Transactions of the ASME®

Journal of Heat Transfer

Published Quarterly by The American Society of Mechanical Engineers

VOLUME 122 • NUMBER 1 • FEBRUARY 2000

TECHNICAL PAPERS

Analytical and Experimental Techniques

Properties and Property Measurements

Conduction Heat Transfer

Natural and Mixed Convection

Boiling and Condensation

(Contents continued on inside back cover)

This journal is printed on acid-free paper, which exceeds the ANSI Z39.48-1992 specification for permanence of paper and library materials. ∞™
♲ 85% recycled content, including 10% post-consumer fibers.

HEAT TRANSFER DIVISION
Chair, **R. A. NELSON**
Vice Chair, **L. C. WITTE**
Past Chair, **W. F. FIVELAND**
Secretary, **Y. BAYAZITOGLU**
Treasurer, **Y. JALURIA**
Technical Editor, **J. R. HOWELL (2000)**

Associate Technical Editors,
C. T. AVEDISIAN (2002)
P. S. AYYASWAMY (2000)
C. BECKERMANN (2001)
F.-B. CHEUNG (2002)
T. Y. CHU (2002)
B. T. F. CHUNG (2001)
R. W. DOUGLASS (2000)
J. P. GORE (2002)
J.-C. HAN (2000)
M. HUNT (2002)
Y. JALURIA (2000)
D. A. KAMINSKI (2001)
R. L. MAHAJAN (2001)
A. MAJUMDAR (2001)
M. P. MENGUC (2000)
M. F. MODEST (2000)
D. POULIKAKOS (2002)
S. S. SADHAL (2002)
D. A. ZUMBRUNNEN (2001)

BOARD ON COMMUNICATIONS
Chairman and Vice President
R. K. SHAH

OFFICERS OF THE ASME
President, **R. E. NICKELL**
Executive Director,
D. L. BELDEN
Treasurer,
J. A. MASON

PUBLISHING STAFF
Managing Director, Engineering
CHARLES W. BEARDSLEY

Director, Technical Publishing
PHILIP DI VIETRO

Managing Editor, Technical Publishing
CYNTHIA B. CLARK

Managing Editor, Transactions
CORNELIA MONAHAN

Production Coordinator
JUDITH SIERANT

Production Assistant
MARISOL ANDINO

Transactions of the ASME, Journal of Heat Transfer (ISSN 0222-1481) is published quarterly (Feb., May, Aug., Nov.) for $240.00 per year by The American Society of Mechanical Engineers, Three Park Avenue, New York, NY 10016. Periodicals postage paid at New York, NY and additional mailing offices. POSTMASTER: Send address changes to Transactions of the ASME, Journal of Heat Transfer, c/o THE AMERICAN SOCIETY OF MECHANICAL ENGINEERS, 22 Law Drive, Box 2300, Fairfield, NJ 07007-2300. **CHANGES OF ADDRESS** must be received at Society headquarters seven weeks before they are to be effective. Please send old label and new address. **PRICES:** To members, $40.00, annually: to nonmembers, $240.00. Add $40.00 for postage to countries outside the United States and Canada. **STATEMENT from By-Laws.** The Society shall not be responsible for statements or opinions advanced in papers or ... printed in its publications (B7.1, Para. 3), **COPYRIGHT © 2000** by The American Society of Mechanical Engineers. Authorization to photocopy material for internal or personal use under circumstances not falling within the fair use provisions of the Copyright Act is granted by ASME to libraries and other users registered with the Copyright Clearance Center (CCC) Transactional Reporting Service provided that the base fee of $3.00 per article is paid directly to CCC, 222 Rosewood Drive, Danvers, MA 01923. Request for special permission or bulk copying should be addressed to Reprints/Permission Department. **INDEXED** by Applied Mechanics Reviews and Engineering Information, Inc. Canadian Goods & Services Tax Registration #126148048.

Downloaded 04 Feb 2011 to 194.85.80.107. Redistribution subject to ASME license or copyright; see http://www.asme.org/terms/Terms_Use.cfm

(Contents continued)

Combustion

Phase Change and Multiphase Heat Transfer

Microscale Heat Transfer

Porous Media, Particles, and Droplets

Heat Transfer Enhancement

Heat Transfer in Manufacturing

TECHNICAL NOTES

(Contents continued on facing page)

(**Contents continued**)

Journal of Heat Transfer **Volume 122, Number 1** **FEBRUARY 2000**

ANNOUNCEMENTS AND SPECIAL NOTES

Journal of Heat Transfer

Editorial

The Millennial Issue of JHT

This issue of the *Journal of Heat Transfer*, Number 1 of Volume 122 for February, 2000, marks the first issue of the year, and celebrates the new millennium as well.

The field of heat transfer is undergoing rapid and remarkable changes, and the Journal is working to report on the research that reflects these changes and also to respond to the changing publication needs of the heat transfer community. This year, JHT will make its debut on the web, complete with the ability to hyperlink to references in each paper.

From discussions with the editors of other journals in the field, it is obvious that research continues in the traditional core areas of conduction, convection, and radiation heat transfer. Much contemporary research is driven by the heat transfer applications, problems and opportunities that arise in diverse fields, from microelectronic cooling through biotechnology to manufacturing processes. These applications have opened new research areas for heat transfer at the nano- and microscale, in biological systems, in beamed energy/material interactions, in nonequilibrium processes, and a host of others. In addition, experimental capability that allows measurement of full-field transient temperature and velocity distributions has opened a new understanding of phenomena that could only be sampled locally and slowly using earlier techniques. The measurement scale has also greatly expanded. From the use of satellite imagery down to the atomic force microscope, heat transfer and energy effects can now be measured and understood across decades of length scale. Time scales that characterize heat transfer phenomena are equally broad, from femtosecond pulsed lasers to geological changes. Further, increases in computational ability change the ways we think about analysis and experimentation, and that capability will surely continue to balloon.

After decades of promise without performance, the tools and capability are now available to bring the computer into the classroom and make it an integral part of the learning process. This capability is causing all of us to rethink our teaching methods, and creativity in this field will certainly change how and whether textbooks are written and marketed and how we gather and transmit both the wealth of historical information in the field and the results of contemporary research.

Future applications in fields that cannot presently be foreseen will involve heat transfer problems, and at the same time new developments in fundamental heat transfer research will drive novel applications and products.

The future of the field of heat transfer really seems to be limitless.

Are there problems? Yes, and a major contemporary one that impacts this and other heat transfer journals is that researchers often choose to report their application-driven results in journals and other channels that are in the field of application, rather than in the core-discipline journals such as JHT. Thus, much useful heat transfer information is dissipated in application journals not generally referred to by our community. Perhaps our increasing ability to search information resources will make this a transitory problem.

There are certainly other challenges and opportunities that we will face. The discipline of heat transfer did not really exist until well into the final century of the previous millennium. It would take a bold person indeed to forecast what the field will be like at the end of the present one. However, we did ask the community to give their ideas of where the field might be going as we enter the next millennium, and the responses from a cross section of members of the heat transfer community follow this editorial.

I hope that at the beginning of the third millennium, an intrepid historian of heat transfer will look at the predictions and comments from our members, and either marvel at our prescience or have a good laugh.

Jack Howell
Technical Editor

A Photothermal Technique for the Determination of the Thermal Conductance of Interfaces and Cracks

K. R. McDonald

J. R. Dryden[1]

A. Majumdar[2]

F. W. Zok
e-mail: zok@engineering.ucsb.edu

Materials Department,
University of California,
Santa Barbara, CA 93106

The paper describes a phase-sensitive photothermal technique for the determination of the thermal conductance of an interface, a thin interlayer, or crack embedded within a plate. The technique involves sinusoidally modulated heating at one point on the surface using a focused laser beam and measurement of the phase shift of the thermal wave at some other point. The technique is demonstrated using a model system comprising two stainless steel disks, placed either in direct contact with each other or with thin polyethylene sheets between them. The use of the technique for determining the conductance of delamination cracks in fiber-reinforced ceramic matrix composite is also demonstrated. [S0022-1481(00)02801-2]

Keywords: Contact Resistance, Heat Transfer, Measurement Techniques, Periodic

1 Introduction

The present article describes a photothermal technique for the determination of the thermal conductance of an interface or thin interlayer embedded within a plate. The technique is based on periodic heating at a point on one surface, using, for example, a focused laser beam, and measurement of the phase lag of the thermal wave at some other point. In the absence of an interface, the technique can be used to determine the thermal diffusivity of the material. The relevant theoretical analysis is presented in a recent paper by Ohsone et al. [1]. The work is motivated by concurrent studies on the thermal conductance of both delamination cracks in fiber-reinforced ceramic matrix composites and interfaces in multilayered structures for electronics packaging.

Photothermal techniques have been used extensively to study the thermal properties of materials ([2–14]). The techniques have been used also as nondestructive tools for detecting subsurface defects ([13,15–20]). The focus of the present work is on one specific subgroup of these techniques, notably, that based upon periodic heating and phase lag measurement. The present technique provides quantitative information about the thermal conductance of interfaces. This information is crucial for thermomechanical analysis and failure prediction.

In the past, thermal contact conductances have been measured predominantly by DC techniques ([21–24]). These techniques require a heat flux, q, to flow through the interface as well as through the bulk of the two contacting solids. The temperature distribution in the bulk solid is measured and extrapolated to the interface to estimate the interfacial temperature jump, ΔT_i. The contact conductance is then estimated by the relation, $h = q/\Delta T_i$. Although this technique is widely used, it suffers from several drawbacks. First, the heat flux must be constant over the bulk of both contacting solids which requires insulation material to be placed around the specimen. Second, it requires a cooling unit to remove the heat from the system; otherwise, the temperature of the sample increases monotonically with time. Finally, since the temperature distribution needs to be measured in the bulk, the samples must be sufficiently thick for at least three thermocouples to be inserted. Consequently, the technique is not easily adapted for measurement in thin and small specimens or structures.

The AC technique described in the present paper has the advantage over the DC techniques that it does not require insulation of the system from the surroundings nor of a cooling unit to extract heat. Moreover, it can be performed relatively quickly on both large and small specimens. The technique is demonstrated using two materials systems:(i) a model system comprising two stainless steel disks, placed either in direct contact with each other or with thin polyethylene sheets between them, and (ii) a unidirectional fiber-reinforced ceramic matrix composite containing a delamination crack along the specimen midplane. A discussion of the sources of error is presented in Ohsone et al. [1].

2 Experimental Techniques and Materials

Measurements of thermal diffusivity and conductance were made using the apparatus shown schematically in Fig. 1. The apparatus consists of a 0.5 W diode laser, mounted on a *x-y-z* translation stage with a precision of ~10 μm, and modulated with a lock-in amplifier. Temperatures were measured using Type T thermocouples with a bead size of ~200 μm. The thermocouples were affixed to the surfaces using epoxy. The phase lag ϕ at the thermocouple location was obtained by comparing the laser input signal with the thermocouple signal using the lock-in amplifier.

To mitigate the effects of the thermal resistance of the thermocouple and the surrounding epoxy, all measurements and subsequent analyses were based on the *differences* of phase lags relative to a reference measurement. For instance, in determining the thermal diffusivity, a series of measurements was made along the top (heated) surface at several locations away from the laser spot (shown by the inset in Fig. 3). The measurements were subsequently compared with the one made at the location nearest to the laser spot, yielding a phase lag difference, $\Delta\phi(\Delta r)$, where Δr is the difference in the distance from the reference point. It is subsequently demonstrated that this measurement approach coupled with the appropriate heat flow analysis yields accurate values of thermal diffusivity. In cases where the crack or interface conductance was to be determined, phase lag measurements were made on the surface opposite to the one being heated, normal to the

---

[1] On sabbatical leave from the Department of Mechanical and Materials Engineering, University of Western Ontario, London, ON N6A 5B9, Canada.

[2] Currently at the Department of Mechanical Engineering, University of California, Berkeley, CA 94720.

Contributed by the Heat Transfer Division for publication in the JOURNAL OF HEAT TRANSFER. Manuscript received by the Heat Transfer Division, Dec. 9, 1998; revision received, Oct. 13, 1999. Associate Technical Editor: M. F. Modest.

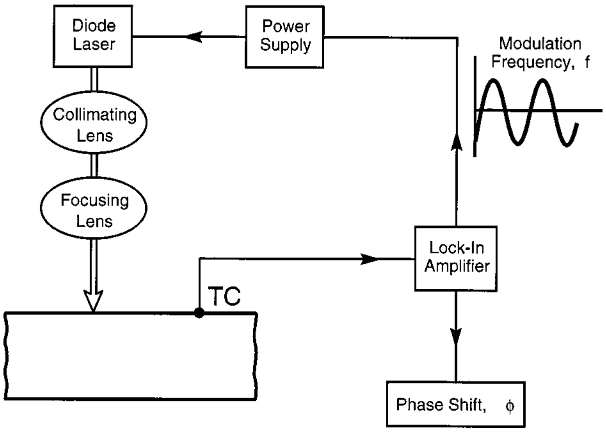

Fig. 1 Schematic of the experimental technique

interface or crack. The corresponding reference measurement was that made on an equivalent specimen in the absence of the interface or crack.

2.1 Interface Conductance in a Model Steel System. The effects of interfaces were studied using a series of model systems comprising two circular stainless steel disks with known thermal properties[3] (Table 1), each ground and polished to a final thickness of 1.25 mm and a diameter of 34 mm. The disks were polished to produce a unidirectional lay. The RMS value of surface roughness, measured orthogonal to the polishing direction using a Sloan Dektak II profilometer, was 0.42 μm. As a check on the current technique, measurements were first made on the steel disks alone and the measurements used to confirm the reported thermal diffusivity, α. The latter measurements were made at frequencies, f, ranging from ~0.05–2.6 Hz, and at three distances from the thermocouple location: $r = 1.5$, 2.0, and 2.5 mm.

Various types of ''interfaces'' were produced between the two steel disks. The first was obtained by simply clamping together the disks with two binder clips, with the polishing directions of the two surfaces oriented perpendicular to one another. The force associated with the clips was measured to be ≈50 N and the calculated average pressure was 0.015 MPa. The laser was focused on the top surface, directly above the thermocouple. Phase lag measurements were made over the frequency range 0.05 to 1 Hz. For comparison, a parallel series of measurements at the same frequencies was made on the pristine sample with the same total thickness (2.5 mm). The differences in phase lags in the two specimens at each frequency were used to determine the interface conductance. In order to study the effects of interlayers, thin sheets of a commercial linear low density polyethylene (LLDPE), ~13-μm thick, were placed between the steel disks, the disks clamped together and the phase lag measurements repeated. Specimens containing 1, 2, and 4 polyethylene sheets were characterized.

To increase the absorption of the incident laser beam, the samples were coated with a sputtered carbon layer that was less than 0.1 μm in thickness. Assuming that the carbon layer is amorphous, a conservative lower-limit estimate for the thermal diffusivity is on the order of 10^{-6} m^2/s. Hence, the upper limit for the phase difference due to the bulk of the carbon layer is about 0.2 mrad at a frequency of 1 Hz. This is negligible compared to the phase difference measured for the bulk samples. The interface between the carbon layer and the underlying sample could also pose a thermal resistance. However, since the interface is chemically bonded, it is expected that this resistance would be much lower than that of the bulk sample studied in this paper.

Table 1 Thermal properties of the stainless steel and the LLDPE

Material	Volumetric Heat Capacity, c (J/m^3 K)	Thermal Conductivity, k (W/mK)	Thermal Diffusivity, α (m^2/s)
Stainless Steel	3.8×10^6 [29,30]	14.3 [29]	3.8×10^{-6}*
LLDPE	2.1×10^6 [31]	0.33 [31]	1.6×10^{-7}*

*Calculated from the other data, using $\alpha = k/c$.

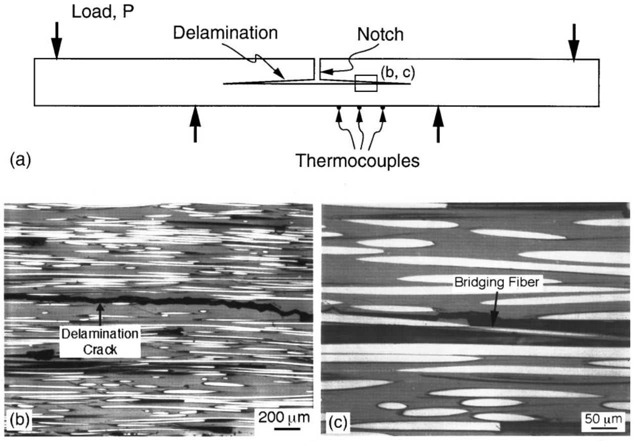

Fig. 2 (*a*) Schematic of the specimen and loading geometry used to cause delamination of the Nicalon/MAS composite specimen and subsequently determine the crack conductance; (*b*) optical micrograph of a typical delamination crack; (*c*) higher magnification view of the crack showing bridging by an inclined fiber

2.2 Thermal Conductance of Delamination Cracks in Ceramic Composites. Experiments were also performed on a unidirectional composite comprising 37 percent Nicalon™ fibers in a matrix of a magnesium aluminosilicate (MAS) glass ceramic. A delamination crack was produced by notching a long rectangular specimen at the center transverse to the fibers, and subsequently loading the specimen in four-point bending. The specimen and loading geometries are shown schematically in Fig. 2(*a*). Thermocouples were attached at several locations on the bottom side of the specimen. Upon loading, delamination cracks initiated from the notch and propagated along the specimen length. One such crack is shown in Figs. 2(*b*) and (*c*). A notable feature in (*c*) is the presence of an inclined fiber spanning the crack faces.

The thermal conductance of the crack at various locations was determined through a series of phase lag measurements across the specimen thickness (directly over the thermocouples) both before and after delamination. In addition, the opening displacement of the delamination crack at the location of measurement was obtained by replicating the side surface of the specimen using cellulose acetate tape and subsequently examining the replicas in an optical microscope. All phase lag measurements and surface replicas were taken under load.

3 Experimental Results and Analysis

3.1 Model Steel System. The experimental measurements for the pristine steel specimen (without interfaces) are plotted in Fig. 3. The results are presented in the form of phase lag *differences*, $\Delta\phi$, obtained at two locations, separated by a distance Δr. Also shown on the figure are the calculated curves, using the analysis presented in Ohsone et al. [1] and the reported thermal

---

[3] Obtained from the NIST Standard Reference Materials Program.

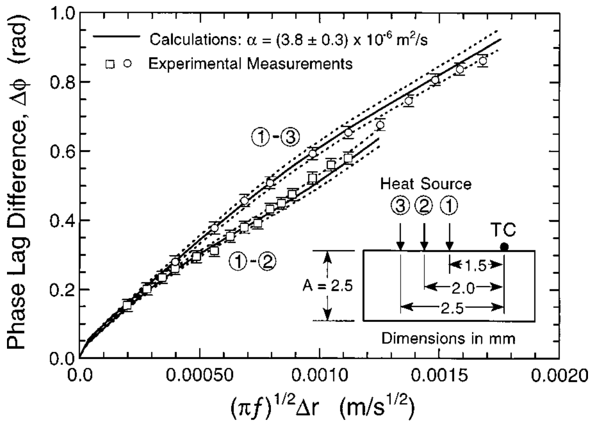

Fig. 3 Phase lag measurements made on pristine steel specimen and the corresponding calculations from the analysis presented in Ohsone et al. [1]. The error bars represent the maximum uncertainty in $\Delta\phi$, (0.017 rad), based on many repeat measurements under the same test conditions. The solid curves were calculated using the reported thermal diffusivity of the steel alloy, whereas the dotted curves represent calculations for thermal diffusivities that are either eight percent higher or lower than the reported value.

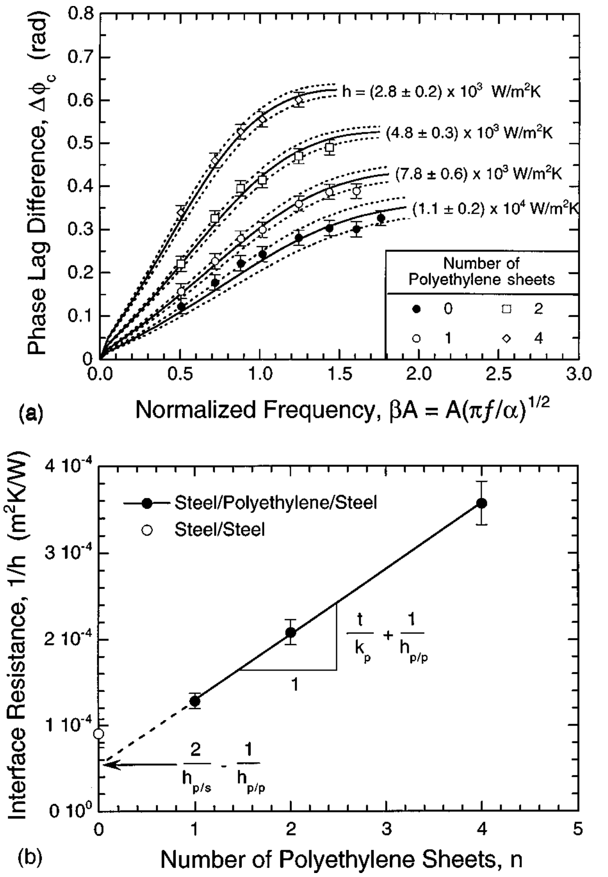

Fig. 4 Experimental data and calculated curves for the stainless steel sandwich specimens, showing the effects of the polyethylene sheets on (*a*) the phase lag, $\Delta\phi_i$, associated with the interface itself, and (*b*) the interface conductance. The error bars in (*b*) represent the range of conductances needed to encompass the experimental data in (*a*). The solid line in (*b*) is a least-squares fit of the data for $n=1$, 2, and 4.

diffusivity of the alloy ($\alpha=3.8\times10^{-6}$ m²/s). Excellent correlations are obtained between the calculated curves and the experimental measurements, providing validation of the test technique and the underlying assumptions in the analysis.

Figure 4(*a*) shows the results for the specimens containing an interface along the midplane. The results are presented in terms of the phase lag difference, $\Delta\phi_i$, associated with the interface. Also shown are the calculated curves that give the best fit to the data for each type of interface along with the corresponding values of the thermal conductance, h. The trends in the calculated phase lag with frequency for a fixed interface conductance closely follow the ones obtained experimentally. This self-consistency provides confidence in both the theoretical results and the measurement technique. The variation in the effective interface resistance, $1/h$, with the number of polyethylene sheets is plotted in Fig. 4(*b*). The trend is linear (with the exception of the point at $n=0$, corresponding to the contact between the two steel disks), and can be rationalized in the following way.

The effective thermal resistance of the interfacial region in the presence of the polyethylene sheets can be partitioned into three components:

$$\frac{1}{h}=\frac{2}{h_{p/s}}+\frac{n-1}{h_{p/p}}+\frac{nt_p}{k_p} \tag{1}$$

where n is the number of sheets. The first term represents the resistance associated with the two interfaces between the polyethylene and the stainless steel, each with a conductance $h_{p/s}$; the second is the resistance of the polyethylene/polyethylene interfaces, with each interface having a conductance $h_{p/p}$; and the third is the resistance of the polyethylene itself, with t_p being the thickness of one sheet and k_p the thermal conductivity of the polyethylene. For the purpose of comparing this model with the data in Fig. 4(*b*), Eq. (1) is rewritten as

$$\frac{1}{h}=\left[\frac{2}{h_{p/s}}-\frac{1}{h_{p/p}}\right]+n\left[\frac{t_p}{k_p}+\frac{1}{h_{p/p}}\right]. \tag{2}$$

The resistance is predicted to increase linearly with n, which agrees well with the measured trend. Upon performing a linear regression analysis of the data and using the reported value for k_p (Table 1) along with Eq. (2), the relevant conductances were determined to be $h_{p/p}=3.0\times10^4$ W/m² K and $h_{p/s}=2.1\times10^4$ W/m² K. By comparison, the measured conductance of the steel/steel interface is $h_{s/s}=1.1\times10^4$ W/m² K.

The ranking of the three conductance values can be further rationalized on the basis of surface roughnesses and the elastic/plastic properties of the constituent phases. Notably, because of the roughness of the stainless steel disks and the high modulus and strength of the steel, the interface conductance $h_{s/s}$ is expected to be the lowest of the three. The polyethylene has extremely low modulus and yield stress and will readily deform locally upon contact with the steel, yielding a more conductive interface ($h_{p/s}>h_{s/s}$). Indeed, the measured values yield a ratio $h_{p/s}/h_{s/s}\approx2$. Moreover, because of the smooth surfaces of the polyethylene sheets, the thermal contact between the polyethylene sheets is expected to be better yet. This, too, is in agreement with the experiments ($h_{p/p}/h_{p/s}\approx1.5$).

At the most rudimentary level, the absolute value of the conductance of the steel/steel contact can be rationalized on the basis of the surface roughness, assuming that heat flow occurs by conduction through the air gap between the two surfaces. (The latter assumption can be justified on the basis of the very low pressures used in clamping the two disks together and thus the low area fraction of contacting asperities.) Thus the interface conductance is predicted to be

$$h\approx k_a/\delta \tag{3}$$

where k_a is the thermal conductivity of air at ambient temperature (0.024 W/mK) and δ is the effective separation between the surfaces. In general, δ depends on the roughness characteristics of the two surfaces, the contact pressure, and the hardness of the material ([21,25,26,27,28,24]). For surfaces with unidirectional lay in two perpendicular directions and for low contact pressures, δ is expected to lie in the range of two to four times the RMS surface roughness measured perpendicular to the direction of the lay. The resulting predicted conductance falls in the range 1.4×10^4 to $2.9\times10^4\ \mathrm{W/m^2\,K}$. The measured value, $1.1\times10^4\ \mathrm{W/m^2\,K}$, falls towards the low end of the predicted range. In light of the approximate nature of the model, the correlation between the model prediction and the experimental measurement is considered to be adequate.

3.2 Thermal Conductance of a Delamination Crack. The results of three sets of measurements on the cracked composite specimen are presented in Fig. 5(*a*). Each corresponds to a different local crack-opening displacement, as indicated on the figure. Clearly the phase lag associated with the delamination crack increases with increasing crack-opening displacement. Also shown on Fig. 5(*a*) are the corresponding calculated curves using crack conductance values that yield the best fits to the experimental curves. In all cases, the shapes of the predicted curves are in good agreement with the measured ones.

The values of the inferred crack conductances are plotted against crack-opening displacement in Fig. 5(*b*). Also shown are the predictions based on the assumption that the crack conductance is dictated by the air gap between the two crack surfaces, given by Eq. (3). The latter prediction underestimates the measured conductance at small crack-opening displacements. However, the two appear to converge at larger crack-opening displacements. The discrepancy can be attributed to the presence of bridging fibers of the type shown in Fig. 2(*c*), which must contribute to the crack conductance. Such bridging is expected to diminish with increasing crack opening because of failure of the bridging fibers. Indeed, once all the bridging fibers have failed, the crack conductance will be dictated by air conduction alone. This trend is in broad agreement with the experimental measurements. Studies are in progress to probe in more detail the contributions to thermal conductance from fiber bridging.

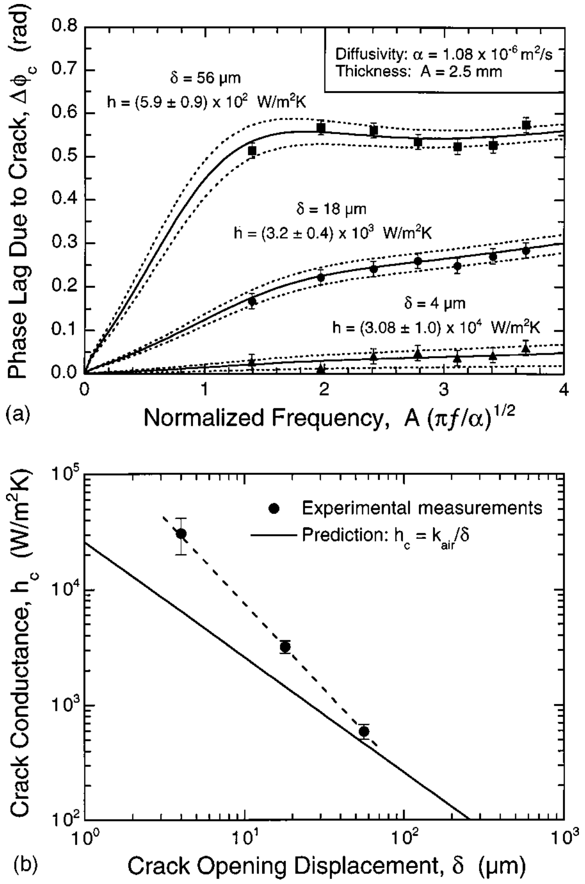

Fig. 5 Experimental data and calculated curves for the Nicalon/MAS composite specimens showing the effects of crack opening displacement on (*a*) the additional phase lag, $\Delta\phi_c$, and (*b*) the crack conductance. The error bars in (*b*) represent the range of conductances needed to encompass the experimental data in (*a*).

4 Concluding Remarks

The present technique of periodic heating and phase lag measurement provides a relatively simple and quick determination of both the thermal diffusivity of solids and the thermal conductance of embedded interfaces, interlayers, and cracks. Temperature measurements can be made using standard thermocouples. The effects of the thermal resistance of the thermocouples are mitigated by using the differences in phase lag measurements relative to an appropriate reference state. In this way, the phase lag associated with the thermocouples is removed and the measurements then become a function only of the thermal properties of the system. The use of thermocouples is restricted to the low-frequency regime, commensurate with the time constant associated with the thermocouple response. For time constants typical of most thermocouples (~10 ms), measurements can be made accurately in the frequency range used in the present experiments, i.e., $f < 3$ Hz. At higher frequencies, alternate techniques for temperature measurement would be needed, such as the reflectance technique described by Ohsone et al. [1].

Acknowledgments

Funding for this work was provided by ONR Contract No. N00014-97-1-0394 along with ARPA AASERT award (Contract No. DAAH04-94-G-0374).

References

[1] Ohsone, Y., Wu, G., Dryden, J. R., Zok, F. W., and Majumdar, A., 1999, ''Optical Measurement of Thermal Contact Conductance Between Wafer-Like Thin Solid Samples,'' ASME J. Heat Transfer, in press.

[2] Hirschman, A., Dennis, J., Derksen, W., and Monahan, T., 1961, ''An Optical Method for Measuring the Thermal Diffusivity of Solids,'' *International Developments in Heat Transfer*, Part IV, ASME, New York, pp. 863–869.

[3] Rosencwaig, A., and Gersho, A., 1976, ''Theory of the Photoacoustic Effect With Solids,'' J. Appl. Phys., **47**, No. 1, pp. 64–69.

[4] Rosencwaig, A., 1978, ''Theoretical Aspects of Photoacoustic Spectroscopy,'' J. Appl. Phys., **49**, No. 5, pp. 2905–2910.

[5] Maglic, K. D., Cezairliyan, A., and Peletsky, V. E., 1984, *Compendium of Thermophysical Property Measurement Methods, Volume 1 Survey of Measurement Techniques*, Plenum, New York, pp. 299–456.

[6] Pessoa, O., Jr., Cesar, C. L., Patel, N. A., Vargas, H., Ghizoni, C. C., and Miranda, L. C. M., 1986, ''Two-Beam Photoacoustic Phase Measurement of the Thermal Diffusivity of Solids,'' J. Appl. Phys., **59**, No. 4, pp. 1316–1318.

[7] Reichling, M., and Gronbeck, H., 1994, ''Harmonic Heat Flow in Isotropic Layered Systems and Its use for Thin Film Thermal Conductivity Measurements,'' J. Appl. Phys., **75**, No. 4, pp. 1914–1922.

[8] Kemp, T., Srinivas, T. A. S., Fettig, R., and Ruppel, W., 1995, ''Measurement of Thermal Diffusivity of Thin Films and Foils Using a Laser Scanning Microscope,'' Rev. Sci. Instrum., **66**, No. 1, pp. 176–181.

[9] Fabbri, L., and Fenici, P., 1995, ''Three-Dimensional Photothermal Radiometry for the Determination of Thermal Diffusivity of Solids,'' Rev. Sci. Instrum., **66**, No. 6, pp. 3593–3600.

[10] DeVecchio, D., Russel, D., and Taborek, P., 1995, ''Measurement of Thermal Diffusivity of Small, High Conductivity Samples Using a Phase Sensitive Technique,'' Rev. Sci. Instrum., **66**, No. 6, pp. 3601–3605.

[11] Preston, S. D., 1995–1996, ''A Review of Techniques for Measuring the Thermal Diffusivity of Thin Films and Coatings,'' High Temp.-High Press., **27–28**, pp. 111–134.

[12] Yu, X. Y., Zhang, L., and Chen, G., 1996, ''Thermal-Wave Measurement of Thin-Film Thermal Diffusivity With Different Laser Beam Configurations,'' Rev. Sci. Instrum., **67**, No. 6, pp. 2312–2316.

[13] Almond, D. P., and Patel, P. M., 1996, *Photothermal Science and Techniques*, Chapman & Hall, London.

[14] Haji-Sheikh, A., Hong, Y. S., You, S. M., and Beck, J. V., 1998, ''Sensitivity Analysis for Thermophysical Property Measurements Using the Periodic Method,'' ASME J. Heat Transfer, **120**, pp. 568–576.

[15] Opsal, J., and Rosencwaig, A., 1982, ''Thermal-Wave Depth Profiling: Theory,'' J. Appl. Phys., **53**, No. 6, pp. 4240–4241.

[16] Monchalin, J. P., Parpal, J. L., Bertrand, L., and Gagne, J. M., 1981, ''Thermal Contact Probing by the Photoacoustic Effect,'' Appl. Phys. Lett., **39**, No. 1, pp. 391–393.

[17] Kuo, P. K., Favro, L. D., Inglehart, L. J., Thomas, R. L., and Srinivasan, M., 1982, ''Photoacoustic Phase Signatures of Closed Cracks,'' J. Appl. Phys., **53**, No. 2, pp. 1258–1260.

[18] Grice, K. R., Inglehart, L. J., Favro, L. D., Kuo, P. K., and Thomas, R. L., 1983, ''Thermal Wave Imaging of Closed Cracks in Opaque Solids,'' J. Appl. Phys., **54**, No. 11, pp. 6245–6255.

[19] Yonushonis, T. M., Stafford, R. J., Ahmed, T., Favro, L. D., Kuo, P. K., and Thomas, R. L., 1992, ''Infrared Thermal Wave Imaging of Thermal Barrier Coatings for Diesel Applications,'' Am. Ceram. Soc. Bull., **71**, No. 8, pp. 1191–1202.

[20] Favro, L. D., Kuo, P. K., Thomas, R. L., and Shepard, S. M., 1993, ''Thermal Wave Imaging for Aging Aircraft Inspection,'' Mater. Eval., **51**, No. 12, pp. 1386–1389.

[21] Cooper, M. G., Mikic, B. B., and Yanovich, M. M., 1969, ''Thermal Contact Conductance,'' Int. J. Heat Mass Transf., **12**, pp. 279–300.

[22] Fletcher, L. S., 1988, ''Recent Developments on Contact Conductance Heat Transfer,'' ASME J. Heat Transfer, **110**, pp. 1059–1070.

[23] Madhusudana, C. V., and Fletcher, L. S., 1983, ''Solid Spot Thermal Conductance of Zircaloy-2/Uranium Dioxide Interfaces,'' Nucl. Sci. Eng., **83**, pp. 327–332.

[24] Williamson, M., and Majumdar, A., 1992, ''Effect of Surface Deformations on Contact Conductance,'' ASME J. Heat Transfer, **114**, pp. 802–810.

[25] Jeevanashankara, Madhusudana, C. V., and Kulkarni, M. B., 1990, ''Thermal Contact Conductance of Metallic Contacts at Low Loads,'' Appl. Energy, **35**, pp. 151–164.

[26] McWaid, T., and Marschall, E., 1992, ''Thermal Contact Resistance Across Pressed Metal Contacts in a Vacuum Environment,'' Int. J. Heat Mass Transf., **35**, No. 11, pp. 2911–2920.

[27] Song, S., Yovanovich, M. M., and Goodman, F. O., 1993, ''Thermal Gap Conductance of Conforming Surfaces in Contact,'' ASME J. Heat Transfer, **115**, pp. 533–540.

[28] Thomas, T. R., and Probert, S. D., 1966, ''Thermal Contact of Solids,'' Chemical and Process Engineering, **47**, pp. 51–60.

[29] Hust, J. G., and Lankford, A. B., 1984, ''Standard Reference Materials 1460, 1461 and 1462: Austenitic Stainless Steel Thermal Conductivity and Electrical Resistivity as a Function of Temperature From 2 to 1200 K,'' National Bureau of Standards Certificate.

[30] Campbell, R., 1998, personal communication, Holometrix, Inc., Beford, MA.

[31] Crawford, R. J., 1987, *Plastics Engineering*, 2nd Ed., Pergamon Press, Oxford, UK, p. 33.

S. Bhattacharjee
e-mail: subrata@voyager5.sdsu.edu

M. King
e-mail: king@rohan.sdsu.edu

W. Cobb
e-mail: cobb@rohan.sdsu.edu

Department of Mechanical Engineering,
San Diego State University,
San Diego, CA 92182

R. A. Altenkirch
Department of Mechanical Engineering and
NSF Engineering Research Center for
Computational Field Simulation,
Mississippi State University,
Mississippi State, MS 39762
e-mail: altenkirch@research.msstate.edu

K. Wakai
Department of Mechanical Engineering,
Gifu University,
Japan
e-mail: wakai@cc.gifu-u.ac.jp

Approximate Two-Color Emission Pyrometry

Approximate methods for the determination of a temperature field using pure emission pyrometry applied to a two-dimensional nonoptically thin flame without variation along a line of sight are presented. In the absence of an absorption measurement, emission pyrometry depends on theoretical spectral information. Limitations of existing techniques stem from the fact that spectral information is a function of temperature only for the optically thin situation, by and large the situation to which current techniques apply, and temperatures above 1000 K. Through extensive narrow-band calculation using a simulated flame over polymethylmethacrylate, we show that the spectral information contained in the equivalent bandwidth ratio is approximately a constant for the 2.8 μm/1.8 μm band pair and appropriate bandwidths. The constant can be evaluated from emission measurements at a point where the temperature is known or can be estimated using, e.g., the maximum flame temperature of a simulated flame and the peak band intensities. The temperature field evaluated with this approximately constant value of the equivalent bandwidth ratio, A_r, is accurate to within five percent for temperatures down to 450 K. [S0022-1481(00)02601-3]

Keywords: Flame, Heat Transfer, Radiation, Temperature

Introduction

Knowledge about temperature and species distribution in a flame is essential for improved design of combustors and for gaining fundamental insight into the combustion process. Numerical simulation, capable of predicting the field variables, still requires extensive validation using experimental data. The experimental approach can be divided into two categories: intrusive probe methods and nonintrusive optical or acoustic methods. The former suffers from a relatively large time response in addition to disturbing the combustion reaction. Optical methods utilize emission ([1]), absorption ([2]) or refraction ([3]) of light by the burnt gases, or laser interaction such as coherent antistokes Raman scattering (CARS) or laser-induced fluorescence (LIF) ([4]), while the acoustic method exploits the transit time of sound ([5]). Most of these methods, however, require radiation sources, which restricts the measurement environment. They are also subject to interference from background radiation.

Emission methods suffer from the fact that without an absorption measurement, theoretical information about the infrared spectra of the radiatively active species is necessary. This spectral information, in general, is a function of temperature and pressure-pathlength of the radiating species. If the optical depth is small, then the spectral information can be shown to depend only on temperature, which has been demonstrated before, e.g., Wakai et al. [6] and Ferriso et al. [7]. The unknown temperature is obtained by iterating between the experimental and theoretical information. Wakai et al. [6] selected two H_2O bands and employed a very small bandwidth to ensure small optical depth. One drawback of ensuring optically thin behavior (through small values of a_λ) is that temperatures lower than 1000 K are difficult to measure as the bands become weaker, and the signal-to-noise ratio is low.

Here we propose a new methodology for obtaining an approximate temperature distribution in a two-dimensional nonoptically thin flame using two-color emission pyrometry. A simulated flame for flame spread over a solid fuel in an opposing flow of oxidizer is used to demonstrate the method. The configuration is that of an experiment aimed at understanding the physics of flame spreading at ‘‘very-low-velocity’’ opposing flows. Such a configuration can only be obtained in microgravity so as to eliminate effectively the influence of buoyancy, and the configuration has implications for spacecraft fire safety, particularly when the spacecraft is experiencing low levels of acceleration ([8,9]).

Simulated Flame

The experimental configuration, which is simulated, is shown in Fig. 1 with regard to infrared imaging. The flame propagates steadily over a 6.35-mm wide, 20-mm thick sample of PMMA flush-mounted on the floor of a square cross-section (10 cm $\times$10 cm) wind tunnel. The opposing flow of the 50 percent O_2/50 percent N_2 (by volume) mixture enters the tunnel with a slug profile at 10 cm/s.

The configuration derives, as mentioned above, from the NASA-supported Diffusion and Radiative Transport in Fire Experiment in which the effects of the radiative environment of a flame spreading in low-velocity flow is investigated ([8,9]). These flames contain, from visual observation and infrared measurements, no soot, and so soot is neglected here. Soot may be included in the technique if desired as attempted by Ferriso et al. [7] for the optically thin situation. The two-dimensional Navier-Stokes equations for species-continuity, x and y-momentum, and energy equations are solved using the SIMPLER algorithm ([10]). Gas-phase combustion is modeled with a single-step, second-order, complete reaction, and fuel pyrolysis with a single-step, first-order, dissociation reaction. Surface and gas-phase radiation including radiation feedback from the gas to the solid surface is modeled with the Global Balance method of ([11]).

Contributed by the Heat Transfer Division for publication in the JOURNAL OF HEAT TRANSFER. Manuscript received by the Heat Transfer Division, Feb. 15, 1999; revision received, Aug. 2, 1999. Associate Technical Editor: J. Gore.

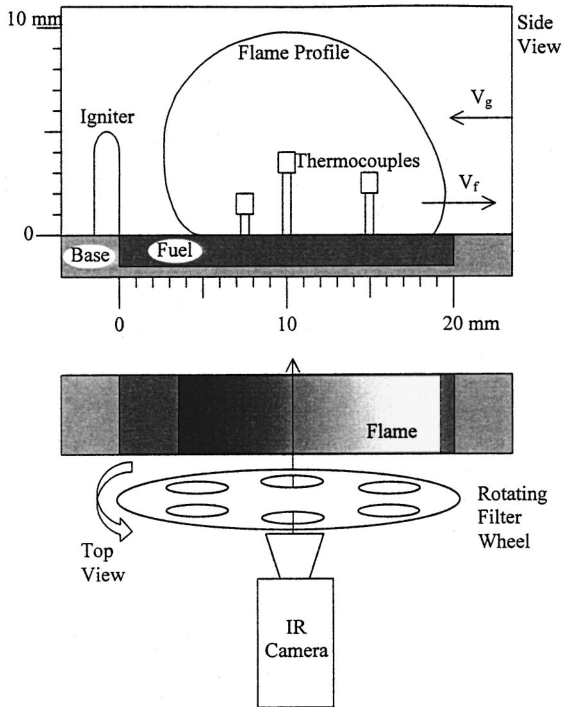

Fig. 1 Schematic of combustion experiment showing: Top, side profile of flame spread experiment with including thermocouples, igniter, fuel bed, and flow characteristics; bottom, top view of flame spread experiment with IR camera and filter wheel arrangement with respect to the flame

The simulated temperature and the partial pressure field for CO_2 are shown in Figs. 2 and 3. For complete combustion of MMA ($C_5H_8O_2$) vapor with the oxidizer, $p_{H_2O}=0.8p_{CO_2}$. Because the temperature and species fields are known, a narrow-band model such as RADCAL ([12,13]) can be used to produce the intensity fields at any wavelength interval (band). Band intensities computed at two such bands, $4.224\,\mu m<\lambda_1<4.33\,\mu m$ and $2.56\,\mu m<\lambda_2<3.02\,\mu m$, are shown in Figs. 4 and 5, respectively. These bands correspond to those of filters used in the experiment mentioned above in conjunction with a PtSi detector video camera (Inframetrics, Inc. Model Infra-Cam PtSi FPZ 256×256 pixel array). They were selected because of filter availability and to ensure sufficient signal for measurement. The simulated fields will be considered the ''data'' for the emission pyrometry method developed here, and the success of the proposed technique will be evaluated by the degree to which it reproduces the simulated temperature field from the simulated intensity fields.

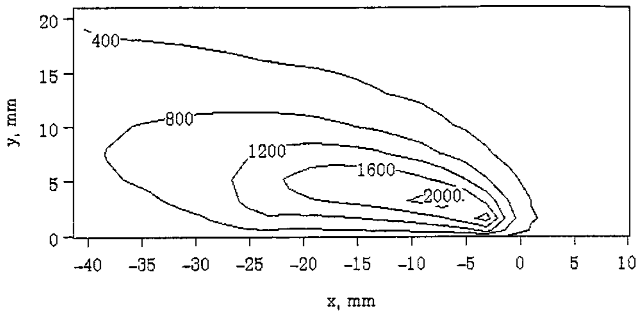

Fig. 2 Simulated flame temperature contours in K (50 percent O_2, $V_g=10$ cm/s)

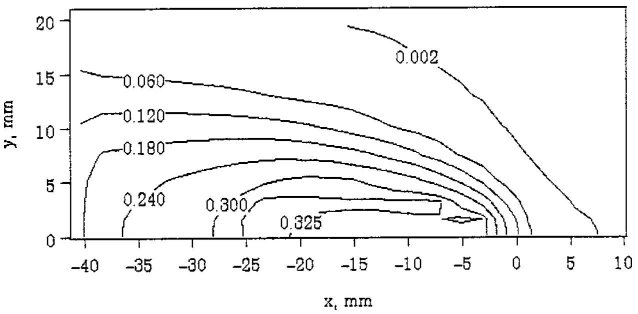

Fig. 3 Simulated partial pressure of CO_2 contours in atm (50 percent O_2, $V_g=10$ cm/s)

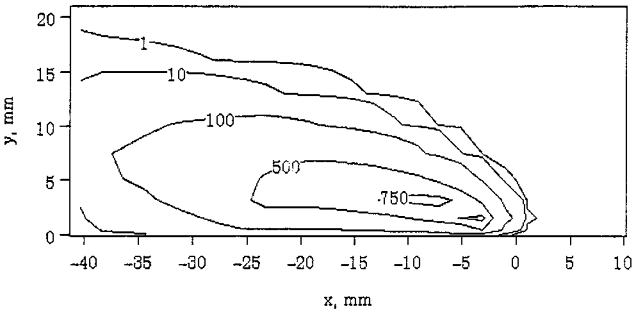

Fig. 4 Simulated band intensity contours for $\Delta\lambda=4.224-4.330$ μm in W/(m^2·Str) (50 percent O_2, $V_g=10$ cm/s)

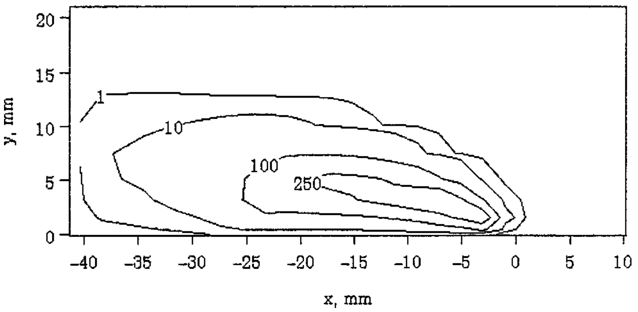

Fig. 5 Simulated band intensity contours for $\Delta\lambda=2.56-3.02$ μm in W/(m^2·Str) (50 percent O_2, $V_g=10$ cm/s)

Hybrid Emission Pyrometry

Two-color pyrometry, when applied to a solid surface, measures signals that are proportional to the intensities $i'_{\lambda1}$ and $i'_{\lambda2}$ emitted at two different wavelengths. If the ratio of the emittance at the two wavelengths, $\varepsilon_{\lambda1}/\varepsilon_{\lambda2}$, is known, the temperature can be obtained from Planck's law.

$$\frac{i'_{\lambda1}}{i'_{\lambda2}}=\frac{\varepsilon_{\lambda1}}{\varepsilon_{\lambda2}}\frac{i'_{\lambda b1}}{i'_{\lambda b2}}=\frac{\varepsilon_{\lambda1}}{\varepsilon_{\lambda2}}P(\lambda_1,\lambda_2,T) \tag{1}$$

When applied to a column of radiating gas at a uniform temperature, small but finite intervals (or bandwidths), $\Delta\lambda_1$ and $\Delta\lambda_2$, at the two bands are used due to practical considerations. The ratio of the band intensities can be expressed in terms of the equivalent bandwidth ratio, referred to here as A_r, and the Planck function as follows:

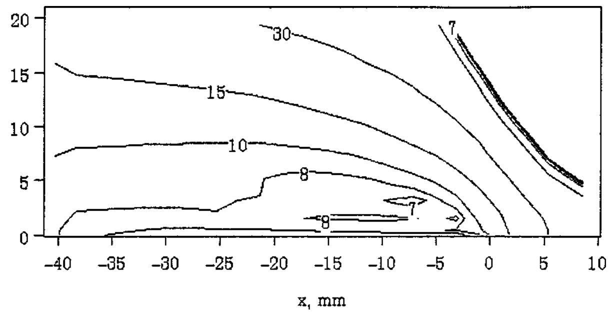

Fig. 6 Simulated equivalent bandwidth ratio, $A_{1.3}/A_{2.8}$, for PMMA in 50 percent O_2, $V_g=10$ cm/s, $lp=2$ cm

$$\frac{i'_1}{i'_2}=\frac{i'_{\lambda b1}}{i'_{\lambda b2}}\frac{A_1}{A_2}=\frac{A_1}{A_2}P(\lambda_1,\lambda_2,T). \tag{2}$$

The A_r can be expressed in terms of more fundamental quantities, namely

$$\frac{A_1}{A_2}=\frac{\int_{\Delta\lambda_1}[1-\exp(-a_\lambda L)]d\lambda}{\int_{\Delta\lambda_2}[1-\exp(-a_\lambda L)]d\lambda} \tag{3}$$

and can be obtained from the spectral structure of the emitting gases. For the simulated flame A_r is computed from the known field variables, T, p_{CO_2}, and p_{H_2O} using the narrow-band model for the two bands used in the computation of intensities. When the computed A_r field, shown in Fig. 6, is used in conjunction with the simulated intensities, the temperature field can be determined from Eq. (2). Because the intensity ratio and the A_r are obtained computationally from the same set of field variables, the temperature obtained from Eq. (2) is identical to the field temperature.

For a real flame, the *i*-ratio is obtained from experiment, while simulation provides the A_r. The accuracy of the resulting hybrid pyrometry depends on the accuracy of simulation and measurements.

Optically Thin Limit

The dependence of a_λ on the species concentration can be factored out as follows:

$$a_\lambda L=a^0_\lambda\frac{\rho}{\rho_0}L=\frac{a^0_\lambda}{R\rho_0}\frac{pL}{T}=a^0_\lambda\left[\frac{(p/p_0)L}{(T/T_0)}\right] \tag{4}$$

where a^0_λ is the spectral absorption coefficient at 1 atm and depends only on temperature. For small values of $a^0_\lambda[(p/p_0)L/(T/T_0)]$, therefore, Eq. (3) simplifies to

$$\frac{A_1}{A_2}=\frac{\int_{\Delta\lambda_1}a^0_\lambda(T)d\lambda}{\int_{\Delta\lambda_2}a^0_\lambda(T)d\lambda}=A_r(T). \tag{5}$$

The A_r now is only a function of temperature and can be determined using any accurate band model without any need for the simulated fields. Once the functional dependence is determined, i.e., $A_r=f(T)$, temperature can be obtained from the *i*-ratio by iterating between $f(T)$ and the Planck function using Eq. (2).

Wakai et al. [6] employed the 1.8 and 2.7 μm bands of H_2O for pyrometric measurement of flame temperature and forced the optically thin limit by utilizing a narrow bandwidth for measurement. The A_r for these two bands and the narrow $\Delta\lambda$'s is shown in Fig. 7 as a function of T for different pressure-pathlengths typical of the configuration considered here. Clearly, the optically thin limit is obtained for all the situations presented, primarily due to the low values of a^0_λ relative to $[(p/p_0)L/(T/T_0)]$. Below 1000 K, the bands are too weak, and the error in the measured value of the *i*-ratio and the calculated value of A_r becomes too high for this method to work ([6]).

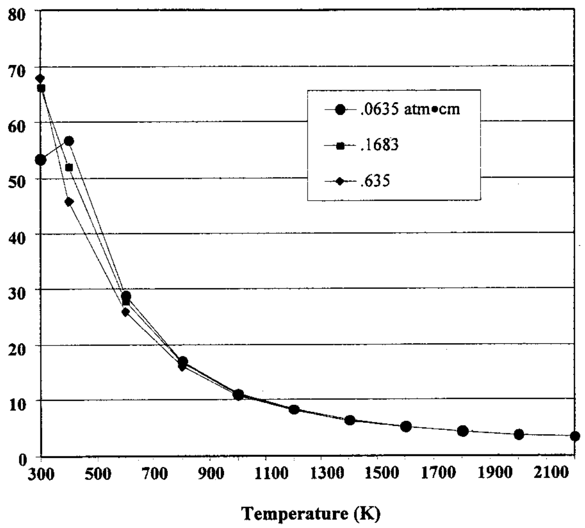

Fig. 7 Narrow-band equivalent bandwidth ratio, $A_{2.8}/A_{1.8}$, over wavelengths ($\Delta\lambda_1=2.474-2.674$, $\Delta\lambda_2=1.86-2.16$ μm) specified by Wakai et al. [6] for a range of pressure-pathlengths

Use of Stronger Bands

The CO_2 bands are considerably stronger than the H_2O bands producing much stronger signal to noise ratios. However, the high relative value of a^0_λ makes it difficult to use the optically thin limit. This is illustrated in Fig. 8, where the A_r for the 4.3 and 2.8 μm bands is evaluated for different values of pL using the wide-band (entire band) model of Edwards and Menard [14] and p. 590, No. 3 in Siegel and Howell [15]. As pL/T decreases, each curve tends towards the optically thin limit as predicted by Eq. (4). Only for $pL<0.003$ atm·cm, a value too small for any practical flame, can the thin approximation be used with these two bands when the entire band is used, which improves the signal to noise ratio over use of narrow-band filtering.

The situation is further complicated by the overlap of the CO_2 band by the H_2O band at 2.8 μm. The A_r computed with the narrow-band model (RADCAL program) using the experimental

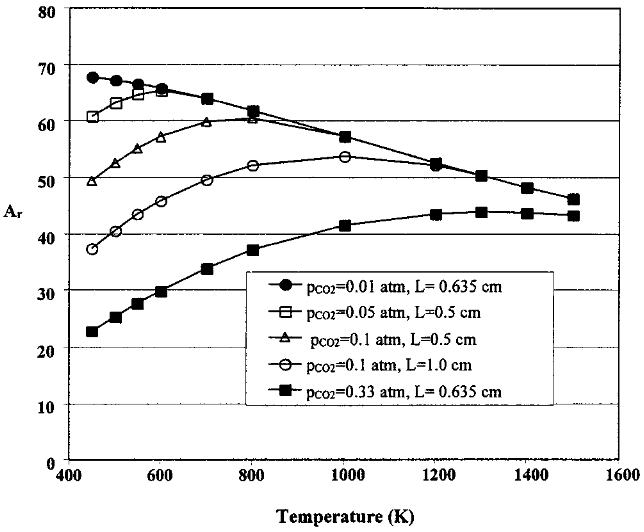

Fig. 8 Wide-band (entire band) model predicted equivalent bandwidth ratio, $A_{4.3}/A_{2.8}$, for CO_2 at various pressure-pathlengths from the maximum simulated pL to that approaching the thin limit

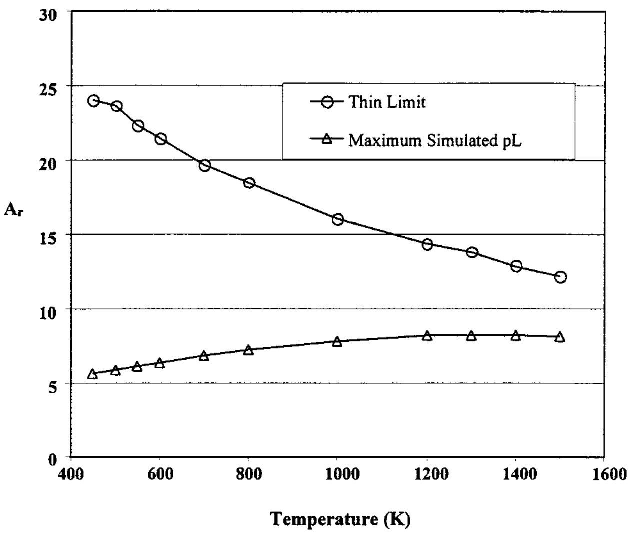

Fig. 9 Narrow-band model ($4.224\,\mu m < \lambda_1 < 4.33\,\mu m$ and $2.56\,\mu m < \lambda_1 < 3.02\,\mu m$) predicted equivalent bandwidth ratio, $A_{4.3}/A_{2.8}$, for CO_2 and H_2O at the maximum simulated pressure-pathlengths and the thin limit

bandwidths of the DARTFire experiment ([9]) of $4.224\,\mu m < \lambda_1 < 4.33\,\mu m$ and $2.56\,\mu m < \lambda_1 < 3.02\,\mu m$ for the thickest and the thinnest cases of Fig. 8 is plotted in Fig. 9. The thickest case has a modest pressure pathlength of $pL = 0.2$ atm·cm that corresponds to a DARTFire experiment ([9,16]). The A_r obtained from the narrow-band model is much smaller than from the wide-band model primarily due to the H_2O overlap resulting in a higher value of A_2. Although the A_r of $pL = 0.2$ atm·cm does not exhibit optically thin behavior within the observed temperature range, it is surprisingly uniform over a wide range of temperature, an observation that will be exploited in the proposed approximate technique that is presented below.

Approximate Technique

The hypothesis behind the proposed approximate technique is that the A_r is approximately a constant for suitable choices of the bands and their bandwidths. Out of all the combinations from the set of 1.8 μm, 2.8 μm, 4.3 μm, and 4.8 μm, the three pairs that look most promising are 2.8/1.8, 4.3/2.8, and 4.3/1.8 bands. The A_r computed for a wide range of temperatures with a $pL = 0.2$ atm·cm is shown in Fig. 10. The dependence of the equivalent bandwidth on temperature is quite different for the H_2O bands from that of the CO_2 bands, which causes a compensating effect for these three pairs of wavelengths. With other combinations where the H_2O contribution is not present, the A_r changes by a factor of 500 or more for the same temperature range.

Having not reached the thin limit, A_r still depends on the pressure-pathlength as can be seen from Fig. 11, where pL is varied as a parameter for the 2.8/1.8 pair for the bandwidths of the experimental filters, i.e., $2.56\,\mu m < \lambda_1 < 3.02\,\mu m$ and $1.768\,\mu m < \lambda_1 < 1.976\,\mu m$. However, the dependence of A_r on pL is relatively moderate. If the $\Delta\lambda$ of Fig. 11 were reduced to those of Fig. 8, the results of Fig. 11 would be squeezed to the left with the A_r at low temperature increased, and the A_r at the higher tempera-

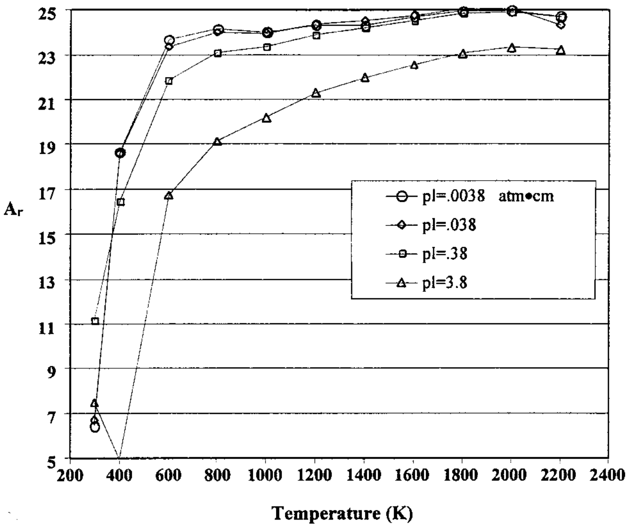

Fig. 11 Narrow-band simulated equivalent bandwidth ratio, $A_{2.8}/A_{1.8}$, for various pressure-pathlengths approaching the thin limit

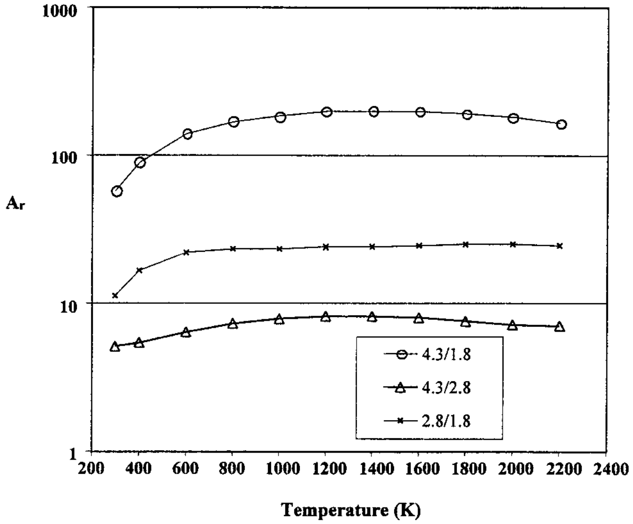

Fig. 10 Narrow-band model predicted equivalent bandwidth ratio, A_1/A_2, for CO_2 and H_2O at the maximum simulated pressure-pathlengths for various bandwidth combinations; $\Delta\lambda_1 = 4.224 - 4.330$, $\Delta\lambda_2 = 2.56 - 3.02$, $\Delta\lambda_3 = 1.768 - 1.976$

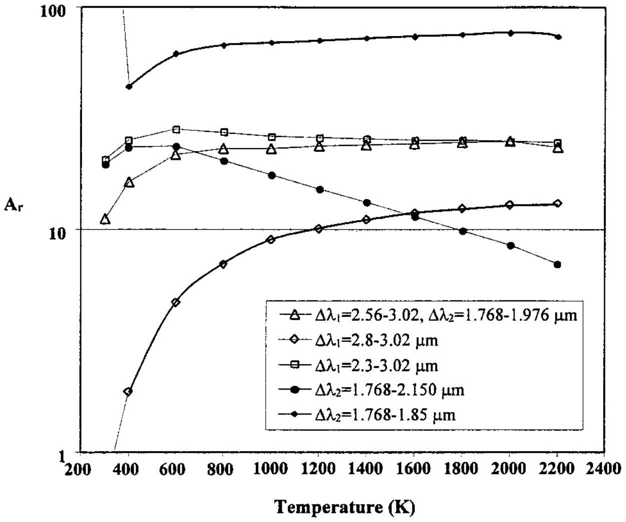

Fig. 12 Narrow-band equivalent bandwidth ratio, $A_{2.8}/A_{1.8}$, for the maximum simulated pressure-pathlength with variations of the filter bandwidth wavelength limits

tures reduced to recover exactly the results of Fig. 7, which is the optically thin behavior exploited by Wakai et al. [6]. In the simulated flame, the value of pL changes by less than a factor of 3 in the bulk of the flame (see Fig. 3), which translates to a variation in the A_r by less than ten percent.

The effect of filter bandwidth on the A_r is presented in Fig. 12, where $\Delta\lambda_1$ and $\Delta\lambda_2$ are treated as parameters. The purpose is to show that the variation of A_r with temperature can be controlled to a large degree by adjusting the filter bandwidth. The sensitivity on $\Delta\lambda_1$, seen in Fig. 12, is due to the contribution of H_2O in the 2.8 μm band.

Application

The approximate technique is applied to the simulated flame by first obtaining the *i*-ratio from simulated fields (using RADCAL) for the 2.8/1.8 band pair. The value of A_r is assumed to remain constant at 24 as indicated by Fig. 11. The resulting temperature field, obtained by solving Eq. (2), is shown in Fig. 13. Except for the outer zone of the flame, the reproduction of the temperature field is excellent. The error, shown in Fig. 14, is within five percent for most of the flame although it exceeds five percent for temperatures below 450 K. When the technique described here is applied to a measured intensity ratio, the experimental uncertainty of that measurement introduces uncertainty into the computed temperature field. By logarithmically differentiating the intensity ratio at two wavelengths, i.e., Eq. (2), we obtain the error in temperature for a combined error in the intensity ratio and equivalent bandwidth ratio. For each 1 percent error in the intensity ratio plus the equivalent bandwidth ratio, the error in temperature is 1.3 K at 1000 K and 5.1 K at 2000 K. Consequently, a ten percent error in the ‘‘experimental’’ data would produce a 13 K uncertainty in temperature at 1000 K (1.3 percent) and 51 K at 2000 K (2.6 percent), which are relatively low uncertainties.

Ferriso et al. [7] applied two-color, or bandwidth ratio, pyrometry to the optically thin situation. They conjectured that the technique may be applied to nonthin gases because of the particular behavior of the bands as they grow thicker, and what we have outlined here is a method that demonstrates what they anticipated, but noted at the time ‘‘is unconfirmed.’’

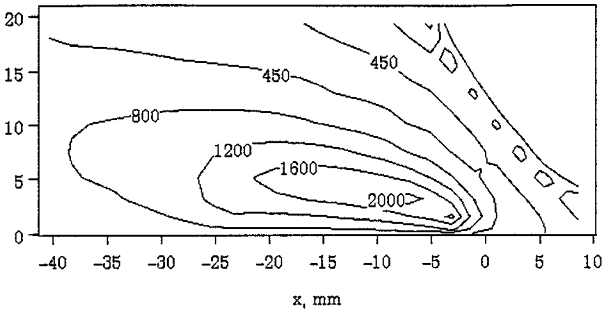

Fig. 13 Calculated flame temperature contours in K using a constant A_r of 24 (50 percent O_2, $V_g = 10$ cm/s, $lp = 2$ cm)

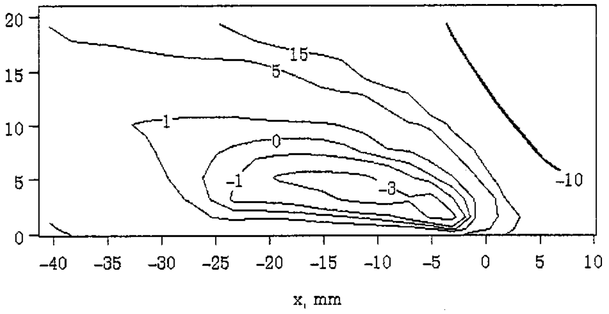

Fig. 14 Percent error between calculated flame temperature contours using a constant A_r of 24 and the simulated temperature contours (50 percent O_2, $V_g = 10$ cm/s, $lp = 2$ cm)

Evaluation of A_r

The assumption of a constant A_r simplifies emission pyrometry for nonthin gases by eliminating the need for evaluation of the A_r field. However, a constant value for the A_r for the nonoptically thin situation has to be chosen for the approximate method. This can be done in various ways. An approximate value of the pressure-pathlength can be obtained from the stoichiometric reaction. For the particular flame examined here, $(p_{CO_2} + p_{H_2O})\ L = 0.38\ \mathrm{atm \cdot cm}$. From Fig. 11, the A_r varies from 23 to 25 between 600 and 2200 K. An average value of 24 is used in Fig. 13. For cases with greater pressure-pathlengths, the A_r may not be as uniform as in the cases presented. Choosing an A_r at a particular temperature assures relatively small error in the neighborhood of that particular temperature.

The A_r can also be experimentally determined. If the temperature at a certain location is known from some other means, Eq. (2) can be used to calculate the value of the constant A_r. Yet another approach is to use the maximum flame temperature as the temperature at the location of peak intensities. The *i*-ratio measured at that location in conjunction with the maximum temperature yields the A_r. Using such an approach an A_r of 24.653 is calculated as from the equilibrium temperature and the *i*-ratio at the location of peak intensity. This is effectively the same at the assumed value of 24 used to compute the temperature field of Fig. 13 giving, for all intents and purposes, the same temperature field back again.

Conclusions

A number of approximate methods for the determination of a temperature field for a nonoptically thin participating medium using pure emission pyrometry is presented. Without an absorption measurement, emission pyrometry depends on theoretical spectral information contained in A_r. Existing techniques are based on the choice of bands and bandwidths, at which A_r is only a function of temperature as the flame becomes optically thin. However, at temperatures below 1000 K, these techniques break down as A_r becomes a function of the pressure-pathlength of the radiating species, and the signal to noise ratio is low.

The behavior of A_r with respect to the choice of the bands, choice of bandwidths, pressure-pathlength, and temperature for a particular two-dimensional flame for flame spread over PMMA is extensively studied. The major finding is that narrow-band radiation calculations suggest that A_r remains approximately constant for the 2.8 μm/1.8-μm band pair for the nonthin situation. This fact is exploited in approximate pyrometry methods used to deduce a temperature field from a ‘‘measured’’ intensity ratio.

In the first proposed approximate method A_r is obtained from a simulated flame. Because the simulated flame here is also the source of the ‘‘experimental’’ intensity ratio, the reproduction of the temperature field is exact. The uncertainty of this method can be judged by combining experimental data with the simulated flame. For a ten percent uncertainty in the intensity ratio plus the bandwidth ratio, a 1.3 percent uncertainty in temperature is obtained at 1000 K and 2.6 percent at 2000 K.

In the second method, the pressure-pathlength is approximated from the stoichiometric reaction, and a constant value, 24, for A_r is chosen from the characteristic spectral curves of the type presented in Fig. 11. Temperatures above 450 K are predicted with less than five percent error using this method.

Because A_r is hypothesized to be a constant, it can be calculated from emission measurements at a point where the temperature is known or can be estimated. Using the maximum flame temperature of the simulated flame and the peak band intensities, A_r is evaluated to be 24.65. Use of this estimate in this third approximate method produces the same degree of accuracy as the second method. For a practical flame, the dissociation temperature can be used to evaluate A_r.

Nomenclature

Symbols (Units)

a^0 = absorption coefficient at 1 atm
A = effective bandwidth
A_r = equivalent bandwidth ratio
ε = emittance over filter band due to all species, ($\mathrm{W/m^2 \cdot sr}$)
i' = radiant intensity, ($\mathrm{W/m^2 \cdot sr}$)
l_p = pyrolysis length (2 cm)
x = direction along fuel surface in direction of flame spread
y = direction perpendicular to fuel surface
p = pressure, (atm)
pL = pressure-pathlength, (atm·cm)
MMA = Methylmethacrylate
R = gas constant (kJ/kg·K)
T = temperature (K)
λ = wavelength (μm)
ρ = density ($\mathrm{kg/m^3}$)

Subscripts

b = blackbody
CO_2 = only due to carbon dioxide
H_2O = only due to water
λ = spectrally dependent
n = filter specific
o = ambient conditions

Acknowledgment

We gratefully acknowledge the support for this work by NASA through Grant No. NCC3-221.

References

[1] Uchiyama, H., Nakajima, M., and Yuta, S., 1985, ''Measurement of Flame Temperature Distribution by IR Emission Computed Tomography,'' Appl. Opt., **24**, No. 23, pp. 4111–4116.

[2] Ray, S. R., and Semerjian, H. G., 1984, ''Laser Tomography for Simultaneous Concentration and Temperature Measurement in Reacting Flows,'' Prog. Astronaut. Aeronaut., **921**, pp. 300–324.

[3] Sato, S., and Kumakura, K., 1988, ''Measurement of Flame Temperature Profiles by Holographic Interferometry and Computed Tomography,'' Trans. Jpn. Soc. Mech. Eng., Ser. B (in Japanese), **55**, No. 511, pp. 841–846.

[4] Bernstein, J., Fein, A., Choi, J., Cool, T., Sausa, R., Howard, S., Locke, R., and Miziolek, A., 1993, ''Laser-Based Flame Species Profile Measurements: A Comparison With Flame Model Predictions,'' Combust. Flame, **92**, pp. 85–105.

[5] Nichols, R. H., 1985, ''An Acoustic Technique for Rapid Temperature Distribution Measurement,'' J. Acoust. Soc. Am., **77**, No. 2, pp. 759–763.

[6] Wakai, K., Kayima, K., Sakai, S., and Shimizu, S., 1992, ''Instantaneous Measurement of Two-Dimensional Temperature and Density Distributions of Flames by a Two-Band-Emission-CT Pyrometer,'' *SPIE Infrared Technology XVIII*, **1762**, pp. 19–22, 564–575.

[7] Ferriso, C. C., Ludwig, C. B., and Boynton, F. P., ''A Band-Ratio Technique for Determining Temperatures and Concentrations of Hot Combustion Gases From Infrared-Emission Spectra,'' *Tenth Symposium (International) on Combustion*. The Combustion Institute, Pittsburgh, PA, pp. 161–175.

[8] Altenkirch, R. A., Olson, S. L., Deering, J. L., Tang, L., Bhattacharjee, S., and Hegde, U., 1999, ''Diffusive and Radiative Transport in Fires (DARTFire): Opposed-Flow Flame Spread in Low-Velocity Flows,'' Fifth International Microgravity Combustion Workshop, NASA/CP-199-208917, pp. 317–320.

[9] Olson, S. L., Altenkirch, R. A., Bhattacharjee, S., Tang, L., and Hegde, U., 1997, ''Diffusive and Radiative Transport in Fire Experiment: DARTFire,'' Fourth International Microgravity Combustion Workshop, NASA/CP 10194, pp. 393–398.

[10] Patankar, S. V., 1980, *Numerical Heat Transfer and Fluid Flow*, Hemisphere, Washington, DC.

[11] Bhattacharjee, S., and Altenkirch, R. A., 1991, ''The Effect of Surface Radiation on Flame Spread in a Quiescent, Microgravity Environment,'' Combust. Flame, **84**, pp. 160–169.

[12] Grosshandler, W. L., 1980, ''Radiative Heat Transfer in Nonhomogeneous Gases: A Simplified Approach,'' Int. J. Heat Mass Transf., **23**, pp. 1447–1459.

[13] Grosshandler, W. L. 1993, ''RADCAL: A Narrow-Band Model for Radiation Calculations in a Combustion Environment,'' NIST Technical Note 1402.

[14] Edwards, D. K., and Menard, W. A., 1964, ''Comparison of Models for Correlation of Total Band Absorption,'' Appl. Opt., **3**, No. 5, pp. 621–625.

[15] Siegel, R., and Howell, J. R., 1992, *Thermal Radiation Heat Transfer*, 3rd Ed., Taylor & Francis, Washington, DC.

[16] Horowitz, J., and Quinn, P., 1994, ''Video Digitization & Processing for the DARTFire Project,'' Project Review, NASA Lewis Research Center, Sept.

Estimation of Local Thermophysical Properties of a One-Dimensional Periodic Heterogeneous Medium by Infrared Image Processing and Volume Averaging Method

M. Varenne
Post-doctorate Student

J.-C. Batsale
Professor
e-mail: batsale@lept-ensam.u-bordeaux.fr

C. Gobbé
Assistant Professor

LEPT-ENSAM,
Esplanade des Arts et Métiers,
F-33405 Talence Cedex, France

The estimation of local thermophysical properties can be of paramount importance in the study of heterogeneous media. The volume averaging method, here reduced to a one-dimensional line averaging, is used to implement an estimation method of local thermal resistivity field, for a stratified medium. The method is tested with experimental transient temperature fields obtained with a calibrated stratified sample by an infrared camera. A large number of images are processed at the transient state. The same intrinsic stationary field is estimated from each image. By repeated estimations, this method reduces the measurement noise influence. [S0022-1481(00)01701-1]

Keywords: Heat Transfer, Image Processing, Inverse, Measurement Techniques, Porous Media

1 Introduction

Composite materials are widely used in aerospace or electronic industry. The methods that are most commonly used to characterize the local behavior of heterogeneous media ([1]) use transient thermal excitation at a small scale, as compared to the heterogeneities' size. For instance, the laser photoreflectance method ([2]) requires two different laser beams of a few micrometers in diameter. The characteristic times associated with the characteristic sizes of the experiment are quite short (the order of magnitude of the excitation frequency is 100 kHz), and experimental devices are very sophisticated and must be very accurate ([3]).

This paper proposes a simpler experiment associated with a suitable estimation method. It consists in applying a transient heat flux on one edge of a heterogeneous sample (see Figs. 1 and 2). The characteristic times of our method are associated with the size of the sample, and not with the size of the heterogeneities. This implies that the heat flux influences an area much larger than the heterogeneity. The data acquisition is also slower than with more classical local measurement methods, such as laser photoreflectance. The experimental device, which is based on infrared thermography, is therefore considerably simplified. But the obtained images are quite noisy and complex, and must be processed with physical models. In the case of a heterogeneous medium, the experimental transient temperature field T can be decomposed into the sum of a macroscopic field $\langle T \rangle$, and a local deviation field $\widetilde{T}$. The volume averaging method ([4]) can then be useful to process infrared images. This method is usually used to compute effective macroscopic properties from local properties, such as the effective thermal conductivities ([5]). In this paper, the volume averaging method is used in a nonclassical way, since transient temperature fields are processed in order to estimate *local* thermophysical properties. The estimation method is partly based on the relation that links the local and the macroscopic temperature fields through the vector **b**. This closure vector is a local stationary field.

The complete estimation method is presented first, and the problems due to measurement noise are processed with a least squares linear estimation ([6]). The experimental validation is then presented with a calibrated multilayered sample.

2 Description of the Method

The experimental method consists of applying a transient heat flux on one edge of a heterogeneous sample (see Figs. 1 and 2). For each time-step of the experiment, an infrared camera records the temperature field at the surface of the sample. The closure problem, which links macroscopic and local temperature fields, is solved first. From its solution **b**, the local field of the thermal conductivities is then deduced.

2.1 Experimental Estimation of the Field *b*. The volume averaging method ([4,7]) allows us to describe the heat transfers in a heterogeneous medium through a macroscopic model associated with an equivalent continuous model. The basic idea of the volume averaging theory is that a temperature field T is the sum of a mean component (or macroscopic field $\langle T \rangle$) and of a local com-

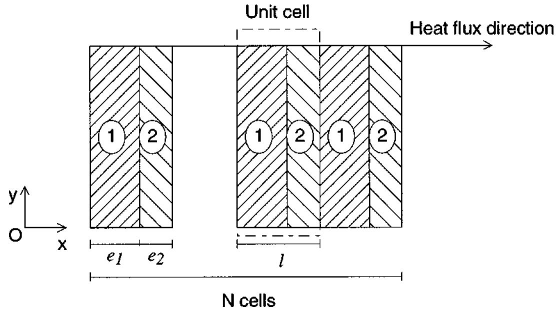

Fig. 1 Diagram of a periodic stratified medium

Contributed by the Heat Transfer Division for publication in the JOURNAL OF HEAT TRANSFER. Manuscript received by the Heat Transfer Division, Mar. 27, 1999; revision received, Sept. 10, 1999. Associate Technical Editor: T. Avedisian.

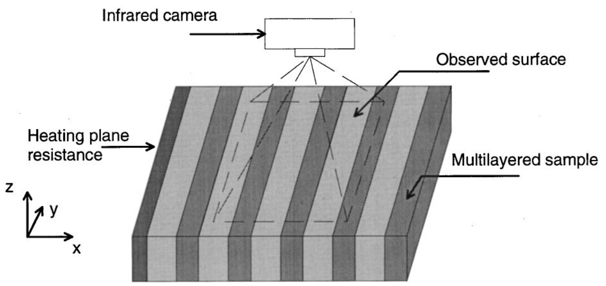

Fig. 2 Schematic of the experimental device

ponent $\tilde{T}$, which describes the spatial deviation around the mean value of the temperature ([8]). The macroscopic temperature $\langle T\rangle$ is an average temperature upon the whole representative elementary volume, which is the unit cell of a periodic heterogeneous medium. In the general case $\langle T\rangle$ is a continuous field defined by a convolution product such as

$$\langle T\rangle = m \otimes T. \tag{1}$$

The weighting function m is defined by

$$m(x) = (H(x+l/2) - H(x-l/2))/l \tag{2}$$

where H is the Heaviside function, and l is the averaging length, or the length of a unit cell ($l = e_1 + e_2$). In the case of a one-dimensional medium, as shown in Fig. 1, $\langle T\rangle$ is defined by

$$\langle T(x,t)\rangle = \frac{1}{l}\int_{x-l/2}^{x+l/2} T(\zeta,t)\,d\zeta. \tag{3}$$

The previously described averaging method also corresponds to a filtering of the signal, which attenuates the fluctuations of spatial frequency greater than the characteristic frequency $1/l$. The intrinsic average temperature for the i phase is given by

$$\langle T_i(x,t)\rangle^i = \frac{1}{e_i}\int_{x-l/2}^{x+l/2} T_i(\zeta,t)\,d\zeta \tag{4}$$

where $T_i(\zeta,t)$ is zero when ζ locates a point that is not in i phase, and e_i is the length of phase i contained within length l.

In some cases, the medium is considered to be in local thermal equilibrium ([9]), that is to say

$$\langle T\rangle = \langle T_1\rangle^1 = \langle T_2\rangle^2 \tag{5}$$

and the two-equation model, considering $\langle T_1\rangle^1$ and $\langle T_2\rangle^2$ separately, yields a one-equation model in which the only macroscopic temperature is $\langle T\rangle$. Gobbé et al. [10] have shown that the local thermal equilibrium hypothesis was always verified under the experimental conditions used in this paper (periodic stratified medium, perpendicular to the heat flux and with Dirichlet boundary conditions). Under the assumption of a local thermal equilibrium, Carbonell and Whitaker [11] propose a closure problem

$$\tilde{T} = \underset{\sim}{b} \cdot \nabla\langle T\rangle. \tag{6}$$

This equation links local variables (spatial deviations $\tilde{T}$) with macroscopic variables (macroscopic temperature gradient field $\nabla\langle T\rangle$). In a general case **b** is a vector. The components of the closure vector **b** are local coefficients and depend on both the geometry and the thermophysical properties of the medium. In a one-dimensional transfer, vector **b** yields a scalar field b, and Eq. (6) is written

$$\tilde{T}(x,t) = b(x)\nabla\langle T(x,t)\rangle. \tag{7}$$

In practice, each infrared image $T(x,y)$ is averaged in the direction perpendicular to the heat flux (Oy-direction), which gives a local temperature profile $T(x)$. The macroscopic temperature field $\langle T\rangle$ is deduced from each profile by use of Eq. (3). The macroscopic temperature gradient field $\nabla\langle T\rangle$ is obtained by differentiating $\langle T\rangle$. The spatial deviation field $\tilde{T}$ is deduced from fields T and $\langle T\rangle$ ([8]). In theory, one thermographic image is enough to estimate the b field, but all the images will be processed in order to have the best estimate of b field.

2.2 Study of the Measurement Noise Influence. The measurement noise in infrared thermography is rather important (about 0.5 K). One of the advantages of the proposed method is that the parameter estimation is made from a great number of experimental results, which statistically decreases the influence of measurement noise. The *observed* temperature field $\hat{T}$ is made up of an *exact* temperature field T and an error field e_T such as

$$\hat{T} = T + e_T. \tag{8}$$

We will consider, in the following, that the measurement noise is sufficiently softened by the spatial convolution, and does not ''reappear'' with spatial derivation. Under this condition, macroscopic variables, and more particularly the macroscopic gradient field $\nabla\langle T\rangle$, are assumed to be known without error. Thus, measurement noise is thoroughly integrated in the spatial deviation field $\tilde{T}$. For the ith experimental time-step, the unknown parameter b is linked to the local deviation field $\tilde{T}$ through the relation

$$\begin{bmatrix} \tilde{T}_1 \\ \tilde{T}_2 \\ \cdot \\ \tilde{T}_M \end{bmatrix}_i = [X]_i \begin{bmatrix} b_1 \\ b_2 \\ \cdot \\ b_M \end{bmatrix} \tag{9}$$

where

$$[X]_i = \begin{bmatrix} \nabla\langle T_1\rangle & & 0 \\ & \cdot & \\ 0 & & \nabla\langle T_M\rangle \end{bmatrix} \tag{10}$$

$[X]_i$ is an M by M sensitivity matrix, if $[\tilde{T}]_i$ is a M by 1 matrix. Equation (9) is related to one time-step. The measurement is repeated N times, Eq. (9) then yields

$$\begin{bmatrix} [\tilde{T}_1 \;\; \tilde{T}_2 \;\; \cdot \;\; \tilde{T}_M]_1^t \\ [\tilde{T}_1 \;\; \tilde{T}_2 \;\; \cdot \;\; \tilde{T}_M]_2^t \\ \cdot \\ [\tilde{T}_1 \;\; \tilde{T}_2 \;\; \cdot \;\; \tilde{T}_M]_N^t \end{bmatrix} = \begin{bmatrix} [X]_1 \\ [X]_2 \\ \cdot \\ [X]_N \end{bmatrix} \begin{bmatrix} b_1 \\ b_2 \\ \cdot \\ b_M \end{bmatrix} \tag{11}$$

which can otherwise be written

$$\tilde{\mathbf{T}} = \mathbf{X}\mathbf{b}. \tag{12}$$

Vector **b** contains the unknown parameters. Matrix **X** is composed of the macroscopic gradients, which are assumed to be known without error. The elements of vector $\tilde{\mathbf{T}}$ are defined with measurement noise. This additive measurement noise has a zero mean value, is noncorrelated, and has a constant standard deviation. The temperature field covariance matrix can then be defined as

$$\mathrm{cov}(\tilde{\mathbf{T}}) = \sigma^2\mathbf{I} \tag{13}$$

where **T** is the identity matrix. The optimal estimator of field **b**, denoted $\hat{\mathbf{b}}$, is obtained ([6]) through the relation

$$\hat{\mathbf{b}} = (\mathbf{X}^t[\mathrm{cov}(\hat{\mathbf{T}})]^{-1}\mathbf{X})^{-1}\mathbf{X}^t[\mathrm{cov}(\hat{\mathbf{T}})]^{-1}\tilde{\mathbf{T}}. \tag{14}$$

According to Eq. (13), Eq. (14) may be simplified

$$\hat{\mathbf{b}} = (\mathbf{X}^t\mathbf{X})^{-1}\mathbf{X}^t\tilde{\mathbf{T}}. \tag{15}$$

We are also able to evaluate the estimation error upon field $\hat{\mathbf{b}}$

$$\mathrm{cov}(\hat{\mathbf{b}})=\mathrm{cov}(\mathbf{e}_{\tilde{\mathbf{b}}})=\sigma^2(\mathbf{X}^t\mathbf{X})^{-1}. \tag{16}$$

Equations (15) and (16) show that dealing with a great quantity of information strongly decreases the measurement noise influence. All data are weighted by the macroscopic gradient. Thus, the estimation of the $\hat{\mathbf{b}}$ field will be improved by dealing with large gradient values.

The best estimate solution $\hat{\mathbf{b}}$, or $\hat{b}$ field, of the closure problem (Eq. (6)) was found, along with the estimation error $\mathrm{cov}(\mathbf{e}_{\tilde{\mathbf{b}}})$, or $\mathrm{cov}(\mathbf{e}_{\mathbf{b}})$.

2.3 Estimation of the Resistivity Field. In the case of a periodic medium with symmetric unit cells, Quintard and Whitaker [4] suggest that the closure vector **b** and the local conductivity field λ be linked through the following relation:

$$\nabla\cdot(\lambda\nabla\mathbf{b})=-\nabla\cdot(\lambda\mathbf{I}). \tag{17}$$

We observe that Eq. (17) is stationary. This is due to the fact that the different time scales are dissociated: The characteristic times related to the transfer at a local scale (local equations) are much smaller than the times related to the transfer between the heated area and the measurement points (macroscopic equations).

In a stratified medium, where the macroscopic gradient field is perpendicular to the strata, heat transfer can be considered one-directional and Eq. (17) is then written

$$\frac{d}{dx}\left(\lambda(x)\frac{db(x)}{dx}\right)=-\frac{d\lambda(x)}{dx}. \tag{18}$$

Integration of Eq. (18) with respect to x gives

$$\lambda(x)=A\bigg/\left(1+\frac{db(x)}{dx}\right) \tag{19}$$

where $db(x)/dx\neq-1$ and A is an integration constant. The case where $db(x)/dx=-1$ will be discussed later in this paper. To avoid the indetermination problems, we will no longer consider the conductivity field, but the thermal resistivity field $R(x)$ defined as

$$R(x)=1/\lambda(x)=\left(1+\frac{db(x)}{dx}\right)\bigg/A. \tag{20}$$

Let us consider a stratified medium (Fig. 1), composed of a stack of identical unit cells, perpendicular to the heat flux. Each unit cell is made up of two different layers, referred to as phase 1 and phase 2. The thickness of the layers is denoted e_1 and e_2, and the thickness of the unit cell is denoted l. Thermal conductivities are, respectively, λ_1 and λ_2. The i phase linear fraction is $\varepsilon_i=e_i/l$. Considering such a stratified medium, Gobbé and Quintard [12] propose an analytical solution to the closure problem (Eq. (7))

$$b(x)=\left(\frac{\varepsilon_1}{2}l+x\right)\frac{\varepsilon_2(\lambda_2-\lambda_1)}{\varepsilon_1\lambda_2+\varepsilon_2\lambda_1};\quad \text{if } -e_1<x<0$$

$$b(x)=\left(\frac{\varepsilon_1}{2}l-\frac{\varepsilon_1}{\varepsilon_2}x\right)\frac{\varepsilon_2(\lambda_2-\lambda_1)}{\varepsilon_1\lambda_2+\varepsilon_2\lambda_1};\quad \text{if } 0<x<e_2. \tag{21}$$

This latter analytical solution is introduced into Eq. (20), and since $R(x)$ is known in each medium ($1/\lambda_i$ in phase i) the integration constant is

$$A=\lambda_1\lambda_2/(\varepsilon_1\lambda_2+\varepsilon_2\lambda_1) \tag{22}$$

where A is the equivalent, or macroscopic, thermal conductivity of a multilayered sample, in which the strata are perpendicular to the heat flux. In most cases, the equivalent conductivity of the heterogeneous medium is not known. It has to be determined from a macroscopic measurement of the thermal diffusivity ([13,14]), when the global heat capacity was previously estimated. In fact, the proposed method estimates a relative distribution of local thermophysical properties (R field).

The main difficulty in estimating the R field is to derive b. Field b is estimated from experimental results, and is therefore noisy, and the estimation of the R field is an ill-posed problem ([15]), since derivation increases the noise influence. To decrease the effects of the noise amplification due to derivation, an optimal Wiener filtering ([16]) is used to estimate the R field. This filter gives more importance to the points of the b field that are estimated with the smaller estimation error e_b.

The estimation of the optimal resistivity field was presented. The estimation method will now be tested with experimental temperature fields.

3 Experimental Results

The experimental device is shown schematically in Fig. 2. The sample (height 25 mm, width 65 mm, and length 50 mm) is made of 25 strata. The strata are 2 mm thick, and are alternatively made of aluminum ($\lambda_1=200\,\mathrm{W\,m^{-1}\,K^{-1}}$) and of epoxy resin ($\lambda_2=0.32\,\mathrm{W\,m^{-1}\,K^{-1}}$). The macroscopic thermal conductivity of the sample was estimated from Eq. (22), and is $0.64\,\mathrm{W\,m^{-1}\,K^{-1}}$. The observed surface is carefully polished and painted black, to ensure a uniform and close to 1 emissivity. The value of the emissivity is not needed in the estimation process, since the b field is defined through a ratio of temperatures. The heat flux (perpendicular to the strata) is applied on one side of the multilayered sample, through a heating plane resistance of the same size as the sample (see Fig. 2). The upper, lower, and lateral sides of the sample are left as they are. The sample is held by the side where the heat flux is applied, and by the opposite end. The thermal perturbation has not reached the opposite end during the time of the experiment. In this experiment, the heat flux is a step function of time, even though the steady state was not reached, as shown in Fig. 4. The measurements are made during transient state. The electric power dissipated by the resistance is 7 W, which implies a temperature increase that is contained between 50 and 0.6°C, according to the point that is taken into consideration. In order to have a sufficiently large macroscopic temperature gradient field, the sample was heated for 15 min before the beginning of the data recording.

No particular precautions have been taken about the lateral convective and radiative heat losses. The reason is that such losses, like transient effects, are noticeable at large scale but negligible at small scale. Under the present experimental conditions, the ratio of the flux that leaves, $\varphi(x=L)$, and that comes in, $\varphi(x=0)$, the observed surface can be deduced from the equation of heat transfer in a fin ([17])

$$\frac{\varphi(x=L)}{\varphi(x=0)}=\exp\left(-\sqrt{\frac{2h}{Ar}}L\right), \tag{23}$$

with $h=10\,\mathrm{W\,m^{-2}\,K^{-1}}$, the heat losses coefficient, $r=23\times10^{-3}\,\mathrm{m}$, the equivalent radius of the sample, $A=0.64\,\mathrm{W\,m^{-1}\,K^{-1}}$, the macroscopic thermal conductivity, and $L=45\times10^{-3}\,\mathrm{m}$, the length of the observed surface. The outgoing heat flux, $\varphi(x=L)$, is 80 percent smaller than the incoming heat flux, $\varphi(x=0)$, which traduces an important effect of the lateral heat losses at a large scale. On the other hand, the ratio of the flux that leaves and that comes in an elementary surface represented by a pixel whose length is $dl=0.23\,\mathrm{mm}$ is given by

$$\frac{\varphi(x+dl)}{\varphi(x)}=\exp\left(-\sqrt{\frac{2h}{Ar}}dl\right). \tag{24}$$

The outgoing flux, $\varphi(x+dl)$, is only one percent smaller than the incoming flux, $\varphi(x)$. The heat losses at the local scale are therefore negligible.

Figure 3 illustrates an example of a thermographic image of the aforementioned sample. This infrared picture was obtained with an AVIO TVS 2000 infrared camera, which can record up to 512 images. Each image is composed of 100×256 pixels. The length of the pixel is measured from a calibrated sample. According to the lens, and to the distance between the camera and the sample

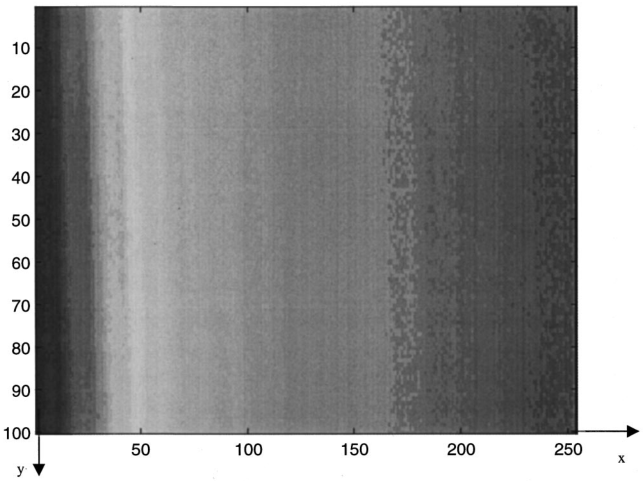

Fig. 3 Infrared image of the multilayered sample at time *t*

that were used in the experiment, the length of each pixel is estimated to be 0.23 mm. The recording frequency is 1 image/s. The large number of experimental data compensates for the poor accuracy of each pixel measurement, through the statistical data processing. Estimation of b and λ parameters is feasible only if the medium's behavior can be described with macroscopic equations. In the case of a stratified medium, Batsale et al. [18] require that the unit cell adjacent to the heat flux not be taken into consideration. The experimenter should then be careful that the observed surface be far enough (about a few cells) from the thermal excitation.

In order to estimate the one-dimensional temperature field in the Ox-direction (parallel to the heat flux), each two-dimensional temperature image is averaged in the Oy-direction (perpendicular to the heat flux). Figure 4 illustrates two local one-dimensional temperature fields, and their related macroscopic temperature fields (obtained with Eq. (3)) for $t=1$ s and $t=300$ s. The bidirectional effect of the heat flux in the sample is limited because the observed surface is not in contact with the edges of the sample.

Figure 5 illustrates examples of b fields estimated with Eq. (7) for $t=1$ s, $t=150$ s, and $t=300$ s. It shows that when macroscopic gradients are large enough, the estimated closure fields b are accurate, and do not depend on time.

The estimation of field $\hat{b}$ is made using Eq. (15). It yields one optimal field, illustrated in Fig. 6. The nondimensional values of the thermal resistivities ($R^*=R/R_2$) are also shown in Fig. 6, so as to illustrate the structure of the medium.

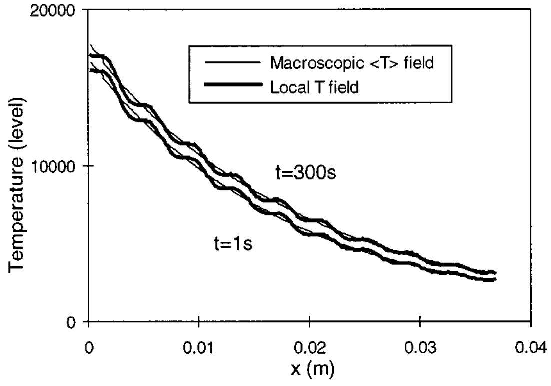

Fig. 4 Local and macroscopic temperature fields, experimental results

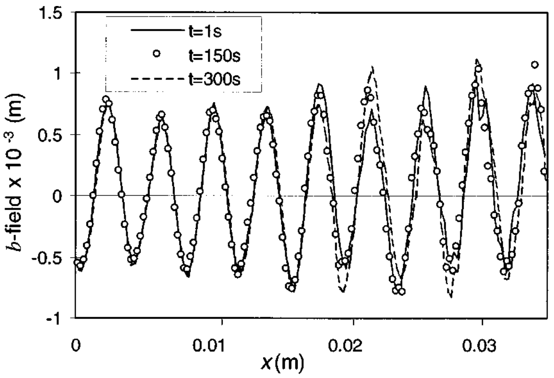

Fig. 5 *b* fields, $t=1$ s, $t=150$ s, and $t=300$ s

The thermal resistivity R field, shown in Fig. 7, is estimated from the $\hat{b}$ field by Eq. (20) with use of a Wiener optimal filtering. The awaited values for the lowest (aluminum) and highest (epoxy resin) resistivities are $R_1=(5.0\pm0.5)\ 10^{-3}\ \mathrm{K\,m\,W^{-1}}$ and $R_2=(3.1\pm0.3)\ \mathrm{K\,m\,W^{-1}}$, respectively. Experimental results for the lowest conductivity (highest resistivity) are very satisfactory. The estimation of thermophysical properties in the most conductive medium is not possible when it is highly more conductive than the other medium. The analytical solution of the b field (Eq. (21)) shows that $db(x)/dx=-1$ in the most conductive medium. This corresponds to an indeterminate thermal conductivity (Eq. (20)),

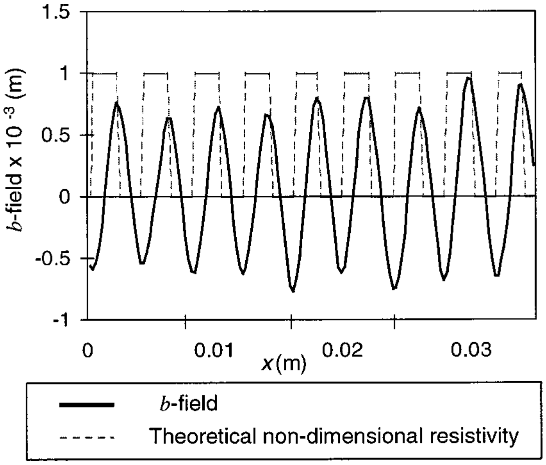

Fig. 6 Optimal *b* field

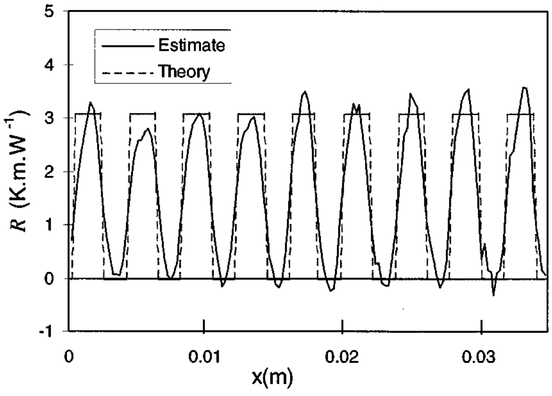

Fig. 7 Experimental thermal resistivity *R* field

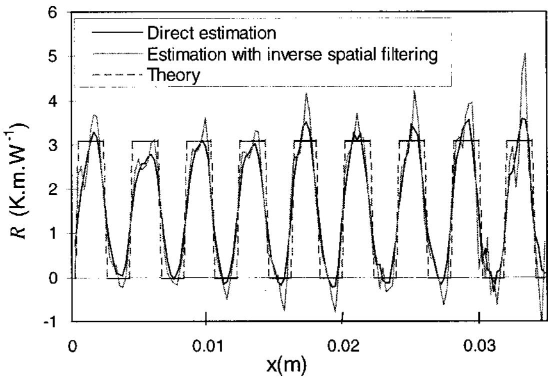

Fig. 8 ***R*** **field with and without spatial inverse filtering**

or to a 0 thermal resistivity. The thermal resistivity of the aluminum strata is very low: $R_1 = (5.0 \pm 0.5)\ 10^{-3}\ \mathrm{K\,m\,W^{-1}}$. Therefore the experimental uncertainties lead to some negative values of the thermal resistivity. Figure 7 clearly illustrates the spatial filtering of the infrared camera, since the phases' boundaries are not sharply defined. The highest spatial frequencies are so attenuated that the square angles of the resistivity field have disappeared. The spatial transfer function of the camera was determined, and its inverse was applied to *R* field, as described in Bougeard et al. ([19]). Although the measurement noise is slightly increased, it yields a field that discriminates the phases better, as shown in Fig. 8.

Up to now, the estimation method did not require the knowledge of the size of the strata in the one-dimensional medium. The accuracy of the estimated *b* field in Fig. 6 allows us to determine the thickness of each stratum. The distance between two consecutive extreme values of the *b* field gives an estimate of the thickness of the considered layer. The average estimated thickness is (2.00 ± 0.10) mm, when the expected value is 2 mm. Making the hypothesis that the resistivity *R* is constant by parts, with every other resistivity being nonzero, there remains only one parameter to estimate. The resistivity of the less conductive medium (here the epoxy resin) is estimated via a least-squares method in Fourier space. The estimated value is $(2.5 \pm 0.2)\ \mathrm{K\,m\,W^{-1}}$. The epoxy resin here is assumed to have a $(3.1 \pm 0.3)\ \mathrm{K\,m\,W^{-1}}$ thermal resistivity, 19 percent higher than the estimated value. Two estimated resistivity profiles are shown in Fig. 9. The first one corresponds to the estimation of *R* when the geometry and both resistivities of media 1 and 2 are searched at the same time. The second profile was obtained with the a priori knowledge of the geometry of the medium and of the lowest thermal resistivity.

The knowledge of the sample's geometry allows us to a posteriori check the validity of the local thermal equilibrium assumption. The macroscopic intrinsic temperatures relative to each phase ($\langle T_i \rangle^i$ defined by Eq. (4)) are thoroughly comparable to the macroscopic temperature ($\langle T \rangle$ defined by Eq. (3)), as shown in Fig. 10.

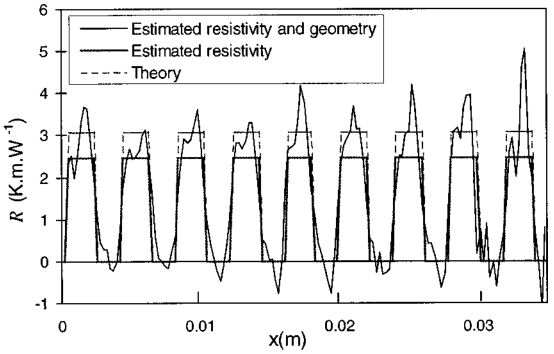

Fig. 9 Resistivity of the sample: estimation of a function, and estimation of the resistivity of one of the media

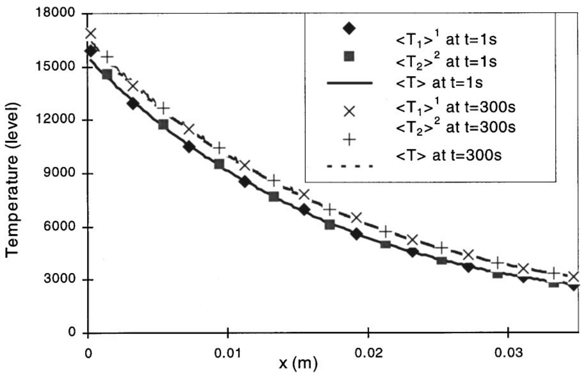

Fig. 10 Validation of the local thermal equilibrium hypothesis

The proposed estimation method gives precise information about the geometry (the unit cell size was very properly estimated) of a periodic multilayered sample. It also estimates the resistivity of the less conductive material with reasonable accuracy.

4 Remarks About the Proposed Method

The method presented in this paper gives an estimation of the thermophysical properties in a multilayered sample, thanks to a one-dimensional volume averaging method, infrared thermography, and inverse techniques. The thermal resistivities of a sample made of epoxy resin and aluminum strata were estimated. Even though the estimation method may seem to be inaccurate, it is an easy-to-use and powerful means to produce a map of thermophysical properties. One of the most important advantages of the method is that it requires a simple experimental device. The only high-tech device is an infrared camera and a local thermophysical properties field is estimated with only one position of the experimental bench.

Although the effects inherent to infrared thermography (measurement noise and spatial filtering) were taken into consideration, the use of an infrared camera with a better spatial filtering should improve the results.

The spatial resolution that can be reached with this technique depends on the lens of the camera. In this study, the unit cell was 4 mm thick, but the estimation method has been tested with a multilayered carbon sample, whose unit cell was 1.3 mm thick. The use of an infrared microscope could make the characterization of electronic components possible, since some stacked components can be assimilated to multilayered materials. The order of magnitude of such stacks is $10 \times 10 \times 20\ \mathrm{mm}^3$.

The estimation method was presented for a one-directional heat transfer. The study of a two-dimensional heterogeneous medium (one phase is dispersed in another phase) is more difficult. The estimation of the **b** vector components is made in the same way as the one-dimensional case, but inversion of Eq. (17) is difficult because it has no simple analytical solution, and requires two macroscopic thermal excitations, in the *Ox* and *Oy*-directions. Some first results obtained with a two-dimensional sample are given in Varenne et al. [20]. The study of three-dimensional heterogeneous media requires physical assumptions, because temperature distribution as a function of *z* (direction perpendicular to the observed surface of the sample) is not accessible with classical infrared measurements.

Nomenclature

A = macroscopic thermal conductivity $(\mathrm{W\,m^{-1}\,K^{-1}})$
$\mathbf{b}$ = vector field that maps $\nabla\langle T\rangle$ onto $\tilde{T}$ in the one-equation model (m)
b = scalar field, analogous to $\mathbf{b}$ in a one-dimensional transfer
dl = length of a pixel (m)
e_i = i layer thickness (m)
$\mathbf{e_V}$ = measurement error on field or vector $\mathbf{V}$
h = heat losses coefficient $(\mathrm{W\,m^{-2}\,K^{-1}})$
$\underset{\sim}{I}$ = identity matrix
L = length of the observed surface (m)
l = length of the unit cell (m)
M = number of measurement points
m = weighting function $(\mathrm{m^{-1}})$
N = number of time steps
R = thermal resistivity $(\mathrm{K\,m\,W^{-1}})$
r = equivalent radius of the sample (m)
T = local temperature field
$\langle T\rangle$ = macroscopic temperature field
$\langle T_i\rangle^i$ = intrinsic phase average temperature for the i phase
$\tilde{T}$ = spatial deviation temperature
$\hat{T}$ = exact temperature field
t = time (s)
$\mathbf{X}$ = sensitivity matrix

Greek

ε_i = linear fraction of the i phase
λ = thermal conductivity $(\mathrm{W\,m^{-1}\,K^{-1}})$
λ_i = thermal conductivity of the i phase $(\mathrm{W\,m^{-1}\,K^{-1}})$
σ = measurement noise standard deviation
φ = heat flux (W)
ξ = integration dumb variable

Superscript

$.^t$ = transposed matrix
$.^*$ = nondimensional quantity
$\hat{\ }$ = best estimate

References

[1] Lepoutre, F., Lefebvre, J., Lhermitte, T., Ainouch, L., Delpech, P., Forge, P., Hirschi, S., and Joulaud, J. L., 1996, ‘‘Mesures Thermiques Microscopiques,’’ Rev. Gen. Therm., **35**, pp. 344–354.

[2] Rosencwaig, A., Opsal, J., Smith, W. L., and Willenborg, D. L., 1985, ‘‘Detection of Thermal Waves Through Modulated Optical Transmittance and Modulated Optical Scattering,’’ Appl. Phys. Lett., **46**, No. 11, pp. 1013–1015.

[3] Gervaise, C., Nouals, C., Calderan, C., Benet, S., and Serra, J. J., 1997, ‘‘Diffusivity Measurements by Photothermal Microscopy,’’ Proceedings of the 24th ITCC, Pittsburgh, PA.

[4] Quintard, M., and Whitaker, S., 1993, ‘‘One- and Two-Equation Models for Transient Diffusion Processes in Two-Phase Systems,’’ Adv. Heat Transfer, **23**, pp. 369–464.

[5] Nozad, I., Carbonell, R. G., and Whitaker, S., 1985, ‘‘Heat Conduction in Multiphase Systems-I. Theory and Experiment for Two-Phase Systems,’’ Chem. Eng. Sci., **40**, pp. 843–855.

[6] Beck, J. V., and Arnold, K. J., 1977, *Parameter Estimation in Engineering and Science*, John Wiley and Sons, New York.

[7] Marle, C. M., 1967, ‘‘Ecoulements Monophasiques en Milieu Poreux,’’ Rev. Inst. Fr. Pet., **22**, pp. 1471–1509.

[8] Gray, W. G., 1975, ‘‘A Derivation of the Equations for Multi-phase Transport,’’ Chem. Eng. Sci., **30**, pp. 229–233.

[9] Whitaker, S., 1991, ‘‘Improved Constraints for the Principle of Local Thermal Equilibrium,’’ Ind. Eng. Chem. Res., **30**, pp. 983–997.

[10] Gobbé, C., Ladevie, B., and Quintard, M., 1995, ‘‘Modèle macroscopique de transfert thermique instationnaire dans un matériau composite comportant des résistances de contact entre phases,’’ *7ièmes Journées Internationales de Thermique*, Marrakech, Vol. 1, pp. 119–128.

[11] Carbonell, R. G., and Whitaker, S., 1984, ‘‘Heat and Mass Transfer in Porous Media,’’ *Fundamentals of Transport Phenomena in Porous Media*, J. Bear, New York, pp. 121–198.

[12] Gobbé, C., and Quintard, M., 1994, ‘‘Macroscopic Description of Unsteady Heat Transfer in Heterogeneous Media,’’ *High Temperatures–High Pressures*, No. 13, ECTP Proceedings, Vol. 26, pp. 535–548.

[13] Varenne, M., Batsale, J. C., and Gobbé, C., 1997, ‘‘Mesure de Diffusivité Thermique Effective d’un Milieu Poreux Bidimensionnel par Thermographie Infrarouge,’’ *Congrès SFT 97*, Elsevier, Paris, pp. 420–425.

[14] Batsale, J. C., Ladevie, B., and Gounot, J., 1998, ‘‘Measurement of Macroscopic Thermophysical Properties of Geological Samples by Infrared Image Processing,’’ *ASME Proceedings of the 2nd International Conference on Inverse Problems in Engineering: Theory and Practice*, ASME, New York, pp. 633–641.

[15] Hensel, E., 1991, ‘‘Inverse Theory and Applications for Engineers,’’ *Prentice-Hall Advanced Reference Series—Engineering*, Prentice-Hall, Englewood Cliffs, NJ.

[16] Press, W. H., Flannery, B. P., Teukolsky, S. A., and Vetterling, W. T., 1992, *Numerical Recipes, The Art of Scientific Computation*, Cambridge University Press, Cambridge.

[17] Carslaw, H. S., and Jaeger, J. C., 1959, *Conduction of Heat in Solids*, Oxford University Press, Oxford, UK.

[18] Batsale, J. C., Gobbé, C., and Quintard, M., 1996, ‘‘Local Non-Equilibrium Heat Transfer in Porous Media,’’ *Recent Res. Development in Heat, Mass and Momentum Transfer*, Trivadrum India, Res. SignPost, Vol. 1, pp. 1–24.

[19] Bougeard, D., Vermeulen, J. P., and Baudoin, B., 1995, ‘‘Mesure du Champ de Température sur une Ailette d’Échangeur par Thermographie Infrarouge. Utilisation d’une Technique de d’Éconvolution d’Image,’’ Rev. Gen. Therm., **34**, No. 400, pp. 325–334.

[20] Varenne, M., Batsale, J. C., and Gobbé, C., 2000, ‘‘Estimation of a Local Thermal Conductivity Field of a Plane Heterogeneous Medium With Infrared Images Processing and the Volume Averaging Method,’’ *High Temperatures–High Pressures*, No. 32, to be published.

D. J. Doss[1]
Assoc. Mem. ASME

N. T. Wright[2]
e-mail: wright@umbc.edu
Mem. ASME

Department of Mechanical Engineering,
University of Maryland,
Baltimore, MD 21250

Simultaneous Measurement of the Orthogonal Components of Thermal Diffusivity in PVC Sheet

An extension of the flash method is described that measures simultaneously the three orthogonal components of thermal diffusivity in specimens of moderate thermal diffusivity. Only part of the top face of the specimen is illuminated and the temperature histories are recorded at three points on the bottom face. A Marquardt parameter estimation algorithm coupled with a finite difference model of the diffusion equation analyzes these temperature histories to determine the components of thermal diffusivity. Illustrative measurements in stainless steel, glass, and PVC demonstrate that accurate three-dimensional thermal diffusivity measurements can be made in this way. The in-plane components of thermal diffusivity of as-supplied PVC sheet are shown to be about 20 percent greater than the out-of-plane component. This anisotropy appears to be due to the manufacturing process and exemplifies the need for such measurements. [S0022-1481(00)70101-0]

Keywords: Conduction, Heat Transfer, Measurement Techniques, Polymers, Thermophysical

Introduction

Initially isotropic polyethylene subjected to large plastic deformation has been found to develop anisotropic thermal conductivity ([1]). Likewise, composite materials (e.g., Refs. [2,3]), polymers in thin films ([4]), and biological tissues ([5]) have been found to have anisotropic thermal conductivities. Multiple components of the thermal conductivity (or diffusivity) tensor are often measured by the sequential application of a one-dimensional measurement method. This in turn often requires that specimens be fabricated uniquely for each component measured (e.g., Refs. [1,2,5]). Requiring multiple specimens, and having to alter their geometry for each direction measured, may add uncertainty in correlating the components of thermal property tensors, especially in materials prone to specimen-to-specimen variability, such as biological tissues. Measuring multiple components using a single specimen has often required substantial contact with the specimen, such as depositing metal lines of varying widths on thin dielectric films ([4]) or sandwiching a mica heater between two carbon-carbon composite specimens and embedding thermocouples into the specimen ([3]). Methods requiring such contact prevent the application of well-defined finite deformation, as might be desired in a study of finite thermoelasticity in elastomers or biological tissues. Furthermore, such methods may be inappropriate for materials requiring a specific chemical state or that are not easily manufactured.

The flash method of thermal diffusivity measurement ([6]) requires little contact with the specimen. Donaldson and Taylor [7] and Chu et al. [8] extended the one-dimensional flash method to measure the out-of-plane and radial in-plane components of thermal diffusivity using a single specimen. Only the center of the specimen was illuminated and the temperature history at two points on the rear surface measured. Maillet et al. [9] and Lachi and Degiovanni [10] refined this two-dimensional flash method to measure the out-of-plane and radial in-plane components of thermal diffusivity simultaneously and developed criteria for the optimal position of the thermocouples for given aperture and specimen sizes. Fujii et al. [11] determine the in-plane components of thermal conductivity of several test materials using a laser flash and measuring the temperature of the illuminated surface using an IR camera. Although they list a three-dimensional boundary value problem for data reduction, only the in-plane components are calculated by comparing temperature histories with finite difference solutions. Sawaf and Özişik [12] suggested using the Marquardt parameter estimation algorithm coupled with a finite difference solution of the heat diffusion equation to determine the three components of thermal diffusivity in an orthotropic material. Their illustrative calculations employed a cubic specimen with constant temperature boundary conditions. Wright et al. [13] proposed further extending the flash method to measure the three diagonal components of the thermal diffusivity tensor $\boldsymbol{\alpha}$ of elastomers and biological tissues subject to finite strain. As with the two-dimensional flash method, a portion of the front face would be illuminated, but now temperatures at three points on the rear surface would be measured. Then, a Marquardt parameter estimation algorithm coupled with a finite difference solution of the heat diffusion equation would be used to determine the three components of thermal diffusivity.

Described here are the simultaneous measurements of the diagonal components of $\boldsymbol{\alpha}$ of plane specimens. Key features are minimal contact with the specimen (required for specimens that may undergo large deformations) and quantification of the role of heat conduction in the air layer underneath the specimen. Conduction in the air layer is shown to be important for materials of moderate thermal conductivity. (Many such materials, for example biological tissues which must remain well hydrated, may not be tested in a vacuum that could eliminate conductive and convective parasitic losses.) The results discussed here are limited to undeformed materials at room temperature. Stainless steel and plate glass illustrate the accuracy of the measurements in isotropic materials. Then, $\boldsymbol{\alpha}$ of PVC sheet is contrasted to that of PVC rod. These results illustrate that manufacturing processes may introduce directional dependence in the thermal properties of polymers, and hence the need for measurements beyond those that presume material isotropy.

Methods and Materials

The one-dimensional flash method ([6]) has evolved to become a standard ([14]) for determining the out-of-plane component of

---

[1] Current address: Black and Decker, Inc., 701 East Joppa Road, Towson, MD 21286.

[2] To whom correspondence should be addressed.

Contributed by the Heat Transfer Division for publication in the JOURNAL OF HEAT TRANSFER. Manuscript received by the Heat Transfer Division, Jan. 30, 1999; revision received, June 18, 1999. Associate Technical Editor: D. Zumbrunnen.

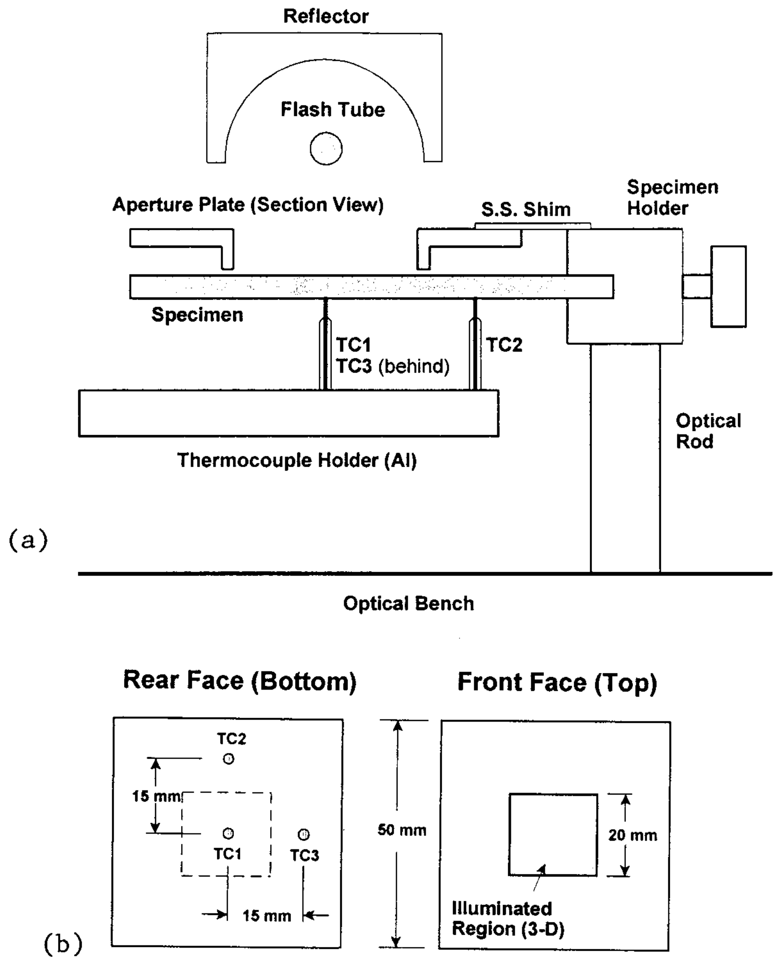

Fig. 1 (*a*) Schematic diagram of the orthogonal thermal diffusivity test device and (*b*) Illustration of the Illuminated central region and the thermocouple locations

thermal diffusivity α_z of solids. Briefly, the front surface of a nominally opaque planar specimen absorbs a burst of intense radiant energy and the temperature history of the rear surface is recorded. Then, α_z can then be estimated simply as

$$\alpha_z=\frac{1.37d^2}{\pi^2 t_{1/2}} \tag{1}$$

where d is the thickness of the specimen and $t_{1/2}$ is the time required for the rear surface to reach one-half its maximum temperature $T_{\max}$. As determined by Eq. (1), α_z is independent of the amount of energy absorbed, requiring only that an ''instantaneous'' burst of energy be absorbed at the front surface. Degiovanni [15] and the ASTM [14] discuss criteria for the flash to be considered instantaneous. Taylor [16] and Balageas [17] have reviewed the flash method and the literature that describes it, and discussed some of the methods used for more accurate data reduction.

In this extension of the flash method to three dimensions, a plane specimen is mounted horizontally such that the top face is illuminated and the temperatures are measured on the bottom. A linear xenon flashtube, mounted in an aluminum reflector, illuminates the top face of the specimen (Fig. 1(*a*)). A 50×50 mm aperture plate with a 20×20 mm opening is mounted between the flash and the specimen. Three 0.254-mm diameter E-type thermocouple probes are mounted into miniature glass pipettes which are in turn glued into holes in an aluminum fixture. The thermocouple probes protrude from the glass pipettes such that the pipettes are not in contact with the specimen. These coplanar thermocouples form the apexes of a right isosceles triangle which has two 15-mm sides and when aligned with the aperture, measure the temperature at the center of the projection of the lighted area and at two points outside this projection (Fig. 1(*b*)). The aperture plate is mounted on a linear translation stage that allows adjustment of the spacing between the aperture and the thermocouples while maintaining accurate alignment. A small amount of high thermal conductivity silicone paste is applied to the thermocouples to insure good contact between the thermocouple probe and the specimen surface. The paste is applied under magnification to aid in consistent application.

Measurements of five flashes with a broad band (320–1100 nm) photodetector indicated that the total flash output is consistent with a standard deviation of less than 0.37 percent and reaches its peak at 400 μs. Greater than 94 percent of the flash energy is released within 1 ms, and at any instant the flash level was repeatable to within 1.4 percent. The ASTM standard stipulates that for Eq. (1) to be valid in the one-dimensional tests, the flash must last less than 6 ms for the most restrictive specimens used here (2.25-mm thick stainless steel). Measurements showed that the region underneath the aperture opening was uniformly illuminated (less than a one percent variation) along the axis of the bulb and that there was an eight percent variation perpendicular to the axis. An opal glass diffuser was added between the flash and the aperture and subsequent measurements indicated about one percent variation across the entire illuminated region.

The amplified thermocouple signal is sent to a temperature-compensated terminal strip, which is connected to an eight-channel A/D board mounted in a 90 MHz Pentium PC. The ability of the temperature measurement system to adequately resolve the temperature history of the polymer specimens for which this system is intended can be evaluated indirectly by measuring the thermal diffusivity of a reference material that has a higher diffusivity. Stainless steel (AISI 304), with a thermal diffusivity roughly 40 times that of PVC, has a $t_{1/2}=0.18$ s for $d=2.25$ mm, as compared with 13 s for 3-mm thick PVC specimen. The measured α_z was 3.91 mm^2/s for the AISI 304 sample, within the range of reference values ($2.84<\alpha<5.04$ mm^2/s ([18])) and within about one percent of 3.95 mm^2/s ([19]). By extension, if the temperature measurement system accurately captures the temperature response of AISI 304, then it is sufficiently fast for measurements made with PVC specimens of similar thickness.

Data Reduction. A Marquardt algorithm ([20]) estimated the components of $\boldsymbol{\alpha}$ from the bottom face temperature histories and the calculations of a finite difference model. Data reduction for the one-dimensional measurements of α_z alone, made by removing the aperture plate, was performed using both Eq. (1) and a Marquardt algorithm with a one-dimensional finite difference model.

The diffusion equation for a nondeforming solid, assuming the absence of stress power and volumetric heat addition, is written as

$$\frac{\partial T(\mathbf{x},T)}{\partial t}=\boldsymbol{\alpha}:\boldsymbol{\nabla}(\boldsymbol{\nabla}T(\mathbf{x},t)) \tag{2}$$

where T is temperature, $\mathbf{x}$ position, and t time. For the one-dimensional measurements, the bottom and, after the flash, the top faces are assumed adiabatic. Before the end of the flash, a time-dependent heat flux is assumed on the top face. Thus, the boundary conditions are

$$z=0 \quad \text{and} \quad t<t_f\rightarrow q''=q''_{\max}f(t)$$

$$z=0 \quad \text{and} \quad t>t_f\rightarrow dT/dz=0$$

$$z=d\rightarrow dT/dz=0$$

where q'' is the top face heat flux, t_f the flash duration, $f(t)$ a time varying function whose form models the output of the photodetector in the aforementioned measurements, and $q''_{\max}$ the maximum heat flux absorbed by the surface. Two parameters are estimated for the one-dimensional tests: α_z and $q''_{\max}/\rho C$, where ρ is the mass density and C the specific heat. A grid of nine nodes was found to converge to within 0.1 percent of the temperature calculated with a grid of 51 nodes; 11 nodes were used in the data reduction. A global energy balance was maintained to better than 0.01 percent.

Figure 2 illustrates the geometry for the three-dimensional model for the data reduction of the components of $\boldsymbol{\alpha}$. Adiabatic boundaries were specified on the symmetry planes and at the distant edges of the specimen. A convective boundary was specified on the top face, except under the aperture opening, where a spatially uniform time-varying heat flux was specified during illumination, followed by a convective boundary condition after the flash. The bottom boundary assumes conduction into the air underneath the specimen. Such boundary conditions may be written

$$z=0,\ t<t_f,\quad \text{and} \quad x\leqslant x_j,\ y\leqslant y_f\rightarrow q''=q''_{\max}f(t)$$

$$z=0,\ t>t_f,\quad \text{and} \quad x\leqslant x_f,\ y\leqslant y_f\rightarrow -k_z dT/dz=h(T-T_\infty)$$

$$z=0 \quad \text{and} \quad x>x_f,\ y>y_f\rightarrow -k_z dT/dz=h(T-T_\infty)$$

$$z=d\rightarrow k_z dT/dz=k_a dT_a/dz$$

$$x,y=0,\ l\rightarrow dT/dn=0$$

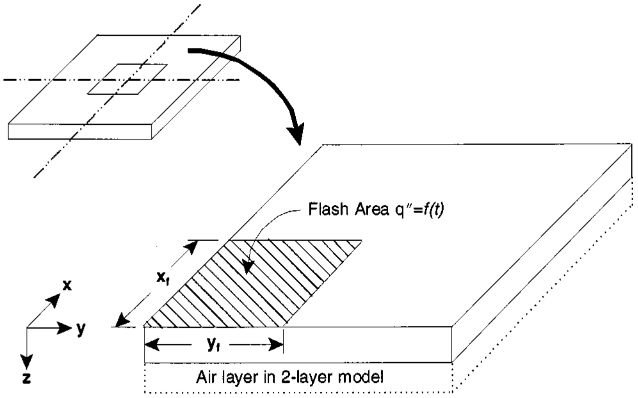

Fig. 2 Schematic diagram of the geometry for the three-dimensional model

where x_f and y_f are the half-lengths of the illuminated region, k_z and k_a the thermal conductivities of the specimen and air, respectively, l the half-length of the specimen, z the out-of-plane direction, T_∞ the ambient temperature, and h the convective heat transfer coefficient. Note, k_z is estimated as part of these tests using the estimated value of α_z and reference values of C and ρ. The Marquardt program for three-dimensional measurements estimates five parameters: the three components of thermal diffusivity (α_x, α_y, and α_z), heat flux term defined $q''_{\max}/\rho C$, and heat loss term defined $2h\,dt/\rho C\,dx$, where dx is the node spacing and dt the timestep. A $7\times21\times21$ grid produced temperature histories within 0.1 percent of a $21\times121\times121$ grid for the three-dimensional model; an $11\times21\times21$ grid was used for data reduction.

Conduction in the air layer underneath the specimen plays a significant role in heating specimens of moderate thermal diffusivity at the transverse thermocouple locations. The aperture opening is 10 mm on a side and the distance between the central and transverse thermocouples is 15 mm, but $d\approx3$ mm. Once the air has been heated by the central region of the bottom face of the specimen, it provides an alternative path for energy transport. Since the total temperature rise of the transverse thermocouples in the three-dimensional tests run here is on the order of 0.3°C, even a small addition of energy from the air can cause significant error in the determination of in-plane thermal diffusivity. The Rayleigh number is small enough to indicate the absence of buoyancy driven flows in the air underneath the specimen ([21]). This was confirmed by measurements of the temperature response of the air and comparison with finite difference modeling. Calculated specimen temperatures were unchanged for included air layers thicker than 13 mm.

Measurement Protocol. The specimen is first coated with flat black paint (≈0.02 mm thick) to enhance absorption of the flash energy at the top surface. Absorption of the flash energy *within* the material requires correction to the data reduction analysis ([22]). Taylor [16] suggested that excessive heat loss, energy addition via conduction or convection, or energy absorption within the material would cause α_z to vary by more than five percent as a function of $\tau(=t/t_{1/2})$. The effectiveness of the paint was thus assured by one-dimensional tests for which α_z varied less than two percent for $1.0<\tau<4.5$ for the otherwise most transparent material examined here (plate glass). After coating, the specimen is placed into the specimen holder, the thermocouples positioned on the bottom face, and the aperture plate adjusted to within 0.5 mm of the top surface. Data acquisition is started, the bulb flashed, and the temperature history recorded for the three thermocouples. Following data acquisition, the specimen is allowed to cool to the ambient temperature before the test is repeated. After testing is complete, the geometry of the illuminated area, as marked by discoloration of the paint, and thermocouple locations, as marked by the high thermal conductivity paste, are

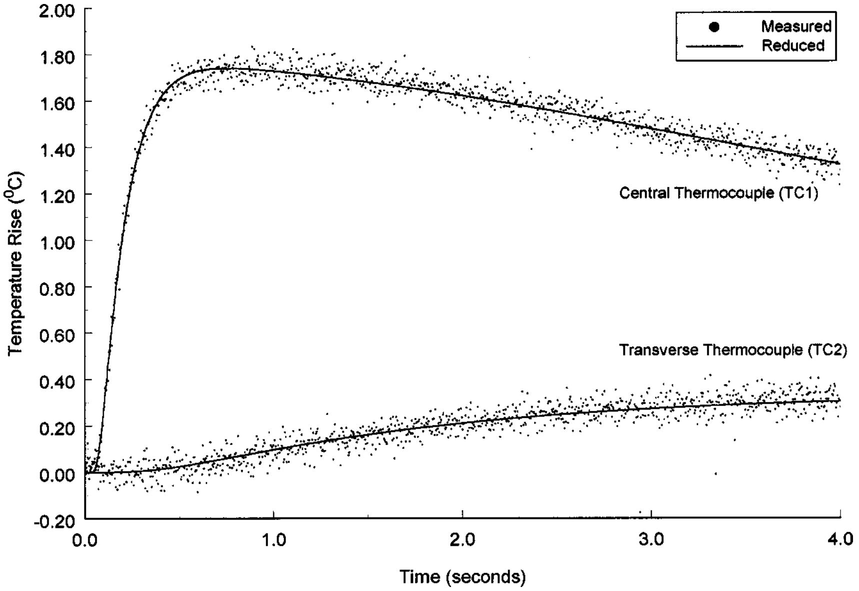

Fig. 3 Measured temperature history for an AISI 304 specimen with the calculated response from the Marquardt algorithm

checked to confirm the pretest values. The thermal diffusivities are then calculated using the Marquardt algorithm.

The one-dimensional tests met ASTM E-1461-92 ([14]) criteria. The uncertainty in the one-dimensional tests can be found using Eq. (1) and the uncertainties of measuring the thickness of the specimen (20 μm) and the time of the temperature history (0.004 s). Using the method of Kline and McClintock [23], the uncertainty of the one-dimensional measurements is 0.12, 0.0072, and 0.0014 mm^2/s for the AISI 304, glass, and PVC measurements, respectively. For the three-dimensional measurements, the temperatures of the three thermocouples were brought into agreement at the start of each test by bringing them to a common initial value based on their pre-flash average readings. These corrections were less than 0.02°C. Analysis revealed the noise in the temperature history data to be randomly distributed, thus not affecting the Marquardt fit. Based on statistical analysis of the three-dimensional results, the uncertainty in the in-plane values is 0.22, 0.017, 0.008 mm^2/s for the AISI 304, glass, and PVC measurements, respectively, and for the out-of-plane values of 0.14, 0.008, 0.004 mm^2/s for AISI 304, glass, and PVC measurements, respectively.

Results

First, three-dimensional measurements were made in materials with isotropic thermal properties, AISI 304 stainless steel and plate glass. As mentioned above, one-dimensional measurements of α_z of AISI 304 were within one percent of a reference value. Typical temperature histories of the central and one of the transverse thermocouples for the three-dimensional tests, along with the Marquardt fits, are shown in Fig. 3; the other transverse thermocouple trace is indistinguishable from the one shown. These curves illustrate the rapid rise in temperature for the central thermocouple as compared with the transverse ones and the relative magnitudes of the thermocouple signals. Also, the rapid decline of the central temperature history, as compared with a standard one-dimensional test, results from only part of the front face being illuminated and the subsequent lateral diffusion. The thermal diffusivity of AISI 304 is large enough that accounting for the heat conduction in the air beneath the specimen changes the measured values by less than one percent. Table 1 lists the average (of ten tests) of values of the components of $\boldsymbol{\alpha}$, the one-dimensional α_z, and the range of reference values ([18]). The three-dimensional values are in good agreement with each other and deviate from the one-dimensional value by less than two percent. The standard deviation is less than 0.1 mm^2/s for each of the components, demonstrating the repeatability of the measurements.

Next, a 2.28 mm specimen of plate glass with unknown composition was cut and its top face painted. Table 1 lists its average α_z measured in a series of 15 one-dimensional flash tests: this value falls within the range for plate glass ([18]), also in Table 1. Ten three-dimensional tests were then run on the coated plate glass specimen. Data reduction included the heat conduction in the air beneath the specimen because neglecting it led to a five percent error. The measured components of diffusivity varied from the one-dimensional value by less than 1.5 percent.

Initial measurements with PVC *sheet* indicated unexpected anisotropy in the thermal diffusivity. Lachi and Degiovanni [10] had measured the out-of-plane and radial in-plane components of $\boldsymbol{\alpha}$ of PVC and found agreement to within three percent in these two directions. Choy et al. [1] demonstrated, however, that initially isotropic semi-crystalline polymers may develop anisotropic thermal diffusivity when subjected to plastic deformation. In order to determine if the initial three-dimensional results were an experimental artifact, other PVC specimens of the same composition were sought that had undergone less deformation during manufacturing. A 102-mm diameter extruded PVC rod of the same composition and from the same manufacturer was chosen because suitable specimens could be cut from its central region. Three specimens were cut so that the normal of each specimen was oriented along an axis of the rectangular coordinate system (Fig. 4). The specimens were then milled to thicknesses of 3.32, 3.28, and 3.26 mm; the specimens were flat to within 0.02 mm. Fifteen one-dimensional tests were run on each of these specimens. The

Table 1 Thermal diffusivities from references and measurements

Material	α_{ref} mm^2/s	One-dimensional α_z mm^2/s	α_x mm^2/s	α_y mm^2/s	α_z mm^2/s
AISI 304	2.84 . . . 5.04	3.91	3.86	3.98	3.88
glass	0.36 . . . 0.62	0.430	0.436	0.433	0.428
PVC rod	0.107 . . . 0.269	0.108	0.109	0.111	0.107
PVC sheet	0.107 . . . 0.269	0.112	0.127	0.130	0.106

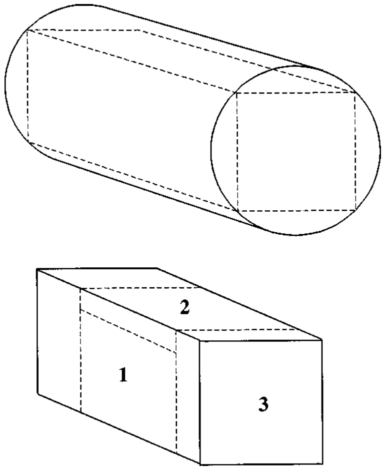

Fig. 4 Specimen orientation with respect to the PVC rod

average one-dimensional α_z for the three specimens is listed in Table 1 along with the range of reference values ([24]). The standard deviation of α_z was 0.004 mm^2/s, indicating the isotropy of the material.

Five three-dimensional tests were then performed on each of the three specimens. Sample temperature histories for thermocouples 1 and 2 are shown in Fig. 5 along with the Marquardt model results. Only half of the measured points are shown so that the Marquardt reduction line is clearly visible. These histories are similar to Fig. 3, except that the response is slower for the PVC. Neglecting heat conduction in the air underneath the specimen would have caused errors of about 20 percent in the in-plane thermal diffusivity values. Heat addition from the air layer to the underside of the specimen at the transverse thermocouple locations was indicated by measuring the temperature history of the air 0.5 mm below the PVC specimen following a flash. The air was hotter than the surface at these locations. (When the tests were repeated for AISI 304, the specimen was hotter than the air.) Similar measurements on the top of the specimen confirmed that convection effects dominate there.

Then, nine specimens were cut from three separate 3.2-mm thick PVC sheets. These sheets were obtained from the supplier at different times, but came from the same manufacturer as the PVC rod and were of the same composition. Five three-dimensional tests were performed on each specimen. All specimens were oriented in the same direction relative to the rolling during manufacturing and heat conduction in the air layer was modeled for all data reduction. Table 1 summarizes the mean values of the measurements of the components of $\boldsymbol{\alpha}$ for the PVC sheet. The out-of-plane (z-direction) diffusivity for the three sheets are not significantly different from the isotropic value measured in the rod. The inplane components are about 15 percent higher than α_z.

Conclusions

The flash method has been extended for measuring the three orthogonal components of thermal diffusivity simultaneously. Careful measurements in AISI 304, plate glass, and PVC rod indicated that the system measures the in-plane and out-of-plane components of thermal diffusivity accurately, over a wide range of thermal diffusivities. The necessity of including heat conduction in the air underneath the specimen has been demonstrated for materials of moderate $\boldsymbol{\alpha}$. This is especially important for materials such as the biological tissues that must be maintained well-hydrated, thus prohibiting their being tested in a vacuum.

Comparing the results of the PVC sheet and rod illustrates the utility of the device described here. The rod and sheet specimens were tested using the same test protocols, experimental apparatus, and data reduction, suggesting that the difference in $\boldsymbol{\alpha}$ is due to the material processing for the sheet PVC. The manufacturer of the PVC stated that the sheet undergoes significantly more deformation during its manufacture. After manufacturing, only small changes in dimension occur when a rod is heated above the glass transition temperature T_g, where as PVC sheets heated above T_g may shrink by 7 to 15 percent ([25]). In addition, the mechanical deformation imposed at the top and bottom surfaces of the sheet by the first roller may induce material orientation in the in-plane directions. Because the overall thickness of the specimen is only about 3 mm, this surface effect may play a role throughout the thickness of the specimen. The rod specimens were cut well below the surface and the specimen thickness is small, about three percent of the total diameter of the rod. Thus, an extrusion reduc-

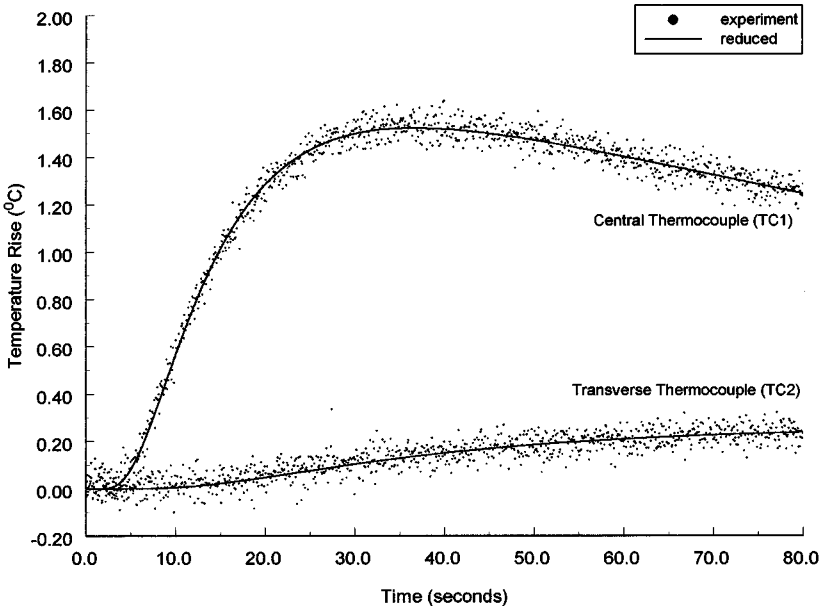

Fig. 5 Measured temperature history for a PVC rod specimen with the calculated response from the Marquardt algorithm

tion of up to 15 percent in the sheet appears to cause a 15 percent change in the in-plane components of thermal diffusivity. This anisotropy in the thermal properties of a common polymer, such as PVC, demonstrates the need for such multiaxial thermal diffusivity testing as described here.

Acknowledgment

The authors gratefully acknowledge the Whitaker Foundation for sponsoring this research under its Biomedical Engineering Research Grants Program, and the Army Research Office for support through grant DAAH-04-95-2-2.

Nomenclature

C = specific heat (J/kg K)
d = specimen thickness (m)
h = convective heat transfer coefficient (W/m^2 K)
k_a = thermal conductivity of air (W/m K)
k_z = through the specimen component of thermal conductivity (W/m K)
l = in-plane half-length of the specimen (m)
n = normal to a boundary surface
q'' = heat flux vector (W/m^2)
t = time (s)
t_f = flash duration (s)
$t_{1/2}$ = time after flash at which rear surface reaches $T_{\max}/2$ (s)
T = temperature (°C)
T_∞ = ambient temperature surrounding specimen (°C)
$T_{\max}$ = maximum bottom face temperature of the specimen (°C)
$\mathbf{x}$ = position vector with components x, y, and z (m)
x_f = half-length of the illuminated region in x-direction (m)
y_f = half-length of the illuminated region in y-direction (m)

Greek Letters

$\boldsymbol{\alpha}$ = thermal diffusivity tensor (mm^2/s)
α = isotropic thermal diffusivity (mm^2/s)
α_i = Component of thermal diffusivity tensor in ith direction (mm^2/s)
ρ = mass density (kg/m^3)
τ = scaled time defined as $t/t_{1/2}$

References

[1] Choy, C. L., Luk, W. H., and Chen, F. C., 1978, ''Thermal Conductivity of Highly Oriented Polyethylene.'' Polymer, **19**, pp. 155–162.
[2] Taylor, R. E., and Kelsic, B. H., 1986, ''Parameters Governing Thermal Diffusivity Measurements of Unidirectional Fiber-Reinforced Composites,'' ASME J. Heat Transfer, **108**, pp. 161–165.
[3] Dowding, K. J., Beck, J. V., and Blackwell, B. F., 1996, ''Estimation of Directional-Dependent Thermal Properties in a Carbon-Carbon Composite,'' Int. J. Heat Mass Transf., **39**, No. 15, pp. 3157–3164.
[4] Ju, Y. S., Kurabayashi, K., and Goodson, K. E., 1999, ''Thermal Characterization of Anisotropic Thin Dielectric Films Using Harmonic Joule Heating.'' Thin Solid Films, **339**, pp. 160–164.
[5] Valvano, J. W., Dalvi, V. P., and Pearce, J. A., 1993, ''Directional Thermal Conductivity Measured in Bovine Aorta.'' *Advances in Bioheat and Mass Transfer*, Vol. 268, ASME, New York, pp. 37–40.
[6] Parker, W. J., Jenkins, R. J., Butler, C. P., and Abbott, G. L., 1961, ''Flash Method of Determining Thermal Diffusivity, Heat Capacity, and Thermal Conductivity,'' J. Appl. Phys., **32**, pp. 1679–1684.
[7] Donaldson, A. B., and Taylor, R. E., 1975, ''Thermal Diffusivity Measurement by a Radial Heat Flow Method,'' J. Appl. Phys., **46**, pp. 4584–4589.
[8] Chu, F. I., Taylor, R. E., and Donaldson, A. B., 1980, ''Thermal Diffusivity Measurements at High Temperatures by the Radial Flash Method,'' J. Appl. Phys., **51**, pp. 336–341.
[9] Maillet, D., Lachi, M., and Degiovanni, A., 1990, ''Simultaneous Measurements of Axial and Radial Thermal Diffusivities of an Anisotropic Solid in a Thin Plate: Application to Multi-layered Materials,'' *Thermal Conductivity 21*, C. J. Cremers and H. A. Fine, eds., Plenum Press, New York, pp. 91–107.
[10] Lachi, M., and Degiovanni, A., 1991, ''Determination des Diffusivites Thermiques des Materiaux Anisotropes par Methode Flash Bidirectionnelle,'' J. Phys. III., **12**, pp. 2027–2046.
[11] Fujii, M., Park, S. C., Tomimura, T., and Zhang, X., 1997, ''A Noncontact Method for Measuring Thermal Conductivity and Thermal Diffusivity of Anisotropic Materials,'' Int. J. Thermophys., **18**, No. 1, pp. 251–267.
[12] Sawaf, B., and Özişik, N., 1995, ''Determination of the Constant Thermal Conductivity of Orthotropic Materials by Inverse Analysis.'' Int. Comm. Heat Mass Transf., **22**, No. 2, pp. 201–211.
[13] Wright, N. T., da Silva, M. G., Doss, D. J., and Humphrey, J. D., 1995, ''Measuring Thermal Properties of Elastomers Subject To Finite Strain,'' *Thermal Conductivity 25*, C. J. Cremers and H. A. Fine, eds., Plenum Press, New York.
[14] ASTM, 1992, ''Standard Test Method for Thermal Diffusivity of Solids by the Flash Method,'' E 1461–92, Philadelphia.
[15] Degiovanni, A., 1987, ''Correction de longueur d'implosion pour la mesure de la diffusivité thermique par méthode flash,'' Int. J. Heat Mass Transf., **30**, No. 10, pp. 2199–2200.
[16] Taylor, R. E., 1975, ''Critical Evaluation of Flash Method for Measuring Thermal Diffusivity,'' Rev. Int. Htes Temp. et Refract., **12**, pp. 141–145.
[17] Balageas, D. L., 1989, ''Thermal Diffusivity Measurement by Pulsed Methods,'' High Temp.-High Press., **21**, pp. 85–96.
[18] Touloukian, Y. S., Powell, R. W., Ho, C. Y., and Klemens, P. G., 1970, *Thermophysical Properties of Matter*, IFI Plenum Press, New York.
[19] Incropera, F. P., and DeWitt, D. P., 1996, *Fundamentals of Heat and Mass Transfer*, 4th Ed., John Wiley and Sons, New York.
[20] Press, W. H., Flanery, B. P., Teukolsky, S. A., and Vettering, W. T., 1986, *Numerical Recipes*, 1st Ed., Cambridge University Press, Cambridge, UK.
[21] Gebhart, B., Jaluria, Y., Mahajan, R. L., and Sammakia, B., 1988, *Buoyancy-Induced Flows and Transport*, Hemisphere, Washington, DC.
[22] McMasters, R. L., Beck, J. V., Dinwiddie, R. B., and Wang, H., 1999, ''Accounting for Penetration of Laser Heating in Flash Thermal Diffusivity Experiments,'' ASME J. Heat Transfer, **121**, pp. 15–21.
[23] Kline, S. J., and McClintock, F. A., 1953, ''Describing Uncertainties in Single-Sample Experiments,'' Mech. Engr., **75**, pp. 3–8.
[24] Titow, W. V., 1990, *PVC Plastics-Properties, Processing and Applications*, Elsevier, New York.
[25] Wagner, J., 1998, personal communication.

M. Becker
Professor Emeritus,
Member ASME,
Oregon Graduate Institute,
P.O. Box 1000,
Portland, OR 97291
e-mail: mbecker@nycap.rr.com

Nonlinear Transient Heat Conduction Using Similarity Groups

Nonlinear response is studied using similarity groups. The nonlinear solution is similar to the linear solution except with properties evaluated at the local temperature and is consistent with reported empirical observations that, near the heat source, high-temperature properties are needed to predict cooling times to high temperatures and that low temperature properties are needed to predict cooling time to low temperatures. For position-dependent characteristics of the solution away from the source, like magnitudes and locations of peak temperatures, nonlinear and linear solutions are similar if local properties are evaluated at current temperatures prevailing near the source.
[S0022-1481(00)02701-8]

Introduction

Heat conduction is a nonlinear problem because thermal properties—conductivity and heat capacity—depend on temperature. Much use of analytical methods has been made in modeling thermal processing of materials. These processes can include very rapid and highly localized transients. Most of this modeling has been based on linear assumptions. Kasuya and Yurioka [1] have presented a comprehensive linear solution, which has provided good agreement with experimental results. This agreement, however, required use of different values of thermal properties for predicting different quantities. Earlier comparison of linear analytical solutions with numerical and experimental results also found that values of properties suitable for predicting certain key parameters were not as good for predicting other important parameters ([2]).

In steady-state situations, a change of variables (Kirchhoff transformation) can be introduced to transform to a linear problem. The new variable is the integral over temperature of the thermal conductivity ([3]). In transient situations, however, the transformed equation depends on the temperature-dependent thermal diffusivity and remains nonlinear. Grosh and Trabant [4] applied the transformation and assumed thermal diffusivity to be independent of temperature, i.e., assumed that thermal conductivity and heat capacity varied with temperature in exactly the same way. Myers et al. [5], however, noted that while heat capacity typically increases with temperature, thermal conductivity generally does not, and that the assumption of heat capacity and thermal conductivity varying in the same manner is of limited utility.

Transient heat conduction with temperature-dependent properties is examined in this paper. The physical significance of the solutions is studied, and the implications for understanding process variables are shown. The restrictions on temperature dependence of properties required to obtain solutions are examined to determine whether or to what degree the resulting solutions have the potential for being realistic. The thermal properties selected by Kasuya and Yurioka and by Moore et al. are compared with what may be expected on the basis of nonlinear analysis. It is shown that the adjustments made to linear solutions in the literature are consistent with nonlinear analysis.

Nonlinear response to a pulsed source has been studied using similarity variables. Ames [6] Logan [7], and Ozisik [8] have reviewed the subject. Early work was published by Zeldovich and Kompaneets [9], Ames [10], Boyer [11], Heaslet and Alskne [12], and Pattle [13] have also contributed.

The similarity solutions entail assuming that thermal conductivity and heat capacity vary as powers of temperature. If the properties increase with increasing temperature, they go to zero at the ambient temperature. Similarly, if the properties decline with increasing temperature, they go to infinity at the ambient temperature. These extreme limiting values raise concern as to whether this form of behavior can be of use in practical thermal cycle situations. It will be shown that, while there are limitations, useful results can be obtained for parameters of practical importance. It also is noted where results are artifacts of extreme limits of properties.

Most attention paid in the literature has been for situations where properties increase with temperature. Zeldovich and Kompaneets [9] present a solution for declining conductivity in plane geometry. The other authors cited consider only properties increasing with temperature. For important materials, such as low-carbon steels, thermal conductivity declines with temperature. This paper will give considerable attention to this case.

The literature has emphasized mathematical aspects of the problem. This paper examines the physical interpretations to solutions, and relates these interpretations to the types of adjustment that have been made to linear solutions to improve agreement with experiment. Two interesting findings are reported. One is that in the vicinity of the heat source, the nonlinear solution is similar to the linear solution with properties evaluated at the current temperature. The second finding is that away from the source, the nonlinear solution is similar to the linear solution with properties evaluated at the current temperature prevailing near the heat source. These findings imply a theoretical basis for practices found in the literature for accommodating linear solutions to experimental results.

Pulse Response

The time-dependent heat conduction equation is

$$\rho c \frac{\partial T}{\partial t} = (1/r^{m-1}) \frac{\partial}{\partial r}\left(r^{m-1} k \frac{\partial T}{\partial r} \right) + Q\,\delta(r)\,\delta(t) \tag{1}$$

where m of 1, 2, and 3 correspond, respectively, to plane, cylindrical, and spherical geometry. The source term involves delta functions, so that the source is zero except at the origin at time zero, and so that the integral over volume and time of the source is Q. Temperature is relative to the reference ambient temperature that prevails everywhere before the introduction of the source.

Contribution by the Heat Transfer Division for publication in the JOURNAL OF HEAT TRANSFER. Manuscript received by the Heat Transfer Division, July 15, 1998; revision received, June 29, 1999. Associate Technical Editor: D. Kaminski.

Thus, the temperature is zero everywhere for $t<0$. In addition, the temperature must go to zero as r goes to infinity for any $t>0$.

Let the conductivity and the heat capacity depend on powers of temperature, i.e.,

$$k=k_0(T/T_0)^s \tag{2}$$

$$\rho c=(\rho c)_0(T/T_0)^p \tag{3}$$

If a new variable U is defined as [8]

$$U=(T/T_0)^{p+1}, \tag{4}$$

then the heat conduction equation for $t>0$ becomes

$$\frac{\partial U}{\partial \tau}=(1/r^{m-1})\frac{\partial}{\partial r}\left(r^{m-1}U^n\frac{\partial U}{\partial r}\right) \tag{5}$$

where the parameter n is defined by

$$n=(s-p)/(p+1) \tag{6}$$

and where a modified time is defined in terms of thermal diffusivity α by

$$\tau=tk_0/(\rho c)_0=\alpha_0 t. \tag{7}$$

Nonlinear diffusion and heat conduction have been addressed by several authors using similarity transformations. With the exception of Zeldovich and Kompaneets [9], who presented a solution for plane geometry for negative n, the literature has concentrated on positive n. The case of negative n is important, however. For important materials, like low-carbon steels that are subjected to pulsed heating, the thermal conductivity declines with increasing temperature (i.e., s is negative) and the heat capacity increases with increasing temperature (i.e., p is positive). For such materials n is negative.

The similarity method and its application to the derivation of temperature distributions are given in the Appendix. For positive n, from Eqs. (A12) and (A15),

$$U=[B^{1/n}/\tau^{m/(2+mn)}]\{1-Br^2/\tau^{2/(2+mn)}\}^{1/n}, \tag{8}$$

where B is the constant of integration. This solution goes to zero at a finite radius. This unusual feature, which is not present in the linear solution

$$T=(B_2/\tau^{m/2})\exp(-r^2/4\tau), \tag{9}$$

has been the focus of much of the attention given to nonlinear solutions.

For negative n, with $q=-n$, Eqs. (A12) and (A18) yield

$$U=\frac{1}{\tau^{m/(2-mq)}}\,\frac{A}{1+\dfrac{qA}{2(2-mq)}\dfrac{r^2}{\tau^{2/(2-mq)}}}^{1/q}. \tag{10}$$

The constant A is obtained by applying

$$\int\int \rho c\, dT\, dV=\frac{(\rho cT)_0}{p+1}\int U\, dV=Q \tag{11}$$

where Q is the amplitude of the pulsed heat source, and V is volume. The integrals in the three standard geometries are evaluated in the Appendix in terms of gamma functions. In cylindrical geometry, A is given by Eq. (A30):

$$A=\left[\frac{Q(p+1)}{4\pi(\rho cT)_0}\right]^{q/(1-q)} \tag{12}$$

The formula is relatively simple because of our ability to evaluate and use recurrence relations for gamma functions when dealing with integers. In plane geometry, the expression for A is more complicated and is given by Eq. (A24):

$$A=\left\{\frac{Q(p+1)\sqrt{q}}{2(\rho cT)_0\sqrt{2(2-q)}}\,\frac{2\Gamma(1/q)}{\Gamma(1/2)\Gamma(1/q-1/2)}\right\}^{2q/(2-q)}. \tag{13}$$

The solution for negative n (positive q), like the linear solution, is finite everywhere except at the origin at the instant of the pulse. It can be shown to go to the linear solution as q goes to zero.

In the nonlinear solution, the power $m/(2-mq)$ of the time variable where it appears alone differs from the corresponding power $m/2$ in the linear solution. It will be shown that the nature of this difference has important physical significance for the manner in which analytical solutions are used in practice.

In the linear solution, while the power of time where it appears alone depends on the geometry, the similarity variable appears in the same manner in all three geometries, depending on space and time by the ratio of the spatial variable to the square root of the time. In the nonlinear problem, the similarity variable depends upon the geometry, with the half power of time in all geometries replaced by the geometry-dependent $1/(2-mq)$.

Features of the Solution Near the Source

The pulse solution often is used to characterize thermal processes [14]. Analytical solutions provide insight into important parameters like cooling times and cooling intervals. In the treatment of steel, for example, the cooling interval between 800 and 500°C determines important characteristics of the resulting material.

For localized applications of heat, cooling times frequently are evaluated by considering regions near the heat sources. Under these circumstances, the spatial dependence term is not a factor, and the temperature varies as

$$T\sim 1/t^{m/(2-mq)(p+1)}. \tag{14}$$

We have converted from the U variable to temperature via the $(p+1)$ factor in the exponent. Noting the relation between $q=-n$ and the powers s and p, and clearing fractions leads to

$$T\sim 1/t^{m/[2+ms+(2-m)(p)]}. \tag{15}$$

Consider the case of cylindrical geometry $(m=2)$. The temperature dependence becomes

$$T\sim 1/t^{1/(1+s)} \tag{16}$$

Observe that near the source in cylindrical geometry, time variation depends on the temperature variation of thermal conductivity (through s in the exponent) but is insensitive to temperature variation of heat capacity. As we will see below, there is dependence on heat capacity variation in the ''constant'' coefficient. Near the heat source, the temperature in cylindrical geometry may be expressed as

$$\frac{T}{T_0}=\frac{A^{1/q(p+1)}}{\tau^{1/(1+s)}}. \tag{17}$$

This can be rearranged to

$$\left(\frac{T}{T_0}\right)^s\frac{T}{T_0}=\frac{k}{k_0}\frac{T}{T_0}=\frac{A^{(1+s)/q(p+1)}}{\tau}=\frac{A^{(1+q)/q}}{\tau}. \tag{18}$$

Note that we have made use of the assumed dependence of conductivity on temperature. Substituting the expression obtained for A, we find that

$$T=\frac{Q(p+1)}{4\pi kt}. \tag{19}$$

This differs from the linear result in that the actual temperature-dependent conductivity is in the denominator instead of the constant conductivity, and by presence of the factor $p+1$ in the numerator. This correspondence between linear and nonlinear solutions is significant relative to the type of data adjustment that has been performed to get linear analytic solutions to agree with experiments. The $p+1$ factor originated in the application of the boundary condition that required an integration of the heat capacity with temperature and gives the appearance, relative to the linear solution, of a reduction in thermal conductivity. This will be discussed further in the section on application.

To examine cooling time, let the terms be rearranged so that

$$t \sim 1/k(T)T. \tag{20}$$

In the linear case,

$$t \sim 1/k_0 T. \tag{21}$$

The physical significance of the nonlinear solution is that the cooling time still depends inversely on the product of conductivity and temperature. As will be seen later, authors who have fitted linear solutions to operating data have found agreement with experiment when parameters (conductivity, heat capacity) are selected corresponding to the temperature regions of interest.

The relation between cooling time, conductivity, and temperature is specific to the form of temperature variation (power of temperature) assumed. Thus, the conclusion that in cylindrical geometry, cooling time varies inversely as the product of conductivity and temperature will have validity to the extent that this power dependence is a reasonable representation over a temperature range of interest. In another section we shall observe that for carbon steel, this is indeed the case.

By a similar procedure as used for cylindrical geometry, we find that for plane geometry temperature varies as

$$T \sim 1/t^{1/(2+s+p)}. \tag{22}$$

We then find that cooling time varies as

$$t \sim 1/k\rho c T^2. \tag{23}$$

Again, this is the same dependence as in the linear case, except that here the actual temperature-dependent parameters are used. In spherical geometry, cooling time is

$$t \sim (\rho c)^{1/3}/kT^{2/3}. \tag{24}$$

Here also, dependence corresponds to the linear case, except that actual temperature-dependent properties are to be used.

The effect of nonlinearity on time variation near the source is a strong function of geometry. In plane geometry, the $2+s+p$ dependence implies that nonlinearities can either reinforce or interfere depending on the relative values of s and p. For stainless steels, s and p are both positive and there is reinforcement. For carbon steels, s is negative while p is positive and there is a tendency toward cancellation. In cylindrical geometry, however, the $1+s$ dependence implies that nonlinearities in conductivity and heat capacity cannot offset one another as in plane geometry. In addition to cooling times, cooling rates also have correspondence between linear and nonlinear solutions. Consider the cylindrical geometry case near the heat source. Rewriting the temperature-time relationship,

$$T^{s+1} = B_3/t, \tag{25}$$

where B_3 is a constant. Differentiating yields

$$(s+1)T^s(dT/dt) = -B_3/t^2 \sim -T^{2s+2}. \tag{26}$$

Noting that conductivity varies as T^s,

$$dT/dt \sim -k(T)T^2. \tag{27}$$

As in the linear case, cooling rate varies with conductivity and square of temperature in cylindrical geometry. In the nonlinear case the actual temperature-dependent conductivity applies.

It is convenient that the relationships for cooling times and cooling rates near the source are similar for linear and nonlinear cases. Next, we shall consider solutions at significant distances from the source.

Features of the Solution Away From the Source

The spatial solution away from the source has been used to develop models of grain growth and precipitate coarsening ([15,16]). Spatial dependence occurs through the similarity variable

$$\eta = r/\tau^{1/(2-mq)}. \tag{28}$$

In linear problems, q is zero and η reduces to

$$\eta_L = r/\tau^{1/2} \tag{29}$$

in all three geometries (plane, cylindrical, and spherical). Thus, in linear problems, the width of the Gaussian distribution is the same at any given time in all three geometries. In nonlinear problems, however, the solutions have different spatial variations in different geometries. Differences arise because of the presence of the $2-mq$ factor in the power to which time is raised.

In one sense, since the exponent of time in the similarity variable is different in each geometry, the form of the spatial dependence varies with geometry. In this regard, the character of the nonlinear solution may be viewed as distinct from the character of the linear solution. In another sense, there is important correspondence between linear and nonlinear solutions.

Consider the time dependence of Eq. (28) in cylindrical geometry $(m=2)$. Let

$$\tau^{1/(1-q)} = \tau^{(p+1)/(s+1)} = \tau\tau^{[(p+1)/(s+1)]-1} = \tau\tau^{(p-s)/(s+1)}. \tag{30}$$

Relating time to temperature near the heat source as per the previous section, and noting the relations between temperature and properties (Eqs. (2) and (3)), we obtain

$$\begin{aligned}\tau^{1/(1-q)} &= \tau\left\{\frac{A^{1/q(p+1)}}{[T(r=0)/T_0]}\right\}^{p-s} \\ &= A\tau\left(\frac{\rho c}{k}\right)_0 \frac{k}{\rho c}(r=0) = \frac{A\alpha(r=0)}{\alpha_0} = A\alpha(r=0)t.\end{aligned} \tag{31}$$

The spatial dependence term in the solution (Eq. (10)) thus becomes

$$\frac{1}{\left[1+\frac{qA}{4(1-q)}\frac{r^2}{\tau^{1/(1-q)}}\right]^{1/q}} = \frac{1}{\left[1+\frac{q}{1-q}\frac{r^2}{4\alpha(r=0,t)t}\right]^{1/q}}. \tag{32}$$

This has a spatial variation like that of the linear solution (Gaussian behavior results when $q \rightarrow 0$) except that properties are evaluated at the current temperature prevailing near the heat source.

Analogous procedures may be followed in other geometries. In plane geometry, for example, we let

$$\tau^{2/(2-q)} = \tau\tau^{2/(2-q)-1}. \tag{33}$$

This again leads to a similarity variable comparable to the linear one with thermal diffusivity evaluated near the heat source.

It therefore is interesting to observe that if properties for linear analysis are chosen so as to correspond to properties evaluated near the heat source at particular times or for particular time intervals, then there is a basis for using these same properties at these same times and time intervals at locations away from the heat source.

The spatial variation away from the source is affected by the magnitude of the heat source. In the nonlinear solution, the magnitude appears through the integration constant in two places. The solution has been given above as Eq. (7)

$$U = \frac{A^{1/q}}{\tau^{m/(2-mq)}}\left\{1+\frac{qA}{2(2-mq)}\eta^2\right\}^{-1/q} \tag{34}$$

To illustrate the dependence consider the value of A for cylindrical geometry (Eq. (12))

$$A=\left\{\frac{(p+1)Q}{4\pi(\rho cT)_0}\right\}^{q/(1-q)}. \tag{35}$$

When q and p go toward zero, i.e., when the problem tends toward linearity, the value of A tends toward unity independent of the magnitude of the heat source (any quantity raised to a zero power is one), and the spatial variation tends to lose dependence on magnitude of heat source.

While the value of A tends to unity, the qth root of A in the numerator does not lose dependence on magnitude in the limit as q goes to zero as can be seen from

$$A^{1/q}=\left\{\frac{(p+1)Q}{4\pi(\rho cT)_0}\right\}^{1/(1-q)}. \tag{36}$$

It is not surprising that the solution to a nonlinear problem does not scale simply with the amplitude of the source. It is worth noting that the complex dependence on the heat source appears primarily in the portion of the solution governing spatial dependence. In the purely time-dependent portion of the solution that governs behavior in the vicinity of the source, amplitude of the heat source does not affect the shape of the time-dependence. The solution exhibits some features that are artifacts of the assumed power form of property variation. When the heat source Q is very small, then A also is small and for nonzero q the spatial dependence of the temperature will be very flat. Alternatively, one can examine the spatial dependence given above in terms of thermal diffusivity at the current time near the heat source. Under such circumstances, heat transfer is dominated by conditions where the thermal conductivity is large tending toward infinity, and where the heat capacity tends toward zero. The thermal diffusivity tends toward infinity and the spatial correction tends toward zero. The nonlinear solutions have the potential for being useful when extreme aspects of property variation are not central to the character of the problem.

A common property of interest is the time at which peak temperature is attained at a particular location. This is obtained by setting the time derivative of the solution to zero. In cylindrical geometry, this leads to

$$\frac{r^2}{4\tau^{1/(1-q)}}=1. \tag{37}$$

In the nonlinear case, the value of q in the power of the time-like variable affects the manner in which peak time varies with position. To see correspondence with the linear solution, the expression may be expressed as

$$\frac{r^2}{4\alpha(r=0,t)t}=1. \tag{38}$$

Here again, results away from the source are similar to linear solution results if properties are evaluated near the heat source location at the current time.

Application

Responses to pulsed heat sources have been used to describe welding problems with rapidly moving heat sources ([14]). For many welding applications, the welding torch traverses a region before a significant amount of heat transfer can take place. Rapidly moving point sources have been represented by pulsed line sources and rapidly moving line sources have been represented by pulsed plane sources. When assumptions of rapid motion are not made, welding problems have been formulated as moving heat source problems ([17,18]). For parameters of particular interest like cooling times, which are evaluated in the immediate vicinity of the heat source, corresponding moving and pulsed problems (e.g., moving point and pulsed line) give similar results.

Cooling times and cooling rates are important in that they determine important characteristics of the product material ([14]). The rate of cooling in the interval between 800°C and 500°C, for example, governs phase and properties. The rate of cooling to 100°C influences susceptibility to stress corrosion cracking.

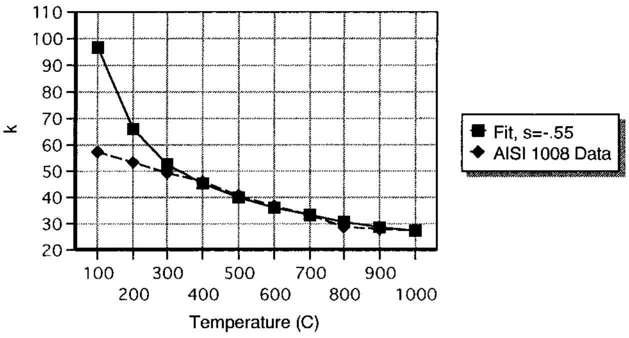

Fig. 1 Thermal conductivity of carbon steel

The pulse solution requires a particular form of temperature dependence, namely a property varying as a power of the temperature. In this relation, the reference temperature is the ambient temperature. Thus, far from the source (i.e., as the space variable goes to infinity), the temperature goes to zero. This boundary condition was applied in obtaining the solution.

For materials, like carbon steels, where the conductivity declines with temperature, a negative power would have to be used. This implies that the approximation to thermal conductivity would go to infinity as the temperature goes to zero. Thus, no matter how good a fit is obtained over some temperature range of interest, at some point the temperature dependence would become unrealistic. Similarly, heat capacity, with a positive power, tends toward zero at zero temperature.

The variation of thermal conductivity for AISI 1008 carbon steel ([19]) is shown in Fig. 1. The tabulated data did not have an entry at 900°C, so that value was obtained by interpolation. Conductivities for other carbon steels would be somewhat different, but not fundamentally so. Also shown in the figure is a power fit with $s=-0.55$. It may be observed that the power fit corresponds reasonably well to the tabulated data over a wide temperature range. As the temperature declines below 300°C, the power fit departs from the tabulated data, and would go to infinity at 0°C, taken as the ambient temperature.

Variation of specific heat for the same material, with tabulated data and a power fit, is shown in Fig. 2. Reasonable correspondence exists above 300°C. Below this temperature, the fit departs from the tabulated data, tending toward zero at 0°C. At temperatures higher than the range shown, there are fluctuations in effective specific heat associated with latent heat of phase transformation. The practice, even in numerical analysis, has been to smooth out these changes.

The essence of Figs. 1 and 2 is that over significant ranges of temperatures, power variation provides good approximation to ac-

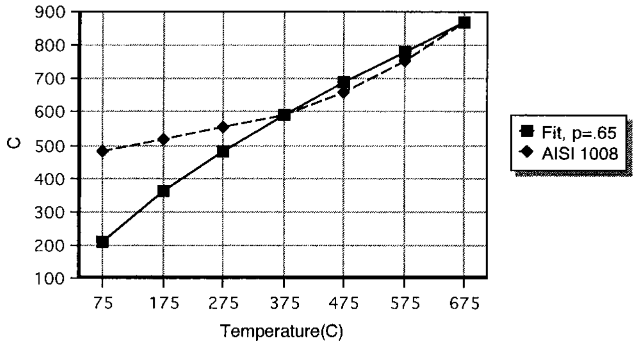

Fig. 2 Specific heat of carbon steel

tual dependence of the thermal properties of carbon steel on temperature. Accordingly, the features of the nonlinear solution may be expected to characterize actual physical situations.

Kasuya and Yurioka [1] compared linear analysis with experimental results. They found good agreement provided that they used different properties for predicting different quantities. To predict the time to cool from 1500°C to 100°C for shielded metal arc welding, they assumed an instantaneous line source (cylindrical model) and employed a thermal conductivity of 54.3 W/m °C. They did not specify the specific steel used, but this value is comparable to the value of conductivity at that temperature in Fig. 1. Similarly, they cited 1.2×10^{-5} m^2/s for thermal diffusivity as appropriate for cooling to 100 °C. This is comparable to low-temperature data cited in the literature. Results were obtained for several thicknesses spanning the range from thin to thick.

In studying cooling between 800°C and 500°C for shielded metal arc welding, Kasuya and Yurioka used an empirical formula for thermal conductivity that depended on the welding heat input energy and on the thermal efficiency of welding. For the cases they reported, thermal conductivity varied between 26.6 and 27.3 W/m °C. This is characteristic of high-temperature thermal conductivity of steel, but is still on the low side for the 800°C–500°C interval in which conductivity varies between roughly 30 and 40 W/m °C (Fig. 1). For two high heat input submerged arc and electrogas welding cases (one each), they report best results with conductivities of 38 and 31 W/m °C, respectively.

Moore et al. [2] previously had compared analytical and finite element predictions of cooling times after welding of thick and thin plates with measurements reported by several investigators. They found that a thermal conductivity of 25 W/m °C gave good predictions of cooling between 800°C and 500°C for both thick and thin plates, but commented that this conductivity value was unrealistically low. (Recall, however, that the $p+1$ term in the numerator of the nonlinear solution creates the appearance of a lower thermal conductivity.) The cooling times to 100°C, though, were substantially in error for thick plates. For thin plates, the value of 25 W/m °C could yield an accurate cooling time if combined with particular surface heat transfer coefficient.

Earlier investigators had used average values of thermal properties to study the entire temperature range. Goldak, Chakravarti, and Bibby [20] had used a conductivity of 41 W/m °C for analytical solutions used to compare with finite element calculations and measured results. Similarly, Myers et al. [5] had used a value of 41 W/m °C in analyzing a variety of welding problems. Moore et al. [2] observed that several values of conductivity in a broad range from 20 to 41 W/m °C had been used to obtain agreement between prediction and experiment.

Both Kasuya and Yurioka [1] and Moore et al. [2] recognize and note that there are simplifications associated with analytical solutions other than temperature-dependence of thermal properties. Moore et al. note that there are remaining simplifications even in sophisticated finite element models. Thus, to some degree, it may be expected that adjusting parameters can compensate somewhat for other assumptions. Moore et al. performed finite element calculations in which various assumptions associated with analytical solutions were studied separately. They found that for thick plates, using a single value of thermal conductivity had large effects on both the 800 °C–500°C interval and on cooling to 100°C, and for thin plates the effect was large for cooling to 100 deg.

Linear heat conduction analysis of weld thermal cycles, with all its simplifications, has proven to be useful in studying weld thermal cycles, especially when modifications have been introduced empirically to improve agreement with experiment. Nonlinear analysis indicates that the type of adjustment that has been made to thermal properties, namely using high-temperature values to predict cooling between 800°C and 500°C, and using low-temperature values to predict cooling to 100°C, has a theoretical basis.

Summary

Heat conduction following a localized pulse (delta function source) has been analyzed accounting for temperature variation of thermal properties. The solution method of similarity groups requires assuming that properties vary as powers of temperature. This form of variation has been shown to be appropriate over a substantial portion of the temperature range of interest. In the vicinity of the heat source, solutions have been found to be analogous to linear solutions, with properties evaluated at the current temperature. This behavior is consistent with findings in the literature that agreement with measurements are obtained when high-temperature properties are used to predict cooling times to high temperatures and low-temperature properties are used to predict cooling times to low temperatures. Away from the heat source, linear and nonlinear solutions correspond when properties found appropriate near the heat source at the same time are used.

Nomenclature

a = parameter in integration formula
A = integration constant
b = parameter in integration formula
B, B_2, B_3 = constants
c = specific heat
D = constant of integration
E = constant of integration
F = arbitrary function
g = function of the similarity variable
j = parameter in integration formula
k = thermal conductivity
m = geometry index (1, 2, 3 for plane, cylindrical, spherical)
n = nonlinearity exponent, $n=(s-p)/(p+1)$
p = nonlinearity exponent for heat capacity
q = negative of n
r = length dimension
Q = amplitude of heat source
s = nonlinearity exponent for thermal conductivity
t = time
T = temperature
U = $(T/T_0)p+1$
V = volume
x = plane geometry space variable
y = dummy variable in integration formula
z = parameter in similarity transformation

Greek Symbols

α = thermal diffusivity
β_1, β_2 = powers with space and time in similarity transformation
g = power with U in similarity transformation
G = gamma function
d = dirac delta function
h = similarity variable
μ = parameter in integration formula
v = parameter in integration formula
p = density
t = product of thermal diffusivity and time

Subscript

0 = reference condition

Appendix

Similarity Group Solution: General Approach. Consider a transformation of the dependent variable

$$\overline{U}=z^{\gamma}U \tag{A1}$$

and of the independent variables

$$\overline{r} = z^{\beta_1} r \tag{A2}$$

$$\overline{\tau} = z^{\beta_2} \tau \tag{A3}$$

where the parameter z is real and nonzero. The exponents are to be chosen such that the equation determining U is invariant under the transformation, i.e.,

$$F(r,\tau,U) = 0 = F(\overline{r},\overline{\tau},\overline{U}). \tag{A4}$$

With the exponents so chosen, we can define a similarity variable

$$\eta = r/\tau^{\beta 1/\beta 2} \tag{A5}$$

such that

$$U(r,\tau) = g(\eta)\tau^{\gamma/\beta_2}. \tag{A6}$$

The partial differential equation for U is reduced to an ordinary differential equation for g. For the transformations to be invariant, the exponents must be related by

$$\gamma/\beta_2 = \frac{2(\beta_1/\beta_2) - 1}{n}. \tag{A7}$$

When the similarity variables are substituted into the equation for U, the result is

$$\frac{d}{d\eta}\left(\eta^{m-1} g^n \frac{dg}{d\eta}\right) - \frac{2(\beta_1/\beta_2)-1}{n}\,\eta^{m-1} g + (\beta_1/\beta_2)\,\eta^m \frac{dg}{d\eta} = 0. \tag{A8}$$

To put this equation in the form of perfect differentials, choose

$$\beta_1/\beta_2 = 1/(2+mn). \tag{A9}$$

This leads to

$$\frac{d}{d\eta}\left(\eta^{m-1} g^n \frac{dg}{d\eta}\right) + \frac{1}{2+mn}\,\frac{d}{d\eta}(\eta^m g) = 0 \tag{A10}$$

with

$$\eta = \frac{r}{\tau^{1/(2+mn)}}. \tag{A11}$$

Upon solving the differential equation for g, U is given by

$$U = g(\eta)/\tau^{m/(2+mn)}. \tag{A12}$$

There are two cases of interest. One is for positive n, which has received the majority of attention in the literature. The other is for negative n, where we set $q=-n$. This case has received very little attention in the literature, but applies to important materials of interest like carbon steels.

Integrating the equation for g once gives

$$\eta^{m-1} g^n \frac{dg}{d\eta} + \frac{1}{2+mn}(\eta^m g) = E = 0. \tag{A13}$$

The integration constant E has been set to zero to satisfy the equation when $\eta = 0$. For $m=2$ and 3, it is clear that the left side is then zero. For $m=1$, note that symmetry requires that the derivative of g be zero. Integrating again yields (with C a constant of integration)

$$g^n/n + \eta^2/2(2+mn) = C. \tag{A14}$$

Rearranging terms and letting $B = Cn$

$$g = B^{1/n}\left\{1 - \frac{n}{2(2+mn)B}\,\eta^2\right\}^{1/n}. \tag{A15}$$

This solution implies that temperature would go to zero at a finite distance from the heat source.

For negative n with $q=-n$, the equation for g becomes

$$\frac{d}{d\eta}\left(\eta^{m-1} g^{-q} \frac{dg}{d\eta}\right) + \frac{1}{2-mq}\,\frac{d}{d\eta}(\eta^m g) = 0. \tag{A16}$$

Integrating, setting the integration constant to zero as with positive n, and integrating again yields

$$-1/qg^q + \frac{1}{2(2-mq)}\,\eta^2 = -D \tag{A17}$$

where D is a constant of integration. Letting $A = Dq$, the result may be expressed as

$$g = \frac{A^{1/q}}{\left\{1 + \dfrac{qA}{2(2-mq)}\,\eta^2\right\}^{1/q}}. \tag{A18}$$

This solution implies that temperature is finite at any finite distance from the heat source.

To evaluate the constant A, we impose the condition that at any time, the total energy in the system (integrated over volume V) is equal to the amount of energy introduced by the pulsed heat source, i.e.,

$$\int\int \rho c\, dT\, dV = \frac{(\rho c T)_0}{p+1}\int U\, dV = Q. \tag{A19}$$

We make use of the general integral relation

$$I = \int_0^\infty \frac{y^{\mu-1}}{(a+by^\nu)^{j+1}}\,dy = \frac{1}{\nu a^{j+1}}\left(\frac{a}{b}\right)^{\mu/\nu} \frac{\Gamma(\mu/\nu)\Gamma(1+j-\mu/\nu)}{\Gamma(1+j)}. \tag{A20}$$

Plane Geometry. In plane geometry, Eq. (A19) becomes

$$\frac{2(\rho c T)_0}{(p+1)\tau^{1/(2-q)}} A^{1/q} \int_0^\infty \frac{dx}{\left[1 + \dfrac{Aq}{2(2-q)\tau^{2/(2-q)}}\,x^2\right]^{1/q}} = Q. \tag{A21}$$

The integral is of the standard form if we identify

$$j+1 = 1/q, \quad \nu = 2, \quad \mu = 1, \quad a = 1 \tag{A22}$$

$$b = \frac{qA}{2(2-q)\tau^{2/(2-q)}}. \tag{A23}$$

This leads to

$$A = \left\{\frac{Q(p+1)\sqrt{q}}{2(\rho c T)_0\sqrt{2(2-q)}}\,\frac{2\Gamma(1/q)}{\Gamma(1/2)\Gamma(1/q-1/2)}\right\}^{2q/(2-q)}. \tag{A24}$$

Cylindrical Geometry. In cylindrical geometry, Eq. (A19) becomes

$$\frac{2\pi(\rho c T)_0}{\tau^{1/(1-q)}} A^{1/q} \int_0^\infty \frac{r\,dr}{\left[1 + \dfrac{Aq}{4(1-q)\tau^{1/(1-q)}}\,r^2\right]^{1/q}} = Q. \tag{A25}$$

For the standard integral, we identify

$$j+1 = 1/q, \quad \nu = 2, \quad \mu = 2, \quad a = 1 \tag{A26}$$

$$b = \frac{qA}{4(1-q)\tau^{1/(1-q)}}. \tag{A27}$$

If we note that

$$\Gamma(1) = 1 \tag{A28}$$

$$\Gamma\left(\frac{1}{q}\right) = \left(\frac{1}{q} - 1\right)\Gamma\left(\frac{1}{q} - 1\right) \tag{A29}$$

then we obtain

$$A = \left[\frac{Q(p+1)}{4\pi(\rho c T)_0}\right]^{q/(1-q)}. \tag{A30}$$

Spherical Geometry. In spherical geometry, Eq. ($A19$) becomes

$$\frac{4\pi(\rho cT)_0}{(p+1)\tau^{3/(2-3q)}}A^{1/q}\int_0^\infty \frac{r^2dr}{\left[1+\dfrac{qA}{2(2-3q)\tau^{2/(2-3q)}}\right]^{1/q}}=Q. \tag{$A31$}$$

If we identify

$$j+1=1/q,\quad \nu=2,\quad \mu=3,\quad a=1 \tag{$A32$}$$

$$b=\frac{qA}{2(2-3q)\tau^{2/(2-3q)}} \tag{$A32$}$$

then the constant of integration becomes

$$A=\left\{\frac{(p+1)Q}{4\pi(\rho cT)_0}\left[\frac{q}{2(2-3q)}\right]^{3/2}\frac{\Gamma\left(\dfrac{1}{q}\right)}{\Gamma\left(\dfrac{3}{2}\right)\Gamma\left(\dfrac{1}{q}-\dfrac{3}{2}\right)}\right\}^{(2q/(2-3q))}. \tag{$A33$}$$

References

[1] Kasuya, D., and Yurioka, N., 1993, ''Prediction of Welding Thermal History by a Comprehensive Solution,'' Weld. J. (Miami), **72**, No. 3, pp. 107s–115s.

[2] Moore, J. E., Bibby, M. J., Goldak, J. A., and Santyr, S., 1986, ''A Comparison of the Point Source and Finite Element Schemes for Computing Weld Cooling,'' *Welding Research: The State of the Art*, E. F. Nippes and D. J. Ball eds., ASM, Miami, pp. 1–9.

[3] Carslaw, H. C., and Jaeger, J. C., 1959, *Conduction of Heat in Solids*, 2nd Ed., Oxford University Press, London.

[4] Grosh, R. J., and Trabant, E. A., 1956, ''Arc Welding Temperatures,'' Weld. J. (Miami), **35**, No. 8, pp. 396–401.

[5] Myers, P. T., Uyehara, O. A., and Borman, G. L., 1967, ''Fundamentals of Heat Flow in Welding,'' Welding Research Council Bulletin, No. 123, pp. 1–46.

[6] Ames, W. F., 1968, *Nonlinear Ordinary Differential Equations in Transport Processes*, Academic Press, New York.

[7] Logan, J. D., 1994, *An Introduction to Nonlinear Partial Differential Equations*, John Wiley and Sons, New York.

[8] Ozisik, M. N., 1980, *Conduction Heat Transfer*, John Wiley and Sons, New York.

[9] Zeldovich, Ya., and Kompaneets, A. S., 1950, ''On the Theory of Propagation of Heat With Temperature-Dependent Thermal Conductivity,'' Izdat. Akad. Nauk SSSR, pp. 61–71.

[10] Ames, W. F., 1964, ''Similarity for the Nonlinear Diffusion Equation,'' Ind. Eng. Chem. Fundam., **4**, pp. 72–76.

[11] Boyer, R. H., 1961, ''On Some Solutions of a Nonlinear Diffusion Equation,'' J. Math. Phys., **40**, No. 1, pp. 41–45.

[12] Heaslet, M. A., and Alksne, A., 1961, ''Diffusion From a Fixed Surface With a Concentration Dependent Coefficient,'' J. SIAM, **9**, No. 4, pp. 584–596.

[13] Pattle, R. E., 1959, ''Diffusion From an Instantaneous Point Source With a Concentration Dependent Coefficient,'' Q. J. Mech. Appl. Math., **12**, No. 4, pp. 407–409.

[14] Radaj, D., 1992, *Heat Effects of Welding*, Springer-Verlag, New York.

[15] Ion, J. C., Easterling, K. E., and Ashby, M. F., 1984, ''A Second Report on Diagrams of Microstructure and Hardness for Heat-Affected Zones in Welds,'' Acta Metall., **32**, pp. 1949–1962.

[16] Svensson, L., 1994, *Control of Microstructures and Properties in Steel Arc Welds*, CRC Press, Boca Raton, FL.

[17] Rosenthal, D., 1941, ''Mathematical Theory of Heat Distribution During Welding and Cutting,'' Weld. J. (Miami), **20**, No. 5, pp. 220s–234s.

[18] Rosenthal, D., 1946, ''The Theory of Moving Sources of Heat and Its Application to Metal Treatments,'' Trans. ASME, **68**, pp. 849–866.

[19] Harvey, P., 1982, *Engineering Properties of Steel*, ASTM, Metals Park, OH.

[20] Goldak, J., Chakravarti, A., and Bibby, M., 1984, ''A New Finite Element Model for Welding Heat Sources,'' Metall. Trans., **15B**, No. 6, pp. 299–305.

A Monte Carlo Solution of Heat Conduction and Poisson Equations

M. Grigoriu
Professor of Structural Engineering,
Cornell University,
Ithaca, NY 14853-3501
e-mail: mdg12@cornell.edu

A Monte Carlo method is developed for solving the heat conduction, Poisson, and Laplace equations. The method is based on properties of Brownian motion and Itô processes, the Itô formula for differentiable functions of these processes, and the similarities between the generator of Itô processes and the differential operators of these equations. The proposed method is similar to current Monte Carlo solutions, such as the fixed random walk, exodus, and floating walk methods, in the sense that it is local, that is, it determines the solution at a single point or a small set of points of the domain of definition of the heat conduction equation directly. However, the proposed and the current Monte Carlo solutions are based on different theoretical considerations. The proposed Monte Carlo method has some attractive features. The method does not require to discretize the domain of definition of the differential equation, can be applied to domains of any dimension and geometry, works for both Dirichlet and Neumann boundary conditions, and provides simple solutions for the steady-state and transient heat equations. Several examples are presented to illustrate the application of the proposed method and demonstrate its accuracy. [S0022-1481(00)02201-5]

Keywords: Keywords: Conduction, Heat Exchangers, Numerical Methods

1 Introduction

The fixed random walk and exodus methods are the most frequently used Monte Carlo solutions of the heat conduction and Poisson equations. The methods are based on random walkers moving on the mesh of finite difference approximations of these partial differential equations in different directions of the space with probabilities derived from the corresponding finite difference operators ([1–6]). Generally, the exodus method is preferred because of its computational efficiency. The floating random walk or spherical process method based on Green functions has also been applied to solve the Laplace and Poisson equations ([2,4,5,7,8]). All these Monte Carlo methods are not efficient for finding the field solution of partial differential equations but can be competitive with the traditional numerical methods if only local solutions are needed, that is, the solutions at a single or a few points of the domain of definition ([1–6]).

Let T be the solution of the Poisson equation

$$\Delta T(\mathbf{x}) = -g(\mathbf{x}), \quad \mathbf{x}\in D\subset\mathbb{R}^d \tag{1}$$

where d is the dimension of the space, g denotes a prescribed real-valued function defined on $\mathbb{R}^d$, and $\Delta = \Sigma_{p=1}^{d}\partial^2/\partial x_p^2$ is the Laplace operator. This equation also gives the steady-state temperature field T in a homogeneous medium subjected to a flux g. If the flux is $g=0$, Eq. (1) becomes the Laplace equation

$$\Delta T(\mathbf{x}) = 0. \tag{2}$$

The solution of Eqs. (1) and (2) requires to specify the boundary conditions. For example, the Dirichlet boundary conditions for these equations are given by

$$T(\mathbf{x}) = T_b(\mathbf{x}), \quad \mathbf{x}\in\partial D, \tag{3}$$

where T_b is a prescribed real-valued function giving the temperature on the boundary ∂D of the domain D. The Neumann boundary conditions for these equations prescribe values of the directional derivatives of T on ∂D.

This paper develops the framework of a Monte Carlo solution of Eqs. (1) and (2). The emphasis is on the Dirichlet boundary value problem. The proposed solution is based on properties of Brownian motion and Itô processes, the Itô formula for differentiable functions of these processes, and the similarities between the generator of Itô processes and the differential operators of Eqs. (1) and (2) and related equations. The proposed and the current Monte Carlo methods are similar in the sense that they are local and are based on Monte Carlo simulation. However, there are notable differences between the proposed and the current Monte Carlo solutions. For example, the first step of the fixed random walk and exodus methods is the discretization of the domain of definition D in a finite difference mesh. In contrast, the proposed method does not require to discretize D. Moreover, the proposed method does not become difficult to apply if the dimension d increases and/or the shape of D become complex and can be applied without difficulties to solve the heat conduction equation for heterogeneous media with Dirichlet and Neumann boundary conditions. For heterogeneous media, the temperature T is the solution of the partial differential equation

$$\sum_{p=1}^{d}\frac{\partial\sigma(\mathbf{x})}{\partial x_p}\frac{\partial T(\mathbf{x})}{\partial x_p} + \sigma(\mathbf{x})\Delta T(\mathbf{x}) = -g(\mathbf{x}), \quad \mathbf{x}\in D, \tag{4}$$

where σ denotes the conductivity field. Conceptually, the floating random walk or spherical process method is the closest related to the proposed method. This relationship can be uncovered by interpreting the Green functions of the differential operators of Eqs. (1), (2), and (4) as probability measures.

The main objectives of this paper are to (1) provide the theoretical foundation for the proposed Monte Carlo method, (2) demonstrate the application of this method to the solution of the heat conduction equation by numerical examples, (3) establish similarities and differences between the current and the proposed Monte Carlo solutions, and (4) outline relevant features of the proposed Monte Carlo method for applications.

Contributed by the Heat Transfer Division for publication in the JOURNAL OF HEAT TRANSFER. Manuscript received by the Heat Transfer Division, June 9, 1997; revision received, Aug. 31, 1999. Associate Technical Editor: S. Ramadhyani.

2 Current Monte Carlo Solutions

Two representative solutions for the differential operators of Eqs. (1) and (2) are reviewed. The solutions are based on finite difference approximations and the mean value theorem.

2.1 First Solution. Consider the finite difference approximation

$$\frac{T_{i+1,j}-2T_{i,j}+T_{i-1,j}}{a^2}+\frac{T_{i,j+1}-2T_{i,j}+T_{i,j-1}}{a^2}=-g_{i,j} \qquad (5)$$

of Eq. (1) for $d=2$ and a mesh of equal step a in both coordinates, where $T_{i,j}$ and $g_{i,j}$ denote the values of functions T and g at node (i,j), respectively. The version

$$T_{i,j}=\frac{1}{4}(T_{i+1,j}+T_{i-1,j}+T_{i,j+1}+T_{i,j-1})+\frac{a^2}{4}g_{i,j} \qquad (6)$$

of this approximation is the basis for the Monte Carlo solution of Eq. (1) by the fixed random walk and exodus methods ([4,5]).

Suppose that the objective is to find the temperature T satisfying Eqs. (1) and (2) at an arbitrary node $\mathbf{x}$ of the finite difference mesh. The method is based on the probabilistic interpretation of Eq. (6) showing that a random walker located at a node of the finite difference mesh may move to the right, left, up, or down with equal probabilities. Consider n_s random walkers starting at $\mathbf{x}$. The walker k travels through the nodes $\{(x_p^{(k)},y_p^{(k)})\}$, $p=1,2,\ldots,m_k$, of the finite difference mesh and exits D at $(x_{m_k}^{(k)},y_{m_k}^{(k)})\in\partial D$. The value of $T(\mathbf{x})$ can be approximated by [3–5].

$$\hat{T}(\mathbf{x})=\frac{1}{n_s}\sum_{k=1}^{n_s}\left[T_b(x_{m_k}^{(k)},y_{m_k}^{(k)})+\frac{a^2}{4}\sum_{p=1}^{m_k}g(x_p^{(k)},y_p^{(k)})\right]. \qquad (7)$$

If $g=0$, the last term of Eq. (7) vanishes and the resulting solution $\hat{T}$ provides an approximation for the solution of the Laplace equation (Eq. (2)).

The methods based on Eq. (7) can calculate the temperature T only at points $\mathbf{x}$ belonging to the nodes of the finite difference mesh considered in the analysis. This restriction may be undesirable in some applications because the finite difference mesh cannot be chosen independently of the points where the temperature needs to be calculated. Difficulties related to this restriction may not be relevant if the mesh step is small.

2.2 Second Solution. The mean value theorem for a homogeneous differential operator $L[T(\mathbf{x})]=0$, $\mathbf{x}\in D$, gives ([9])

$$T(\mathbf{x})=\int_{S(\mathbf{x},r)}k(\mathbf{x},\mathbf{y})T(\mathbf{y})d\sigma(\mathbf{y}) \qquad (8)$$

where $S(\mathbf{x},r)=\{\mathbf{y}:\|\mathbf{y}-\mathbf{x}\|=r\}\subset D$ is a sphere of radius $r>0$ centered at $\mathbf{x}\in D$, k is the kernel of the differential operator L, and $d\sigma(\mathbf{y})$ denotes the element of area on $S(\mathbf{x},r)$. If k is positive, it can be used to define a probability measure on $S(\mathbf{x},r)$ so that $T(\mathbf{x})$ can be interpreted as the mean value of a random variable $\mathbf{Y}$ taking values on $S(\mathbf{x},r)$ and having a probability measure defined by the kernel k.

Suppose L is the Laplace operator Δ of Eq. (2) and the solution T satisfies the boundary conditions of Eq. (3). The kernel of this operator is constant and equal to $1/a_d$, where $a_d=2\pi^{d/2}r^{d-1}/\Gamma(d/2)$ is the area of $S(\mathbf{x},r)$ so that $(1/a_d)\int_{s(\mathbf{x},r)}d\sigma(\mathbf{y})=1$. Hence, $T(\mathbf{x})=\int_{s(\mathbf{x},r)}T(\mathbf{y})[d\sigma(\mathbf{y})/a_d]$ so that it can be viewed as the average value of a random variable $\mathbf{Y}$ uniformly distributed on $S(\mathbf{x},r)$.

Let $\mathbf{x}_0=\mathbf{x}$ be an arbitrary point of D and $S(\mathbf{x}_0,r(\mathbf{x}_0))$ the largest sphere centered at $\mathbf{x}_0$ that can be inscribed in D. Let $\mathbf{x}_1(\omega)$ be a randomly selected point on $S(\mathbf{x}_0,r(\mathbf{x}_0))$ and $S(\mathbf{x}_1(\omega),r(\mathbf{x}_1(\omega)))$ the largest sphere centered at $\mathbf{x}_1(\omega)$ that can be inscribed in D. Select now a random point $\mathbf{x}_2(\omega)$ on $S(\mathbf{x}_1(\omega),r(\mathbf{x}_1(\omega)))$. This algorithm generates a sequence of points $\{\mathbf{x}_0,\mathbf{x}_1(\omega),\mathbf{x}_2(\omega),\ldots\}$, referred to as spherical process, that converges to a point $\mathbf{y}(\omega)$ of ∂D ([2,7,8,10,11]). The value of T at this limit point is known and equal to $T_b(\mathbf{y}(\omega))$ by the boundary conditions. Then

$$T(\mathbf{x}_0,\omega)=\left[\prod_{i=1}^{N(\omega)}k(\mathbf{x}_{i-1}(\omega)\mathbf{x}_i(\omega))\right]T_b(\mathbf{y}(\omega)) \qquad (9)$$

is the value of T at $\mathbf{x}_0$ on sample ω, where $\mathbf{x}_0(\omega)=\mathbf{x}_0$ and $N(\omega)$ denote the number of steps of the spherical process. An estimate of $T(\mathbf{x})=T(\mathbf{x}_0)$ is given by the arithmetic average of the sample values $\{T(\mathbf{x}_0,\omega)\}$. The algorithm can be modified to solve partial differential equations with Neumann boundary conditions ([7,8,10]).

3 Fundamentals for the Proposed Solution

This section reviews essential properties of the Brownian motion and the Itô processes and gives the version of the Itô formula needed for the proposed Monte Carlo solution of the heat equation.

3.1 Brownian Motion. The $\mathbb{R}^d$-valued Brownian motion $\mathbf{B}(t)$, $t\geqslant 0$, is a stochastic process with the properties:

(a) The initial value $\mathbf{B}(0)=\mathbf{x}$ of $\mathbf{B}$ can be any point $\mathbf{x}$ in $\mathbb{R}^d$.

(b) The increment $\mathbf{B}(t)-\mathbf{B}(s)$, $s<t$, of $\mathbf{B}$ in an arbitrary time interval (s,t) is a d-dimensional random vector whose coordinates are independent Gaussian variables with mean zero and variance $t-s$. Hence, the Gaussian vector $\mathbf{B}(t)-\mathbf{B}(s)$ has mean zero and covariance matrix $\mathbf{i}(t-s)$, where $\mathbf{i}$ denotes the (d,d)-identity matrix. Because the properties of the increments of $\mathbf{B}$ depend on only the duration $t-s$ of the time interval (s,t), the process is said to have stationary increments.

(c) The increments of $\mathbf{B}$ in nonoverlapping time intervals are independent, that is, the increments $\mathbf{B}(t)-\mathbf{B}(s)$ and $\mathbf{B}(u)-\mathbf{B}(v)$, $v<u\leqslant s<t$, of $\mathbf{B}$ are independent random vectors. Hence, $\mathbf{B}$ has stationary and independent increments.

(d) The samples of $\mathbf{B}$ are continuous and nondifferentiable everywhere. The lack of differentiability is caused by the rapid oscillations of the samples of $\mathbf{B}$ and has implications on the way in which various operations can be performed on this process. For example, integrals involving Brownian motions as integrators cannot be defined in the classical Riemann-Stieltjes sense because these types of integrals exist for relatively smooth integrators. The integrators of Riemann-Stieltjes integrals must be of bounded variation on bounded intervals and the samples of the Brownian motion do not have this property.

(e) The generation of samples of an $\mathbb{R}^d$-valued Brownian motion process $\mathbf{B}$ is simple irrespective of the dimension d and involves three steps:

1. Select a time step $\Delta t>0$ and a starting point $\mathbf{x}$.
2. Consider a time sequence $t_k=k\Delta t$, $k=0,1,\ldots$, and generate samples of the increments $\Delta\mathbf{B}_k=\mathbf{B}(t_{k+1})-\mathbf{B}(t_k)$ of $\mathbf{B}$ during each time interval (t_k,t_{k+1}).
3. Apply the recurrence formula

$$\mathbf{B}(t_{k+1})=\mathbf{B}(t_k)+\Delta\mathbf{B}_k, \quad k=0,1\ldots \qquad (10)$$

to obtained samples of $\mathbf{B}$, where $\mathbf{B}(t_k)$ is the current value, $\Delta\mathbf{B}_k$ denotes the increment of the Brownian motion, and $\mathbf{B}(t_0)=\mathbf{B}(0)=\mathbf{x}$.

Simple algorithms can be developed to generate samples of $\mathbf{B}$ in any dimension d with a specified time step Δt. For example, the function

```
function [time,br]=brown(d,x,Δt,nstep, nseed)
dts=sqrt(Δt);
randn('seed',nseed)
time(1)=0;
br(:,1)=x;
for i=1:nstep,
```

```
    time(i+1)=time(i)+Δt;
    br(:,i+1)=br(:,i)+dts*randn(d,1);
  end
```

can be used to generate a sample of the Brownian motion process **B** in $\mathbb{R}^d$ starting at **x** with time step Δt in the time interval $[0,(\text{nstep})(\Delta t)]$. The generation uses the MATLAB function randn giving independent Gaussian samples with mean zero and variance one. A set of samples of **B** can be obtained by running the MATLAB function brown for different values of nseed.

3.2 The Itô Process.

The stochastic differential equation

$$d\mathbf{X}(t)=\mathbf{a}(\mathbf{X}(t))dt+\mathbf{c}(\mathbf{X}(t))d\mathbf{B}(t), \quad t\geqslant 0, \tag{11}$$

defines an $\mathbb{R}^d$-valued stochastic process **X** depending on the $(d,1)$ and (d,d_b) matrices **a** and **c**, called drift and diffusion, and the $\mathbb{R}^{d_b}$-valued Brownian motion **B**. The dimensions d and d_b may differ as demonstrated by an example presented in the paper (Eq. (33)). The diffusion **c** controls the magnitude of the driving noise **B**. Both the drift and the diffusion coefficients may depend on the state **X**. The process **X** is called in the probability literature diffusion or Itô process. To avoid confusion with common terms used in engineering, **X** is referred to as Itô's process in this paper.

If **a** and **c** are relatively smooth functions satisfying the so-called Lipschtz conditions, the solution

$$\mathbf{X}(t)=\mathbf{X}(0)+\int_0^t \mathbf{a}(\mathbf{X}(s))ds+\int_0^t \mathbf{c}(\mathbf{X}(s))d\mathbf{B}(s), \tag{12}$$

of Eq. (11) exits and is unique ([12–14]). This solution depends on the Riemann and the Itô integrals $\int_0^t \mathbf{a}(\mathbf{X}(s))ds$ and $\int_0^t \mathbf{c}(\mathbf{X}(s))d\mathbf{B}(s)$, respectively. As previously indicated, the integral $\int_0^t \mathbf{c}(\mathbf{X}(s))d\mathbf{B}(s)$ cannot be defined in the Riemann-Stieltjes sense because the samples of **B** are of unbounded variation.

The generation of samples of the Itô process **X** can be based, for example, on the finite difference approximation

$$\mathbf{X}(t+\Delta t)\simeq \mathbf{X}(t)+\mathbf{a}(\mathbf{X}(t))\Delta t+\mathbf{c}(\mathbf{X}(t))\Delta\mathbf{B}(t) \tag{13}$$

of Eq. (11). This recurrence formula and the algorithm for generating samples of **B** discussed in the previous section can be used to produce samples of **X** with a specified time step Δt in any dimension d starting at an arbitrary point **x**. More accurate recurrence formulas for generating samples of **X** can be found in [15].

3.3 Itô's Formula.

The tools of the classical calculus cannot be applied to perform operations on Brownian motion and Itô processes. A very efficient computation tool is the Itô formula

$$T(\mathbf{X}(t))-T(\mathbf{X}(0))=\int_0^t \mathcal{A}T(\mathbf{X}(s))ds + \sum_{i=1}^{d}\sum_{k=1}^{d_b}\int_0^t \mathbf{c}(\mathbf{X}(s))_{i,k}\frac{\partial T(\mathbf{X}(s))}{\partial x_k}dB_k(s) \tag{14}$$

valid for any function T with continuous second-order partial derivatives, where

$$\mathcal{A}T(\mathbf{x})=\lim_{t\downarrow 0}\frac{E[T(\mathbf{X}(t))]-T(\mathbf{x})}{t} =\sum_i a_i(\mathbf{x})\frac{\partial T_b(\mathbf{x})}{\partial x_i}+\frac{1}{2}\sum_{i,j}(\mathbf{c}(\mathbf{x})\mathbf{c}(\mathbf{x})^T)_{i,j}\frac{\partial^2 T(\mathbf{x})}{\partial x_i\partial x_j} \tag{15}$$

is the generator of the Itô process **X** for $\mathbf{X}(0)=\mathbf{x}$, [12–14]. $a_i(\mathbf{x})$ denotes the element i of $\mathbf{a}(\mathbf{x})$, and $(\mathbf{c}(\mathbf{x})\mathbf{c}(\mathbf{x})^T)_{i,j}$ is the element (i,j) of $\mathbf{c}(\mathbf{x})\mathbf{c}(\mathbf{x})^T$. The generator $\mathcal{A}T(\mathbf{x})$ gives the average rate of change of function $T(\mathbf{X}(t))$ at an arbitrary time given that the process is equal to **x** at this time. The formulas of Eqs. (14)–(15) represent a generalization of the change of variables formula of the classical calculus. The only difference between Eqs. (14) and (15) and the change of variables formula of the classical calculus is the term of Eq. (15) involving the second derivatives of T that is absent in the classical calculus.

The expectation or the mean of Eq. (14) is

$$E[T(\mathbf{X}(t))]-T(\mathbf{x})=E\left[\int_0^t \mathcal{A}T(\mathbf{X}(s))ds\right] \tag{16}$$

because $\mathbf{X}(0)=\mathbf{x}$ so that $E[T(\mathbf{X}(0))]=T(\mathbf{x})$ and the increments of B have mean zero so that the average of the last term of Eq. (14) vanishes, where $E[\mathbf{Z}]$ denotes the mean value of a random variable **Z** and is called the mean, average, or expectation operator.

The formula of Eq. (16) holds for any initial value $\mathbf{X}(0)=\mathbf{x}$ and time t. For the proposed Monte Carlo method, the time t needs to be replaced with a random time $\tau(\mathbf{x})$ corresponding to the first exit of **X** from a bounded domain D under the condition $\mathbf{X}(0)=\mathbf{x}\in D$, that is, the time

$$\tau(\mathbf{x})=\inf\{t\geqslant 0:\mathbf{X}(t)\notin D\}. \tag{17}$$

The version of Eq. (16) with t replaced by $\tau(\mathbf{x})$ is

$$E[T(\mathbf{X}(\tau(\mathbf{x})))]-T(\mathbf{x})=E\left[\int_0^{\tau(\mathbf{x})}\mathcal{A}T(\mathbf{X}(s))ds\right]. \tag{18}$$

The special case of the Brownian motion **B** can be obtained from Eqs. (15) and (18) by taking **a** equal to zero, $d=d_b$, and $\mathbf{c}=\mathbf{i}$ in these equations, as it can be seen from Eq. (11). The generator of **B** is

$$\mathcal{A}T(\mathbf{x})=\lim_{t\downarrow 0}\frac{E[T(\mathbf{B}(t))]-T(\mathbf{x})}{t}=\frac{1}{2}\Delta T(\mathbf{x}) \tag{19}$$

so that Eq. (18) becomes

$$E[T(\mathbf{B}(\tau(\mathbf{x})))]-T(\mathbf{x})=\frac{1}{2}E\left[\int_0^{\tau(\mathbf{x})}\Delta T(\mathbf{B}(s))ds\right] \tag{20}$$

for $\mathbf{B}(0)=\mathbf{x}$. The last formula shows that the Brownian motion process can be used to solve the Laplace equation but it cannot be applied to find the solution of differential equations defined by differential operators different from the Laplace operator.

4 Proposed Solution of the Heat Equation

The solution of the heat equation can be based on the Brownian motion and Itô processes depending on the functional form of the differential operators defining these equations. The framework is established for solving the heat equation by the proposed method for both homogeneous and heterogeneous media. Several examples are used to illustrate the application of the proposed method.

4.1 General Formulation.

Consider the solution of Eqs. (1) and (4) with the Dirichlet boundary conditions given by Eq. (3). The objective is to calculate the temperature T at an arbitrary point **x** in D. The proposed Monte Carlo method uses the Brownian motion process for solving Eq. (1) but Itô processes are needed to find the local solution of Eq. (4).

First, consider the local solution of Eq. (1). The formula of Eq. (20) with T being the solution of Eq. (1) gives

$$T(\mathbf{x})=E[T_b(\mathbf{B}(\tau(\mathbf{x})))]+\frac{1}{2}E\left[\int_0^{\tau(\mathbf{x})} g(\mathbf{B}(s))ds\right] \tag{21}$$

because $\mathbf{B}(\tau(\mathbf{x}))\in\partial D$ so that $T(\mathbf{B}(\tau(\mathbf{x})))=T_b(\mathbf{B}(\tau(\mathbf{x})))$ by the boundary condition of Eq. (3) and because $\mathbf{B}(s)\in D$ for $s<\tau(\mathbf{x})$ so that $\Delta T(\mathbf{B}(s))=-g(\mathbf{B}(s))$ by Eq. (1). Hence, the temperature $T(\mathbf{x})$ at an arbitrary point $\mathbf{x}\in D$ depends on the known functions g

and T_b. The method works because the generator of **B** has the same functional form as the differential operator of Eq. (1) so that the value of $\mathcal{A}\mathbf{B}(s)$ is know for $s \in [0,\tau(\mathbf{x}))$.

Generally, it is not possible to obtain the expectations of Eq. (21) analytically but they can be estimated from samples of **B**. Let $\{\mathbf{b}_i(t)\}, i=1,\ldots,n_s$, be n_s independent samples of **B** starting at **x** and $\{\tau_i(\mathbf{x})\}$ the first exit times of these samples from D. The expectations of Eq. (21) can be approximated by

$$E[T_b(\mathbf{B}(\tau(\mathbf{x})))] \simeq \frac{1}{n_s}\sum_{i=1}^{n_s} T_b(\mathbf{b}_i(\tau_i(\mathbf{x})))E\left[\int_0^{\tau(\mathbf{x})} g(\mathbf{B}(s))ds\right]$$

$$\simeq \frac{1}{n_s}\sum_{i=1}^{n_s} \int_0^{\tau_i(\mathbf{x})} g(\mathbf{b}_i(s))ds, \tag{22}$$

that is, the arithmetic averages of the samples $T_b(\mathbf{b}_i(\tau_i(\mathbf{x})))$ and $\int_0^{\tau_i(\mathbf{x})} g(\mathbf{b}_i(s))ds$ of the random variables $T_b(\mathbf{B}(\tau(\mathbf{x})))$ and $\int_0^{\tau(\mathbf{x})} g(\mathbf{B}(s))ds$, respectively.

The solution of Eq. (2) with the Dirichlet boundary conditions given by Eq. (3) can be obtained from Eq. (2) with $g=0$, that is,

$$T(\mathbf{x}) = E[T_b(\mathbf{B}(\tau(\mathbf{x})))]. \tag{23}$$

The estimated value of $T(\mathbf{x})$ based on n_s independent samples of the Brownian motion is

$$T(\mathbf{x}) \simeq \frac{1}{n_s}\sum_{i=1}^{n_s} T_b(\mathbf{b}_i(\tau_i(\mathbf{x}))). \tag{24}$$

Second, consider the solution of the heat equation for a heterogeneous medium with a conductivity field σ. The formula of Eq. (18) holds for T being the solution of Eq. (4). The Brownian motion **B** cannot be used for solution because the generator of **B** is proportional to the Laplace operator and the differential operator on the left-hand side of Eq. (4) has a different structure. Let **X** be an Itô process such that its generator $\mathcal{A}T(\mathbf{x})$ coincides with the left-hand side of Eq. (4). Then the equality $\mathcal{A}T(\mathbf{x}) = -g(\mathbf{x})$ holds for each $\mathbf{x} \in D$ so that

$$T(\mathbf{x}) = E[T_b(\mathbf{X}(\tau(\mathbf{x})))] + E\left[\int_0^{\tau(\mathbf{x})} g(\mathbf{X}(s))ds\right] \tag{25}$$

by Eq. (18) and the boundary conditions (Eq. (3)). It remains to show that such an Itô process can be constructed. The functional form of Eqs. (4) and (15) shows that there exists an Itô process **X** with the required properties. The process **X** is defined by Eq. (11) with the drift and diffusion coefficients

$$a_i(\mathbf{x}) = \frac{\partial \sigma(\mathbf{x})}{\partial x_i}, \quad i=1,\ldots,d,$$

$$\mathbf{c}(\mathbf{x}) = \mathbf{i}\sqrt{2\sigma(\mathbf{x})}. \tag{26}$$

4.2 Examples. Two examples are considered to demonstrate the use of the proposed Monte Carlo method, illustrate some features of this method, and explore the relationships between the current and proposed Monte Carlo techniques.

Example 1. Consider the solution of Eq. (2) with the Dirichlet boundary condition given by Eq. (3) and a spherical domain D defined by the interior of a sphere $S(\mathbf{x},r)$ of radius $r>0$ and centered at **x**. Suppose that the temperature $T(\mathbf{x})$ at the center of the sphere needs to be determined.

The required temperature is $T(\mathbf{x}) = E[T_b(\mathbf{B}(\tau(\mathbf{x})))]$ by Eq. (23). Because $\mathbf{B}(\tau(\mathbf{x}))$ is uniformly distributed on $S(\mathbf{x},r)$ [11], $T(\mathbf{x})$ is equal to the expectation $E[T_b(\mathbf{Y})]$, where **Y** denotes a random variable uniformly distributed on $S(\mathbf{x},r)$. This result coincides with the solution by the mean value theorem (Eqs. (8) and (9)). The example shows the close relationship between the method based on the mean value theorem and the proposed Monte Carlo solution.

Example 2. Suppose that T is the solution of Eq. (2) defined on the domain $D=(0,a)\times(0,b)$, $0<a$, $b<\infty$, with the boundary temperatures 100 on the side $x_1=a$ and zero on all the other sides of D. The exact solution is given by the infinite series ([16]),

$$T(\mathbf{x}) = \frac{400}{\pi}\sum_{n=1,3,\ldots}^{\infty} \frac{\sinh(n\pi x_1/b)\sin(n\pi x_2/b)}{\sinh(n\pi a/b)}. \tag{27}$$

The approximate value of $T(\mathbf{x})$ by the proposed Monte Carlo solution is (Eq. (24))

$$T(\mathbf{x}) \simeq 100\,\frac{n_{s,1}}{n_s}, \tag{28}$$

where n_s and $n_{s,1}$ denote the total number of samples generated from a Brownian motion process **B** starting at **x** and the number of these samples exiting D through the side $x_1=a$ of D. Comparisons of values of T given by Eqs. (27) and (28) show differences less two percent for $n_s=2000$ samples of **B**, time steps Δt in the range (0.0005, 0.001), and $a=b=1$ for a large set of points **x** covering the domain of definition D. The proposed Monte Carlo solution improves as the sample size n_s increases. For example, the estimates given by Eq. (28) are 30, 25.8, and 25.5 at point (0.5, 0.5) for $n_s=100$, 500, and 1000, respectively, and a time step of $\Delta t=0.001$. The corresponding errors relative to the exact temperature at this point, $T(0.5,0.5)=25$, are 20, 3.2, and 2 percent, respectively.

This example can be generalized in several directions. First, suppose that T is the solution of the heterogeneous heat equation,

$$\frac{\partial^2 T}{\partial x_1^2} + 3\,\frac{\partial^2 T}{\partial x_2^2} = -16, \tag{29}$$

with $g \neq 0$ (Eq. (1)). The Brownian motion cannot be used for solution because the differential operator of Eq. (29) differs from the Laplace operator. The Itô process **X** required for solution is (Eqs. (11) and (26))

$$\begin{aligned} dX_1(t) &= dB_1(t) \\ dX_2(t) &= \sqrt{3}\,dB_2(t) \end{aligned} \tag{30}$$

because the generator of this process is proportional with the left-hand side of Eq. (29). The proposed solution is

$$T(\mathbf{x}) = E[T_b(\mathbf{X}(\tau(\mathbf{x})))] + 8E[\tau(\mathbf{x})] \tag{31}$$

by Eq. (21) because the generator of **X** is equal to the left hand side of Eq. (29) divided by two so that $\int_0^{\tau(\mathbf{x})} \mathcal{A}T(\mathbf{X}(s))ds = -8\int_0^{\tau(\mathbf{x})} ds = -8\tau(\mathbf{x})$. Samples of **X** can be used to estimate the averages $E[T_b(\mathbf{X}(\tau(\mathbf{x})))]$ and $E[\tau(\mathbf{x})]$ in the expression of $T(\mathbf{x})$ using similar estimates as in Eq. (22).

Table 1 gives solutions of Eq. (29) at six points in the domain of definition $D=(0,1)\times(0,1)$ of this equation obtained by the finite element and the proposed Monte Carlo methods. The Monte Carlo solution is based on $n_s=1000$ samples of the Itô process defined by Eq. (30) and a time step $\Delta t=0.0001$. The difference between the finite element and the proposed solutions are given in percentages in the last column of the table. The largest difference occurs at location (0.5, 0.5). The result by the proposed method for another set of 1000 samples at point (0.5, 0.5) is 9.3930 so that the estimate of T at this point based on 2000 samples is (9.3930

Table 1 Finite element and proposed Monte Carlo solutions

Point	Finite element	Monte Carlo	Difference (%)
(0.25, 0.25)	1.788	1.8019	0.78
(0.50, 0.25)	6.35	6.2490	−1.59
(0.75, 0.25)	23.87	23.9758	0.44
(0.25, 0.50)	2.48	2.4064	−2.97
(0.50, 0.50)	8.94	8.4766	−5.18
(0.75, 0.50)	32.43	33.2928	2.66

$+8.4766)/2=8.9348$ and differs from the finite element solution by -0.058 percent. The finite element solution is based on a very refined mesh so that it can be considered to be nearly exact.

Second, suppose that Eq. (29) must satisfy Dirichlet and Neumann boundary conditions. The proposed Monte Carlo method can be extended to find the local solution for this type of problem. The extension is based on a generalized version of the Itô formula that incorporates the values of the directional derivatives of temperature at the Neumann boundaries. Theoretical considerations on this version of the Itô formula can be found in [12] and are not presented in this paper.

5 Comments on Current and Proposed Solutions

The proposed, the fixed random walk, and the exodus methods have some notable common features. These methods (1) are based on probabilistic interpretations of deterministic partial differential equations and use of Monte Carlo simulation for solution and (2) are local in the sense that they can deliver the value of the unknown function at an arbitrary point of the domain of definition directly. In contrast, finite element, finite difference, and other traditional numerical methods have to calculate the field solution even if the solution is required at a point or a small set of points of the domain of definition.

The relationship between the proposed Monte Carlo method and the Monte Carlo approach based on the mean value theorem is illustrated by the first example of the previous section. The relationship between the proposed method, the exodus, and the fixed random walk methods is examined here. Consider the solutions of Eq. (1) with the Dirichlet boundary conditions of Eq. (3) given by Eq. (7) and Eq. (21). The first term $(1/n_s)\Sigma_{k=1}^{n_s} T_b(x_{m_k}^{(k)}, y_{m_k}^{(k)})$ of Eq. (7) is an estimate of the expectation $E[T_b(\mathbf{B}(\tau(\mathbf{x})))]$ in Eq. (21). The connection between the second terms of Eqs. (7) and (21) is less visible. It is sufficient to show that $(a^2/2)\Sigma_{p=1}^{m_k} g(x_p^{(k)}, y_p^{(k)})$ approximates $\int_0^{\tau(\mathbf{x})} g(\mathbf{B}(s))\,ds$ because the summation on k scaled by n_s in Eq. (7) provides an estimate for the expectation of the integral in Eq. (21). The integral $\int_0^{\tau(\mathbf{x})} g(\mathbf{B}(s))\,ds$ can be approximated by the sum $\Sigma_{p=1}^{m_k} g(x_p^{(k)}, y_p^{(k)})\Delta S_p^{(k)}$, where $\{(x_p^{(k)}, y_p^{(k)})\}$ are points on path k of $\mathbf{B}$ equally spaced at distance a and $\{\Delta S_p^{(k)}\}$ denote the corresponding time steps. The time steps $\{\Delta S_p^{(k)}\}$ are independent identically distributed random variables with mean a^2/d because $\{\Delta S_p^{(k)}\}$ represent first exit times of $\mathbf{B}$ from a sphere of radius a provided $\mathbf{B}$ starts at the center of this sphere [14]. If $g=1$ in D, the integral $\int_0^{\tau(\mathbf{x})} g(\mathbf{B}(s))\,ds$ is equal to $\tau(\mathbf{x})$ and the sum $\Sigma_{p=1}^{m_k} g(x_p^{(k)}, y_p^{(k)})\Delta S_p^{(k)}$ becomes $\Sigma_{p=1}^{m_k}\Delta S_p^{(k)}$. If m_k is large, this sum can be approximated by its average $m_k(a^2/2)$ according to the central limit theorem. If g is a smooth function in D and m_k is sufficiently large, the central limit theorem holds so that the sum $\Sigma_{p=1}^{m_k} g(x_p^{(k)}, y_p^{(k)})\Delta S_p^{(k)}$ can be approximated by its mean value $(a^2/2)\Sigma_{p=1}^{m_k} g(x_p^{(k)}, y_p^{(k)})$ and this approximation coincides with the formula of Eq. (7). If m_k is not large, the random variable $\Sigma_{p=1}^{m_k} g(x_p^{(k)}, y_p^{(k)})\Delta S_p^{(k)}$ cannot be approximated by $(a^2/2)\Sigma_{p=1}^{m_k} g(x_p^{(k)}, y_p^{(k)})$ because its variance is not negligible. This observation suggests to use a refined finite difference mesh for calculating values of solution T at point $\mathbf{x}\in D$ close to ∂D to assure that m_k is relatively large for most walks originating at these points.

The proposed method has some attractive features that are not shared by most of the current Monte Carlo techniques. The proposed method:

1 does not require to discretize the domain of definition D of the differential equation. In contrast, the discretization of D is the first step of the solution by the fixed random walk and exodus methods. Because the calculations related to the generation of the paths of the random walkers and the averaging of these paths needed for solution are similar in the current and the proposed methods (Eqs. (7) and (21)), the computational effort in the proposed method is reduced.

2 can be applied without any difficulty to domains of arbitrary shape and dimension. For example, suppose the domain of definition of Eq. (2) is multiply connected with boundary $\partial D = U_{r=1}^{m}\partial D_r$, $\partial D_r \cap D_r{}' = \emptyset$, $r \neq r'$, and the solution T takes constant values on these boundaries, that is $T(\mathbf{x})=k_r$ for $\mathbf{x}\in\partial D_r$, $r=1,\ldots,m$. The expectation $E[T_b(\mathbf{B}(\tau(\mathbf{x})))]$ of Eq. (23) becomes

$$E[T_b(\mathbf{B}(\tau(\mathbf{x})))]=\sum_{r=1}^{m} k_r p_r(\mathbf{x}) \tag{32}$$

where $p_r(\mathbf{x})$ denotes the probability that the Brownian motion starting at $\mathbf{x}\in D$ exits D for the first time through ∂D_r. The probabilities $p_r(\mathbf{x})$ cannot be calculated analytically for arbitrary domains but can be estimated by the ratio $n_{s,r}/n_s$, where n_s and $n_{s,r}$ denote the total number of samples and the number of samples exiting D through ∂D_r. The accuracy of the resulting estimates is very good as demonstrated by a numerical example in [10]. On the other hand, the meshing of the domain required by the fixed random walk and exodus methods results in some difficulties when dealing with domains D of complex geometry and/or high dimension.

3 can be applied to solve both Dirichlet and Neumann boundary value problems using the same conceptual framework. The incorporation of the Neumann boundary conditions requires the use of a generalized version of the Itô formula.

4 can be used for the solution of the transient heat equation. For example, the $\mathbb{R}^3$-valued Itô process $\mathbf{X}$ defined by

$$\begin{aligned} dX_1(s) &= dB_1(s) \\ dX_2(s) &= dB_2(s) \\ dX_3(s) &= -\,ds \end{aligned} \tag{33}$$

with the initial conditions $X_1(0)=x_1$, $X_2(0)=x_2$, and $X_3(0)=t$ can be used to calculate the local solution $T(t,\mathbf{x})$ for $\mathbf{x}=(x_1,x_2)$ and time $t>0$ of the transient heat equation $\partial T/\partial t=(1/2)(\partial^2/\partial x_1^2+\partial^2/\partial x_2^2)T$ defined on a domain $D\subset\mathbb{R}^2$ for $t>0$ and specified initial and boundary conditions. The solution of this problem can be based on Eq. (21) corresponding to the cylindrical domain $D^*\subset\mathbb{R}^3$ with base D extending in the positive direction of time to infinity and boundary conditions given by the specified initial and boundary conditions of the transient heat equation. Because the generator of the Itô process $\mathbf{X}$ defined by Eq. (33) coincides with the differential equation of T, the temperature at $(t,\mathbf{x})$ is equal to the average of the temperatures on the boundaries of D^* at the exit points of $\mathbf{X}$ by Eq. (21). Numerical results for the one-dimensional transient heat conduction equation can be found in [10].

6 Conclusions

A Monte Carlo solution was proposed for calculating the local solution of the Poisson and heat conduction equations, that is, the solution of these equations at a point or a small set of points of the domain of definition. The method is based on properties of the Brownian motion and Itô processes, the Itô formula for differentiable functions of these processes, and similarities between the generators of Itô processes and the differential operators of the Poisson and heat equations. In contrast to the fixed random walk and exodus Monte Carlo simulation methods that are based on random walks with a fixed step specified by the finite difference approximations of the differential operators of the Poisson and heat equations, the proposed method is based on walks with random steps. The proposed Monte Carlo method has some attractive features. The method does not require to descretize the domain of definition of the differential equation, can be applied to domains of arbitrary dimension and geometry, works for both Dirichlet and Neumann boundary conditions, and provides simple solutions for both steady-state and transient heat equations. Examples were presented to illustrate the application of the proposed method and demonstrate its accuracy.

Nomenclature

$\mathcal{A}$ = the generator of **B** or **X**
a = drift coefficients
c = diffusion coefficients
B = Brownian motion
D = domain of definition for the heat equation
∂D = boundary of D
E = the expectation, mean, or average operator
$k(\mathbf{x},\mathbf{y})$ = Green's function
$\mathbb{R}^d$ = d-dimensional space
t = time
T = temperature
$\tau(\mathbf{x})$ = first exit time of **B** or **X** starting at $\mathbf{x} \in D$ from D
X = Itô's process
x = arbitrary point in D

References

[1] Emery, A. F., and Carson, W. W., 1968, ''A Modification to the Monte Carlo Method—The Exodus Method,'' ASME J. Heat Transfer, **90**, pp. 328–332.
[2] Haji-Sheikh, A., and Sparrow, E. M., 1967, ''The Solution of Heat Conduction Problems by Probability Methods,'' ASME J. Heat Transfer, **89**, pp. 121–130.
[3] Klahr, C. N., 1960, ''A Monte Carlo Method for the Solution of Elliptic Partial Differential Equation,'' *Mathematical Methods for Digital Computers*, A. Ralston and H. S. Wilf, eds., John Wiley and Sons, New York, pp. 157–164.
[4] Sadiku, M. N. O., and Hunt, D. T., 1992, ''Solution of Dirichlet problems by Exodus Methods,'' IEEE Trans. Microwave Theory Tech., **40**, No. 1, pp. 89–95.
[5] Sadiku, M. N. O., Ajose, S. O., and Fu, Z., 1994, ''Applying the Exodus Methods to Solve Poisson's Equation,'' IEEE Trans. Microwave Theory Tech., **42**, No. 4, pp. 661–666.
[6] Zinsmeister, G. E., and Sawyerr, J. A., 1974, ''A Method for Improving the Efficiency of Monte Carlo Calculations of Heat Conduction Problems,'' ASME J. Heat Transfer, **96**, pp. 246–248.
[7] Suresh, K., 1966, ''Fast Point Solution Techniques in Engineering Analysis,'' *Advances in Mechanical Engineering*, T. S. Mruthyunjava, ed., Narosa Publishing House, New Delhi, India, pp. 385–400.
[8] Zagajac, J., 1995, ''A Fast Method for Estimating Discrete Field Values in Early Engineering Design,'' *Proceedings of the Third Symposium on Solid Modeling and Applications*, C. Hoffmann and J. Rossignac, eds., Salt Lake City, UT, May, pp. 420–430.
[9] Courant, R., and Hilbert, D., 1966, *Methods of Mathematical Physics*, Vol. 2, John Wiley and Sons, New York.
[10] Grigoriu, M., 1997, ''Local Solutions of Laplace, Heat, and Other Equations by Itô Processes,'' ASCE J. Eng. Mech., **123**, No. 8, pp. 823–829.
[11] Muller, M. E., 1956, ''Some Continuous Monte Carlo Methods for the Dirichlet Problem,'' Ann. Math. Stat., **27**, No. 3, pp. 569–589.
[12] Chung, K. L., and Williams, R. J., 1990, *Introduction to Stochastic Integration*, 2nd Ed., Birkhäuser, Boston.
[13] Grigoriu, M., 1995, *Applied Non-Gaussian Process: Examples, Theory, Simulation, Linear Random Vibration, and MATLAB Solutions*, Prentice-Hall, Englewood Cliffs, NJ.
[14] Øksendal, B., 1992, *Stochastic Differential Equations*, 3rd Ed., Springer-Verlag, New York.
[15] Kloeden, P. E., and Platen, E., 1980, *Numerical Solution of Stochastic Differential Equations*, Springer-Verlag, New York.
[16] Greenberg, M. D., 1978, *Foundations of Applied Mathematics*, Prentice-Hall, Englewood Cliffs, NJ.

Y. Z. Li
Research Student

C. V. Madhusudana[1]
Associate Professor
e-mail: madhu@cfd.mech.unsw.edu.au

E. Leonardi
Professor

School of Mechanical and
Manufacturing Engineering,
The University of New South Wales,
Sydney 2052, Australia

On the Enhancement of the Thermal Contact Conductance: Effect of Loading History

A resistance to heat flow exists at the junction of two surfaces. It has long been recognized that there exists a hysteresis effect, that is, the value of thermal contact resistance in the unloading process is less than that in the loading process at the same load. However, little work has been done in utilizing this phenomenon to enhance the thermal contact conductance. The present experimental work investigated the effect of loading history; in particular the number of load cycles and overloading pressure, on the thermal contact conductance. It was found that the value of the thermal contact conductance might be enhanced by up to 51 percent. A cost-effective way of enhancing the contact conductance is suggested. [S0022-1481(00)01601-7]

Keywords: Heat Transfer

1 Introduction

A detailed examination of solid surface reveals that there exist a large number of microscopic peaks and valleys on any surface. Therefore, when two rough flat surfaces are brought into contact under pressure, they touch each other at only a few discrete spots. The real contact area is only a fraction of the nominal area (typically less than one percent). When heat flows through the interface, it is constrained to flow through the separated contact spots. This constriction causes an additional resistance to the heat flow, namely the thermal contact resistance. The thermal contact conductance is the reciprocal of the contact resistance.

Extensive reviews on the current state of the thermal contact conductance may be found in Madhusudana and Fletcher [1] and Fletcher [2]. It is generally agreed that the value of thermal contact conductance is related to the surface roughness, material properties, and the load applied to the surfaces in contact. Theoretical and experimental studies conducted by Cooper et al. [3], Mikic [4], and Song and Yovanovich [5] indicate that the nondimensional conductance and load are related by equations of the form

$$\frac{h\sigma}{mk_S}=c\left(\frac{P}{H}\right)^n. \tag{1}$$

Yovanovich [6], for example, proposed $c=1.25$ and $n=0.95$. This is applicable for initial loading assuming plastic deformation.

Experiments conducted by Madhusudana and Williams [7] and Williamson and Majumdar [8] found that there existed a hysteresis effect, that is, the values of contact conductance in the unloading process are higher than those in the initial loading process ([9]). McWaid and Marshall [10] found that hysteresis occurred on the surfaces with different machining processes. Experimental work by Li et al. [11] investigated the effect of overloading on the contact conductance. Their results confirmed that hysteresis existed between the contact of stainless steel/stainless steel and mild steel/mild steel specimen pairs.

Mikic [4] analyzed the hysteresis effect in his theoretical work. He concluded that due to the change of deformation mode in the loading and unloading process, the contact conductance is expected to be higher in the unloading process, provided the asperities deform plastically in the initial loading. The possible change of asperity shape due to elastic recovery was not mentioned in his analysis.

Experimental work by Pullen and Williamson [12] and Williams and Idrus [13] demonstrated that the shape of contacting asperities change and the rms roughness of the surface decrease as the result of thermal and mechanical load. Their results also suggest that some fundamental change may remain on the rough surface upon removal of the applied load. Thus, the assumption that the shape of asperities on the contact surface stays unchanged in the loading and unloading process may not be valid.

Although some previous investigations have studied hysteresis, the effect of the number of loading cycles, and the effect of mechanically overloading the contact have received little attention. The present work reports an experimental investigation into these two effects. Also, an explanation of the observed effects of cyclic loading and overloading is offered, taking into account the change of asperity shapes.

2 Experimental Investigation

A detailed description of the experimental procedure, including specimen preparation, experimental apparatus, and the uncertainty analysis have been reported by Li et al. [11]. A brief description is given below.

The experimental apparatus contains three major parts: two stainless plates and a Pyrex glass tube forms an enclosed vacuum chamber. A rotary vacuum pump is linked to the chamber. The vacuum level was maintained at 2×10^{-2} mbar during the test. Four steel rods and a middle plate secure the test column in place during the initial assembly. The test column contains a heater block, two heat flux meters, two test specimens, a cooler, and two insulators. The heater block has a 250 W band heater attached to it. A voltage stabilizer is used to keep a constant voltage for the band heater. Cooling water circulates through the cooler. Two insulators, made of reinforced concrete, isolate the test column from the environment. A radiation shield was also installed in the test apparatus. A lever arm system located outside the vacuum chamber is employed to apply load to the test column. 16 calibrated type T thermocouples (ϕ 1 mm) were used in the system. The outputs from the thermocouples were fed into a 16-bit Sensory-419 data acquisition board, which converts the signals from the thermocouples into PC for analysis.

Test specimens were made of AISI304 stainless steel and AISI1020 mild steel. Table 1 lists the surface roughness test results and the material properties of the specimens used. The test

---

[1] Author to whom correspondence should be addressed.

Contributed by the Heat Transfer Division for publication in the JOURNAL OF HEAT TRANSFER. Manuscript received by the Heat Transfer Division Jan. 15, 1999; revision received, Sept. 22, 1999. Associate Technical Editor: A. Majumdar.

Table 1 Roughness data and material properties of the test specimens

Specimen	SS 54	SS 137	MS 12	MS 43	SS 34	SS 48
σ_q	1.981	2.137	3.401	3.353	4.771	4.329
σ	2.914		4.776		6.442	
m_a	0.317	0.342	0.336	0.341	0.268	0.259
m	0.466		0.478		0.373	
W_a	0.325	0.375	0.823	0.985	0.956	0.866
Wm_a	0.002	0.061	0.046	0.052	0.002	0.048
T_m	348		352		358	
K	12.72		48.18		12.88	
H	2940		2385		2940	

specimens were cleaned with acetone prior to assembly. A light load of 100 kPa was applied to the test column to secure the alignment. The system was left to degas over 12 hours before the heater was switched on. The system was considered to reach steady state based on two observations: (1) Temperature measurement did not vary by 0.2°C over a period of 15 minutes for each thermocouple. (2) The heat fluxes in the two test specimens differed by less than three percent.

3 Results and Discussion

3.1 Hysteresis Effect. Two pairs of specimens were tested for the hysteresis effect. After the initial assembly, the test column was loaded from 0.865 to 6.425 MPa in six steps during the loading process. Thermal contact conductance was measured at each step. When the loading process was completed, the test column was unloaded back to 0.865 MPa in six steps and the contact conductance was again measured at each step. The results are plotted in Fig. 1.

It is clear from Fig. 1 that hysteresis effect existed in the tests conducted. For both pairs of specimens, the measured thermal contact conductance was higher in the unloading process than in the loading process, even though the test column was subjected to the same contact pressure.

For the pair of stainless steel specimens (SS54-137), the difference in the value of contact conductance reached its peak at the contact pressure of 1.977 MPa. At this pressure, the value of thermal contact conductance was 60 percent higher in the unloading process than in the loading process. At the end of the unloading process, the conductance was still 33 percent higher than the corresponding value during loading.

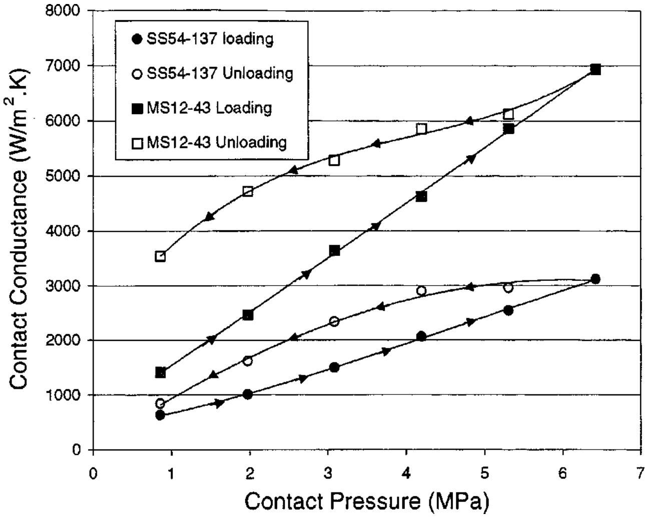

Fig. 1 Results for specimens SS54-137 and MS12-43 in loading and unloading process

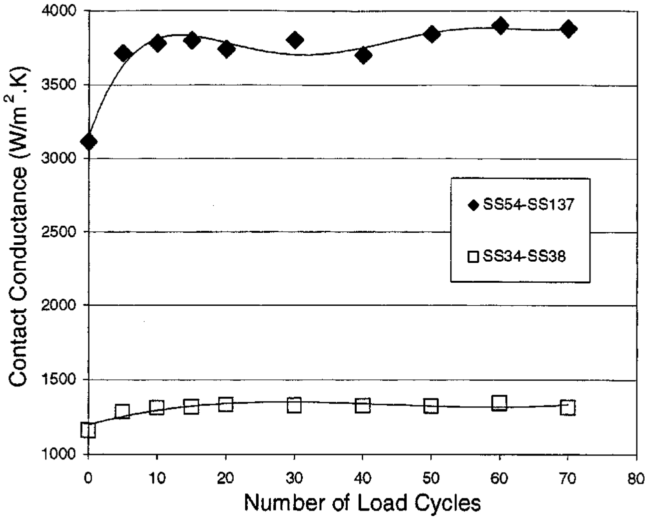

Fig. 2 Number of loading cycles versus contact conductance for SS 34-48 and SS54-137 at operation pressure of 6.425 MPa

For the pair of mild steel specimens (MS12-43), the largest difference in the value of contact conductance appeared at the end of unloading process. The value of thermal contact conductance had increased by 150 percent compared to that at initial loading.

3.2 Number of Load Cycles. Two pairs of stainless steel specimens were tested to study the effect of the number of load cycles applied on thermal contact conductance. After the initial assembly, the test column was loaded to the operating pressure of 6.425 MPa in six steps. The values of thermal contact conductance were measured at each step, and the test column was unloaded back to 0.865 MPa. Next, the test column was loaded back to the operation pressure of 6.425 MPa in a single step. This procedure was repeated a number of times. When a certain number of load cycles was completed, the value of the contact conductance was measured and recorded. The numbers of load cycles applied to the test column were 5, 10, 15, 20, 30, 40, 50, 60, and 70. The test results are shown in Fig. 2.

It is clear from Fig. 2 that the number of load cycles applied does affect the thermal contact conductance. The increase in thermal contact conductance mainly occurred in the first five load cycles. At the end of the first five load cycles, specimen pair SS54-137 had an increase of 19 percent, while specimen pair SS34-48 had an increase of 11 percent in the value of contact conductance, compared to the value in initial loading. From five to 30 load cycles, specimen pair SS54-137 showed an improvement of only two percent, while for specimen pair SS34-48, the improvement was three percent. Thus, at the end of 30 load cycles, specimens SS54-137 had an increase of 22 percent, while specimens SS34-48 had an increase of 15 percent in contact conductance, compared to the value in initial loading. Once the number of load cycles was over 30, there was no significant increase in contact conductance.

It was also noticed that the surface roughness might also influence the effect of load cycles. It appeared that the effect of load cycles was more evident on a smooth surface than on a relatively rough surface.

The reason for the effect of the number of load cycle applied, we believe, is the substitution of asperities deformation mode. At the operation pressure of 6.425 MPa, in the initial loading process, the majority of plastic deformation had occurred and been completed, and asperities deformed elastically in the following load cycles. We recorded a dramatic increase in the value of thermal contact conductance after only five load cycles. However, for some asperities, plastic deformation may not have been fully complete at the end of five cycles. These asperities completed their

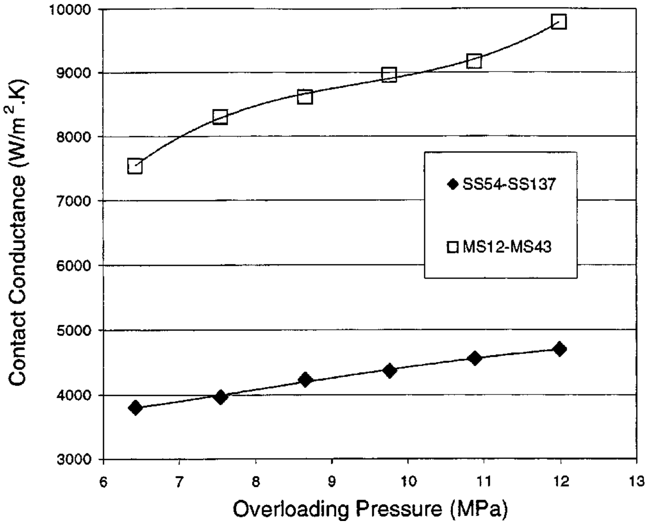

Fig. 3 Overloading pressure versus contact conductance for SS54-137 and MS 12-43 at operation pressure of 6.425 MPa

plastic deformation in the following load cycles, deformed elastically at the end of plastic deformation, and were responsible for the increase in the value of thermal contact conductance in 5–30 load cycles. After the application of 30 load cycles, almost all of the asperities have completed their plastic deformation. The asperities in contact deformed elastically in the following load cycles, and the measured contact conductance values tended to be constant. Elastic deformation requires more contact area and number of contact spots to sustain the same load as plastic deformation. Thus, the value of thermal contact conductance after 30 load cycles is higher compared to that in the initial loading process.

3.3 Overloading Pressure. It was verified in the last section that repeatedly loading the test column produced an increase in thermal contact conductance. It is logical to expect that overloading, that is loading the test column beyond the normal operating pressure, will also enhance the contact conductance.

Two pairs of specimens were tested to verify the effect of overloading. After initial assembly, the test column was loaded to an operation pressure of 6.425 MPa in six steps and the values of thermal contact conductance were measured in each step. The test column was than unloaded back to 0.865 MPa. Stainless steel specimen pair SS54-137 went through a number of load cycles at 6.425 MPa, as shown in the last section, before the start of the overloading session. Mild steel specimens MS12-43 also went through 30 load cycles at 6.425 MPa.

The test column was then overloaded to a predetermined pressure for 30 load cycles and unloaded back to 0.865 MPa. A contact pressure of 6.425 MPa was then applied to the test column, and the value of contact conductance was measured. The overloading pressures applied in this investigation were: 7.537, 8.649, 9.761, 10.873, and 11.985 MPa.

From the experimental results shown in Fig. 3, it is clear that the overloading had significant effect on contact conductance. For both specimens pairs tested, it was found that the values of contact conductance measured after the overloading operation were much higher than the values that were obtained without the overloading, *even though the test column was loaded at the same operation pressure*. It is also clear that the value of contact conductance increased with the overloading pressure. When the specimens were overloaded to 11.985 MPa, SS54-137 had an increase of 23 percent, while MS12-43 had an increase of 30 percent in contact conductance, compared to the value obtained after cycling the load 30 times. When they were compared to the values obtained in the *initial* loading process, the improvements were 51 percent and 41 percent for SS54-137 and MS12-43, respectively.

No previous theory may be applied to predict the effect of overloading on thermal contact conductance. The experimental results on the overloading effect lead us to believe that the shape of asperities may have changed in the elastic recovery process, as discussed below.

Considering a single asperity in contact with a flat surface, the asperity has a tip radius R_0 prior to the initial loading, and it deforms plastically under the normal operation pressure of P_0. As the load is removed, the plastically deformed asperity recovers elastically. But it does not recover back to its original shape due to the existence of residual stress. The asperity recovers to a tip radius of R_1. Obviously R_1 is greater than R_0. Provided the contact pressure is not greater than P_0 in the following load cycles, the asperity deforms elastically at the radius of R_1. The contact area corresponding to the elastic deformation is larger than that of initial plastic deformation at the same intermediate pressure.

The number of contact spots on the contacting surface also increases at an intermediate contact pressure. This is due to the fact that for the same amount of deflection, the elastic deformation sustains less load than the plastic deformation. When the asperity deforms elastically, it needs to deform further in order to sustain the same load as the plastic deformation. Therefore, the total number of contact spots increases at the intermediate contact pressure.

Because the total contact area increases due to the elastic deformation, and the total number of contact spots increases due to the greater deflection, the thermal contact conductance increases as well. This is one of the reasons that contact conductance is enhanced by repeated loading.

When the asperity is subjected to a new overloading pressure of P_1, greater than P_0, it deforms plastically again. It starts with an initial radius of R_1, then undergoes plastic deformation at the overloading pressure of P_1. When the load is removed, the asperity will recover back to a radius of R_2 ($R_2 > R_1$). The asperity then deforms elastically in the new recovered radius of R_2 in the following load cycles, provided the pressure does not exceed P_1. As R_2 is greater than R_1, when the normal operation pressure of P_0 is applied again, the asperity will yield a larger radius of contact, thus a larger contact area. The thermal contact conductance is therefore increased at the end of overloading operation even though the contact pressure applied remains the same.

4 Conclusions

This experimental program has demonstrated that

1 hysteresis effect exists for the contact of stainless steel/stainless steel and mild steel/mild steel surfaces for different degrees of surface finish.

2 number of load cycles applied affects the value of thermal contact conductance. In general, increasing number of load cycles results in higher contact conductance.

3 cycling the load cannot increase the value of contact conductance indefinitely. It was found that 30 load cycles might be sufficient to get the maximum benefit from repeated loading.

4 further increase in the value of thermal contact conductance may be gained by overloading the contact surfaces beyond the normal operation pressure for a number of load cycles. The overloading operation may increase the value of thermal contact conductance by as much as 51 percent, depending on the overloading pressure applied.

5 the reason for the effect of overloading, we believe, is that the asperities change shape during the unloading process.

6 engineers working in the area of thermal contact conductance may use preoverloading as a cost-effective tool to enhance the thermal performance of the components.

Further work is currently underway to develop a detailed theoretical analysis for the overloading process.

Acknowledgment

The support of the Australian Research Council under Grant No. A-9530286 to C. V. Madhusudana is gratefully acknowledged.

Nomenclature

σ_q = rms roughness, μm
σ = combined rms surface roughness of two surfaces, μm
m_a = mean absolute slope
m = combined mean absolute slope of two surfaces
P = external pressure applied to the joint, MPa
W_q = rms waviness, μm
Wm_q = rms waviness slope
T_m = mean contact temperature, K
H = microhardness of the softer material in contact, MPa
k_s = harmonic mean of the thermal conductivity of the two contacting solids, W/m K
c = a constant
n = load exponent

References

[1] Madhusudana, C. V., and Fletcher, L. S., 1986, ''Contact Heat Transfer—The Last Decade,'' AIAA J., **24**, pp. 510–523.
[2] Fletcher, L. S., 1990, ''A Review of Thermal Enhancement Technique for Electronic System,'' IEEE Trans. Compon., Hybrids, Manuf. Technol., **13**, pp. 1012–1021.
[3] Cooper, M. G., Mikic, B. B., and Yovanovich, M. M., 1969, ''Thermal Contact Conductance,'' Int. J. Heat Mass Transf., **12**, pp. 279–300.
[4] Mikic, B. B., 1971, ''Analytical Studies of Contact of Nominally Flat Surface; Effect of Previous Loading,'' Trans. ASME J. Lub. Technol., **92**, pp. 451–456.
[5] Song, S., and Yovanovich, M. M., 1988, ''Relative Contact Pressure: Dependence on Surface Roughness, and Vickers Microhardness,'' J. Thermophys., **2**, No. 1, pp. 43–47.
[6] Yovanovich, M. M., 1982, ''Thermal Contact Correlations, Spacecraft Radiative Transfer and Temperature Control,'' *Progress in Astronautics and Aeronautics*, Vol. 83, T. E. Horton, ed., AIAA, New York, pp. 83–95.
[7] Madhusudana, C. V., and Williams, A., 1973, ''Heat Flow Through Metallic Contacts—The Influence of Cycling the Contact Pressure,'' *1st Australian Conference on Heat Mass Transfer*, Section 4.1, Monash University, Melbourne, Australia, pp. 33–40.
[8] Williamson, M., and Majumdar, A., 1992, ''Effect of Surface Deformations on Contact Conductance,'' Trans. ASME J. Heat Transfer, **114**, pp. 802–809.
[9] Madhusudana, C. V., 1996, *Thermal Contact Conductance*, Springer, New York, pp. 130–134.
[10] McWaid, T. H., and Marshall, E., 1992, ''Thermal Contact Resistance Across Pressed Metal Contacts in a Vacuum Environment,'' Int. J. Heat Mass Transf., **35**, pp. 2911–2920.
[11] Li, Y. Z., Madhusudana, C. V., and Leonardi, E., 1998, ''On The Enhancement Of Thermal Contact Conductance: Effect Of Over Loading,'' Heat Transfer 1998, *Proceeding of 11th International Heat Transfer Conference*, Vol. 7, pp. 27–32.
[12] Pullen, J., and Williamson, J. B. P., 1966, ''On the Plastic Contact of Rough Surface,'' Proc. R. Soc. London, Ser. A, **327**, pp. 159–173.
[13] Williams, A., and Idrus, N., 1977, ''Changes of Surface Shapes due To Contact Loading With Thermal and Pressure Cycling,'' paper presented at AIAA 12th Thermophysics Conference, Albuquerque, NM.

Experimental Analysis of Thermal Instability in Natural Convection Between Horizontal Parallel Plates Uniformly Heated

O. Manca
B. Morrone
Dipartimento di Ingegneria Aerospaziale,
Seconda Università, degli studi di Napoli,
Via Roma 29,
81031 Aversa CE, Italy

S. Nardini
Dipartimento di Energetica, DETEC
Termofluidodinamica applicata e
Condizionamenti ambientali,
Università degli studi Federico II,
Piazzale Tecchio,
80125 Napoli, Italy

An experimental investigation of natural convection between horizontal, heated, parallel plates in air was carried out by visualizing the flow and measuring the air temperature. Grashof numbers, based on the plate spacing, varied in the 1.22×10^5–1.06×10^6 range. Flow patterns and probable onset of secondary motions were observed for three heating modes: (1) both plates heated, (2) upper plate heated and lower one unheated, and (3) upper plate unheated and lower one heated. The main flow pattern resembled a C shape (C loop) for all modes. In fact, the flow penetrated inside the cavity close to the leading edge of the lower plate and exited from the upper part, by reversing its motion between the plates. When the lower plate was heated, flow visualization showed that secondary flows were added to the C loop main flow. Such secondary structures arose as thermals, then changed into longitudinal vortices and, in the upper region of the open-ended cavity, a chaotic motion was detected. The existence of these structures was confirmed by measurements of instantaneous temperature values. They showed that the greater the Grashof number the more chaotic the flow in the outflow branch of the C loop when the lower plate was heated and the upper one was unheated. [S0022-1481(00)01801-6]

Keywords: Heat Transfer, Instability, Natural Convection, Three Dimensional, Visualization

Introduction

The growing attention to natural convection is related to its importance in several engineering applications as well as different natural phenomena, and a thorough investigation is required for some basic configurations, as was pointed out by Goldstein and Volino [1] in their recent review.

The configuration of two horizontal, heated, flat, parallel plates, in particular, has many technological applications such as the cooling of electronic components, solar cells, and chemical vapor deposition (CVD) systems. These aspects of technical interest can involve thermal instabilities in plane air layers ([2]). The flow can show very complex patterns due to an interaction between the horizontal plate and other surfaces. The study of such flows has been extensive, and much information exists concerning their heat transfer characteristics, particularly under steady or quasi-steady conditions. In spite of many studies, the structures and heat transfer mechanisms of these flows are not completely described. This is particularly true for thick layers under both transient and quasisteady conditions.

One of the first experimental investigations on a uniformly heated upward-facing horizontal plate shrouded by a parallel insulated surface placed above, was carried out by Sparrow and Carlson [3]. They determined the local and average natural convection heat transfer characteristics. The existence of longitudinal vortices between horizontal parallel isothermal plates was investigated by Fukui et al. [4]. They analyzed the vortex patterns for laminar natural and forced convection. Maughan and Incropera [5,6] studied experimentally ([5]) and numerically ([6]) the heat transfer for laminar mixed convection in horizontal and inclined channels. Evans and Greif [7,8] studied thermally unstable flow and heat transfer of a gas in a horizontal channel with a heated bottom surface and a cooled top surface by means of a numerical approach. Their interest was focused on the applications of the CVD. Cheng and Shi [9] made use of a visualization technique to study the developing secondary flow patterns in mixed convection caused by buoyancy forces in horizontal rectangular channels with isothermally heated upper and bottom plates. Lin and Lin [10,11] carried out, by means of a visualization technique and velocity and temperature measurements, an investigation on mixed convection of air in bottom heated horizontal and slightly inclined ducts. More recently, Chang et al. [12] carried out an experimental investigation by means of flow visualization and temperature measurement for a mixed convection of air in a horizontal plane channel.

Natural convection between two horizontal parallel plates is similar to natural convection in horizontal open-ended cavities, since the former configuration shows a temperature and flow symmetry in the transversal plane. As far as natural convection in open-ended cavities is concerned, Vafai and Ettefagh [13,14] numerically studied the transient behavior of the flow field between two isothermal walls. For a more complete review of this topic, readers should refer to Vafai et al. [15].

The almost complete lack of studies on natural convection between horizontal parallel plates and in open-ended cavities with isoflux heated walls should be noticed. One of these studies was carried out by Hart [16], who performed an experimental study in order to detect the patterns of the instabilities that take place in convective flows between inclined plates. He analyzed the configurations with an inclination angle ranging from 10 deg to 90 deg with regards to the vertical, with the plates heated from below. Recently Manca et al. [17,18] performed experimental analyses by means of visualization for natural convection in horizontal and slightly inclined isoflux heated channels.

In this paper, the authors describe an experimental analysis for horizontal parallel plates heated with uniform heat flux, carried out by means of a visualization technique and air temperature measurements by means of hot-wire probes, to evaluate the tem-

---

Contributed by the Heat Transfer Division for publication in the JOURNAL OF HEAT TRANSFER. Manuscript received by the Heat Transfer Division, Dec. 9, 1998; revision received, Dec. 10, 1999. Associate Technical Editor: B. Chung.

perature fluctuations and the average thermal field. The most relevant configurations have been analyzed for different plate distances and heat flux values.

Experimental Apparatus

The experimental test section was made of two principal parallel isoflux heated walls and two unheated side walls. Each principal wall consisted of two 400×530-mm sandwiched phenolic fiberboard plates. The side walls were made of Plexiglas rectangular rods, machined to an accuracy of ±0.03 mm. The plate spacing was measured to an accuracy of ±0.25 mm by a dial-gauge equipped caliper.

The cavity was 400 mm long, 2 L, and 475 mm wide (W) and was open to the ambient along its right and left edges (Fig. 1(*a*)). In order to reduce conductive heat losses, a 150-mm Polystyrene block was affixed to the rear face of each plate. The plate facing the channel was 3.2 mm thick and its surface adjacent to the internal air was coated with a 35-μm-thick nickel plated copper layer, as shown in Fig. 1(*b*). The low emissivity of nickel (0.05) minimized radiation effects on heat transfer. The rear plate was 1.6 mm thick. Its back surface was coated with a 17.5-μm-thick copper layer, which was the heater. The plates were heated by passing a direct electrical current through each of the heaters, which had a serpentine shape. Its runs were 19.6 mm wide with a gap of nearly 0.5 mm between each one, giving each heater a total length of 9.0 m. Its expected electrical resistance was 0.50 Ω. The narrow gaps between the runs, together with the relatively high thickness (4.8 mm) of the resulting low-conductive fiberglass, were suitable to maintain a nearly uniform heat flux at the plate surface ([19]). The plates were heated by passing a direct electrical current through the heaters: this was accomplished by using a Hewlett-Packard 6260B DC power supply. The electrical power supplied by each heater was evaluated by measuring the voltage drop across the plates and the current passing through them. The voltage drop was measured by a HP-3465A digital multimeter, while the current was calculated by the measured voltage drop across a reference resistance. A variable power resistor was connected in series with one of the heaters to allow the symmetric heating of the cavity. To avoid electrical contact resistances, thick copper bars soldered to both the electric supply wire and the ends of each heater were bolted together. The dissipated heat flux per board was evaluated to an accuracy of ±2 percent. The entire apparatus was located within a room, sealed to eliminate extraneous air currents.

Wall temperatures were measured by 36 0.50-mm o.d. ungrounded iron–constantan thermocouples embedded in each fiberboard plate and in contact with the outer layer. They were located at 12 longitudinal stations at three different *z* values. Fifteen thermocouples were affixed to the rear surface of the plates and embedded in the Polystyrene to enable the evaluation of conductive heat losses.

The ambient air temperature was measured by a shielded thermocouple placed near the leading edge of the channel. A Kaye instrument K170 ice point was used as a reference for thermocouple junctions. Their voltages were recorded to 1 μV by a HP 3497A acquisition unit connected to a 486-66 PC. Calibration of the temperature measuring system showed an estimated precision of the thermocouple-readout system of ±0.1°C.

The temperature of the air in the channel was measured by a Dantec 5600 hot-wire system. The measurements were carried out by using a 55P15 special miniature probe connected to a 56C01-56C20 constant current bridge. The probe was calibrated in air, in the 15–80°C temperature range. The maximum uncertainty was ±0.1°C. The probe could be manually positioned anywhere in the cavity using a micrometer traversing mechanism supported on one side of the frame. It allowed positioning of the probe along *x* and *y*-axes to an accuracy of not less than 0.03 mm and along the *z*-coordinate to an accuracy not less than 0.1 mm.

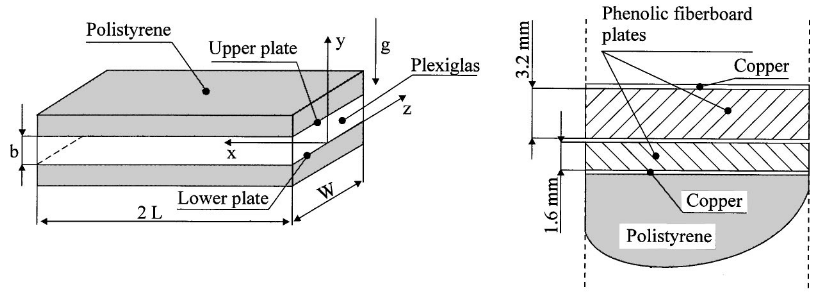

(a) (b)

Fig. 1 (*a*) View of the test section; (*b*) Sketch of heated sandwiched plate

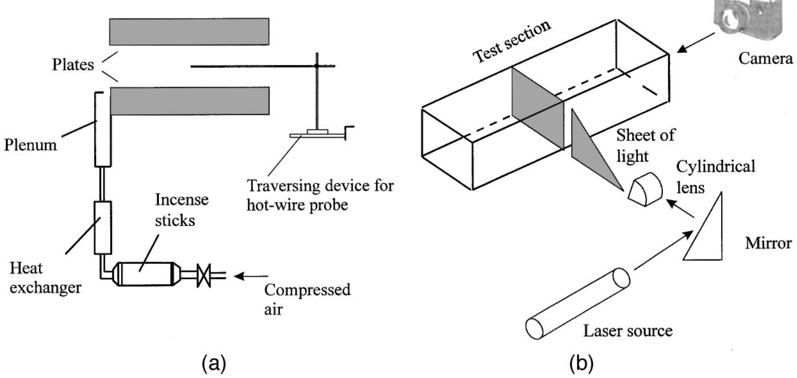

(a) (b)

Fig. 2 Sketch of the visualization and anemometric arrangement

The anemometric signal was acquired and recorded by the data acquisition system and reduced by means of a PC through the Labview™ [20] program. The set of measurements was carried out 8–9 h after the modification of the configuration. In fact, this time interval was long enough for the eventual wall temperature fluctuations to attain a quasisteady state, with regard to constant time average value.

Smoke for flow visualization was generated by burning incense sticks in a steel tube connected to a compressor. The smoke was injected through a glass heat exchanger to reduce the temperature of the smoke, and then sent into a plenum. Its temperature, measured by a thermocouple, turned out to be close to that of the ambient air entering the cavity. It was then driven to the test section through a small slot situated under the leading edge of the bottom plate along the plate width. A sketch of the apparatus is reported in Fig. 2. The longitudinal view of the arrangement for the air temperature measurements is reported in Fig. 2(*a*), while in Fig. 2(*b*) the sketch of the visualization setup is shown. Preliminary tests were carried out to determine the plenum location so as not to interfere with the air flow at the inlet section. The visualization was made possible by means of a laser sheet, generated by a He–Ne laser source. The laser sheet was produced by placing a mirror near the end of the test section at an angle of 45 deg in the direction of the main flow, behind which a cylindrical lens was placed to enlarge the beam as needed. Small adjustments were allowed by means of a micrometer screw system, in order to take photographs at different locations along the z-axis. The same arrangement was used to obtain pictures in the y-z plane at several x locations. The still camera was a programmable Minolta 7000 and the film was a Kodak TMAX™ 3200.

Data Reduction and Analysis of Air Temperatures

Three heating modes are taken into account in the analysis: Mode I, both plates heated; Mode II, upper plate heated and lower one adiabatic; Mode III, lower plate heated and upper one adiabatic.

The Grashof number is defined as

$$\mathrm{Gr}=\frac{g\beta\overline{q_c}b^4}{\nu^2k} \tag{1}$$

where $\overline{q_c}$ is the average convective heat flux

$$\overline{q_c}=\frac{1}{2}\frac{1}{2L}\left[\int_0^{2L}q_{c,b}(x)dx+\int_0^{2L}q_{c,t}(x)dx\right]. \tag{2}$$

The thermophysical properties are evaluated at the reference temperature

$$T_r=\frac{\overline{T_w}+T_0}{2} \tag{3}$$

with

$$\overline{T_w}=\frac{1}{2}\frac{1}{2L}\left[\int_0^{2L}T_{w,b}(x)dx+\int_0^{2L}T_{w,t}(x)dx\right] \tag{4}$$

where $T_{w,b}(x)$ and $T_{w,t}(x)$ are the spanwise average values.

Local convective heat flux, $q_c(x)$, was not uniform because of radiation and conduction heat losses. Experimental data were reduced by first introducing, in the equations presented above, the local convective heat flux

$$q_c(x)=q_\Omega(x)-q_k(x)-q_r(x) \tag{5}$$

where $q_\Omega(x)$ is the local heat flux due to ohmic dissipation, assumed uniform along x, $q_k(x)$ the local conduction heat losses from the plate, and $q_r(x)$ the local radiative heat flux from the plate. For each run, the terms $q_k(x)$ were calculated by means of a numerical procedure, where a three-dimensional distribution of the temperature is assumed in the Polystyrene. Therefore, q_k on the plate wall was a function of both x and z-coordinates, and its values were averaged along z. The predicted temperatures for some configurations of the system were previously compared with those measured by thermocouples embedded in the Polystyrene insulation and the agreement was very good, the maximum deviation being three percent.

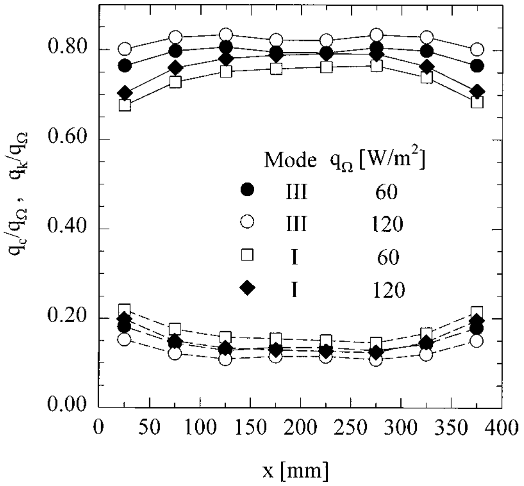

Fig. 3 Relative heat fluxes distributions along the length of the plate: (——) convective and (– – –) conductive

A two-dimensional radiative cavity was made of the two plates, considered as diffuse-gray surfaces and the two black edge sections at room temperature. In all cases the radiative heat losses were not greater than two percent of the ohmic dissipated power. The $q_r(x)$ terms were calculated for each temperature distribution of the wall, ambient temperature, and plate spacing, dividing each plate into 16 strips along its length. Each strip was assumed at the spanwise average temperature.

In Fig. 3 the convective as well as conductive heat flux distributions, normalized with regard to the ohmic heat flux at each x location, are reported for two heating Modes I and III and two wall heat fluxes (60 and 120 W/m^2) for $b=32.2$ mm. A nearly uniform distribution of the heat losses is observed for the cases shown in this figure. Analogous trends were observed for open-ended cavities with $b=20.0$ and 40.0 mm. The maximum value of the heat losses was 28 percent of the ohmic dissipated rate for a wall heat flux of 240 W/m^2, $b=40.0$ mm, and Mode I.

The detection test points were placed at several x locations, in the longitudinal section, and at five y-coordinates. 512 data samples were taken in order to measure the time-averaged air temperatures and the fluctuations of the air flow temperature. The response of the hot-wire anemometer was about 2 kHz ([21]) and, according to the procedure suggested by Bruun [22], the signal was sampled every 0.50 s.

The uncertainty in the calculated quantities was determined according to the standard single sample analysis recommended by Kline and McClintock [23] and Moffat [24]. The uncertainty of the Grashof number was ±7 percent.

Results and Discussion

The preliminary tests carried out showed that no conductive regime was set up, in accordance with the findings of Lavine [25]. This is well understandable from a physical point of view: When the system is either heated with a prescribed wall heat flux on one plate and the other one insulated or both plates heated with heat flux, no quasi-steady state regime would be attained without any flow incoming into the cavity from the ambient. In fact, a flow penetration inside the cavity was detected for any considered Grashof number. In addition, the flow entered the cavity to a greater extent, the greater the Grashof number was, for fixed plate

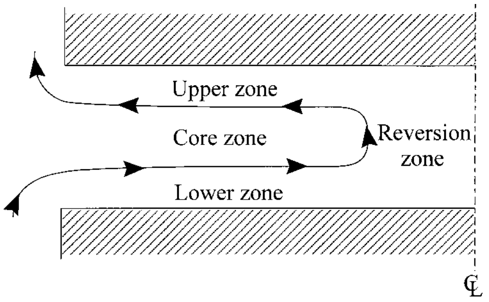

Fig. 4 Subdivision of the main flow in the longitudinal section

spacing b. A sketch of the main flow patterns in the longitudinal section at $z=0$ is shown in Fig. 4. The main flow is subdivided into four zones identified as follows:

1. the *lower zone*, the boundary layer where the fluid flows adjacent to the lower plate from the leading edge to the middle plane of the open ended cavity;
2. the *reversion zone* where the main flow reverses its motion;
3. the *upper zone*, the boundary layer where the fluid flows adjacent to the upper plate from the reversion zone to the trailing edge; and
4. the *core zone* separates the lower and the upper zones.

In the following the above described flow will be referred to as C loop. This schematic view takes into account the numerical results presented by Vafai and Ettefagh [14], when the lowest values of the longitudinal aspect ratio were considered, as already observed experimentally by Manca et al. [17,18]. In these two experimental papers a different behavior for the two investigated gaps ($b=20.0$ mm and $b=40.0$ mm) was observed. At $b=20.0$ mm, the stabilizing effect of the heated upper plate affected the main flow in such a way as to sweep away the fluid, only then could any secondary motion start. In this case the core zone nearly vanished and two boundary layers, the upper and lower ones, came into contact with each other. This implied that the temperature profile was nearly uniform along y (in the direction orthogonal to the main flow). Thus, the thermal gradient along y was weak and did not determine secondary motions along the same direction. On the contrary, for the widest analyzed gap ($b=40.0$ mm), the heat flux dissipated by the upper plate could not prevent the onset of secondary flows since the plates were too far away.

The experimental tests that were run in the present investigation showed that Mode II always presented a steady, laminar regime, up to the investigated values of Grashof equal to 6.0×10^5 and $L/b=5.0$ ($b=40.0$ mm and $q_\Omega=120$ W/m^2). Instead, Mode I presented a flow regime steady up to $\mathrm{Gr}=4.0\times10^4$ and $L/b=10$ ($b=20.0$ mm and $q_\Omega=60$ W/m^2). Mode III, which was the most interesting and investigated herein, showed a steady regime, inside the C loop, up to $\mathrm{Gr}=1.9\times10^4$ and $L/b=10$ ($b=20.0$ mm and $q_\Omega=60$ W/m^2).

Flow Visualization. Results were obtained for a cavity gap equal to 32.2 mm. This value corresponded to an aspect ratio of $L/b=6.2$. The ohmic heat flux was set equal to 60, 120, and 240 W/m^2. The aforementioned parameters yield Grashof numbers in the following range: 1.24×10^5–4.65×10^5.

Longitudinal sections, with an ohmic wall heat flux of 60 W/m^2, for the three heating modes are shown in Fig. 5. It is worth noting that all three modes present a main flow with the peculiar shape indicated in Fig. 4. For these configurations, the reversion zone of the C loop takes place at about $x=200$ mm. For heating Mode II, Fig. 5(b), ($\mathrm{Gr}=1.22\times10^5$), the flow is laminar, as already observed for $b=20.0$ and 40.0 mm in Manca et al. [17,18]. For heating Mode III, Fig. 5(c) ($\mathrm{Gr}=1.24\times10^5$), a vortex is

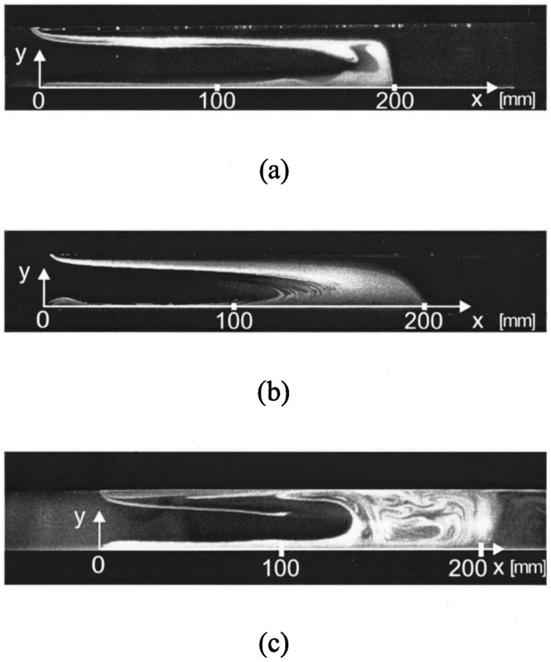

Fig. 5 Longitudinal section at $z=0.0$ mm for $b=32.2$ mm, $q_\Omega=60$ W/m^2; (*a*) Mode I ($\mathrm{Gr}=2.42\times10^5$); (*b*) Mode II ($\mathrm{Gr}=1.22\times10^5$); (*c*) Mode III ($\mathrm{Gr}=1.24\times10^5$)

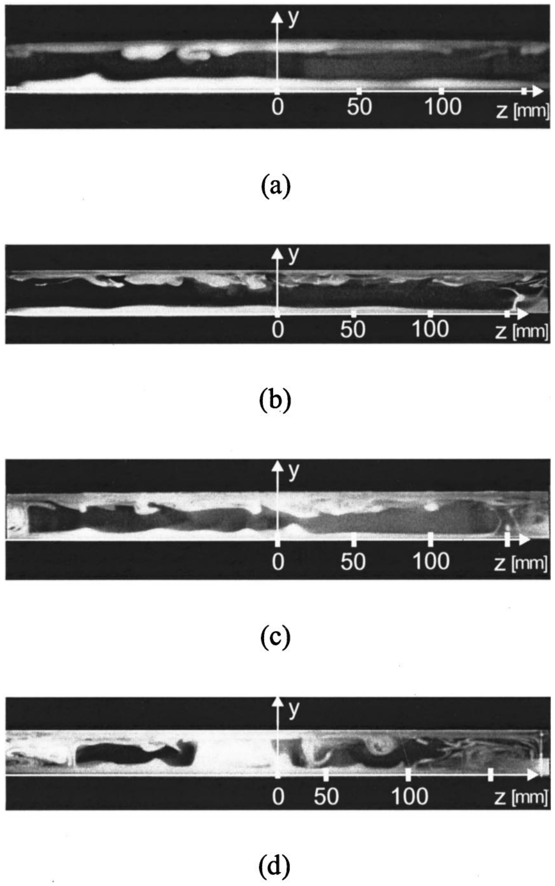

Fig. 6 Cross-stream sections for $b=32.2$ mm, $q_\Omega=60$ W/m^2, and $\mathrm{Gr}=1.24\times10^5$, Mode III at (*a*) $x=20$ mm; (*b*) $x=60$ mm; (*c*) $x=100$ mm; (*d*) $x=150$ mm

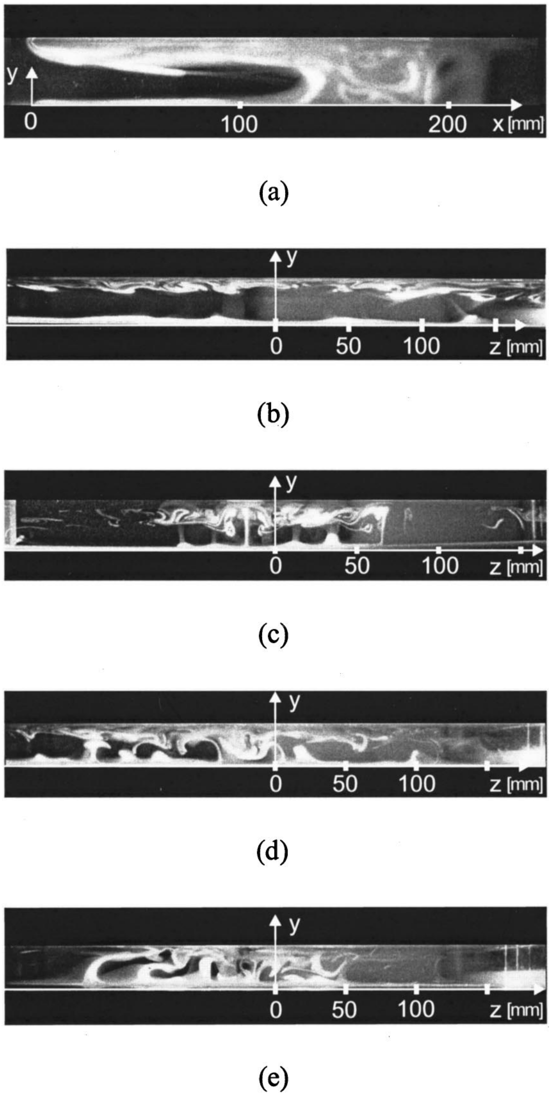

Fig. 7 $b=32.2$ mm, $q_\Omega=120$ W/m^2, and Gr$=2.35\times10^5$, Mode III: (*a*) longitudinal section $z=0.0$ mm; cross-stream section at (*b*) $x=20$ mm; (*c*) $x=60$ mm; (*d*) $x=100$ mm; (*e*) $x=160$ mm

present in the core region of the longitudinal section between $x=140$ mm and $x=200$ mm, and at about $x=100$ mm the flow transition starts. Figure 5(*a*) (Mode I and Gr$=2.42\times10^5$) exhibits an almost regular flow pattern up to about $x=120$ mm. Moreover, the flow adjacent to the upper plate presents more regular patterns than the previous configuration. Therefore, for this plate spacing b, the stabilizing effects of the upper heated plate becomes significant. Mode III is the most interesting configuration with regard to the secondary motion. For this reason in the following only the results for Mode III are presented.

The cross-stream sections for Mode III are reported in Fig. 6 with the same geometric and heating parameters in Fig. 5. At $x=20$ mm (Fig. 6(*a*)), the flow is nearly laminar in the lower zone, while in the upper zone there are small perturbations of the flow leaving the open-ended cavity. At $x=60$ mm (Fig. 6(*b*)) a chaotic motion is observed in the upper zone, whereas in the lower zone the flow is still laminar. The disturbances are clearer in the inner part of the cavity and tend to modify the flow pattern due to the secondary motion. This is seen in Fig. 6(*c*), $x=100$ mm, where the flow in the lower zone is less regular and presents starting thermals. At a larger x, $x=150$ mm (Fig. 6(*d*)), the cross-stream section is located in the reversion zone and the flow lifts up.

For the same heating Mode III, $b=32.2$ mm and $q_\Omega=120$ W/m^2 (Gr$=2.35\times10^5$) the longitudinal and cross-stream sections are presented in Fig. 7. Figure 7(*a*) (longitudinal section) shows patterns similar to that for $q_\Omega=60$ W/m^2, whereas in the cross-stream sections the flow appears to be more unstable. In fact, at $x=20$ mm (Fig. 7(*b*)) the flow is disordered in the upper zone, due to the motion in the inner of the cavity. Moreover, this figure shows slight differences of smoke layer thickness on the heated bottom plate; this denotes that thermals are starting up. At $x=60$ mm (Fig. 7(*c*)) this occurrence is evident and at $x=80$ mm (not shown in figure) the mushroom structures already exist. These patterns are still present at $x=100$ mm, as Fig. 7(*d*) points out. Here, the mushroom patterns start turning into longitudinal vortices. These secondary motions produce an interaction between the two opposite flows. In particular, the lower unstable flow provokes secondary motions rising toward the upper plate. The flow adjacent to the top plate (upper zone) drags this flow toward the open-ended cavity exit. This causes a disordered motion. At $x=160$ mm (Fig. 7(*e*)) the main flow goes toward the top plate. The patterns become disordered in the whole cross-stream section.

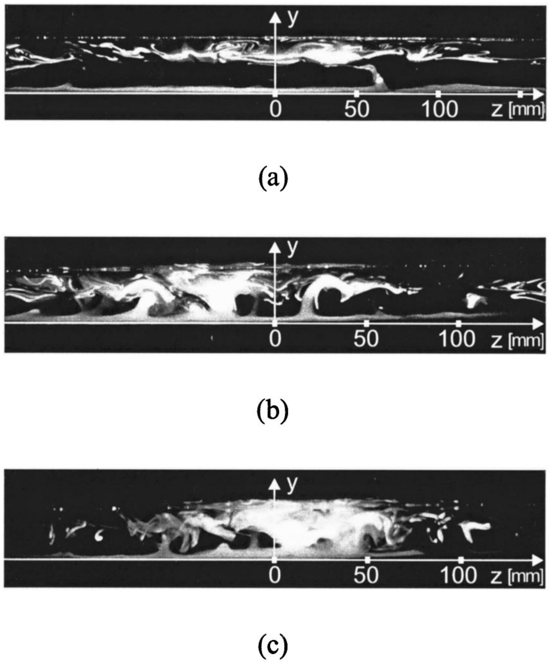

Fig. 8 Cross-stream section for $b=32.2$ mm, $q_\Omega=240$ W/m^2, and Gr$=4.65\times10^5$, Mode III: (*a*) $x=20$ mm; (*b*) $x=60$ mm; (*c*) $x=100$ mm

For greater heat flux, $q_\Omega=240$ W/m^2, Gr$=4.65\times10^5$, and $b=32.2$ mm (Fig. 8), at $x=20$ mm a higher thickness of the flow is observed in the upper zone, Fig. 8(*a*), and a disordered pattern is clearer, owing to the secondary motions produced by the instability started at lower values of the axial coordinate. In fact, the convective structures are similar to those presented in Fig. 7, but they are clearer and start at lower x coordinates (Figs. 8(*b*), $x=60$ mm, and 8(*c*), $x=100$ mm).

Air Flow Temperature Measurements. Air temperature as function of time, in the $z=0.0$ mm plane is presented in Figs. 9, 10, and 11. In Fig. 9 the temperature traces at $y=8$ mm ($y/b=0.25$) for $b=32.2$ mm and $q_\Omega=60$ W/m^2 (Gr$=1.24\times10^5$) and $b=32.2$ mm and $q_\Omega=120$ W/m^2 (Gr$=2.35\times10^5$) are shown. The temperature measurements show a laminar flow regime at $x=60$ mm for the lower Grashof number (Fig. 9(*a*)), as already observed in Fig. 6(b). Farther downstream, at $x=150$ mm and for the same Grashof number, quasi-periodical oscillation was observed. By doubling the Grashof number (Gr$=2.35\times10^5$), Fig. 9(*b*), temperature peaks are detected at $x=60$ mm, which were

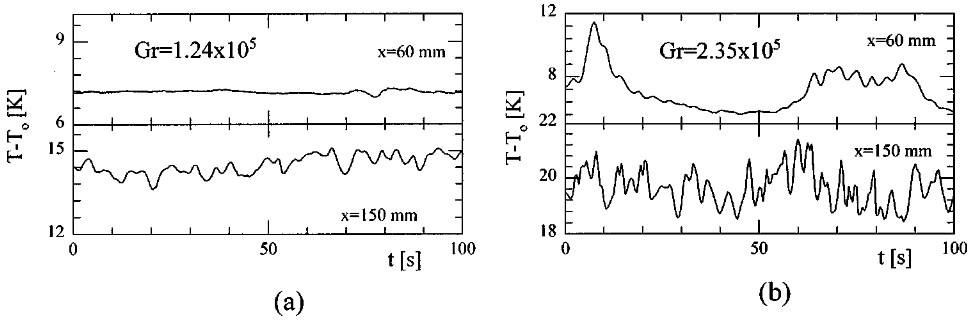

Fig. 9 Time records of the air temperature at selected *x*-coordinate and $y=8$ mm for $b=32.2$ mm and (*a*) $q_\Omega=60\ \mathrm{W/m^2}$ ($\mathrm{Gr}=1.24\times10^5$); (*b*) $q_\Omega=120\ \mathrm{W/m^2}$ ($\mathrm{Gr}=2.35\times10^5$)

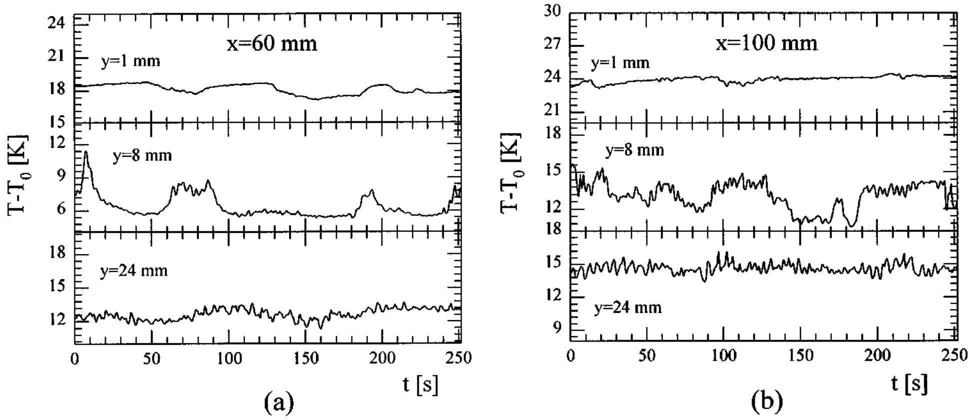

Fig. 10 Time records of the air temperature at selected *y*-coordinate for $b=32.2$ mm and $q_\Omega=120\ \mathrm{W/m^2}$ ($\mathrm{Gr}=2.35\times10^5$) at (*a*) $x=60$ mm; (*b*) $x=100$ mm

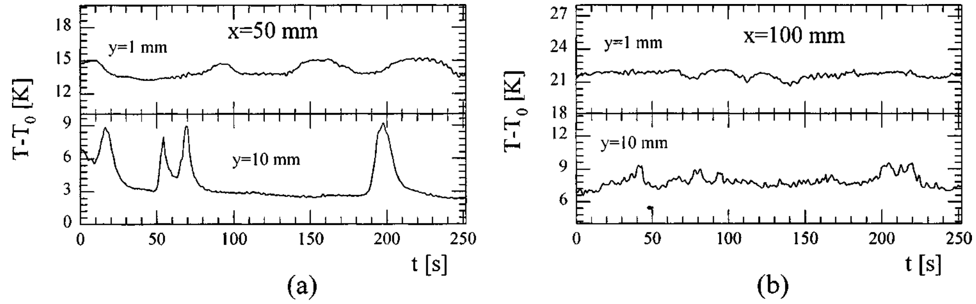

Fig. 11 Time records of the air temperature at selected *y*-coordinate for $b=40.0$ mm and $q_\Omega=120\ \mathrm{W/m^2}$ ($\mathrm{Gr}=5.56\times10^5$) at (*a*) $x=50$ mm; (*b*) $x=100$ mm

due to the thermals lifting from the lower plate, as shown by photographs in Fig. 7(*c*). At $x=150$ mm the fluctuations assume chaotic patterns with quite high amplitude and frequency.

Figure 10 presents time temperature traces at some locations, already shown in the previous flow visualization results for $b=32.2$ mm, $q_\Omega=120\ \mathrm{W\,m^{-2}}$, and $\mathrm{Gr}=2.35\times10^5$. In detail, the time traces at $x=60$ mm (Fig. 10(*a*)) and $x=100$ mm (Fig. 10(*b*)) and three y locations ($y=1$, 8, and 24 mm) are presented. The temperature plots in the zone close to the lower plate ($y=1$ and 8 mm), at $x=60$ mm, indicate the existence of thermals, whereas in the upper zone ($y=24$ mm) the trace shows evidence of a chaotic motion, which was already detected from the corresponding picture. The time temperature traces at $x=100$ mm (Fig. 10(*b*)) always show greater frequency oscillations, related to more intense secondary motions, as seen in Fig. 7(*d*). In addition, the time trace at the upper position ($y=24$ mm) indicates a chaotic motion. The traces which identify chaotic motions close to the upper plate are characterized by fluctuations with low amplitude and high frequency.

A comparison with the time temperature traces for $b=40.0$ mm, $q_\Omega=120\ \mathrm{W\,m^{-2}}$, and $\mathrm{Gr}=5.56\times10^5$ can be carried out by looking at Fig. 11. In fact, sudden peaks, associated with the rise of thermals or nonstationary plumes, are shown at $x=60$ mm (Fig. 11(*a*)) and at a distance from the lower plate equal to $y=10$ mm, whereas at $y=1$ mm ($y/b=0.025$) the fluctuations are damped, as in the case of Fig. 10. At the other y locations, not shown in Fig. 11, the temperature patterns were typical of a chaotic motion. At $x=100$ mm, Fig. 12(*b*), no temperature peaks appear when $y=10$ mm and the fluctuation frequencies are higher than those at $x=60$ mm for any y value.

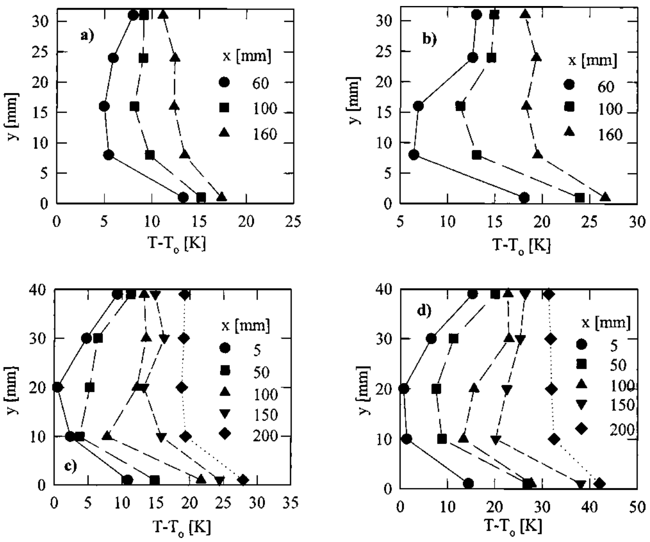

Fig. 12 Time-average temperature along the *y*-direction at $z=0.0\text{ mm}$ and several *x*-coordinates for Mode III: (*a*) $b=32.2\text{ mm}$ and $q_\Omega=60\text{ W/m}^2$ ($\text{Gr}=1.24\times10^5$); (*b*) $b=32.2\text{ mm}$ and $q_\Omega=120\text{ W/m}^2$ ($\text{Gr}=2.35\times10^5$); (*c*) $b=40.0\text{ mm}$ and $q_\Omega=120\text{ W/m}^2$ ($\text{Gr}=5.56\times10^5$); (*d*) $b=40.0\text{ mm}$, $q_\Omega=240\text{ W/m}^2$ ($\text{Gr}=1.06\times10^6$)

Average air temperature profiles as a function of the y-coordinate, in the $z=0$ mm plane, at different values of x and y-coordinates, heat flux, and channel spacing are presented in Fig. 12. The temperature profile at $x=60\text{ mm}$, $b=32.2\text{ mm}$, and $q_\Omega=60\text{ W m}^{-2}$ ($\text{Gr}=1.24\times10^5$), Fig. 12(*a*), shows that the central region of the temperature profile is cooler than that adjacent to the plates. The lower zone spreads up to about 0.25 b, where the thermal gradient along y is very steep. This is in accordance with the picture at this section reported in Fig. 6(*b*). At $x=100\text{ mm}$ the temperature profile is nearly uniform in the upper zone, and this is mainly due to the chaotic mixing in that zone, as previously observed in Fig. 6(*c*). At higher x values the temperature in the same region is more uniform, also due to the interaction of the outflow fluid with the cooler flow rising up from the lower region. Figure 12(*b*), $b=32.2\text{ mm}$ and $q_\Omega=120\text{ W m}^{-2}$ ($\text{Gr}=2.35\times10^5$), shows a greater difference between the main flow in the C loop and the flow in the core of the open-ended cavity when the heat flux is greater. In fact, on the upper side of the C loop the air is completely mixed because of the chaotic motion determined by the secondary flows and the reversion of the flow, as observed in Figs. 7(*b*)–7(*e*). For $b=40.0\text{ mm}$, $q_\Omega=120\text{ W m}^{-2}$ ($\text{Gr}=5.56\times10^5$), Fig. 12(*c*) shows that the temperatures in the midpart of the cavity ($10\text{ mm}<y<30\text{ mm}$), at $x=5$ mm and $x=50$ mm, are lower than those in the previous case because of the greater distance between the plates. In the bottom part of the cavity the temperature distribution is still similar to that of the previous investigated cases. Note that the temperature profile at $x=200\text{ mm}$ is uniform in the $y=10-39\text{ mm}$ range. This is due to the mixing of the fluid determined by the rising flow. The average temperature profiles for $b=40.0\text{ mm}$ and $q_\Omega=240\text{ W m}^{-2}$ ($\text{Gr}=1.06\times10^6$), presented in Fig. 12(*d*), are very similar to those at $q_\Omega=120\text{ W m}^{-2}$, even if the temperature values are greater as expected. Temperatures in the upper region ($y>30\text{ mm}$) are nearly uniform for $x=100\text{ mm}$. At $x=50\text{ mm}$ the lower the y coordinate in the $20<y<40\text{ mm}$ range, the lower the temperature, probably because of the motion along x which mixes the hot thermals rising from the lower regions and the cooler air coming from the ambient.

Conclusions

Air natural convection between two parallel horizontal heated plates was experimentally investigated. The test section was open to the ambient air at two cross sections. The C loop main flow induced in the test section was very similar to flows peculiar to open-ended cavities. The results obtained by the visualization confirm the numerical results obtained by Vafai and Ettefagh [14] from a qualitative point of view, when the lowest values of the longitudinal aspect ratio are taken into account.

The flow visualization showed that the main C loop flow extended as far as half the length of the plate. Secondary flows were absent when only the upper plate was heated, whereas for the other heating modes thermals started in the inflow side of the C loop over the lower heated plate, and then they changed into longitudinal vortices. These vortices then broke out in the reversion region of the flow, and a chaotic motion originated in the outflow branch of the C loop, adjacent to the upper plate. The chaotic flow extended as far as to the exit section of the open-ended cavity. Some locations showed temperature peaks, during the time observation, due to plumes or thermals. On the other hands the time temperature traces presented high frequency fluctuations with variable amplitude where the motion was chaotic. Average temperature values suggest similar observations. Namely, in Mode III the uniformity of the average temperature was noticed in the C loop both in the flow reversion region and near the upper plate.

Acknowledgments

This study was supported by the Consiglio Nazionale delle Ricerche with the grant on Bilateral research project No. 97.03198.07 and by the MURST with a 1997 grant research program ‘‘Termofluidodinamica mono e bifase.’’

Nomenclature

b = plate spacing, m
g = acceleration of gravity, ms^{-2}
Gr = Grashof number, Eq. (1), dimensionless
k = thermal conductivity, $\text{W m}^{-1}\text{ K}^{-1}$
L = half length of the plate, m
q = heat flux, W m^{-2}
T = temperature, K
x = coordinate along the channel length, m
y = coordinate along the channel spacing, m
z = coordinate along the channel width, m
W = width of the plate, m

Greek symbols

β = volumetric coefficient of expansion, K^{-1}
ν = kinematic viscosity, $\text{m}^2\text{ s}^{-1}$

Subscripts

b = bottom
c = convective
k = conductive
o = ambient air
r = radiative, reference
t = top
w = wall
Ω = ohmic dissipation

A bar over a symbol indicates mean values along the plate.

References

[1] Goldstein, R. J., and Volino, R. J., 1995, ‘‘Onset and Development of Natural Convection Above a Suddenly Heated Horizontal Surface,’’ ASME J. Heat Transf., **117**, pp. 808–821.
[2] Mahajan, R. L., 1996, ‘‘Transport Phenomena in Chemical Vapor Deposition Systems,’’ Adv. Heat Transfer, **28**, pp. 339–425.
[3] Sparrow, E. M., and Carlson, C. K., 1986, ‘‘Local and Average Natural Convection Nusselt Numbers for a Uniformily Heated, Shrouded or Unshrouded Horizontal Plate,’’ Int. J. Heat Mass Transf., **29**, pp. 369–379.

[4] Fukui, K., Nakajima, M., and Ueda, H., 1983, ''The Longitudinal Vortex Effects on the Transport Process in Combined Free and Forced Laminar Convection Between Horizontal and Inclined Parallel Plates,'' Int. J. Heat Mass Transf., **26**, pp. 109–119.

[5] Maughan, J. R., and Incropera, F. P., 1987, ''Experiments on Mixed Convection Heat Transfer for Airflow in a Horizontal and Inclined Channel,'' Int. J. Heat Mass Transf., **30**, pp. 1307–1318.

[6] Maughan, J. R., and Incropera, F. P., 1990, ''Regions of Heat Transfer Enhancement for Laminar Mixed Convection in a Parallel Plate Channel,'' Int. J. Heat Mass Transf., **33**, pp. 555–570.

[7] Evans, G., and Greif, R., 1989, ''A Study of Traveling Wave Instabilities in a Horizontal Channel Flow with Applications to Chemical Vapor Deposition,'' Int. J. Heat Mass Transf., **32**, pp. 895–911.

[8] Evans, G., and Greif, R., 1993, ''Thermally Unstable Convection With Applications to Chemical Vapor Deposition Channel Reactors,'' Int. J. Heat Mass Transf., **36**, pp. 2769–2781.

[9] Cheng, K. C., and Shi, L., 1994, ''Visualization of Convective Instability Phenomena in the Entrance Region of a Horizontal Rectangular Channel Heated From Below and/or Cooled From Above,'' Exp. Heat Transfer, **7**, pp. 235–248.

[10] Lin, W. L., and Lin, T. F., 1996, ''Experimental Study of Unstable Mixed Convection of Air in a Bottom Heated Horizontal Rectangular Duct,'' Int. J. Heat Mass Transf., **39**, pp. 1649–1663.

[11] Lin, W. L., and Lin, T. F., 1996, ''Unstable Aiding and Opposing Mixed Convection of Air in a Bottom-Heated Rectangular Duct Slightly Inclined from the Channel,'' ASME J. Heat Transf., **118**, pp. 47–55.

[12] Chang, M. Y., Yu, C. H., and Lin, T. F., 1997, ''Changes of Longitudinal Vortex Roll Structure in a Mixed Convective Air Flow Through a Horizontal Plane Channel: An Experimental Study,'' Int. J. Heat Mass Transf., **40**, pp. 347–363.

[13] Vafai, K., and Ettefagh, J., 1990, ''Thermal and Fluid Flow Instabilities in Buoyancy-Driven Flows in Open-Ended Cavities,'' Int. J. Heat Mass Transf., **33**, pp. 2329–2344.

[14] Vafai, K., and Ettefagh, J., 1990, ''The Effects of Sharp Corners on Buoyancy-Driven Flows With Particular Emphasis on Outer Boundaries,'' Int. J. Heat Mass Transf., **33**, pp. 2311–2328.

[15] Vafai, K., Desai, C. P., Iyer, S. V., and Dyko, M. P., 1997, ''Buoyancy Induced Convection in a Narrow Open-Ended Annulus,'' ASME J. Heat Transf., **119**, pp. 483–494.

[16] Hart, J. E., 1971, ''Transition of a Wavy Vortex Regime in Convective Flow Between Inclined Plates,'' J. Fluid Mech., **48**, Part 2, pp. 265–271.

[17] Manca, O., Morrone, B., and Nardini, S., 1997 ''Visualization of Natural Convection in Inclined Parallel Plates,'' *Thermal Managment of Electronic System*, Vol. II, Kluwer Academic, Dordrecht, pp. 283–292.

[18] Manca, O., Morrone, B., and Nardini, S., 1997, ''Flow Visualization of Natural Convection between Horizontal Heated Parallel Plates,'' *Proceedings of the 4th World Conference on Experimental Heat Transfer, Fluid Mechanics and Thermodynamics*, Brussels, 2–6 June, Vol. 4, pp. 2251–2258.

[19] Chyu, M. C., 1987, ''On the Boundary Condition and Data Reduction of Heat Transfer Experiment,'' Int. Commun. Heat Mass Transfer, **14**, pp. 543–550.

[20] Labview Reference Manual, 1993, National Instruments, Austin.

[21] DANTEC, 1996, ''Probes for Hot-Wire Anemometry,'' Dantec Meas. Tech. Publ. No. 196-105-01.

[22] Bruun, H. H., 1995, ''Hot-Wire Anemometry: Principles and Signal Analysis,'' Oxford University Press, New York.

[23] Kline, S. J., and McClintock, F. A., 1953, ''Describing Uncertainty in Single Sample Experiments,'' Mech. Eng., **75**, pp. 3–12.

[24] Moffat, R. J., 1988, ''Describing the Uncertainties in Experimental Results,'' Exp. Therm. Fluid Sci., **1**, pp. 3–17.

[25] Lavine, A., 1993, ''On the Linear Stability of Mixed and Free Convection Between Inclined Parallel Plates With Fixed Heat Flux Boundary Conditions,'' Int. J. Heat Mass Transf., **36**, pp. 1373–1387.

Stabilization of Buoyancy-Driven Unstable Vortex Flow in Mixed Convection of Air in a Rectangular Duct by Tapering Its Top Plate

W. S. Tseng
W. L. Lin
C. P. Yin
C. L. Lin
T. F. Lin
Department of Mechanical Engineering,
National Chiao Tung University,
Hsinchu, Taiwan, R.O.C.

Stabilization of the buoyancy-driven unstable mixed convective vortex air flow in a bottom heated rectangular duct by tapering its top plate is investigated experimentally. Specifically, the duct is tapered so that its aspect ratio at the duct inlet is 4 and gradually raised to 12 at the exit of the duct. In the study the secondary flow in the duct is visualized and the steady and transient thermal characteristics of the flow are examined by measuring the spanwise distributions of the time-average temperature. The effects of the Reynolds and Grashof numbers on the vortex flow structure are studied in detail. Moreover, the spanwise-averaged Nusselt numbers for the horizontal rectangular and tapering ducts are also measured and compared. Furthermore, the time records of the air temperature are obtained to further detect the temporal stability of the flow. Over the ranges of the Re and Gr investigated for $5 \leqslant Re \leqslant 102$ *and* $1.0 \times 10^4 \leqslant Gr \leqslant 1.7 \times 10^5$*, the vortex flow induced in the rectangular duct exhibits temporal transition from a steady laminar to time periodic and then to chaotic state at increasing buoyancy-to-inertia ratio. Substantial change in the spatial structure of the vortex flow is also noted to accompany this temporal transition. The results for the tapering duct indicate that more vortex rolls can be induced due to the increase in the aspect ratio of the duct with the axial distance. But the vortex rolls are weaker and are completely stabilized by the tapering of the top plate.*
[S0022-1481(00)70301-X]

Keywords: Heat Transfer, Mixed Convection, Vortex

1 Introduction

At high buoyancy-to-inertia ratio frequently encountered in various heat transfer equipment, the buoyancy-driven secondary vortex flow in a forced laminar flow through a bottom heated rectangular duct is rather unstable. Heat transfer augmentation associated with the buoyancy-driven vortex flow is desirable and welcome in many technological applications in which the efficient energy transport is of major concern. However, in the chemical vapor deposition (CVD) processes used to grow thin crystal films on semiconductor substrates, the presence of the vortex flow at a high buoyancy and a low inertia for the Reynolds number ranging from 1 to 100 will result in a nonuniform chemical vapor deposition, producing a thin crystal film of nonuniform thickness. Moreover, the unsteady vortex flow will provoke a time-dependent deposition rate. These unsteady vortex flows are not welcome and should be avoided in the CVD processes. A simple mean often used to suppress and stabilize the vortex flow is to accelerate the main flow so that the buoyancy-to-inertia ratio decreases in the flow direction. This experimental study intends to explore the change in the vortex flow structure of air caused by the flow acceleration when the top plate of a bottom-heated horizontal rectangular duct is slightly tapered.

In a horizontal parallel plane channel with the bottom plate at a higher uniform temperature than the top one by ΔT, the critical Rayleigh number for the onset of the vortex flow was found to be around 1708, as predicted from experimental measurements and linear stability theory ([1,2]). Ostrach and Kamotani [3] and Kamotani and Ostrach [4] experimentally noted that the longitudinal vortex rolls appear when the temperature difference becomes larger than a critical value corresponding to $Ra = 1708$. Above the critical point, the heat transfer rate is increased by the thermal instability and the temperature field is strongly influenced by the motion of the vortex rolls. When $Ra > 8000$, the vortex rolls become irregular. Hwang and Liu [5] visualized the onset of secondary flow and showed that the wave number of vortex rolls remains constant along the flow direction. Experiments conducted by Incropera et al. [6] and Maughan and Incropera [7] disclosed four flow regimes along the bottom plate-laminar forced convection, laminar mixed convection, transitional mixed convection, and turbulent free convection. The transition to turbulent flow was attributed to the breakdown of the vortices due to the hydrodynamic instability. Besides, a correlation for the onset points was proposed. Criteria for the onset of vortex instability and the start of the transition from two-dimensional laminar flow to three-dimensional vortex flow in mixed convection air flow over an isothermally heated horizontal flat plate were established by Moharreri et al. [8]. The vortex flow regime started with a stable laminar flow region where vortices develop and grow gradually and ended with an unstable flow region where the vortices mix together and collapse to form a two-dimensional turbulent flow regime.

In the mixed convection of the nitrogen gas between two horizontal, differentially heated parallel plates, Chiu and Rosenberger [9,10] showed that the critical Ra for the appearance of the transverse convection rolls increased with Re. They also found that at a high Ra, the longitudinal rolls were unsteady and snaking. Besides, they showed the regime of Ra and Re leading to a steady or unsteady flow. Nyce et al. [11] showed the variations of velocity field in both the axial and transverse directions which were consistent with the presence of both longitudinal roll and transverse wave instabilities. The transverse rolls were noted at a very low Reynolds number by Ouazzani et al. [12,13]. They also refined the regime map to include the transverse rolls. The recent flow visualization from Yu et al. [14] showed that at a fixed Ra but in

---

Contributed by the Heat Transfer Division for publication in the JOURNAL OF HEAT TRANSFER. Manuscript received by the Heat Transfer Division, Feb. 7, 1999; revision received, July 27, 1999. Associate Technical Editor: F. Cheung.

reducing Re the vortex flow transforms from the structure prevailed by the longitudinal rolls to transverse waves in sequence of stable longitudinal rolls, unstable longitudinal rolls, mixture of the longitudinal rolls and transverse waves, and transverse waves. Photographic results from Cheng and Shi [15] revealed the convective instability and chaotic phenomena caused by the buoyancy forces. Koizumi and Hosokawa [16] presented the sidewall temperature profile in a horizontal rectangular duct heated from below which simulated a horizontal thermal CVD reactor. They found that although the flow was unsteady but the time-averaged local mass transfer rate on the bottom wall can be almost uniform.

Recently, in a series of studies ([17–20]) we unraveled the complex flow characteristics in an air flow through a bottom-heated horizontal rectangular duct of aspect ratio $AR=2$ & 4. The formation, merging, and splitting of the longitudinal vortex rolls were numerically and experimentally predicted for the laminar steady, laminar time periodic, transitional quasi-periodic, and irregular chaotic flow at increasing buoyancy-to-inertia ratio.

The above literature review clearly reveals that there has been a substantial amount of research carried out in the past on various aspects of the vortex flow and heat transfer in mixed convection of gas in a horizontal rectangular duct. However, very little is known on the processes of how the vortex flow is suppressed by the flow acceleration resulting from reducing the cross-sectional area of the duct. An experimental investigation combining flow visualization and temperature measurements will be conducted in the present study to unravel the effects of tapering the top plate of rectangular duct on the detailed changes in the vortex flow structure in a mixed convective air flow through a bottom heated trapezoid duct. Attention will be focused on the flow stabilization and weakening of the vortex flow by the acceleration of the primary flow for various Reynolds and Grashof numbers.

2 Experimental Apparatus and Procedures

2.1 Experimental Apparatus. Figure 1 shows a schematic arrangement of the mixed convective experimental apparatus established for the present study. The apparatus consists of three parts: wind tunnel, test section, and measuring probes along with a data acquisition unit. Two different test sections have been designed, one for the rectangular duct without tapering the top plate and another for the trapezoid duct with the top plate tapered downwards from the duct inlet to exit. The test section for the rectangular duct is constructed of 9-mm-thick plexiglass top and side walls to facilitate flow visualization. The rectangular cross section is 30 mm in height and 120 mm in width and the duct has a total length of 800 mm, providing an aspect ratio of $AR=4$ for the duct. The tapering duct is also 800 mm long and is made of 10-mm-thick plexiglass top and 9-mm-thick plexiglass side walls. The top plate is inclined downwards so that the aspect ratio of the duct cross section increases from 4 at the inlet to 12 at the exit with the duct height reduced from 30 mm at the inlet to 10 mm at the exit. The inclined angle of the top plate is rather small at 1.432 deg when measured from the horizontal. The details of the mixed convective loop were already described in Lin and Lin [19]. Besides, the experimental procedures and method to analyze the temperature fluctuation were also given in that study.

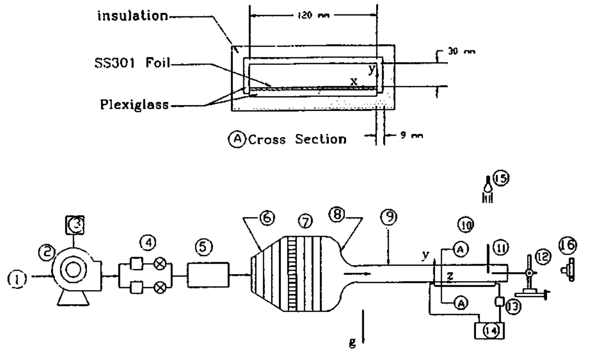

1.air flow ; 2.blower ; 3.frequency regulator ; 4.flowmeters and valves ; 5.smoke container ; 6.diffuser with screens ; 7.straightener with honeycomb and screens ; 8.nozzle ; 9.developping channel ; 10.test section ; 11.probes ; 12.three-way traversing device ; 13.ammeter ; 14.D.C.power supply ; 15.lamp ; 16.camera.

Fig. 1 Schematic diagram of the experimental apparatus

2.2 Data Reduction for Heat Transfer Coefficient. The spanwise-averaged Nusselt number defined as

$$\mathrm{Nu}_d=\frac{hd_{\mathrm{in}}}{k}=\frac{q''_{\mathrm{conv}}d_{\mathrm{in}}}{(\overline{T}_w-T_{\mathrm{in}})k} \tag{1}$$

is obtained from measuring the spanwise-averaged bottom wall temperature $\overline{T}_w$ and local convective heat flux q''_{conv}. Note that the heat transfer coefficient $\overline{h}$ is based on the temperature difference $(\overline{T}_w-T_{\mathrm{in}})$ instead of $(\overline{T}_w-T_b)$ since the heated section is not long $(L/d_{\mathrm{in}}=26.7)$ and the convective heat transfer in it mainly takes place in the entrance region. The surface energy balance relating the total energy dissipated in the heater plate due to the electric resistance heating per unit surface area q''_{tot} to the heat fluxes associated with the convection from the surface to the flow q''_{conv}, net radiation heat loss from the surface q''_{rad} and conduction loss through the insulation q''_{insul} is

$$q''_{\mathrm{tot}}=q''_{\mathrm{conv}}+q''_{\mathrm{rad}}+q''_{\mathrm{insul}}. \tag{2}$$

The convective heat flux is therefore determined by measuring the total dissipated heat flux and applying appropriate correlations for the nonconvective components. An implication of the expression in Eq. (2) is that although uniform heat generation q''_{tot} is achieved in the heated plate, variations in the radiation and conduction losses with the location induce nonuniformities in the convective heat flux. The axial variations in q''_{conv} were estimated to be less than 20 percent of the average q''_{conv}. The radiation and conduction losses were estimated to range from 32 percent to 36 percent and 13 percent to 17 percent, respectively.

Uncertainties in the Nusselt, Reynolds, and Grashof numbers were estimated according to the standard procedures proposed by Kline and McClintock [21]. This analysis indicated that through the combination of many measurements together with the uncertainties in the conductive and radiative losses, the uncertainties in Re, Gr, and Nu_d are 2 percent, 11 percent, and 4 percent, respectively.

3 Discussion of Experimental Results

In what follows, only a small sample of the results obtained are presented to illustrate the effects of the top plate tapering on the flow stabilization by examining the resulting vortex flow structures and time history of the air temperature. In addition, the spanwise average Nusselt number affected by the plate tapering is also inspected. More detailed results are available from the thesis of Tseng [22].

3.1 Spanwise Average Heat Transfer Coefficient. The axial distributions of the steady spanwise average Nusselt number was obtained first for the limiting cases of forced convection with the Grashof number Gr $(=g\beta q''_{\mathrm{conv}}d^4_{\mathrm{in}}/k\nu^2)$ below 2000 for the rectangular and tapering ducts. The data for the rectangular duct were very close to that calculated for the forced convection in that duct from the previous numerical computation ([18]). This was verified in our previous studies ([19,20]). In the exit region the Nusselt number for the tapering duct is slightly above that for the rectangular duct due to the acceleration of the main flow.

Effects of the Grashof number on the time-averaged axial variations of the spanwise average Nusselt number in the two different

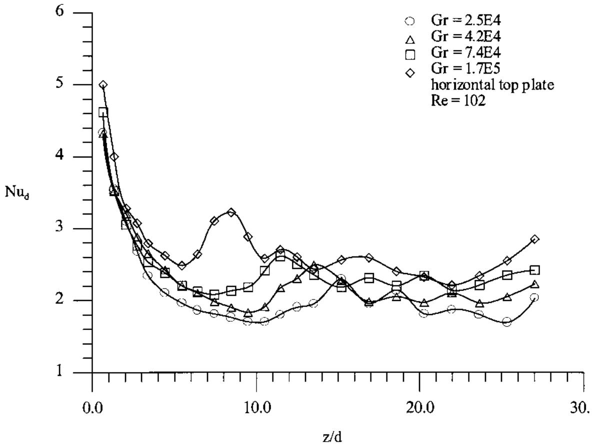

(a)rectangular duct

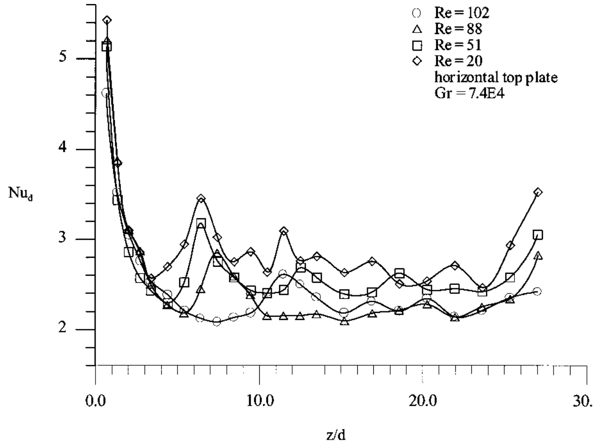

(a)rectangular duct

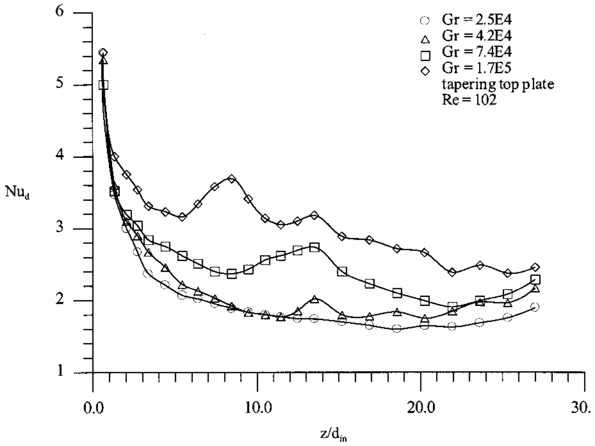

(b)tapering duct

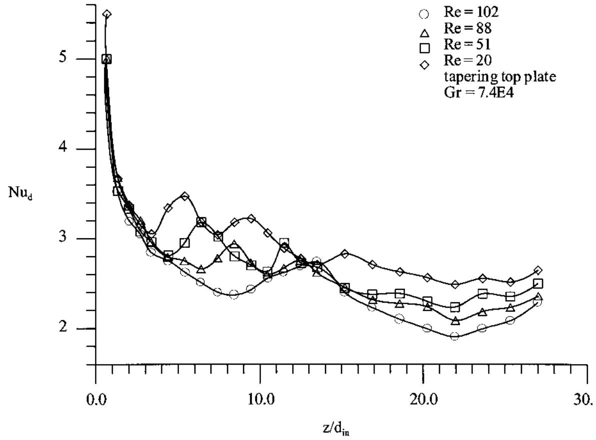

(b)tapering duct

Fig. 2 Effects of Grashof number on the spanwise-averaged Nusselt number distribution for Re=102 for (*a*) rectangular duct and (*b*) tapering duct

Fig. 3 Effects of Reynolds number on the spanwise-averaged Nusselt number distribution for Gr=7.4×10^4 for (*a*) rectangular duct and (*b*) tapering duct

ducts are shown in Fig. 2 for Re=102. The results in Fig. 2(*a*) for the horizontal top plate indicate that at a given Gr near the duct entry the Nusselt number decreases monotonically in the flow direction. At a certain axial location Nu_d reaches a minimum and rises gradually. This location corresponds to the onset of the buoyancy-induced vortex flow. More specifically, the onset point is defined as the axial station where the spanwise average Nusselt number enhanced by the vortex flow exceeds that for the forced convection by three percent. At a higher Grashof number this onset location appears at a shorter distance from the duct inlet. The monotonic decay in the Nusselt number in the upstream is associated with the dominated laminar forced convection there. Beyond the onset point plumes of warm fluid rise from the heated surface resulting in a developing secondary flow and the plate temperature is reduced by the cool air descending from the duct core. Thus, the flow circulation provides an effective mechanism for heat transfer enhancement. As the secondary flow strengthens, the Nusselt number rises well above the forced convection limit. Further downstream the core flow has been warmed up and Nu_d reverses its trend to decrease in the flow direction. Thus, we have oscillatory Nu_d distributions in the axial direction for a high Gr. The results for the tapering duct (Fig. 2(*b*)) resemble those for the rectangular duct (Fig. 2(*a*)) except that in the tapering duct the onset of the vortex flow moves a little downstream as compared with that for the horizontal duct for the same Re and Gr. Note that the duct height at the duct inlet is used in defining Gr for the tapering duct. It is further noted that the axial rise in Nu_d due to the vortex flow are slightly smaller for the tapering duct, implying the induced secondary flow being weaker. Also note that Nu_d is lower for the tapering duct in the downstream region of the duct. These results indicate that the Nusselt number increases with the Grashof number except in the region near the exit of the tapering duct. Near the exit region, the flow accelerates so rapidly that the transport process is dominated by forced convection. Therefore, the Grashof number only exhibits a mild effect on the heat transfer near the duct exit.

The data in Fig. 3 for illustrating the effects of the Reynolds number on the Nu_d distributions for both ducts indicate that the onset of secondary flow moves downstream at increasing Reynolds number for Gr fixed at 7.4×10^4. This trend is in compliance with the fact that the velocity boundary layer gets thinner at a higher Re and thereby increases its resistance to thermal instability, and hence impedes secondary flow development. Oscillatory Nu_d variations with the axial distance are also noted for these curves. More intense oscillations result for a higher buoyancy-to-inertia ratio. Moreover, at the same Re and Gr the onset point moves downstream in the tapering duct as compared with that for the corresponding case in the rectangular duct. Besides, Nu_d is also lower in the tapering duct.

It is of interest to note that the onset points for various cases covered here for both ducts can be correlated as

$$\mathrm{Gr}_z = 3637\,\mathrm{Re}_z^{1.66} \tag{3}$$

where Gr_z and Re_z are the local Grashof and Reynolds numbers, $\mathrm{Gr}_z = g\beta q''_{\mathrm{conv}} z^4/k\nu^2$ and $\mathrm{Re}_z = \overline{w}z/\nu$. Here $\overline{w}$ is the local mean velocity of the air in the ducts, which increases linearly with the axial distance for the tapering duct. But for the rectangular duct $\overline{w}$ is constant.

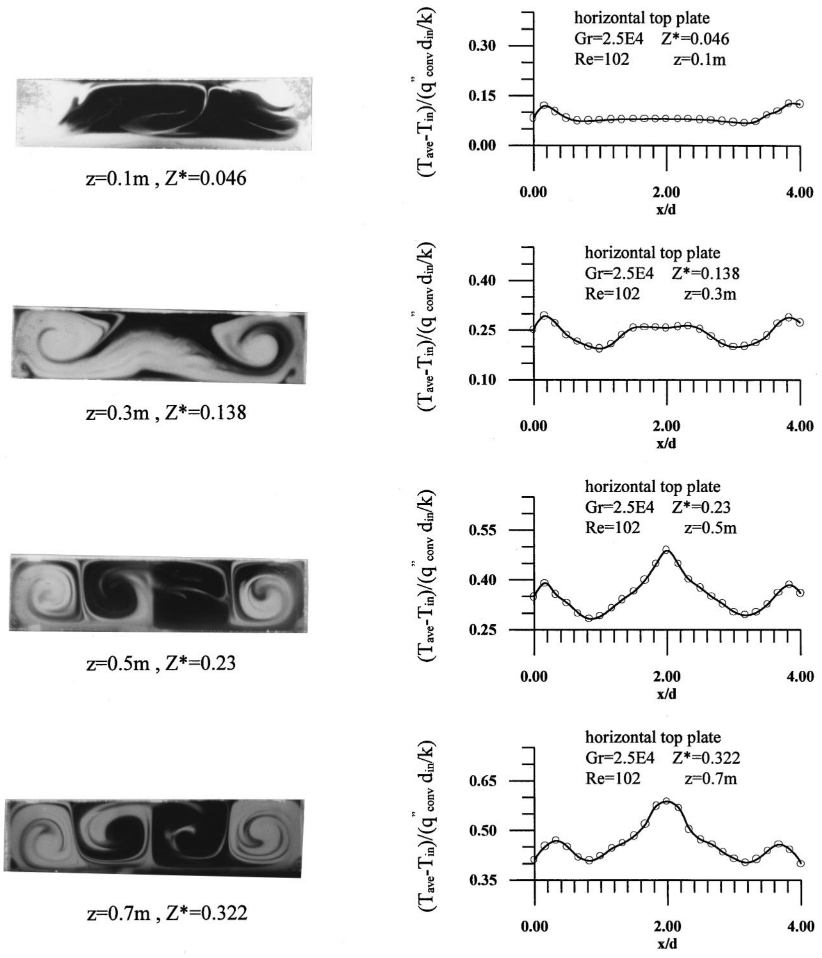

(a) (b)

Fig. 4 (***a***) **Instantaneous flow photos and** (***b***) **time-averaged spanwise temperature distributions at** $y=1.5$ **cm at selected cross sections in rectangular duct for** $Re=102$ **and** $Gr=2.5\times10^4$

3.2 Vortex Flow Structure and Spanwise Temperature Distributions. Flow visualization was conducted to detect the resulting buoyancy-induced vortex flow patterns at steady or statistical state for both rectangular and tapering ducts for various Reynolds and Grashof numbers. They were carried out by using a 1.5–3-mm plane light beam shone through the flow field containing small incense smoke particles as light scattering centers.

Side views of the instantaneous flow photos taken at the central vertical plane at $x=6$ cm for various Reynolds and Grashof numbers clearly showed the uplift of the streamlines from the bottom plate at certain axial locations, suggesting the onset of the vortex flow there. The onset points were also found to advance upstream for a higher Grashof number or a lower Reynolds number. The photos are not shown here due to the limited availability of the space for the article. Tapering the top plate was noted to cause significant delay in the onset of vortex flow at low buoyancy-to-inertia ratio (Gr/Re^2). The delay gradually diminished at increasing Gr/Re^2. At a high Gr/Re^2 no noticeable delay in the onset of vortex flow was detected. Inspecting these side view flow photos for the low Reynolds and high Grashof numbers revealed the presence of irregular recirculating cells and the associated secondary flow was somewhat unstable. This recirculating flow became highly irregular when reaching the downstream portion of the duct. It was also noted that at this high buoyancy-to-inertia ratio the induced vortex flow was so strong that the forced flow entering the duct was seriously blocked and hence was reversed near the duct inlet resulting in a returning flow there ([23]). More specifically, the returning flow was formed by a part of warm air ascending from the bottom plate slightly upstream of the onset point and penetrating towards the top plate. When the warm air reached the top plate, it split into two streams. One moved upstream and another downstream along the top plate over a certain distance. Meanwhile the upstream moving stream was slowed down by the main forced flow. Finally, it merges with the main flow around the inlet of the heated section. Thus an elongated recirculating cell is formed in the duct entry. It is also noted that after the onset point of thermal instability, most of the test section is dominated by the natural convection for $Gr/Re^2 \geqslant 40$.

To illustrate the effects of the top plate inclination on the detailed vortex flow structures, the instantaneous flow photos from the top and end views were also examined. It was noted from the results for the rectangular duct that at a low buoyancy-to-inertia ratio for $Re=102$ and $Gr=2.5\times10^4$ a symmetric pair of longitudinal rolls were induced near the side walls beginning at $z \approx 15$ cm. Slightly downstream at $z \approx 31$ cm another symmetric pair of longitudinal rolls were generated. This four-roll structure prevailed beyond that. Raising Gr to 7.4×10^4 caused an earlier

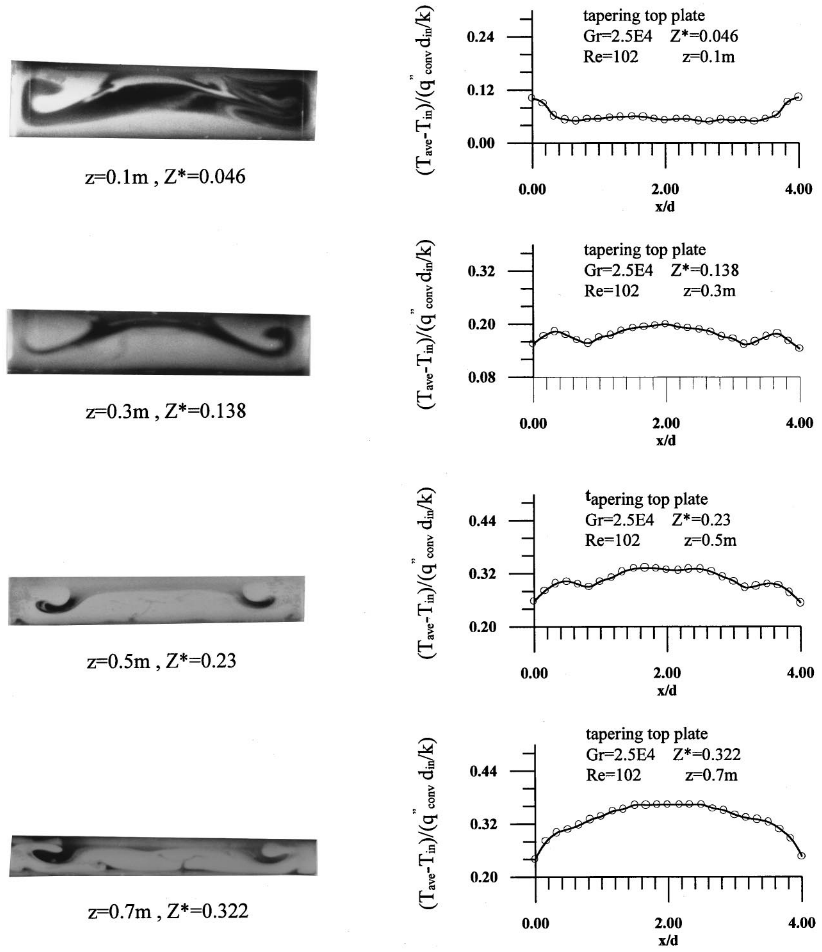

(a) (b)

Fig. 5 (***a***) **Instantaneous flow photos and** (***b***) **time-averaged spanwise temperature distributions at** $\boldsymbol{y=1.5}$ **cm at selected cross sections in tapering duct for Re=102 and Gr=2.5×10**^{4}

onset of the rolls. The vortex flow in the downstream still consisted of four-roll structure. Lowering the Reynolds number from 102 to 88 for Gr fixed at 7.4×10^4 resulted in the generation of a new pair of longitudinal rolls so that there were six longitudinal rolls in the duct. But at this higher Gr/Re^2 the vortex flow is slightly asymmetric with respect to the central vertical plane at $x=6$ cm. At an even higher Gr/Re^2 the longitudinal rolls were somewhat irregular and were obviously asymmetric. Additional flow photos for the very low Reynolds numbers of Re=15 and 9 indicated that the vortex flow still consisted of symmetric longitudinal rolls when Gr was not too high. Next, snapshots of the flow viewing from the top for the tapering duct at the same Re and Gr were inspected. Note that for the low buoyancy-to-inertial ratio case with Re=102 and Gr=2.5×10^4, a symmetric pair of longitudinal rolls induced in the entry half of the tapering duct were rather weak. At the higher Gr of 7.4×10^4 a pair of stronger longitudinal rolls were induced near the side walls beginning at $z\approx8$ cm. At $z\approx22$ cm, two plumes of warm air rose near the central vertical plane ($x=6$ cm) and formed two new pairs of longitudinal rolls. Thus, beyond that we had three pairs of longitudinal rolls in the tapering duct. Lowering the Reynolds number from 102 to 88 for Gr fixed at 7.4×10^4 again caused an earlier appearance of the three pairs of longitudinal rolls. At the even lower Reynolds number of Re=51, three symmetric pairs of vortex rolls started to appear at $z\approx15$ cm. The results for the low Reynolds number of Re=15 and 9 with Gr fixed at 1.0×10^4 for the tapering duct indicated that for Re=15 only one symmetric roll pair was induced near the side walls and no noticeable roll was induced in the center region of the heated section. The rolls near the side walls were suppressed by the accelerating air flow and were weaker than those in the rectangular duct at the same Re and Gr. At a lower Reynolds number of Re=9 two pairs of longitudinal rolls began to appear at $z\approx16$ cm, one adjacent to the center vertical plane at $x=6$ cm and another near the side walls. Note that for $z\geqslant30$ cm the two vortex pairs were significantly suppressed by the accelerating main forced flow and their strength got weaker with the downstream distance.

The above observation of the vortex structure changes with the Grashof and Reynolds numbers and with the duct tapering can be further illustrated by the end-view photos for the cross-plane secondary flow at selected cross sections. The corresponding spanwise distributions of the time-averaged air temperature at the mid-height of the duct are also given to quantitatively show the intensity of the vortex rolls. Figure 4 distinctly manifests the evolution of the vortex pattern in the rectangular duct from the uni-

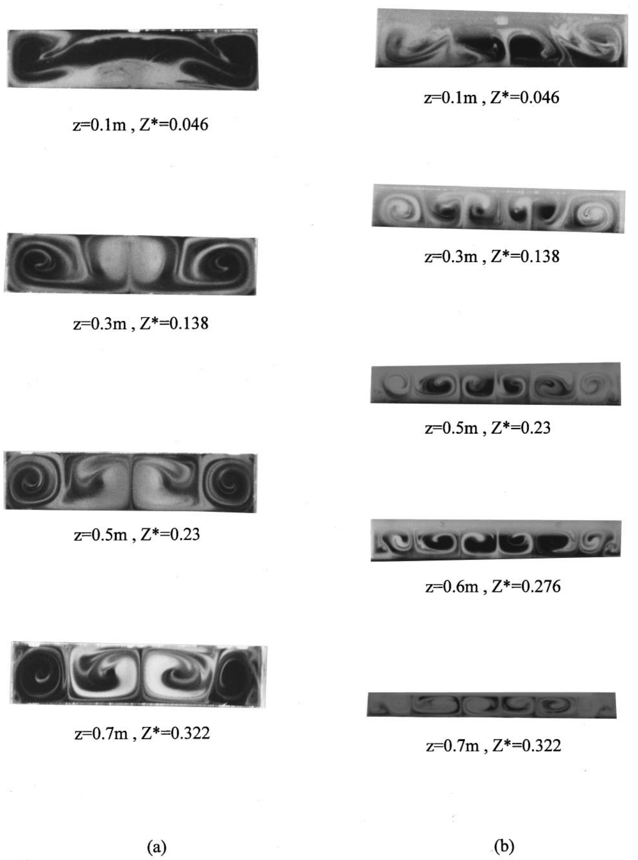

Fig. 6 Instantaneous and view flow photos at selected cross sections for Re=102 and Gr=7.4×10^4 for (*a*) rectangular duct and (*b*) tapering duct

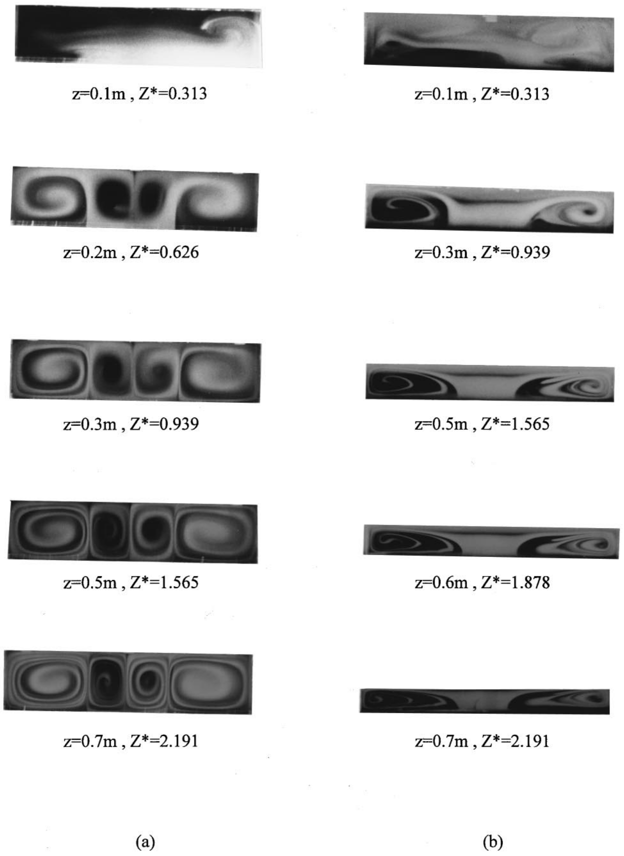

Fig. 7 Instantaneous end view flow photos at selected cross sections for Re=15 and Gr=1.0×10^4 for (*a*) rectangular duct and (*b*) tapering duct

directional flow in the duct entry to the two-roll structure slightly downstream and then to the four-roll structure in the exit half of the duct for Re=102 and Gr=2.5×10^4. It is also noted from the flow photos and time-averaged temperature distributions that in the upstream ($z<0.4$ m) the rolls near the duct sides are stronger than those in the duct core. In the downstream the reverse is the case. The corresponding results for the tapering duct at the same Re and Gr are shown in Fig. 5. Note that in the tapering duct one pair of longitudinal rolls clearly exist near the side walls in nearly the entire test section. In the downstream the second pair of longitudinal rolls are rather weak and can be barely seen in the photos for $z=0.5$ and 0.7 m. It is also noted from the time-averaged temperature distributions (Figs. 4(*b*) and 5(*b*)) that the strength of the vortex rolls for the tapering duct is much weaker than that in the rectangular duct at the same Re and Gr. Further comparison of the results for the higher buoyancies (Gr=4.2×10^4 & 7.4×10^4) was also made. We noted that the photos for the rectangular duct (Fig. 6(*a*)) showed a similar vortex flow evolution to that at a lower buoyancy for Gr=2.5×10^4 except the appearance of an additional pair of small vortex rolls near the duct sides in the exit end of the duct. This newly formed vortex pair circulates downwards near the side walls. It should be pointed out that this new vortex pair is small and mainly appears in the duct corners, and hence is not detected by the top view flow photos discussed above in which the secondary flow at the horizontal plane at the mid-height of the duct $y=1.5$ cm was pictured. Moreover, at these higher buoyancies the rolls in the core region grow significantly as the flow moves downstream. While in the tapering duct an increase of the Grashof number to 4.2×10^4 resulted in three pairs of weak longitudinal rolls in the secondary half of the duct. The vortex rolls were obviously weaker than those in the horizontal duct. For a higher Grashof number of Gr=7.4×10^4 (Fig. 6(*b*)) the vortex flow in the tapering duct consists of two weak longitudinal roll pairs in the entry region of the duct core ($z<28$ cm), three vortex roll pairs in the middle portion of the duct (28 cm$\leqslant z\leqslant$55 cm), and four pairs in the exit end. Note that due to the flow acceleration in the axial direction associated with the top plate tapering the vortex intensity of the longitudinal rolls does not always increase with the axial distance. For example, the rolls at the cross section $z=0.7$ m are much weaker than those at the cross section $z=0.6$ m. These vortex rolls are also weaker than those in the horizontal duct at the same Re and Gr (Fig. 6(*a*)).

The Reynolds number can have a dramatic impact on the vortex flow development, as discussed above. This is further manifested by inspecting the end-view photos for Gr=1.0×10^4 and Re=15 and 9. Note that at these lower Reynolds numbers the vortex rolls in the rectangular duct get stronger with the axial distance but do not merge together (Fig. 7(*a*)). Moreover, the degree of the vortex flow asymmetry is largest in the duct entry where the vortex flow is relatively weak. Downstream the four vortex rolls are in fact spanwisely symmetric. Note that in the tapering duct only one vortex pair forms at Re=15 (Fig. 7(*b*)) and the vortex flow is much weaker. At Re=9 there were four rolls induced shortly after the flow entered the duct. But the rolls in the duct core were substantially suppressed by the top plate tapering to nearly disappear in the duct exit. The rolls near the duct sides were also weaker and are in triangular shape. Again the vortex intensity of the flow in the tapering duct is much weaker. For a further reduction of the Reynolds number to 5 the vortex flow quickly evolved to one pair of strong, symmetric longitudinal rolls in the rectangular duct. In the tapering duct the four-pair structure prevailed in the entry half of the duct. Downstream the rolls in the duct core were significantly suppressed. These downstream rolls were slightly asymmetric. The vortex flow was weakened again by the top plate tapering but in a smaller degree at this low Reynolds number of Re=5.

To reveal the temporal characteristics of the vortex flow, the time variations of the detected instantaneous air temperature at selected locations for various cases for the rectangular and trapezoid ducts were examined. It was of interest to note that the flow oscillation in the rectangular duct at high buoyancy-to-inertia ratios was completely suppressed by the flow acceleration in the tapering duct. This clearly shows the effective stabilization of the buoyancy driven unstable flow by the top plate tapering.

4 Concluding Remarks

We have performed an experimental study to investigate the effects of the top plate tapering on the stabilization of the buoyancy driven vortex flow in mixed convection of air through the bottom heated horizontal rectangular and tapering ducts by systematic measurement of the time-averaged spanwise temperature distributions and the time histories of the air temperature. Instantaneous flow visualizations were also conducted. The experiments were carried out for the Reynolds number ranging from 5 to 102 and Grashof numbers from 1.0×10^4 to 1.7×10^5. The major results can be brightly summarized in the following.

1 In the rectangular duct the onset of thermal instability was found to move upstream for increasing Grashof number and/or decreasing Reynolds number. The results for the tapering duct resemble those for the rectangular duct except that the onset point moves a little downstream as compared with that for the horizontal duct for the same Re and Gr.

2 Due to the increase of the aspect ratio from 4 at the duct inlet to 12 at the duct exit, more vortex rolls are induced in the tapering duct than in the rectangular duct in the downstream region.

3 In the tapering duct, the main forced flow accelerates so rapidly in the downstream region that the vortex intensity of the longitudinal rolls are much weaker.

4 The unstable vortex flow at high buoyancy-to-inertia ratio in the rectangular duct can be completely stabilized by tapering the top plate over the range of the parameters covered in the present study.

During the course of this study it has been realized that although the top plate tapering results in the complete stabilization of the vortex flow, the weaker vortices still dominate the secondary flow in the tapering duct. Methods to eliminate these vortices need to be investigated in the future.

Acknowledgment

The financial support of this study by the engineering division of National Science Council of Taiwan, R.O.C. through the contract NSC 87-2212-E-009-029 is greatly appreciated.

Nomenclature

AR = aspect ratio, b/d
b, d = duct width and duct height
g = gravitational acceleration
Gr = Grashof number, $g\beta q''_{\text{conv}} d_{\text{in}}^4/k\nu^2$
Gr_z = local Grashof number, $g\beta q''_{\text{conv}} z^4/k\nu^2$
h = local convection heat transfer coefficient
k = thermal conductivity
L = length of the test section
Nu_d = Nusselt number, hd_{in}/k
Pr = Prandtl number, ν/α
q''_{conv} = local convective heat flux
q''_{insul} = local conduction heat loss through the insulation
q''_{rad} = local radiation heat loss from the surface
q''_{tot} = the total heat flux in the plate
Ra = Rayleigh number, Gr·Pr
Re = Reynolds number, $\overline{w_{\text{in}}}d_{\text{in}}/\nu$
Re_z = local Reynolds number, $\overline{wz}/\nu$
T = temperature
w = velocity component in axial direction
x, y, z = Cartesian coordinates
X, Y, Z = dimensionless Cartesian coordinate, x/d_{in}, y/d_{in}, and z/d_{in}
Z^* = modified Z-coordinate, $z/d_{\text{in}}\cdot\text{Re}\cdot\text{Pr}$
β = thermal expansion coefficient
ν = kinematic viscosity

Subscripts

b = of buck quantities
in = values at the inlet of the test section
w = of heated wall quantities

Superscripts

$-$ = average value

References

[1] Mori, Y., and Uchida, Y., 1996, ''Forced Convective Heat Transfer Between Horizontal Flat Plates,'' Int. J. Heat Mass Transf., **9**, pp. 803–817.
[2] Akiyama, M., Hwang, G. J., and Cheng, K. C., 1971, ''Experiments on the Onset of Longitudinal Vortices in Laminar Forced Convection Between Horizontal Plates,'' ASME J. Heat Transfer, **93**, pp. 335–341.
[3] Ostrach, S., and Kamotani, Y., 1975, ''Heat Transfer Augmentation in Laminar Fully Developed Channel Flow by Means of Heating From Below,'' ASME J. Heat Transfer, **97**, pp. 220–225.
[4] Kamotani, Y., and Ostrach, S., 1976, ''Effect of Thermal Instability on Thermally Developing Laminar Channel Flow,'' ASME J. Heat Transfer, **98**, pp. 62–66.
[5] Hwang, G. J., and Liu, C. L., 1976, ''An Experimental Study of Convective Instability in the Thermal Entrance Region of a Horizontal Parallel-Plate Channel Heated From Below,'' Can. J. Chem. Eng., **54**, pp. 521–525.
[6] Incropera, F. P., Knox, A. L., and Maughan, J. R., 1987, ''Mixed-Convection Flow and Heat Transfer in the Entry Region of a Horizontal Rectangular Duct,'' ASME J. Heat Transfer, **109**, pp. 434–439.
[7] Maughan, J. R., and Incropera, F. P., 1990, ''Regions of Heat Transfer Enhancement for Laminar Mixed Convection in a Parallel Plate Channel,'' Int. J. Heat Mass Transf., **33**, pp. 555–570.
[8] Moharreri, S. S., Armaly, B. F., and Chen, T. S., 1988, ''Measurements in the Transition Vortex Flow Regime of Mixed Convection Above a Horizontal Heated Plate,'' ASME J. Heat Transfer, **110**, pp. 358–365.
[9] Chiu, K. C., and Rosenberger, F., 1987, ''Mixed Convection Between Horizontal Plate—I. Entrance Effects,'' Int. J. Heat Mass Transf., **30**, pp. 1645–1654.
[10] Chiu, K. C., Ouazzani, J., and Rosenberger, F., 1987, ''Mixed Convection Between Horizontal Plates—II. Fully Developed Flow,'' Int. J. Heat Mass Transf., **30**, pp. 1655–1662.
[11] Nyce, T. A., Ouazzani, J., Durand-Daubin, A., and Rosenberger, F., 1992, ''Mixed Convection in a Horizontal Rectangular Channel-Experimental and Numerical Velocity Distributions,'' Int. J. Heat Mass Transf., **35**, pp. 1481–1494.
[12] Ouazzani, M. T., Caltagirone, J. P., Meyer, G., and Mojtabi, A., 1989, ''Etude Numerique et Experimental de la Convection Mixte Entre Deux Plans Horizontaux,'' Int. J. Heat Mass Transf., **32**, pp. 261–269.
[13] Ouazzani, M. T., Platten, J. K., and Mojtabi, A., 1990, ''Etude Experimental de la Convection Mixte Entre Duex Plans Horizontaux a Temperatures Differents—II,'' Int. J. Heat Mass Transf., **33**, pp. 1417–1427.
[14] Yu, C. H., Chang, M. Y., and Lin, T. F., 1996, ''Structures of Moving Transverse and Mixed Rolls in Mixed Convection in a Horizontal Plane Channel,'' Int. J. Heat Mass Transf., **40**, pp. 333–346.
[15] Cheng, K. C., and Shi, L., 1994, ''Visualization of Convective Instability Phenomena in the Entrance Region of a Horizontal Rectangular Channel Heated From Below and/or Cooled From Above,'' Exp. Heat Transfer, **7**, pp. 235–248.
[16] Koizumi, H., and Hosokawa, I., 1993, ''Unsteady Behavior and Mass Transfer Performance of the Combined Convective Flow in a Horizontal Rectangular Duct Heated From Below,'' Int. J. Heat Mass Transf., **36**, pp. 3937–3947.
[17] Huang, C. C., and Lin, T. F., 1994, ''Buoyancy Induced Flow Transition in Mixed Convective Flow of Air Through a Bottom Heated Horizontal Rectangular Duct,'' Int. J. Heat Mass Transf., **37**, pp. 1235–1255.
[18] Huang, C. C., and Lin, T. F., 1995, ''Vortex Flow and Thermal Characteristics in Mixed Convection of Air in a Horizontal Rectangular Duct: Effects of

Reynolds and Grashof Numbers,'' Int. J. Heat Mass Transf., **38**, pp. 1661–1674.

[19] Lin, W. L., and Lin, T. F., 1996, ''Experimental Study of Unstable Mixed Convection of Air in a Bottom Heated Horizontal Rectangular Duct,'' Int. J. Heat Mass Transf., **39**, pp. 1649–1663.

[20] Lin, W. L., Ker, Y. T., and Lin, T. F., 1996, ''Experimental Observation and Conjugate Heat Transfer Analysis of Vortex Flow Development in Mixed Convection of Air in a Horizontal Rectangular Duct,'' Int. J. Heat Mass Transf., **39**, pp. 3667–3683.

[21] Kline, S. J., and Mcclintock, F. A., 1953, ''Describing Uncertainties in Single-Sample Experiments,'' Mech. Eng., **75**, pp. 3–8.

[22] Tseng, W. S., 1996, ''Stabilization of Mixed Convective Air Flow in a Bottom Heated Rectangular Duct by Tapering its Top Plate,'' M.S. thesis, National Chiao Tung University, Hsinchu, Taiwan, R.O.C.

[23] Visser, E. P., Kleijn, C. R., Govers, C. A. M., and Hoogendoorn, C. J., 1989, ''Return Flows in Horizontal MOCVD Reactors Studied With the Use of TiO_2 Particle Injection and Numerical Calculations,'' J. Cryst. Growth, **94**, pp. 929–946.

Experimental Analysis of the Heat Transfer Induced by Thermocapillary Convection Around a Bubble

P. Arlabosse
e-mail: patricia@iusti.univ-mrs.fr

L. Tadrist
e-mail: ltadrist@iusti.univ-mrs.fr

H. Tadrist

J. Pantaloni

I.U.S.T.I.-CNRS UMR 6595,
Universite de Provence,
Technopole de Chateau Gombert,
5 rue Enrico Fermi,
13453 Marseille Cedex 13,
France

The surface tension driven flow in the liquid vicinity of gas bubbles on a heated wall and its contribution to the heat transfer are investigated experimentally in a configuration where surface tension force and buoyancy forces oppose one another. This liquid flow caused by the temperature gradient along the interface is called thermocapillary or thermal Marangoni convection. The studies were made with silicone oils of different viscosities so that a wide range of dimensionless numbers were encountered. The velocity fields are determined from the motion of carbon particles in the meridian plane of the bubble. The influence of the temperature gradient, the oil viscosity, and the bubble shape on the profiles along the interface and in the direction normal to the interface is analyzed. The temperature field is determined by holographic interferometry. For the axisymmetric problem, the interferograms are evaluated by solving the Abel-integral equation. From the isotherms, the temperature distribution along the bubble surface and in the liquid beneath the bubble is measured. To quantify the contribution of thermocapillarity to the heat transfer, the heat flux transferred by thermocapillarity is measured. A heat exchange law giving the increase in heat flux due to Marangoni convection in comparison to the conductive regime is proposed. [S0022-1481(00)70501-9]

Keywords: Convection, Experimental, Heat Transfer, Instability, Thermocapillary

1 Introduction

The extensive studies on nucleate boiling heat transfer have resulted in a considerable increase in the understanding of the boiling process. But one of the questions remaining to be answered concerns the detailed mechanism by which heat is transferred from the heating surface to the boiling liquid. The classical theories describing boiling on earth make an extensive use of parameter ''gravitational acceleration'' ([1]), which could explain the high heat transfer coefficient owing to the bubble's detachment from the heater. For quite a long time, no evidence had been obtained to experimentally check whether the influence of gravity was modeled correctly. Since the 1960s, numerous experiments have been performed to draw some conclusions about the role of the gravitational acceleration first in high gravity levels ([2,3]) and later in microgravity environments ([4,5,6]). This leads to short experimental times during which it is difficult to extrapolate the behaviors observed in the short tests conducted in drop towers ([5]). Insufficient time exists for transients to decay and the long-term behavior of the vapor formed in the vicinity of the surface is as yet unknown. To avoid natural convection, the gravitational acceleration should be as small as possible, but residual fluctuations can induce the bubble's detachment from the heater ([7]). Doubt remains as to the contribution of this residual convection to the boiling heat transfer. Many works on boiling using wires and tubes appear in the literature and any general conclusion must be considered very carefully because surface tension effects associated with the curvature of the heater may overshadow other effects. Owing to these experimental constraints, no clear quantitative conclusion can be drawn about the role of gravity in boiling heat transfer. Nevertheless, the following general trend comes out: The characteristic curve ([8]) remains largely valid for nucleate pool boiling in low gravity fields.

In nucleate pool boiling, the departure radius of the bubble is essentially determined by the balance of Archimedes forces which tend to tear the bubble away from the heater and surface tension forces which act to retain it on the surface. This leads to the well-known relation deduced by Fritz [9], which gives the detachment radius of the bubble (assimilated to an equivalent sphere of radius R_d) as a linear function of $g^{-1/2}$ so that an increase in the bubble size associated with the accelerated onset of film boiling and a decrease in the heat transfer coefficient were expected in a microgravity environment.

The contradiction between the theoretical predictions and the much debated experimental results confirms that the physics of the boiling process is still poorly understood. The question of whether the classical theory is still valid, and if so to what extent, is thus still open. Since boiling is a complex phenomenon, it is difficult to put it into a simple theoretical frame. Among the mechanisms neglected in the normal gravity field, some authors ([4,10,11]) point out that the thermocapillary flow around the growing bubble could be important in microgravity.

Interferometric measurements performed by Mayinger [12] and Beer [13] show that the first bubble generated on the heater grows in an undisturbed temperature field and that the interface is surrounded by the isotherm of saturation. But for the subsequent bubbles, the wake's flows disturb the temperature field and strong temperature gradients appear along the interface near the base of the bubble. These gradients along the interface of the growing bubble cause local changes in the surface tension at the interface and thereby generate a motion of the interface towards the higher surface tension regions. The tangential force generated on the interface acts as a shear stress applied by the interface to the adjoining fluids. Since the surface tension usually decreases with

---

Contributed by the Heat Transfer Division for publication in the JOURNAL OF HEAT TRANSFER. Manuscript received by the Heat Transfer Division, June 30, 1998; revision received, Jan. 12, 1999. Associate Technical Editor. M. Kaviany.

Table 1 Thermophysical properties of the silicone oil at 298 K

ν (m^2/s)	ρ (kg/m^3)	β (K^{-1})	Cp (J/kg K)	λ (W/m K)	$\partial\gamma/\partial T$ (N/m K)	n	$\partial n/\partial T$ (K^{-1})
$2\ 10^{-5}$	950	$1.07\ 10^{-3}$	1630	0.14	$-6.23\ 10^{-5}$	1.400	$-3.66\ 10^{-4}$
$5\ 10^{-5}$	959	$1.05\ 10^{-3}$	1460	0.16	$-6.8\ 10^{-5}$	1.402	$-3.74\ 10^{-4}$
10^{-4}	965	$9.45\ 10^{-4}$	1460	0.16	$-6.57\ 10^{-5}$	1.403	$-3.77\ 10^{-4}$

increasing temperature, the fluid along the surface of the growing bubble will usually move from the overheated base of the bubble towards its cooler rear.

Our interest in Marangoni convection arises from its possible importance in boiling heat transfer. In the following, we will focus our attention on thermocapillary flows around bubbles. Nevertheless, there is an abundant literature on thermocapillary-buoyancy-driven convection induced along planar interfaces in rectangular pools heated from one side and cooled on the other ([14–18]) and on migration of bubbles under the combined action of buoyancy and thermocapillarity ([19]).

Mc Grew et al. [10] were the first to describe the thermocapillary convection around a vapor bubble qualitatively and to express the hypothesis that it can contribute to the boiling heat transfer. When vigorous boiling occurs, the liquid is exuded downward in a stream with a velocity of 1 to 2 cm/s near the liquid-vapor interface. At lower boiling rates, the flow pattern is different: The liquid tends to produce rotating vortices near the heating surface.

The fullest description of the motion was proposed by Huplik and Raithby [20] who investigated this phenomenon in boiling on a downward-facing heated surface. Most of the experiments were conducted with the liquid at a temperature lower than the saturation temperature. A strong jet-type flow is created immediately after the appearance of a bubble on the surface. The liquid is projected downward from the center of the bubble with cooler liquid being drawn inward toward the heater surface and the upper portion of the bubble. As the vapor volume increases, the interface motion is observed to decrease near the bubble crown. The coalescing bubbles form a blanket of vapor which covers a large portion of the heated surface and vigorous Marangoni convection is observed along the portion of the blanket near the heated surface.

The interpretation of the flow pattern observed under nucleate boiling conditions is, at first, not evident. Gaddis [21] simulated Marangoni convection around vapor and gas bubbles and came to the conclusion that the thermocapillarity is all the more important as the heat transfer coefficient on the liquid vapor interface is low.

Raake et al. [22] evaluated the temperature distribution around an air bubble in silicone oil of variable viscosity with a Schlieren interferometer. The convective heat transport deforms the isotherms in the direction of the temperature gradient. A locally larger temperature gradient appears below the colder apex of the bubble than in an undisturbed fluid. With increasing convection, the temperature along the interface is nearly constant and the convective mechanism only operates along a small part of the bubble interface near the wall. An oscillatory instability is reported in experiments with low oil viscosities at a temperature gradient greater than a critical one.

More recently, Wozniak et al. experimentally investigated the flow pattern in both normal ([23]) and low gravity ([24]) fields using Particle Image Velocimetry (PIV) with liquid crystal tracer particles. Earth-bound experiments were carried out in a configuration where buoyancy and surface tension forces act in opposite direction. Due to hydrostatic pressure, the shape of the bubble is flattened in the direction parallel to the gravity. A toroidal vortex is active along the entire contour of the bubble. Secondary vortices appear in the lower part of the liquid, resulting from the interaction of buoyancy and surface tension forces. In microgravity, thermocapillarity leads to a jet-like flow. The convection penetrates much deeper into the bulk.

This bibliographical review reveals that many of the experimental results are qualitative and no systematic analysis has been performed. So far the increase in the heat flux due to Marangoni convection has not been measured. Since the mechanisms involved in boiling (vaporization, condensation, oscillations, drift current, etc.) make the quantification of the contribution of thermocapillarity to the boiling heat transfer difficult, in this paper we propose an experimental study to investigate the thermocapillary flow around a bubble under non-boiling conditions (air bubble inside a liquid layer) and its contribution to the heat transfer. The geometric configuration chosen to investigate the thermocapillarity around an air bubble the relevant dimensionless parameters that describe the phenomena are presented in Section 2. The experimental setup and the measurement techniques are detailed in Section 3. To determine the flow field, the shifting of carbon particles is measured. To investigate the contribution of thermocapillarity to the heat transfer, interferometry and heat flux sensors are used. The method to evaluate the interferograms is briefly described. Section 4 concerns the results. The first part is devoted to the analysis of the flow field: The flow pattern is, first, described; then, a systematic analysis of the influence of the relevant parameters on the velocity field in the liquid is achieved. The second part concerns the analysis of the temperature field in the liquid. The contribution of the Marangoni convection to the heat transfer is measured and a heat exchange law is proposed.

2 Physical Model and Mathematical Formulation

For liquids with a negative temperature coefficient of surface tension, the flow is directed from the hot to the cold. So that natural convection may not overshadow the thermocapillary effects, the liquid layer is heated from above and an air bubble is generated on the underside of the upper wall. In this case, the thermocapillary force, which drives hot fluid downward, acts in the opposite direction to the buoyancy force. Silicone oil was chosen as the working fluid. Its surface tension is insensitive to contamination, which will minimize the problem of experimental reproducibility, and the temperature coefficient of surface tension is nearly the same (regardless of the oil viscosity) between $2\ 10^{-5}$ and 10^{-4} m^2/s, which is the range of viscosity we considered. Table 1 provides the fluid properties at the mean temperature of 25°C.

An analysis ([26]) of the physical problem leads us to determine the relevant dimensionless parameters that describe the phenomena. We use the following reference scales: $L_{\mathrm{ref}}=R$, $V_{\mathrm{ref}}=(\partial\gamma/\partial T(T_h-T_c)R)/(\mu_{\mathrm{oil}}E)$, $t_{\mathrm{ref}}=L_{\mathrm{ref}}/V_{\mathrm{ref}}$, $P_{\mathrm{ref}}=\mu_{\mathrm{oil}}V_{\mathrm{ref}}/L_{\mathrm{ref}}$ and $\Delta T_{\mathrm{ref}}=(T_h-T_c)R/E$. We take the bubble radius as the reference length because this characteristic length should be proportional to the interface length, which drives the flow. For the reference temperature difference, we must consider the temperature difference between the overheated base of the bubble and its cooler rear. As the temperature of the apex is unknown, we assume in a first approximation that the change in temperature is linear between the upper and lower walls and we determine the temperature of the cooler rear of the bubble. In addition to the ratios between the properties of the gas and liquid phases, the four relevant dimensionless parameters are defined by

$$\mathrm{Ma}=-\frac{\frac{\partial\gamma}{\partial T}(T_h-T_c)R^2}{\mu_{\mathrm{oil}}a_{\mathrm{oil}}E} \tag{1}$$

$$\mathrm{Pr}=\frac{\nu_{\mathrm{oil}}}{a_{\mathrm{oil}}} \tag{2}$$

$$\mathrm{Ca}=\frac{\frac{\partial\gamma}{\partial T}(T_h-T_c)R}{\gamma E} \tag{3}$$

$$\mathrm{Bo}=\frac{\rho_{\mathrm{oil}}\beta_{\mathrm{oil}}gR^2}{\frac{\partial\gamma}{\partial T}} \tag{4}$$

where Ma, Pr, and Ca are the classical Marangoni, Prandtl, and Capillary numbers whereas Bo is a modified Bond number.

The modified Bond number is a ratio of the thermocapillary force to the buoyancy force and can be related to the ratio between the Rayleigh and the Marangoni numbers. In the selected configuration, the Marangoni number characterizes the destabilizing effects while the Prandtl and Rayleigh numbers correspond to the stabilizing effects.

3 Experimental Setup

The heart of the experimental setup is the test cell containing the test liquid. The cell is a cavity with horizontal brass endwalls, the temperature of which could individually be kept uniform and constant in order to establish a vertical temperature gradient within the liquid. To achieve stable stratification inside the fluid, the top plate is heated via an electrical heater while the bottom one is cooled by means of a Peltier element. Two bore holes with tube connections are located on the upper wall for fluid volume compensation during heating and bubble injection. A further capillary opening in the middle of the upper wall is connected to a syringe for bubble injection.

Two test cells are used in the present study. A cell with a 30×6 mm^2 interior section and a height of 10 mm is used for interferometric measurements and fluid flow analysis. The vertical walls are made of glass. A second experimental chamber, sketched in Fig. 1, is used to quantify the contribution of the thermocapillary convection to the heat transfer. The interior square section is 40×40 mm^2 and the distance between the horizontal walls is adjustable between 3 and 10 mm. The vertical walls are made of polycarbonate for visualization purposes and a 2-mm thick air layer is added to the side walls to limit heat exchange with the outside environment.

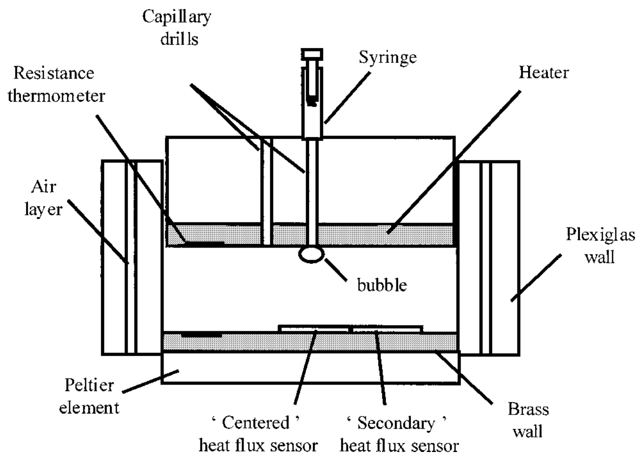

Fig. 1 Experiment chamber

Two heat flux sensors, of surface 10×10 mm^2, sensitivity 0.34 μV/[W/m^2] and response time 0.2 sec, are glued in the middle of the bottom wall, just beneath the bubble, and 10 mm from the center of this wall, respectively (see Fig. 1). The thin foil heat flux sensor, manufactured by M.A.H.T. (France), is a multilayer sensor [25] which measures the average density of conductive, convective, and radiant heat transfer between an area on which the sensor is mounted and the surrounding environment. Since the sensitivity depends on the number of thermoelements distributed over the sensing surface, the area must be estimated to obtain the desired sensitivity. The signal delivered by the two heat flux sensors is so small ($0.17\,10^{-3}$ V for a heat flux of 500 W/m^2) that two low-noise and low-offset operational amplifiers (LT 1051 circuits manufactured by Linear Technology, USA) are used. The gain is set to 1000.

The procedure for measuring the velocity is based on a particle image velocimetry method. Carbon particles of about 40 μm in diameter, whose density is matched with the density of the silicone oil, are added to the fluid for the flow analysis. Since the flow under investigation is axisymmetric, illumination of the mid-plane is sufficient to capture the characteristics of the entire flow field. The vertical meridian plane is uniformly illuminated with a thin laser light sheet. The light flux diffused by the particles is collected by a CCD camera equipped with a 100 mm macro lens and set in the direction perpendicular to the illuminated plane. This camera is connected to a video screen and a video recorder. The particles images are recorded every 0.2 sec. These images are analyzed to identify the particles which move nearby the interface and then their shifting between two successive images is measured. This method enables to determine the liquid velocity near the bubble.

The temperature distribution in the liquid is determined by holographic interferometry. The experimental setup has been described elsewhere ([26]). The reference state used in the experiments corresponds to a liquid at uniform temperature and any deviations from this reference state result in the appearance of interference fringes. Light rays fumish an integral information about the refractive index distribution of the medium they have traveled through. Using the relationship between the refractive index and the temperature, one can easily evaluate the temperature distribution of a two-dimensional field from an interferogram. In such a two-dimensional field, the refractive index along the ray traversing through the medium is constant and the interference fringes correspond to the isotherms. But for axisymmetrical thermal field, the interferogram must be evaluated with suitable methods to determine the distribution of the temperature in the meridian plane. The thermocapillary convection around the bubble induces an axisymmetrical thermal field about the vertical axis through the apex of the bubble. To evaluate the interferograms, the method of Matekunas and Winter [27] is used. An influence area is associated to the bubble: inside this area, the refractive index field is axisymmetric whereas, outside this area, the refractive index field is two-dimensional. The optical pathlength difference between a light ray passing through the bubble influence area and another passing through the undisturbed medium is given by an Abel integral type of equation, which should be inverted to determine the radial distribution of the refractive index, $\Delta n(r)$. Finally, the equation to be solved can be written as

$$\Delta n(r)=\frac{1}{\pi}\frac{\Delta L'(R)}{1-R/R_I}\log\frac{r/R_I}{1+[1-(r/R_I)^2]^{0.5}}-\left[1-\left(\frac{r}{R_I}\right)^2\right]^{0.5} \tag{5}$$

where R_I and $\Delta L'$ are the size of the bubble influence area and the slope of the interference fringe on the interface weighted by the ratio of the laser wave length and the distance between two consecutive fringes in the two-dimensional area.

The experimental procedure is as follows: first, the chamber is filled with silicone oil up to a level exceeding the upper wall by about 10 mm. The liquid is heated from above and cooled from below until a steady temperature difference between the horizontal plates is established. Then, an air bubble is injected and after a few seconds the steady convective flow is developed. The bubble size is continuously controlled so that it is constant on the video screen. The motion of the tracer in the meridian plane of the bubble and/or the variation of heat flux due to thermocapillary convection are recorded.

4 Results and Discussion

4.1 Analysis of the Flow Pattern.

4.1.1 Qualitative Description of the Flow Pattern. Immediately after the bubble injection, two convective vortices, shown in Fig. 2 around a 1.5-mm diameter air bubble immersed in a 2 10^{-5} m^2/s silicone oil, appear on both sides of the bubble. The liquid flows along the heated wall toward the bubble; then the interface drives the hot fluid downward toward the lower cold pole of the bubble. This pole corresponds to a stagnation point, where the projection of the temperature gradient is zero. The continuity of motion, together with the buoyancy, brings the fluid up again resulting in a toroïdal vortex. The thermocapillarity is active along the entire contour of the bubble and, in the immediate vicinity of the bubble surface, it prevails over the buoyancy-driven convection. For higher temperature gradients, weak secondary contrarotative vortices can be observed beneath the first two. They result from the interaction of surface tension and gravity forces. Indeed, in an earth gravity environment, both effects are coupled: the thermocapillarity destroys the stable temperature stratification which causes natural convection as a secondary effect. These secondary vortices reduce the size of the main cells.

4.1.2 Quantitative Analysis of the Flow Field. The physical analysis of the thermocapillary convection brings to the fore the four relevant parameters which have an influence on the magnitude of the velocity. As the capillary number ranges in values from 7.6 10^{-4} to 3 10^{-3}, its influence on the flow field is not analyzed. In the following, we investigate the influence of the Marangoni, Prandtl, and Bond numbers on the magnitude of the flow.

Marangoni convection was analyzed around two different bubble shapes, plotted in Fig. 3. The projection of the area of the bubble in the camera plane is of elliptical shape. Up to a radius of 1.3 mm, the bubble remains spherical in shape. Beyond, the bubble flattens in the vertical direction due to the hydrostatic pressure in the oil layer. The radius, as well as the contact angle between the bubble and the wall, is detailed in Fig. 3. To evaluate the Marangoni and Bond numbers, we took the radius R_{eq} of the sphere which will have the same volume as the bubble. The range of dimensionless numbers investigated is $0 \leqslant \mathrm{Ma} \leqslant 250$, $220 \leqslant \mathrm{Pr} \leqslant 880$, and $\frac{1}{3} \leqslant \mathrm{Bo} \leqslant \frac{2}{3}$.

The sources of uncertainties attributed to the velocity measurement come from the measurements of the shifting of the particles and the time. The uncertainties on the shifting and the time are estimated to 0.0 125 mm and 0.04 sec, respectively.

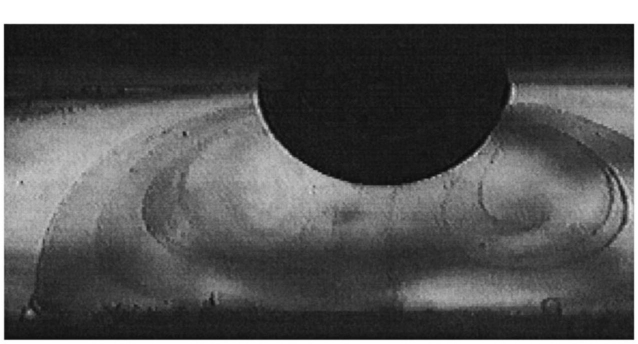

Fig. 2 Flow pattern around a 1.5-mm diameter air bubble immersed in a 2 10^{-6} m^2/s silicone oil

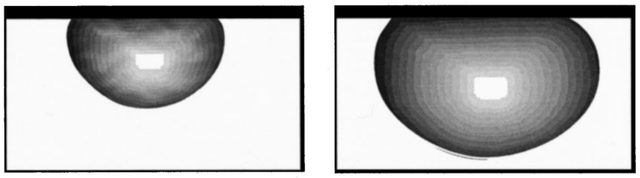

(a) (b)

Fig. 3 Areas of the investigated bubble shapes in the camera plane: (a) smaller bubble (R_{eq}=1.5 mm and contact angle 71.5 deg), (b) flattaned bubble (R_{eq}=2 mm and contact angle 52 deg)

Since $\mathrm{Ma} \neq 0$, the interface at least drives partially the flow both in the bubble and in the oil. The tangential velocity is maximum near the interface and decreases rapidly in the direction perpendicular to the interface. This decrease in the ''r'' direction, which connects the center of the bubble to the center of the primary vortex, is shown in Fig. 4 for Pr=220, Bo=0.35, and Ma=40 and 80. The tangential velocity is divided by the maximum velocity measured in the liquid near the interface. Experimentally, we can measure the velocity at best 50 μm from the interface and this measured maximum velocity is equal to 0.36±0.02 mm/s for Ma=40 and 0.64±0.05 mm/s for Ma=80. According to the velocity profile in the direction perpendicular to the interface, one can extrapolate the velocity on the interface, which is 15 percent greater than the magnitude of the velocity measured at 50 μm from the interface.

Apart from the magnitude of the velocity on the interface, the most important datum one can extract from the velocity field in the liquid is the thickness of the viscous boundary layer. A systematic study of the influence of the temperature gradient and the viscosity has been performed but no notable influence of these parameters on the position of the vortex center was found. The thickness of the viscous boundary layer can be estimated at $0.385R_{eq}$ from the Fig. 4.

The influence of the Marangoni, Bond, and Prandtl numbers on the tangential velocity profiles are now successively studied.

Influence of Marangoni number. To analyze the influence of the temperature gradient on the magnitude of Marangoni convection, we changed this parameter in the range $40 \leqslant \mathrm{Ma} \leqslant 120$ and we measured the velocity profiles along the interface. The magnitude

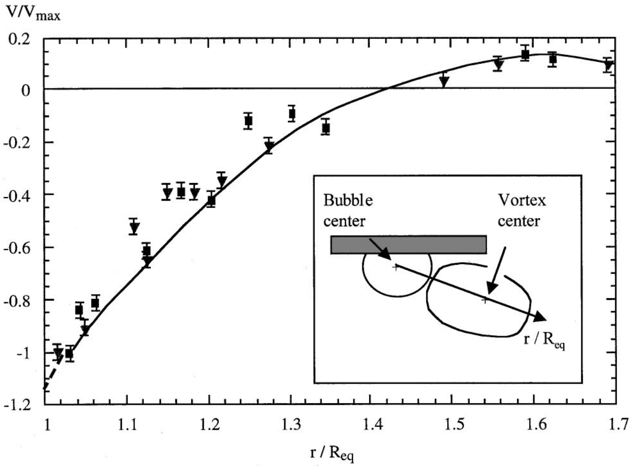

Fig. 4 Nondimensional velocity profile in the direction normal to the interface of the 1.5-mm diameter bubble for Pr=220, Bo=0.35, and ▼ Ma=40 and a ■ Ma=80

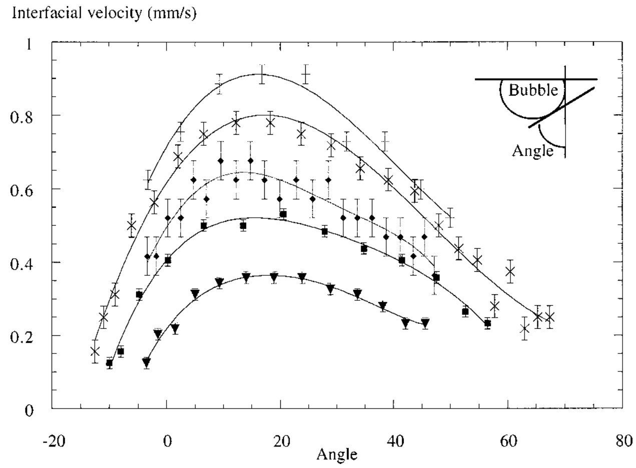

Fig. 5 Velocity profile along the interface of the 1.5-mm diameter bubble for Pr=220, Bo=0.35, and ▼ Ma=40, ■ Ma=60, ◆ Ma=80, × Ma=100, and + Ma=120

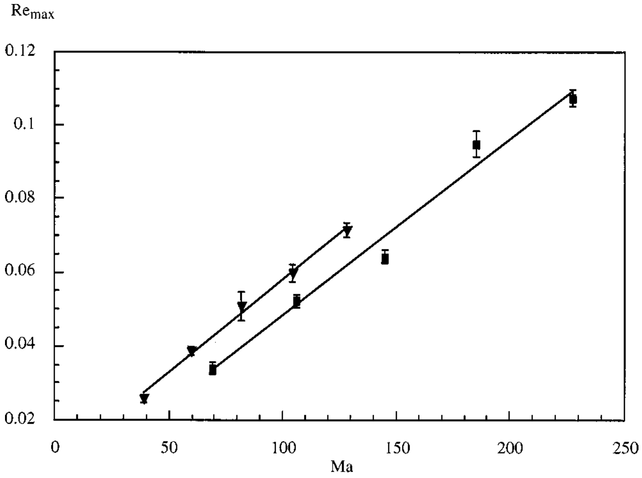

Fig. 7 Maximum Reynolds number versus the Marangoni number for Pr=220, ▼ Bo=0.35, and ■ Bo=0.64

of the velocity is plotted in Fig. 5 versus the angle between the tangent to the interface and the vertical axis for the 1.5-mm diameter bubble with $\mathrm{Pr}=220$ and $\mathrm{Bo}=0.35$. Regardless of the values of the Marangoni number, the behavior is similar. The velocity increases from zero on the heated wall to a maximum, then it decreases as the crown of the bubble is approached, which corresponds to a stagnation point. We notice that the magnitude of the velocity increases with the Marangoni number and that the location of the maximum is nearly independent of the Marangoni number. Therefore, all the velocity profiles obtained for this bubble can be gathered on a single curve, as shown in Fig. 6 for $\mathrm{Ma}=40$ and $\mathrm{Ma}=80$. The maximum is reached for an angle of 17.5 deg in the case of the smallest bubble ($R_{eq}=1.5\,\mathrm{mm}$). The same systematic study was performed for the second bubble shape ($R_{eq}=2$ mm). The velocity profiles are similar to those plotted in Fig. 5 but the maxima are located at an angle of five degrees.

Influence of the Bond number. A change in the bubble size modifies both the Marangoni and the Bond numbers. For the 1.5-mm diameter bubble, the range of nondimensional numbers investigated is $40\leqslant\mathrm{Ma}\leqslant 120$, $\mathrm{Pr}=220$, and $\mathrm{Bo}=0.35$ whereas it is $70\leqslant\mathrm{Ma}\leqslant 250$, $\mathrm{Pr}=220$, and $\mathrm{Bo}=0.64$ for the 2-mm diameter bubble. To compare all the results, we introduce the Reynolds number defined in the nomenclature. The velocity and the characteristic length used to evaluate this parameter are the maximum velocity measured in the liquid and R_{eq}. Whatever the Bond number, the maximum Reynolds number in the liquid increases linearly with the Marangoni number, as shown in Fig. 7. But there is a shift between the two straight lines corresponding to the two Bond numbers investigated. For a fixed Marangoni number, the maximum Reynolds is smaller when the Bond number is high. Indeed, the Bond number represents the ratio of the buoyancy to the thermocapillary forces and in the chosen configuration, buoyancy is a stabilizing effect which counteracts the thermocapillary-driven convection.

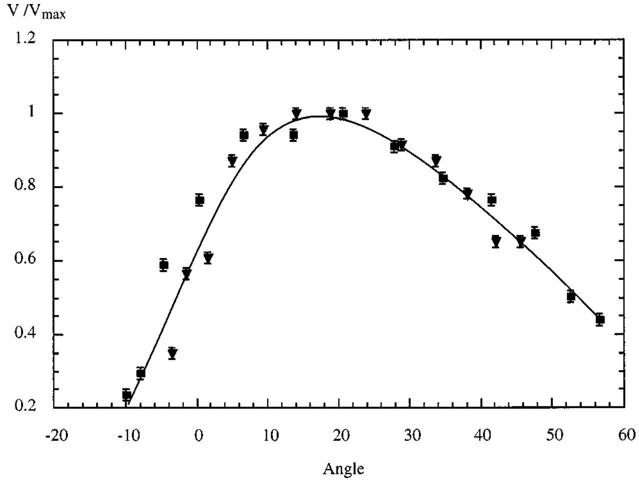

Fig. 6 Nondimensional velocity profile along the interface of the 1.5-mm diameter bubble for Pr=220, Bo=0.35, ▼ Ma=40, and ■ Ma=80

Influence of the Prandtl number. To analyze the influence of the Prandtl number, we changed this parameter in the range $220\leqslant\mathrm{Pr}\leqslant 880$ and we measured the velocity profiles for $\mathrm{Bo}=0.35$ and $10\leqslant\mathrm{Ma}\leqslant 250$. As previously, the maximum Reynolds number was used to compare all the results. For the same Marangoni number, an increase in the Prandtl number reduces the magnitude of the maximum velocity and thus that of the Reynolds number since the Prandtl number characterizes the second stabilizing effect.

4.1.3 Law of Change of the Maximum Reynolds Number. To generalize our results, we determined the relation between the maximum Reynolds number and the previous parameters for all the investigated configurations. This law of change is plotted in Fig. 8 and can be written for the range of dimensionless parameters investigated $0\leqslant\mathrm{Ma}\leqslant 250$, $210\leqslant\mathrm{Pr}\leqslant 880$ and $\frac{1}{3}\leqslant\mathrm{Bo}\leqslant\frac{2}{3}$:

$$\mathrm{Re}_{\mathrm{max}}=0.077\,\mathrm{Bo}^{-1/3}\frac{\mathrm{Ma}}{\mathrm{Pr}}. \tag{6}$$

The above relation gives the value of the maximum Reynolds number in the liquid with great accuracy for the geometric configuration and the range of dimensionless parameters investigated. This reported correlation is the best estimate for the result, and with a resolution coefficient R^2 of 0.984. This number is related to a surface effect through the Marangoni number and to volume effects through the Prandtl and Bond numbers. $\mathrm{Re}_{\mathrm{max}}$ varies linearly with the ratio Ma/Pr. This law and the above velocity profiles, plotted in Figs. 4 and 5, enable us to determine the velocity field in the liquid from the knowledge of the liquid properties and the boundary conditions.

4.2 Analysis of the Temperature Field. The interference fringe distribution was measured by means of a holographic interferometer around the 1.5-mm diameter bubble for $0\leqslant\mathrm{Ma}\leqslant 120$, $\mathrm{Pr}=220$, and $\mathrm{Bo}=0.35$.

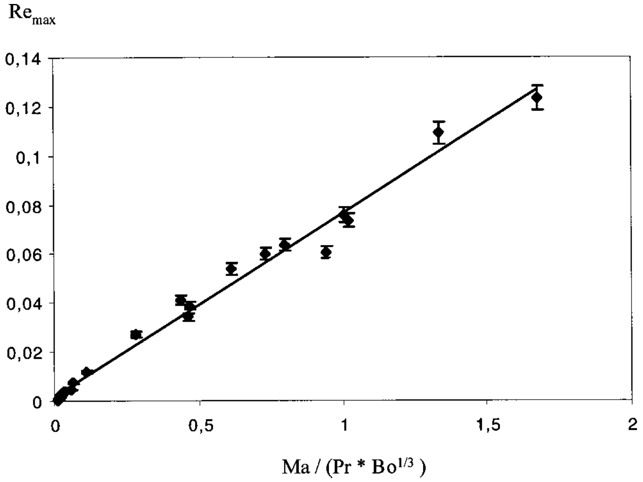

Fig. 8 Law of change of the maximum Reynolds number with the ratio between the Marangonl and the Prandtl numbers for $0 \leqslant Ma \leqslant 250$ and $220 \leqslant Pr \leqslant 880$

When $\mathrm{Ma}=0$ (in the absence of a bubble inside the liquid layer), the interference fringe pattern is a succession of alternating dark and light horizontal lines. Since the phenomenon is two-dimensional, the interference fringes correspond to the isotherms in the liquid and are characteristic of a conductive heat transfer between the two horizontal walls. When $\mathrm{Ma}\neq 0$, the temperature gradient along the interface induces a motion of liquid around the bubble which consequently distorts the interference fringe in the close vicinity of the bubble, as shown in Fig. 9 for $\mathrm{Ma}=60$. The curvature of the interference fringes expresses a heat transfer from the upper wall toward the lower cold one. Far from the bubble, the interference fringes are horizontal which are characteristic of a conductive heat transfer regime between the upper and the lower walls. The convective regime extends in the vertical direction up to one bubble diameter.

The temperature distribution along the bubble interface was evaluated with the method presented in Section 3. The temperature on the interface decreases from the upper wall to the lower pole of the bubble but the temperature gradient along the bubble interface is not linear, as shown in Fig. 10. The main sources of uncertainties are introduced by the estimate of the slope of the interference fringe on the interface and of the distance between two consecutive fringes, the error bars are plotted in Fig. 10. When the Marangoni number increases, the temperature difference between the bottom of the bubble and the apex increases. For example, this difference reaches 0.6°C for $\mathrm{Ma}=40$ and 3°C for $\mathrm{Ma}=100$.

4.3 Contribution to the Heat Transfer. The evaluation of the contribution of Marangoni convection to the heat transfer from the interferograms is rather difficult. Thus, systematic measurements of the heat flux transferred by Marangoni effect around a 1.5-mm diameter air bubble were performed for different Marangoni, Bond, and Prandtl numbers. The range of dimensionless parameters investigated is $0 \leqslant \mathrm{Ma} \leqslant 700$, $\mathrm{Bo} \approx 0.25$, and $220 \leqslant \mathrm{Pr} \leqslant 880$.

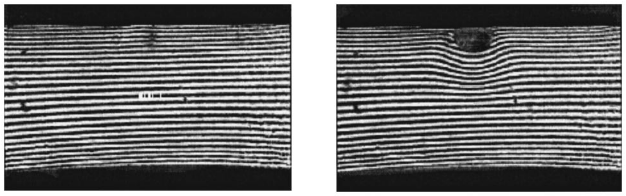

Fig. 9 Interferograms for Pr=220, Bo=0.35, and Ma=60

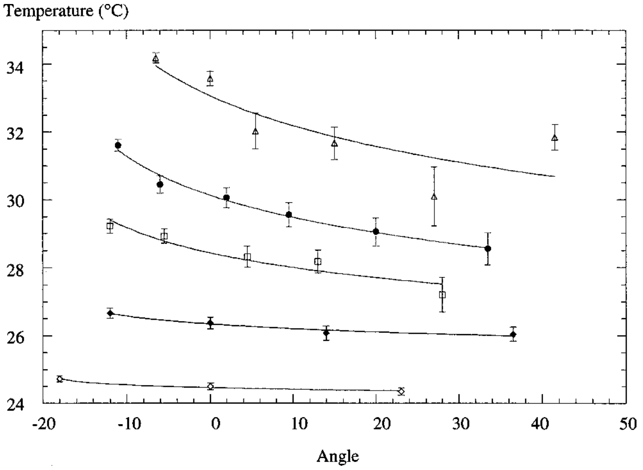

Fig. 10 Temperature distribution along the interface of the 1.5-mm diameter air bubble for Pr=250, Bo=0.35, and ◇ Ma=40, ◆ Ma=60, □ Ma=80, ● Ma=100 and △ Ma=120

The change of the heat fluxes through the heat flux sensors is recorded as a function of time. Before the bubble injection, the heat is exchanged by conduction between the two horizontal walls. When the stationary conductive state is reached in the liquid, the heat fluxes through the two sensors remain constant versus time. Immediately after the bubble injection, the heat flux through the sensor glued beneath the bubble increases, as shown in Fig. 11 for $\mathrm{Ma}=350$, $\mathrm{Bo}=0.25$, and $\mathrm{Pr}=220$. After a few seconds, a new stationary state is reached and the heat flux remains constant. The second sensor measures a small decrease in heat flux, because the main flow induces contrarotative vortices by viscosity in the liquid. When the bubble is removed, the heat fluxes return to their initial values.

We noticed the influence of the distance between the heat flux sensors and the bubble interface. When the heat flux sensors are far from the bubble, the increase in the heat transfer is smaller. For a 5-mm thick liquid layer, the increase is of the order of the experimental error. Beyond this thickness, contrarotative vortices are generated in the oil beneath the bubble, which results in a decrease in the heat flux measured by the sensor pasted in the

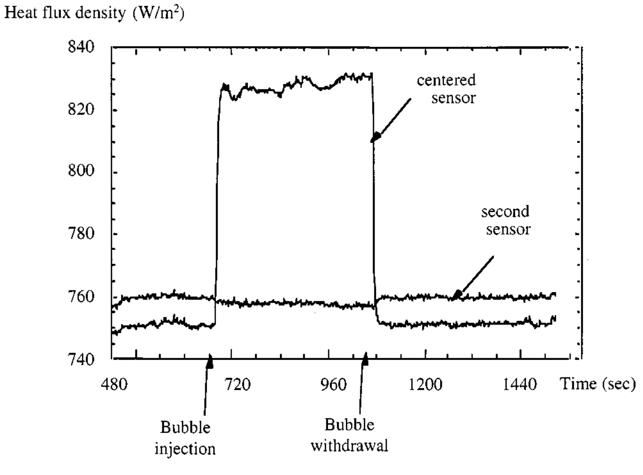

Fig. 11 Heat flux through the heat sensors versus time for Ma=350, Pr=220, and Bo=0.25 (liquid layer thickness *E* =4 mm)

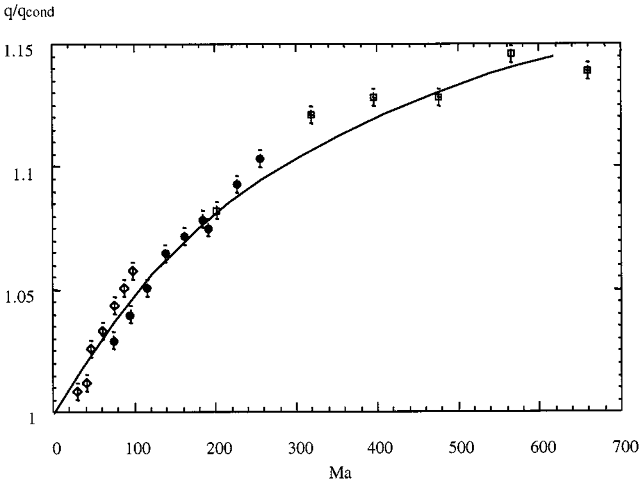

Fig. 12 Change of the ratio between the heat transferred with the bubble and without the bubble with the Marangoni number for Bo≈0.25, 0≤Ma≤700, and □ Pr=220, ● Pr=440 and ◇ Pr =880, −empirical best fit

middle of the bottom wall and an increase in the heat flux measured by the second sensor. According to this conclusion, the liquid layer thickness was fixed at 3 mm for all the results presented in the following.

To quantify the contribution of the thermocapillarity to the heat transfer, we introduced the ratio between the heat flux transferred with the bubble to the conductive one. The sources of uncertainties in estimate this ratio are introduced by the uncertainty on the sensitivity of the heat flux sensor ($\pm 0.01\ \mu\mathrm{V}/[\mathrm{W/m^2}]$), on the gain ($\pm 1$) and on the measurement of the signal delivered by the sensor ($\pm 6\ 10^{-5}\ \mathrm{V}$). The change in this ratio with the Marangoni number is presented in Fig. 12 for the three Prandtl numbers investigated, together with the error bars. The ratio increases with the Marangoni number and the same behavior is observed for the three Prandtl numbers. An analysis of these results leads us to derive the following heat exchange correlation:

$$\frac{q}{q_{\mathrm{cond}}}=1+8.410^{3}\mathrm{Ma}^{0.5}. \tag{7}$$

When the Marangoni number is equal to zero (without any temperature gradient or without a bubble), q/q_{cond} equals 1, which corresponds to conductive heat transfer. When thermocapillarity acts, this ratio increases with the square root of the Marangoni number. In the investigated configuration, thermocapillarity contributes to the heat transfer but its action is relatively small (the same order of magnitude as the conductive regime) for the range of nondimensional parameters investigated.

5 Conclusions and Outlook

The influence of the Marangoni, Prandtl, and Bond numbers on the velocity profiles along and in the direction normal to the bubble interface and on the magnitude of the maximum velocity was analyzed. An experimental flow law, which gives the change in the Reynolds number versus the ratio between the Marangoni and the Prandtl numbers, is proposed.

The increase in the heat flux due to thermocapillarity is measured in the close vicinity of the bubble but, beyond two bubble diameters, heat transfer is dominated by conduction. According to these experimental results, the ratio between the heat flux transferred with an air bubble to the conductive one changes with the square root of the Marangoni number. In the selected configuration, where thermocapillary and gravity effects oppose one another, the contribution of the thermocapillarity to the heat transfer is relatively small for the range of nondimensional parameters investigated ($0 \leq \mathrm{Ma} \leq 700$).

Further experiments will focus on the analysis of the thermocapillary flow for liquids with lower Prandtl numbers, such as those met in boiling experiments.

Acknowledgment

We thank Messrs. Sanchez and Clifton, from the LGC of the University Paul Sabatier (Toulouse, France) for their help during interferometric measurements and Mr. Faure, from IUSTI (Marseille, France), for his technical assistance.

Nomenclature

a = thermal diffusivity ($\mathrm{m^2/s}$)
C_p = specific heat (J/kg K)
E = liquid layer thickness (m)
g = gravitational acceleration ($\mathrm{m/s^2}$)
k = thermal pressure (W/m K)
n = unit normal vector
P = pressure
q = heat flux ($\mathrm{W/m^2}$)
R = bubble radius (m)
s = curvilinear coordinate
T = temperature (K)
t = time (s)
V = velocity (m/s)

Greek Letters

β = volume expansion coefficient ($\mathrm{K^{-1}}$)
δ_{th} = thermal boundary layer (m)
γ = surface tension (N/m)
μ = dynamic viscosity (kg/ms)
ν = kinematic viscosity ($\mathrm{m^2/s}$)
ρ = density ($\mathrm{kg/m^3}$)
τ = unit tangential vector

Subscript

α = air or oil
c = cold
cond = conduction
h = hot
max = maximum

Dimensionless Parameters

Bo = $(\rho_{\mathrm{oil}}\beta_{\mathrm{oil}} g R^2)/(\partial\gamma\partial T)$=Bond number
Ca = $((\partial\gamma/\partial T)(T_h-T_c)R)/(\gamma E)$=capillary number
Ma = $-(\partial\gamma/\partial T)(T_h-T_c)R^2/\mu a E$ = Marangoni number
Pr = ν/a=Prandtl number
Ra = $\beta g(T_h-T_c)R^4/\nu a E$ =Rayleigh number
Re = $V_{\max}R/\nu$= Reynolds number

References

[1] Rohsenow, W. M., 1962, ''A Method of Correlating Heat Transfer Data for Surface Boiling of Liquids,'' ASME J. Heat Transfer, **84**, p. 969.
[2] Merte, H., Jr., and Clark, J. A. 1961, ''Pool Boiling in an Accelerating System,'' ASME J. Heat Transfer, **83**, pp. 233–242.
[3] Costello, C. P., and Tuthill, W. E., 1961, ''Effects of Acceleration on Nucleate Pool Boiling,'' Chem. Eng. Prog., **57**, pp. 189–196.
[4] Siegel, R., 1968, ''Effects of Reduced Gravity on Heat Transfer,'' Adv. Heat Transfer, **4**, pp. 143–227.
[5] Merte, H., 1990, ''Nucleate Pool Boiling in Variable Gravity,'' Am. Inst. Aeronaut. Astronaut., pp. 15–69.
[6] Straub, J., and Miko, S., 1996, ''Boiling on a Wire Under Microgravity Conditions: First Results From a Space Experiment Performed in May 1996,'' *Proceedings Eurotherm N°48, Pool Boiling 2*, D. Gorenflo et al., eds., Edition ETS Pisa, Italy, pp. 275–282.
[7] Zell, M., 1991, ''Untersuchung des Siedevorgangs unter reduzierter Schwerkraft,'' Ph.D. thesis, University of Munich, Germany.
[8] Nukiyama, S., 1934, ''The Maximum and Minimum Values of the Heat Transmitted From Metal to Boiling Water Under Atmospheric Pressure,'' Int. J. Heat Mass Transf., **27**, No. 7, pp. 959–970.

[9] Fritz, W., 1935, ‘‘Berechnungen des Maximalvolumens von Dampfblasen,’’ Phys. Z., **36**, pp. 379–384.
[10] Mc Grew, J. L., Bamford, F. L., and Rehm, T. R., 1966, ‘‘Marangoni Flow: An Additional Mechanism in Boiling Heat Transfer,’’ Science, **153**, No. 3740, pp. 1106–1107.
[11] Straub, J., 1994, ‘‘The Role of Surface Tension for Two Phase Heat and Mass Transfer in the Absence of Gravity,’’ Exp. Therm. Fluid Sci., **9**, pp. 253–273.
[12] Mayinger, F., 1975, ‘‘Blasenbildung und Wärmeübergang beim Sieden in freier und erzwungener Konvektion,’’ Chem. Ing. Tech., **47**, No. 18, pp. 737–748.
[13] Beer, H., 1979, ‘‘Interferometry and Holography in Nucleate Boiling,’’ *Boiling Phenomena*, Hemisphere. Washington, DC, pp. 821–843.
[14] Mundrane, M., and Zebib, A., 1993, ‘‘Two and Three Dimensional Buoyant Thermocapillary Convection,’’ Phys. Fluids A, **5**, p. 810.
[15] Ostrach, S., 1977, ‘‘Motion Induced by Capillarity,’’ V. G. Birthday Levich Conference, Oxford England Publisher, pp. 571–589.
[16] Kamotani, Y., Ostrach, S., and Pline, A., 1995, ‘‘A Thermocapiliary Convection Experiment in Microgravity,’’ ASME J. Heat Transfer, **117**, pp. 611–618.
[17] Braunsfurth, M. G., and Homsy, G. M., 1997, ‘‘Combined Thermocapillary-Buoyancy Convection in a Cavity. Part II: An Experimental Study,’’ Phys. Fluids, **9**, No. 5, p. 1277.
[18] Villers, D., and Platten, J. K., 1986, ‘‘Separation of Marangoni Convection From Gravitational Convection in Earth Experiments,’’ PhysicoChem. Hydrodyn., **8**, No. 2, pp. 173–183.
[19] Wei, H., and Subramanian, R. S., 1995, ‘‘Migration of a Pair of Bubbles Under the Combined Action of Gravity and Thermocapillarity,’’ J. Colloid Interface Sci., **172**.
[20] Huplik, V., and Raithby, G. D., 1972, ‘‘Surface Tension Effects in Boiling From a Downward-Facing Surface,’’ ASME J. Heat Transfer, **94**, pp. 403–409.
[21] Gaddis, E. S., 1972, ‘‘The Effects of Liquid Motion Induced by Phase Change and Thermocapillarity on the Thermal Equilibrium of a Vapor Bubble,’’ Int. J. Heat Mass Transf., **15**, pp. 2241–2250.
[22] Raake, D., Siekmann, J., and Chun, Ch-H., 1989, ‘‘Temperature and Velocity Fields Due to Surface Tension Driven Flow,’’ Exp. Fluids, **7**, pp. 164–172.
[23] Wozniak, K., and Wozniak, G., 1990, ‘‘Particle Image Velocimetry Applied to Thermocapillary Convection,’’ Exp. Fluids, **10**, pp. 12–16.
[24] Wozniak, G., Wozniak, K., and Bergeit, H., 1996, ‘‘On the Influence of Buoyancy on the Surface Tension Driven Flow Around a Bubble on a Heated Wall,’’ Exp. Fluids., **21**, No. 3.
[25] Herih, Ph., and Thery, P., 1992, ‘‘Measurements on the Thermoelectric Properties of Thin Layers of Two Metals in Electrical Contact: Application for Designing New Heat Flow Sensors,’’ Meas. Sci. Technol., **3**, No. 5, p. 495.
[26] Arlabosse, P., 1997, ‘‘Etude des transferts de chaleur et de masse par effet Marangoni: Application à la compréhension des mécanismes de l’ébullition en apesanteur,’’ Ph.D. Thesis, University of Provence, Marseille, France.
[27] Matekunas, F. A., and Winter, E. R. F., 1971, ‘‘An Interferometric Study of Nucleate Boiling,’’ International Symposium of Two Phase Systems, Haífa (Israel).

Critical Heat Flux During Natural Circulation Boiling of Saturated Liquid in Annulus With Uniformly Heated Outer Tube

M. Monde[1]
Professor
e-mail: monde@me.saga-u.ac.jp

Y. Mitsutake
Professor

Department of Mechanical Engineering,
Saga University,
1 Honjo-machi, Saga-shi,
Saga 840-8502, Japan

Critical heat flux has been measured during natural circulation boiling of water and R113 on a uniformly heated outer tube in a vertical annular tube. The experiment was carried out using water at atmospheric pressure and R113 at a pressure of 0.1–0.4 MPa for the annular gap width of $S=1.0$–4.0 mm, the heated tube diameter of 9–17 mm, and the annular tube length of 100–1000 mm. The similarity of critical heat flux between annular configurations of either inner or outer heated tubes and a simple heated tube can be clearly elucidated based on the characteristics of the heated equivalent diameter. The critical heat flux measured for $S=1$ mm can be predicted accurately by existing correlation for the annular tube and for clearance larger than $S=4$ mm by existing correlation for the single tube. A new correlation for medium clearances from $S=1$ to 4 mm has been developed to connect between both the existing correlations. [S0022-1481(00)01901-0]

Keywords: Annular Flow, Boiling, Heat Transfer, Natural Convection, Phase Change

1 Introduction

Critical heat flux during natural convective boiling in confined channels, such as a tube and an annulus, are important as a fundamental study of the critical heat flux phenomenon as well as for its application to industrial problems related to superconducting devices and a cooling of microelectric devices. The critical heat flux is recently recalled to play an essential role in predicting a safety cooling of pressurized water reactor and boiling water reactor reactors after its loss of coolant accident happened such as the Three Mile Island-2 (TMI-2) accident. On the other hand, a two-phase thermosyphon, which is another type of confined flow, is widely applied to cool an electric device. In order to improve critical heat flux of the thermosyphon, Islam et al. [1] inserted a tube into the thermosyphon to avoid a counter-current flow of liquid and vapor at the exit of the thermosyphon. They succeeded in improving the critical heat flux about eight times at optimum operation. Under the condition, the critical heat flux is found to closely relate to flow condition to which a tube in annular passage is heated, although the flow mode becomes very complicated.

One of the authors ([2,3]) has extensively measured critical heat flux during natural circulation boiling in a vertical tube and annular tube with a wide range of density ratio, ρ_l/ρ_g and a combination of heated tube length to tube diameter. The following correlations (1), (2), and (3), are proposed to predict the critical heat flux in vertical tube and annular tube.

For the tube ([2]), the characteristic of critical heat flux can be categorized according to tube diameter into two regimes and the corresponding correlations become,

in the case of a small tube

$$\frac{q_{\mathrm{co}}/\rho_g h_{lg}}{\sqrt[4]{\sigma g(\rho_l-\rho_g)/\rho_g^2}}=\frac{0.16}{1+0.025(L/D)} \tag{1}$$

for $D/\sqrt{\sigma/g(\rho_l-\rho_g)}<13$

in the case of a large tube

$$\frac{q_{\mathrm{co}}/\rho_g h_{lg}}{\sqrt[4]{\sigma g(\rho_l-\rho_g)/\rho_g^2}}=\frac{0.16}{1+0.003\ \ \mathrm{Bo}^{1/2}} \tag{2}$$

for $D/\sqrt{\sigma/g(\rho_l-\rho_g)}>13$.

For the annular tube with an inner tube heated ([3]), its characteristic appears in a single mode independent of $D_{\mathrm{he}}/\sqrt{\sigma/g(\rho_l-\rho_g)}$ and the correlation becomes

$$\frac{q_{\mathrm{co}}/\rho_g h_{lg}}{\sqrt[4]{\sigma g(\rho_l-\rho_g)/\rho_g^2}}=\frac{0.16}{1+0.075(L/D_{\mathrm{he}})}. \tag{3}$$

Comparing Eqs. (1) and (3), one may notice that both equations become the same in form except for the factors on L/D or L/D_{he}.

Recently, Islam et al. [1] measured critical heat flux in a concentric-tube thermosyphon in which an outer tube is heated and a tube inserted serves as a feed supplying liquid from a liquid reservoir at the top of the thermosyphon. The paper implied that the characteristic of the critical heat flux appears to gradually shift from Eq. (3) to Eq. (1) with increasing clearance of annular passage through which vapor generated on the outer heated tube flows out. The transition of the critical heat flux from Eq. (3) to Eq. (1) may be attributed to the characteristics of heated equivalent diameter, which is defined for the inner or outer heated tubes, respectively, as

for the inner heated tube

$$D_{\mathrm{he}}=d_o\left(\left(\frac{D_i}{d_o}\right)^2-1\right)$$

for the outer heated tube

$$D_{\mathrm{he}}=\frac{d_o^2}{D_i}\left(\left(\frac{D_i}{d_o}\right)^2-1\right).$$

According to the definition of the heated equivalent diameter, for example, in the case where the outer diameter of the inner tube d_o becomes close to the inner diameter of the outer tube D_i, namely $d_o\rightarrow D_i$, each of the heated equivalent diameters approaches the same value for either of the heated tubes. As a result, the critical heat flux for both cases may be predicted by Eq. (3). The characteristics for both critical heat flux seem to be similar

---

[1] Author to whom correspondence should be addressed.

Contributed by the Heat Transfer Division for publication in the JOURNAL OF HEAT TRANSFER. Manuscript received by the Heat Transfer Division, May 13, 1999: revision received Sept. 26, 1999. Associate Technical Editor: T. Chu.

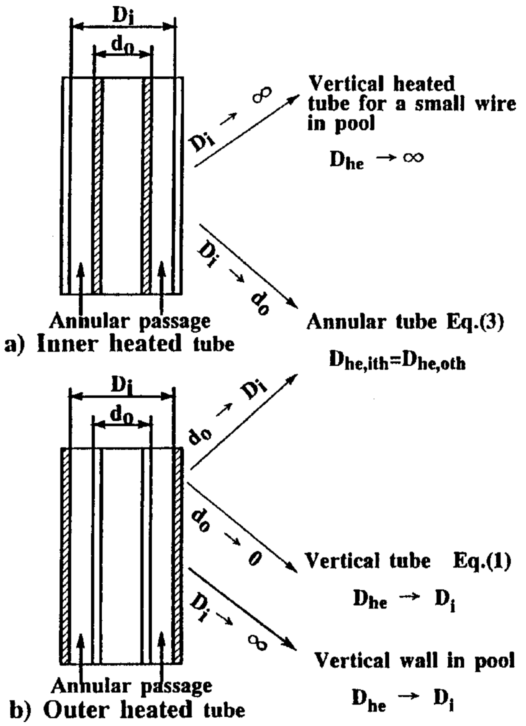

Fig. 1 Classification of critical heat flux characteristics in vertical natural circulation flow

for a narrow annulus. For the case of a wide annular passage, conversely, both the heated equivalent diameters approach a different limiting value, respectively. The heated equivalent diameter for the heated inner tube becomes infinity, namely $D_{\mathrm{he}} \to \infty$ so that the flow condition may become similar to pool boiling on a vertical heated surface. On the other hand, the heated equivalent diameter for the heated outer tube approaches the tube diameter for both limiting cases of $d_o \to 0$ and $D_i \to \infty$, namely $D_{\mathrm{he}} \to D_i$. As for flow aspect on the heated tube in the case of $d_o \to 0$, its flow configuration becomes close to natural circulation in a vertical tube. For $D_i \to \infty$, pool boiling on a vertical heated wall is approached, for which no correlation is yet proposed, except for a short wall ([4]). Therefore, the case of $D_i \to \infty$ is omitted here since a further study would be required. Another limiting case is a vertical rectangular channel, that is both d_o and D_i become equally large enough to retain a narrow space. As for the critical heat flux in this case, Monde et al. [5] also proposed the following correlation:

$$\frac{q_{\mathrm{co}}/\rho_g h_{lg}}{\sqrt[4]{\sigma g(\rho_l-\rho_g)/\rho_g^2}} = \frac{0.16}{1+6.7\times 10^{-4}(\rho_l/\rho_g)^{0.6}(L/S)}. \tag{4}$$

Monde et al. [3] note that the critical heat flux value predicted by Eq. (4) comes close to that by Eq. (3) when L/S is replaced by heated equivalent diameter and then other correlations for the critical heat flux in a vertical rectangular channel also give a similar trend to Eq. (4).

Flow configurations for these cases can be finally categorized into four different types depending on whether the annular passage has space enough for vapor to flow or not and on which tube is heated, as shown in Fig. 1.

Recently, the critical heat flux during pool boiling on a vertical heated wire was proposed by Monde et al. [6] as follows:

$$\frac{q_{\mathrm{co}}/\rho_g h_{lg}}{\sqrt[4]{\sigma g(\rho_l-\rho_g)/\rho_g^2}} = \begin{cases} 0.42\ \mathrm{Bo}^{-1/4} & \text{for } \mathrm{Bo}<30 \\ 0.18 & \text{for } \mathrm{Bo}>30. \end{cases} \tag{5}$$

Equation (5) was derived for the critical heat flux which occurred under the condition that discontinuous coalesced bubbles surrounded the wire and rose along it. However, for the case of medium size tubes where the tube diameter is too large for the coalesced bubbles to surround the tube, no correlation has been derived yet due to less interest in it from an engineering point of view.

According to the trend in the critical heat flux as shown in Fig. 1, the critical heat flux on a vertical heated wire in a large vertical tube may become theoretically similar to that on the vertical wire heated in the pool. As given in Eqs. (2) and (5), there is a large effect of the Bond number on the critical heat flux. What causes the effect, however, is still unknown although a difference may exist in the flow aspect between inward and outward surfaces.

Incidentally, in correlating critical heat flux for forced convective boiling in an annulus using few available critical heat flux data, Katto [7] pointed out an important role of the heated equivalent diameter. When his correlations proposed for the uniformly heated tube are extended to the critical heat flux for the inner heated tube, the factor only related to an effect of L/D on the critical heat flux should be replaced by another one, while for the outer heated tube, his correlations do not need any change.

Deriving correlations for critical heat flux during forced convective boiling in an annulus based on that tube, Shah [8] also pointed out that the heated equivalent diameter played an essential role in critical heat flux in place of the hydrodynamic equivalent diameter. Furthermore, there is no difference in correlations of the critical heat flux between inner and outer heated tubes except that the tube diameter D in the parameter, that only related to an effect of L/D on the critical heat flux, is replaced by the heated equivalent diameter D_{he}, although the accuracy of prediction for annulus slightly deteriorates compared with that for the tube.

In the present study, in order to elucidate the characteristics of the heated equivalent diameter for critical heat flux, the critical heat flux has been measured for water at atmospheric pressure and R113 at a pressure of 0.1–0.4 MPa in the vertical annulus, in which only the outer tube is heated. The effect of the clearance of the annulus on critical heat flux and the estimation mentioned before will be discussed.

2 Experimental Apparatus and Procedure

Figure 2 shows the whole system of the experimental apparatus. A test annulus built by two concentric stainless tubes is settled at the center of a pressure vessel. The outer tube of the annulus is directly heated by dc current. The level of test liquid in the vessel was always kept at 150 mm higher than the exit of the test tube. Two C-A (Chromel-Alumel) thermocouples which are calibrated with the minimum division of 0.1 K are mounted at a position of 7 mm below the exit of the outer tube and 50 mm above from the entrance to measure the surface temperature. The position of 7 mm was chosen to avoid end effects. The heat flux was calculated with a relative accuracy higher than 0.1 percent from the electric input. The radial heat flow loss from the outer side of the heated surface is estimated to be less than one percent of electric input by air enclosed between the outer tube (4) and the test assembly (13) and the bakelite (14) used as a spacer. This estimation results from the following reasons: the temperature difference between saturated liquid and the back side of the heated tube is usually less than 20 K before the occurrence of critical heat flux and then boiling heat transfer on the tube wall becomes extremely high. The axial heat loss from the end tube to the electrode is also limited close near the electrode from a calculation for heat transfer in a finned surface and then can be ignored except for the part near the electrode.

The experiment was carried out by increasing the electric input to the outer tube with increments that are less than five percent of each preceding heat flux under the condition that the pressure inside the vessel is kept at a designated pressure. The steady state condition can be reached within a few minutes after setting the

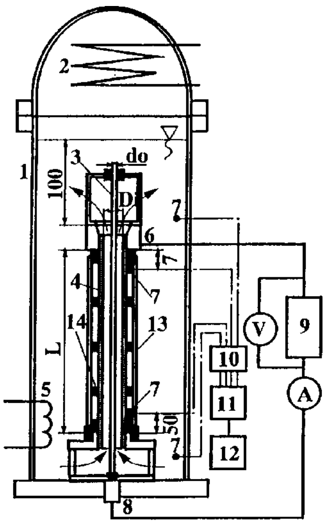

Fig. 2 Experimental apparatus: (1) pressure vessel, (2) cooling coil, (3) inner tube, (4) heated outer tube, (5) auxiliary heater, (6) upper heater, (7) thermocouple, (8) lower electrode, (9) DC power supply, (10) multiplexer, (11) digital volt meter, (12) computer, (13) test assembly, (14) bakelite

Table 1 Experimental range

Test liquid		Water	R113	
Pressure (MPa)		0.1	0.1, 0.2, 0.4	
D_i	mm	9	12	17
d_o	mm	3, 5, 7	4, 6, 8, 10	5, 9, 13, 15
S	mm	1, 2, 3	1, 2, 3, 4	1, 2, 4, 6
L	mm		100, 250, 500, 1000	

heat flux, since the heat capacity of the outer tube is rather small compared with heat input and heat transfer coefficient of evaporation that is large enough. The critical heat flux was determined by the following means: when heat flux is increased in increments that are less than five percent of each preceding heat flux and finally a point is reached where the tube temperature monitored runs away. At this point, the critical heat flux is determined with an estimated uncertainty of less than five percent.

The experimental range is summarized in Table 1.

3 Experimental Result and Discussion

3.1 Boiling Curve. Figure 3 shows typical boiling curves at two different positions of 7 and 450 mm for $D_i = 12$ mm, $d_o = 8$ mm, and $L = 500$ mm. Two boiling curves clearly show that boiling near the exit reaches a fully developed boiling from a heat flux less than 10^{-2} MW/m^2, while boiling near the entrance may not appear until about 3×10^{-2} MW/m^2 at which excursion of the wall temperature due to incipient boiling is observed. The critical heat flux takes place near the exit since the temperature at the position of 7 mm from the exit first starts rising at a heat flux of 4×10^{-1} MW/m^2. A small decrease in the wall temperature (as shown in Fig. 3) always appears under the steady condition at heat fluxes a little smaller than the critical heat flux before the critical heat flux condition is reached. This may be caused by an enhancement of heat transfer, which results from evaporation of a very thin liquid film covering the heated surface. The same phenomenon was always observed in annular flow in forced convective boiling ([9]) in which heat transfer is enhanced and boiling is suppressed by evaporation of thin liquid film.

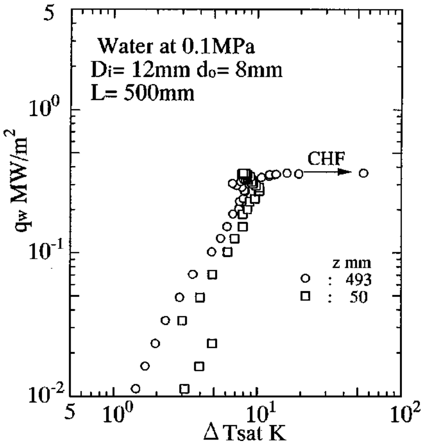

Fig. 3 Boiling curve (*z*: distance from entrance of heated tube)

Finally, the arrow of critical heat flux in Fig. 3 and some points near the arrow show that the wall temperature monitored for a short time is just running away under unsteady condition after occurrence of the critical heat flux.

3.2 Position of Critical Heat Flux Occurrence. As shown in Fig. 3, the critical heat flux first takes place near the exit and then the critical heat flux condition propagates toward the entrance. A similar result would be obtained for the case of the inner

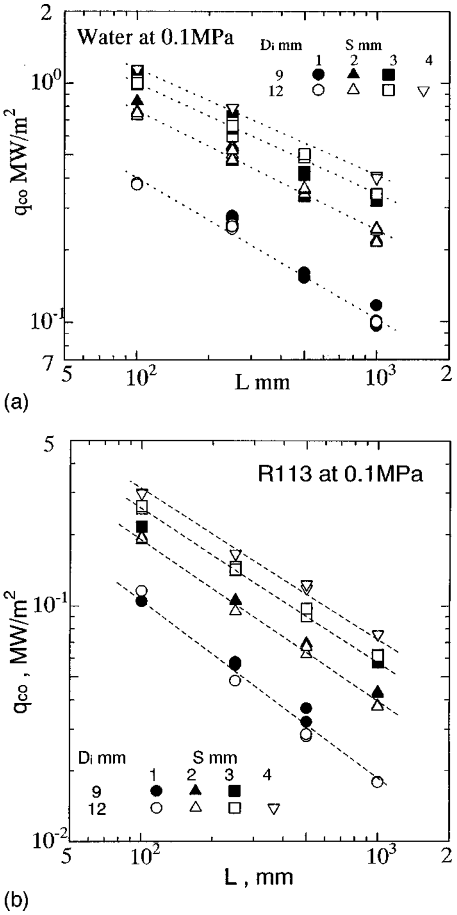

Fig. 4 (*a*) Relationship between heated length and critical heat flux for water; (*b*) relationship between heated length and critical heat flux for R113

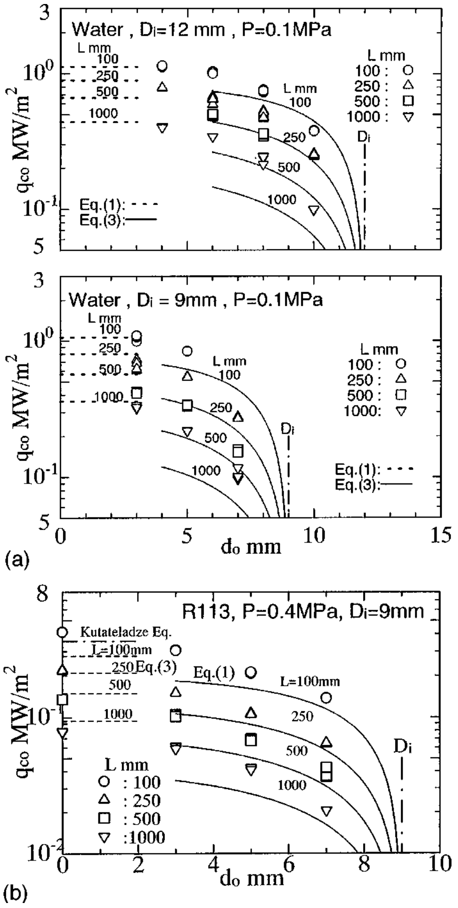

Fig. 5 (*a*) Effect of inserted (inner) tube on critical heat flux for water; (*b*) effect of inserted (inner) tube on critical heat flux for R113

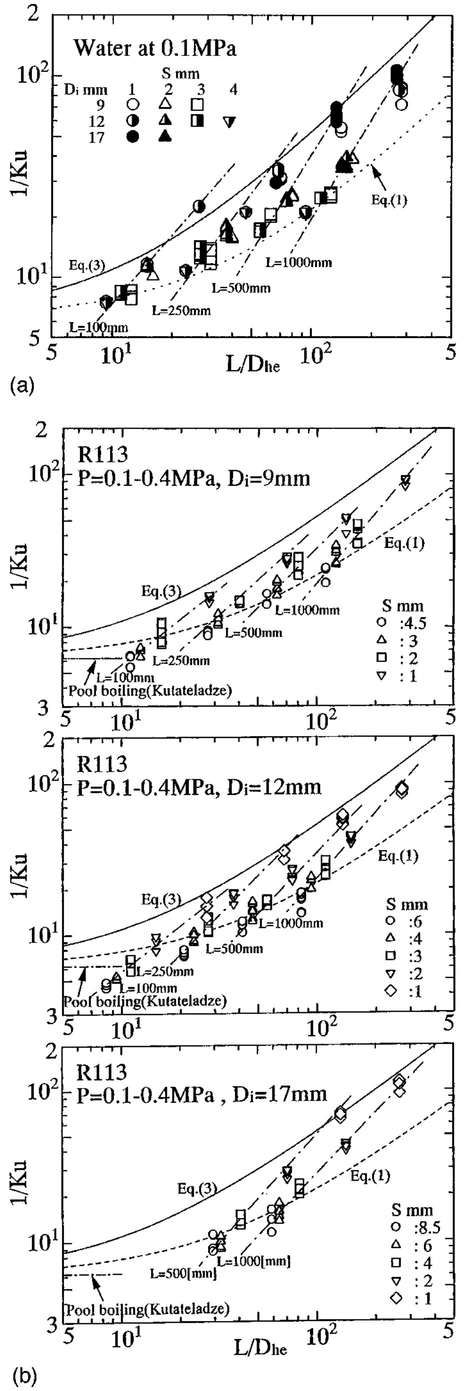

Fig. 6 (*a*) 1/Ku versus L/D_{he} for water; (*b*) 1/Ku versus L/D_{he} for R113

heated tube where the critical heat flux position was identified by a rise in the temperature of the heated tube near the exit ([3]). There seems to be no difference at the point of critical heat flux occurrence between the outer and inner heated tubes.

3.3 Characteristics of Critical Heat Flux. Figure 4 shows the critical heat flux values measured for two different tube diameters of $D_i = 9$ and 12 mm plotted against the heated tube length L. A broken line in Fig. 4 as a reference shows appropriate lines drawn in parallel to the line for the same condition predicted by Eq. (3).

It is found from Fig. 4 that the critical heat flux linearly decreases with the heated tube length and then decreases with diameter of the inner tube or a decrease in the clearance of annular passage. This trend agrees with that predicted by Eqs. (1) and (3). In order to clarify the effect of diameter of the inner tube on the critical heat flux and for a comparison of Eqs. (1) and (3), the critical heat flux data are rearranged and plotted against the inner diameter as shown in Fig. 5. A dashed line and a solid line are Eqs. (1) and (3), respectively.

Figure 5 shows clearly that as the diameter of the inner tube becomes smaller, the critical heat flux values gradually approach Eq. (1), and when the inner tube diameter approaches the outer tube diameter, the critical heat flux value leaves from Eq. (1) and approaches Eq. (3). This trend with the clearance of annulus is attributed to the characteristic of the heated equivalent diameter mentioned in Section 1.

3.4 Correlation of Critical Heat Flux. Figure 6 shows nondimensional values of the critical heat flux in order to compare Eqs. (1) and (3) in which the critical heat flux data with the same heated tube length are connected by dot-and-dashed lines.

It may be noticed from Fig. 6 that most of the critical heat flux data are predicted accurately for a small clearance of $S = 1$ mm by Eq. (3), while for a large clearance by Eq. (1), the critical heat flux data for the annular clearance of $1 \leqslant S \leqslant 4$ are sandwiched by Eqs. (3) and (1). Consequently, the factor in the denominator of Eqs. (1) and (3) may change from $C = 0.025$ to 0.075, depending on whether the clearance of the annular passage is sufficient or not. This trend in critical heat flux due to the clearance can be effectively estimated from the characteristic of the heated equivalent diameter.

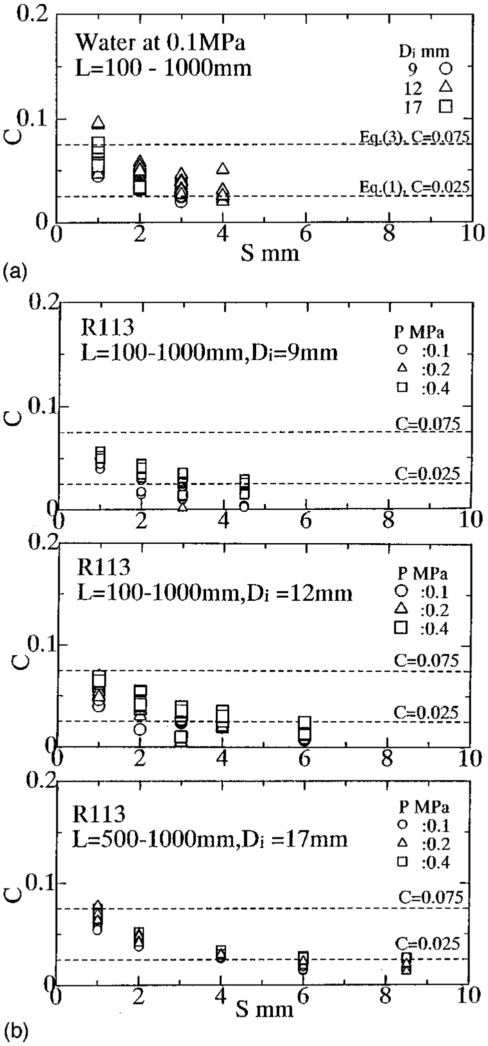

Fig. 7 (***a***) **Effect of clearance on constant in Eqs. (1) and (3) for water; (*b*) effect of clearance on constant in Eqs. (1) and (3) for R113**

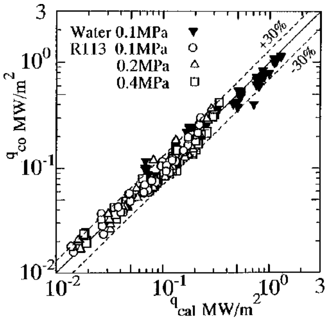

Fig. 8 Correlation of critical heat flux data with Eqs. (1), (3), and (7)

3.5 Effect of Clearance on Critical Heat Flux. Figure 7 shows the effect of clearance on the factor in the denominator of Eqs. (1) and (3). The value of the factor clearly shifts from $C = 0.025$ to 0.075 with a certain scattering of data by increasing the clearance. It is found that the space clearance clearly influences the critical heat flux characteristics. However, it is still unclear at present how the clearance influences the critical heat flux together with which physical properties concern the critical heat flux or flow condition near the critical heat flux, since this effect is considered to be a secondary one and this effect may merge into uncertainties of measurement accuracy.

4 Correlation of Critical Heat Flux for Medium Clearance

It is found from Fig. 7 that the critical heat flux for $S=1$ mm can be predicted well by Eq. (1), while the critical heat flux for $S \geqslant 4$ mm by Eq. (3). Therefore, in order to correlate the critical heat flux data in the medium clearance of $1 \leqslant S \leqslant 4$, one may start improving a functional form in light of Eqs. (1) and (3) as follows:

$$\frac{q_{\infty}/\rho_g h_{lg}}{\sqrt[4]{\sigma g(\rho_l-\rho_g)/\rho_g^2}} = \frac{0.16}{1+C(L/D_{\mathrm{he}})} \tag{6}$$

and from Fig. 7, a functional form for the constant C can be tentatively employed as

$$C = k\left(1 - a\left(\frac{\rho_l}{\rho_g}\right)^n \frac{S}{\sqrt{\sigma/[g(\rho_l-\rho_g)]}}\right)^2 + 0.025 \quad 1 \leqslant S \leqslant 4 \ \mathrm{mm} \tag{7}$$

where the constants, k, a, and n are: $k=0.089$, $a=0.060$, and $n=0.30$, respectively, connecting between Eqs. (1) and (3) smoothly.

The reason that the clearance of $S=4$ mm beyond which the critical heat flux characteristic for the annular channel with the outer heated tube becomes close to that for the vertical tube is not influenced by the inner tube diameter or heated equivalent diameter as well as the tube length, is hardly explained from a physical point of view. On the other hand, for the clearance $S \leqslant 1$ mm, the reason that the critical heat flux characteristic becomes independent of which tube is heated can be easily understood from the viewpoint of the heated equivalent diameter, although the physical meaning of $S=1$ mm is also not explained.

Figure 8 shows a comparison of the critical heat flux data ob-

Table 2 Accuracy of prediction

			Eqs. (1), (3), and (6)			Equations revised with 0.188		
	P (MPa)	N	E_1	E_2	E_3	E_1	E_2	E_3
Water	0.1	111	0.145	0.177	0.211	−0.005	0.153	0.190
R113	0.1	63	0.124	0.131	0.202	0.010	0.118	0.171
	0.2	66	0.100	0.137	0.178	−0.0409	0.136	0.174
	0.4	66	0.074	0.112	0.152	−0.053	0.114	0.160

(N means number of the critical heat flux data)

$$E_1=\frac{1}{N}\sum\frac{(q_{\mathrm{co}}-q_{\mathrm{cal}})}{q_{\mathrm{co}}} \quad E_2=\frac{1}{N}\sum\frac{|(q_{\mathrm{co}}-q_{\mathrm{cal}})|}{q_{\mathrm{co}}} \quad E_3=\sqrt{\frac{1}{N}\sum\left(\frac{q_{\mathrm{co}}-q_{\mathrm{cal}}}{q_{\mathrm{co}}}\right)^2}$$

tained and Eq. (6) with Eq. (7) and Eqs. (1) and (3). In addition, Table 2 gives a statistical result of accuracy in evaluating the critical heat flux data with the correlations (1), (3), and (6).

As shown in Fig. 8 and Table 2, all the critical heat flux data seem to become about 10 percent larger than that predicted by Eq. (6) with Eq. (7) and Eqs. (1) and (3) and most of the critical heat flux data fall within a range of ±30 percent when compared with those equations. Incidentally if the constant of 0.16, which is commonly used for critical heat flux in pool boiling, can be replaced by another value of 0.188, then all the critical heat flux data are found to be correlated well as given in Table 2. It may be of interest to note that the critical heat flux for a small vertical heated wire can be predicted by Eq. (5) whose constant of 0.18 is adopted in place of the value of 0.16. The physical reason why the constant changes from 0.16 to 0.188 is not yet clear.

5 Similarity of Critical Heat Flux in Concentric Thermosyphon

Islam et al. [1] measured the critical heat flux in a concentric-tube open thermosyphon in which the inner tube serves as a liquid supplier from a top liquid reservoir to the bottom and the outer tube is heated. They mentioned that in the case of a relatively large inner tube diameter inserted, the flow situation in the thermosyphon becomes similar to that in the outer heated tube in the annulus, since the annular passage for vapor to escape from the thermosyphon becomes narrow, while the inner tube is large enough for liquid to be supplied to it from the bottom. As a result, the critical heat flux obtained there was predicted well by Eq. (3). In addition, the characteristic of the critical heat flux also gradually changed from Eqs. (3) to (1) with an increase of the clearance. This is because of the clearance effect on critical heat flux as mentioned in Section 3.5.

6 Conclusions

The critical heat flux during natural circulation boiling in the vertical annulus in which the outer tube is uniformly heated was measured for water at atmospheric pressure. The key results are:

1. For the annular tubes, either of which is heated, the role of heated equivalent diameter on critical heat flux becomes important.
2. The characteristic of critical heat flux depends on annular space as shown in Fig. 1.
3. The critical heat flux can be predicted well for the clearance of $S=1$ mm by Eq. (3) and of $S\geqslant 4$ mm by Eq. (1).
4. For medium clearance of $1\leqslant S\leqslant 4$ mm, the critical heat flux can be predicted by Eqs. (6) and (7).

Acknowledgments

The authors express their appreciation to K. Nakashima for his valuable assistance in making experimental apparatus and M. Hayashi, Y. Izumi, K. Tsumura, H. Ueda, and Y. Kuroki for their valuable assistance in making the experimental apparatus and collecting data.

Nomenclature

Bo = bond number $(=L^2/(\sigma/g(\rho_l-\rho_g)))$
D = tube diameter
D_i = inner diameter of outer tube in annulus
d_o = outer diameter of inner tube in annulus
D_{he} = heated equivalent diameter (=4(flow area)/heated perimeter)
g = acceleration due to gravity
h_{lg} = latent heat of evaporation
Ku = Kutateladze number$(=(q_\infty/\rho_g h_{lg})/(\sqrt[4]{\sigma g(\rho_l-\rho_g)/\rho_g^2}))$
L = length of heated tube
q = heat flux
q_{co} = critical heat flux
S = clearance of annular passage
ΔT_{sat} = wall superheat
ρ_g, ρ_l = density of vapor and liquid
σ = surface tension

References

[1] Islam, M. A., Monde, M., Hasan, M. Z., and Mitsutake, Y., 1998, ‘‘Experimental Study of critical heat flux in Concentric-tube Open Thermosyphon,’’ Int. J. Heat Mass Transf., **43**, pp. 3691–3704.
[2] Monde, M., and Yamaji, K., 1990, ‘‘Critical Heat Flux During Natural Convective Boiling in a Vertical Uniformly Heated Tubes Submerged in Saturated Liquid,’’ J. Heat Transfer, **2**, pp. 111–116.
[3] Monde, M., Mitsutake, Y., and Kubo, S., 1994, ‘‘Critical Heat Flux During Natural Convective Boiling on Uniformly Heated Inner Tubes in Vertical Annular Tubes Submerged in Saturated Liquid,’’ Wärme-Stoffübertragung, **29**, pp. 271–276.
[4] Park, K. A., and Bergles, A. E., 1988, ‘‘Effect of Size of Simulated Microelectronic Chip on Boiling and Critical Heat Flux,’’ ASME J. Heat Transfer, **110-3**, pp. 728–734.
[5] Monde, M., Kusuda, H., and Uehara, H., 1982, ‘‘Critical Heat Flux During Natural Convective Boiling in Vertical Rectangular Channels Submerged in Saturated Liquid,’’ J. Heat Mass Transf., **104**, pp. 300–303.
[6] Monde, M., Inoue, T., and Mitsutake, Y., 1997, ‘‘Critical Heat Flux in Pool Boiling on Vertical Heater,’’ Heat Mass Transfer, **32**, pp. 435–440.
[7] Katto, Y., 1981, ‘‘Generalized Correlations of Critical Heat Flux for the Forced Convection Boiling in Vertical Uniformly Heated Annuli,’’ Int. J. Heat Mass Transf., **24**, pp. 541–544.
[8] Shah, M. M., 1980, ‘‘A General Correlation for Critical Heat Flux in Annuli,’’ Int. J. Heat Mass Transf., **23**, pp. 225–234.
[9] Collier, J. G., 1981, *Convective Boiling and Condensation*, 2nd Ed., McGraw-Hill, New York, p. 135.

S. Nozu[1]
Professor,
Department of Systems Engineering,
Okayama Prefectural University,
111, Kuboki, Soja,
Okayama 719-1197, Japan
e-mail: nozu@cse.oka-pu.ac.jp

H. Honda
Professor,
Institute of Advanced Material Study,
Kyushu University,
6-12, Kasuga-Kouen, Kasuga,
Fukuoka 816-8580, Japan

Condensation of Refrigerants in Horizontal, Spirally Grooved Microfin Tubes: Numerical Analysis of Heat Transfer in the Annular Flow Regime

A method is presented for estimating the condensation heat transfer coefficient in a horizontal, spirally grooved microfin tube. Based on the flow observation study performed by the authors, a laminar film condensation model in the annular flow regime is proposed. The model assumes that all the condensate flow occurs through the grooves. The condensate film is segmented into thin and thick film regions. In the thin film region formed on the fin surface, the condensate is assumed to be drained by the combined surface tension and vapor shear forces. In the thick film region formed in the groove, on the other hand, the condensate is assumed to be driven by the vapor shear force. The present and previous local heat transfer data including four fluids (CFC11, HCFC22, HCFC123, and HFC134a) and three microfin tubes are found to agree with the present predictions to a mean absolute deviation of 15.1 percent. [S0022-1481(00)01501-2]

Keywords: Keywords: Annular Flow, Condensation, Enhancement, Finned Surfaces

Introduction

Enhancement of condensation heat transfer in horizontal tubes has received considerable attention in air-conditioning and refrigeration systems with relatively small size. In recent years microfin tubes are commonly used due to their high condensation heat transfer performance with moderate pressure loss. Numerous experimental and analytical studies on the condensation in microfin tubes were reported. Recent studies that are representative of the work in this area include: Khanpara et al. [1], Schlager et al. [2–4], Hori and Shinohara [5], Koyama et al. [6], Haraguchi [7], and Chamra and Webb [8]. Most of the work cited above measured the effects of fin geometry, fin dimensions, and fluid properties on the condensation characteristics, and developed empirical equations for the heat transfer and pressure drop. A few detailed works, however, were performed to explain the condensation enhancement mechanism (e.g., Webb [9], Fujii [10], and Srinivasan and Shah [11]). Recently, Shikazono et al. [12,13] considered the circumferential distribution of condensate liquid, and proposed a heat transfer equation for a horizontal, spirally grooved microfin tube. The equation, however, is derived on the basis of an equation for a smooth horizontal tube in which the surface tension effect is not included.

Referring to the condensation of vapors in horizontal smooth tubes (e.g., Dobson and Chato [14]), the condensate is controlled by the combined vapor shear and gravity forces. At high vapor velocities, significant vapor shear forms a vapor core with a circumferentially uniform condensate film around the inner surface of the tube. At low vapor velocities, the condensate film formed on the inner tube surface drains towards the tube bottom due to gravity force and the liquid stratification is formed in the lower part of the tube.

Characteristics of condensate flow in a microfin tube would become more complex than that in a smooth tube. This is due to the effect of surface tension force that pulls a thin condensate film on the fin surface into the groove between adjacent fins. Nozu et al. [15] condensed CFC11 vapor in horizontal, smooth, and microfin tubes. The experiment includes the flow observation studies with use of industrial borescopes as well as the local heat transfer and pressure drop measurements. The results of the condensing two-phase flow patterns observed just downstream of the tube exit have implied that two major flow patterns exist during complete condensation of a vapor. One would fit the annular flow regime and the other the stratified flow, as can be observed in horizontal smooth tubes, while the condensation mechanism in the microfin tubes may be much different from that in smooth tubes.

In this paper, condensate flow between fins observed in a horizontal, spirally grooved microfin tube is discussed, and a prediction method is proposed for estimating the condensation heat transfer coefficient in the annular flow regime. The model includes the combined effects of the surface tension and vapor shear forces acting on the condensate surface, and comparisons of the local heat transfer coefficients are made between the measured and predicted values.

Experimental Apparatus and Procedure

The experimental apparatus, shown schematically in Fig. 1, consists of forced circulation loops of test fluid and cooling water. The vapor generated in an electrically heated boiler (1) flows through superheaters (2), a mixing chamber (3) and a sight glass (4) to a test section (5). The vapor condenses almost completely in the test section, and the condensate flows downward through a condensate receiver (6), then through a circulation pump (7), a flow control valve (8), and a strainer (9), and returns to the boiler. The cooling water is pumped from a cooling water tank (10) by a feed water pump (11) to the test section through a calibrated rotameter (12). After exchanging heat with the test fluid, the cooling water returns to the tank. Cooling water temperature at the test section inlet is regulated by a chiller (13) and a heater (14).

The test section is a horizontal double-tube condenser with the vapor condensing in the inner tube and the cooling water passing countercurrently through the annulus. A smooth tube and two mi-

---

[1] Corresponding author.

Contributed by the Heat Transfer Division for publication in the JOURNAL OF HEAT TRANSFER. Manuscript received by the Heat Transfer Division, Aug 27, 1998; revision received, Aug. 1, 1999. Associate Technical Editor: P. S. Ayyaswamy.

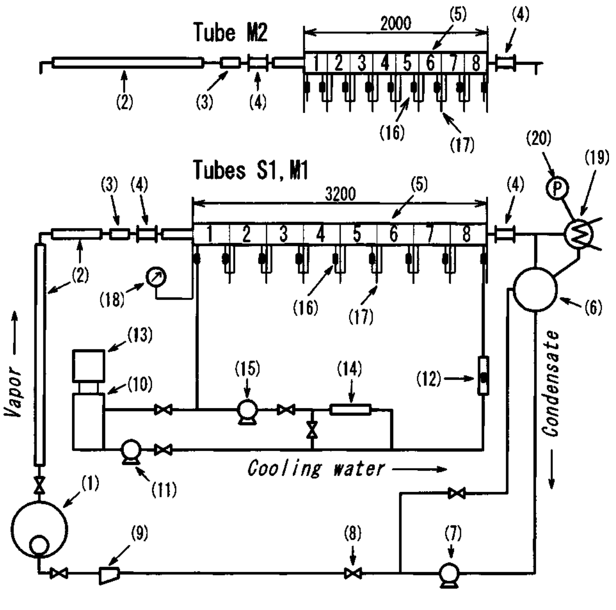

1 Boiler
2 Superheater
3 Mixing chamber
4 Sight glass
5 Test section
6 Condensate receiver
7 Circulation pump
8 Needle valve
9 Strainer
10 Cooling water tank
11 Feed water pump
12 Rotameter
13 Chiller
14 Feed water heater
15 Feed water pump
16 Mixing chamber
17 Pressure tap
18 Pressure gauge
19 Dump condenser
20 Vacuum pump

Fig. 1 Schematic diagram of experimental apparatus

crofin tubes, each having an outer diameter of about 9.5 mm, are used as the test tubes to study the effects of fin dimensions on the condensation characteristics. Figure 2 illustrates the fin profiles per one-half of fin pitch and Table 1 lists the dimensions of fin and tube, where tube S1 is a smooth tube and tubes M1 and M2 are microfin tubes. Also shown in Fig. 2 and Table 1 are the details of tube M3 tested by Haraguchi [7], and the heat transfer data obtained in the tube will be cited in this paper. It should be noted that the values of fin dimensions are cross-sectional ones normal to the groove and the fin profiles are illustrated in dimensionless form. Among the microfin tubes, tube M1 has larger fin spacing and higher fin height than tube M2, and tube M3 has smaller fin half tip angle as compared to tube M2. Lengths of the test sections are 3.2 m for tubes S1 and M1, and 2.0 m for tube M2. Tube M3 is 6.0 m in length and the test section consists of 14 subsections.

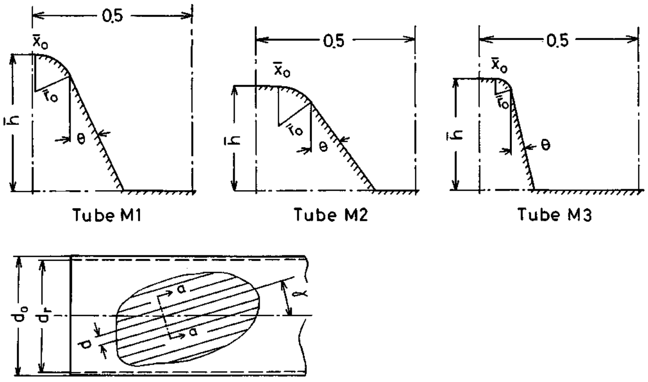

Fig. 2 Fin profile per one half of fin pitch in *a*-*a* cross section; nondimensionalized by fin pitch

Table 1 Fin and tube dimensions at cross-section normal to groove

Tube designation			S1	M1	M2	M3
Outside diameter	d_o	mm	9.41	9.53	9.50	10.0
Fin root diameter	d_r	mm	8.18	8.44	8.82	8.48
Number of fins	n		-	47	65	60
Helix angle	γ	rad	-	0.350	0.419	0.314
Fin pitch*	p	mm	-	0.53	0.39	0.42
Fin height	$\bar{h}$	-		0.43	0.33	0.35
Fin half tip angle*	θ	rad	-	0.43	0.60	0.24
Radius of curvature at corner of fin tip*	$\bar{r}_o$	-	-	0.12	0.13	0.05
Length of flat portion at fin tip*	$\bar{x}_o$	-	-	0.01	0.07	0.05
Area enhancement ratio		-	1.00	1.49	1.32	1.50
Tube length		mm	3,200	3,200	2,000	6,000

* dimension in a cross section normal to groove

To measure the axial distributions of the heat transfer rate, tube wall temperature, and static pressure, the test section is equipped with nine spacers to subdivide the annulus into eight equilength subsections. Illustration of a subsection is shown in Fig. 3. For the test sections with tubes S1 and M1, the outer duct is made of polyvinyl chloride pipe with inner diameter of 16.0 mm, and the length of the subsection Δl is 0.4 m. For the test section with tube M2, the outer duct is made of polyvinyl chloride plate and is constructed to form the annulus with a diameter of 16.0 mm, and the value of Δl is 0.25 m. Each subsection is provided with a cooling water inlet and outlet, and a mixing chamber, having a 1-mm-dia type-K sheathed thermocouple, is located between adjoining subsections. This provides reliable data on the axial distribution of the cooling water temperature T_c. The same type mixing chambers are also installed at both ends of the test section.

For tubes S1 and M1, local wall temperatures are measured at seven points in each subsection, spaced axially in groups of two or five. As shown in Fig. 3, in a cross section of 0.1 m downstream from the subsection inlet, two fine grooves are cut on the outer surface of the inner tube at circumferential angles ψ of $\pi/2$ and $3\pi/2$ rad from the tube top. In the other cross section of 0.3 m downstream from the inlet, fine grooves are machined at angles of $\psi=0$, $\pi/2$, $3\pi/4$, π and $3\pi/2$ rad. Teflon-coated, 0.127-mm-dia constantan wires with bare tips are soldered in these grooves. This allows seven wall thermocouples between the wires and the inner tube itself, and the area-averaged value is adopted as the measured wall temperature $T_{\rm wm}$ for each subsection. For tube M2, the inner tube is electrically insulated from the test loop to measure the $T_{\rm wm}$ by the resistance thermometry. The inner tube and a standard resistor of 1 m Ω are connected in series by a lead wire to a DC power supply, and a constant current of 30 A is passed through the circuit. Voltage taps are soldered to the outer surface of the inner tube at the same positions of the spacers. To avoid the effect of parasitic voltage, readings of the voltage drops are repeated by reversing the DC current and the averages of the two measurements are adopted as the experimental data. The calibration curve of the resistance–temperature relation is determined by the preliminary experiments.

Eight pressure taps with 1-mm-dia holes are drilled through the bottom of the inner tube at the inlet of each subsection, and the same type pressure tap is also installed at the exit of the test section. The adjoining pressure taps are connected to inverse U-tube manometers, reading to 1 mm, to measure the difference in condensate level. Static pressure at the vapor inlet is measured by a precision Bourdon tube, reading to 10^3 Pa and a Fortin barom-

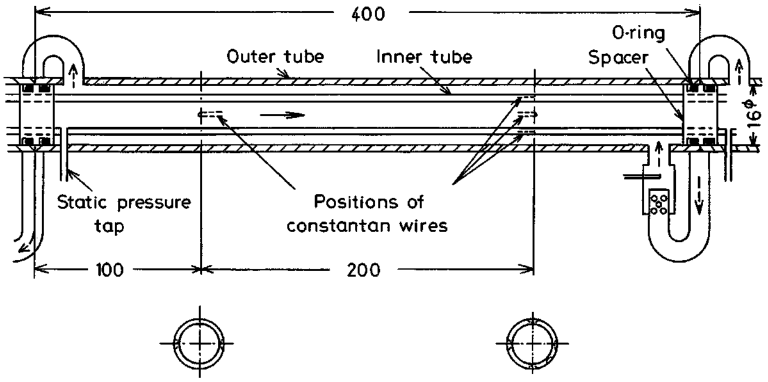

Tubes S1, M1

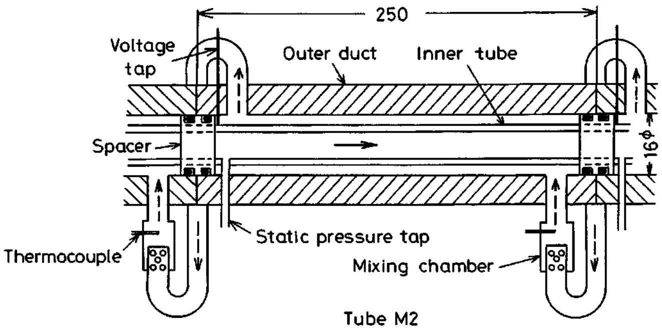

Tube M2

Fig. 3 Illustration of a subsection

eter. The mixed mean temperatures of the test fluid at the vapor inlet and in the strainer are measured by 1-mm-dia type-K sheathed thermocouples.

For tube M1, the behavior of condensate in the inner tube is observed using industrial borescopes installed at the tube exit. Two types of scopes are used: one is a direct-viewing type and the other is a side-viewing type. Figure 4 shows the observation device with the side-viewing type scope. The scope with outer diameter of 2.7 mm is provided with a lens and an illumination near the tip. The scope is inserted in the inner tube and is turned on its axis to enable viewing of the circumferential variations of condensate flow between fins.

After the steady state is reached, the thermocouple outputs and the voltage drops of tube M2 and the standard resistor are read five times to 1 μV using a data acquisition system. Experiments were conducted using CFC11 as the test fluid. For each test run, the static pressure and the degree of vapor superheat, both at the vapor inlet, are maintained at 0.17 MPa ($T_s \cong 313$ K) and less than 2 K, respectively. The mass velocity of the test fluid G is obtained from the heat balance of the boiler by application of a steady flow energy balance for the test fluid. The G value ranged from 80 to 460 kg/m^2 s. In the flow observation study, the vapor mass quality at the tube exit is changed in three steps for a few prescribed values of G.

The local heat flux q_n and the local heat transfer coefficient α_n are defined on the basis of the nominal surface area (i.e., surface area of a smooth tube with d_n) as

$$q_n = \Delta Q/(\pi d_n \Delta l), \tag{1}$$

$$\alpha_n = q_n/(T_s - T_w) \tag{2}$$

where ΔQ is the heat transfer rate in a subsection calculated from the flow rate and enthalpy change of the cooling water, T_s is the saturation temperature corresponding to the measured local static pressure, T_w is the inner wall temperature obtained from the measured T_{wm} value, making a small correction for the radial wall conduction, d_n is the nominal diameter of the test tube, where the inner diameter d_i is adopted for tube S1, and fin root diameter d_r for tubes M1, M2, and M3. The vapor mass quality X is calculated successively from the vapor inlet, on the assumption of negligible condensate subcooling, using the values of G and ΔQ. In the data reduction, the condensate properties are evaluated at the reference temperature $T_w + 0.3(T_s - T_w)$.

Referring to Eqs. (1) and (2), the uncertainty of α_n is affected by that of ΔQ and $(T_s - T_w)$. The ΔQ is obtained from the temperature rise and flow rate of the cooling water, each having uncertainties of 0.05 K and ±2 percent, respectively. In the same way, the uncertainty of $(T_s - T_w)$ depends on the uncertainties of the local static pressure and wall temperature. In the present experiment, the inverse U-tube manometers, reading to 1 mm in

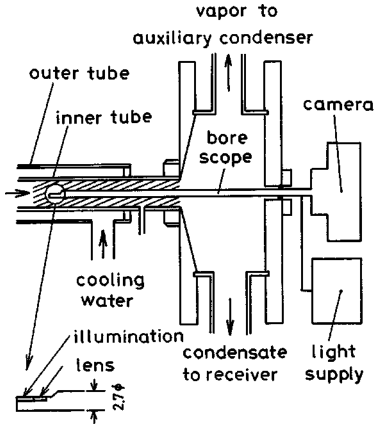

Fig. 4 Details of observation devices attached to tube exit; side-viewing type scope

condensate level, are used to measure the distribution of the static pressure with high resolution. The uncertainty of $(T_s - T_w)$ is estimated to be 0.05 K. The propagation-of-error analyses, based on the above considerations, provide the typical uncertainty of ±11 percent for α_n.

Experimental Results and Discussion

Heat Transfer. The experimental data for tube S1 are compared with the recommendation equation of a smooth tube for obtaining reliability of the apparatus and measurements. The heat transfer coefficient α_s for a smooth tube recommended by Fujii [10] is expressed as

$$\alpha_s = \lambda_l \mathrm{Nu}_d / d_n \tag{3}$$

where

$$\mathrm{Nu}_d = (\mathrm{Nu}_d)_v \quad \text{for} \quad (\mathrm{Nu}_d)_v \geqslant (\mathrm{Nu}_d)_g \tag{4a}$$

$$\mathrm{Nu}_d = (\mathrm{Nu}_d)_g \quad \text{for} \quad (\mathrm{Nu}_d)_v < (\mathrm{Nu}_d)_g \tag{4b}$$

In Eq. (4), $(\mathrm{Nu}_d)_v$ and $(\mathrm{Nu}_d)_g$ denote the Nusselt numbers in the shear-controlled and gravity-controlled regimes, respectively. Expressions for $(\mathrm{Nu}_d)_v$ and $(\mathrm{Nu}_d)_g$ are given by

$$(\mathrm{Nu}_d)_v = 0.0125(\mathrm{Re}_l\sqrt{\rho_l/\rho_v})^{0.9}(X/(1-X))^{0.1X+0.8}\mathrm{Pr}_l^{0.63} \tag{5a}$$

$$(\mathrm{Nu}_d)_g = 0.725\left(\frac{\mathrm{GaPr}_l}{\mathrm{Ph}}\right)^{0.25}\frac{\{1+0.003\sqrt{\mathrm{Pr}_l}\,a^{(3.1-0.5/\mathrm{Pr}_l)}\}^{0.3}}{(1+bc)^{0.25}} \tag{5b}$$

$$a = \frac{0.47\sqrt{\rho_l/\rho_v}(\mathrm{Ph}/\mathrm{Pr}_l)^{1/12}(\mathrm{Re}_l X/(1-X))^{0.9}}{(\mathrm{GaPr}_l/\mathrm{Ph})^{1.1/4}} \tag{5c}$$

$$b = \frac{1.55\{1+1.6\times10^{11}(\mathrm{Ph}/\mathrm{Pr}_l)^5\}^{0.25}}{\sqrt{\rho_l/\rho_v}}\left\{\frac{(\mathrm{GaPr}_l/\mathrm{Ph})^{0.25}}{\mathrm{Re}_l X/(1-X)}\right\}^{1.8} \tag{5d}$$

$$c = 40\exp\{-2.6\times10^{-4}\,\mathrm{Re}_l/(1-X)\} \tag{5e}$$

where $\mathrm{Ga} = g d_n^3/\nu_l^2$ denotes the Galileo number, $\mathrm{Ph} = c_{pl}\Delta T/h_{fg}$ the phase change number, $\mathrm{Re}_l = G(1-X)d_n/\mu_l$ the liquid Reynolds number, and $\Delta T = T_s - T_w$ the vapor-to-wall temperature difference. The measured heat transfer coefficients for tube S1 were found by the prediction of Eq. (3) to have a mean absolute deviation of 10.3 percent. This indicates the reliability of the apparatus and measurements.

Figure 5 shows the axial distributions of $\alpha_n, q_n, T_s, T_w, T_c$, the wetness fraction $(1-X)$ and the static pressure drop from the vapor inlet $(P_{\mathrm{in}} - P)$ at $G \approx 300\ \mathrm{kg/m^2\,s}$. Results for tubes S1, M1, and M2 are shown in Figs. 5(*a*), 5(*b*), and 5(*c*), respectively. Also shown in Fig. 5 are the heat transfer coefficients α_s for a smooth tube calculated from Eq. (3). Comparison of the results for tubes S1 and M1, each having the test-section length of 3.2 m, reveals that the vapor-to-wall temperature difference $T_s - T_w$ is smaller for tube M1 that leads a maximum condensation enhancement ratio of 2.6 with an increase in pressure loss by about 50 percent. Comparison of Figs. 5(*b*) and 5(*c*) for different fin dimensions shows that the heat transfer enhancement ratio α_n/α_s for tube M1 is larger than for tube M2. The observed values of α_n/α_s take 2.0–2.6 for tube M1 and 1.8–2.0 for tube M2, and the α_n/α_s are larger than the area enhancement ratios.

Flow Observation. Figure 6 shows the circumferential variations of the behavior of condensate for $G = 170\ \mathrm{kg/m^2\,s}$ at $X = 0.4$. Figures 6(*a*) and 6(*c*) show the condensate behavior in the neighborhood of the tube top and tube bottom, respectively. Also Figs. 6(*b*) and 6(*d*) present the results in the neighborhood of the left and right sides of the tube, respectively. The photographs were taken at intervals of a few seconds by use of a side-viewing

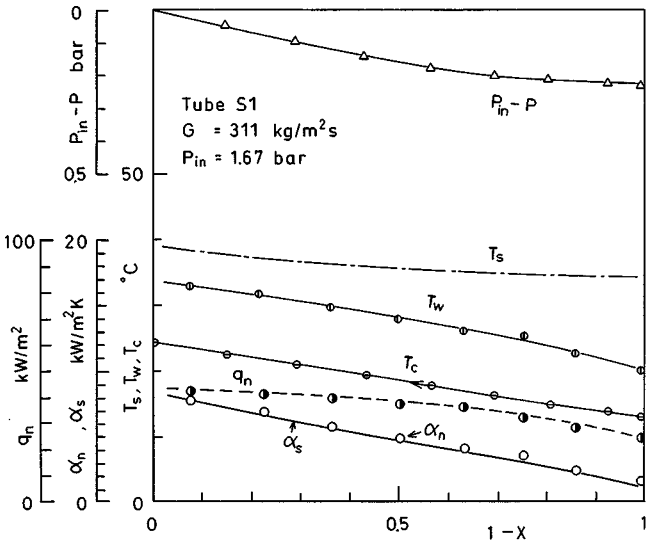

(a) Tube S1

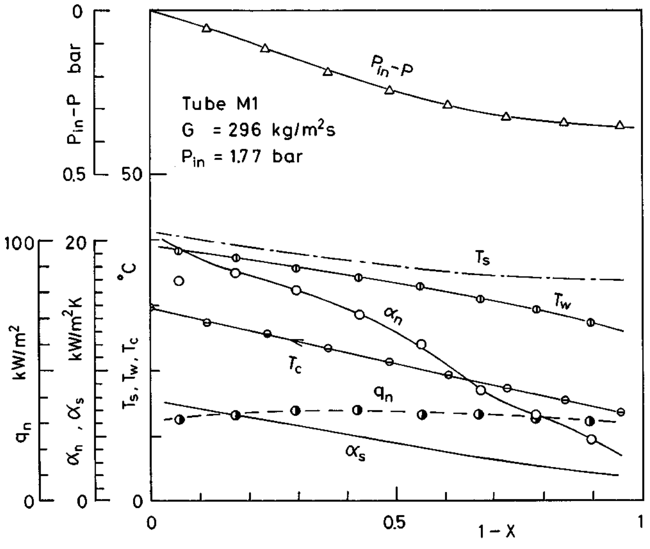

(b) Tube M1

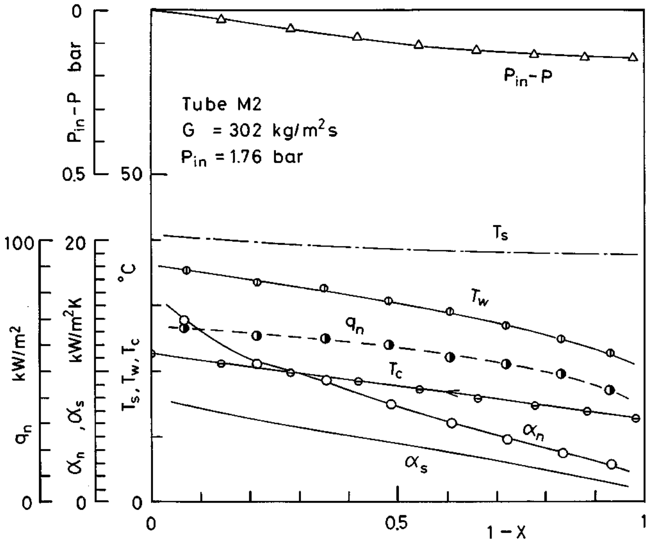

(c) Tube M2

Fig. 5 Axial distributions of measured quantities, $G \cong 300\ \mathrm{kg/(m^2 s)}$: (*a*) tube S1, (*b*) tube M1, (*c*) tube M2

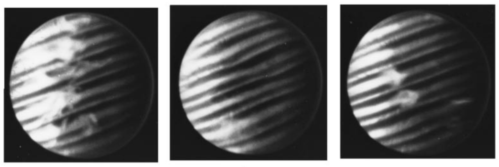

(a) Flow direction →

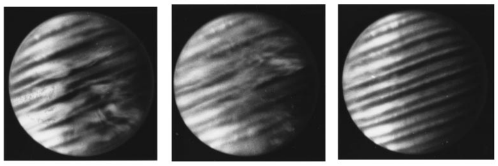

(b) Flow direction →

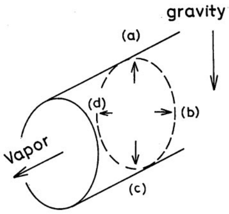

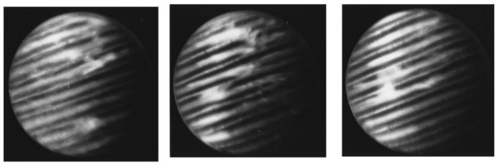

(c) Flow direction →

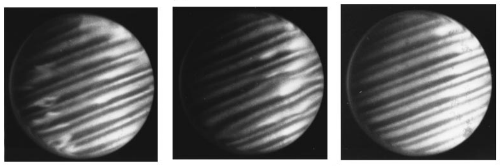

(d) ← Flow direction

Fig. 6 Circumferential variation of condensate behavior: tube M1, $G=170\ \mathrm{kg/(m^2s)}$, $X=0.4$

type scope. Comparison of Figs. 6(*a*)–6(*d*) for different circumferential positions shows that few marked variations of the film flow are observed, and most of the condensate flows through the grooves with a smooth liquid-vapor interface. A close inspection of Fig. 6 suggests that the film flows without apparent turbulent mixing in the film. However, a continuous wavy liquid-vapor interface that covers a number of fins is observed in some of the photographs. According to the previous study ([15]), this may be due to the disturbance wave traveling on the thin condensate film.

It may be possible, from the previous and present observation studies, to define two extreme flow patterns in a horizontal, spirally grooved microfin tube. (1) At high vapor velocities, most of the condensate flows through the grooves without apparent turbulent mixing in the film. Also no significant condensate stratification exists in the lower part of the tube. This means that all microfins act to augment condensation. This regime is referred to as the annular flow regime. (2) At low vapor velocities, most of the condensate flows through the lower part of the tube in the form of stratified condensate. This means that only upper microfins exposed to the vapor core enhance the condensation. This regime is referred to as the stratified flow. The results of the flow observation studies provide important findings for us to elucidate the condensation enhancement mechanism.

Prediction Method of Heat Transfer in the Annular Flow Regime

Numerical Analysis of Condensate Film. Figure 7 defines the geometry on which our model is based. A side view of a horizontal, spirally grooved microfin tube with n grooves and a spiral angle of γ is shown in Fig. 7(*a*). The coordinate z is measured along the groove from the vapor inlet at which the laminar film condensation starts. The model assumes that all the condensate flows through the grooves with smooth liquid-vapor interface, since the objective of the present analysis is the prediction of condensation heat transfer in the annular flow regime. Figure 7(*b*) shows the fin cross section normal to the groove. The T_s and T_w refer to the saturation and wall temperatures, respectively. The coordinates along the surface and normal to the surface are x and y, respectively. The dimensions specifying the fin geometry are: fin pitch p, fin height h, fin half tip angle θ, and radius of curvature at the corner of fin tip r_0, and those characterizing the condensate film are: film thickness δ and radius of curvature at the condensate surface r.

Neglecting the effect of gravity force, it can be considered that the condensate flow is controlled by the combined surface tension and vapor shear forces. To facilitate the numerical analysis, the condensate film is, with reference to Honda and Nozu [16], divided into two regions. One is the thin film region, referred to as region I, where the combined effects of the surface tension and vapor shear forces are taken into consideration, i.e., the condensate is pulled by the surface tension force in the x-direction and is driven by the vapor shear force in the z-direction. The other is the thick film region, referred to as region II, where the condensate surface is approximated by a circular arc with radius r_b and the condensate is drained by the vapor shear force in the z-direction.

The condensate profile between adjacent fins depends on the combination of the fin geometry and condensate flow rate. Two possible cases may exist as shown in Fig. 7(*b*). Case A corresponds to the case of large interfin space with small condensate flow rate, where the condensate film is divided into the thin film regions $0\leqslant x\leqslant x_b$ and $x_b'\leqslant x\leqslant x_c$, and the thick film region $x_b\leqslant x\leqslant x_b'$. Case B corresponds to the case of small interfin space with large condensate flow rate, where the thin condensate film is formed in the region $0\leqslant x\leqslant x_b$ and the rest of the surface is covered with the thick condensate film. Simplifying assumptions are introduced that permit fundamental assessment of the heat transfer rate: (1) the condensate flow is laminar; (2) the wall temperature T_w is uniform; (3) the inertia term in the momentum equation and

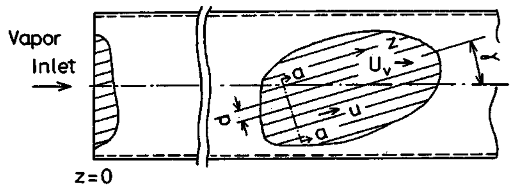

(a) side-view of microfin tube

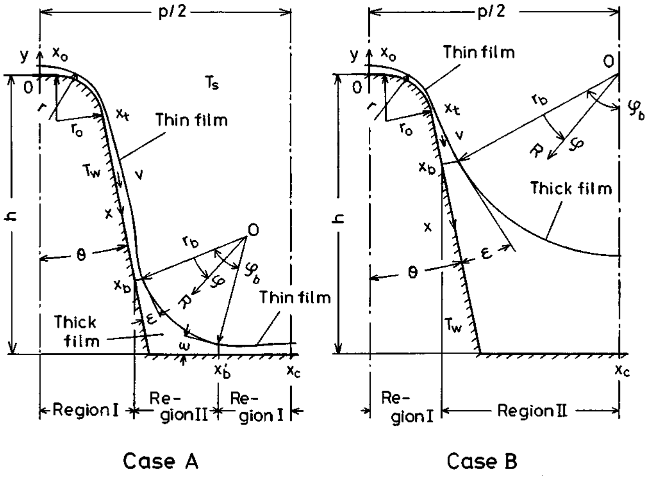

(b) a-a cross section

Fig. 7 Physical model and coordinates

the convection term in the energy equation can be neglected; (4) the effect of gravity force can be neglected; and (5) fin pitch is sufficiently smaller than the groove length.

The procedure for the formulation of the problem is basically similar to the case of condensation on a horizontal integral-fin tube reported in Honda and Nozu [16]. The momentum equations in region I are given by

$$\mu_l \frac{\partial^2 u}{\partial y^2} = 0, \tag{6}$$

$$\mu_l \frac{\partial^2 v}{\partial y^2} - \frac{dP}{dx} = 0 \tag{7}$$

where u and v denote the velocity components in the z and x-directions, respectively. The boundary conditions are

$$u = v = 0 \quad \text{at } y = 0 \tag{8}$$

$$\mu_l \frac{\partial u}{\partial y} = \tau_i, \tag{9}$$

$$\frac{\partial v}{\partial y} = 0 \quad \text{at } y = \delta \tag{10}$$

where τ_i is the shear stress at the condensate surface. The continuity and energy equations yield

$$\rho_l \left(\frac{\partial}{\partial z} \int_0^\delta u\, dy + \frac{\partial}{\partial x} \int_0^\delta v\, dy \right) = \frac{\lambda_l}{\delta} \frac{\Delta T}{h_{fg}} \tag{11}$$

where $\Delta T = T_s - T_w$ is the vapor-to-wall temperature difference. Substitution of the solutions of Eqs. (6) and (7) subject to the boundary conditions, Eqs. (8)–(10) into Eq. (11) yields

$$S_v \bar{\delta} \frac{\partial \bar{\delta}}{\partial \bar{z}} - \frac{1}{3} S_s \frac{\partial}{\partial \bar{x}} \left\{ \frac{d}{d\bar{x}} \left(\frac{1}{\bar{r}} \right) \bar{\delta}^3 \right\} = \frac{1}{\bar{\delta}} \tag{12}$$

where $\bar{x} = x/p$, $\bar{z} = z/p$, $\bar{\delta} = \delta/p$, $\bar{r} = r/p$, $S_v = \tau_i p^2 h_{fg} / (\lambda_l \nu_l \Delta T)$, $S_s = \sigma p h_{fg} / (\lambda_l \nu_l \Delta T)$. Expressions for $\bar{r}$ are given by for $0 \leqslant \bar{x} \leqslant \bar{x}_o$ and $\bar{x}_t \leqslant \bar{x}$

$$\frac{1}{\bar{r}} = -\frac{(d^2 \bar{\delta}/d\bar{x}^2)}{\{1 + (d\bar{\delta}/d\bar{x})^2\}^{3/2}} \tag{13a}$$

for $\bar{x}_o \leqslant \bar{x} \leqslant \bar{x}_t$

$$\frac{1}{\bar{r}} = \frac{\{1/\bar{r}_o + (2/\bar{r}_o^2 + \bar{\delta}/\bar{r}_o^3)\bar{\delta} + 2(d\bar{\delta}/d\bar{x})^2/\bar{r}_o - (1 + \bar{\delta}/\bar{r}_o)(d^2\bar{\delta}/d\bar{x}^2)\}}{\{(1 + \bar{\delta}/\bar{r}_o)^2 + (d\bar{\delta}/dx)^2\}^{3/2}}. \tag{13b}$$

We further assume that the change of the film thickness in the z-direction, $\partial\bar{\delta}/\partial\bar{z}$ is small compared with that in the x-direction $\partial\bar{\delta}/\partial\bar{x}$, due to the rapid condensate drainage by the surface tension force to the groove. Thus Eq. (12) is reduced to

$$-\frac{S_s}{3} \frac{d}{d\bar{x}} \left\{ \frac{d}{d\bar{x}} \left(\frac{1}{\bar{r}} \right) \bar{\delta}^3 \right\} = \frac{1}{\bar{\delta}}. \tag{14}$$

The boundary conditions are

for Case A

$$d\bar{\delta}/dx = d^3\bar{\delta}/d\bar{x}^3 = 0 \quad \text{at } \bar{x} = 0 \text{ and } \bar{x} = \bar{x}_c \tag{15}$$

$$d\bar{\delta}/d\bar{x} = \tan \varepsilon \tag{16}$$

$$\bar{r} = -\bar{r}_b \quad \text{at } \bar{x} = \bar{x}_b \text{ and } \bar{x} = \bar{x}_b' \tag{17}$$

for Case B

$$d\bar{\delta}/dx = d^3\bar{\delta}/d\bar{x}^3 = 0 \quad \text{at } \bar{x} = 0 \tag{18}$$

$$d\bar{\delta}/d\bar{x} = \tan \varepsilon \tag{19}$$

$$\bar{r} = -\bar{r}_b \quad \text{at } \bar{x} = \bar{x}_b \tag{20}$$

where x_c is the coordinate at the midpoint of the interfin space. The set of conditions, Eqs. (16) and (17) for Case A and Eqs. (19) and (20) for Case B, describe smooth connection of condensate surface between regions I and II.

Equation (14) is solved numerically as the steady-state solution of an unsteady condensate flow subject to an arbitrary initial distribution of $\bar{\delta}$. After adding the unsteady term to the left-hand side of Eq. (14), the resultant equation

$$\frac{\partial\bar{\delta}}{\partial\Theta} - \frac{S_s}{3} \frac{\partial}{\partial\bar{x}} \left\{ \frac{d}{d\bar{x}} \left(\frac{1}{\bar{r}} \right) \bar{\delta}^3 \right\} = \frac{1}{\bar{\delta}} \tag{21}$$

is solved using an implicit finite difference scheme. Three different grid sizes with finer grids at the tip and corner and coarser grids at the fin side are chosen along $\bar{x}$, with a total of 51–101 points. Convergence is accepted when the criterion $|1 - \bar{\delta}_i/\bar{\delta}_i^*|/\Delta\Theta \leqslant 0.01$ is satisfied, where $\bar{\delta}_i$ and $\bar{\delta}_i^*$ are the old and new values of $\bar{\delta}$ between successive iterations at grid point i and $\Delta\Theta$ the grid size of the dimensionless time. Changing the criterion to 0.1 altered the heat transfer result in region I by less than one percent. The value of ε is restricted by the geometrical conditions of fin and condensate profile, and is assumed as $\pi/20$. The deviations in the average Nusselt number Nu_d, obtained from Eq. (34), calculated by changing the ε value between $\pi/20$ and $\pi/6$ are always less than one percent. This means that the ε value has little effect on Nu_d.

The fluid flow and heat transfer in region II are analyzed using the cylindrical coordinates (R, φ) with the origin O at the center of the circular arc as shown in Fig. 7(b). The momentum and energy equations are described in dimensionless form as

$$\frac{\partial}{\partial\bar{R}} \left(\bar{R} \frac{\partial\tilde{u}}{\partial\bar{R}} \right) + \frac{\partial}{\partial\varphi} \left(\frac{\partial\tilde{u}}{\bar{R}\partial\varphi} \right) = 0 \tag{22}$$

and

$$\frac{\partial}{\partial\overline{R}}\left(\overline{R}\frac{\partial\tilde{T}}{\partial\overline{R}}\right)+\frac{\partial}{\partial\varphi}\left(\frac{\partial\tilde{T}}{\overline{R}\partial\varphi}\right)=0 \tag{23}$$

where $\overline{R}=R/p$, $\tilde{u}=up/\nu_l$ and $\tilde{T}=(T-T_w)/(T_s-T_w)$. The boundary and compatibility conditions are

$$\tilde{u}=0 \text{ and } \tilde{T}=0 \text{ at the wall} \tag{24}$$

$$\frac{\partial\tilde{u}}{\partial\overline{R}}=\mathrm{Re}_p^2 \text{ and } \tilde{T}=1 \text{ at the condensate surface} \tag{25}$$

and the continuities of $\tilde{u}$ and $\tilde{T}$ at the connecting point of the two regions. For Case B, the symmetries of $\tilde{u}$ and $\tilde{T}$ also hold along the centerline axis between adjacent fins. $\mathrm{Re}_p=\sqrt{\tau_i/\rho_l}\,p/\nu_l$ in Eq. (25) is obtained from

$$\mathrm{Re}_p=\sqrt{\frac{f_i}{2}\frac{\rho_l}{\rho_v}}\;\frac{GXp}{\mu_l} \tag{26}$$

where the friction factor f_i at the condensate surface is defined by

$$\tau_i=\frac{f_i}{2}\rho_v U_v^2. \tag{27}$$

Expression for f_i is, on the basis of the earlier work ([15]), assumed to be

$$f_i=0.046\,\mathrm{Re}_v^{-0.2}(1+300\delta/d_n)+\frac{V_1}{U_v} \tag{28}$$

where $\mathrm{Re}_v=GXd_n/\mu_v$ is the vapor Reynolds number, $V_i=\dot{m}/\rho_v$ is the suction velocity at the condensate surface, U_v is the axial vapor velocity, and $\dot{m}$ is the condensation mass flux. The first term on the right-hand side of Eq. (28) is the same as the expression for annular film flow in a smooth tube proposed by Wallis [17], and the second one shows the effect of vapor suction at the condensate surface. The present heat transfer model assumes that the condensate is flowing only through the grooves. This permits an assumption that the axial vapor velocity U_v is satisfactorily expressed by

$$U_v=GX/\rho_v. \tag{29}$$

The solutions of Eqs. (22) and (23) subject to the boundary and compatibility conditions are obtained iteratively using a control-volume-based, finite difference procedure after introducing the following coordinates transformation

$$\xi=\varphi, \tag{30}$$

$$\overline{R}=\overline{r_b}+\overline{\delta}\eta. \tag{31}$$

A 10×10 or 20×20 equally spaced mesh, depending on the depth of the condensate pool, is used and a convergence criterion of 0.01 percent is adopted during the iteration. The local Nusselt number $\mathrm{Nu}_p=\alpha p/\lambda_l$ for the fin surface is obtained from

for region I

$$\mathrm{Nu}_p=1/\overline{\delta} \tag{32a}$$

for region II

$$\mathrm{Nu}_p=(-\partial\tilde{T}/\partial\overline{R})_{\overline{R}=\overline{R}_w}. \tag{32b}$$

The average Nusselt number $\mathrm{Nu}_{pm}=\alpha_m p/\lambda_l$ for the fin surface is calculated from

for case A

$$\mathrm{Nu}_{pm}=2\left(\int_0^{\overline{x_b}}(1/\overline{\delta})d\overline{x}+\int_0^{\varphi_b}(-\partial\tilde{T}/\partial\overline{R})_{\overline{R}=\overline{R}_w}\overline{R}_w d\varphi\right.$$
$$\left.+\int_{\overline{x}'_b}^{\overline{x_c}}(1/\overline{\delta})d\overline{x}\right) \tag{33a}$$

for case B

$$\mathrm{Nu}_{pm}=2\left(\int_0^{\overline{x_b}}(1/\overline{\delta})d\overline{x}+\int_0^{\varphi_b}(-\partial\tilde{T}/\partial\overline{R})_{\overline{R}=\overline{R}_w}\overline{R}_w d\varphi\right). \tag{33b}$$

The average Nusselt number $\mathrm{Nu}_d=\alpha_n d_n/\lambda_l$ for the microfin tube, nominal surface area basis, is related to Nu_{pm} as

$$\mathrm{Nu}_d=\mathrm{Nu}_{pm}(d_n/p). \tag{34}$$

The liquid Reynolds number Re_l

$$\mathrm{Re}_l=G(1-X)d_n/\mu_l \tag{35}$$

can be expressed in another form using $\tilde{u}$ and γ as

$$\mathrm{Re}_l=4\cos\gamma\left(2\int_{\overline{F}}\tilde{u}\,d\overline{F}\right) \tag{36}$$

where $\overline{F}=F/p^2$, F is the cross-sectional area of the condensate per one half of fin pitch. The $\tilde{u}$ in Eq. (36) for region I is obtained from the solution of Eq. (6), and that for region II is given by the solution of Eq. (22). The Re_l determined by Eq. (36) becomes larger for smaller $\overline{x_b}$ and larger τ_i, taking a finite value together with $\overline{r_b}\to\infty$. In this paper, the liquid Reynolds number at an extreme condition that the interfin space is almost completely filled with condensate is denoted as $(\mathrm{Re}_l)_{\mathrm{fl}}$. This will be related to an applicable range of the present prediction method. To discuss the validity of the present prediction method, the numerical analysis is executed by the following procedure for a set of experimental conditions of G, X, ΔT, and the dimensions of fin and tube (values of $\overline{h}$, $\overline{r_o}$, $\overline{x_o}$, θ, p, and d_n in Table 1).

(i) Calculate measured Re_l from Eq. (35).
(ii) Solve Eqs. (14) and (22) subject to the boundary and compatibility conditions by assuming

$$\overline{x_b}=\overline{x_o}+\overline{r_o}\varepsilon+\Delta\overline{x} \tag{37}$$

and then calculate $(\mathrm{Re}_l)_{\mathrm{fl}}$ from Eq. (36). The values of $\Delta\overline{x}$ and ε, which provide the extreme condensate profile with $\overline{r_b}\to\infty$, are assumed as 10^{-4} and $\pi/20$, respectively.
(iii) If the relation $\mathrm{Re}_l\leqslant(\mathrm{Re}_l)_{\mathrm{fl}}$ is satisfied, continue the following steps. On the other hand, if $\mathrm{Re}_l>(\mathrm{Re}_l)_{\mathrm{fl}}$, calculate Nu_d from Eq. (34) by assuming $\mathrm{Re}_l=(\mathrm{Re}_l)_{\mathrm{fl}}$ for our reference.
(iv) Assume $\overline{x_b}$ and solve Eqs. (14) and (22), and then calculate Re_l from Eq. (36).
(v) Repeat (iv) until an agreement of within ±0.1 percent is obtained between the two Re_l values calculated in (i) and (iv).
(vi) Calculate Nu_d from Eqs. (33) and (34) after the convergence criterion in (v) is satisfied.

To ensure the numerical accuracy of Nu_d, the convergence criterion in (v) is changed from ±0.1 percent to ±0.01 percent. It is found that the deviations in Nu_d calculated with the two criterions are always less than 0.1 percent. Thus the numerical method proposed here is considered to be accurate to predict the condensation heat transfer characteristics.

Comparison With Experiments and Discussion. Numerical predictions of the local heat transfer coefficient are compared with available experimental data including four fluids and three microfin tubes. Figure 8 shows the axial distributions of the measured and predicted heat transfer coefficients for tubes M1 and M2 at $G\cong 300\ \mathrm{kg/(m^2\,s)}$, where Nu_d is plotted versus $(1-X)$. Also shown in Fig. 8 is the distribution of $(\mathrm{Re}_l)_{\mathrm{fl}}$. In Fig. 8, the symbol

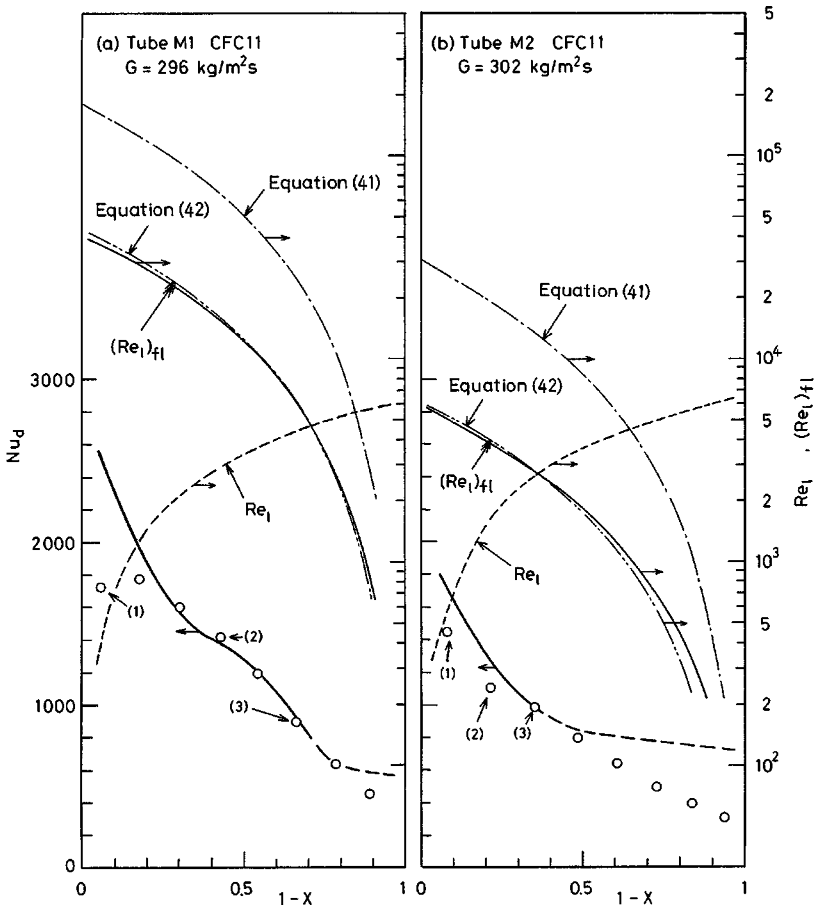

Fig. 8 Comparison of measured and predicted Nu_d values; effect of fin dimensions, tubes M1 and M2

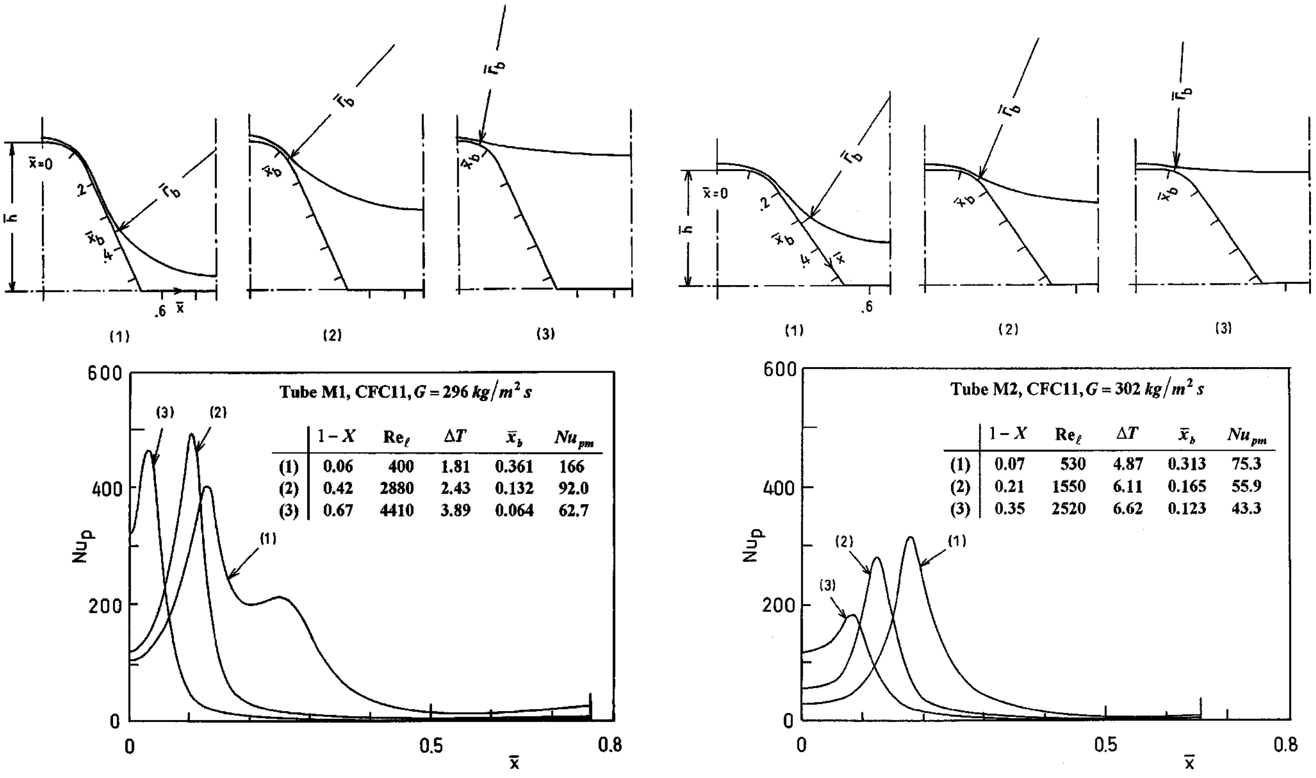

Tube M1, CFC11, $G = 296\ kg/m^2 s$

	$1-X$	Re_ℓ	ΔT	$\bar{x}_b$	Nu_{pm}
(1)	0.06	400	1.81	0.361	166
(2)	0.42	2880	2.43	0.132	92.0
(3)	0.67	4410	3.89	0.064	62.7

Tube M2, CFC11, $G = 302\ kg/m^2 s$

	$1-X$	Re_ℓ	ΔT	$\bar{x}_b$	Nu_{pm}
(1)	0.07	530	4.87	0.313	75.3
(2)	0.21	1550	6.11	0.165	55.9
(3)	0.35	2520	6.62	0.123	43.3

(a) Tube M1

(b) Tube M2

Fig. 9 Axial development of condensate profile: (*a*) tube M1, (*b*) tube M2

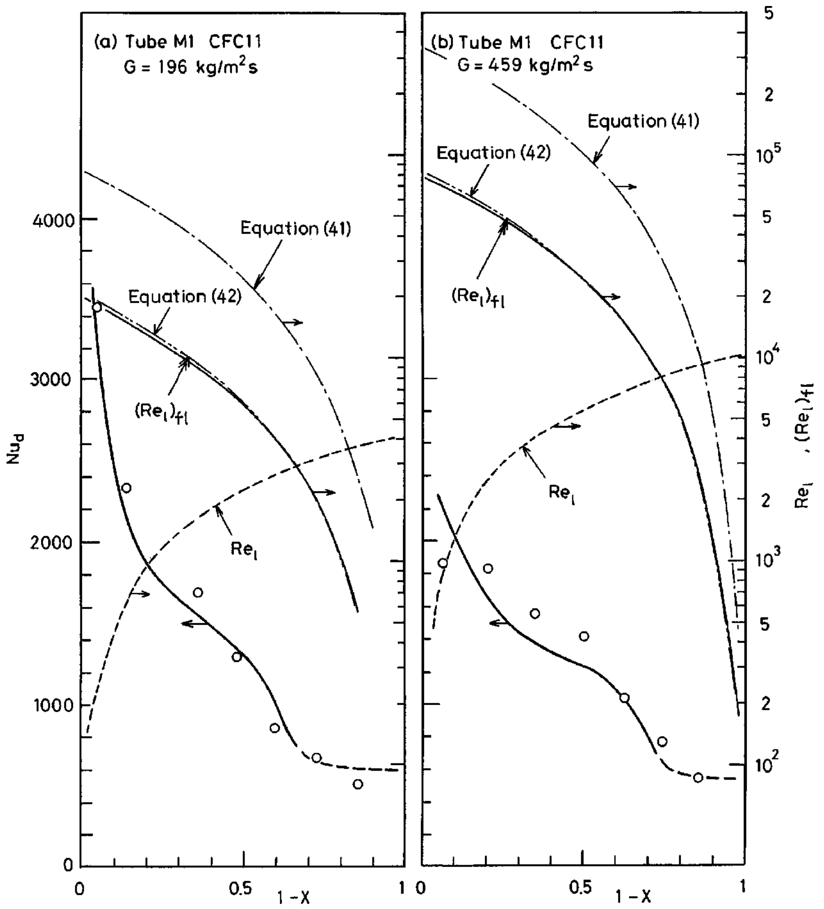

Fig. 10 Comparison of measured and predicted Nu_d values: effect of mass velocity, tube M1

○ shows the measured Nu_d. The thick and thin solid lines present the predicted Nu_d and $(\mathrm{Re}_l)_{\mathrm{fl}}$ values, respectively. Comparisons of Nu_d between the measured and predicted values in the region $\mathrm{Re}_l \leqslant (\mathrm{Re}_l)_{\mathrm{fl}}$ are meaningful since the annular flow is assumed. For each tube, Re_l increases monotonically, whereas $(\mathrm{Re}_l)_{\mathrm{fl}}$ decreases monotonically with increasing $(1-X)$. Then Re_l agrees with $(\mathrm{Re}_l)_{\mathrm{fl}}$ at 4600 for tube M1 and 2600 for tube M2. It is seen that the measured Nu_d is in good agreement with the prediction in the region $\mathrm{Re}_l \leqslant (\mathrm{Re}_l)_{\mathrm{fl}}$.

The change of the condensate profile along the groove is of interest in understanding the heat transfer mechanism. The upper and lower columns of Fig. 9, respectively, illustrate the condensate profile and the variation of Nu_p with $\bar{x}$ for tubes M1 and M2 at three points indicated by (1)–(3) in Fig. 8. It can be seen from Fig. 9 that the condensate profile is affected strongly by the flow conditions and fin dimensions as expected. For each tube, the depth of the condensate flowing through the groove increases with $(1-X)$. As a result, the thin film region shifts towards the fin tip. This leads to the decrease in the heat transfer rate, as is clearly seen in the lower column of Fig. 9. It is also interesting to observe that the depth of the condensate for tube M2 increases more rapidly than that for tube M1 due to the smaller interfin space. For example, the $(1-X)$ values at which the interfin space is almost completely filled with condensate is around 0.7 for tube M1 and 0.36 for tube M2. These facts indicate that the flow pattern transition from the annular to stratified flow depends on both the flow conditions and fin dimensions.

Figures 10 and 11 present similar comparisons as shown in Fig. 8, where Fig. 10 shows the effects of the mass velocity and Fig. 11 the effects of the fluid properties. The measured Nu_d for tube M3 is recalculated using Eq. (2) from the data of Haraguchi [7]. A quick inspection of Figs. 10 and 11 reveals that the prediction method proposed here performs quite well in the region $\mathrm{Re}_l \leqslant (\mathrm{Re}_l)_{\mathrm{fl}}$. The model can be applied in a wider Re_l range for larger G, and the region $\mathrm{Re}_l \leqslant (\mathrm{Re}_l)_{\mathrm{fl}}$ is wider for HCFC123 than for HCFC22 because the vapor density is smaller for HCFC 123 than for HCFC22.

In summary, the present theory is applicable in the region $\mathrm{Re}_l \leqslant (\mathrm{Re}_l)_{\mathrm{fl}}$. Now we develop an approximate expression of $(\mathrm{Re}_l)_{\mathrm{fl}}$ for practical use. First let us consider a shear-controlled laminar liquid film with a thickness equal to fin height h. The momentum equation is expressed as

$$\frac{d^2\tilde{u}}{d\bar{y}^2}=0 \tag{38}$$

where $\bar{y}=y/p$. The boundary conditions are

$$\tilde{u}=0 \quad \text{at } \bar{y}=0 \tag{39}$$

$$\frac{d\tilde{u}}{d\bar{y}}=\mathrm{Re}_p^2 \quad \text{at } \bar{y}=\bar{h} \tag{40}$$

where $\bar{h}=h/p$ and Re_p in Eq. (40) is calculated from Eqs. (26) and (28) on the assumptions of $\delta=h$ and $V_i=0$. After solving Eq. (38) with the boundary conditions given by Eqs. (39) and (40), substitution of $\tilde{u}$ into Eq. (36) yields

$$\mathrm{Re}_l=2\cos(\gamma)(\mathrm{Re}_p\bar{h})^2. \tag{41}$$

In Figs. 8, 10, and 11, the prediction of Eq. (41) is compared with the numerical results of $(\mathrm{Re}_l)_{\mathrm{fl}}$. It can be seen that the prediction is in good agreement with $(\mathrm{Re}_l)_{\mathrm{fl}}$ in trend, but takes up to a 4.5 times larger value than $(\mathrm{Re}_l)_{\mathrm{fl}}$. This is due to neglecting the ef-

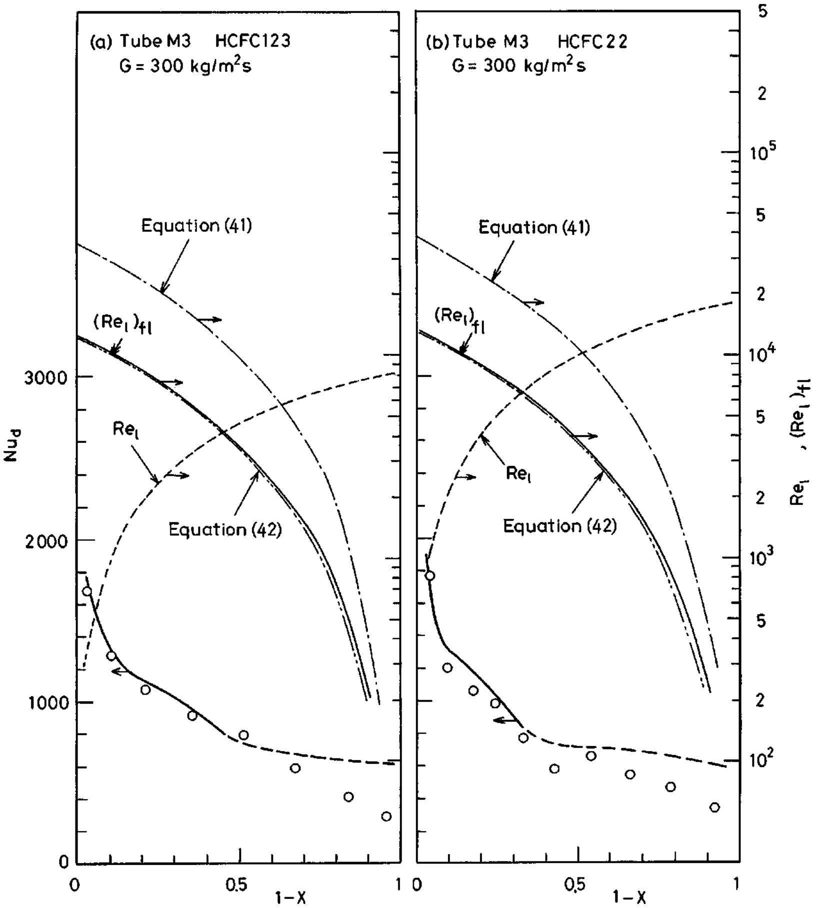

Fig. 11 Comparison of measured and predicted Nu_d values: effect of fluid properties, tube M3

fects of fin surface on the fluid flow. By reference to Eq. (41), the numerical results of $(\mathrm{Re}_l)_{\mathrm{fl}}$ for the three tubes can be approximated by

$$(\mathrm{Re}_l)_{\mathrm{fl}} = \cos(\gamma)(\mathrm{Re}_p \overline{h})^2 \{\overline{s} - \overline{h}_t^2 \tan(\theta + \pi/15)\} \qquad (42)$$

where $\overline{s} = s/p$, $\overline{h}_t = \overline{h} - \overline{r}_0(1 - \cos\theta)$ and s denotes the fin spacing measured at a distance of one half of fin height from fin root. In Figs. 8, 10, and 11, prediction of Eq. (42) is shown by dash double-dot curves. It is seen that Eq. (42) can predict $(\mathrm{Re}_l)_{\mathrm{fl}}$ with sufficient accuracy except in the region $(1 - X) \geqslant 0.7$ for tube M2. As a result, for given conditions of the mass velocity, dimensions of fin and tube, and fluid properties, the maximum Re_l below which the present heat transfer model can be applied is obtained by first, finding out a X value that satisfies the right-hand sides of Eqs. (35) and (42) simultaneously, and then calculate Re_l from Eq. (35).

In Figs. 8, 10, and 11, the thick dashed lines in the region $\mathrm{Re}_l > (\mathrm{Re}_l)_{\mathrm{fl}}$ show the Nu_d predicted on the assumption of $\mathrm{Re}_l = (\mathrm{Re}_l)_{\mathrm{fl}}$. In this region, the measured Nu_d deviate toward lower values than the predictions as the condensation proceeds. This may be due to a rapid increase in the depth of stratified condensate in the lower part of the tube not considered in the present model.

All the available experimental data in the region $\mathrm{Re}_l \leqslant (\mathrm{Re}_l)_{\mathrm{fl}}$ for tubes M1, M2, and M3 are compared with the present predictions in Figs. 12 and 13, where $(\mathrm{Nu}_d)_{\mathrm{mea}}$ and $(\mathrm{Nu}_d)_{\mathrm{pre}}$ denote the measured and predicted Nu_d values, respectively. It is seen from Figs. 12 and 13 that the prediction method proposed here provides satisfactory predictions with a mean absolute deviation of 15.1 percent.

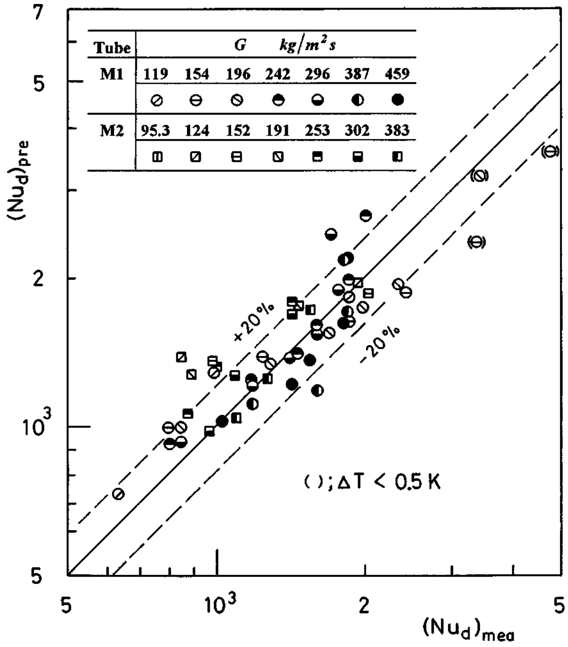

Fig. 12 Comparison of measured and predicted local heat transfer coefficients: tubes M1 and M2

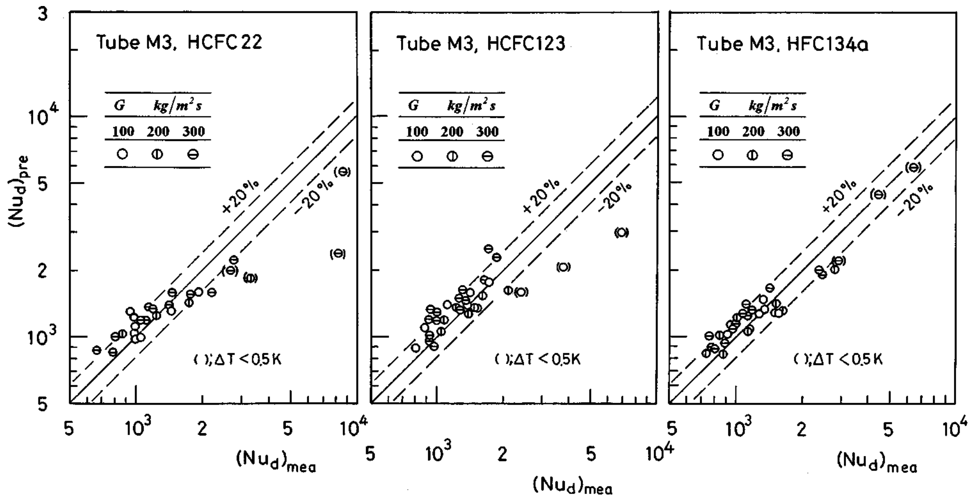

Fig. 13 Comparison of measured and predicted local heat transfer coefficients: tube M3

Conclusions

Experimental and numerical studies have been performed for the condensation of a vapor in horizontal, smooth, and spirally grooved microfin tubes. Two microfin tubes have been tested to study the effects of fin dimensions on the axial variation of the heat transfer coefficients. Based on the flow observation study with use of an industrial bore scope, the film flow model between fins in the annular flow regime has been proposed. The conclusions are summarized as follows:

1 The flow observation study has revealed that the condensing two-phase flow pattern is divided into two major flow regimes in a horizontal, spirally grooved microfin tube. One is the annular flow, where most of the condensate flow through the grooves without apparent turbulent mixing in the condensate film. The other is the stratified flow, where a stratified condensate flowing through the lower part of the tube exists.

2 Numerical analysis has been performed for the condensation heat transfer in the annular flow regime. The model assumes that all the condensate flow occurs through the grooves. For each groove, laminar condensate film is divided into the thin and thick film regions to facilitate the numerical analysis. In the thin film region formed on the fin surface, the condensate flow under the influences of combined surface tension and vapor shear forces has been considered, while in the thick film region formed in the groove, the condensate profile has been approximated by a circular arc and the shear-controlled condensate flow has been taken into consideration.

3 The available experimental data of the local heat transfer coefficient including four fluids and three microfin tubes have been found by the present prediction method to have a mean absolute deviation of 15.1 percent.

4 For a set of conditions of the mass velocity, dimensions of fin and tube, and condensing fluid, the maximum liquid Reynolds number below which the present prediction method can be applied is obtained as follows. First, find out the vapor mass quality that satisfies the right-hand sides of Eqs. (35) and (42) simultaneously, then calculate the liquid Reynolds number from Eq. (35).

Acknowledgment

This work is partly supported by a Grant-in-Aid for Scientific Research (No. 09650252) by the Ministry of Education, Science, Sports and Culture, Japan.

Nomenclature

a, b, c = dimensionless number, Eq. (5)
c_{pl} = specific heat of condensate
d_n = nominal diameter
d_o = tube outer diameter
d_r = fin root tube diameter
$2F$ = cross-sectional area of condensate between fins
f_i = friction factor at condensate surface, Eq. (27)
g = gravitational acceleration
h = fin height
h_{fg} = specific enthalpy of evaporation
G = test fluid mass velocity
Ga = Galileo number $= g d_n^3 / \nu_l^2$
Δl = length of subsection
$\dot{m}$ = condensation mass flux$= \dot{m}/\rho_\nu$
n = number of grooves
Nu_d = Nusselt number for tube, nominal surface area basis
$(\mathrm{Nu}_d)_g$ = Nusselt number for smooth tube, gravity-controlled regime, Eq. (5*b*)
$(\mathrm{Nu}_d)_v$ = Nusselt number for smooth tube, vapor shear-controlled regime, Eq. (5*a*)
Nu_p = local Nusselt number for fin surface, Eq. (32)
Nu_{pm} = average Nusselt number for fin surface, Eq. (33)
P = static pressure
p = fin pitch
Ph = phase change number$= c_{pl}\Delta T / h_{fg}$
Pr_l = liquid Prandtl number
ΔQ = heat transfer rate in subsection
q = heat flux
q_n = heat flux, nominal surface area basis
R = radial coordinate, Fig. 7
r = radius of curvature of liquid-vapor interface
r_b = radius of curvature of condensate surface in thick film region
r_o = radius of curvature at corner of fin tip, Fig. 7
Re_l = liquid Reynolds number, Eqs. (35), (36)
$(\mathrm{Re}_l)_{\mathrm{fl}}$ = liquid Reynolds number under extreme condition that interfin space is almost completely filled with condensate
Re_p = shear Reynolds number$= \sqrt{\tau_i/\rho_l}\, p/\nu_l$
Re_v = vapor Reynolds number$= G X d_n / \mu_v$
s = fin spacing measured at a distance of one-half of fin height from fin root
S_s = dimensionless number$= \sigma \mathrm{p} h_{fg} / (\lambda_l \nu_l \Delta T)$

S_v = dimensionless number$=\tau_i p^2 h_{fg}/(\lambda_l \nu_l \Delta T)$
T = temperature
T_s = vapor saturation temperature
T_w = inner wall temperature
T_{wm} = measured wall temperature
T_c = cooling water temperature
ΔT = vapor-to-wall temperature difference$=T_s-T_w$
$\tilde{T}$ = dimensionless temperature$=(T-T_w)/(T_s-T_w)$
U_v = axial vapor velocity$=GX/\rho_v$
u = velocity component in z-direction
$\tilde{u}$ = dimensionless velocity$=up/\nu_l$
V_i = suction velocity at condensate surface$=\dot{m}/\rho_\nu$
v = velocity component in x-direction
X = vapor mass quality
x,y,z = coordinates, Fig. 7
x_o, x_t = coordinates at connecting points between straight and round portions of fin, Fig. 7
x_b, x_b' = coordinates at connecting points between thin and thick film regions, Fig. 7
x_c = coordinate at midpoint of interfin space, Fig. 7
α = heat transfer coefficient
α_n = heat transfer coefficient, nominal surface area basis
α_s = heat transfer coefficient for smooth tube, Eq. (3)
γ = helix angle
δ = condensate film thickness
ε = angle, Fig. 7
η = coordinate, Eq. (31)
θ = fin half tip angle, Fig. 7
λ = thermal conductivity
μ = viscosity
ν = kinematic viscosity
ξ = coordinate, Eq. (30)
ρ = density
σ = surface tension
τ = shear stress
τ_i = shear stress at condensate surface
φ = angular coordinate, Fig. 7
φ_b = angle subtended at origin O by an arc with radius r_b, Fig. 7
ψ = circumferential angle measured from tube top
Θ = dimensionless time

Subscripts and Superscripts

b = boundary of thin and thick film regions
c = cooling water; also center of interfin space
g = gravity-controlled regime
i = condensate surface
in = vapor inlet
l = condensate
n = nominal surface area basis
s = saturation; also surface tension-controlled regime
ν = vapor; also vapor shear-controlled regime
w = wall
$\overline{}$ = nondimensionalized by p or p^2

References

[1] Khanpara, J. C., Bergles, A. E., and Pate, M. B., 1986, ''Augmentation of R-113 In-tube Condensation With Micro-fin Tubes,'' in *Heat Transfer in Air Conditioning and Refrigeration Equipment*, J. A. Kohler and J. W. B. Lu, eds., ASME, NY, pp. 21–32.
[2] Schlager, L. M., Pate, M. B., and Bergles, A. E., 1989, ''Heat Transfer and Pressure Drop During Evaporation and Condensation of R22 in Horizontal Micro-fin Tubes,'' Int. J. Refrig., **12**, pp. 6–14.
[3] Schlager, L. M., Pate, M. B., and Bergles, A. E., 1990, ''Evaporation and Condensation Heat Transfer and Pressure Drop in Horizontal, 12.7-mm Microfin Tubes with Refrigerant 22,'' J. Heat Transfer, **112**, pp. 1041.
[4] Schlager, L. M., Pate, M. B., and Bergles, A. E., 1990, ''Condensation of Refrigerant-Oil Mixture in Smooth and Augmented Tubes,'' *Proceedings of the 2nd International Symposium on Condensers and Condensation*, Mar. 28–30, University of Bath, Bath, UK, pp. 451–460.
[5] Hori, M., and Shinohara, Y., 1990, ''Heat Transfer Characteristics of Internally Grooved Tubes,'' Shindo-Gizyutsu Kenkyuukai-shi, **29**, pp. 65–70.
[6] Koyama, S., Miyara, A., Takamatsu, H., and Fujii, T., 1990, ''Condensation Heat Transfer of Binary Refrigerant Mixtures of R22 and R114 Inside a Horizontal Tube with Internal Spiral Grooves,'' Int. J. Refrig., **13**, pp. 256–263.
[7] Haraguchi, H., 1994, ''Study on Condensation of HCFC22, HFC134a and HCFC123 Inside Horizontal Tubes,'' Dr. Eng. thesis, Kyushu University.
[8] Chamra, L. M., and Webb, R. L., 1996, ''Advanced Micro-Fin Tubes for Condensation,'' Int. J. Heat Mass Transf., **39**, pp. 1839–1846.
[9] Webb, R. L., 1994, *Principles of Enhanced Heat Transfer*, John Wiley and Sons, New York.
[10] Fujii, T., 1995, ''Enhancement to Condensing Heat Transfer–New Developments,'' J. Enhanced Heat Transfer, **2**, pp. 127–137.
[11] Sirnivasan, V., and Shah, R. K., 1997, ''Condensation in Extended Surfaces and Small Hydraulic Diameter Channels,'' *Compact Heat Exchangers for the Process Industries*, R. K. Shah, et al., eds., Begell House, New York, pp. 101–118.
[12] Shikazono, N., Itoh, M., Uchida, M., Fukushima, T., and Hatada, T., 1997, ''Prediction Method for Condensation Heat Transfer Coefficient of Pure Refrigerants in Horizontal Microfin Tubes,'' Trans. Jpn. Soc. Mech. Eng., Ser. B, **63**, pp. 2436–2443.
[13] Shikazono, N., Itoh, M., Uchida, M., Fukushima, T., and Hatada, T., 1998, ''Predictive Equation Proposal for Condensation Heat Transfer Coefficient of Pure Refrigerants in Horizontal Microfin Tubes,'' Trans. Jpn. Soc. Mech. Eng., Ser. B, **64**, pp. 196–203.
[14] Dobson, M. K., and Chato, J. C., 1998, ''Condensation in Smooth Horizontal Tubes,'' J. Heat Transfer, **120**, pp. 193–213.
[15] Nozu, S., Katayama, H., Nakata, H., and Honda, H., 1998, ''Condensation of a Refrigerant CFC11 in Horizontal Microfin Tubes (Proposal of a Correlation Equation for Frictional Pressure Gradient),'' Exp. Therm. Fluid Sci., **18**, pp. 82–96.
[16] Honda, H., and Nozu, S., 1987, ''A Prediction Method for Heat Transfer During Film Condensation on Horizontal Low Integral-Fin Tubes,'' J. Heat Transfer, **109**, pp. 218–225.
[17] Wallis, G. B., 1969, *One-Dimensional Two-Phase Flow*, McGraw-Hill, New York.

Flammability Measurements of Difluoromethane

W. L. Grosshandler
e-mail: wgrosshandler@nist.gov

M. K. Donnelly

C. Womeldorf

Building and Fire Research Laboratory,
National Institute of Standards and Technology,
Gaithersburg, MD 20899

Difluoromethane (CH_2F_2, or R-32) is a candidate to replace ozone-depleting chlorofluorocarbon refrigerants. Because CH_2F_2 is flammable, it is necessary to assess the hazard posed by a leak in a refrigeration machine. The currently accepted method for determining flammability, ASTM E 681 has difficulty discerning the flammability boundary for weak fuels such as CH_2F_2. This article describes an alternative approach to identify the limits of flammability, using a twin, premixed counterflow flame. By using the extinction of an already established flame, the point dividing flammable from nonflammable becomes unambiguous. The limiting extinction mixture changes with stretch rate, so it is convenient to report the flammability limit as the value extrapolated to a zero stretch condition. In the burner, contoured nozzles with outlet diameters of 12 mm are aligned counter to each other and spaced 12 mm apart. The lean flammability limit of CH_2F_2 in dry air at room temperature was previously reported by the authors to be a mole fraction of 0.14, using the twin counterflow flame method. In the current study, relative humidity was not found to affect the lean limit. Increasing the temperature of the premixed fuel and air to 100°C is shown to extend the flammability limit in the lean direction to 0.13. The rich limit of CH_2F_2 found using the counterflow method is around 0.27. The uncertainties of the measurements are presented and the results compared to data in the literature. [S0022-1481(00)02501-9]

Keywords: Combustion, Fire, Flame, Heat Transfer, Refrigeration

Background

An accepted method for determining the flammability limits of gaseous fuels is described in ASTM Standard E 681 [1]. The minimum and maximum concentrations of the fuel in air for flame propagation are based upon the observed ignition and growth of a flame in a vessel filled with a quiescent fuel/air mixture at a specified uniform temperature and pressure. A clear distinction is sought between a mixture which creates a nonpropagating flicker and a flame which has enough horizontal propagation to be hazardous. When applied to fuels like methane or propane, these tests give well-defined results. Weak fuels like difluoromethane (CH_2F_2, or R-32), however, have a greater sensitivity to the test conditions and provide ambiguous limits (see Table 1 and references therein). The ignition energy and type (spark, match-head, heated wire), the complex geometry of the flame, and wall effects all contribute to this ambiguity.

Many of the difficulties associated with the ASTM measurements of flammability are not present in the approach suggested in the papers by Wu and Law [2] and Law et al. [3]. The earlier paper employed a laminar flame impinging on a flat plate to determine the speed at which different concentrations of hydrocarbon/air mixtures burn. By repeating the experiments at diminishing flow rates, it was possible to plot the measured flame speed versus the flow rate, and to extrapolate the results to identify the flame speed corresponding to an experimentally unattainable zero-flow condition. In the second paper ([3]) the authors replaced the flat plate with a counterflowing mixture of the fuel and air, which produced twin flat flames separated by a close-to-adiabatic stagnation plane. They determined the gradient of velocity normal to the flame at the extinction condition as a function of the concentration of methane and propane in the mixture. By repeating the experiment at lower and lower velocities, it is possible to extrapolate to a concentration that would exist at zero flow, which is proposed here to be an equivalent definition of flammability limit. Unlike the ASTM apparatus, the counterflow burner method entirely avoids issues surrounding the design of an ignition mechanism, it minimizes heat loss and wall effects, and also it is amenable to computational analysis.

A twin-flame counterflow burner was selected by Womeldorf and Grosshandler [4] to determine the lean flammability limit (LFL) of CH_2F_2 in dry air at ambient temperature. At the limiting lean mixture, the reaction rate is slowed to the point that the residence time in the flame (which is maintained about constant since the velocity and spacing are fixed) is insufficient for complete combustion to occur, leading to flame extinction. On the other hand, when a fixed concentration of the fuel is maintained, increasing the jet velocity forces the flames towards the stagnation plane lying equidistant between the two burner jet outlets. At a sufficiently high velocity the time through the reaction zone becomes so short that the reactants pass through faster than they can burn, decreasing the combustion efficiency to a point that not enough heat is released to propagate the flame. Again, extinction follows.

The effect of jet velocity and spacing can be combined into a single parameter called the global stretch rate, K_g, defined as the average velocity at the exit of the burner jet divided by the distance between the exit plane and the stagnation plane (i.e., half the nozzle separation). The mole fraction of refrigerant at extinction can be plotted against diminishing values of K_g, and linear extrapolation used to determine the minimum mole fraction of fuel required to propagate a flame at the zero-flow ($K_g = 0\ s^{-1}$) condition. This is the LFL of the fuel for the given initial conditions (ambient temperature, pressure, and relative humidity).

Difluoromethane has a molecular weight of 0.052 kg/mol, a boiling temperature of -51.7°C at 101 kPa, a saturation pressure of 1.69 MPa at 25°C, a specific heat (gas phase) of 0.843 kJ/kg-°C, and an enthalpy of combustion of $-9.35\ MJ/kg_{fuel}$. The complete, stoichiometric combustion of CH_2F_2 in dry air is given by the following expression:

$$CH_2F_2 + (O_2 + 3.76\ N_2) \rightarrow CO_2 + 2\ HF + 3.76\ N_2. \qquad \{R1\}$$

Contributed by the Heat Transfer Division for publication in the JOURNAL OF HEAT TRANSFER and presented at the Fifth ASME/JSME Joint Thermal Engineering Conference, Mar. 15–19, San Diego, CA. Manuscript received by the Heat Transfer Division, Jan. 6, 1999; revision received, Aug. 11, 1999. Associate Technical Editor: J. Gore.

Table 1 Lean flammability limits of CH_2F_2/air at ambient temperature (unless indicated otherwise) using different experimental methods

Author(s)	Method	Ignition	Lean Limit Equiv. Ratio	Lean Limit Mole Fract.
Dekleva et al. (1993)	5 cm tube (ICI)	hot wire	1.11	0.189
Richard and Shankland (1992)	4 liter tube	match	0.84	0.150
Dekleva et al. (1993)	ASTM E 681, 5 liter	hot wire	0.81	0.145
Grob, D. (1991)	ASTM E 681, 12 liter	hot wire	0.81	0.145
Richard and Shankland (1992)	ASTM E 681, 5 liter	hot wire	0.79	0.142
Womeldorf and Grosshandler (1999)	counter-flow twin flame, linear extrapolation	(extinction)	0.78 ± 0.04	0.141 ± 0.006
Dekleva et al. (1993)	ASTM E 681, 5 liter	hot wire	0.77	0.139
Dekleva et al. (1993)	ASTM E 681, 12 liter	match	0.77	0.139
Dekleva et al. (1993)	Autoclave, 8 liter	hot wire	0.75	0.136
Richard and Shankland (1992)	ASTM E 681, 5 liter	spark	0.74	0.134
present work (50 % RH, 100 °C)	counter-flow twin flame, linear extrapolation	(extinction)	0.72 ± 0.02	0.131 ± 0.004
Ohnishi, H. (1993)	ASTM E 681, 5 liter	paper match	0.71	0.130
Richard and Shankland (1992)	ASTM E 681, 5 liter	match	0.69	0.127

Data from References [4,6,7,22,23].

The stoichiometric mole fraction of CH_2F_2, $X_{CH_2F_2}$, in dry air is 0.1736. The equivalence ratio, Φ (defined as the fuel-to-air mole ratio divided by the stoichiometric fuel-to-air mole ratio), is related to the mole fraction by $\Phi = 4.76\, X_{CH_2F_2}/(1 - X_{CH_2F_2})$; in the counterflow burner Φ is equal to 4.76 times the ratio of the volume flow of CH_2F_2 to the volume flow of air.

The temperature and products of combustion of difluoromethane at adiabatic, equilibrium conditions were determined by Womeldorf and Grosshandler [4] for different values of equivalence ratio. For CH_2F_2/dry air mixtures, initially at 25°C and 101 kPa, the peak temperature, 1940°C, occurs when $\Phi = 1.05$. At approximately the same Φ, the CO_2 reaches a peak mole fraction of about 0.13. The mole fraction of HF at stoichiometric conditions is close to 0.30, and it continues to increase with Φ. The mole fraction of H_2O in the dry flame is over two orders-of-magnitude less than the mole fractions of HF and CO_2.

Womeldorf and Grosshandler [4] estimated the adiabatic, stoichiometric laminar flame speed of CH_2F_2/air to be 67 mm/s. They also measured the lean flammability limit mole fraction to be 0.14 ± 0.006, which corresponds to a limiting lean equivalence ratio of 0.78 ± 0.04, when the air is dry and at 35°C±5°C.

The refrigeration industry is interested in identifying the hazard associated with a leaking refrigerant as installed in the field, where the temperature and humidity differ from the above experimental conditions. Mixtures at higher temperatures are expected to be more flammable, while the impact of changing the relative humidity is less clear. The current paper addresses these points, and describes experiments in which the temperature is increased to 100°C and the dew point of the air is set at 12°C (equivalent to 50 percent relative humidity at 23°C and 101 kPa). Estimates of the rich flammability limit and the global stretch rates at extinction for all mixtures between the lean and rich limits are also provided.

Facility Design and Operation

Figure 1 is a schematic of the experimental facility. The counterflow burner is cylindrical, about 100 mm in outside diameter and 450 mm high. The critical dimensions are the nozzle separation and the nozzle diameter, both of which are fixed at 12.0 mm±0.2 mm. Air premixed with the fuel enters the upper and lower sections of the burner. The flow is straightened and made uniform with honeycomb, fine mesh screens, and a converging nozzle with an area contraction ratio of 44:1. Nitrogen flows in a concentric annulus to quench the reactants as they escape from the flame, to prevent the flame from stabilizing on the nozzle rim, and to reduce entrainment of air. To eliminate unwanted air currents around the burner and direct the exhaust gases upward, the entire burner is enclosed within a 300-mm diameter Plexiglas tube.

The burner flanges directly exposed to the flames are water-cooled to maintain their integrity and to minimize heat transfer upstream into the reactant flow. Water flows through a copper tube coiled around the upper chamber of the burner to prevent the exhaust gases from preheating the upper section. Thermocouples are located on the centerline just upstream of the contraction nozzles to monitor the incoming mixture temperatures. Flammability measurements at temperatures above the ambient are conducted by heating the air/refrigerant mixtures and controlling the temperatures of the upper and lower burner sections.

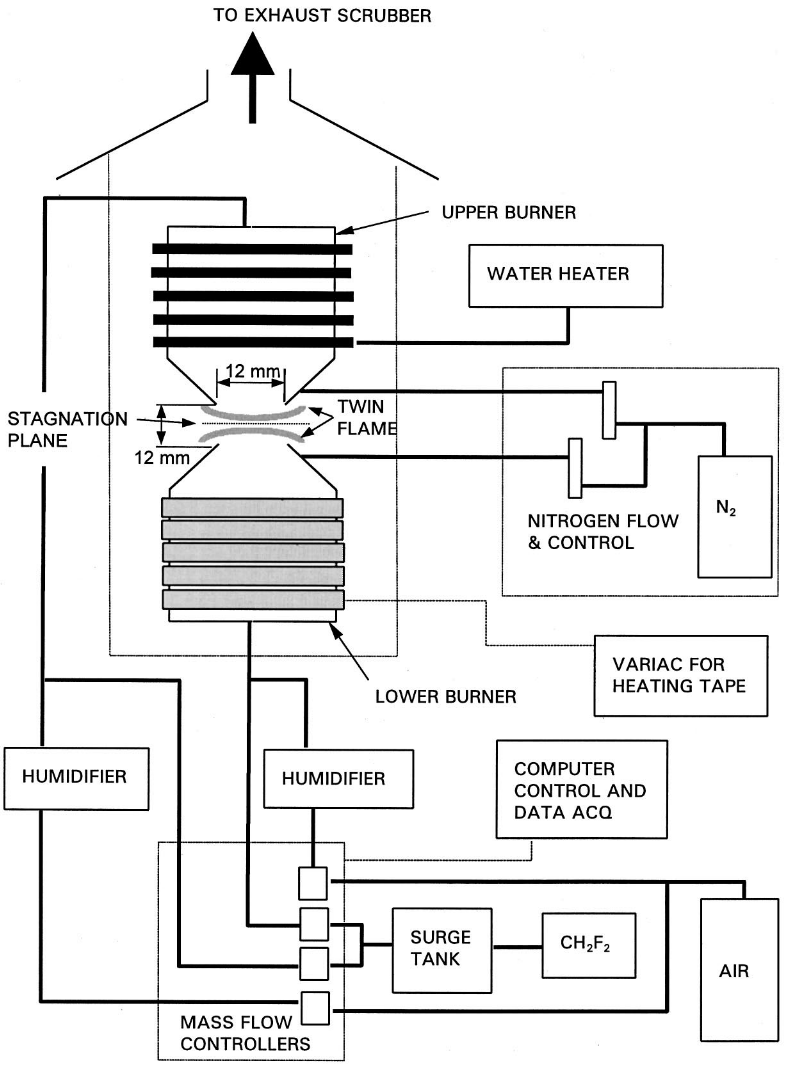

Fig. 1 Block diagram of counterflow burner experimental facility

The reactants are stored in individual pressurized cylinders. The air is certified to have a mole fraction of O_2 equal to 0.2110 ± 0.0002, with water and hydrocarbon levels below 10^{-6}. The remaining components (N_2, Ar, and CO_2) are as taken from the atmosphere. The air is routed through a humidifier prior to reaching the burner. The CH_2F_2 is a liquid at room temperature and 1.69 MPa, and is claimed by the manufacturer to contain mass fractions of water and nonvolatile residues of less than 10^{-5} and noncondensable contaminates of less than 1.5 percent by volume. The CH_2F_2 supply bottle is connected to a lower pressure expansion tank to minimize pulsation in the flow of gas. The air and the refrigerant are combined at the upper and lower sections of the burner. The concentration of gases in the mixture is maintained through electronic mass flow controllers. All flow controllers are calibrated to ± 2 percent of value with the gas used during testing. Hydrofluoric acid in the exhaust stream is removed using a water spray scrubber. Complete details of the facility design can be found in the final report by Grosshandler et al. [5].

A computer controls the flow and monitors the inlet temperatures and pressure. Either the mole fraction of fuel or the global stretch rate can be chosen as the independent experimental variable. The other then becomes the dependent parameter. Before beginning an experiment, the burner is preheated and measurements of the air humidity are taken. An initial lighting condition is chosen which is robust enough for easy ignition, but has a flow velocity greater than the flame speed to prevent flashback into the burner. Depending on the conditions, the luminescent region is 10 mm to 20 mm in diameter and the gap between the flames is about 4 mm or less. Once the flame has stabilized, the flow settings are changed in small increments to bring the conditions closer to extinction. Refer to [5] for operational details.

Experimental Results

The effect of humidity on the extinction stretch rate of close to room temperature, lean CH_2F_2 flames was determined by repeating the experiments of Womeldorf and Grosshandler [4] with air at a relative humidity of 43 percent. The dotted line in Fig. 2 is a least-squares fit of the data (solid diamonds), with the mole fraction of CH_2F_2 in the mixture plotted versus the global stretch rate at extinction. The spread in the data points is indicative of the experimental uncertainty. Mole fractions above and to the left of the line are flammable; below and to the right of the line a steady flame cannot be maintained. The dashed line in the figure represents a least-squares fit of the dry air experiments (open diamonds) conducted at the same initial temperature. The difference in the intercept of the two lines is well within the experimental uncertainty (estimated in a following section to be $\pm$ 0.004), indicating that humidity does not significantly alter the lean flammability limit. This implies that even though the H/F ratio in the

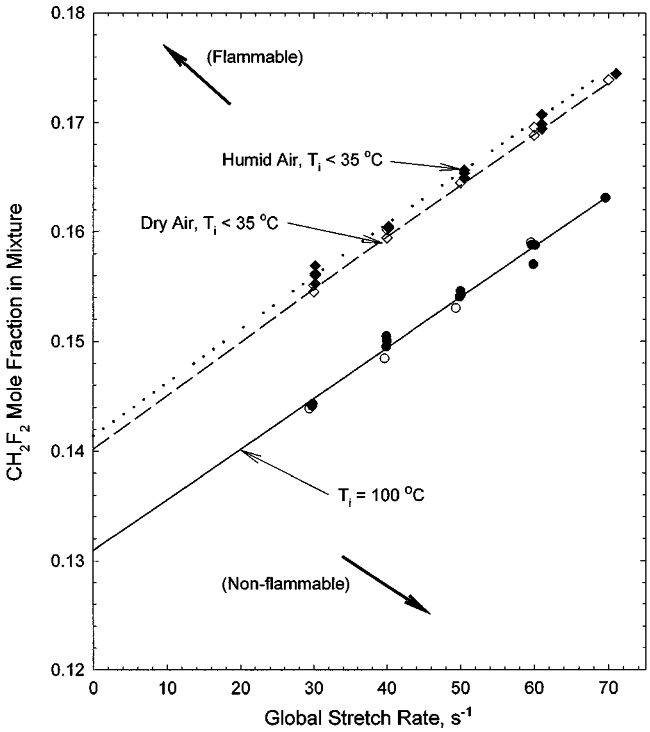

Fig. 2 Lean extinction mole fraction of CH_2F_2 in air as function of global stretch rate, comparing effect of humidity and initial temperature: solid symbols, $T_{dp}=12°C$; open symbols, dry

fuel is unity, enough water vapor is formed during combustion that the addition of more H_2O is in excess of the minimum necessary to supply the critical H and OH chain carrying radicals.

The temperature of the mixture was increased to 100°C±5°C and experiments were conducted under dry and humid conditions to assess any impact on the lean flammability limit. The dew point was maintained between 11.6°C and 13.4°C for the results plotted as the solid circles in Fig. 2. The open circles correspond to dry conditions. The solid line is a linear fit through the dry and moist data for global stretch rates between 30 and 70 s^{-1}. An extrapolation of the line to a zero stretch condition yields a lean flammability limit CH_2F_2 mole fraction of 0.131 ± 0.004. The temperature can be seen to have a measurable impact on the LFL, decreasing the lean limit almost seven percent as the initial conditions are changed from 30°C to 100°C. While the intercepts of the three curve-fits change with the temperature, the lines remain almost parallel. The slope of the extinction mole fraction versus stretch rate curves lie between 0.46 ms-mole/mole and 0.48 ms-mole/mole.

The equivalence ratio that leads to the maximum extinction stretch rate is dependent upon the fuel. For example, Law et al. [3] found that for methane/air mixtures, the highest extinction stretch rate occurs for $\Phi = 0.95$, while for propane/air mixtures, the most robust mixture is associated with an equivalence ratio near 1.20. To determine the mixture of CH_2F_2 in air that leads to the most difficult flame to extinguish, additional experiments were performed for stoichiometric and rich conditions.

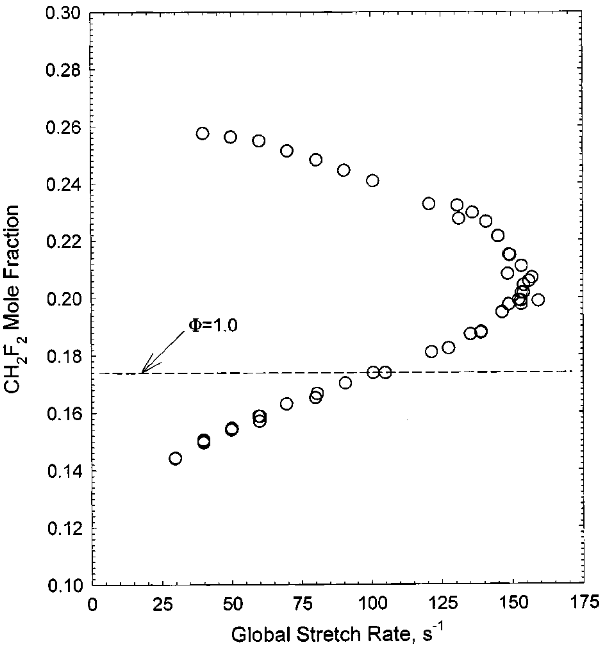

Fig. 3 Extinguishing stretch limits of CH_2F_2 in air mixtures initially at 100°C and $T_{dp}=12°C$

Figure 3 is a plot of the data, taken at a nominal temperature of 100°C and a dew point of 12°C. The lower portion of the curve, for K_g less than 70 s^{-1}, includes some of the same data shown in Fig. 2. The horizontal line corresponds to $\Phi = 1.0$ ($X_{CH2F2} = 0.1736$). It is evident that the stoichiometric condition is not the most difficult to extinguish. Operating at a CH_2F_2 mole fraction of 0.202 increases the extinction stretch rate to 156 s^{-1}, compared to 102 s^{-1} for a stoichiometric flame. The peak mole fraction corresponds to an equivalence ratio of about 1.20, which is similar to the behavior of propane/air flames. The shift to fuel-rich conditions for maximum flame stability cannot be attributed to a higher temperature since at $\Phi = 1.2$ the equilibrium adiabatic condition produces a temperature well below the peak, which occurs when $\Phi = 1.05$. The difference in equivalence ratios corresponding to peak stretch rates for propane and methane has been attributed ([3]) to the less than unity Lewis numbers (defined as the thermal diffusivity divided by the deficient reactant mass diffusivity), which occur for propane under rich conditions and for methane under lean conditions. The Lewis number for the CH_2F_2/air flame is, as for propane, less than one for rich mixtures.

The structure of rich flames is more complex than flames in lean mixtures because recombination reactions lead to multicarbon species and soot, and preferential diffusion of the H-atom is enhanced among the field of larger hydrofluorocarbon molecules. Even so, inspection of the upper branch of the flammability curve in Fig. 3 suggests that a linear extrapolation to a zero-stretch condition can yield an identifiable upper limit. A straight-line fit through the data with $X_{CH2F2} \geqslant 0.24$ has a y-intercept of 0.271; excluding data with stretch rates greater than 60 s^{-1} produces a slightly lower value, 0.263. These values are less than most of those reported in the literature, which range for ambient initial conditions from 0.269 using a flame tube and fuse wire ([6]) to 0.334 measured in the ASTM E-681 apparatus with a match ignitor ([7]).

Analysis and Discussion

Uncertainty Analysis. The measured flammability limits are subject to uncertainties from several sources, including errors in flow measurements; variations in temperature, pressure and composition; the rate at which the extinction point is approached; changes in burner geometry; and nonlinear effects near the zero-stretch rate condition. Flow calibration and measurement uncertainties were examined and described in detail by Grosshandler et al. [5]. An uncertainty in mole fraction of ±0.006, with a 95 percent confidence interval, was estimated based upon the assumed linear relation between the LFL and stretch rate, and the dependence of each on the uncertainty in measured flows. In the current work, additional mass flow controllers have been added, which are sized to operate close to the middle of their dynamic range during most of the experiments, and to allow independent control of the upper and lower burner sections. Both of these conditions lead to less uncertainty in the flow.

The impact on the uncertainty of the results caused by variations in humidity, unknown concentrations of trace species in the reactants, and variations in inlet temperature cannot be expressed in a simple mathematical expression because of the complex relationships between these parameters and the flame chemistry. The uncertainty in dew point is about ±1°C, which, based upon the measurements with and without any moisture added, is an insignificant variation. One would not expect small changes of the barometric pressure, which ranges between about 98 and 100 kPa, to affect flame stability. The average temperature of the reactants as they enter the burner nozzle varies less than 10°C, and the maximum difference in temperature between the upper and lower sections is approximately the same. Higher temperatures are known to stabilize the flame, but since the actual temperature at extinction varies in the experiment in a non-systematic way, the uncertainty in flammability limits caused by variations in reactant temperature can be reduced by replication. The high degree of repeatability of the extinction conditions indicate that such random errors are smaller than the uncertainty in flow.

The extinction process is dynamic and the response times of the electronic flow controllers and burner are nonzero. This means that the exact conditions at the nozzle exit and in the flame during the precise point of extinction are not measured. The uncertainty due to this behavior is reduced by ensuring that changes in flow conditions occur at a rate slower than the response time of the burner and control system, which is estimated from the volume of the burner and the typical flow rate to be about 10 s. The conditions at extinction are taken to be the readings just after the change in flow setting. The uncertainty can be estimated to be one half the increment between the previous and final step if the flow controllers do not overshoot the new set point. This value varies among tests, but is typically less than 0.5 percent of the recorded stretch rate or mole fraction.

The effect of intentionally changing the burner geometry on the measured LFL has been found to be significant ([5]). This is distinct from small changes due to imperfections in the burner or misalignment in assembly. The burner was disassembled for cleaning a number of times and physically relocated from one laboratory to another. No extraordinary care was taken to reassemble the nozzles precisely in the same manner each time. It is estimated that the nozzle spacing and centerline alignment could have varied by as much as 0.5 mm. (The measured separation distance ±0.2 mm was always used to compute the global stretch rate.) As long as an entire test sequence was conducted without disassembling the burner, no additional uncertainty in LFL was found distinct from the random errors associated with run-to-run variations. Table 1 lists the lean flammability limit of CH_2F_2/air mixtures found in the literature using alternative techniques. Exact temperature, pressure, and humidity were not always listed in these other studies, nor were the uncertainties quantified. However, the values of the LFL reported bracket those determined in the current study.

Nonlinear Extrapolation and Flame Radiation. The basis for assuming that the LFL can be obtained by a linear extrapolation of the extinction mole fraction to a zero-stretch condition is the satisfactory agreement between the experimental measurements and a straight-line fit to the global stretch rate. (An identical approach was used effectively by Wang et al. [8] for prevaporized benzene/air mixtures.) Although a strong correlation ($R^2 = 0.988$) is undeniable from a statistical analysis over stretch rates between about 30 and 60 s^{-1}, the critical lower stretch conditions necessary to confirm linearity are unattainable in the burner due to the presence of buoyant instabilities.

There are two major difficulties with the linear extrapolation approach: First, the global stretch rate is not equal to the local stretch rate at the flame front; and second, a microgravity study ([9]) and theoretical analysis ([10]) indicate that the approach to a zero-stretch condition is not linear, and is affected by radiation and the fuel Lewis number. The impact on the LFL of using the global stretch rate is lessened if K_g is proportional to the local stretch rate, even if the two values differ significantly in magnitude. Kobayashi and Kitano [11] found the proportionality to be about constant in their counterflow burner. Preliminary LDA measurements of the axial velocity profile led to the conclusion that the seed particles have a negative impact on the low stretch CH_2F_2/air flames, causing them to extinguish prematurely. As a result, the analysis conducted in the present paper is based upon the assumption that the global stretch rate is proportional to the local stretch rate over the range of conditions examined.

Sorhab et al. [12] established a theoretical role for radiation loss in the extinction of a gaseous diffusion flame at a stagnation point. The existence of a blow-off limit in laminar diffusion flames controlled by radiation losses under slightly stretched conditions was shown to exist by T'ien [13]. The extent to which radiation heat loss affects the zero-stretch condition in our premixed, counterflowing twin flame is investigated by first assuming that at extinction, the chemical reaction time (τ_c) is about equal to the residence time of the fluid in the flame front (τ_f), as done by Chung et al. [14]. The characteristic residence time scales with the inverse of K_g. If the reaction rate, which scales with the inverse of τ_c, is taken to be first order in CH_2F_2 and oxygen concentration and Arhenius in form, then the following empirical expression can be used to model the extinction stretch rate:

$$\text{reaction rate} \propto 1/\tau_c \approx 1/\tau_f \approx K_g \propto [CH_2F_2][O_2]\exp(-c_1/T_f), \tag{1}$$

where c_1 is an effective activation temperature and T_f is the flame temperature. The adiabatic equilibrium temperature of a lean CH_2F_2/air flame can be approximated in terms of the stoichiometric value, $T_{ad,st}$, the inlet temperature, T_i, and the mole fraction of fuel (assuming the excess air acts as a heat sink with constant specific heat):

$$T_f = T_i + (T_{ad,st} - T_i)X_{\mathrm{CH2F2}}/(0.1215X_{\mathrm{CH2F2}} + 0.1525). \tag{2}$$

The concentrations are proportional to their respective mole fractions and the molar density, which decreases with increasing inlet temperature, or

$$[CH_2F_2][O_2] \propto X_{\mathrm{CH2F2}}(1 - X_{\mathrm{CH2F2}})/T_i^2, \tag{3}$$

and Eq. (1) can be written as

$$K_g = c_2[X_{\mathrm{CH2F2}}(1 - X_{\mathrm{CH2F2}})/T_i^2]\exp(-c_1/T_f), \tag{4}$$

where c_2 is a proportionality constant.

The extinction stretch rates for the lean data shown in Fig. 3 are replotted in Fig. 4, with the best fit of Eq. (4) drawn through the points with the dot-dash line (labeled ''adiabatic, nonlinear extrapolation''). The activation temperature, c_1, and proportionality constant, c_2, are 15,900 K and 1.3×10^{11} K^2/s, respectively. Although the data match the line down to the leanest conditions attainable in the burner, following the curve to a stretch rate of zero suggests that the lower flammability limit is zero. A more useful and physically meaningful result is obtained when radiation from the flame is considered.

Treating the radiative heat loss, Q_{rad}, as a fractional decrease in enthalpy of combustion, ΔH_c, the flame temperature with heat loss, $T_{f,\mathrm{rad}}$, can be found by modifying Eq. (2) to be

$$\begin{aligned} T_{f,\mathrm{rad}} = {} & T_i + (1 - |Q_{\mathrm{rad}}/\Delta H_c|) \\ & \times [(T_{ad,st} - T_i)X_{\mathrm{CH2F2}}/(0.1215X_{\mathrm{CH2F2}} + 0.1525)]. \end{aligned} \tag{5}$$

The flame is approximated as a uniform column of optically thin gas with a height one-half its diameter, *D*. The energy radiated from the gas per unit time can be shown to be $0.5\pi D^3 \sigma k_p T_{f,\mathrm{rad}}^4$,

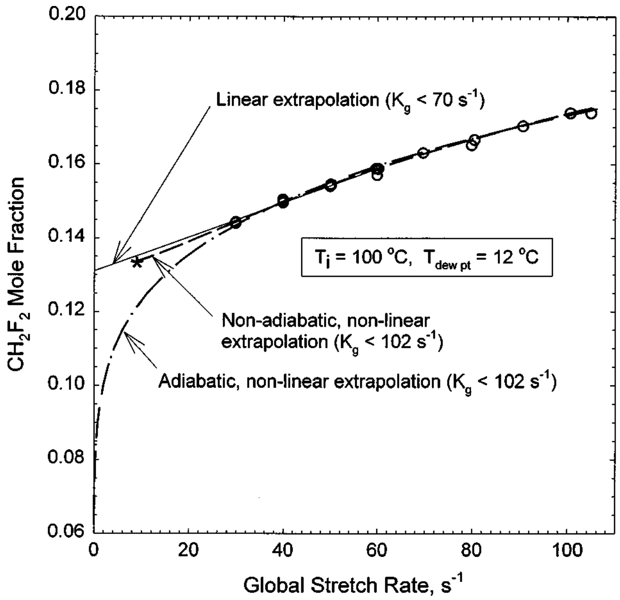

Fig. 4 Nonlinear extrapolation of CH_2F_2 extinction mole fraction to a zero-stretch flame

where k_p is the absorption coefficient and σ is the Stefan-Boltzmann constant [15]. The radiation loss in Joules per kilogram of CH_2F_2 can thus be estimated to be

$$Q_{\rm rad}=4\tau_f\sigma k_p T^4_{f,\rm rad}(RT_{f,\rm rad}/P)/(0.052X_{\rm CH2F2}). \qquad (6)$$

Equation (6) indicates that the radiation loss increases in an unbounded fashion directly with the flow time; hence, as K_g ($\approx 1/\tau_f$) approaches zero, the chemical reaction will be quenched. The absorption coefficient was estimated with RADCAL [16] from the equilibrium temperature and products assuming HF has about the same band strength as CO. It was found to vary between 0.66 m^{-1} at stoichiometric conditions and 1.12 m^{-1} when $X_{\rm CH2F2}$ equals 0.11, so a single value for k_p of 0.8 m^{-1} was chosen to be representative over the range of mole fractions. Using 373 K and 101 kPa for the initial temperature and pressure, and -9.35 MJ/$kg_{\rm CH2F2}$ for ΔH_c, the flame temperature accounting for radiative loss can thus be expressed as

$$T_{f,\rm rad}=373+[1-3.08\times10^{-17}(T^5_{f,\rm rad}/K_g)/X_{\rm CH2F2}]$$
$$\times[1838X_{\rm CH2F2}/(0.1215X_{\rm CH2F2}+0.1525)]. \qquad (7)$$

The temperature from Eq. (7) can be inserted into Eq. (4), producing the best fit to the experimental data with $c_1=12{,}000$ K and $c_2=3.1\times10^{11}$ K^2/s. The dashed line in Fig. 4, labeled ''nonadiabatic, nonlinear extrapolation,'' shows the result. Accounting for radiative heat loss does two things; first, it shifts the extinction mole fraction curve upward, and second, it demonstrates a true lower limit, as indicated by the * in Fig. 4. No solutions are mathematically obtainable for $X_{\rm CH2F2}<0.134$. The nonadiabatic, nonlinear theory predicts an LFL very close to the simple linear extrapolation (solid line in Fig. 4), validating the use of a linear extrapolation for yielding a conservative value for the LFL.

Other affects such as conduction losses, preferential diffusion, and flame distortion due to buoyancy act to move the LFL upward. (See, e.g., the series of reports by Hertzberg [17–20]). By contrast, negative flame stretch ([2]) and reabsorbed radiation ([21]) both act to widen the limits of flammability. All of these phenomena contribute to the hazard posed by the leak of a flammable fluid, and an assessment of the actual application is always required to assure safety. The LFL determined by extrapolation to the zero-stretch limit in the counterflowing flame provides an unambiguous starting point for this assessment.

Conclusion

In this work, a counterflow burner has been used to determine the extinction stretch limits of CH_2F_2/air flames for differing mixture inlet conditions. The following conclusions are made based upon the experimental results and analysis:

- An increase in relative humidity from 0 to 50 percent (based upon an air temperature of 23°C) has no measurable effect above the experimental uncertainty on the extinction limits of a lean CH_2F_2/air stretched flame.
- An increase in initial temperature from 30°C to 100°C widens the lean flammability limit in a measurable way. The LFL recommended for CH_2F_2/air (dew point of 12°C±1°C) mixtures is 0.13±0.004 when the inlet temperature is 100°C±5°C and the pressure is 99 kPa±1 kPa.
- The rich flammability limit for CH_2F_2/air at 100°C and a dew point of 12°C is estimated to lie between 0.26 and 0.29, based on linear extrapolation of a limited amount of data to a stretch rate of zero. Additional studies are required to better understand the behavior of fuel rich flames.
- The maximum extinction global stretch rate for CH_2F_2/air flames is 156±10 s^{-1} for initial mixture conditions of 100°C and a dew point of 12°C. This occurs when the mole fraction of CH_2F_2 is 0.202 ($\Phi\approx1.2$).
- If a nonlinear extrapolation to the zero-stretch condition is used and radiative loss is taken into account, the LFL at 100°C is about the same as for the linear extrapolation method (within experimental uncertainty), giving credence to the linear extrapolation technique for lean mixtures in air of fuels similar to CH_2F_2.

Acknowledgments

This work was supported by the Air-Conditioning & Refrigeration Technology Institute, MCLR Project No. 660-52401, Steven R. Szymurski program manager. The contributions of Carolyn White to the exhaust scrubber design and data taking are gratefully acknowledged.

Nomenclature

c_1 = effective activation temperature, K
c_2 = proportionality constant in Eq. (3), $K^2\ s^{-1}$
ΔH_c = enthalpy of combustion, $J/kg_{\rm fuel}$
k_p = radiative absorption coefficient, m^{-1}
K_g = global stretch rate, s^{-1}
LFL = lean flammability limit, mole fraction of fuel in mixture
P = pressure, Pa
$Q_{\rm rad}$ = radiative heat loss, $J/kg_{\rm fuel}$
R = ideal gas constant
$T_{ad,st}$ = adiabatic, equilibrium, stoichiometric flame temperature, K
T_{dp} = dew point temperature, K
T_f = flame temperature, K
$T_{f,\rm rad}$ = flame temperature with radiative cooling, K
T_i = mixture inlet temperature, K
X_i = mole fraction of species *i*
σ = Stefan-Boltzmann constant
τ_c = characteristic chemical reaction time, s
τ_f = characteristic fluid residence time, s
Φ = fuel/air equivalence ratio
[ ] = concentration of species, moles/m^3

References

[1] ASTM E 681, 1994, ''Standard Test Method for Concentration Limits of Flammability of Chemicals,'' American Society for Testing and Materials, Philadelphia, PA.
[2] Wu, C. K., and Law, C. K., 1985, ''On the Determination of Laminar Flame Speeds From Stretched Flames,'' *Twentieth Symposium (International) on Combustion*, The Combustion Institute, pp. 1941–1949.
[3] Law, C. K., Zhu, D. L., and Yu, G., 1986, ''Propagation and Extinction of

Stretched Premixed Flames,'' *Twenty-First Symposium (International) on Combustion*, The Combustion Institute, pp. 1419–1426.

[4] Womeldorf, C., and Grosshandler, W., 1999, ''Flame Extinction Limits in CH_2F_2/Air Mixtures,'' Combust. Flame, **118**, pp. 25–36.

[5] Grosshandler, W., Donnelly, M., and Womeldorf, C., 1998, ''Lean Flammability Limit as a Fundamental Refrigerant Property,'' Final Technical Report, DOE/CE/23810-98, ARTI MCLR Project No. 660-52401, Mod. 3, Aug.

[6] Dekleva, T. W., Lindley, A. A., and Powell, P., 1993, ''Flammability and Reactivity of Select HFCs and Mixtures,'' ASHRAE Trans., **35**, Dec., pp. 40–47.

[7] Richard, R. G., and Shankland, I. R., 1992, ''Flammability of Alternative Refrigerants,'' ASHRAE Trans., **34**, No. 4, pp. 20–24.

[8] Wang, C.-H., Ueng, G.-J., and Tsay, M.-S., 1998, ''An Experimental Determination of the Laminar Burning Velocities and Extinction Stretch Rates of Benzene/Air Flames,'' Combust. Flame, **113**, pp. 242–248.

[9] Maruta, K., Yoshida, M., Ju, Y., and Niioka, T., 1996, ''Experimental Study on Methane-air Premixed Flame Extinction at Small Stretch Rates in Microgravity,'' *Twenty-Sixth Symposium (International) on Combustion*, The Combustion Institute, pp. 1283–1289.

[10] Ju, Y., Guo, H., Maruta, K., and Niioka, T., 1998, ''Flame Bifurcations and Flammable Regions of Radiative Counterflow Premixed Flames With General Lewis Numbers,'' Combust. Flame, **113**, pp. 603–614.

[11] Kobayashi, H., and Kitano, M., 1991, ''Flow Fields and Extinction of Stretched Cylindrical Premixed Flames,'' Combust. Sci. Technol., **75**, pp. 227–239.

[12] Sorhab, S. H., Linan, A., and Williams, F. A., 1982, ''The Asymptotic Theory of Diffusion Flame Extinction With Radiant Loss from the Flame Zone,'' Combust. Sci. Technol., **27**, p. 143.

[13] T'ien, J. S., 1986, ''Diffusion Flame Extinction at Small Stretch Rates: The Mechanism of Radiative Loss,'' Combust. Flame, **65**, pp. 31–34.

[14] Chung, S. H., Chung, D. H., Fu, C., and Cho, P., 1996, ''Local Extinction Karlovitz Number for Premixed Flames,'' Combust. Flame, **106**, pp. 515–520.

[15] Siegel, R., and Howell, J., 1981, *Thermal Radiation Heat Transfer*, 2nd Ed., Hemisphere Publishing Corp., New York, pp. 615–620.

[16] Grosshandler, W., 1993, ''RADCAL: A Narrow-Band Model for Radiation Calculations in a Combustion Environment,'' NIST Technical Note 1402, National Institute of Standards and Technology, Gaithersburg, MD.

[17] Hertzberg, M., 1976, ''The Theory of Flammability Limits: Natural Convection,'' Bureau of Mines Report of Investigation, RI-8127.

[18] Hertzberg, M., 1980, ''The Theory of Flammability Limits: Conductive-Convective Wall Losses and Thermal Quenching,'' Bureau of Mines Report of Investigation, RI-8469.

[19] Hertzberg, M., 1982, ''The Theory of Flammability Limits: Radiative Losses and Selective Diffusional Demixing,'' Bureau of Mines Report of Investigation, RI-8607.

[20] Hertzberg, M., 1984, ''The Theory of Flammability Limits: Flow Gradient Effects and Flame Stretch,'' Bureau of Mines Report of Investigation, RI-8865.

[21] Ju, Y., Masuya, G., and Ronney, P., 1998, ''Effects of Radiative Emission and Absorption on the Propagation and Extinction of Premixed Gas Flames,'' *Twenty-Seventh Symposium (International) on Combustion*, The Combustion Institute, pp. 2619–2626.

[22] Grob, D., 1991, ''Flammability Characteristics of R-32 and R-32 Mixtures,'' *Proceedings of the Symposium to Evaluate R-32 and R-32 Mixtures in Refrigeration Applications*, Environmental Protection Agency, Washington, DC, Mar. 19–20.

[23] Ohnishi, H., 1993, ''Relationship Between Flammability and Composition Ratio of HFC-32/HFC-134a Blend,'' *Proceedings of the ASHRAE/NIST Refrigerants Conference: R-22/R-502 Alternatives*, ASHRAE, Atlanta, GA.

Modeling of Conjugate Two-Phase Heat Transfer During Depressurization of Pipelines

Y. V. Fairuzov
Senior Scientist,
Institute of Engineering,
P.O. Box 70-472,
National Autonomous University of Mexico,
Mexico City 04510, Mexico
e-mail: fairuzov@servidor.unam.mx
Assoc. Mem. ASME

Transient conjugate two-phase heat transfer during depressurization of pipelines containing flashing liquids is examined in this paper. A numerical model for transient flashing liquid flow in a pipe is formulated. The model takes into account the transient radial heat conduction and the forced convection effects. Numerical simulation of flashing two-component (propane and butane) flow is performed in order to investigate the effect of wall friction on the heat transfer conditions in the pipe. The simulation results are compared with predictions of the model that are based on a new formulation of energy equation proposed by the author in an early study. A comparison of the results obtained allows one to determine the range of applicability of the new energy equation formulation. A procedure is proposed for choosing an appropriate model for predicting transient conjugate two-phase heat transfer during releases of flashing liquids from pipes. A criterion of thermodynamic similarity for flashing liquids flows in pipes or channels is formulated. The proposed criterion provides the basis for selecting model fluids and for constructing experimental models of systems containing flashing (volatile) liquids with scaled thermodynamic conditions. An example of its use is given. [S0022-1481(00)02001-6]

Keywords: Conjugate, Heat Transfer, Modeling, Two-Phase, Unsteady

Introduction

The depressurization (blowdown) of a pipeline conveying a flashing (volatile) liquid may lead to a significant drop in the fluid temperature. The temperature difference between the flashing liquid flowing through the pipeline and the pipe wall, produced in this process, causes the transfer of energy stored in the wall to the fluid. In many technical applications, the pipe wall has a finite thickness and the thermal boundary condition is known at the outer surface of the wall. This situation presents a conjugate heat-transfer problem since the heat transfer rate at the wall-fluid interface and local fluid conditions are not known a priori, and therefore need to be simultaneously calculated.

A growing number of multiphase technology applications in the petroleum, chemical, aerospace, power, and process industries stimulate the development of reliable methods for analyzing transient processes in two-phase systems in which the temperature field in the moving fluid and the temperature field in the bounding walls are directly dependent on each other. Examples of such types of processes include; controlled or accidental blowdowns of subsea oil/gas pipelines, the loss of coolant accident in a nuclear power plant, and release of highly volatile multicomponent liquids during accidents in chemical plants.

Much research has been carried out to investigate the conjugate heat transfer in single-phase flows. Existing methods of solving the problem include exact, approximate, and numerical techniques. The early attempts to treat the problem are based on the exact and approximate methods, in which simplifying assumptions are made regarding the thermal capacity of the fluid, the thermal capacity, and conductivity of the wall ([1–3]). The most rigorous mathematical formulation of the problem ([4]) takes into account the radial heat conduction, the axial heat conduction, and the thermal capacity effects both in the fluid and in the pipe wall. In this case, the governing equations both for the fluid flow and for the pipe wall are solved numerically.

Solving the problem of the conjugate heat transfer in a flashing liquid flow is a complex task because of the difficulties associated with modeling of the forced convection under two-phase flow conditions. The traditional approach to solving the two-phase conjugate heat transfer problem is based on experimental correlations for boiling heat transfer and a numerical model of transient heat conduction in the wall. The fluid flow is modeled by a system of equations for two-phase flow, in which the energy equation includes a source term governing the wall-to-fluid heat transfer. The transient heat conduction in the walls that bounds the flow is modeled by the heat conduction equation. Many two-phase heat transfer correlations have been proposed for forced-convection boiling (for example, Chen [5], Klimenko [6], and Shah [7]). Unlike the boiling process in which the change of phase is the result of heating of the fluid, flashing of the liquid occurs due to its depressurization. The issue regarding the applicability of the boiling heat transfer correlations to the prediction of forced convection in flashing liquid flows has not been studied.

Fairuzov [8] proposed a new approach to solving the problem of transient conjugate heat transfer in flashing liquid flows. This approach is based on the assumption that the pipe wall and fluid flow are in local thermal equilibrium. The energy equation is formulated for a control volume comprising an element of the fluid and an adjoining element of the pipe wall. The effect of thermal capacity of the wall is incorporated into the energy equation for the fluid flow in the form of an additional term. Hence, a model based on this approach does not require predicting the heat conduction within the pipe wall in order to take the wall-to-fluid heat transfer into account. This enables one to simplify the governing equations and reduce significantly the computer running time. More recently Fairuzov [9] found a numerical solution for the blowdown problem based on the modified energy equation and introduced a dimensionless parameter, the factor of adiabaticity of flashing flow or Fa, that governs the effect of the pipe-wall thermal capacity on the two-phase flow behavior. This parameter allows one to quantify the departure from adiabatic conditions caused by the transfer of heat from the wall to the flow. For a single-component flashing liquid flowing through a channel of cross-section area A bounded by a wall of cross-section area A_w, the factor of adiabaticity is defined as

---

Contributed by the Heat Transfer Division for publication in the JOURNAL OF HEAT TRANSFER. Manuscript received by the Heat Transfer Division, Apr. 26, 1999; revision received, Oct. 7, 1999. Associate Technical Editor: C. Beckermann.

$$\mathrm{Fa}=\frac{\rho_w c_w T v_{fg} A_w}{h_{fg} A}. \qquad (1)$$

According to Eq. (1), Fa provides a measure of the energy stored in the pipe wall (the reference temperature is (absolute) zero) relative to the energy required for vaporizing the liquid by means of its depressurization. The temperature of the fluid in Eq. (1) must be in Kelvin.

The formulation of energy equation proposed in a previous article ([9]) provides a simple and convenient method for solving transient conjugate two-phase heat-transfer problems. This is particularly true for flashing liquid flows bounded by solids of complicated shape. However, the assumption of local thermal equilibrium underlying the proposed formulation is not always valid. The effects of two-phase forced convection and transient heat conduction in the wall may result in a large local temperature difference between the flow and the pipe wall. Hence, it is very important to determine under what conditions the new formulation may be used with reasonable accuracy.

In this paper, a numerical model for transient flashing liquid flow is formulated. The model rigorously takes into account the transient radial heat conduction and the forced convection effects. Numerical simulation of flashing two-component (propane and butane) flow is performed. The effect of wall friction on the heat transfer condition is studied and the range of applicability of the solution based on the modified energy equation is determined. Relying on the results obtained in this study, a procedure is proposed for choosing an appropriate model for predicting transient conjugate two-phase heat transfer during release of flashing liquids from pipes. A criterion of thermodynamic similarity of flashing flows that interchange heat with solids, which bound these flows, is formulated.

Formulation of the Problem

The problem considered in this study is schematically shown in Fig. 1. A horizontal pipeline of internal radius R_i and length L has the thickness of the pipe wall δ. The pipeline is filled with flashing liquid at a high pressure ($p>p_a$). Initially, the fluid and the pipe wall are at a uniform temperature, and both ends of the pipeline are closed. At $t=0$, a rupture or valve opening at one of the ends of the pipeline initiates a depressurization process. The other end of the pipeline remains closed. A detailed description of physical processes occurring during the pipeline blowdown is given by Richardson and Saville [10] and Fairuzov [8]. The depressurization process is divided into three stages: (1) depressurization wave propagation in single-phase liquid flow that may be accompanied by pressure undershoot, (2) flashing boundary propagation, and (3) two-phase discharge that is characterized by continuous changes of the flow pattern and two-phase choking at the open end.

For long pipelines, modeling of depressurization wave propagation is usually of no real practical significance, unless the effects of fluid–structure interaction have to be accounted for. In this paper, only the second and third stages of blowdown are considered using two mathematical models. The assumptions underlying each model and basic equations are presented in the next two sections.

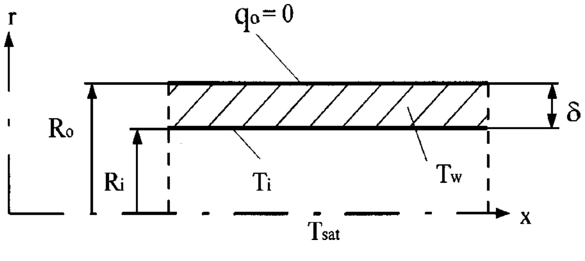

Fig. 1 Conjugate two-phase heat-transfer problem

Solution Based on a Rigorous Conjugate Heat Transfer Model

The model of pipeline blowdown based on the rigorous approach to the conjugate two-phase transfer has been divided into two parts: the hydrodynamic model and the heat transfer model. These individual models are discussed below.

Hydrodynamic Model. The hydrodynamic model describes transient, flashing liquid flow in the pipeline. The homogeneous equilibrium model is used here to formulate the hydrodynamic model. The applicability of the homogeneous equilibrium theory to the analysis of two-phase flows in long horizontal pipes is discussed in a number of papers, for example, Wallis [11] and Chen et al. [12].

The governing equations are written as follows:

continuity equation

$$\frac{\partial\rho}{\partial t}+\frac{\partial}{\partial x}(\rho V)=0 \qquad (2)$$

momentum equation

$$\frac{\partial V}{\partial t}+V\frac{\partial V}{\partial x}=-\frac{1}{\rho}\frac{\partial p}{\partial x}-KV|V| \qquad (3)$$

energy equation

$$\frac{\partial(\rho h)}{\partial t}-\frac{\partial p}{\partial t}+\frac{\partial}{\partial x}(\rho h V)-V\frac{\partial p}{\partial x}=q \qquad (4)$$

equation of state

$$\rho=\rho(p,h,z_1,z_2,\ldots,z_{M-1}). \qquad (5)$$

A computer program for predicting multicomponent vapor–liquid equilibrium (the EQFASES computer package, Solorzano et al. [13]), based on a cubic equation of state (the Redlich–Kwong–Soave equation) and separate liquid-phase correlations, is used for the pressure-enthalpy flash calculation. The error in property estimates is less then two percent.

Closure Relationships. The closure of the system of governing equations of the hydrodynamic model requires the specification of constitutive relationships for the wall friction term K and the heat source term q.

The wall friction term K is estimated using the two-phase friction multiplier correlation based on the McAdams et al. [14] expression for the two-phase mean viscosity and the Colebrook correlation for single-phase friction factor.

The heat source term in the energy equation is assumed to be of the form

$$q=\frac{4h(T_i-T_{\mathrm{sat}})}{D}. \qquad (6)$$

The published literature on forced convection boiling of multicomponent mixtures is very limited. Collier [15] proposed to modify the calculation of the nucleate boiling contribution in the well-known Chen correlation based on the procedure proposed by Stephan and Korner [16] for pool boiling in order to account for the presence in a multicomponent mixture of several components having different volatility. He also proposed a correlation for predicting the convective heat transfer contribution for multicomponent mixtures. However, the Chen correlation is valid only for situations where the internal surface of the pipe wall remains wet. Therefore, the application of the modified Chen correlation for two-phase flows in horizontal pipes, in which phase segregation can occur, may result in inaccurate predictions of wall-to-fluid heat transfer rate. Because of lack of information on heat transfer under flashing conditions, the correlation proposed by Shah [7] for boiling heat transfer in single-component two-phase flow has been used here to estimate h. This correlation has the advantage that it can be applied to partially stratified flows in horizontal channels.

Initial and Boundary Conditions for Hydrodynamic Model. The boundary conditions for the hydrodynamic model are (for $t > 0$)

at the closed end

$$x=0\colon \quad G=0;$$

at the open end

$$x=L\colon \quad \begin{aligned} G&=G_{\mathrm{cr}} \quad \text{if } p \geqslant p_{\mathrm{cr}} \\ p&=p_a \quad \text{if } p < p_{\mathrm{cr}} \end{aligned} \tag{7}$$

where P_{cr} is critical pressure calculated by the choked flow model ([8]).

The initial conditions are at $t=0$, for $0<x<L$:

$$V=0, \ p=p_i, \ T=T_a. \tag{8}$$

Heat Transfer Model. The heat transfer model describes the transient heat conduction in the pipe wall. The heat conduction equation for an infinitely long, hollow cylinder can be written in the following form:

$$\rho_w c_w \frac{\partial T_w}{\partial t} = \frac{1}{r}\frac{\partial}{\partial r}\left(r k_w \frac{\partial T_w}{\partial r}\right). \tag{9}$$

If the axial temperature gradient in the pipe wall is not negligible, for example, in a short pipe with an orifice plate producing large fluid pressure (and hence, temperature) difference, a two-dimensional formulation of Eq. (9) should be used.

The pipeline is divided into a number of segments. Each pipe segment has the same length as an adjoining fluid element. Equation (9) is solved for each pipe segment to calculate the radial temperature distribution and heat flux at the wall-fluid interface.

Initial and Boundary Conditions for Heat Transfer Model. The boundary conditions for the heat transfer model are specified at the wall-fluid interface and at the outer surface of the pipe wall. The temperature is prescribed at the wall-fluid interface at $r=R_i$, for $t>0$

$$T_w=T_i. \tag{10}$$

The external heat transfer between the pipeline and surroundings is assumed to be negligible (the pipeline is isolated from the surroundings): at $r=R_0$, for $t>0$

$$q_O=0. \tag{11}$$

Initial condition for the heat transfer model is at $t=0$, for $R_0 > r > R_i$

$$T_w=T_a \tag{12}$$

Coupling Hydrodynamic Model With Heat Transfer Model. The energy balance equation is used to couple the hydrodynamic model with the heat transfer model. The amount of heat conducted to the wall-fluid interface must be equal to the amount of heat removed from the pipe wall by the fluid flowing through the pipeline. The energy balance can be formulated in the following form:

$$k_w \left.\frac{\partial T_w}{\partial r}\right|_{r=R_i} = q\frac{D}{4}. \tag{13}$$

The temperature gradient on the left-hand side of Eq. (13) is calculated numerically.

Equation (13) is a nonlinear equation in one unknown, the temperature at the wall-fluid interface T_i. It has been brought into the standard form $f(x)=0$ and solved numerically using the Newton-Raphson method.

Solution Based on Modified Energy Equation

The modified energy equation for a single-component flashing liquid in a pipe can be written as follows ([9]):

$$\frac{\partial(\rho h)}{\partial t} + (\mathrm{Fa}-1)\frac{\partial p}{\partial t} + \frac{\partial}{\partial x}(\rho h V) - V\frac{\partial p}{\partial x} = q \tag{14}$$

where

$$\mathrm{Fa} = \frac{4\rho_w c_w T v_{fg}}{h_{fg}}\left[\frac{\delta}{D} + \left(\frac{\delta}{D}\right)^2\right]. \tag{15}$$

For a multicomponent mixture, Eq. (14) takes the following form:

$$(1+\mathrm{Fa}_2)\frac{\partial(\rho h)}{\partial t} + (\mathrm{Fa}_1-1)\frac{\partial p}{\partial t} + \frac{\partial}{\partial x}(\rho h V) - V\frac{\partial p}{\partial x} = q \tag{16}$$

where

$$\mathrm{Fa}_1 = 4\rho_w c_w \left(\frac{\partial T}{\partial p}\right)_{\rho h}\left[\frac{\delta}{D} + \left(\frac{\delta}{D}\right)^2\right] \tag{17}$$

$$\mathrm{Fa}_2 = 4\rho_w c_w \left(\frac{\partial T}{\partial \rho h}\right)_{p}\left[\frac{\delta}{D} + \left(\frac{\delta}{D}\right)^2\right]. \tag{18}$$

The continuity and momentum equations are the same as in the model described in the preceding section. To take the slip between the phases into account this formulation of the energy equation, Eqs. (14) or (16), can be extended to the other models of two-phase flow (for example the drift-flux model).

Numerical Methods

In this section, a brief description of the numerical methods that were used for solving the equations of the hydrodynamic model and the heat transfer model is given.

Numerical Method for Hydrodynamic Model. The system of partial differential equations, Eqs. (2), (3), (4), or (14), is solved using the RELAP5 numerical solution scheme ([17]). The method is based on replacing the system of differential equations with a system of finite difference equations, which are partially implicit in time. The scalar quantities (pressure, density, enthalpy) are obtained at the cell centers, and vector quantities are defined at the cell boundaries, as shown in Fig. 2. All implicit terms are linear in the new time variables.

The finite difference equations for the partially implicit method are

$$\rho_i^{n+1} - \rho_i^n = \frac{\Delta t}{\Delta x}\left[(\rho^n V^{n+1})_{i-(1/2)} - (\rho^n V^{n+1})_{i+(1/2)}\right] \tag{19}$$

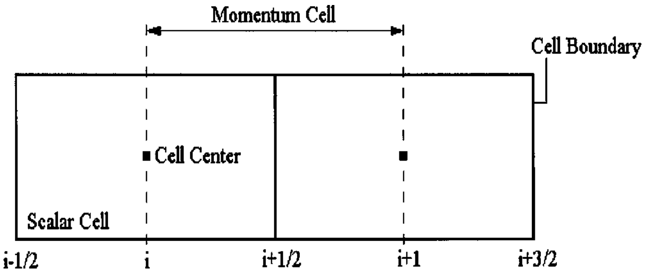

Fig. 2 Staggered difference scheme used for hydrodynamic model

$$\frac{V^{n+1}_{i+(1/2)}-V^{n}_{i+(1/2)}}{\Delta t}=-V^{n}_{i+(1/2)}\left(\frac{V^{n}_{i+1}-V^{n}_{i}}{\Delta x}\right)-\frac{1}{\rho^{n}_{i+(1/2)}}\,\frac{P^{n+1}_{i+1}-P^{n+1}_{i}}{\Delta x}-K^{n}_{i+(1/2)}V^{n+1}_{i+(1/2)}|V^{n}_{i+(1/2)}| \tag{20}$$

$$\frac{(\rho h)^{n+1}_{i}-(\rho h)^{n}_{i}}{\Delta t}+(\mathrm{Fa}-1)^{n}_{i}\frac{p^{n+1}_{i}-p^{n}_{i}}{\Delta t}+\frac{(\rho h)^{n}_{i+(1/2)}V^{n+1}_{i+(1/2)}-(\rho h)^{n}_{i-(1/2)}V^{n+1}_{i-(1/2)}}{\Delta x}-V^{n}_{i}\frac{P^{n+1}_{i+(1/2)}-P^{n+1}_{i-(1/2)}}{\Delta x}=q^{n}_{i}\,. \tag{21}$$

To ensure stability of the numerical scheme, a donor formulation is used to compute the scalar quantities at cell boundaries where they are now defined

$$\Phi_{i+(1/2)}=\frac{1}{2}(\Phi_i+\Phi_{i+1})+\frac{V_{i+(1/2)}}{|(V_{i+(1/2)})|}(\Phi_i-\Phi_{i+1}) \tag{22}$$

where

$$\Phi_{i+(1/2)}=\{\rho_{i+(1/2)},(\rho h)_{i+(1/2)}\}.$$

A donorlike formulation is used to define the momentum flux term in the momentum equation

$$V_{i+1}-V_i=\begin{cases}V_{i+(1/2)}-V_{i-(1/2)},V_{i+(1/2)}\geqslant 0\\ V_{i+(3/2)}-V_{i+(1/2)},V_{i+(1/2)}<0.\end{cases} \tag{23}$$

The finite difference equations (19)–(21) contain four unknowns: ρ^{n+1}_i, $(\rho h)^{n+1}_i$, p^{n+1}_i, and $V^{n+1}_{i+(1/2)}$. The forth equation needed for closure is the equation of state, Eq. (5). A Taylor-series expansion about old time-step values yields

$$\rho^{n+1}_i=\rho^n_i+\left(\frac{\partial\rho}{\partial p}\right)^n_{\rho h}(p^{n+1}_i-p^n_i)+\left(\frac{\partial\rho}{\partial\rho h}\right)^n_p[(\rho h)^{n+1}_i-(\rho h)^n_i]. \tag{24}$$

The system of algebraic Eqs. (19)–(21) and Eq. (24) can be reduced to a single finite difference equation for the new time pressure values

$$b_i p^{n+1}_{i-1}+a_i p^{n+1}_i+c_i p^{n+1}_i=s^n_i\,. \tag{25}$$

Equation (25) is written for N cells of the mesh. The resulting $N\times N$ system of algebraic equations is solved using the Thomas algorithm. After the new pressure values have been calculated, all remaining variables are evaluated by back substitution. Twenty-five mesh cells were used in the numerical simulations. A further increase in the number of cells did not have a significant influence on the results of calculations. The time-step was limited by the material Courant condition

$$\Delta t<\min\left|\frac{\Delta x_{i+(1/2)}}{V_{i+(1/2)}}\right|. \tag{26}$$

Numerical Method for Heat Transfer Model. The transient heat conduction equation for each pipe segment is solved numerically. A control volume formulation ([18]) is employed to obtain a system of discretized equations describing transient heat conduction in the radial direction. The control volume formulation provides the overall balance between the heat fluxes and sources (sinks) for any number of grid points. This circumstance is very important for an accurate prediction of the heat flux at the wall-fluid interface in the study of the effect of the pipe wall on flow behavior. The solution of the discretized equations was obtained by using the Thomas algorithm. A grid with 25 cells was used for each pipe segment. A time step of 0.01 s was used for both the heat-transfer model and for the hydrodynamic model.

Results and Discussion

Model Validation. The model based on the rigorous conjugate two-phase heat transfer calculation has been validated using the experimental data of Tam and Cowley [19]. Although some of the parameters, such as the wall roughness, pipe-wall thickness, and uncertainty in the mixture composition, are not reported by Tam and Cowley [19], the results of their experiments include a complete set of transient measurements of the (instantaneous) fluid mass in the pipeline (inventory), void fraction, fluid pressure, and temperature at ten different locations along the pipe. Fluid temperatures were measured by ten thermocouples with time constants of 50 ms. A more detailed description of the experiments can be found in the works by Chen et al. [12], and Richardson and Saville [20]. Blowdown conditions of the experiments conducted by Tam and Cowley [19] are summarized in Table 1. Because of the lack of experimental data for longer pipelines, these data have been used to validate the solution based on the new formulation of energy equation ([9]). To obtain a good agreement between the data and the solution based on the modified energy equation, an additional parameter (the thickness of the thermally penetrated layer) has been introduced in the above-mentioned article. This was done because in the experiments thermal equilibrium between the fluid flow and the pipe wall was not achieved. The rigorous calculation of heat transfer in the pipeline allows one to obtain good agreement between predicted and measured values of the fluid temperature at the closed end without any adjustment, as shown in Fig. 3. As Tam and Cowly do not report on the schedule of the steel pipe used in their experiments, the calculations have been carried out for two possible values of wall thickness (accord-

Table 1 Summary of blowdown test conditions

Length, m	100 (horizontal)
Diameter, m	0.15
Wall thickness, m	0.0063 and 0.0088 (assumed)
Roughness, mm	0.05 (assumed)
Fluid	LPG
Overall mixture composition	95mole% propane and 5mole% butane (assumed)
Initial fluid pressure, bar	11.25
Initial fluid temperature, K	293.05
Ambient pressure, bar	1.013
Size of the rupture	Full-bore
Density of steel, kg/m^3	7,801
Thermal conductivity of steel, W/(m K)	43
Thermal capacity of steel, J/(kg K)	473

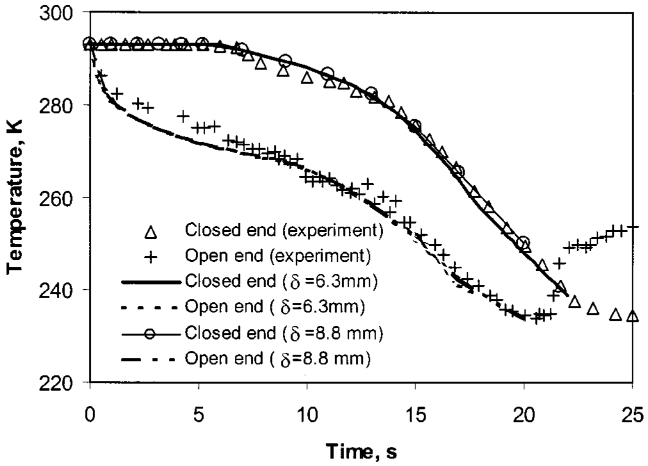

Fig. 3 Temperature histories at closed and open ends of pipeline

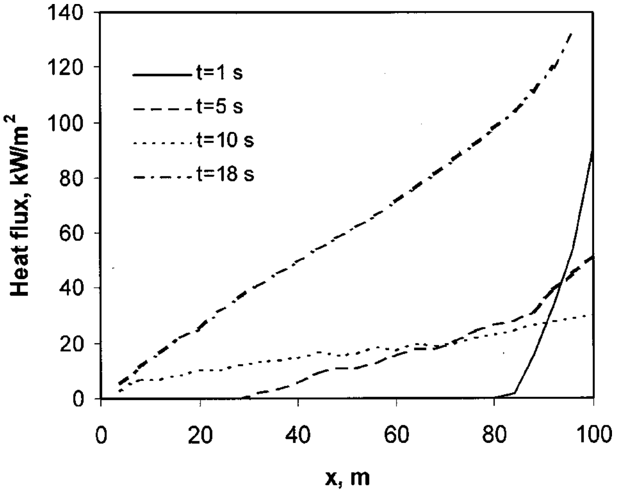

Fig. 4 Predicted heat fluxes

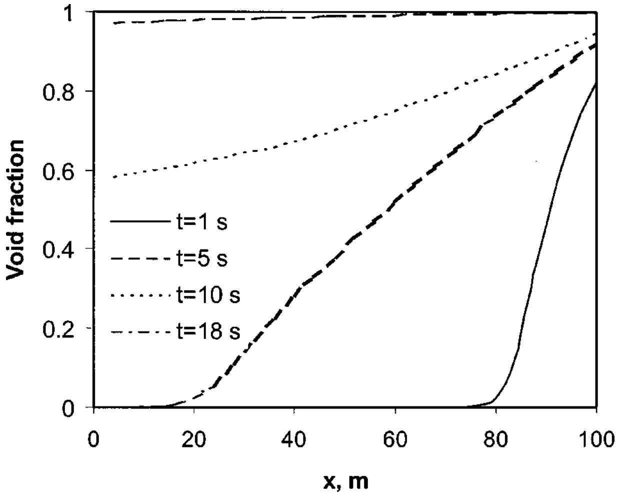

Fig. 6 Predicted transient void fraction profiles

ing to ISO 336-1974 and BS-3600-1973) of a pipe 150 mm in diameter, namely 6.3 and 8.8 mm. Agreement between the predictions and the experiment is good in both cases.

Figures 4–7 illustrate the predicted heat fluxes, transient mass velocity profiles, void fraction profiles, and temperature distributions within the pipe segments adjoining the closed and open end of the pipeline, respectively. After 5 s, the flashing front has not yet reached the closed end (Fig. 6) and therefore, the fluid temperature and the wall temperature are unchanged at this location of the pipe (Fig. 7). At the open end, the flashing process results in a significant fluid temperature drop. The wall temperature drops less quickly than the fluid temperature because of the finite thermal conductivity of the wall and the short time of the fluid release. The test pipeline is relatively short. The rate of the fluid temperature decay is so high that the thermal equilibrium within pipe wall is not achieved. At 18 s, the temperature difference between the inner and outer surfaces of the pipe reaches 10 K. The closed end of the pipe starts to ''feel'' the drop in fluid temperature only by the end of the blowdown process (Fig. 7). This occurs for the following two reasons. First, according to Fig. 3 the closed end of the pipe is exposed to a low fluid temperature during a very short period of time (approximately 15 s). Second, the flow velocity at the closed end is significantly smaller than at the open end (Fig. 5). This leads to a low heat transfer rate (Fig. 4) and, consequently, to a large temperature difference between the fluid and the internal surface of the pipe.

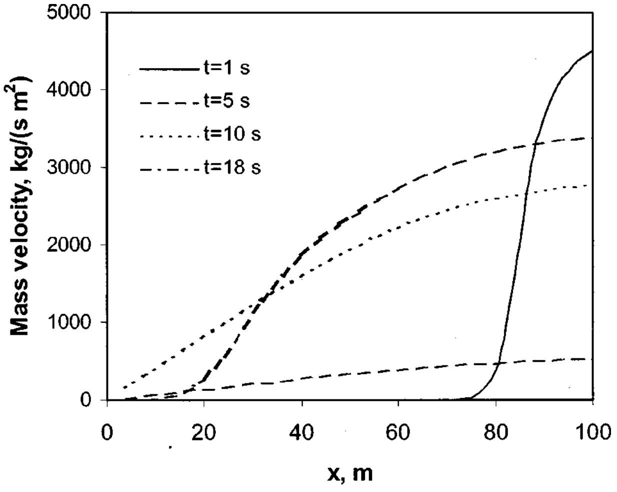

Fig. 5 Predicted transient mass velocity profiles

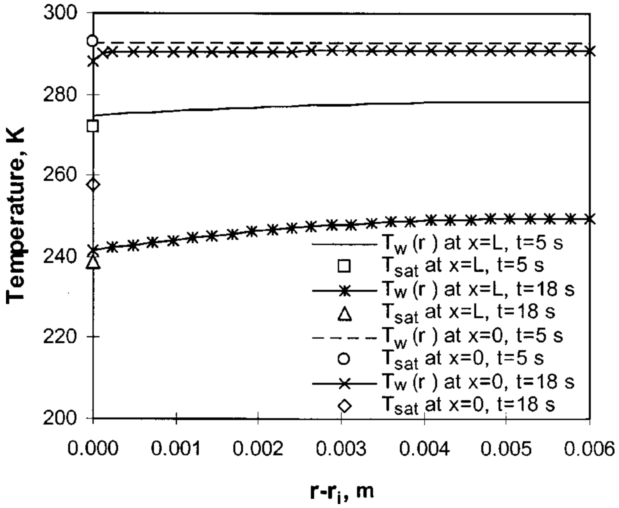

Fig. 7 Transient temperature distributions in the pipe wall at open and closed ends

Effect of Friction on Heat Transfer Conditions. The applicability of the flashing flow model based on the modified energy equation (Eq. (14)) depends on the ratio between characteristic times of two processes: the fluid temperature decay and transient heat conduction in the wall. Wall friction in single-phase flow is usually characterized by the fL/D ratio. The frictional pressure drop in two-phase flow is governed by a larger number of parameters (void fraction, flow pattern, etc.). The prediction of two-phase pressure drop relies on the calculation of the friction coefficient for liquid or both phases (for example, the homogeneous model or the Lockhart-Martinelli correlation) and on the prediction of some two-phase multiplier. Furthermore, due to large flow acceleration during blowdown motion of both phases occurs in the region dominated by wall roughness. Hence, the single-phase friction coefficients are functions of roughness only. Therefore, the range of applicability of the new formulation is found here in terms of fL/D ratio, one of the most important parameters affecting the wall friction. Another parameter affecting the depressur-

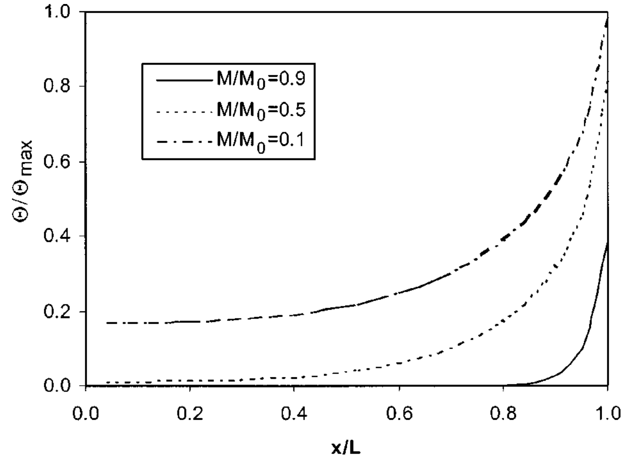

Fig. 8 Transient temperature profiles along pipeline based on the new energy equation formulation, *fL/D*=200

ization rate is the area through which the fluid discharge is carried out. The present study is limited by the analysis of full-bore ruptures.

The characteristic time of the heat transfer process within the wall is the time required to achieve a new steady-state temperature distribution after a sudden change of temperature or heat flux at the wall-to-fluid interface. This time depends on the pipe geometry, thermodynamic, and transport properties of the wall material. In this paper, a typical pipeline used in the transport of flashing hydrocarbon mixtures is considered. The pipe is assumed to be made of one percent carbon steel and has the δ/D ratio of 0.04.

Figure 8 shows transient temperature distributions along the pipeline predicted by a model that assumes local thermal equilibrium for $fL/D=200$, Fa$=117$ at T_{sat} ($P_a=1.013$ bar) of 232.6 K. The fluid in the pipeline is the LPG containing 95 mole percent propane and 5 mole percent butane. The results of calculations are presented in terms of the ratio between the local temperature drop and the maximum temperature drop (the difference between the initial temperature and the saturation temperature corresponding to ambient pressure)

$$\frac{\theta}{\theta_{\max}}=\frac{T_0-T}{T_0-T_{\text{sat}}(p_a)} \tag{27}$$

at the initial ($M/M_0=0.9,\tau=0.025$), middle ($M/M_0=0.5,\tau=0.29$), and final ($M/M_0=0.1,\tau=0.75$) stages of the depressurization process.

The same depressurization process has been modeled using the model based on the rigorous heat-transfer calculation. Figure 9 shows the discrepancies in the temperature predictions based on these two models for the two-phase flow (legend ''fluid''), wall-to-fluid interface and outer surface of the pipe wall. These results are presented in terms of ''relative error:'' $(T_r-T_e)/\theta_{\max}\times 100$ percent. As can be observed, the state of the pipe wall and the fluid is not far from thermal equilibrium. The error in the prediction of outer surface temperature associated with the assumption of thermal local equilibrium is less than two percent (<1 K, $M/M_0=0.5,\tau=0.29$). The discrepancy between the predictions of the fluid temperature does not exceed 0.3 percent. The exceptions are two regions. Near the pipe exit at the beginning of blowdown thermal equilibrium is not achieved ($M/M_0=0.9,\tau=0.025$). In a small region near the closed end of the pipeline at the end of the blowdown low fluid flow velocities result in small heat transfer rates and, consequently, in a nonzero temperature difference between the fluid and the internal surface of the pipe wall ($M/M_0=0.1,\tau=0.75$). However, the maximum discrepancy does not exceed six percent of the maximum possible temperature drop (that is 3 K) in the case considered and the length of pipe sections, where the temperature differences are not negligible, are very short compared to the total length of the pipeline (less than six percent). Furthermore, taking into account that uncertainties of known convective two-phase heat transfer correlations are at least 20 percent, the predictions based on the model that assumes local

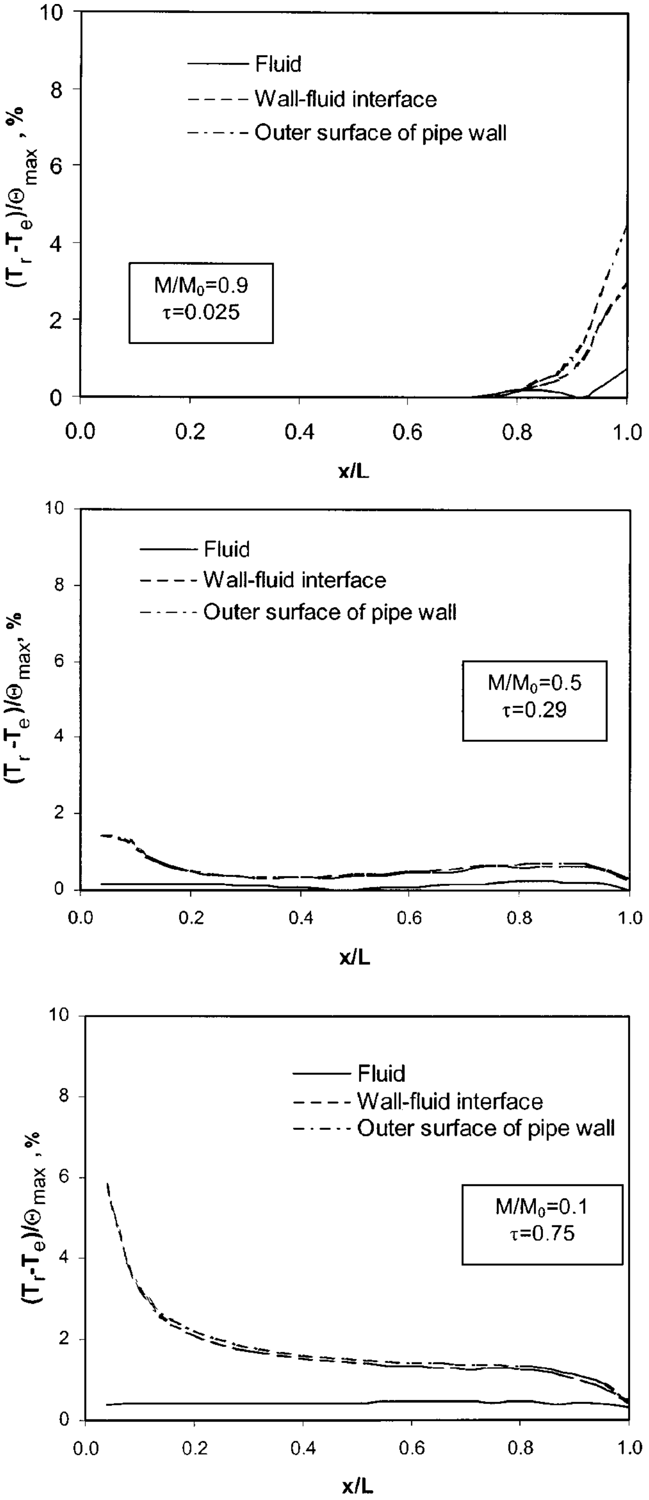

Fig. 9 Discrepancy in the predictions of temperature between the simplified and rigorous heat-transfer models, *fL/D*=200

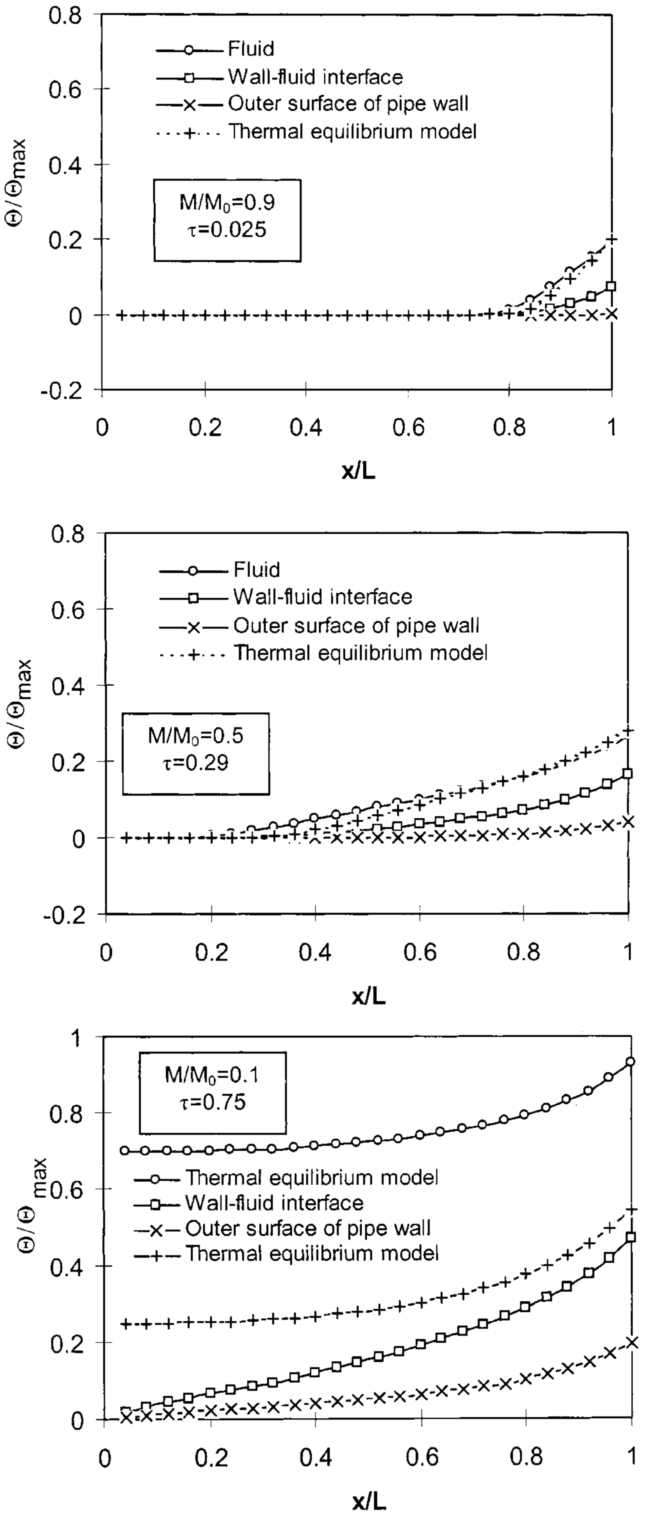

Fig. 10 Comparison of temperature distributions along pipeline predicted by simplified and rigorous heat-transfer models, $fL/D=2$

thermal equilibrium in many cases will be in the range of uncertainty of much more complex rigorous conjugate two-phase heat transfer models.

Similar numerical simulations were carried out for a short pipe ($fL/D=2$). All other blowdown conditions are the same as in the preceding case. The results obtained are shown in Fig. 10. Contrary to the previous case, the local temperature differences between the fluid and the wall are not negligible from the very beginning of the depressurization process. Moreover, they become very large by the end of the blowdown ($M/M_0=0.1, \tau=0.75$). The blowdown time is too small to achieve the thermal equilibrium between the fluid and the wall. Hence, the model based on the local thermal equilibrium assumption is not appropriate for short pipes.

The Use of the Factor of Adiabaticity. Problems of the prediction of transient two-phase flows and heat transfer often arise in the design and operation of system containing flashing liquids (for example, processes of startup, shutdown, controlled or accidental blowdowns in such systems). Based on the results of present study the following procedure for choosing an appropriate model of conjugate two-phase heat transfer can be suggested. The first step in the analysis should be calculating Fa. If Fa is much less than unity the problem can be solved with high accuracy by neglecting the wall-to-fluid heat transfer. As Fa increases with a decrease in the fluid temperature, to ensure the condition $\mathrm{Fa} \ll 1$ during the whole blowdown process, it should be calculated at the minimum temperature that can be produced by the fluid depressurization, for example at $T_{\mathrm{sat}}(P_a)$. For large values of Fa, the effect of thermal capacity of the pipe wall must be accounted for. In this case, two solutions can be used. For long pipes ($fL/D > 10^2$), the simplified formulation can be applied with reasonable accuracy. For short pipes, an analysis based on rigorous conjugate heat transfer calculations should be done.

The dimensionless parameter Fa can also be useful in formulating scaling (modeling) laws in order to generalize experimental data. Consider a two-phase system in which blowdown from a long copper pipe occurs during its operation. If the design of this system requires experimental validation, in the test facility used for this purpose the copper pipe (pipe 1) can be replace by a less expensive pipe (of the same length and internal diameter) made of carbon steel (pipe 2) ensuring that

$$\left(\frac{\rho_w c_w T v_{fg} A_w}{h_{fg} A}\right)_1 = \left(\frac{\rho_w c_w T v_{fg} A_w}{h_{fg} A}\right)_2 \qquad (28)$$

and the roughness of the internal walls of both pipes is of the same length scale. If these two conditions are satisfied, flashing liquid flows in both pipes will behave identically (see Eq. (14)). In this sense the condition expressed by Eq. (28) is a criterion of thermodynamic similarity of flashing flows that interact with solids bounding these flows.

Most flashing liquids that are used in the industry are toxic, flammable, or explosive (ammonia, LPG, volatile oil, liquid hydrogen, etc.) If the thermal effect of the wall on flashing flow behavior is of primary interest, the criterion of thermodynamic similarity Eq. (28) in conjunction with the conditions of geometric and cinematic similarity can provide the basis for constructing scaled experimental models of systems containing such liquids or for selecting model fluids. Although full similarity hardly can be achieved in this case, the proposed criterion may be useful for scaling thermodynamic conditions and extending the results obtained on the model fluids to real flashing (volatile) liquids.

Conclusions

The problem of transient, two-phase, conjugate heat transfer during the depressurization of pipelines conveying flashing liquids is examined in this study. A numerical model for transient flashing liquid flow has been developed. The model rigorously takes into account the transient radial heat conduction and the forced convection effects. The model has been validated using previously published experimental data. The effect of friction on the heat transfer conditions in pipes has been studied. Numerical simulation of flashing two-component liquid flow was performed to determine the range of applicability of the solution based on the new formulation of energy equation. Relying on the simulation results a procedure was proposed for choosing an appropriate model for predicting transient conjugate two-phase heat transfer during release of flashing liquids from pipes. A criterion of thermodynamic similarity for flashing liquid flows in pipes or channels has been formulated. The proposed condition provides the basis for selecting model fluids, as well as for constructing experimental models of systems containing flashing (volatile) liquids with scaled thermodynamic conditions.

Nomenclature

A = area
D = pipe internal diameter
c = thermal capacity
G = mass velocity
Fa = factor of adiabaticity of flashing liquid flow, Eq. (1)
f = friction factor in single-phase liquid flow
h = specific enthalpy; heat transfer coefficient
h_{fg} = latent heat of vaporization
K = wall friction coefficient
L = length
M = total instantaneous mass
N = total number of mesh cells
p = pressure
q = external heat flux per unit volume of the fluid
r = radial coordinate
T = temperature
t = time
V = fluid velocity
v = specific volume
x = axial coordinate
z = concentration
ρ = density

Subscripts

a = ambient
i = internal, wall-to-fluid interface
fg = difference between properties of vapor (gas) and liquid
e = model that assumes local thermal equilibrium
M = total number of components of the mixture
O = external
r = rigorous conjugate two-phase heat transfer model
sat = saturation
τ = dimensionless time (time divided by the total blowdown time)
w = pipe wall
0 = initial condition

References

[1] Sucec, J., 1975, ''Unsteady Heat Transfer Between a Fluid With Time Varying Temperature and a Plate: An Exact Solution,'' Int. J. Heat Mass Transf., **18**, pp. 25–34.

[2] Sucec, J., 1981, ''An Improved Quasi-Steady Approach for Transient Conjugated Forced Convection Problems,'' Int. J. Heat Mass Transf., **24**, pp. 1711–1722.

[3] Lin, Y. K., Yin, C. P., and Yan, W. M., 1991, ''Transient Laminar Mixed Convective Heat Transfer in a Flat Duct,'' ASME J. Heat Transfer, **113**, pp. 384–390.

[4] Lin, Y. K., and Kuo, J. C., 1988, ''Transient Conjugated Heat Transfer in Fully Developed Laminar Pipe Flows,'' Int. J. Heat Mass Transf., **31**, pp. 1093–1102.

[5] Chen, J. C., 1966, ''Correlation for Boiling Heat Transfer to Saturated Liquids in Convective Flow,'' Int. Eng. Chem. Process Design Development **5**, pp. 322–333.

[6] Klimenko, V. V., 1988, ''A Generalized Correlation for Two-Phase Forced Flow Heat Transfer,'' Int. J. Heat Mass Transf., **31**, pp. 541–552.

[7] Shah, M., 1976, ''A New Correlation for Heat Transfer During Boiling Flow Through Tubes,'' ASHRAE Trans., **82**, pp. 66–72.

[8] Fairuzov, Y. V., 1998, ''Blowdown of Pipelines Carrying Flashing Liquids,'' AIChE. J., **44**, pp. 245–254.

[9] Fairuzov, Y. V., 1998, ''Numerical Solution for Blowdown of Pipeline Containing Flashing Liquid,'' AIChE. J., **44**, pp. 2124–2128.

[10] Richardson, S. M., and Saville, G., 1991, ''Blowdown of Pipelines,'' *Proceedings of Offshore Europe 91*, Aberdeen, U.K., SPE Paper No. 23070.

[11] Wallis, G. B., 1980, ''Critical Two-Phase Flow,'' Int. J. Multiphase Flow, **6**, pp. 97–112.

[12] Chen, J. R., Richardson, S. M., and Saville, G., 1995, ''Modelling of Two-Phase Blowdown from Pipelines-II. A Simplified Numerical Method for Multi-Component Mixtures,'' Chem. Eng. Sci., **50**, pp. 2173–2187.

[13] Solorzano, M., Barragán-Arroche, F., and Bazua-Rueda, E., 1996, ''Comparative Study of Mixing Rules for Cubic Equations of State in the Prediction of Multicomponent Vapor-Liquid Equilibria,'' J. Phase Equilib., **122**, pp. 99–106.

[14] McAdams, W. H., Woods, W. K., and Heroman, L. C., 1942, ''Vaporization Inside Horizontal Tubes. II-Benzane-Oil Mixtures,'' Trans. ASME, **64**, pp. 193–200.

[15] Collier, J. G., 1981, ''Multicomponent Boiling and Condensation,'' *Two-Phase Flow and Heat Transfer in the Power and Process Industries*, Bergels, A. E., Collier, J. G., Delhaye, J. M., Hewitt, G. F., and Mayinger, F., eds., Hemisphere, Washington, D.C., pp. 520–557.

[16] Stephan, K., and Korner, M., 1969, ''Calculation of Heat Transfer in Evaporating Binary Liquid Mixtures,'' Chem. Ing. Technik. **41**, pp. 409–417.

[17] Ransom, V. H., and Trapp, J. A., 1978, ''RELAP5 Progress Summary,'' PILOT Code Hydrodynamic Model and Numerical Scheme, Idaho National Engineering Laboratory Report No. CD-AP-TR-005.

[18] Patnakar, V. S., 1980, *Numerical Heat Transfer and Fluid Flow*, Hemisphere, Washington, D.C.

[19] Tam, V. H. Y., and Cowley, L. T., 1988, ''Consequences of Pressurised LPG Releases: The Isle of Grain Full-Scale Experiments,'' Proceedings of GASTECH 88, 13th International LNG/LPG Conference, Kuala Lumpur, pp. 2–25.

[20] Richardson, S. M., and Saville, G., 1996, ''Blowdown of LPG Pipelines, Process Environmental Protection,'' Trans. Inst. Chem. Eng., **74**, pp. 235–245.

S. C. Chen
Department of Mechanical Engineering,
University of California,
Berkeley, CA 94720-1740

D. G. Cahill
Department of Materials Science and
Engineering, University of Illinois,
Urbana, IL 61801

C. P. Grigoropoulos
Department of Mechanical Engineering,
University of California,
Berkeley, CA 94720-1740
cgrigoro@me.berkeley.edu

Melting and Surface Deformation in Pulsed Laser Surface Micromodification of Ni-P Disks

The nanosecond pulsed laser-induced transient melting and miniature surface deformation of Ni-P hard disk substrates has been investigated experimentally. A photothermal displacement method has been developed to detect the transient melting and surface deformation process with nanosecond time resolution. The deflection signals show the variation of the feature shape in response to different pulse energies of the near-infrared pulsed nanosecond heating laser beam. A laser flash photography system is also developed to visualize the growth dynamics of the entire feature with nanosecond time resolution and submicron spatial resolution. The feature formation is explained as a result of surface tension driven flow. The surface tension depends not only on the surface temperature, but also on the surfactant concentration. Competition between the thermocapillarity and a surfactant concentration effect is revealed in the course of the bump formation process. Smaller features with diameters of 5 μm are obtained by using visible pulsed laser radiation. On-line monitoring of the transient growth process of such small features is achieved by a new laser flash deflection microscope. [S0022-1481(00)00301-7]

Introduction

Laser-assisted melting and surface modification processes are important in a variety of industrial applications. A well proven technology to solve the stiction problem of hard disk drives for low-flying-height media is the laser zone texturing (LZT) ([1–3]), using a nanosecond pulsed laser to modify Ni–P hard disk substrates. The laser-materials interaction involves surface melting and resolidification to precisely control the surface topography. It was shown that single pulse topographic features (‘‘bumps’’) are sensitively dependent on laser pulse energy, substrate material and surface preparation procedure ([4]). The mechanism of bump formation was studied by numerical simulations ([5,6]). However, all these studies were based on final topography profile data. Time- and space-resolved experimental investigations are needed for unveiling the physical mechanisms responsible for the feature formation.

Since the transient feature formation process lasts only several hundred nanoseconds and the features typically have diameters less than 20 μm and rim heights in the range of tens of nanometers, fast and nondestructive techniques need to be developed to detect the transient process of bump growth. Photothermal displacement (PTD) techniques have been developed to measure slight displacements due to laser heating by using a probing beam ([7]). However, conventional PTD schemes require high-frequency modulation of the heating beam in order to detect a minute deflection signal due to small temperature change or small deformation on the sample surface in the thermoelastic regime ([8]). Moreover, conventional PTD setups are not technically practical for detecting the bump growth dynamics with the required stability and alignment reproducibility. Recently, Chen et al. [9] developed a novel PTD setup to study the transient melting and surface deformation of materials upon single pulsed-laser heating. This setup provides a robust and high-resolution tool in both time and space for measuring transient deformation on the material surface.

Laser flash photography (LFP) has been shown useful for studying transient laser materials interaction processes, such as the pulsed laser ablation of absorbing liquids ([10]), laser melting of solid thin film ([11]). This technique utilizes a low power laser with a very short pulse width as the illumination source, providing a fine time resolution. One advantage of this technique is that it can visualize the transient growth process of the entire bump.

This paper reports on a study of laser-induced topography via atomic force microscopy (AFM), results of direct observations of transient melting and surface deformation using PTD measurement and imaging of transient bump growth dynamics by LFP during pulsed laser heating on nanosecond time scale and micrometer spatial scale. The mechanism of bump formation is explained as a result of surface tension driven flow in the molten pool. The surface temperature gradient-induced thermocapillary flow drives the molten material outward. However, possible desorption of the native oxide layer upon laser heating tends to induce a surface tension gradient reversing the flow towards the center of the heated spot. The competition between thermocapillarity and surfactant concentration effects determines the nature of the flow and the final topography. In order to meet recent industry demands for smaller bumps, a texturing system utilizing visible laser radiation is developed to generate bumps with diameters of 5 μm. A laser flash deflection microscope is constructed for the first time to visualize the growth of such small features.

Experimental Parametric Studies of the Laser-Induced Topography

The experimental setup for the surface micromodification is shown in Fig. 1. An infrared (IR) heating beam is emitted from a polarized Q-switched Nd:YLF laser (λ=1,047 nm, FWHM=15 ns). The beam is expanded, attenuated, and focused onto the

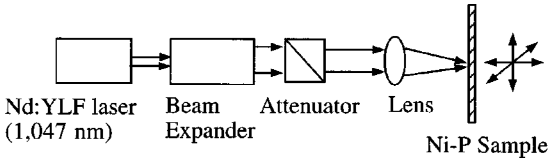

Fig. 1 Experimental setup of the laser surface modification of Ni-P disk substrates

---

Contributed by the Heat Transfer Division for Publication in the JOURNAL OF HEAT TRANSFER. Manuscript received by the Heat Transfer Division, March 29, 1999; revision received, Sept. 1, 1999. Associate Technical Editor: D. Poulikakos.

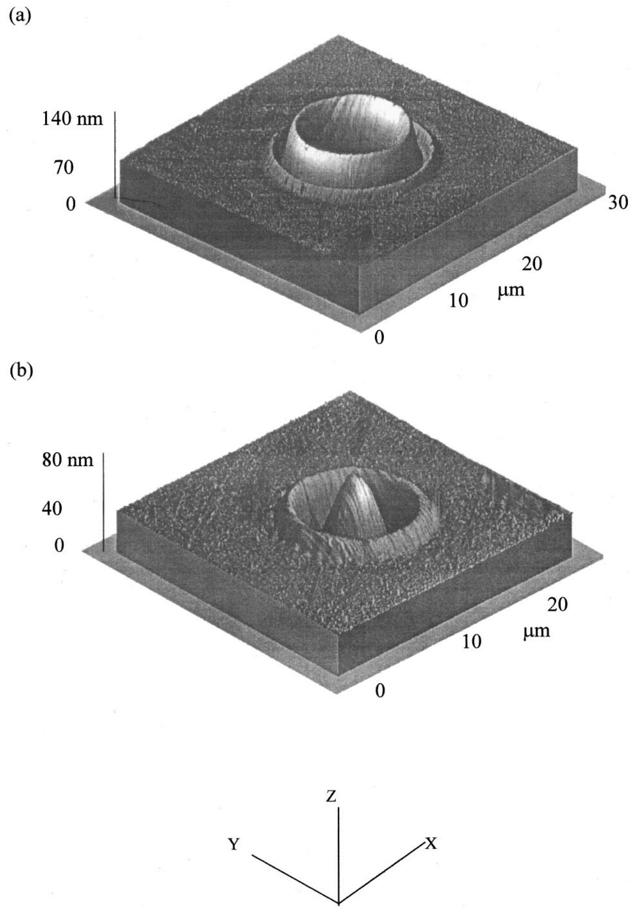

Fig. 2 Typical features (measured by AFM) produced by laser heating at (*a*) high laser energy, (*b*) intermediate laser energy

sample, which is a Ni-P hard disk substrate (12 wt.% P). The laser beam spot on the sample is about 17 μm, which was measured using knife-edge profiling.

Typical bumps produced by laser heating are shown in Fig. 2, measured by AFM. The diameters of the bumps are about 17 μm, and the rim height varies from 10 to 50 nm. The dependence of the bump shape (measured by AFM) on the incident energy of the IR heating beam is shown in Fig. 3. When the incident heating beam energy is 4.0 μJ, the bump has a deep crater at the center and a low peripheral rim. As the pulse energy decreases, the center of the crater starts moving upwards, forming ''double-rim'' and ''W'' shapes. When the laser energy reaches 2.0 μJ, a rounded, smooth central dome is formed, which is called a 'sombrero' shape. At even lower laser intensity, the central dome shrinks, decreases in height and eventually disappears, forming a bowl-like shape.

Experimental in-situ Investigations of Feature Formation

Photothermal Displacement Detection. The schematic of the PTD experimental setup is shown in Fig. 4. The Nd:YLF laser is used as the heating source. The beam is reflected through a dichroic mirror and focused onto the sample by an achromat lens with an aperture of approximately 10 mm and focal length of 25 mm. A probing beam from a linear polarized He-Ne laser ($\lambda = 632.8\,\mathrm{nm}$) is expanded, reflected by three mirrors, passes through a polarizing beam splitter, a quarter wave plate, a dichroic mirror and is focused onto the target surface by an achromat lens. Two of the mirrors are mounted on micropositioning motors whose movement (with 1 μm resolution) allows the He-Ne beam to scan the sample surface in both the x and y directions. At the sample surface, the Nd:YLF laser beam diameter is approximately 17.2 μm while the He-Ne laser beam diameter is about 4.8 μm (both at the $1/e^2$ intensity point). The depths of focus for the Nd:YLF and the He-Ne beams have been determined at about ±

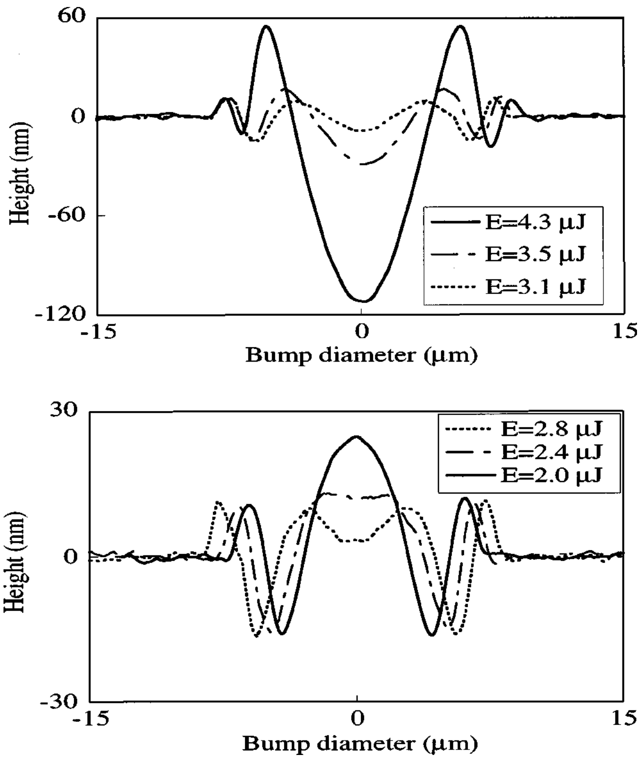

Fig. 3 Bump shape (cross section, measured by AFM) variation due to the incident heating beam energy change

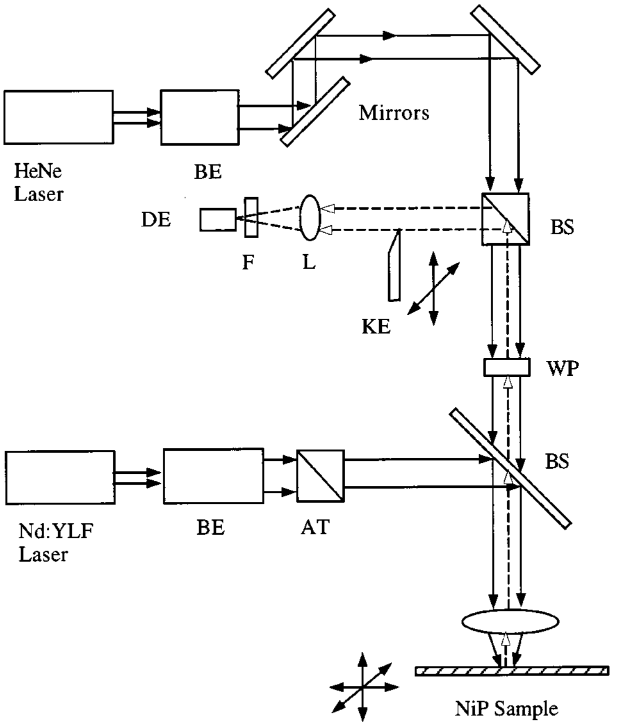

Fig. 4 Experimental setup of the photothermal displacement method (AT) attenuator, (BE) beam expander, (BS) beam splitter, (DE) detector, (F) filter, (KE) knife-edge, (L) lens, (WP) quarter wave plate

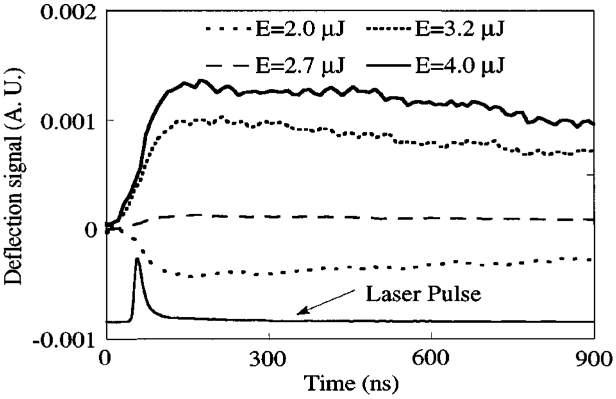

Fig. 5 Transient deflection signals at various heating laser energies. The deflection signal is enhanced due to the crater formation, and weakened for the Sombrero case

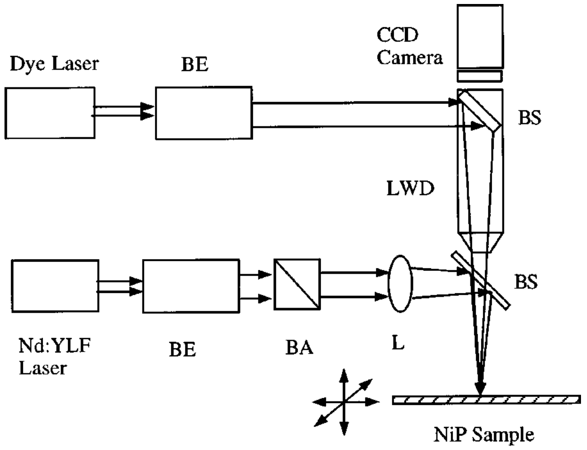

Fig. 6 Experimental setup of the laser flash photography system (BA) beam attenuator, (BE) beam expander, (BS) beam splitter, (LWD) long-working distance microscope, (L) lens

70 μm and ± 10 μm, respectively by using knife-edge profiling. The focusing lens was of special multielement design optimized for achromatic performance at the wavelengths of 1047 and 632.8 nm, allowing accurate placement of the focal points of the heating and probing beams within 10 μm.

The reflected or deflected beam from the sample surface passes through the same dichroic mirror, the quarter-wave plate, the polarizing beam splitter, a He-Ne interference filter, and is finally focused onto a photodetector. The photodetector is connected to a digitizing oscilloscope (1 ns time resolution), which is triggered by the Nd:YLF laser pulse. A knife-edge, cutting half of the reflected beam is used to obtain the deflection signal. The two beams form spots on the sample surface that are separated by approximately 2 μm. When a single pulse is fired onto the target, the surface experiences thermoelastic expansion, melting and deformation, leading to changes in the reflected He-Ne beam. The detected signal comprises contributions steming from optical property change upon melting as well as from the evolving topography. The procedure for extracting the deflection contribution due to the surface topography is outlined in Chen et al. [9]. By detecting the deflection signal of the probe He-Ne beam, the transient deformation of the surface can be tracked with nanosecond time resolution.

The time resolution of this system is on the order of nanosecond, limited mainly by the response time of the photodetector and the sampling speed of the oscilloscope. The spatial resolution is limited by the beam size of the probing HeNe laser beam (4.8 μm).

Figure 5 shows the probing beam deflection signals for various laser pulse intensities. At lower heating beam energies, such as 2.0 μJ for the sombrero case, the growth of a central peak decreases the deflection signal. However, at heating beam energies exceeding 2.7 μJ, the deflection signal is enhanced, exhibiting a reversal in direction that is characteristic of the concave surface of a crater feature since the location of the probing He-Ne beam is fixed. A previous study has shown that the surface reflectivity change of this amorphous material as a function of temperature is negligible ([12]). Therefore, the surface deformation is the main contributor to the deflection signal.

The deflection signals also reveal transient information on the surface deformation process. For example, at the heating laser pulse energy of 4.0 μJ, the deflection signal increases to a maximum value at approximately 130 ns after the heating laser pulse. It then decreases gradually to a permanent value at about 800 ns. This transient process indicates that a crater is formed after melting. The crater becomes deeper and deeper until 130 ns, causing an increase of the slope of the crater with a correspondingly increasing deflection signal. Beyond this point and until complete resolidification, the deflection signal exhibits a small decrease indicating a slight recovery of the crater depth.

Laser Flash Photography. A LFP system is developed to visualize the dynamic process of bump growth as shown in Fig. 6. A pulsed nitrogen laser-pumped dye laser ($\lambda = 650$ nm, FWHM=4 ns) is utilized to illuminate the sample surface through a long-working distance objective lens. Both the Nd:YLF laser and the dye laser are externally triggered by a pulse generator. The time interval between the two lasers is varied by the pulse generator and accurately measured by two identical photodiodes connected to an oscilloscope. This procedure eliminates the delay variation due to possible jitter of the laser pulses. It is noted that the technique can produce only a single image for each firing of the heating laser pulse. The image sequences are obtained by repeating the experiment under the same conditions based on the fact that the heating laser has very good pulse-to-pulse stability, and the sample is uniform, thus yielding highly reproducible laser texture. The spatial resolution of the imaging system is about 0.5 μm. The time resolution is within several nanoseconds, limited mainly by the dye laser pulse width. Thermal emission contribution to the images has been examined by blocking the dye laser illumination. No significant thermal emission image can be captured even at the pulse energy of 6 μJ. Since the reflectivity change for Ni-P during the pulsed laser heating is insignificant, the reflectivity effect to the image captured by the charge coupled device (CCD) camera can be neglected.

The visualization of the entire bump growth has been conducted for various pulse energies. Figure 7(*a*) shows the sequence of images for the double-rim case with laser pulse energy equal to 4.0 μJ. A rim and a central hole become visible in the early stage, having formed right after melting. The melt pool expands and the hole diameter keeps increasing and deepening until 121 ns. The photos from 121 to 682 ns show partial recovery at the central hole. After 682 ns, no change is discernible and the solidification process has concluded. For the ''sombrero'' case, a similar sequence of images is shown in Fig. 7(*b*). A small and shallow depression is observed initially at the center of the growing protrusion. This ''dimple'' vanishes after about 100 ns, leaving the shiny central peak surrounded by a low-height peripheral rim, depicted in the micrograph as a faint halo.

Mechanism of Bump Formation

Normally, for most pure liquids, $\partial\sigma/\partial T<0$. Here σ is surface tension. However, Kingery [13] found that $\partial\sigma/\partial T$ can also be positive for certain liquids such as SiO_2,B_2O_3 melts due to disso-

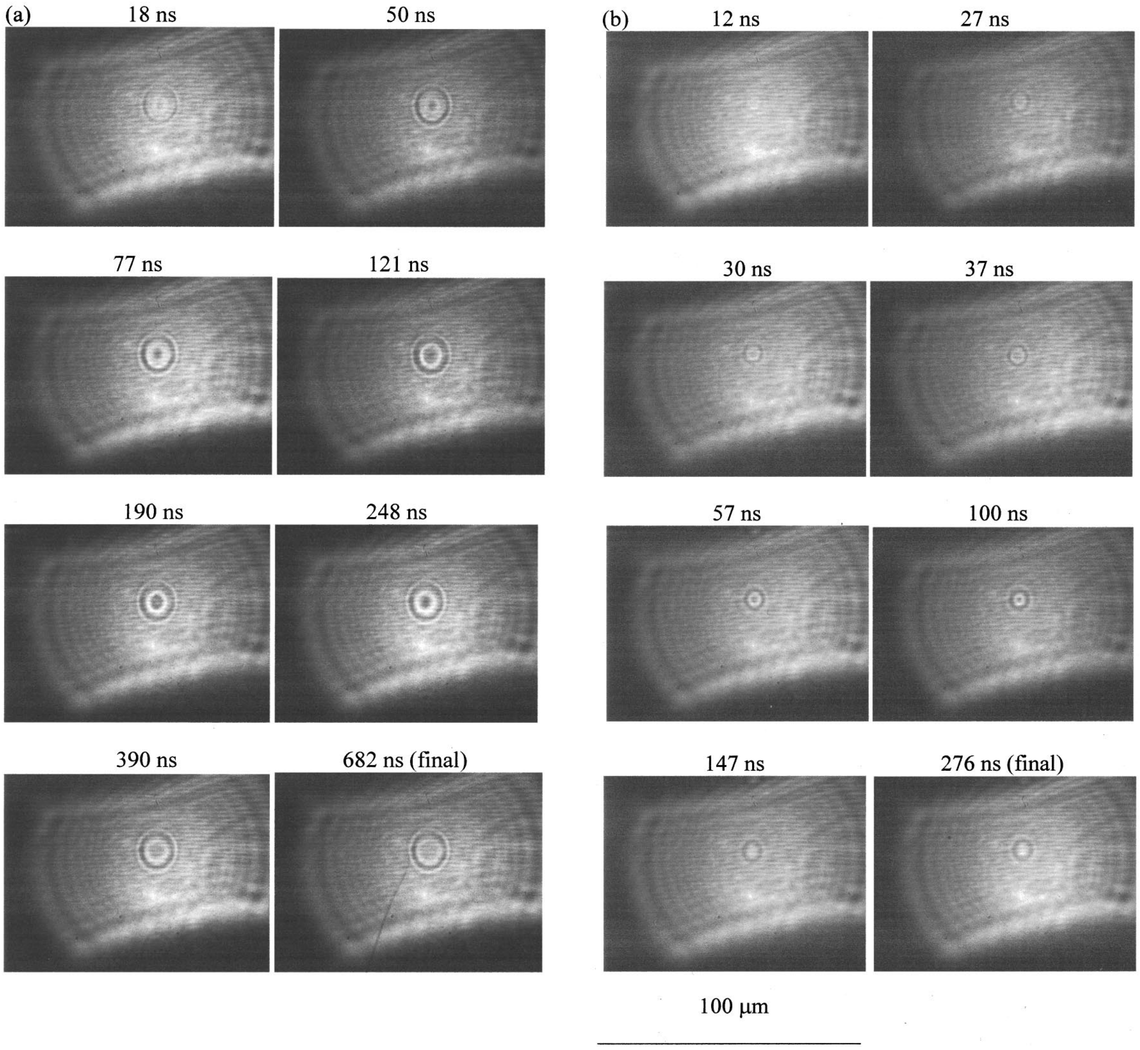

Fig. 7 A sequence of images of bumps with laser pulse energy of (*a*) 4.0 μJ and (*b*) 2.0 μJ produced by the laser flash photography system

ciation with temperature. It is believed that the surface tension of a liquid depends not only on the surface temperature, but also on the surfactant concentration ([14]). The temperature gradient effect acts to drive materials towards the cooler region of higher surface tension, while the surfactant effect tends to move the material to lower surfactant concentration regions ([15]). Bennett et al. [5] have studied the laser-induced topography by numerical simulation and ascribed the establishment of the surfactant composition gradient mainly to the vaporization of phosphorous. However, it was reported that the amount of phosphorous vaporized is negligible and the resolidified Ni–P has very similar properties (amorphous microstructure, chemical composition, reflectivity and hardness) to the starting material ([16]). Even though the model correctly pointed to the importance of surface chemistry, it could not adequately explain the diminishing of the central dome for the ''sombrero'' case when a train of laser pulses is delivered onto the same spot ([16]). If surface oxide is considered as the major surfactant, its supply is limited and subject to desorption upon the laser heating even at moderate laser pulse energies. Pulses following the first one would therefore be expected to drive less significant compositional capillarity, ultimately suppressing the central dome. Furthermore, positive protrusion growth at the heated spot center has been observed in nanosecond laser heating of gold films ([17]). Vaporization of adsorbed oxygen and water was believed the main reason for generating gradients of surfactant composition.

For the case of laser-induced bump formation, pulsed heating creates a temperature gradient following the Gaussian beam intensity profile along the radial direction. The temperature gradient induces thermocapillary flow, driving the material from the hot center to the cold periphery and forming a bowl-shaped feature. However, as previously mentioned, laser heating can at least partially remove the native oxide layer if the induced surface temperature is high enough. This situation establishes a gradient of surfactant concentration, which carries material towards the center. If the surfactant compositional effect is dominant, a sombrerotype feature is formed. At even higher laser power, the center part of the molten zone attains higher temperature and hence thermocapillarity again becomes dominant in the center region, forming a double-rim surface feature.

The transient process observed by both experimental LFP visualization and PTD detection shows competition between the thermocapillarity and the surface compositional effect. In Fig. 7(*a*), at the beginning of melting and deformation, the surface temperature is so high that the thermocapillary effect dominates at the melt pool, moving the material outward. It is seen that the melt pool expands and the crater diameter keeps increasing and deepening. An outer rim is formed due to thermocapillary effect immediately after melting. This freezes quickly because of temperature drop after the expiration of the laser pulse. However, most of the melt pool still experiences thermocapillary and compositional surface tension gradients that pile up an inner rim. In Fig. 5, the deflection signal keeps increasing, indicating a deepening and expanding crater. After about 100 ns, the surface cools down and the thermocapillary effect decreases. Thus the surface compositional effect becomes dominant, carrying material inward, and causing recovery of the center hole in Fig. 7(*a*) and deflection signal reduction in Fig. 5. A similar phenomenon happens for the ''sombrero'' bump case.

Visible Laser Texturing and in-situ Diagnostics

In order to meet recent demands for smaller features in the computer industry, visible pulsed laser radiation is applied, enabling tighter focusing without compromising the focal depth. In this study, texturing utilizing visible radiation is combined with a ''deflection'' microscope to visualize small bumps. Figure 8 shows a schematic of the apparatus. A frequency-doubled *Q*-switched Nd:YLF laser ($\lambda = 524$ nm, FWHM=15 ns) is used as the heating beam. The beam is attenuated and then focused onto the Ni–P sample (12 wt.% of P) by a microscope objective (40×, NA=0.85). The pulse energy is adjusted to create smooth bumps with a diameter of about 5 μm.

The deflection microscope was deigned on the basis of the same principle employed in the localized PTD measurement. The

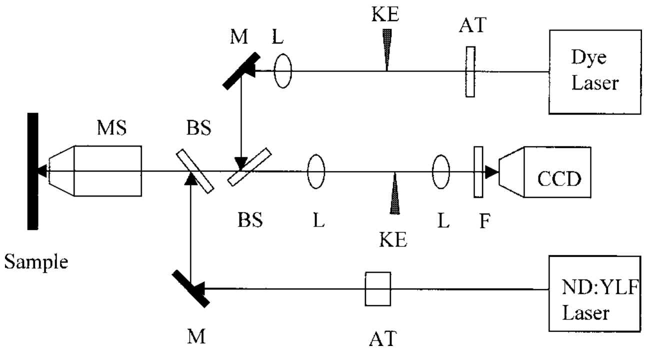

Fig. 8 Experimental setup of the green laser texturing and the laser flash deflection microscope: (AT) attenuator, (BS) beam splitter, (F) filter, (KE) knife-edge, (L) lens, (M) mirror, (MS) microscope

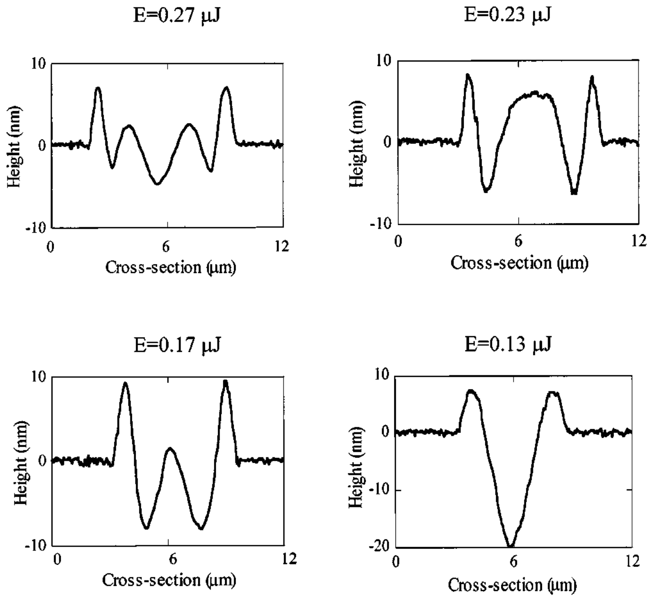

Fig. 9 Laser energy dependence of bump shape (cross section, measured by AFM) in green laser texturing

(a) V-type

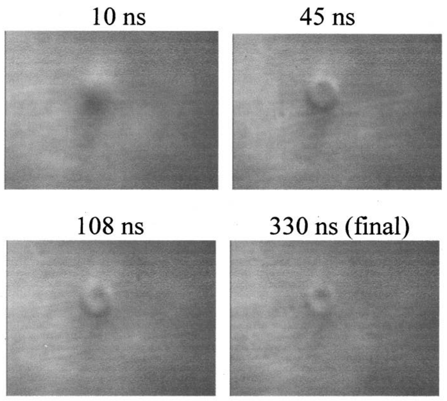

(b) Sombrero type

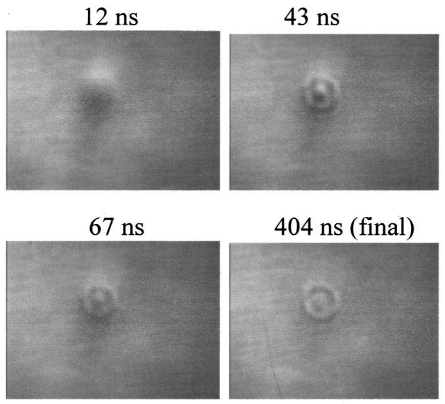

(c) Double-rim type

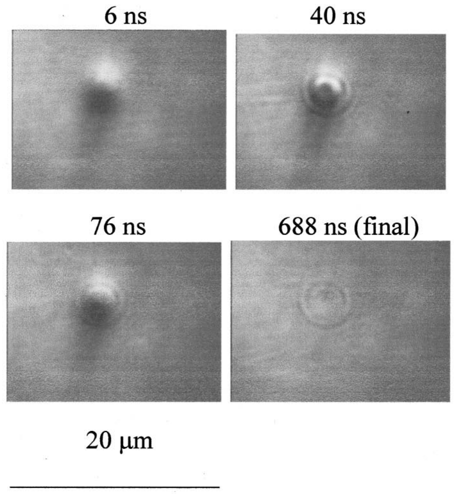

Fig. 10 A sequence of images of bumps with green laser pulse energy of (*a*) 0.13 μJ (V type), (*b*) 0.17 μJ (sombrero type), and (*c*) 0.27 μJ (double-rim type) produced by a laser flash deflection microscope

pulsed nitrogen laser-pumped dye laser ($\lambda = 650$ nm, FWHM $= 4$ ns) provides illumination on the sample surface. The illumination beam is aligned collinearly with the heating beam through the microscope objective lens. A knife edge is utilized to cut half of the illuminating beam. The slope of the deforming surface deflects the reflected illumination beam, producing enhanced or weakened image intensity in the CCD camera. Another knife edge is inserted in the illumination path and used to adjust the contrast of the image.

The dependence of the bump shape (measured by AFM) on the incident energy of the IR heating beam is shown in Fig. 9. The bumps have diameters of about 5 μm and rim heights varying from 5 to 20 nm. The visualization of the entire bump growth by the laser flash deflection microscope has been conducted for various pulse energies as shown in Fig. 10 for (*a*) a V-type bump, (*b*) a sombrero bump, and (*c*) a double-rim bump.

Concluding Remarks

The transient surface deformation of Ni-P substrates upon pulsed laser heating has been investigated experimentally. A photothermal displacement method has been developed to detect the transient melting and surface deformation process with nanosecond time resolution. The deflection signals show distinctly the variation of the produced surface features resulting from different pulse energies of the heating laser beam. A laser flash photography system of nanosecond time resolution and submicron spatial resolution has also been constructed to visualize the growth dynamics of the entire feature. Surface deformation is explained as a result of surface tension induced flow, which depends not only on the surface temperature, but also on the surfactant concentration. In the process of bump formation, both PTD detection and LFP visualization reveal competition between thermocapillary and concentration-induced capillary effects. This competition determines the nature of flow in the liquid pool and eventually the final topography. Green laser texturing has been utilized to produce smaller bumps. A laser flash deflection microscope has been developed to visualize the growth of 5-μm-dia features with striking resolution and clarity.

Acknowledgments

This work was conducted at the Laser Thermal Laboratory of the University of California at Berkeley. Part of this work was supported by the IBM Manufacturing Technology Center, Boca Raton, Florida. Chen thanks Dr. A. C. Tam, Dr. D. S. Kim, and Dr. H. K. Park for helpful discussions.

References

[1] Ranjan, R., Lambeth, D. N., Tromel, M., Goglia, P., and Li, Y., 1991, ''Laser Texturing for Low-Flying-Height Media,'' J. Appl. Phys., **69**, pp. 5745–5747.

[2] Kuo, D., et al., 1996, ''Design of Laser Zone Texture for Low Glide Media,'' IEEE Trans. Magn., **32**, pp. 3753–3758.

[3] Baumgart, P., Krajnovich, D. J., Nguyen, T. A., and Tam, A. C., 1995, ''A New Laser Texturing Technique for High Performance Magnetic Disk Drives,'' IEEE Trans. Magn., **31**, pp. 2946–2951.

[4] Park, H. K., Kerstens, P., Tam, A. C., and Baumgart, P., 1998, ''Issues on High-Speed Laser Zone Texturing of Magnetic Disk Substrates with Improved Quality,'' IEEE Trans. Magn., **34**, pp. 1807–1809.

[5] Bennett, T. D., Krajnovich, D. J., Grigoropoulos, C. P., Baumgart, P., and Tam, A. C., 1997, ''Marangoni Mechanism in Pulsed Laser Texturing of Magnetic Disk Substrates,'' J. Heat Transfer, **119**, pp. 589–593.

[6] Iwamoto, M., Ye, M., Grigoropoulos, C. P., and Greif, R., 1999, ''Numerical Analysis of Pulsed Laser Heating of Metals,'' Num. Heat Transfer A, **34**, pp. 791–804.

[7] *Progress in Photothermal and Photoacoustic Science and Technology*, edited by A. Mandelis (Elsevier, New York, 1992), Vol. 1.

[8] Olmstead, M. A., Amer, N. M., Kohn, S., Fournier, D., and Boccara, A. C., 1983, ''Photothermal Displacement Spectroscopy: An Optical Probe for Solids and Surfaces,'' Appl. Phys. A: Solids Surf., **32**, pp. 141–154.

[9] Chen, S. C., Grigoropoulos, C. P., Park, H. K., Kerstens, P., and Tam, A. C., 1998, ''Photothermal Displacement Measurement of Transient Melting and Surface Deformation During Pulsed Laser Heating,'' Appl. Phys. Lett., **73**, pp. 2093–2095.

[10] Kim, D., and Grigoropoulos, C. P., 1998, ''Phase-Change Phenomena and Acoustic Transient Generation in the Pulsed Laser Induced Ablation of Absorbing Liquids,'' Appl. Surf. Sci., **127–129**, pp. 53–58.

[11] Willis, D. A., Xu, X., Poon, C. C., Tam, A. C., 1998, ''Laser-Assisted Surface Modification of Thin Chromium Films,'' Opt. Eng. (Bellingham), **37**, pp. 1033–1041.

[12] Chen, S. C., and Grigoropoulos, C. P., 1997, ''Non-contact Nanosecond-time-resolution Temperature Measurement in Excimer Laser Heating of Ni–P Disk Substrates,'' Appl. Phys. Lett., **71**, pp. 3191–3193.

[13] Kingery, W. D., 1959, ''Surface Tension of Some Liquid Oxides and Their Temperature Coefficients,'' J. Am. Ceram. Soc., **42**, pp. 6–10.

[14] Guthrie, R. I. L., and Iida, T., 1994, ''Thermodynamic Properties of Liquid Metals,'' Mater. Sci. Eng., A, **A178**, pp. 35–41.

[15] Balandin, V. Yu, Otte, D., and Bostanjoglo, O., 1995, ''Thermocapillary Flow Excited by Focused Nanosecond Laser Pulses in Contaminated Thin Liquid Iron Films,'' J. Appl. Phys., **78**, pp. 2037–2044.

[16] Tam, A. C., Pour, I. K., Nguyen, T. A., Krajnovich, D. J., Baumgart, P., Bennett, T., and Grigoropoulos, C. P., 1996, ''Experimental and Theoretical Studies of Bump Formation During Laser Texturing of Ni-P Disk Substrates,'' IEEE Trans. Magn., **32**, pp. 3771–3773.

[17] Bostanjoglo, O., and Nink, T., 1997, ''Liquid Motion in Laser Pulsed Al, Co and Au Films,'' Appl. Surf. Sci., **109–110**, pp. 101–105.

N. Bianco
Dipartimento di Energetica,
Termofluidodinamica Applicata
E Condizionamenti ambientali,
Universita degli Studi di Napoli Federico II,
P. le Tecchio 80,
Napoli 80125, Italy
e-mail: nibianco@unina.it

O. Manca
Professor,
Dipartimento di Ingegneria Aerospaziale,
Seconda Universita degli Studi di Napoli,
Real Casa Dell' Annunziata,
via Roma 29, Aversa (CE) 81031, Italy
e-mail: manca@unina.it
Mem. ASME

Two-Dimensional Transient Analysis of Absorbing Thin Films in Laser Treatments

In this paper the transient coupled conductive-radiative field, due to a laser heat source impinging on a thin film deposited on a substrate, has been solved in the hypothesis of one dimensionality of the optical field and of two dimensionality of the thermal field. Results have been obtained with the matrix method for the optical field and the finite volume method for the thermal field. The results show that when the investigation is localized to the center of the spot, the one-dimensional model describes the thermal field quite well. Instead, if knowledge of the temperature is required elsewhere, the two-dimensional model is needed. The investigation herein presented shows that for low-conductivity materials (a–Si) the temperature peaks are placed inside the thin film for the absorption function distribution, determined by interference phenomena. [S0022-1481(00)01301-3]

Keywords: Conjugate, Heat Transfer, Laser, Manufacturing, Thin Film

Introduction

Pulsed laser heating of thin films is important for its applications in annealing, damage of optical coatings, and optical recording. In fact, thermal treatment of thin film structures with a heat source, emitting in the thermal radiation spectrum, is a common procedure in numerous electronic and optical material processes ([1]). Temperature prediction and control during such processes is critical and a thorough understanding of the thermal coupled conductive-radiative phenomena involved is required. This is due to the temperature dependence of the optical properties. Absorption of optical energy by a layer or a multilayer structure and the consequent temperature rise within the structure have a wide range of interest.

Depending on the wavelength of the heating laser pulse, the optical properties of materials in thin films are generally temperature dependent. These induce a thermally optical nonlinearity ([2]).

The one-dimensional coupled problem was investigated for a single and multilayer thin film on a glass substrate. One of the first studies was that of Tamura et al. [3]. They investigated the behavior of a thin SiO_2 film on a silicon substrate during laser annealing. Colinge and Van de Wiele [4] determined the laser power absorbed in a silicon on insulator structure by means of a numerical approach employing the matrix method. Park et al. [5] modeled a probe laser response during nanosecond pulse laser heating of amorphous silicon thin films by means of matrix formulation in optical multilayer theory. Grigoropoulos et al. [6] solved the coupled optical-thermal problem, and the evaluation of energy absorption was obtained by a thin film optic model. They took into account the effects of a continuously varying complex index of refraction with temperature. A similar one-dimensional model was employed by Chen and Tien [2] to examine the effects of the temperature-dependent optical constants and the nonuniform absorption in a cadmium sulfide (CdS) thin film and a zinc selenide (ZnSe) interference filter.

The coupled optical-conductive problem in two-dimensional model description has been developed by several investigators and a short review is presented here. Multilayered films with simulations in which only the recording layer absorbed the laser beam were studied by Mansuripur et al. [7]. For a multithin film structure, irradiated by a circular Gaussian laser beam, a numerical model was proposed by Nakano et al. [8]. They considered an absorbed laser power density with an exponential decay for each layer in the thermal model, and the optical properties were constant with temperature. Madison and McDaniel [9] obtained a solution for a scanned and pulsed Gaussian laser beam for an *N*-layer film structure with arbitrary absorption across one layer. A local Green's function theory for temperature evaluation in isotropic multilayer materials that involved exact optical absorption for axisymmetric chopped-beam laser heating was presented by McGahan and Cole [10]. Cole and McGahan [11] extended the theory presented in the previous paper to include anisotropic thermal properties and contact resistance between the layers.

In this paper a coupled optical-thermal model related to a pulsed laser source on a thin film-glass substrate is analyzed and numerically solved. The stationary laser beam is orthogonal to the target and the radiative field related to the absorption-reflection-transmission process in the thin film structure is locally one dimensional, whereas the transient conductive field inside the solid is two dimensional. The solid dimension along the normal direction to the laser beam is infinite. Optical and thermal properties are temperature dependent. The one-dimensional optical model is solved by means of the matrix method in multilayer theory, and the two-dimensional heat conduction equation, in cylindrical coordinates, is numerically solved by means of a finite volume method.

The analysis is related to thin films with a single layer. Amorphous and crystalline silicon are considered. The solid structure is irradiated by a pulsed laser with a wavelength of 1064 nm. A time-dependence triangular shape of the laser beam is taken into account, whereas the spatial dependence is Gaussian or donut. The results in terms of temperature distributions are presented. A comparison with a coupled one-dimensional optical-thermal model is analyzed in terms of temperature profiles.

Thermal and Optical Analysis

The structure consists of a thin film deposited on a glass substrate, as shown in Fig. 1. The film thickness is much smaller than that of the glass substrate, so the latter can be considered thermally semi-infinite. A pulsed Nd-YAG laser beam illuminates the surface of the thin film. For the nanosecond time scales considered in this work, nonequilibrium and non-Fourier thermal wave effects are negligible as suggested by Chen and Tien [2]. The

---

Contributed by the Heat Transfer Division for publication in the JOURNAL OF HEAT TRANSFER and presented at 1998 ASME IMECE. Manuscript received by the Heat Transfer Division, Jan. 6, 1999; revision received, July 22, 1999. Associate Technical Editor: T. Avedisian.

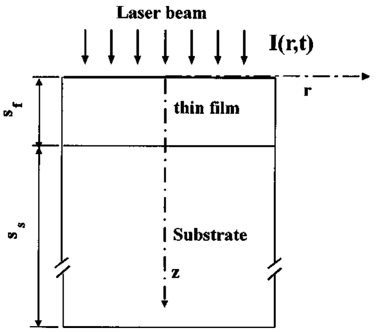

Fig. 1 Sketch of the structure

thermal and the optical properties are considered temperature dependent and the materials are considered isotropic.

The heat conduction equation in the thin film is

$$\frac{1}{r}\frac{\partial}{\partial r}\left(rk_f(T)\frac{\partial T_f}{\partial r}\right)+\frac{\partial}{\partial z}\left(k_f(T)\frac{\partial T_f}{\partial z}\right)+\dot{u}'''(T,r,z,t)=\rho_f c_f\frac{\partial T_f}{\partial t} \tag{1}$$

with $0\leqslant r<+\infty$, $0\leqslant z\leqslant s_f$, $t>0$. For the glass substrate the thermal properties are constant, then the heat conduction equation is

$$\frac{1}{r}\frac{\partial}{\partial r}\left(r\frac{\partial T_s}{\partial r}\right)+\frac{\partial^2 T_s}{\partial z^2}=\frac{1}{a_s}\frac{\partial T_s}{\partial t} \tag{2}$$

with $0\leqslant r<+\infty$, $s_f<z<+\infty$, $t>0$. Since the energy absorbed in the thin film is 10,000 times higher than the surface energy losses, these can be neglected and the thin film surface can be considered adiabatic [6]. The initial and boundary conditions are

$$T_f(r,z,0)=T_{\text{in}} \quad 0\leqslant r<+\infty;\ 0\leqslant z\leqslant s_f \tag{3a}$$

$$T_s(r,z,0)=T_{\text{in}} \quad 0\leqslant r<+\infty;\ s_f<z<+\infty \tag{3b}$$

$$\frac{\partial T_s(r,0,t)}{\partial z}=0 \quad t\geqslant 0;\ 0\leqslant r<+\infty \tag{3c}$$

$$k_f\frac{\partial T_f(r,s_f,t)}{\partial z}=k_s\frac{\partial T_s(r,s_f,t)}{\partial z} \quad t\geqslant 0;\ 0\leqslant r<+\infty \tag{3d}$$

$$T_f(r,s_f,t)=T_s(r,s_f,t) \quad t\geqslant 0;\ 0\leqslant r<+\infty \tag{3e}$$

$$T_s(r,z\rightarrow\infty,t)=T_{\text{in}} \quad t\geqslant 0;\ 0\leqslant r<+\infty \tag{3f}$$

$$T_f(r\rightarrow\infty,z,t)=T_{\text{in}} \quad t\geqslant 0;\ 0\leqslant z\leqslant s_f \tag{3g}$$

$$T_s(r\rightarrow\infty,z,t)=T_{\text{in}} \quad t\geqslant 0;\ s_f<z<+\infty. \tag{3h}$$

The term $\dot{u}'''(T,r,z,t)$ is related to the Poynting vector S and is a function of the optical properties of materials. Its evaluation is obtained following the matrix method ([12]). A plane, monocromatic, and linearly polarized wave is orthogonally incident on the structure. Its amplitude is $E_a(r)$. The corresponding energy flow along the z-direction is

$$I(r)=\frac{n_a}{2\mu c'}|E_a(r)|^2 \tag{4}$$

and the absorbed power per unit volume is ([6,2])

$$\dot{u}'''(r,z,t)=f(t)\frac{\partial S(r,z)}{\partial z} \tag{5}$$

where $f(t)$ is a function of the time and characterizes the temporal shape of the pulse. In this work a triangular time profile is considered and $f(t)=t/t_p$ for $0\leqslant t\leqslant t_p$, $f(t)=(t_l-t)/(t_l-t_p)$ for $t_p<t\leqslant t_l$, $f(t)=0$, for $t>t_l$ with $t_p=6$ ns and $t_l=30$ ns.

The incident intensity distribution can be written

$$I(r)=I_0\left[\xi\exp\left(-\frac{r^2}{r_0^2}\right)+(1-\xi)r^2\exp\left(-\frac{r^2}{r_0^2}\right)\right] \tag{6}$$

where r_0 is the radius of the beam and $0\leqslant\xi\leqslant 1$ (for Gaussian heat source $\xi=1$ and for donut heat source $\xi=0$).

Due to the nonlinearity induced by the temperature-dependent thermophysical and optical properties, the conductive temperature field is numerically obtained by means of a fully implicit finite volume method. The numerical solution of the model has been obtained iteratively at each time-step with the temperature-dependent source distribution by means of the alternating direction implicit method. The domain is a semi-infinite region, then a preliminary evaluation of the finite computational domain was accomplished to simulate this semi-infinite body with the associated initial and boundary conditions, Eq. (3). A finite cylinder was obtained with the radius equal to five times the spot radius and the height equal to 21 times the thin film thickness. In fact increasing the dimensions of the cylinder up to six times the spot radius along the r-direction and 26 times the thin film thickness along the z-direction, the maximum temperature difference between the two fields was less than 0.1 percent for the considered time period (50 ns). Both in the thin film and in the glass substrate the spatial step along the z-direction was uniform. The distance between two nodes along the r-direction was nonuniform and it was equal to $I\Delta r_0$, with $\Delta r_0=15.6$ nm and I equal to $1,2,\ldots,N_r$. Halving the spatial steps along r and z-directions, the maximum temperature difference between the two fields was less than 0.5 percent. Similar behavior was observed for the time-step. A time-step of 5.0×10^{-2} ns and a relative error in the iteration procedure of 10^{-6} were chosen.

Results and Discussion

Numerical calculations were performed for a single amorphous silicon ($a-$Si) thin film or a crystalline silicon ($c-$Si) thin film. In each case the thin film was deposited on a glass substrate. The optical and thermal properties of materials are reported in Table 1. As it has already been observed in the previous section, a triangular pulse was considered. The duration of the ON phase was $t_l=30$ ns and the peak time t_p was equal to 6 ns. The laser irradiation wavelength was 1.064 μm for the $a-$Si and 0.532 μm for the $c-$Si. The heat flux distributions were Gaussian ($\xi=1$) and donut ($\xi=0$). The I_0 value was 3.0×10^{11} W/m^2 for $a-$Si and 1.5×10^{11} W/m^2 for $c-$Si. A beam radius of 20 μm was chosen. The thin film layer was 0.50 μm thick and was subdivided into 80 nodes. The entire period of time was 50 ns in this study, and a depth of 10 μm was sufficient to consider the glass substrate as a

Table 1 Optical and thermophysical properties

	k [W/mK]	$\rho\, c_p$ [J/m^{3}K]	$\overline{n}=n-ik_{\text{est}}$
Glass	1.4 [6]	$2.64\cdot 10^6$ [6]	$1.0-i0.0$ [6]
$c-$Si	$2.99\cdot 10^4/(T-99)$ [6]	$1.474+0.171\cdot T/300)\cdot 10^6$ [6]	$4.153-i\cdot[0.038\cdot\exp((T-293)/430)](\lambda=532\ \text{nm})$ [6]
$a-$Si	$1.3\cdot 10^{-9}(T-900)^3+1.3\cdot 10^{-7}(T-900)^2$ $+10^{-4}(T-900)+1.0$ [13]	$952.0+(171.0\cdot T)/685]\cdot 2330$ [14]	$3.8-i\ [0.0443+6.297\cdot 10^{-5}$ $(T-273.15)](\lambda=1064\ \text{nm})$ [15]

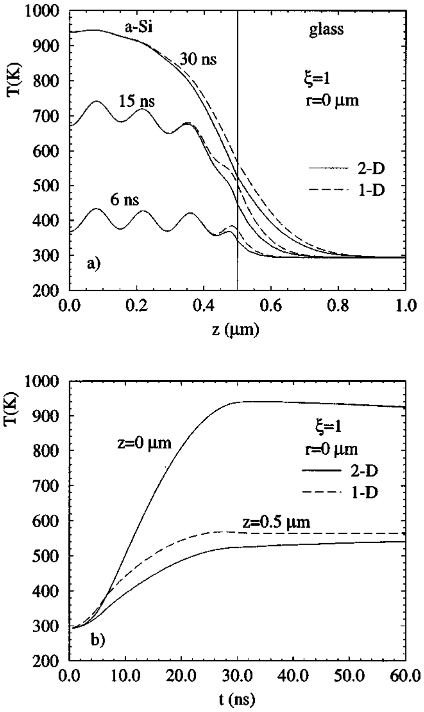

Fig. 2 Temperature profiles versus *z* (*a*) and *t* (*b*) in the *a*–Si/glass structure illuminated with a Gaussian source, for the one-dimensional (1-D) and two-dimensional (2-D) models

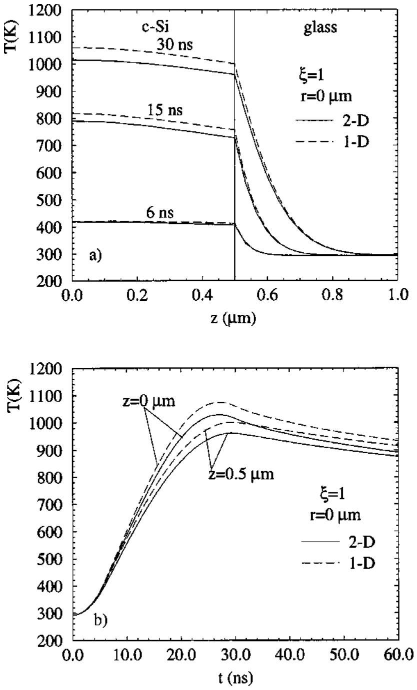

Fig. 3 Temperature profiles versus *z* (*a*) and *t* (*b*) in the *c*–Si/glass structure illuminated with a Gaussian source, for the one-dimensional (1-D) and two-dimensional (2-D) models

thermally semi-infinite body. In all cases the number of nodes in the substrate was 500 and the number of nodes in the *r*-direction was $N_r = 100$.

The $a-$Si temperature profiles along the *z*-coordinate at $r = 0$ are shown in Fig. 2(*a*). Here the two-dimensional profiles are compared with those obtained with the one-dimensional model for the $a-$Si, at $t = 6$, 15 and 30 ns. The profiles of the two models are undistinguishable up to $z = 0.50\ \mu$m for $t = 6$ ns. The abscissa value, where the two profiles start differentiating, decreases with increasing time, and more exactly it reads $z = 0.45\ \mu$m and 0.40 μm for $t = 15$ ns and $t = 30$ ns, respectively. Moreover the discrepancies are not greater than six percent. It can be observed from these figures that temperature oscillations are present within the $a-$Si, because of the interference between the reflected and transmitted waves and of the low thermal conductivity value. The discrepancies between the one-dimensional and two-dimensional profiles can be better appreciated in Fig. 2(*b*), where the profiles

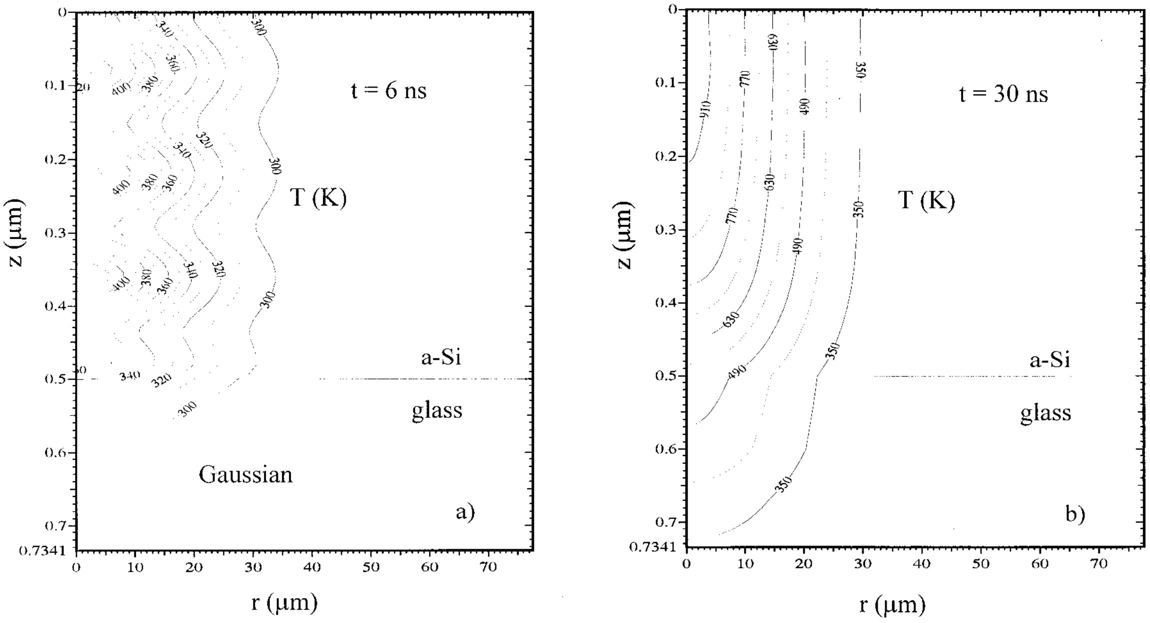

Fig. 4 Isotherms for the *a*–Si/glass structure illuminated with a Gaussian source at different times (*t*=6 and 30 ns)

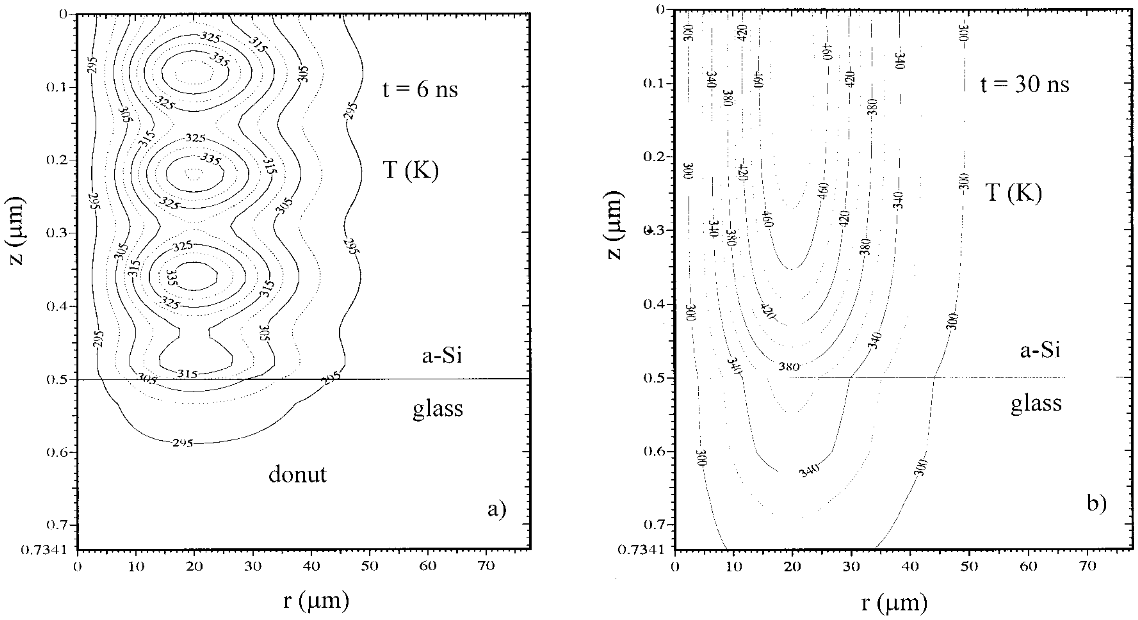

Fig. 5 Isotherms for the $a-$Si/glass structure illuminated with a donut source at different times ($t=6$ and 30 ns)

as functions of time at $r=0$ and $z=0$, i.e., on the surface, as well as at $a-$Si/glass interface ($z=0.5\,\mu$m) are reported.

The $c-$Si temperature profiles as a function of the z-coordinate both for the one-dimensional and two-dimensional models at $t=6$, 15 and 30 ns are reported in Fig. 3(a). Those profiles are quite uniform along z inside the thin film for the aforementioned times. This is mainly due to the greater thermal diffusion inside the $c-$Si. This leads to slightly greater discrepancies as time increases between the two models. In fact, the difference is negligible at $t=6$ ns, it is about four percent at $t=15$ ns, and about five percent at $t=30$ ns. The temperature profiles as function of the time at $r=0$ and $z=0$ (two-dimensional model) and at the $c-$Si/glass interface ($z=0.5\,\mu$m) are shown in Fig. 3(b). The absolute maximum discrepancy between the two models is attained for $t=30$ ns; after this time value the difference almost remains the same. It is worth noting that the comparison between one-dimensional and two-dimensional models at $r=0$ shows an excellent agreement, in accordance with Chen and Tien [2], Grigoropoulos et al. [6], and Angelucci et al. [16].

The isotherms for a Gaussian source at different times, i.e., $t=6$ and 30 ns, are presented in Fig. 4 for the $a-$Si/glass structure. The isotherms for $t=6$ ns are shown in Fig. 4(a); they exhibit an oscillating behavior along z, while the oscillations are dumped along r, giving quite a uniform profile along z. The maximum temperature values are attained inside the thin film according to the spatial absorption function distribution. This can be, perhaps,

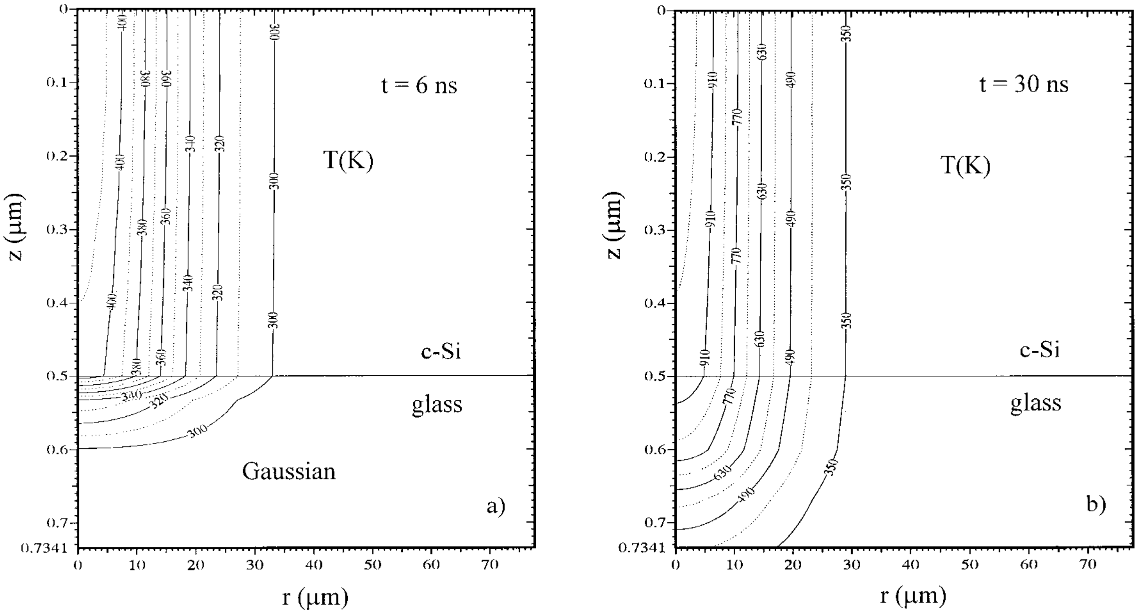

Fig. 6 Isotherms for the $c-$Si/glass structure illuminated with a Gaussian source at different times ($t=6$ and 30 ns)

due more to the lower diffusion of the thermal disturbance rather than to the localized thermal energy generation. As time goes by, the trend is more oriented toward uniform temperature values in the region where the source is stronger than toward diffuse thermal energy along the radius, where the source has very little intensity. This is also due to the existence of higher thermal gradients along z. Furthermore, the diffusion along r is very weak for these elapsed times, as can be seen in Fig. 4(*b*). It can be stated that, in material processing, the heat affected zone is limited to that directly irradiated by the laser for interaction times on the order of 10 ns.

The isotherms at $t=6$ and 30 ns for amorphous silicon, related to a donut laser distribution, are presented in Fig. 5. Even in this case the maximum temperature values at $t=6$ ns are obtained at $z>0$. In this case, it can be observed that thermal gradients along the z-axis are smaller with respect to the Gaussian spot. This is also due to the spot distribution, in fact, the donut presents two symmetrical maxima with respect to the centerline; at $r=0$ the heat flux value is zero. Thus, the solid thermally diffuses along both $r>20\ \mu$m and $r<20\ \mu$m. At $t=30$ ns it can be noted that the thermal fields present the maximum temperature value at $z=0$ and the spatial profiles along the z-axis are smoother than the previous ones.

In Fig. 6 the isothermal lines at $t=6$ and 30 ns for crystalline silicon ($c-$Si) and a Gaussian laser spot are presented. The maximum temperature values are also attained on the external thin film surface for smaller times (6 ns). Isothermal curves assume the same qualitative shape at each time value considered. These curves are almost parallel to the z-axis, the more parallel the higher r is; at r values greater than 20 μm the isotherms are cylindrical surfaces with axis at $r=0$. As can be seen in Fig. 6 the greater the time the smaller the z dependence. This is related to the conductivity of $c-$Si.

Conclusions

The coupled thermal-optical problem inside a multilayer thin film structure irradiated by a laser source was investigated. The optical field was assumed to be one-dimensional, while the thermal one was two-dimensional. Both the thermal and optical properties were assumed to be temperature dependent. The present investigation was carried out for the two silica thin films, $c-$Si and $a-$Si, layered on a glass substrate. A comparison between the present results and those for a coupled fully one-dimensional model was performed. This comparison shows that the hypothesis of one dimensionality of the thermal field is quite accurately verified in the core zone of the Gaussian spot, where the discrepancy between the two models, one dimensional and two dimensional, is negligible for the $a-$Si, and less than five percent for the $c-$Si.

For low-conductivity materials ($a-$Si), the absorption function strongly influences the thermal fields and the maximum values are attained inside the thin film. For high-conductivity materials ($c-$Si), the absorption function does not determine high gradients along z, and these are of the same order of magnitude along r. It can be stated, in conclusion, that for technological processes where the knowledge of temperature is of central importance both on the surface and inside the thin film, that a two-dimensional model should be employed.

Acknowledgment

This work was supported by a grant from Regione Campania by means of Legge 41/1994.

Nomenclature

c = specific heat, J kg^{-1} K^{-1}
c' = speed of light, m s^{-1}
E = electric field, N C^{-1}
k = thermal conductivity, W m^{-1} K^{-1}
k_{ext} = extinction coefficient
n = real part of refractive index
$\overline{n}$ = complex refractive index
r,z = cylindrical coordinate, radial and axial, m
S = Poynting vector, W m^{-2}
s = material thickness, m
T = temperature, K
t = time, s
$\dot{u}'''$ = generation function, W m^{-3}

Greek symbols

λ = wavelength, m
μ = magnetic permeability, N s^{2} C^{-2}
ρ = density, kg m^{-3}

Subscripts

a = air
f = film
in = initial
l = length
p = peak
s = substrate

References

[1] Grigoropoulos, C. P., 1994, ‘‘Heat Transfer in Laser Processing of Thin Films,’’ *Annual Review of Heat Transfer*, C. L. Tien, ed., CRC, Boca Raton, FL, Vol. 5, Chap. 2, pp. 77–130.
[2] Chen, G., and Tien, C. L., 1994, ‘‘Thermally Induced Optical Nonlinearity During Transient Heating of Thin Films,’’ ASME J. Heat Transfer, **116**, pp. 311–316.
[3] Tamura, H., Miyao, M., and Tokuyama, T., 1979, ‘‘Laser-Annealing Behavior of a Phosphorus-Implanted Silicon Substrate Covered with a SiO_2 Film,’’ J. Appl. Phys., **50**, pp. 3783–3784.
[4] Colinge, J. P., and Van de Viele, F., 1981, ‘‘Laser Light Absorption in Multilayers,’’ J. Appl. Phys., **52**, pp. 4769–4771.
[5] Park, H. K., Xu, X., Grigoropoulos, C. P., Do, N., Klees, L., Leung, P. T., and Tam, A. C., 1993, ‘‘Transient Optical Transmission Measurement in Excimer-Laser Irradiation of Amorphous Silicon Films,’’ ASME J. Heat Transfer, **115**, pp. 178–183.
[6] Grigoropoulos, C. P., Park, H. K., and Xu, X., 1993, ‘‘Modeling of Pulsed Laser Irradiation of Thin Silicon Layers,’’ Int. J. Heat Mass Transf., **36**, pp. 919–924.
[7] Mansuripur, M., Connell, G. A. N., and Goodman, J. W., 1982, ‘‘Laser-Induced Local Heating of Multilayers,’’ Appl. Opt., **21**, pp. 1106–1114.
[8] Nakano, S., et al., 1986, ‘‘Laser Patterning Method for Integrated Type a–Si Solar Cell Submodules,’’ Jpn. J. Appl. Phys., Part 1, **25**, pp. 1936–1943.
[9] Madison, M. R., and McDaniel, T. W., 1989, ‘‘Temperature Distributions Produced in an *N*-Layer Film Structure by Static or Scanning Laser or Electron Beam With Application to Magneto-Optical Media,’’ J. Appl. Phys., **66**, pp. 5738–5748.
[10] McGahan, W. A., and Cole, K. D., 1992, ‘‘Solutions of Heat Conduction Equation in Multilayers for Photothermal Deflection Experiments,’’ J. Appl. Phys., **72**, pp. 1362–1373.
[11] Cole, K. D., and McGahan, W. A., 1993, ‘‘Theory of Multilayers Heated by Laser Absorption,’’ ASME J. Heat Transfer, **115**, pp. 767–771.
[12] Knittl, Z., 1976, *Optics of Thin Films*, John Wiley and Sons, London, UK.
[13] Ong, C. K., Tan, H. S., and Sin, E. H., 1986, ‘‘Calculation of Melting Threshold Energies of Crystalline and Amorphous Materials due to Pulsed-Laser Irradiation,’’ Mater. Sci. Eng., **79**, pp. 79–85.
[14] Kiyama, S., Hirono, Y., Hosokawa, H., Moriguchi, T., Nakano, S., and Osumi, M., 1990, ‘‘Temperature Distribution Analysis in Multi-Layer Thin Film Structures by Laser Beam Irradiation,’’ Jpn. Soc. Precision Eng., **56**, pp. 1500–1506.
[15] Do, N., Klees, L., Leung, P. T., Tong, F., Leung, W. P., and Tam, A. C., 1992, ‘‘Temperature Dependence of Optical Constants for Amorphous Silicon,’’ Appl. Phys. Lett., **60**, pp. 2186–2188.
[16] Angelucci, N., Bianco, N., and Manca, O., 1997, ‘‘Thermal Transient Analysis of Thin Film Multilayers Heated by Pulsed Laser,’’ Int. J. Heat Mass Transf., **40**, pp. 4487–4491.

J. E. Kennedy

G. M. Roach, Jr.

M. F. Dowling

S. I. Abdel-Khalik

S. M. Ghiaasiaan
e-mail: seyed.ghiaasiaan@me.gatech.edu

S. M. Jeter

G. W. Woodruff School
of Mechanical Engineering,
Georgia Institute of Technology,
Atlanta, GA 30332-0405

Z. H. Quershi
Westinghouse Savannah River Company,
Aiken, SC 29802

The Onset of Flow Instability in Uniformly Heated Horizontal Microchannels

Onset of nucleate boiling and onset of flow instability in uniformly heated microchannels with subcooled water flow were experimentally investigated using 22-cm long tubular test sections, 1.17 mm and 1.45 mm in diameter, with a 16-cm long heated length. Important experimental parameter ranges were: 3.44 to 10.34 bar channel exit pressure; 800 to 4500 kg/m^{2}s mass flux (1 to 5 m/s inlet velocity); 0 to 4.0 MW/m^2 channel wall heat flux; and 7440–33,000 Peclet number at the onset of flow instability. Demand curves (pressure drop versus mass flow rate curves for fixed wall heat flux and channel exit pressure) were generated for the test sections, and were utilized for the specification of the onset of nucleate boiling and the onset of flow instability points. The obtained onset of nucleate boiling and onset of flow instability data are presented and compared with relevant widely used correlations. [S0022-1481(00)02101-0]

Introduction

Two-phase flow instability is of great concern in the design and operation of heated channels with subcooled liquid through-flow, and can lead to serious safety problems ([1–4]). Two-phase flow instabilities are divided into dynamic and static categories. The dynamic instabilities involve transient inertial dynamic and feedback effects ([2]). The static instabilities can be analyzed based on the pressure drop-flow rate characteristics (the demand curve) of heated channels. When the channel is part of a forced or natural circulatory loop, the segment of the heated channel demand curve with negative slope can be unstable. The onset of flow instability point is defined as the relative minimum point on the demand curve, and is a crucial operational threshold.

The occurrence of the onset of flow instability is due to an increase in the channel pressure drop resulting from voidage in subcooled boiling. In experiments with steady heat flux (or steady mass flow rate), onset of flow instability is known to occur at a flow rate slightly lower (or a heat flux slightly higher) than the flow rate (or heat flux) which leads to the onset of significant void. The onset of significant void point can thus be considered as a conservative estimate for the onset of flow instability.

The onset of significant void and subcooled boiling void fraction development have been studied extensively in the past, leading to successful empirical correlations for the onset of nucleate boiling ([5]) and the onset of significant void ([6,7]) and semi-analytical models for the onset of significant void ([8,9,10]). The relevance of the aforementioned predictive methods to microchannels is questionable, however. In microchannels (where $D_e \lesssim \sqrt{\sigma/g(\rho_L-\rho_G)}$) the gas-liquid interfacial phenomena associated with Taylor instability are mostly irrelevant, and the surface tension is predominant and significantly reduces the vapor-liquid velocity slip, thereby affecting the two-phase flow hydrodynamic characteristics ([11,12]). The predominance of surface tension force, and the occurrence of very large temperature and velocity gradients near the channel walls, also imply that the bubble ebullition phenomena associated with boiling in common large channels do not apply to microchannels. Recent experimental studies have confirmed these observations ([13–15]). Systematic experiments addressing the onset of nucleate boiling, significant void, flow instability, and other related subcooled boiling phenomena in microchannels are thus needed.

Experimental Test Facility and Procedures

Figure 1 is a schematic of the experimental test facility. Important hardware (items labeled with letters) and instrumentation (items labeled numerically) are listed in Tables 1 and 2, respectively. The flow loop is a flexible and carefully designed system for experiments on various aspects of microchannel thermal hydraulics, including the onset of flow instability, critical heat flux, two-phase pressure drop, etc.

Water flow rate over a wide range is provided using two different pumps, *A* and *B*, and flow rates through the test section and the bypass line are finely controlled using the throttle valves *D* and *E*. Fine control of the test section inlet water temperature is provided using the in-line heater *F*. The exit pressure of the test section is controlled via the bellows-type accumulator *M*, where the gas volume in the accumulator is allowed to vary in order to maintain the desired pressure on the liquid side.

The test facility includes a water degassing assembly, where all the water in the test loop is boiled in the reservoir *S*, under vacuum (vacuum pump not shown in Fig. 1), leading to the removal of virtually all the dissolved noncondensables. The dissolved oxygen content of water in the test loop is regularly monitored, and is determined using a galvanic-cell dissolved oxygen sensor (10), which is a pressure-compensated device, and is temperature rated to cover the experimental temperature range.

Instrumentation for the flow loop (Table 2) allows water temperature, pressure, flow rate, and dissolved gas content to be extensively monitored and controlled. Pressure sensors (5) and thermocouples (7) measure the test section water inlet and exit temperatures and pressures, while the pressure drop across the test section is directly measured using the differential pressure transducer (6).

Contributed by the Heat Transfer Division for publication in the JOURNAL OF HEAT TRANSFER. Manuscript received by the Heat Transfer Division, Dec. 1, 1998; revision received, Aug. 3, 1999. Associate Technical Editor: A. Majumdar.

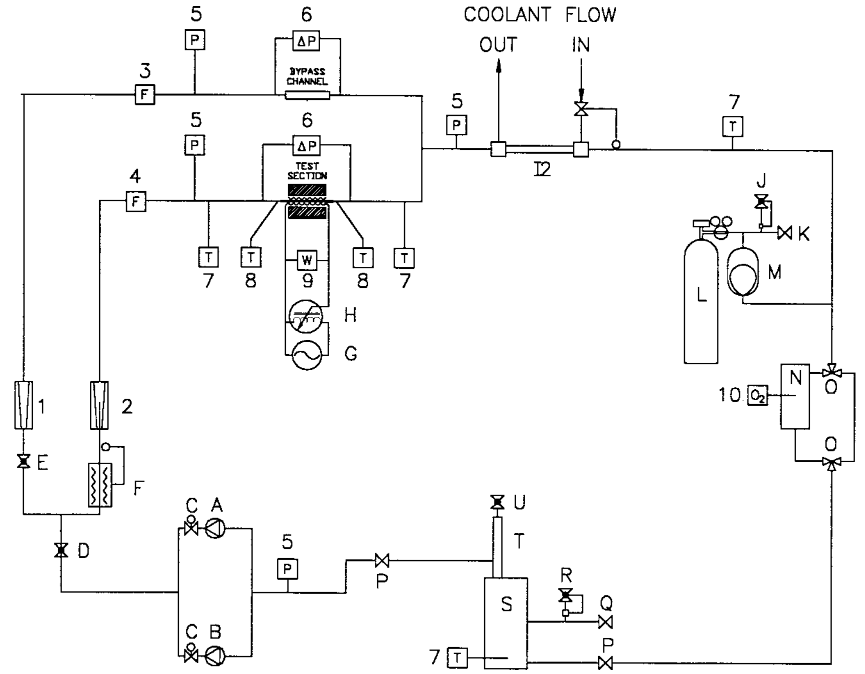

Fig. 1 Schematic of the test facility

Accurate wall temperature readings are made within the heated segment of the test section. Three fine-gauge thermocouples (8) are permanently mounted near each end of the test section in radial configuration, in thermocouple wells drilled accurately to within 0.25 mm of the channel surface, using electrical discharge machining.

Test sections with circular flow cross-sectional geometries, and two diameters, 1.17 mm and 1.45 mm, are used in the experiments. Details of one test section are displayed in Fig. 2. The test sections are constructed from free-machining copper (tellurium copper, *C* 14,500), using the electrical discharge machining technique with extreme care to insure accurate dimensions. The surface roughness of the test sections and their cross-sectional dimensions were measured by cutting separate manufactured samples and placing them in a profilometer. The mean surface roughness was 2 μm and the estimated standard deviation representing the uncertainty in channel hydraulic diameters was only 2.5 μm. The test section is surrounded by thick high-temperature insulation; the calculated heat input to the water (based on overall energy balance) and the applied power typically agree to within two percent.

Table 1 Experimental system hardware components

A	variable-speed positive displacement pump
B	multistage centrifugal booster pump
C	pump isolation ball valve
D	system throttling valve
E	bypass line throttling valve
F	test section in-line heater, thermostatically controlled
G	voltage source, 208 VAC, single phase
H	variable AC power supply
I	heat exchanger, tube-in-tube, thermostatically controlled
J	accumulator relief valve
K	bleed valve
L	nitrogen gas tank
M	accumulator, bellows type
N	oxygen sensor housing
O	three-way valve
P	degassing tank isolation valve
Q	system filling port/valve
R	system relief valve
S	degassing tank
T	noncondensable gas separation column
U	noncondensable gas bleed valve

Deionized and degassed water is used in the experiments. Experiments to measure the onset of flow instability point are performed in two ways. In most cases the tests are pursued by starting with a very high flow rate, and slowly reducing the flow rate and continuously recording all measured parameters. These experiments provide pressure drop versus mass flux characteristics. Some tests, however, are conducted by maintaining the liquid flow rate constant, and increasing the channel heat load until the onset of flow instability occurs at channel exit. The latter tests provide pressure drop versus heat flux characteristics. The onset of flow instability point in both groups of tests is encountered when the pressure drop across the test section passes through a minimum. Each onset of flow instability experiment is repeated at least twice, to ensure reproducibility.

An error propagation analysis was performed for the reported mass and heat fluxes following the standard procedures described in Bevington and Robinson [16], the details of which can be found in Kennedy [17]. Uncertainty in mass flux was assumed to result from errors in the measured volumetric flow rates (see Table 2), and channel diameters. The channel diameters were measured by precision ground pins with a known tolerance of ± 0.013 mm; the latter was therefore used as the error in channel diameter. The calculated mass flux uncertainties in all tests were less than 1.5 percent. The uncertainty in heat flux was assumed to result from errors in measured input power (see Table 2), and the channel heated surface area; and the latter was estimated using the aforementioned tolerance associated with the measurement of channel diameters. The calculated uncertainty associated with heat flux was less than one percent.

In addition to the standard error propagation analysis, an overall energy balance was performed on the test section for each test, whereby the total measured input power was compared with the power calculated from

$$\dot{Q}=\dot{m}_L(\hat{h}_E-\hat{h}_{L,I}) \tag{1}$$

where the enthalpy at the channel exit was calculated using the

Table 2 Experimental system instrumentation components

Label*	Sensor Description	Range	Accuracy†
1	Rotameter	0.8 - 9.5 liters/min	0.4 l/min
2	Rotameter	7.6 - 79.5 l/hr	1.9 l/hr
3	Liquid flow transducer	0-32 l/min	0.3 l/min
4	Liquid flow transducer	0.0560 - 0.5800 l/min	0.0003 l/min
5	Pressure transducer	0 - 1375.0 kPa	3.4 kPa
6	Differential pressure transducer	0 - 186.4 kPa	0.4 kPa
7	Thermocouple, type E	-200 - 425°C	0.1°C
8	Thermocouple, type E, fine gauge	-200 - 425°C	0.1°C
9	Wattmeter, ac power	0 - 5408 kW	0.2% reading
10	Dissolved oxygen probe	0 - 200% saturated air at 25°C, 101 kPa	0.1% reading

* Identification labels refer to the numbered components shown on Figure 1.
† Observed limits of error following calibration in system.

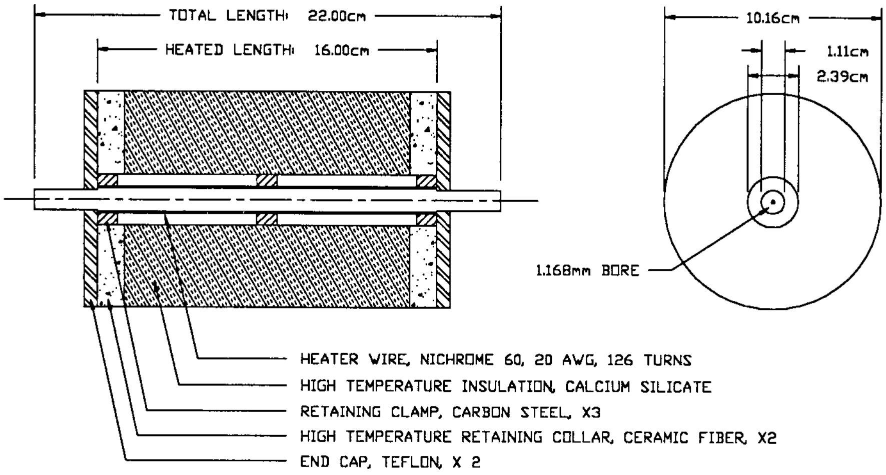

Fig. 2 Cut-away of a test section

measured exit bulk temperature and pressure. The measured and calculated total powers agreed typically within two percent, with a maximum deviation of about four percent.

It should be noted that the aforementioned small uncertainties in G and q'' can lead to relatively large uncertainties for the onset of flow instability data due to the integral nature of the experiments. This can be understood from Eq. (1). Assuming a constant specific heat for water, and noting that the onset of flow instability occurs when the liquid leaving the test section is only slightly subcooled, a mere two percent error in $\dot{Q}/\dot{m}_L$ in a test where the inlet water is subcooled by 60 K leads to an error in $T_{L,E}$ of about 1.2 K. The impact of the latter uncertainty on the local subcooling at the onset of flow instability is significant.

Results and Discussion

General Trends. A total of 70 experiments were performed; in each experiment, measurements providing a complete demand curve for a specific test section at a specified wall heat flux, exit pressure, and bypass flow status (closed or open) were generated. All the experiments presented here were performed using degassed water. The test section pressure drop, ΔP_{TS}, was calculated everywhere by subtracting the pressure drops associated with the test section inlet and exit from the measured pressure difference between the entrance and exit plena, the latter obtained by using the loss coefficients recommended by Idelchick [18].

Typical demand curves (test section pressure drop versus mass flux for constant test section thermal load) are displayed in Fig. 3, and demonstrate the general trends in the data. In this figure each data point represents a separate experiment, and each demand curve represents experiments with a constant heat flux. Each curve depicts only a part of the characteristic pressure drop-mass flux curve, and the onset of flow instability point associated with each heat flux is the relative minimum on its corresponding curve. The segment of the curve to the right of the onset of flow instability point is stable, and instability can develop once the flow rate is reduced below the flow rate associated with the onset of flow instability point, where the curve has a negative slope. Further reduction of the flow rate will lead to a sharp increase in ΔP, the occurrence of a relative maximum, followed by a segment with positive slope ([4]). In the experiments reported here, however,

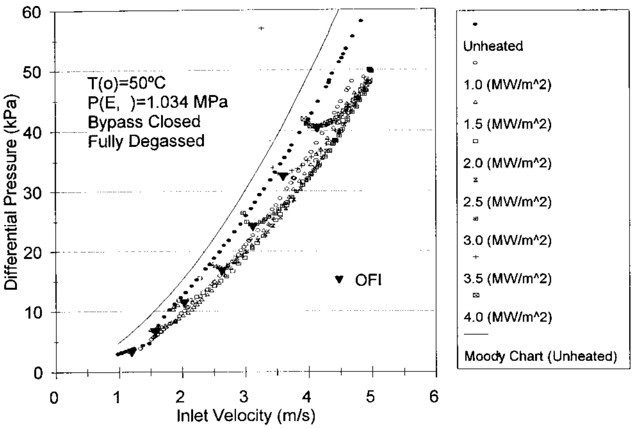

Fig. 3 Experimental demand curves for the 1.17-mm diameter test section (P_E=10.34 bar)

the conditions leading to the onset of flow instability were of interest, and complete demand curves were not obtained. The flow bypass status (bypass open or closed) is not included, since all important test results were found to be insensitive to it. The measured pressure drops obtained in unheated test sections are also shown and do not coincide with the measured liquid pressure drops in the tests with heated channels, even at high liquid velocities. The liquid temperature variations in the experiments with heating are relatively large and affect the liquid viscosity, thereby reducing the liquid single-phase friction factor and leading to smaller channel pressure drops.

Onset of Nucleate Boiling. During experiments, an easily audible whistle-like sound could be heard from the test section, before the flow rate was reduced to the level which led to the onset of flow instability. The generation of this whistle-like sound was evidently due to the appearance of vapor bubbles at the test section exit, and can be attributed to the occurrence of the onset of nucleate boiling. Alternatively, the location of the onset of nucleate boiling point on the demand curve can be specified by comparing the experimental demand curve with a curve representing the calculated channel pressure drops assuming single-phase liquid flow. The latter calculations must, of course, utilize a friction factor representative of the test section, and must correctly account for the dependence of the liquid viscosity on temperature. The experimental and calculated curves will have similar gradients for single-phase liquid flow (i.e., at very high flow rates), and their gradients will be different when boiling occurs. The onset of nucleate boiling point on the characteristic curve, representing the conditions that lead to the occurrence of the onset of nucleate boiling at the channel exit, can thus be specified as the point beyond which the gradients of the two curves become noticeably different ([19]). The aforementioned two methods for the specification of the onset of nucleate boiling conditions were both applied to some tests and compared, and the results were found to be in good agreement. The experimental results to be discussed below were obtained using the aforementioned method based on the gradient of the demand curves.

Table 3 is a summary of the experimental conditions leading to the onset of nucleate boiling. These nucleate boiling conditions are compared with the correlation of [5] in Figs. 4 and 5. The latter correlation represents an empirical fit to the predictions, for water, of a simple model which defines the onset of nucleate boiling as the minimum wall superheat for the growth of hemispherical bubbles assumed to reside on wall crevices. Crevices of all sizes are assumed, and the growth of bubbles of any size is assumed to be sufficient for triggering the onset of nucleate boiling. The correlation of Bergles and Rohsenow [5] can be represented as

Table 3 Parameters leading the onset and nucleate boiling (ONB) at test section exit (liquid inlet temperature=50°C)

Small Diameter (1.168 mm) Circular Tube		
q'' (MW/m^2)	Exit Pressure (Bars)	Experimental U_L(m/s)
4.0	10.34	4.1219
3.5	10.34	3.6011
3.0	10.34	3.1322
3.0	6.90	3.5675
3.0	3.45	4.3576
2.5	10.34	2.6426
2.0	10.34	2.016
2.0	3.45	2.9353
1.5	10.34	1.5
1.0	10.34	1.0467
Larger Diameter (1.448 mm) Circular Tube		
q'' (MW/m^2)	Exit Pressure (Bars)	Experimental U_L (m/s)
3.0	10.34	2.6474
2.5	10.34	2.2880
2.0	10.34	1.7295
1.5	10.34	1.3060
1.5	6.90	1.5726
1.5	3.45	1.9978
1.0	10.34	1.0467

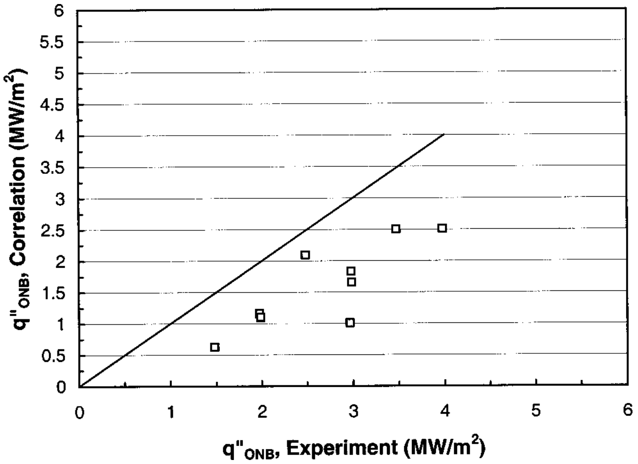

Fig. 4 Comparison between the onset of nucleate boiling (ONB) data and the correlation of Bergles and Rohsenow [5] (D=1.17 mm)

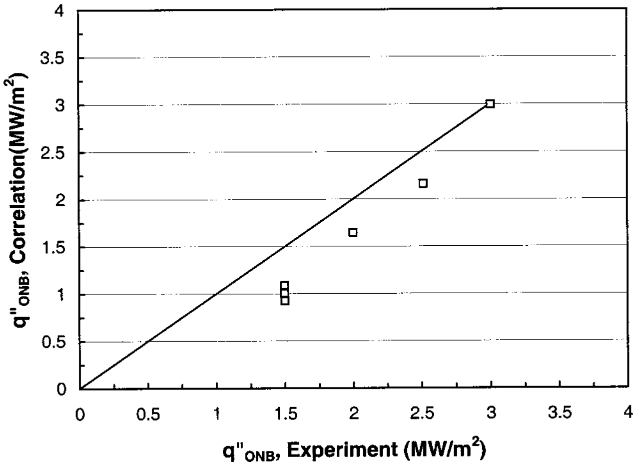

Fig. 5 Comparison between the onset of nucleate boiling (ONB) data and the correlation of Bergles and Rohsenow [5] (D=1.45 mm)

Table 4 Summary of measured local conditions leading to the onset of flow instability (OFI)

D_e	Bypass	$P_{E,}$	Heat Flux*	T_L*	Re_L	Pe	St
(m)		(bar)	(MW/m^2)	(C)			
0.0011684	Closed	10.34	1.39	173.1	12131	11487	0.01498
0.0011684	Closed	10.34	1.88	174.8	15787	14949	0.01692
0.0011684	Closed	10.34	2.37	162.3	22145	20969	0.00787
0.0011684	Closed	10.34	2.9	172.1	24978	23652	0.01373
0.0011684	Closed	10.34	3.38	174.7	28541	27026	0.01688
0.0011684	Closed	10.34	3.85	175.1	32636	30903	0.01727
0.0011684	Closed	6.9	1.9	159.7	16326	16853	0.01952
0.0011684	Closed	6.9	2.89	160.3	25282	26098	0.02088
0.0011684	Closed	3.45	1.8	137.6	17530	21518	0.01443
0.0011684	Closed	3.45	2.86	135.6	26430	32443	0.02252
0.0011684	Closed	10.34	1.42	175.2	11461	10852	0.03406
0.0011684	Closed	10.34	1.92	173.2	15608	14780	0.02516
0.0011684	Closed	10.34	2.4	174.8	19416	18385	0.02997
0.0011684	Closed	10.34	2.89	176.6	22956	21737	0.04002
0.0011684	Closed	10.34	3.37	173.3	27763	26289	0.02447
0.0011684	Closed	10.34	4.06	168.9	34705	32863	0.01587
0.0011684	Closed	6.9	1.93	155.4	16791	17333	0.01986
0.0011684	Closed	3.45	1.92	130	18210	22353	0.01687
0.0011684	Closed	6.9	2.89	155.1	25255	26070	0.01964
0.0011684	Open	10.34	1.33	156.5	13237	12534	0.00606
0.0011684	Open	10.34	1.83	157.6	18288	17317	0.00615
0.0011684	Open	6.9	1.87	158.7	16628	17165	0.01733
0.0011684	Open	3.45	1.75	131.2	17401	21360	0.01306
0.0011684	Open	10.34	1.37	175	11098	10509	0.03049
0.0011684	Open	10.34	1.86	165.1	16504	15627	0.01166
0.0011684	Open	10.34	2.4	174.7	19572	18533	0.02901
0.0011684	Open	6.9	1.93	154.1	16952	17499	0.01783
0.0011684	Open	3.45	1.93	132.7	17844	21904	0.02540
0.001448	Open	10.34	0.93	170.5	7930	7509	0.02147
0.001448	Open	10.34	1.47	172.7	12200	11553	0.02857
0.001448	Open	10.34	1.95	166.4	16649	15765	0.01617
0.001448	Open	10.34	2.5	169.8	22293	21109	0.01366
0.001448	Open	10.34	2.98	169.4	25358	24012	0.02044
0.001448	Open	10.34	3.52	173.4	28609	27091	0.03098
0.001448	Open	10.34	4.06	167.6	34819	32971	0.01757
0.001448	Open	6.9	1.39	153.9	12380	12780	0.02078
0.001448	Open	6.9	2.51	152.3	22024	22735	0.01851
0.001448	Open	3.45	1.5	124.5	13151	16143	0.37103
0.001448	Open	3.45	2.51	130.1	24196	29701	0.02108
0.001448	Closed	10.34	0.94	173.1	7859	7442	0.02966
0.001448	Closed	10.34	1.44	173.5	11853	11224	0.03108
0.001448	Closed	10.34	1.98	169.4	16920	16022	0.01975
0.001448	Closed	10.34	2.48	167.5	21276	20147	0.01763
0.001448	Closed	10.34	2.97	168.9	25448	24097	0.01926
0.001448	Closed	6.9	1.49	146.3	13671	14113	0.01335
0.001448	Closed	3.45	1.46	128.2	14398	17674	0.01625

* Obtained from energy balance assuming no evaporation

$$q''_{\rm ONB}=5.30P^{1.156}[1.8(T_w-T_{\rm sat})_{\rm ONB}]^n \tag{2}$$

where $n=2.41/P^{0.0234}$. Here, q''_{ONB}, represents the wall heat flux leading to the onset of nucleate boiling, is in W/m^2, P is in kPa, and T_w and $T_{\rm sat}$ are wall and saturation temperatures, both in K. In the above correlation, $q''_{\rm ONB}$ and T_w are related according to

$$q''_{\rm ONB}=h(T_w-T_L)_{\rm ONB}. \tag{3}$$

To apply the above correlation, h, the local convective heat transfer coefficient was calculated using the Dittus and Boelter correlation ([20]). The correlation of Bergles and Rohsenow [5] was applied to the data the following way. For each experimental data, T_L at the channel exit was first calculated using a simple energy balance. Knowing T_L and pressure, Eqs. (2) and (3) were then iteratively solved for T_w and $q''_{\rm ONB}$.

The correlation of Bergles and Rohsenow [5], as noted, systematically underpredicts the onset of nucleate boiling heat flux associated with data representing the 1.17-mm diameter test section, typically by a factor of two, and it agrees reasonably well with the data representing the 1.45-mm diameter test section. These results are consistent with the findings of Inasaka et al. [19] who noted similarly reasonable agreement between their data representing the onset of nucleate boiling in microchannels with 1 mm and 3-mm inner diameters and the correlation of Bergles and Rohsenow [5].

Onset of Flow Instability and Onset of Significant Void The points, as noted earlier, are defined as the minima on the demand curves. Table 4 is a summary of the experimental local conditions leading to the onset of flow instability, and includes the local values of the following important dimensionless parameters:

$$\mathrm{St}=\frac{q''}{\rho_L U_L C_{PL}(T_{\rm sat}-T_L)} \tag{4}$$

$$\mathrm{Pe}=\frac{GD_eC_{PL}}{k_L}. \tag{5}$$

The onset of significant void point generally occurs at a slightly higher mass flux than the onset of flow instability point on pressure drop-mass flux channel characteristics, and it occurs at a slightly lower heat flux than the onset of flow instability point on pressure drop-heat flux channel characteristics. As a result, correlations for onset of significant void can provide a conservative estimate of the range of operational parameters leading to the onset of flow instability ([4]). The correlation of Saha and Zuber [6] has been relatively successful in predicting various experimental significant void and flow instability data ([21–23]). Our flow instability experimental data, which all fall in the thermally controlled range of Pe<70,000 ([6]) (see Table 4), are compared with the latter correlation in Fig. 6. The large uncertainty bands represent ±2 percent uncertainty in heat flux (see the discussion following Eq. (1)), and are a result of the integral nature of onset of flow instability experiments. Although uncertainties associated with heat flux and mass flow rate are quite low in these experiments, their effect on the local fluid temperature at the test section exit can be significant. Notwithstanding these large uncertainties, the correlation of Saha and Zuber [6] appears to overpredict the Stanton number, St, for our onset of flow instability data for Pe ⩽25,000, and is in reasonable agreement, within about a factor of 2 scatter, with our data for Pe⩾25,000.

The agreement between our onset of flow instability data and the correlation of Saha and Zuber [6] for thermally controlled onset of significant void at Pe⩾25,000 is consistent with the results of the study reported by Inasaka et al. [19], who experimentally studied the onset of significant void phenomenon in channels 1 mm and 3 mm in diameter. Their experiments included Pe $\approx 4.8\times10^4$, 8.9×10^4, and 13.7×10^4, and their data representing the lower Pe value compared with the correlation of Saha and Zuber [6] relatively well. The data with Pe$\approx 13.7\times10^4$ of the latter authors evidently fall in the hydrodynamically controlled range, where in large channels the models based on the bubble departure mechanism ([8–10]) should apply. Inasaka et al. [19] compared their data with the model of Levy [8] and noted relatively poor results, however.

Simple and purely empirical correlations for the onset of flow instability data can be developed by comparing flow and boundary conditions leading to the onset of flow instability, with those leading to saturation ([24]). Figure 7 shows a comparison between the experimental heat flux values at the onset of flow instability $q''_{\rm OFI}$, and 90 percent of the heat flux, $q''_{\rm sat}$, which would result in bulk exit saturation for the same geometry, mass flux, inlet temperature, and exit pressure. The value of $q''_{\rm sat}$ can be calculated using a simple energy balance:

$$g''_{\rm sat}=\frac{GA(\hat{h}_f-\hat{h}_I)}{p_HL_H}. \tag{6}$$

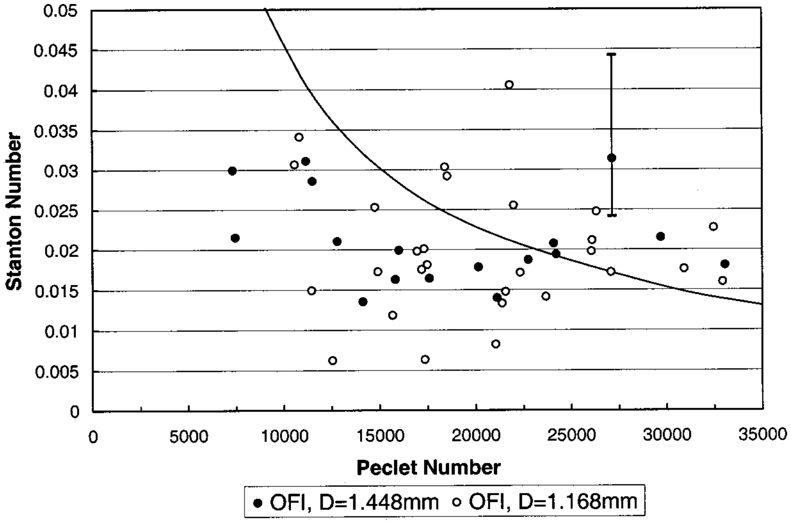

Fig. 6 Variation of experimental values of the Stanton number at onset of flow instability (OFI) with the Peclet number and comparison with the correlation of Saha and Zuber [6] for the onset of significant void (OSV)

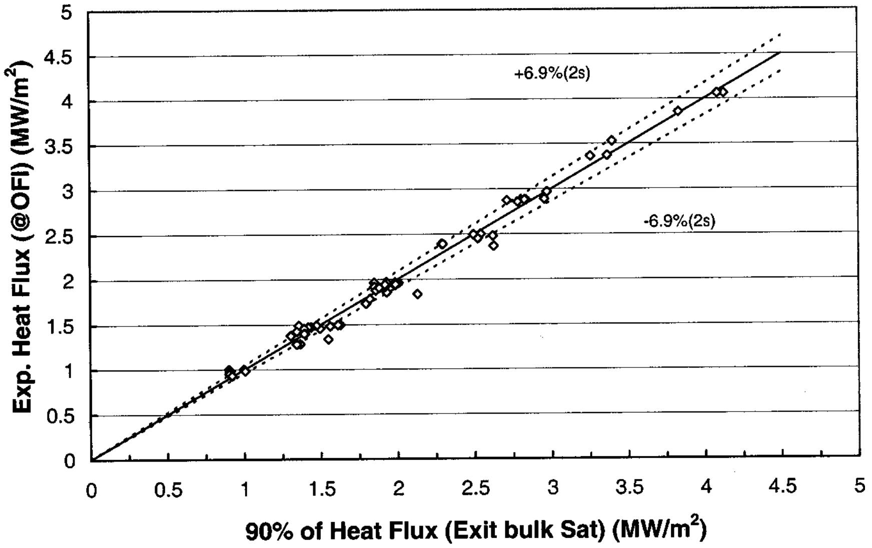

Fig. 7 Comparison between the heat flux values at the onset of flow instability (OFI) and 90 percent of the values required for bulk exit saturation

Figure 7 indicates that the heat flux at the onset of flow instability can be predicted using the relation

$$q''_{\mathrm{OFI}} = 0.9 q''_{\mathrm{sat}}. \tag{7}$$

The above correlation predicts the data within 6.9 percent, with 95 percent confidence level.

A comparison similar to that shown in Fig. 7, for the mass flux at the onset of flow instability, G_{OFI}, and the mass flux corresponding to bulk exit saturation, G_{sat}, for the same geometry, heat flux, inlet temperature and exit pressure, was also performed. The value of G_{sat} can be calculated from

$$G_{\mathrm{sat}} = \frac{q'' p_H L_H}{A(\hat{h}_f - \hat{h}_I)}. \tag{8}$$

The results indicated that the mass flux at the onset of flow instability can be predicted from the following correlation within 6.45 percent, with 95 percent confidence:

$$G_{\mathrm{OFI}} = 1.11 G_{\mathrm{sat}}. \tag{9}$$

As mentioned earlier, the bubble ebullition phenomena in microchannels are likely to be significantly different from the commonly applied large channels, due to the occurrence of extremely large-temperature and velocity gradients in the former. Large-temperature gradients near the wall result in a strong thermocapillary (Marangoni) force which resists the departure of bubbles from wall crevices. Once released, furthermore, small bubbles in a microchannel are acted on by a significant lift force resulting from the extremely large liquid velocity gradients ([13]). Observations confirming that the bubble ebullition phenomenology in microchannels is different from large channels have been reported by Peng and Wang [14,15]. The latter authors did not observe visible bubbles in their experiments dealing with boiling of deionized water and Methanol in rectangular cross section microchannels, even under conditions clearly representing fully developed boiling. Evidently, experiments addressing the basic phenomenology of boiling in microchannels are needed.

Concluding Remarks

The onset of nucleate boiling and the onset of flow instability in uniformly heated microchannels with subcooled water flow were experimentally investigated in this study. The test sections were 22-cm long channels with circular cross sections, with 1.17-mm and 1.45-mm inner diameters, and had 16-cm long heated lengths. Important experimental parameter ranges were: 3.44 to 10.34 bar channel exit pressure; 800 to 4500 kg/m^{2}s mass flux (1 to 5 m/s inlet velocity); 0 to 4.0 MW/m^2 channel wall heat flux; and 7440 to 33,000 Peclet number at the onset of flow instability. Demand curves (pressure drop versus mass flow rate curves for constant wall heat flux and channel exit pressure) were generated. The correlation of Bergles and Rohsenow [5] underpredicted the heat flux at the onset of nucleate boiling typically by a factor of two for the smaller channel and agreed reasonably well with the experimental data for the larger channel. The empirical correlation of Saha and Zuber [6] for the onset of significant void when directly compared with the onset of flow instability data, significantly overpredicted the heat flux leading to the onset of flow instability for Peclet numbers less than about 25,000, and agreed reasonably well with the data for higher Peclet numbers.

Nomenclature

A = channel cross-sectional area (m^2)
C_p = specific heat (J/kg K)
D = channel diameter (m)
D_e = hydraulic diameter (m)
G = mass flux (kg/m^{2}s)
g = gravitational constant (m/s^2)
h = convection heat transfer coefficient (W/m^2 K)
$\hat{h}$ = enthalpy (J/kg)
k = thermal conductivity (W/m K)
L_H = heated length (m)
$\dot{m}$ = mass flow rate (kg/s)
P = pressure (Pa)
ΔP = pressure drop (Pa)
p_H = heated perimeter (m)
Pe = Peclet number
$\dot{Q}$ = total power (W)
q'' = wall heat flux (W/m^2)
St = Stanton number
T = temperature (K)
U = velocity (m/s)

Greek Letters

ρ = density (kg/m^3)
σ = surface tension (N/m)

Subscripts

E = test section exit
f = saturated liquid
G = vapor
I = inlet
L = liquid
OFI = onset of flow instability
sat = saturation

References

[1] Bouré, J. A., Bergles, A. E., and Tong, L. S., 1973, ''Review of Two-Phase Flow Instability,'' Nucl. Eng. Desned., **25**, pp. 165–192.

[2] Ishii, M., 1976, ''Study of Flow Instabilities in Two-Phase Mixtures,'' Argonne National Laboratory Report, ANL-76-23.

[3] Bergles, A. E., 1977, ''Review of Instabilities in Two-Phase Systems,'' *Two-Phase and Heat Transfer*, **2**, S. Kakac and F. Mayinger, eds., Hemisphere, Washington, DC, pp. 383–422.

[4] Yadigaroglu, G., 1981, ''Two-Phase Flow Instabilities and Propagation Phenomena,'' *Thermohydraulics of Two-Phase Systems for Individual Design and Nuclear Engineering*, M. Delhaye, M. Giot, and L. M. Riethmuller, eds., Hemisphere, Washington, DC, pp. 353–403.

[5] Bergles, A. E., and Rohsenow, W. M., 1964, ''The Determination of Forced-Convection Surface Boiling Heat Transfer,'' ASME J. Heat Transfer, **C86**, pp. 365–372.

[6] Saha, P., and Zuber, N., 1974, ''Point of Net Vapor Generation and Vapor Void Fraction in Subcooled Boiling,'' *Proceedings of the 5th International Heat Transfer Conference*, Tokyo, Japan, pp. 175–179.

[7] Ünal, H. C., 1975, ''Determination of the Initial Point of Net Vapor Generation in Flow Boiling Systems,'' Int. J. Heat Mass Transf., **18**, pp. 1095–1099.

[8] Levy, S., 1967, ''Forced Convection Subcooled Boiling: Prediction of Vapor Volumetric Fraction,'' Int. J. Heat Mass Transf., **28**, pp. 1116–1129.

[9] Staub, F. W., 1975, ''The Void Fraction in Subcooled Boiling: Prediction of the Initial Point of Net Vapor Generation,'' Int. J. Heat Mass Transf., **8**, pp. 1095–1099.

[10] Rogers, J. T., Salcudean, M., Abdullah, Z., McLeod, D., and Poirier, D., 1987, ''The Onset of Significant Void in Up-Flow Boiling of Water at Low Pressures and Velocities,'' Int. J. Heat Mass Transf., **30**, pp. 2247–2260.

[11] Triplett, K. A., Ghiaasiaan, S. M., Abdel-Khalik, S. I., and Sadowski, D. L., 1999, ''Gas-Liquid Two-Phase Flow in Microchannels, Part I: Two-Phase Flow Patterns,'' Int. J. Multiphase Flow, **25**, pp. 377–394.

[12] Triplett, K. A., Ghiaasiaan, S. M., Abdel-Khalik, S. I., LeMouel, A., and McCord, B. N., 1999, ''Gas-Liquid Two-Phase Flow in Microchannels, Part II: Void Fraction and Pressure Drop,'' Int. J. Multiphase Flow, **25**, pp. 395–410.

[13] Vandervort, C. L., Bergles, A. E., and Jensen, M. K., 1992, ''Heat Transfer Mechanisms in Very High Heat Flux Boiling,'' *Fundamentals of Subcooled Flow Boiling*, ASME, New York, pp. 1–9.

[14] Peng, X. F., and Wang, B. X., 1993, ''Forced Convection and Flow Boiling Heat Transfer for Liquids Flowing Through Microchannels,'' Int. J. Heat Mass Transf., **36**, pp. 3421–3427.

[15] Peng, X. F., and Wang, B. X., 1994, ''Liquid Flow and Heat Transfer in Microchannels With/Without Phase Change,'' *Proceedings of the 10th International Heat Transfer Conference*, **5**, pp. 159–177.

[16] Bevington, P. R., and Robinson, D. K., 1992, *Data Reduction and Error Analysis for the Physical Sciences*, 2nd Ed., McGraw-Hill, New York.

[17] Kennedy, J. E., 1997, ''Onset of Flow Instability in Uniformly Heated Microchannels,'' M.S. thesis, Georgia Institute of Technology, Atlanta, GA.

[18] Idelchick, I. E., 1994, *Handbook of Hydraulic Resistances*, 3rd Ed., CRC Press, London.

[19] Inasaka, F., Nariai, H., and Shimura, T., 1989, ''Pressure Drops in Subcooled Flow Boiling in Narrow Tubes,'' Heat Transfer–Japanese Research, **18**, pp. 70–82.

[20] Dittus, P. W., and Boelter, L. M. K., 1930, ''Heat Transfer in Automobile Radiators of Tubular Type,'' Univ. of CA Pub. Engng. **2**, No. 13, pp. 443–461.

[21] Hino, R., and Ueda, T., 1985, ''Studies on Heat Transfer and Flow Characteristics in Subcooled Flow Boiling—Part I: Boiling Characteristics,'' Int. J. Multiphase Flow, **11**, pp. 29–281.

[22] Johnston, J. S., 1989, ''Subcooled Boiling of Downward Flow in a Vertical Annulus,'' ASME *Proceedings of the National Heat Transfer Conference*, ASME, New York, pp. 149–156.

[23] Hu, L. W., and Pan, C., 1995, ''Prediction of Void Fraction in Convective Subcooled Boiling Channels Using a One-Dimensional Two-Fluid Model,'' ASME J. Heat Transfer, **117**, pp. 799–803.

[24] Forgan, R., and Whittle, R. H., 1966, ''Pressure Drop Characteristics for the Flow of Subcooled Water at Atmospheric Pressure in Narrow Heated Channels,'' UK Atomic Energy Research Establishment Report AERE-M 1739.

Analysis of In-Flight Oxidation During Reactive Spray Atomization and Deposition Processing of Aluminum

J.-P. Delplanque
Division of Engineering,
Colorado School of Mines,
Golden, CO 80401-1887

E. J. Lavernia

R. H. Rangel
e-mail: rhrangel@uci.edu

Department of Mechanical and Aerospace
Engineering and Department of Chemical and
Biochemical Engineering and Materials Science,
University of California,
Irvine, CA 92697-3975

This work defines a model to predict the characteristics of materials processed using reactive spray atomization and deposition. The materials considered are aluminum alloys while target dispersoids are primarily oxides. These may be obtained by the reaction of oxygen-containing atomization gas mixtures with molten alloy droplets. Droplet position and velocity histories are obtained from the numerical solution of the one-dimensional equation of motion. The energy equation inside the droplet is solved numerically using finite differences to predict the spatially resolved temperature field. The solid/liquid interface progression rate is estimated using a power law while an oxidation rate expression based on the Mott-Cabrera theory is used for the oxide thickness. Such a model should prove very valuable in determining the parameters controlling the volume fraction and the size distribution of the dispersoids for various systems. [S0022-1481(00)02901-7]

Keywords: *Droplet, Heat Transfer, Manufacturing, Materials, Modeling, Solidification*

Introduction

Reactive spray atomization and deposition is a materials processing technique which combines atomization, chemical reaction, and consolidation ([1–3]). It potentially allows in situ, continuous control over alloy composition and chemical reaction between molten alloy droplets and reactive atomization gas ([3]). During reactive spray deposition, a molten alloy is atomized using a reactive gas mixture. The atomized droplets are subsequently deposited on a substrate. Chemical reactions occur between the matrix material and the reactive gas during both atomization and deposition. By carefully selecting alloying additive and reactive gas combinations on the basis of thermodynamic considerations, it is possible to synthesize materials containing in situ dispersoids such as carbides, nitrides, and oxides, leading to grain refinement ([1]).

Dai et al. [2] have shown experimentally that adding oxygen to the atomization gas results in a significant grain size reduction (from 41 μm for processing with nitrogen only down to 18 μm when ten percent (vol.) oxygen is added to the atomization gas). The experimental data indicates that the volume fraction and the size distribution of the dispersoids are critical to the grain refinement mechanisms. However, a tangible understanding of the role played by the dispersoids in grain growth limitation is still in development. A model for Ni_3Al droplet solidification and oxidation was developed by Liu et al. [3]. That model included a crude numerical solution of the droplet energy equation as well as a very simple oxidation model that could not reproduce the variations of the oxide volume fraction with the atomization gas oxygen content observed by Dai et al. [2].

The primary goal of the present work is to define a model that will allow the prediction of the oxide volume fraction in the deposited material as a function of processing parameters such as the atomization gas oxygen content or the melt superheat. The configuration used here as a reference is that employed by Dai et al. [2]. In this setup, the starting alloy is melted and superheated in a graphite crucible and then transported through a graphite delivery tube to the atomizer. In the atomizer, the liquid metal jet (typical diameter: 3–5 mm) flows along the axis. It is surrounded by 18 orifices, each having a diameter of 0.8 mm, providing supersonic jets of a N_2/O_2 mixture. The interactions between the liquid metal jet, the high-speed gaseous jet, and the shock wave pattern result in atomization. The droplets thus formed exchange momentum, heat, and react with the surrounding gas to eventually impinge on a substrate where they deform, spread, and solidify. The model presented here focuses on in-flight droplet behavior. The liquid-metal jet breakup and droplet deposition phases are not modeled.

This model is based on Liu et al.'s model ([3]) but includes a refined solution of the droplet energy equation thus allowing a more accurate prediction of the location of the oxide/solid and solid/liquid interfaces. Furthermore, the oxidation process is described using a model based on the Mott-Cabrera theory ([4,2]). The materials considered are aluminum alloys while target dispersoids are primarily oxides. These may be obtained by the reaction of oxygen-containing atomization gas mixtures with molten alloy droplets or with minor alloy additives that exhibit a high affinity for oxygen. This modeling effort considers only the former.

Analysis

Consider a spherical metal droplet traveling in a colder, oxidizing gas. If the metal oxide is stable and forms relatively quickly (as it is the case for aluminum), it forms a continuous layer at the periphery of the droplet. As the droplet advances, it is cooled by convection and, eventually, starts solidifying. The oxide layer provides heterogeneous nucleation sites and solidification proceeds from the oxide interface towards the center of the droplet (see Fig. 1).

The thermal energy transfer in the droplet is described using a spherically symmetric unsteady conduction equation:

$$\frac{\partial T}{\partial t} = \alpha \frac{1}{r^2} \frac{\partial}{\partial r}\left(r^2 \frac{\partial T}{\partial r}\right). \tag{1}$$

This equation has to be solved in the oxide, solid, and liquid regions. Since heat release occurs at both the oxide/solid (or

---

Contributed by the Heat Transfer Division for publication in the JOURNAL OF HEAT TRANSFER. Manuscript received by the Heat Transfer Division, Feb. 10, 1999; revision received, Oct. 19, 1999. Associate Technical Editor: T. Avedisian.

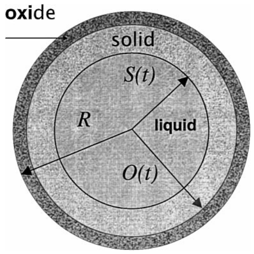

Fig. 1 Oxide, solid, and liquid regions in the droplet

oxide/liquid) and solid/liquid interfaces, their positions, $O(t)$ and $S(t)$, must be determined and heat balances must be written at these locations:

$$\rho_s \Delta H_m \frac{dS}{dt} = k_s \left.\frac{\partial T}{\partial r}\right|_{r=S(t)} - k_l \left.\frac{\partial T}{\partial r}\right|_{r=S(t)} \tag{2}$$

$$\frac{1}{2}\frac{\rho_{\mathrm{At}}}{W_{\mathrm{At}}} \Delta \overline{H}_{\mathrm{ox}} \frac{dO}{dt} = k_{\mathrm{ox}} \left.\frac{\partial T}{\partial r}\right|_{r=O(t)} - k_d \left.\frac{\partial T}{\partial r}\right|_{r=O(t)} \tag{3}$$

where the subscript ''d'' (droplet) refers to either solid or liquid since both situations are possible. Furthermore, a symmetry condition is enforced at the droplet center:

$$\left.\frac{\partial T}{\partial r}\right|_{r=0} = 0 \tag{4}$$

and a convective cooling condition is applied at the droplet surface:

$$k_l \left.\frac{\partial T}{\partial r}\right|_{r=R} = h(T_g - T_s). \tag{5}$$

Since the boundary conditions described by Eqs. (2) and (3) are applied at moving boundaries, it is useful to transform Eq. (1) in order to immobilize these interfaces. In general, if a one-dimensional domain has two time-dependent boundaries ($r = f(t)$ and $r = g(t)$), it can be mapped to a domain where both boundaries are not time-dependent using the following transformation:

$$\xi = \frac{r - f(t)}{g(t) - f(t)}. \tag{6}$$

This mapping results in the appearance of pseudo-convective term in the transformed equation

$$\frac{\partial T}{\partial t} + A(\xi,t)\frac{\partial T}{\partial \xi} = B(\xi,t)\frac{\partial}{\partial \xi}\left(C(\xi,t)\frac{\partial T}{\partial \xi}\right) \tag{7}$$

where

$$\begin{cases} A(\xi,t) = [\xi(\dot{f} - \dot{g}) - \dot{f}]/(g-f) \\ B(\xi,t) = \alpha/\{(g-f)^2[(g-f)\xi + f]^2\}. \\ C(\xi,t) = [(g-f)\xi + f]^2. \end{cases} \tag{8}$$

In the case considered here, $f(t)$ and $g(t)$ are defined in each of the three regions as follows:

$$\begin{cases} 0 < r < S(t): & f(t) = 0, & g(t) = S(t) \\ S(t) < r < O(t): & f(t) = S(t), & g(t) = O(t) \\ O(t) < r < R: & f(t) = O(t), & g(t) = R. \end{cases} \tag{9}$$

Nonequilibrium Solidification. In the case of equilibrium solidification, phase change occurs at the melting temperature, T_L, and Eq. (2) is used to determine the solid growth rate, dS/dt. However, as it will be shown in the Results Section, the droplet cooling rates in the type of process considered here are so high (of the order of 10^5 K/s) that the achievable undercooling is significant and the solid growth is kinetically driven. Hence, a typical liquid metal droplet will undergo liquid cooling until its surface temperature reaches the nucleation temperature. The homogeneous nucleation temperature, $T_{n,0}$, depends on the cooling rate, $-dT/dt$, the droplet size, D, and the rate of nucleation, $\mathfrak{I}$, through Hirth's equation ([5]):

$$\frac{0.01\mathfrak{I}(\pi D^3/6)\Delta T_0}{(-\dot{T})} = 1 \tag{10}$$

where $\Delta T_0 (= T_L - T_{n,0})$ is the achievable homogeneous undercooling. Furthermore, the homogeneous nucleation rate may be estimated by Flemings [6] and Lawrynowicz et al. [7].

$$\mathfrak{I} = N \exp\left[-\frac{16\pi}{3}\frac{\Omega^2 T_L^2 \sigma^3}{\kappa(T_L - \Delta T_0)\Delta T_0^2 \Delta \overline{H}_m^2}\right] \tag{11}$$

where $N = 10^{46}\ \mathrm{m}^{-3}\mathrm{s}^{-1}$. Equations (10) and (11) are solved numerically to yield ΔT_0. In order to evaluate the heterogeneous undercooling, the method proposed by Mathur et al. [8] is used here (see also [7]). The degree of heterogeneous undercooling, ΔT, is then related to ΔT_0 as

$$\Delta T = \Delta T_0 \exp\left(-2.2\times 10^{12}\frac{\pi d^3}{6}\right). \tag{12}$$

Once the nucleation temperature is reached, solidification starts. The solidification rate is assumed to follow a linear law ([3]):

$$\frac{dS}{dt} = K(T_L - T_{s/l}) \tag{13}$$

where $T_{s/l}$ is the temperature of the solid/liquid interface and K is the kinetic parameter as defined by Levi and Mehrabian [9]. Equations (2) and (13) are then solved together to determine $T_{s/l}$.

Oxidation Model. The present oxidation model for aluminum is based on the Mott-Cabrera theory for very thin oxide films recently proposed by Dai et al. [2]. They argue that since the droplet travel time is typically a few milliseconds (the results presented herein confirm it), the oxidation reaction occurs at very short times compared to the several minutes corresponding to the ''initial period.'' Hence, very thin oxide films (less than a few hundred Angstroms) are expected. The Mott-Cabrera theory is based on the assumption that oxidation is limited by the ion transport through the oxide layer. At relatively low temperatures, ion diffusion is extremely slow, but electrons can go through the oxide film by tunnel effect. An electric field is therefore established across the oxide layer that drives ion transport across the film. The oxidation rate can then be evaluated as ([4]):

$$\frac{dO}{dt} = -2A_0 \exp\left(-\frac{Q}{\kappa T}\right)\exp\left(K_0 \frac{P_{\mathrm{O}_2}^{1/2}}{\kappa T}\right) \tag{14}$$

where P_{O_2} is the oxygen partial pressure and $A_0 = 2.5\times 10^6$ Å/s, $Q = 1.6$ eV, and $K_0 = 0.139\ \mathrm{eV/Torr}^{1/2}$ ([2]). Equations (3) and (14) are then solved simultaneously to yield the oxide interface temperature.

Droplet Dynamics. In the reactive spray atomization and deposition process, the droplet dynamics is significantly complicated by compressibility effects and possible interaction with the shock pattern existing in the atomizer. However, the goal here is not to simulate the complete reactive spray atomization and deposition process but rather to gain some valuable insight regarding the processing step which directly controls dispersoid volume fraction, droplet transport. Nevertheless, the convective heat transfer coefficient in Eq. (5) is estimated using the Ranz-Marshall correlation ([10]). This requires that the droplet/gas relative velocity be determined. To this end, a simplified equation for the droplet motion

$$\frac{dV_d}{dt} = g\left(1 - \frac{\rho_g}{\rho_d}\right) + \frac{3}{4D}\frac{\rho_g}{\rho_d}|V_d - V_g|(V_d - V_g)C_d(\mathrm{Re}) \quad (15)$$

is integrated. This equation assumes that the Basset, Saffman, and Magnus forces are negligible. Droplet-droplet interactions are also neglected (dilute spray). Droplets are assumed to remain spherical because of aluminum's large surface tension (the Weber number is typically of order 1) and because deformation is further hindered by the formation of the oxide film. Therefore, an approximation of the standard drag curve for solid spheres can be used to evaluate the drag coefficient ([3]).

A second integration is performed to determine the droplet position. The gas velocity one-dimensional field is specified using the following correlation:

$$V_g = V_{g,0}\exp\left(-\frac{z}{3.04\times10^{-4}V_{g,0}^{1.24}}\right). \quad (16)$$

This is a correlation of the centerline gas velocity originally developed by Grant et al. [11] using a setup with characteristics similar to those used in the present work (as described in the Introduction) and for Al/nitrogen. This correlation is generally suitable for the conditions that are present during close-coupled atomization of molten metals. Although the value of the exponent may vary somewhat, depending on atomizer design, it has been reported to provide an acceptable accuracy ([1]).

Numerical Solution and Accuracy. Equations (2)–(5), (7), (8), and (13)–(16) are solved numerically. Equation (7) and the related boundary conditions were discretized using a forward-time-centered-space (FTCS) scheme with a time step less than 1 μs. The resulting equation system is solved using the tri-diagonal matrix algorithm (TDMA) ([12]). In the particular case of interest here (aluminum droplets) the oxide film is expected to be extremely thin (between one Angstrom and a few hundred Angstroms). Hence, the temperature in the oxide layer can be assumed uniform and the convective cooling boundary condition at the droplet surface is modified to include the energy source due to oxidation. The droplet equation of motion (Eq. (15)) is solved using a Runge-Kutta-Fehlberg algorithm ([13]).

The accuracy of the computations was assessed by varying both the time step and the number of nodes used. The resulting effect on the predicted droplet surface temperature in Case #1 (defined in Table 1) is shown in Fig. 2. The results show that, in this case, the time step used should be maintained below 1 μs and the number of nodes above 40 per region. The former is necessary to obtain a satisfactory time-resolution of recalescence, whereas the latter is required for an accurate prediction of the heat flux at interfaces.

Table 1 Cases considered

Case No.	D [μm]	$T_0(T_0 - T_L)$ [K]	O_2 vol. [%]
1	80	1033 (100)	0
2	40	1033 (100)	0
3	120	1033 (100)	0
4	120	1273 (340)	0
5	50	1073 (140)	0
6	20	1073 (140)	0
7	120	1073 (140)	0
8	50	1073 (140)	3
9	50	1073 (140)	5
10	50	1073 (140)	10
11	80	1033 (100)	10
12	20	1073 (140)	10
13	120	1073 (140)	10
14	50	1173 (240)	10
15	50	1273 (340)	10

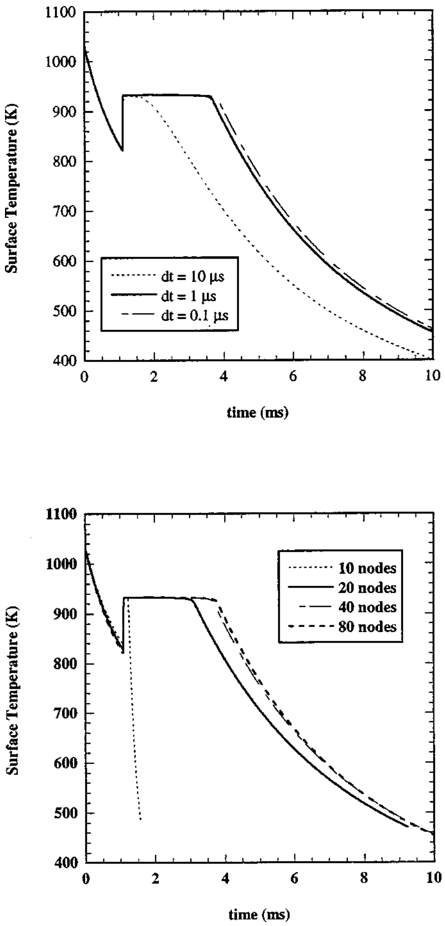

Fig. 2 Numerical accuracy. Variations of the predicted droplet surface temperature for various time-steps and mesh spacings.

Results

The cases presented here consider an aluminum droplet with an initial velocity of 2 m/s injected in a N_2/O_2 gas mixture at 220 K and 520 m/s. Droplet sizes range from 20 to 120 μm, injection temperatures from 1033 to 1273 K (100 to 340 K superheat), and oxygen volume fractions in the atomization gas from 0 to 10 percent. A numbered list of these cases is provided in Table 1 for easy reference.

Droplet Dynamics. The predicted droplet velocity is shown Fig. 3 for 40 μm, 80 μm, and 120 μm droplets together with the correlated gas velocity (Cases 1–3). In all cases, the droplets are rapidly accelerated by drag forces until their velocity exceeds the local gas velocity at which point the droplets decelerate. Smaller droplets (e.g., 40μm) expectedly follow the gas more closely than larger droplets (e.g., 120 μm) which adopt a more inertial trajectory. As stated above, these results neglect compressibility effects and possible interaction with the shock pattern existing in the atomizer.

Droplet Heat Transfer and Solidification. A direct consequence of the predicted droplet velocities is the heat transfer coefficient behavior shown in Fig. 4. The heat transfer coefficient is initially very high (from 1 to 2 10^4 W/m^2/K) because of the large droplet/gas relative velocity. When the droplet switches from acceleration to deceleration and the relative velocity goes through

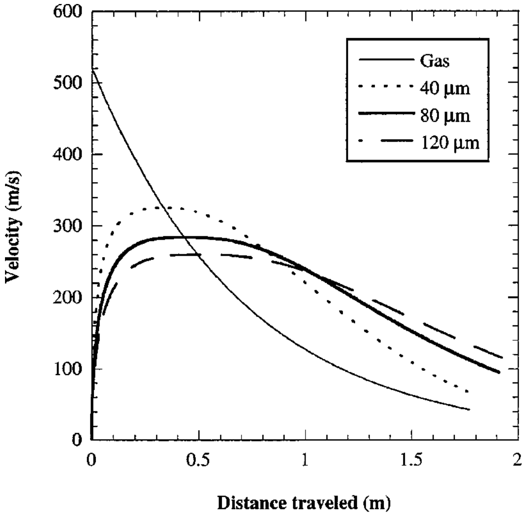

Fig. 3 Influence of size on predicted droplet velocity history (Cases 1–3). The correlated gas velocity is shown for reference.

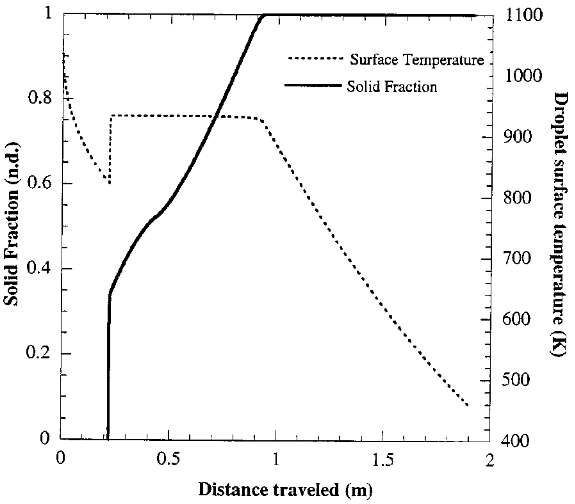

Fig. 5 Predicted solidification behavior of a 80 μm Al droplet (Case 1)

zero (at $z \approx 0.3$ m for a 40 μm droplet), the heat transfer coefficient exhibits a sharp local minimum and then increases again as the absolute value of the relative velocity increases. Eventually, the relative velocity asymptotes back to zero and the heat transfer coefficient decreases again. This is more marked for smaller droplets as they tend to follow the gas velocity more closely. The spike, seen for instance at 0.1 m for the 40 μm droplet, is the result of the sudden rise in droplet surface temperature caused by recalescence and evidences the influence of the droplet surface temperature on the thermophysical properties in the gas film around the droplet. The value of the heat transfer coefficient remains relatively high ($\approx 0.5 \times 10^4$ W/m^2/K) throughout the droplet trajectory for all sizes considered.

The surface temperature and solid fraction histories for a 80 μm Al droplet at 1033 K in a nitrogen atmosphere (no oxidation, Case 1) are shown in Fig. 5. The predicted droplet surface temperature exhibits a behavior typical of rapid solidification. First, the droplet cools down until its surface temperature reaches the nucleation temperature (869 K) corresponding to the calculated undercooling (64 K) 1.09 ms after injection (at 0.218 m). Solidification is then initiated. The rate of solidification is initially so high (cf. the slope of the solid fraction curve in Fig. 5 during recalescence) that the associated heat release is too large for the convective cooling to evacuate the heat generated and the droplet surface temperature increases. This recalescence phase is short (about 750 μs) and is followed by a longer post-recalescence solidification phase (1.85 ms) during which the solid fraction increases from its value at the end of recalescence (0.52) to 1. Finally, the droplet undergoes solid cooling for the rest of its trajectory.

The temperature profiles within the droplet remain relatively uniform except at the inception of recalescence (Fig. 6) when the heating rate becomes positive and very large. Figure 6 also shows that the radial temperature gradient is still negative in the droplet core (up to about 27 μm) as a result of the cooling that the droplet was undergoing up until recalescence started. This result shows that a lump-parameter formulation is not adequate to model droplet behavior in nonequilibrium solidification processes if a detailed description of the recalescence phase is to be obtained.

The droplet-surface heating rate history, as provided in Fig. 7 for the case of a 120 μm droplet (340 K superheat, Case 4), yields more insight regarding the droplet thermal behavior. The four

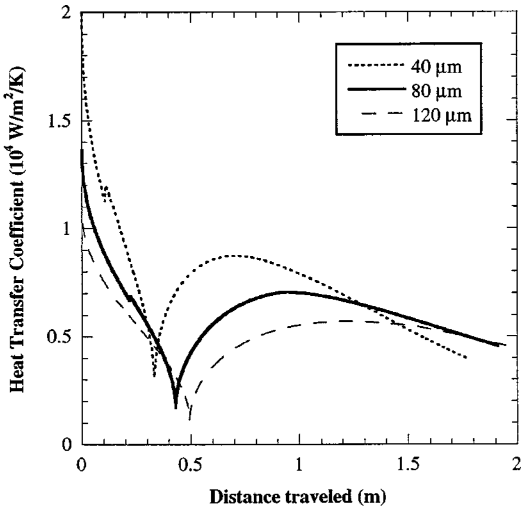

Fig. 4 Influence of droplet size on predicted heat transfer coefficient (Cases 1–3)

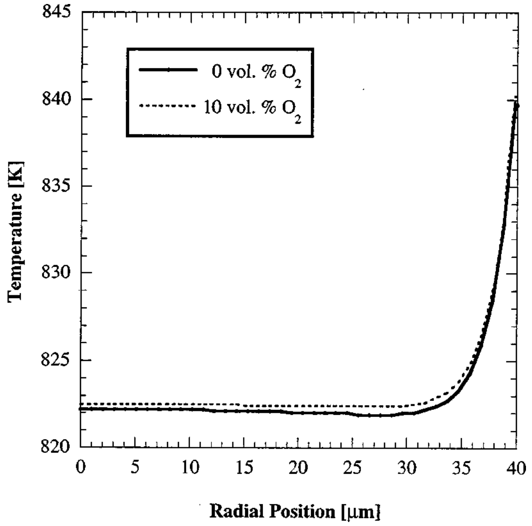

Fig. 6 Computed radial temperature profile in a 80 μm Al droplet when recalescence starts (Cases 1 and 11)

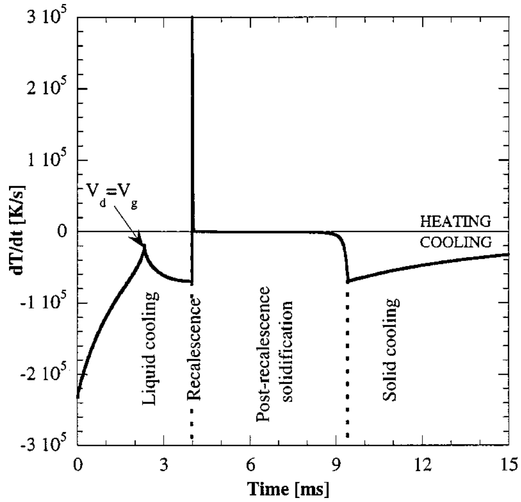

Fig. 7 Heating rate history for a 120 μm Al droplet (Case 4)

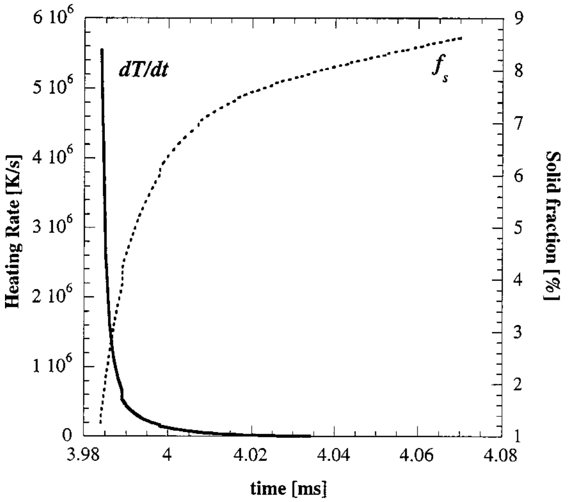

Fig. 8 Solid fraction and heating rate history during recalescence in a 120 μm Al droplet (Case 4)

phases of the droplet solidification process: liquid cooling, recalescence, post-recalescence solidification, and solid cooling are clearly identifiable.

During liquid cooling, the droplet heating rate is controlled by the droplet/gas relative velocity (see also Figs. 3 and 4). At 2.3 ms, the droplet velocity equals that of the gas (flow reversal) and the convective heat transfer coefficient is at its minimum. In the particular case of Fig. 7, flow reversal occurs before recalescence. However, recalescence was found to occur before flow reversal for smaller droplets because their higher heat transfer coefficient causes their surface temperature to reach the nucleation value sooner (even though they exhibit a significantly higher degree of undercooling).

In the case presented in Fig. 7 (Case 4: 120 μm droplet; 340 K superheat), recalescence is even shorter (88 μs) than for the case presented in Fig. 5 (Case 1: 80 μm droplet, 100 K superheat). As a result, recalescence seems to be a singularity on the droplet thermal history. However, as evidenced by Fig. 8, recalescence is well resolved (a time step of 1 μs is used in the computations).

Influence of Droplet Size. Figures 9 and 10 show how the droplet solidification behavior is affected by the droplet size (Cases 5–7). Case 5 (50 μm droplet, 140 K superheat) is used as a base case for the purposes of the following discussion whereas the smaller (Case 6: 20 μm) and larger (Case 7: 120 μm) sizes exemplify two extreme behaviors around this base case.

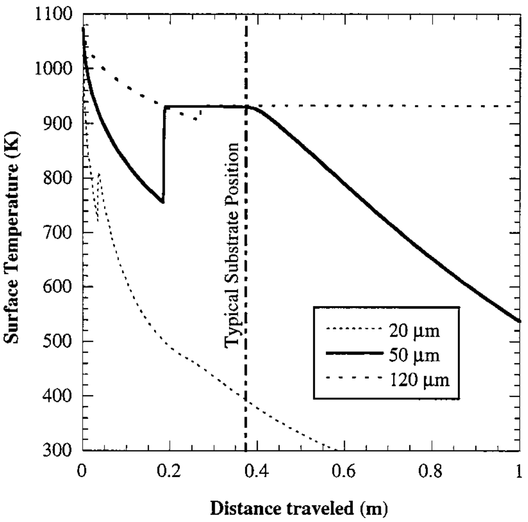

Fig. 9 Influence of droplet size on the predicted surface temperature history (Cases 5–7)

As indicated by Eq. (10), the achievable undercooling decreases as the droplet size increases (20 μm: 211 K; 50 μm: 177 K; 120 μm: 27 K). Nevertheless, recalescence occurs earlier for smaller droplets as a result of their larger heat transfer coefficient and cooling rate. After nucleation at 0.19 ms, solidification proceeds fast enough for the 20 μm droplet to completely solidify before the droplet surface temperature approaches the melting point. On the contrary, the 120 μm droplet reaches the nucleation temperature after 1.45 ms and recalescence lasts about 869 μs (versus 432 μs for the 50 μm droplet and 42 μs for the 20 μm droplet). Recalescence is longer for larger droplets because of their higher nucleation temperature which result in slower solidification (cf. Eq. (13)). The following solidification phase is also relatively slow: At the end of computation (4.33 ms) the solid fraction is only 0.474.

A typical injector to substrate distance is between 200 and 400 mm. For instance, Dai et al. [2] indicate that their substrate is positioned 380 mm below the injector. The present computations show that, all other parameters being equal, an aluminum droplet

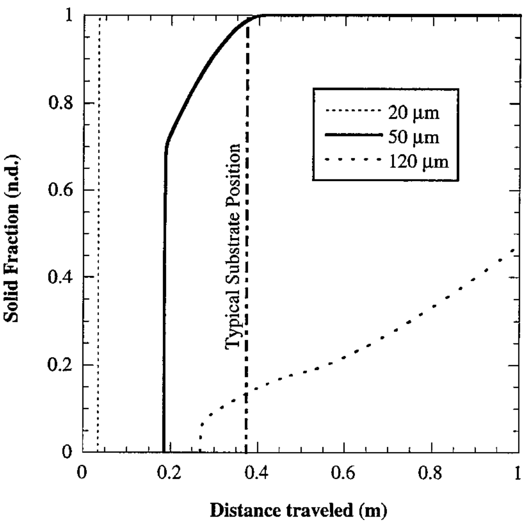

Fig. 10 Influence of droplet size on the predicted solid fraction history (Cases 5–7)

with a diameter of the order of the Sauter Mean Diameter of practical droplet size distributions (about 100 μm) would reach the substrate partially solidified. It has been argued ([1]) that in order to minimize porosity the droplets should not reach the substrate in a completely liquid state. On the other hand, the droplets should not be fully solidified at impact if overspray is to be minimized.

Oxidation. If oxygen is added to the atomization gas, oxidation occurs. Three parameters are expected to influence the oxide film thickness: droplet diameter, melt superheat, and oxygen concentration in the atomization gas. The evolution of the oxide film thickness for a 50 μm droplet, 1073 K superheat, and 10 vol. percent O_2 is shown in Fig. 11. The oxidation is initially high and decreases as liquid cooling proceeds. At 980 μs, nucleation occurs and the sudden increase in droplet surface temperature (Fig. 12) results in a sharp increase of the oxidation rate. Finally, the film thickness asymptotes to about 400 Å. In this case (10 vol. percent O_2) oxidation is found to affect the droplet temperature history (Fig. 12): The heat generated by the oxidation reaction delays slightly the onset of nucleation (by 146 μs). As evidenced in Fig. 6, this is only a time-lag, with little influence on the temperature profile itself.

At lower oxygen concentrations, 3 vol. percent (Case 8) and 5 vol. percent (Case 9), the predicted oxide film thickness is two orders of magnitude smaller than for 10 vol. percent, dropping to less than 0.2 Å and about 2 Å, respectively. This highly nonlinear behavior is directly related to the fact that the oxidation rate is an exponential function of the square root of the oxygen partial pressure (see Eq. (14)). This functional relation reflects the increase in the probability of ion migration along interstitial lattice sites in the direction of the electric field created by the oxygen ions adsorbed at the oxide/gas interface ([4]). These results confirm the argument put forward by Dai et al. [2] to explain why no oxide particles could be found in the deposits produced with an atomization gas containing less than 10 vol. percent O_2.

Oxidation was also found to have a very minor effect on the droplet thermal behavior at lower oxygen concentrations. For instance, the surface temperature predicted for Case 9 (50 μm, 1073 K, 5 vol. percent O_2) remains with 1 K of that predicted for the same droplet in an inert environment (Case 5).

Both droplet size and melt superheat were found to affect the oxide film thickness (Figs. 13 and 14). These effects are both related to the influence that both parameters have on the droplet thermal history. As described above, the temperature of a 20 μm

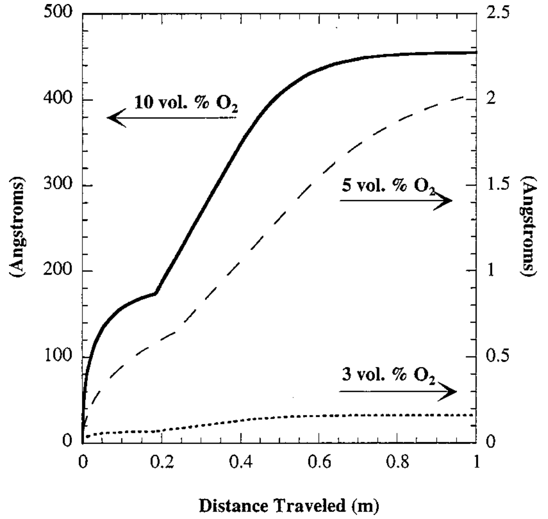

Fig. 11 Predicted oxide film thickness for a 50 μm Al droplet (140 K superheat) at selected oxygen volume fractions (Cases 8–10)

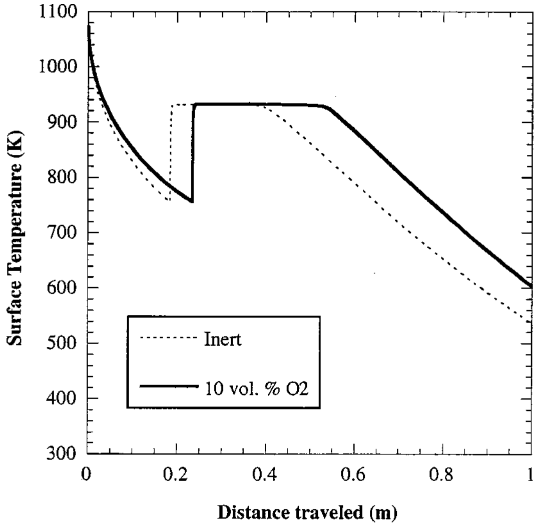

Fig. 12 Effect of oxidation on the predicted droplet surface temperature (Cases 5 and 10)

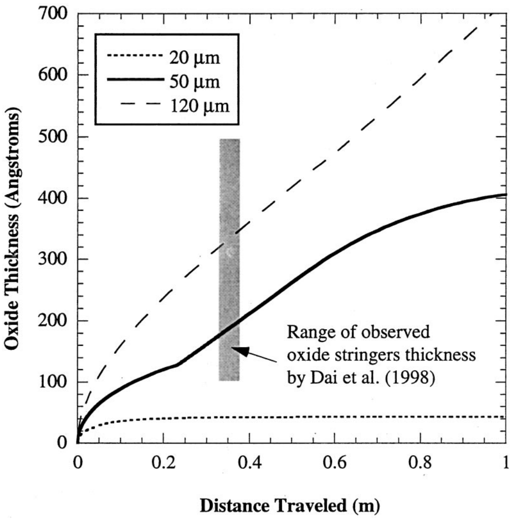

Fig. 13 Effect of droplet size on the predicted oxide film thickness for an Al droplet (140 K superheat, 10 vol. percent O_2; Cases 10, 12, and 13)

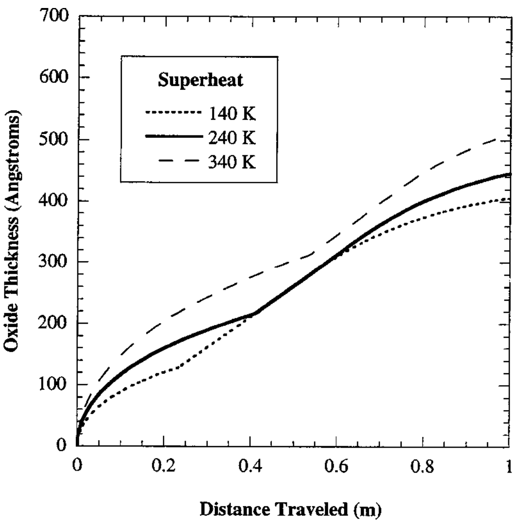

Fig. 14 Effect of superheat on the predicted oxide film thickness for a 50 μm Al droplet (10 vol. percent O_2; Cases 8–10)

droplet decreases much faster than that of a 120 μm droplet because of the higher heat transfer coefficient and lower total thermal inertia of the smaller droplet. Consequently, the oxide film that forms on a 20 μm droplet is much smaller than that on a 120 μm droplet (43 Å versus 510 Å at 3 ms). The melt superheat has a noticeable but relatively less important effect (Fig. 14).

Comparison With Experimental Observations. There is no direct measurement available of the oxide film thickness forming on metal droplets at conditions relevant to reactive atomization and spray deposition. However, a qualitative validation may be obtained by comparing the width of oxide stringers in the deposit to the predicted oxide film thickness. The former is expected to be roughly double the latter ([14]), most likely as the result of the impact of subsequent droplets ([2]). Figure 15 shows that the range of oxide stringer thickness as observed by Dai et al. [2] is indeed about twice the oxide film thickness predicted using the present model at 380 mm (the deposition distance used in the experiments) and for droplet sizes from 20 μm to 120 μm.

This model can be used to test hypotheses regarding the process parameters which potentially control grain refinement. For instance, Fig. 16 shows that the predicted oxide volume fraction that would be obtained with a mono-sized (50 μm) spray and less than five percent O_2 in the atomization gas is too small ($<2.10^{-5}$) to induce grain growth retardation. This is consistent with the measured grain size for this range of oxygen concentration ($>$ 35 μm). However, at ten percent O_2, the predicted oxide volume fraction jumps to 2.10^{-3} and the measured grain size drops to 17 μm. Of course, this is only an example provided to demonstrate the usefulness of this model. More quantitative conclusions could be obtained using the actual droplet size distribution.

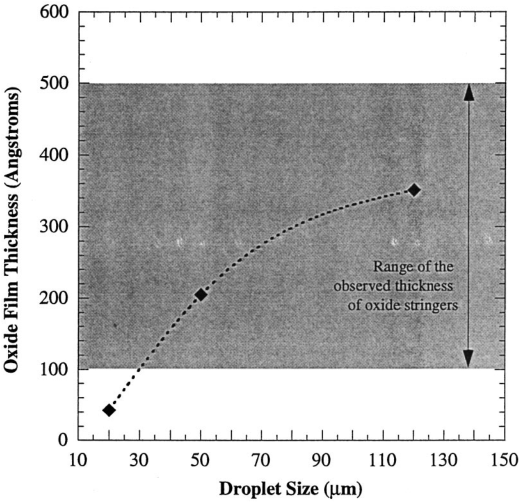

Fig. 15 Comparison of the predicted oxide film thickness with the observed thickness of oxide stringers (10 vol. percent O_2; Cases 10, 12, and 13)

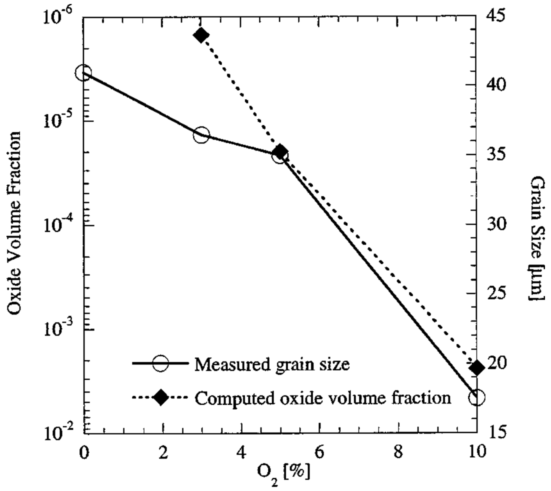

Fig. 16 Variations of predicted oxide volume fraction for a 50 μm Al droplet and measured grain size with atomization gas O_2 content (Cases 5, 8, 9, and 10)

Conclusions

A numerical model for the prediction of droplet in-flight behavior during Reactive Atomization and Spray Deposition processes has been developed. This model can be used to obtain qualitative estimates of the droplet surface temperature, solid fraction, and oxide thickness. The predictions are consistent with available experimental observations, but the model still needs to be quantitatively validated by comparison with relevant experimental data. Such a model could eventually be used to determine the influence of process parameters on the volume fraction and the size distribution of the oxide dispersoids for various systems.

Acknowledgments

This work was sponsored in part by the National Science Foundation (DMI 95-28684 and CTS 96-14653) and a Collaborative UC/Los Alamos Research (CULAR) grant while the first author was at the University of California, Irvine.

Nomenclature

D = droplet diameter (m)
$\Delta \underline{H}_m$ = heat of fusion (J/kg)
ΔH_{ox} = heat of oxidation (J/mol)
h = convective heat transfer coefficient (W/m^2/K)
$\Im$ = nucleation rate (1/m^3/s)
k_i = thermal conductivity of i (W/m/K)
$O(t)$ = position of the oxide/(liquid or solid) interface (m)
r = radial coordinate (m)
R = droplet radius (m)
$S(t)$ = position of the solid/liquid interface (m)
t = time (s)
T = temperature (K)
T_L = melting temperature (K)
T_n = heterogeneous nucleation temperature (K)
$T_{n,0}$ = homogeneous nucleation temperature (K)
ΔT = heterogeneous undercooling (K)
ΔT_0 = homogeneous undercooling (K)
$\dot{T}$ = droplet heating rate (K/s)
V = velocity (m/s)
W_i = molecular weight of i (kg/mol)
z = axial position measured from the nozzle (m)

Greek Letters

α = thermal diffusivity (m^2/s)
ρ = density (kg/m^3)
σ = solid/liquid interfacial energy (J/m^2)
Ω = molar volume (m^3/mol)
κ = Boltzmann's constant ($=1.38\times10^{-23}$) (J/K)

Subscripts

s = solid
Al = aluminum
l = liquid
ox = oxide, oxidation
m = melting
g = gas

Diacritical

– = molar quantity

References

[1] Lavernia, E. J., and Wu, Y., 1996, ''Spray Atomization and Deposition,'' Wiley, New York.

[2] Dai, S. L., Delplanque, J.-P., and Lavernia, E. J., 1998, ''Microstructural Characteristics of 5083 Al Alloys Processed by Reactive Spray Deposition for Net-Shape Manufacturing,'' Metall. Mater. Trans. A, **29A**, pp. 2597–2611.

[3] Liu, H., Rangel, R. H., and Lavernia, E. J., 1994, ''Modeling of Reactive Atomization and Deposition Processing of Ni3Al,'' Acta Metall. Mater., **42**, No. 10, pp. 3277–3289.

[4] Kubaschewski, O., and Hopkins, B. E., 1953, ''Oxidation of Metals and Alloys,'' Butterworths, London.

[5] Hirth, J. P., 1978, ''Nucleation, Undercooling and Homogeneous Structures in Rapidly Solidified Powders,'' Metall. Trans. A, **9A**, pp. 401–404.

[6] Flemings, M. C., 1974, *Solidification Processing*, McGraw-Hill, New York.

[7] Lawrynowicz, D. E., Li, B., and Lavernia, E. J., 1997, ''Particle Penetration During Spray Forming and Co-Injection of Ni_3Al+B/Al_2O_3 Intermetallic Matric Composite,'' Metall. Mater. Trans. B, **28B**, No. 5, pp. 877–897.

[8] Mathur, P., Applian, D., and Lawley, A., 1989, ''Analysis of the Spray Deposition Process,'' Acta Metall. Mater., **37**, No. 2, pp. 429–443.

[9] Levi, C. G., and Mehrabian, R., 1982, ''Heat Flow During Rapid Solidification of Undercooled Metal Droplets,'' Metall. Trans. A—Physical Metallurgy and Materials Science, **13A**, No. 2, pp. 221–234.

[10] Ranz, W. E., and Marshall, W. R., 1952, ''Evaporation From Drops (Part I),'' Chem. Eng. Prog., **48**, No. 3, pp. 141–180.

[11] Grant, P. S., Cantor, B., and Katgerman, L., 1993, ''Modelling of Droplet Dynamics and Thermal Histories During Spray Forming—I. Individual Droplet Behavior,'' Acta Metall. Mater., **41**, No. 11, pp. 3097–3108.

[12] Thomas, L. H., 1949, ''Elliptic Problems in Linear Difference Equations Over a Network,'' Report, Watson Scientific Computing Laboratory, Columbia University, New York.

[13] Burden, R. L., and Faires, J. D., 1997, *Numerical Analysis*, Brooks/Cole, Pacific Grove, CA.

[14] Staniek, G., 1982, ''Observation of Oxide Skin in Powder Metallurgy,'' Technical Report, Air Force Wright Aeronautical Laboratory.

Heat Transfer and Friction Characteristics of Internal Helical-Rib Roughness

R. L. Webb
Department of Mechanical Engineering,
Pennsylvania State University,
University Park, PA 16802
e-mail: rlwebb@psu.edu

R. Narayanamurthy

P. Thors

Wolverine Tube,
Decatur, AL 35609

This paper provides heat transfer and friction data for single-phase flow in seven 15.54-mm inside diameter tubes having internal helical-rib roughness. The range of geometric parameters were number of rib starts (18 to 45), helix angle (25 to 45 deg), and rib height (0.33 to 0.55 mm). These geometries provide data on a new class of internal enhancement that is typical of commercially rough tubes presently used. The tested geometries provide enhancement by flow separation at the ribs, and by a significant surface area increase. The data were taken with water having 5.08≤Pr≤6.29. Two different correlations were employed to predict the Stanton number and friction factor as a function of geometric variables and Reynolds number. The average deviation of the multiple regression heat transfer and correlations were 2.9 percent and 3.8 percent, respectively. Heat transfer and friction correlations based on the heat-momentum transfer analogy for rough surfaces yielded standard deviations of 1.4 percent and 5.4 percent, respectively. The correlations were shown to reasonably predict the heat transfer and friction for commercially used helical-rib roughened tubes. [S0022-1481(00)03001-2]

Keywords: Enhancement, Forced Convection, Heat Transfer, Roughness

Introduction

Internally enhanced tubes for liquid flow have become important in commercial applications. The refrigeration industry routinely uses roughness on the water-side of large refrigeration evaporators and condensers, as described by Webb [1,2]. Such evaporators and condensers have water flow inside the tubes with evaporation (or condensation) on the outside of tubes in a bundle. As shown by Fig. 1, a variety of internally enhanced geometries have evolved since the mid 1970s. These tubes provide water-side enhancement in the range of 70–250 percent. Considerable data have been published on water-side heat transfer enhancements such as shown in Fig. 1, and these data are summarized in Chapter 9 of Webb [2].

The Fig. 1 tubes that have an outside diameter of 19 mm are described as helical rib roughened tubes. The Fig. 1(*a*) Wolverine Turbo-Chil tube having ten starts ($N_s=10$) was commercially introduced in the early 1970s. This tube was replaced in 1988 by the Turbo-C tube having 30 starts, and followed by the Turbo-CII tube (Fig. 1(*b*)) in 1995 having 38 starts. Hence, as the technology advanced, the number of starts was increased. The basic geometric variables of the helically ribbed tube are the rib helix angle (α), the rib height (e), and the rib axial pitch $p_a=\pi D_i/(N_s \tan\alpha)$. As the number of starts increases, the axial rib pitch decreases and the ribs provide considerable surface area increase. The ten-start Figure 1(*a*) Turbo-Chil tube has $p_a/e=11$, and these ribs provide a surface area increase of only 17 percent. However, the surface area increase of the 38-start Fig. 1(*b*) Turbo-CII start tube is approximately 60 percent.

The ten-start Fig. 1(*a*) tube is historically called a ''rough'' tube, because it provides enhancement by local boundary layer separation and reattachment between the ribs. Figure 9.7 of Webb [2] shows that the boundary layer in a ''transverse-rib''tube ($\alpha=90$ deg) reattaches six to eight rib heights downstream from the rib. The maximum heat transfer coefficient occurs at the reattachment point. For $p_a/e>10$, as the helix angle is reduced from 90 deg to 47 deg (Fig. 1(*a*)), the same basic enhancement mechanism exists, and is discussed by Gee and Webb [3].

Webb [2] further shows that the heat transfer coefficient decreases if the rib pitch is reduced below that needed for boundary layer reattachment. However, as the number of starts increases, the rib axial pitch is significantly reduced. The 38-start Fig. 1(*b*)

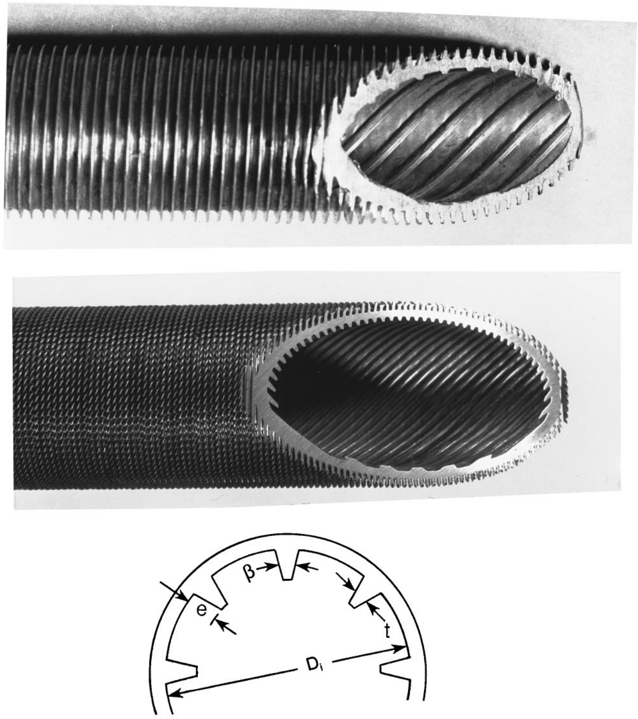

Fig. 1 Photos of commercially used helically ribbed tubes; (*a*) Wolverine Turbo-Chil, (*b*) Wolverine Turbo-CII, (*c*) illustration of internally finned tube

---

Contributed by the Heat Transfer Division for publication in the JOURNAL OF HEAT TRANSFER. Manuscript received by the Heat Transfer Division, Feb. 3, 1999; revision received, Oct. 2, 1999. Associate Technical Editor: B. Chung.

tube has $p_a/e=3.73$. Based on present understanding of the roughness enhancement mechanism, one would not expect boundary layer reattachment to occur. Because of the large number of starts, the Fig. 1(*b*) tube provides significant surface area increase, as does the ''internally finned'' tube whose end view is illustrated in Fig. 1(*c*). Traditional ''internally finned'' tubes, such as illustrated in Fig. 1(*c*), have larger e/D_i than the Fig. 1(*a*) tube and provides significant area increase. Local flow separation is assumed to not occur if the helix angle is small (e.g., less than 15 deg). So the enhancement is principally caused by the area increase alone.

Hence, the Fig. 1(*b*) tube having a large number of starts and high helix angle cannot be described as either a classic ''rough'' tube, or a large e/D_i ''internally finned'' tube. It probably provides some of the attributes of a rough tube (local flow separations) and some of an internally finned tube (large surface area increase). It is likely that the flow will tend to swirl, although it is expected that the swirl angle will be significantly less than the helix angle. Very little understanding exists of the flow and enhancement mechanism of a tube typical of Fig. 1(*b*). No flow visualization experiments or numerical simulations have been reported in the literature for this geometry.

The purpose of this paper is to provide data to define the effect of rib height, rib axial pitch, and helix angle on the tube performance. Work was done to obtain data on seven different tubes having geometries for which the range of rib height (e), the number of starts (N_a), and the helix angle (α) was varied. This is the first work to report the effect of the geometric variables on this class of tube geometry. The data are also correlated to provide a design equation to predict the effect of the geometric variables on the tube performance.

Tube Geometries Tested

Figure 2 shows the seven internally enhanced tube geometries specially manufactured by Wolverine Tube, Inc., for test in this work. Figure 3 shows a drawing of the rib geometry taken normal to the ribs of Tube 5. In the actual tubes, the ribs are slightly asymmetric, because of the manufacturing process. The rib asymmetry provides a small flow directional effect on pressure drop, amounting to a few percent.

The geometry dimensions of the tubes are summarized in Table 1. All eight tubes have $D_i=15.54$ mm (0.612 in.), and were made with 1024 fins/in. (0.90 mm high) on the outer surface. Tube 1 has a plain interior surface while the other seven have internal enhancement. The geometries vary the number of starts (N_s), helix angle (α), and rib height (e). The rib height given in Table 1 is the average of the asymmetric fin. All the ribs have a 41 deg included angle.

The major tube geometry variables are e, N_s, and α and the rib shape geometry parameters are t_b (fin base thickness), t_t (fin tip

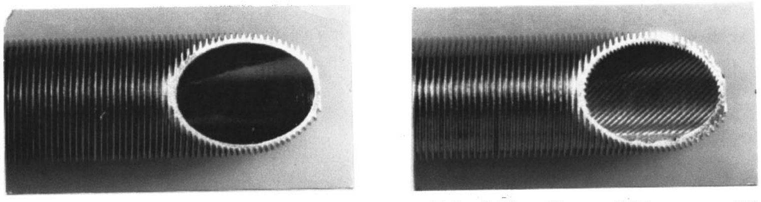

Tube 1: plain I.D. tube

Tube 2: $N_s = 45$, $e_h = 0.36$ mm, $\alpha = 45°$

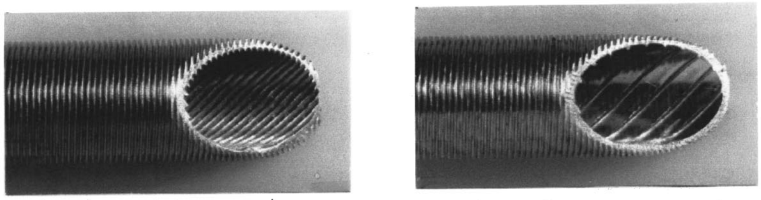

Tube 3: $N_s = 30$, $e_h = 0.43$ mm, $\alpha = 45°$

Tube 4: $N_s = 10$, $e_h = 0.46$ mm, $\alpha = 45°$

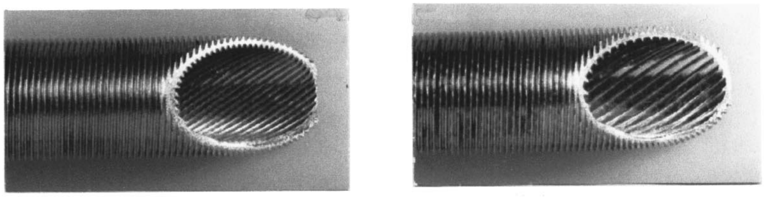

Tube 5: $N_s = 40$, $e_h = 0.50$ mm, $\alpha = 35°$

Tube 6: $N_s = 25$, $e_h = 0.53$ mm, $\alpha = 35°$

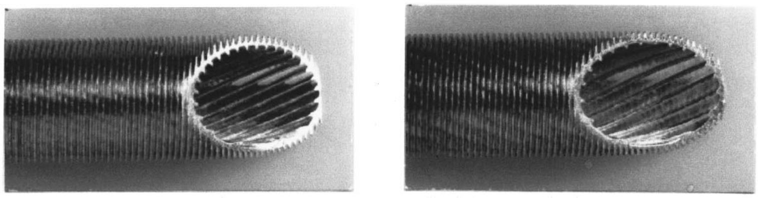

Tube 7: $N_s = 25$, $e_h = 0.57$ mm, $\alpha = 25°$

Tube 8: $N_s = 18$, $e_h = 0.57$ mm, $\alpha = 25°$

N_s = number of starts, e_h= highest fin height, α = helix angle

Fig. 2 Tubes tested in present work

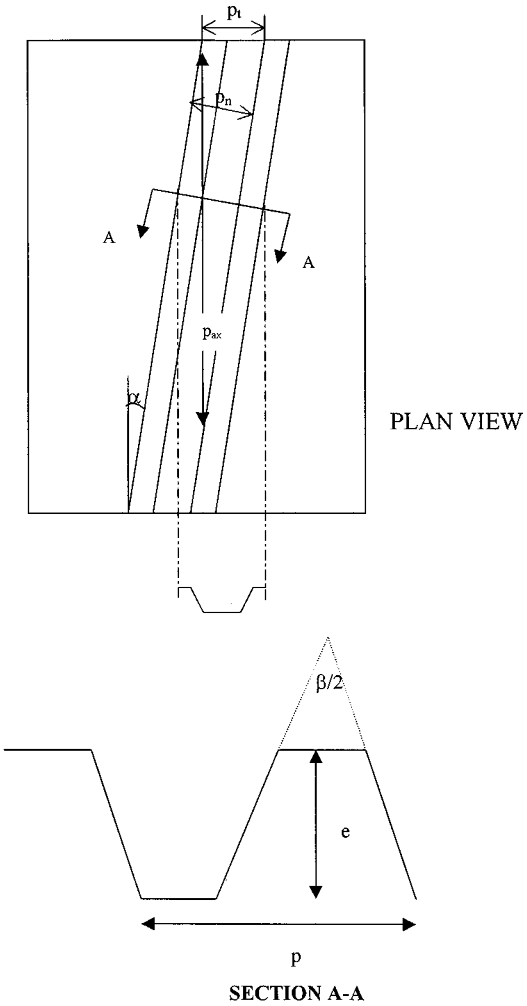

Fig. 3 Cross section drawing of fin

thickness), β (rib included angle), and rib height asymmetry. All tubes, except Tube 4, have $0.029 \leq t_b \leq 0.032$ mm which has a t_b of 0.042 mm.

Table 1 also includes a convenient geometry code for each tube. For example, the code for Tube 2 is 0.33/30/45 where 0.33 is the average rib height in mm, 30 is the number of starts, and 45 is the helix angle in degrees. Table 1 also presents other geometry factors, which include (1) the rib axial pitch/rib height ratio (p_a/e), (2) the actual total inside surface area, relative to that of a plain tube (A/A_p), and (3) the tube material volume ratio (V/V_p) relative to a plain tube. Tube 2 having 45 starts has the greatest V/V_p (20 percent increase) compared to eight percent for the ten-start Tube 4.

Table 1 Tube geometry ($D_i = 15.54$ mm, $t_t = 0.24$ mm, $\beta = 41$ deg)

Tube	Code	e (mm)	N_s (mm)	α (deg)	t_b (mm)	p_a/e	A/A_p	V/V_p
1	Plain	-	-	-	-	-	-	1.00
2	0.33/45/45	0.327	45	45	0.029	2.81	1.59	1.20
3	0.40/30/45	0.398	30	45	0.032	3.50	1.48	1.17
4	0.43/10/45	0.430	10	45	0.041	9.88	1.17	1.08
5	0.47/40/35	0.466	40	35	0.031	3.31	1.65	1.19
6	0.49/25/35	0.493	25	35	0.032	5.02	1.43	1.21
7	0.53/25/25	0.532	25	25	0.032	7.05	1.42	1.19
8	0.55/18/25	0.554	18	25	0.032	9.77	1.31	1.05

Tube 4 having ten thread starts is typical of the geometry used in the 1970s. Advances in manufacture have resulted in tubes having a larger number of starts. Tubes 2, 3, and 5 are similar to enhanced tubes used today. These tubes have between 25 to 45 starts. As the number of rib starts increase, the fins are more closely spaced, and the internal surface area increases. As will be shown, the greater number of starts used in Tubes 2, 3, and 5 provide higher heat transfer coefficients for water flow than the ten-start Tube 4.

Test Procedure

The heat transfer data were taken for cooling of water inside a 2.5-m long double-pipe heat exchanger. Water flowed inside the tube and R-12 at a p_{sat} of 517 kPa (75 psia) boiled on the shell side. The R-12 vapor was condensed against cold aqueous ethylene glycol in a separate condenser. The average heat flux and refrigerant saturation temperature were held constant during the test. The friction factor (f) was measured for isothermal flow.

Data were taken for a series of six flow rates, spanning 20,000 to 80,000 Reynolds number. The modified Wilson plot procedure as described by Briggs and Young [4] was used to obtain the water-side heat transfer coefficient. The Wilson plot requires that the shell-side boiling coefficient be held constant, while data are obtained for different water side velocities. The shell-side boiling coefficient is a function of heat flux, wall superheat, and refrigerant saturation temperature. The saturation temperature was held constant by using PID controllers to control the glycol flow. The average heat flux was held constant by adjusting the inlet water temperature. With the enhanced outside surfaces. For each data point, the inlet water temperature was adjusted to obtain 10.55 kW (36,000 Btu/hr) heat removal. Two sets of data were taken for each tube, which provided 12 test points on each tube. Using instrumental accuracies, the uncertainty in the Sieder-Tate coefficient was estimated to be seven percent.

The measured $1/UA$ value is the total thermal resistance and is the sum of the water-side $(1/h_iA_i)$, the wall (R_w), and the condensing side $(1/h_iA_i)$ thermal resistances. Thus

$$\frac{1}{UA} = \frac{1}{h_iA_i} + R_w + \frac{1}{h_oA_o}. \tag{1}$$

Because the boiling coefficient (h_o) is held constant, the second and third terms on the right-hand side of Eq. (1) are constant values for all test points. The water-side coefficient is assumed to be of the form

$$\frac{h_iD_i}{k} = C_{\mathrm{ST}}\,\mathrm{Re}^{0.8}\,\mathrm{Pr}^{1/3}\left(\frac{\mu}{\mu_w}\right)^{0.14}. \tag{2}$$

Equation (2) is of the form of the Seider-Tate equation as developed by Seider and Tate [5] for turbulent heat transfer in plain tubes. The C_{ST} in Eq. (2) is called the Seider-Tate coefficient. For plain tubes, Seider and Tate found $C_{\mathrm{ST}} = 0.027$. Hence, Eq. (1) is of the form

$$\frac{1}{UA} = C_1\,\mathrm{Re}^n + C_2 \tag{3}$$

where $C_1 = [C_{\mathrm{ST}}A_i(k/D_i)\mathrm{Pr}^{1/3}(\mu/\mu_w)^{0.14}]^{-1}$, and $C_2 = R_w + 1/(h_oA_o)$. Both C_1 and C_2 are constant for all data points in the test of a given tube geometry. Hence, Eq. (3) is a linear equation, of the form $Y = AX + B$, in which the water-side Reynolds number (Re^{-n}) may be interpreted as the variable X.

Figure 4 shows a typical Wilson plot, which is given for Tube 2. The x axis is proportional to the water-side thermal resistance (R_i). The y axis is the total thermal resistance (R_{tot}), less the tube wall conduction resistance (R_w). The shell-side R-12 thermal resistance is given by the intercept of the curve fit with the y-axis at $X = 0.0$. Figure 4 shows that the ratio of the tube side to total thermal resistance was between 0.4 and 0.65 for the data range.

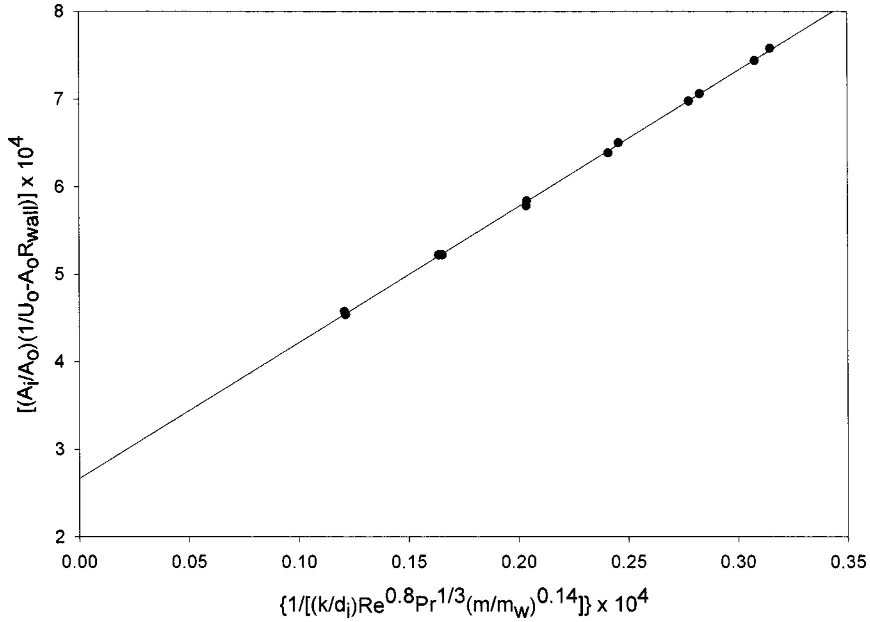

Fig. 4 Modified Wilson plot for Tube 2

The water-side thermal resistance (R_i) is calculated using the derived shell-side thermal resistance and the measured total resistance ($R_{\mathrm{tot}}=1/UA$) by the equation

$$R_i = R_{\mathrm{tot}} - R_o - R_w. \tag{4}$$

The tube-side heat transfer coefficient is then calculated by

$$h_i = \frac{1}{A_iR_i}. \tag{5}$$

The slope of the line through the data points on Fig. 4 gives the Sieder-Tate coefficient (C_{ST}) in Eq. (2) for the tube geometry tested. For the Tube 2 data of Fig. 4, one obtains $C_2 = R_w + 1/(h_oA_o) = 4.7\times10^{-5}$ m^2-K/W, and $C_{\mathrm{ST}}=0.0644$. The C_{ST} ranged from 0.02775 for the plain tube to 0.06457 for Tube 3. Note that the plain tube C_{ST} is in good agreement with the 0.027 value recommended by Seider and Tate [5].

The heat transfer coefficient for the rough tubes is based on the nominal inside surface area defined by $A_i/L = \pi D_i$, where D_i is the tube diameter to the rib root. Because the water inlet temperature was changed for each test point to maintain constant heat flux and T_{sat} on the shell side, the Prandtl number is not constant for all Reynolds numbers for each tube. For example, for Tube 3, the Pr varied from 5.29 to 6.08 over the test range. Eq. (2) properly accounts for this small Pr variation.

Tubes with the same exterior surface should have a common *y* axis intercept, if all tubes have identical external surface geometries. However, Tubes 2 through 8 did not have precisely the same *y*-intercept. This is due to slight variations in rib height and a corresponding difference in external area caused by manufacturing processes and experimental error.

Tube Performance

Figures 5(*a*) and 5(*b*) show the *f* and *j* factors versus Reynolds number for all tubes, respectively. The measured plain tube friction factor is three to four percent higher than the Blasius friction factor ($f = 0.079\,\mathrm{Re}^{-0.25}$). As noted above, the asymmetry causes a small directional effect on the friction factor. Pressure drop data were taken for each flow direction. The friction data are given as the average value determined from pressure drop measurements in each flow direction. The rib asymmetry has negligible effect of flow direction on heat transfer.

The heat transfer coefficient for each test point was converted to the *j*-factor ($\mathrm{StPr}^{2/3}$) using the Prandtl number for each test point. Figure 5(*b*) also compares the experimental *j*-factor with that predicted by the Seider-Tate [5] equation and the Petukhov equation (Eq. (8.62) of Incropera and Dewitt [6]). The data points on Fig. 5(*b*) span $5.08 \leq \mathrm{Pr} \leq 6.29$. The predicted data points are evaluated at the Prandtl number of the experimental data point. Note that plotting Fig. 5(*b*) in the form of the *j* factor ($\mathrm{StPr}^{2/3}$) inherently assumes that $\mathrm{Nu} \propto \mathrm{Pr}^{1/3}$. However, this Prandtl number dependence has not been confirmed by test data at different Prandtl numbers. Such work is presently in progress.

Figure 5(*c*) shows the "efficiency index," $\eta = (j/j_p)/(f/f_p)$. This η parameter compares the *j*-factor increase with the friction factor increase. The j_p and f_p are calculated using the Sieder-Tate equation and the Blasius equations, respectively. The ratio shown for the plain tube is ratio of the calculated values (using the Sieder-Tate and Blasius equations) and the experimental plain tube *j* and *f* values. Figure 5(*c*) shows that the plain tube experimental values agree within three percent of the predicted values. Figure 5(*c*) shows that Tubes 2 and 5 have $\eta > 1.0$. Thus, these tubes provide higher *j* factor increase than the friction factor increase. Figure 5(*c*) shows that $0.85 < \eta < 1.07$. Tube 4 has the lowest efficiency of those tested (approximately 0.85). Note that the η factor is influenced by the Prandtl number. Chapter 9 of Webb [2] discusses the effect of Prandtl number on the efficiency index (η) for roughness.

Based on curve fitted *j* and *f* versus Re values, Table 2 compares the performance characteristics of the tubes at Re=27,000 and Pr=5.2. This Re is an approximate design condition for water chiller evaporators. Parameters compared are h/h_p, the "efficiency index" $[\eta = (h/h_p)/(f/f_p)]$ and $(h/h_p)/(A/A_p)$. If $(h/h_p)/(A/A_p) > 1$, the heat transfer coefficient increase is greater than the area increase. Tubes 2, 3, and 5 show the highest h/h_p values, and their h/h_p are almost equal. Tube 2 also shows the highest efficiency index (1.18) and Tube 4 has the lowest value (0.95). Tube 3 has the highest friction factor for the test range, $20{,}000 < \mathrm{Re} < 80{,}000$.

The A/A_p increases with increasing number of starts and rib height. Among Tubes 2 through 8, Tube 5 has the highest A/A_p, but Tube 2 is close with $A/A_p = 1.59$. These two tubes have $(h/h_p)/(A/A_p)$ values of 1.37 and 1.45, respectively. Thus, the h/h_p is significantly higher than the area increase, so one should

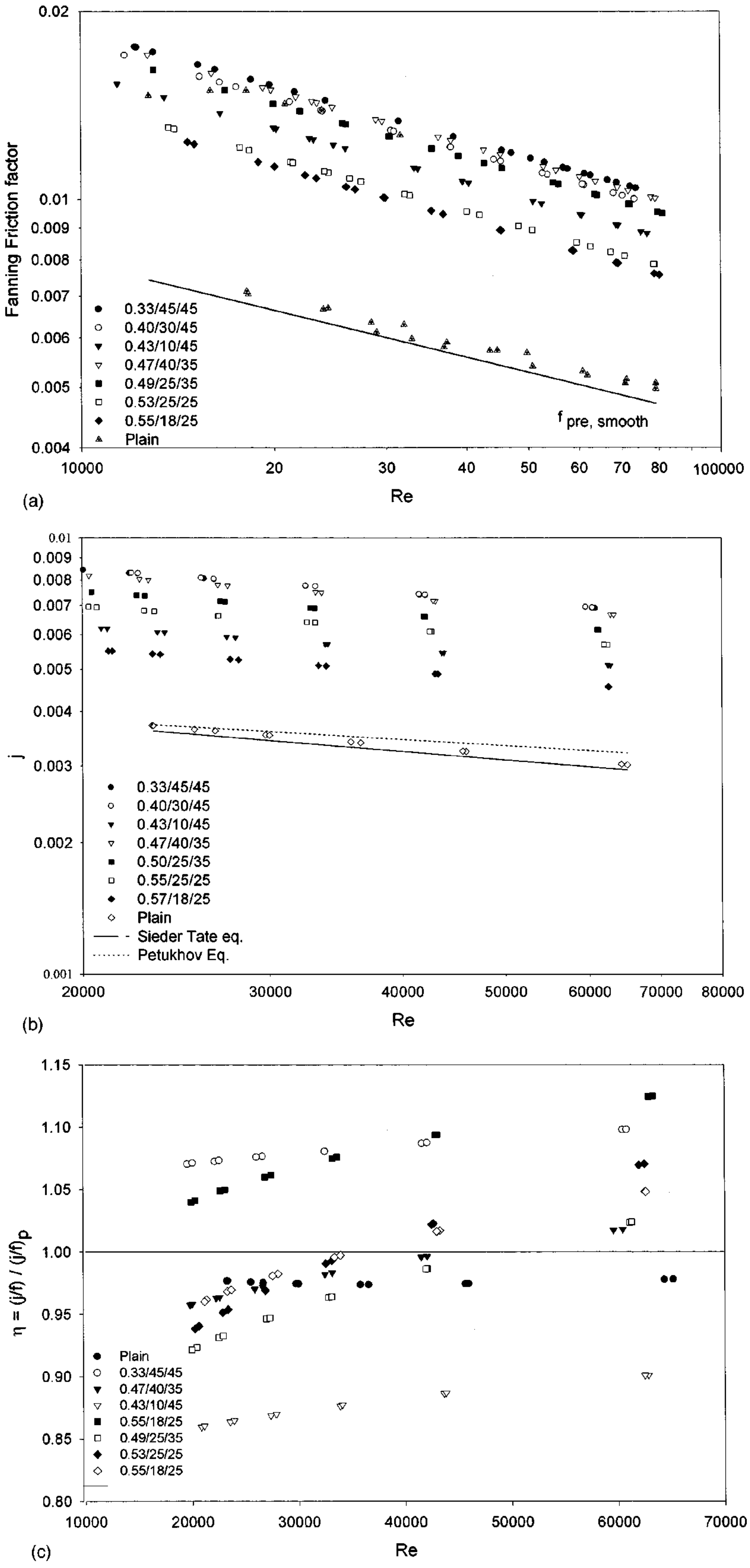

Fig. 5 Table 1 tube performance characteristics: (*a*) *f* versus Re, (*b*) *j* versus Re, (*c*) $[j/(f/2)]/[j/(f/2)]_p$ versus Re

Table 2 Comparative tube performance ($T_b=32°C$, $u=1.33$ m/s, Re=27,000, $h_p=6730$ W/m^2 K, $f_p=0.0257$)

Tube	Code	C_{ST}	h/h_p	η	$(h/h_p)/(A/A_p)$
1	Plain	0.0277	1.0	1.0	1.0
2	0.33/45/45	0.0644	2.32	1.18	1.60
3	0.40/30/45	0.0646	2.33	1.05	1.71
4	0.43/10/45	0.0482	1.74	0.95	1.53
5	0.47/40/35	0.0628	2.26	1.04	1.44
6	0.49/25/35	0.0577	2.08	1.01	1.51
7	0.53/25/25	0.0535	1.93	1.05	1.37
8	0.55/18/25	0.0431	1.51	0.98	1.15

not conclude that $h/h_p \propto A/A_p$. The rib height and helix angle also have important effects on h/h_p. For example, Tube 4 having a small value of $A/A_p(1.17)$ yields $(h/h_p)/(A/A_p)=1.48$. However, its h/h_p of 1.74 is significantly less than that for Tubes 2, 3, and 5.

It appears that there are two key factors, which affect the enhancement level (h/h_p). These are the area increase and fluid mixing in the interfin region caused by flow separation and reattachment. Webb et al. [7] described the enhancement mechanism in tubes having transverse rib roughness ($\alpha \cong 90$ deg). They stated that the flow separates at the rib, with reattachment occurring six to eight rib heights downstream. The highest heat transfer coefficient exists at the reattachment point. Gee and Webb [3] extended the helical-rib roughness tests using $p_a/e=15$ to cover $0 \leqslant \alpha \leqslant 90$ deg and found that the best performance occurred for $\alpha \cong 45$ deg. The Webb et al. and the Gee and Webb studies were for tubes having small number of starts (e.g., similar to the present Tube 4) and hence small A/A_p. The present Tubes 2, 3, and 5 have significantly higher A/A_p, and smaller p_a/e than Tube 4. It is possible that the enhancement mechanism associated with the high performance Tubes 2, 3, and 5 is flow separation/reattachment, combined with area increase.

Correlations for *j* and *f*

We have developed linear multiple regression correlations to predict the heat transfer coefficient and friction factor as a function of the enhancement dimensions. The correlation is given as follows:

$$f=0.108\,\mathrm{Re}^{-0.283}N_s^{0.221}(e/D_i)^{0.785}\alpha^{0.78}. \tag{6}$$

The heat transfer correlation is given in terms of the *j* factor by

$$j=\mathrm{StPr}^{2/3}=0.00933\,\mathrm{Re}^{-0.181}N_s^{0.285}(e/D_i)^{0.323}\alpha^{0.505}. \tag{7}$$

The correlations show that both *f* and *j* increase with increasing N_s, e/D_i, and α. However, the friction factor is a stronger function of e/D_i and α than is the *j* factor. Figure 6 shows an error plot of Eq. (6), for which the average deviation is 3.8 percent and the standard deviation is 4.9 percent. Examination of Fig. 6 shows that the data of Tube 7 (0.53/25/25) are approximately ten percent below the 1.0 line, and the data for Tube 8 (0.55/18/25) are approximately eight percent above the line. It is possible that there is experimental error associated with these two tubes. Figure 7 is an error plot for Eq. (7), which has an average deviation of 2.9 percent and the standard deviation is 3.9 percent. Note that the *j*-factor data for Tubes 7 (0.53/25/25) and 8 (0.55/18/25) show similar deviations from the 1.0 line as were observed in the friction error plots.

All tubes tested in the present work have $D_i=15.54$ mm inside diameter. The parameter N_s may be interpreted for any tube diameter using the relation $N_s=\pi D_i/p_n=\pi D_i/[p_a\tan(\alpha)]$ where p_n is the transverse rib pitch, as viewed from the end of the tube and p_a is the axial pitch. The correlations are valid for the following range of dimensions for any tube inside diameter: $0.024 \leqslant e/D \leqslant 0.041$, $2.39 \leqslant p_e/e \leqslant 12.84$, $25 \leqslant \alpha \leqslant 45$ deg, $\beta=41$ deg, $t_t/D_i=0.015$. It was previously noted that data have not been taken over a wide range of Pr to justify that $\mathrm{St} \propto \mathrm{Pr}^{-2/3}$. Hence, care should be exercised in applying Eq. (7) at Prandl numbers significantly different from the test range.

Correlations for *j* and *f* were also developed based on the heat-momentum transfer analogy for rough surfaces developed by Webb et al. [7] and described in Chapter 9 of Webb [2]. The friction correlation derived from use of the ''friction similarity function'' is given by

$$B(e^+)=4.762(e^+)^{0.2138}N_s^{-0.1096}\alpha^{-0.297}. \tag{8}$$

One predicts the friction factor using Eq. (8) as

$$\sqrt{2/f}=B(e^+)-2.5\ln(2e/D_i)-3.75. \tag{9}$$

Use of the ''heat transfer similarity function'' resulted in the correlation

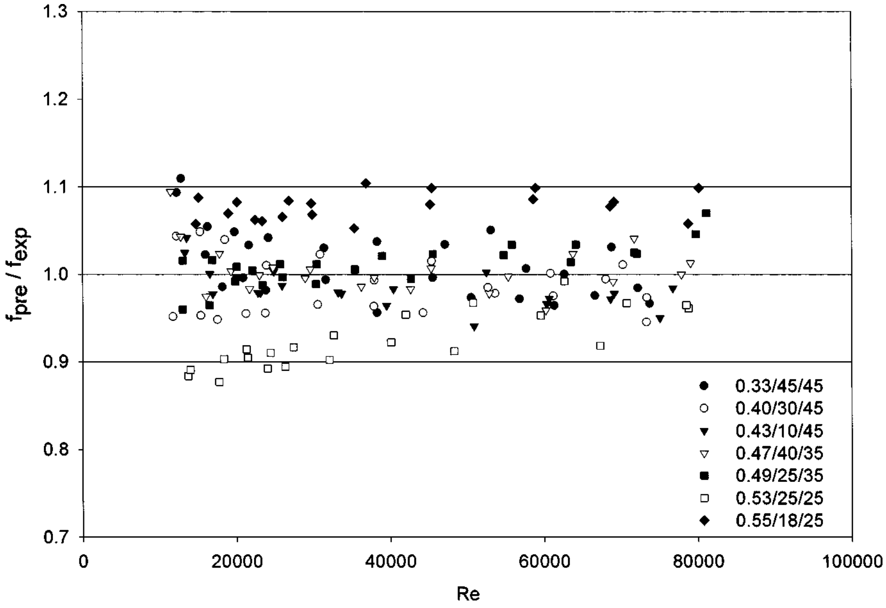

Fig. 6 Error plots showing f_{pre}/f_{exp} versus Re for the Eq. (6) friction factor correlation

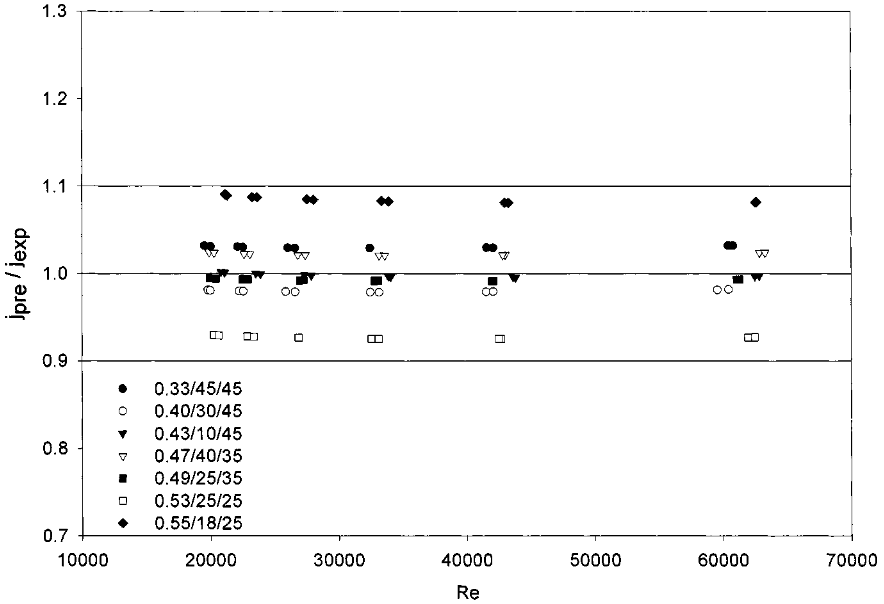

Fig. 7 Error plot showing versus $j_{\mathrm{pre}}/j_{\mathrm{exp}}$ Re for the Eq. (7) *j*-factor correlation

Table 3 Commercial tube geometries from Thors et al. (1997) (t_t=0.24 mm, β=41 deg, Re=27,000, T_{ave}=10°C)

Tube	D_i (mm)	e (mm)	N_s	α (deg)	p_a/e	h/h_p	f/f_p	$h_{\mathrm{pred}}/h_{\mathrm{exp}}$	$f_{\mathrm{pred}}/f_{\mathrm{exp}}$
Turbo-B	16.05	0.56	30	34	4.23	2.02	2.08	1.07	1.08
Turbo-BII	16.05	0.38	38	49	2.80	2.39	2.08	1.04	1.11
Turbo-BIII	16.38	0.41	34	49	3.23	2.54	2.29	0.97	1.03
Turbo-BIII LPD	16.38	0.37	34	49	3.56	2.39	2.03	1.00	1.07

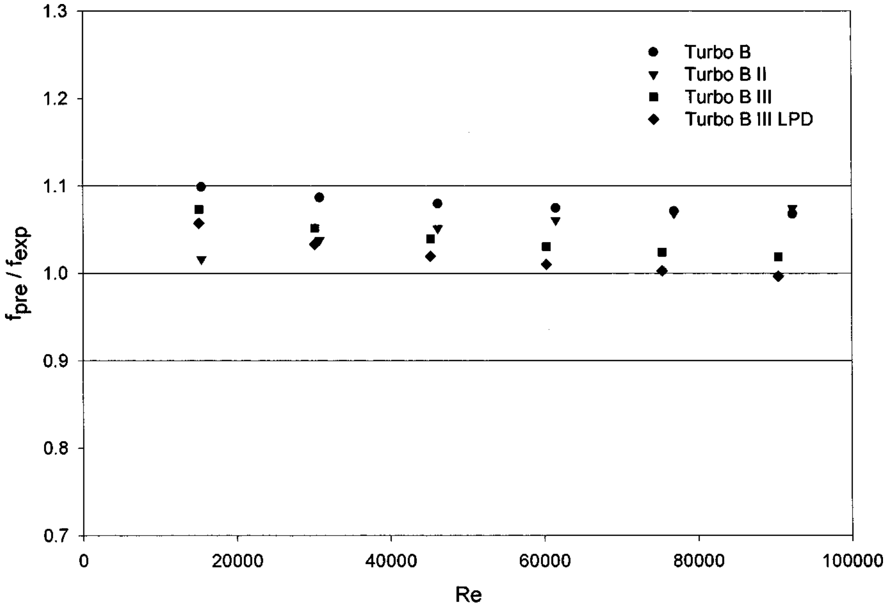

Fig. 8 Error plot showing $f_{\mathrm{pre}}/f_{\mathrm{exp}}$ versus Re for the *f*-factor correlation for tubes in patent

$$\overline{g}(e^{+})=1.714(e^{+})^{0.06}N_s^{-0.21}\alpha^{-0.16}. \tag{10}$$

Using Eq. (10), one calculates the heat transfer coefficient as

$$\mathrm{St}=\frac{f/2}{1+\sqrt{f/2}[\overline{g}(e^{+})\mathrm{Pr}^{n}-B(e^{+})]}. \tag{11}$$

As shown in Table 9.8 of Webb [2], rib-roughened surfaces typically show that the Prandtl number exponent in Eq. (11) is approximately equal to 0.57. Although Eqs. (6) and (7) are simpler to use, greater accuracy may be obtained, for Prandtl numbers different from the test data, using Eqs. (10) and (11). The average deviation of the friction and heat transfer correlations are 5.4 per-

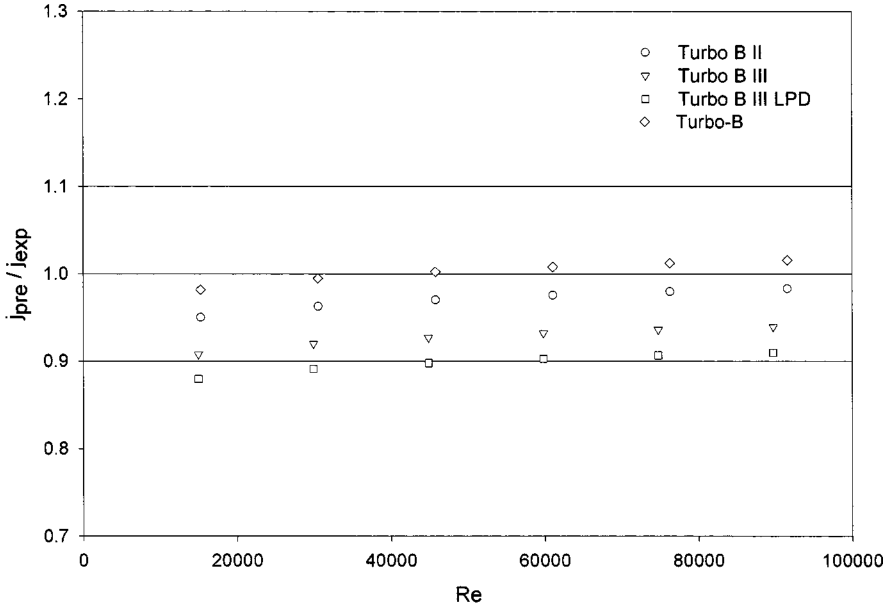

Fig. 9 Error plot showing $j_{\mathrm{pre}}/j_{\mathrm{exp}}$ versus Re for the *j*-factor correlation for tubes in patent

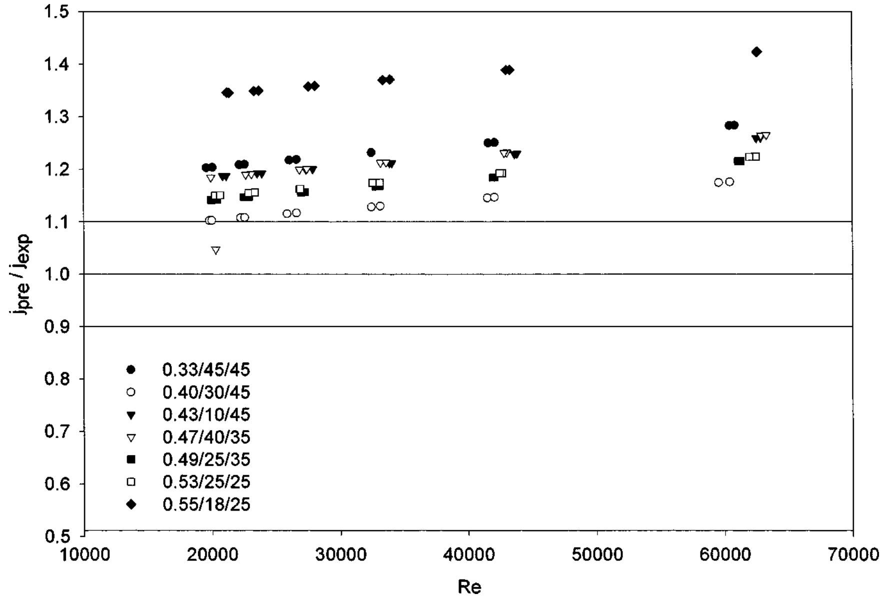

Fig. 10 Error plot showing $j_{\mathrm{pre}}/j_{\mathrm{exp}}$ for the Ravi and Bergles [8] correlation

cent and 1.4 percent, respectively. These deviations are comparable to those of Eqs. (6) and (7).

The heat transfer and friction characteristics of the Fig. 2 tubes were also predicted using empirical correlations published by Ravigururajan and Bergles [8] for single-phase flow in internally enhanced tubes. The heat transfer correlation applies a geometry correction factor to the Petukhov heat transfer equation, and assumes $\mathrm{St} \propto \mathrm{Pr}^{-2/3}$. Figure 10 shows that the correlation overpredicts the heat transfer coefficient of the Fig. 2 tubes by 10 to 45 percent. Although not shown here, the friction data were predicted with an error of ∓ 30 percent.

Additional Predictions

A recent patent by Thors et al. [9] describes commercial versions of helically ribbed tubes developed by Wolverine. The geometry of these commercial tubes are given in Table 3. Comparison of the geometry parameters of Tables 1 and 3 show that the Turbo-Chil Tube is very close to Tube 2 of Table 1. However, the other tubes in Table 3 have rib heights, number of starts, and helix angles somewhat different from the Table 1 tubes.

The Turbo-B, Turbo-BII, and Turbo-BIII tubes are each sequential design evolutions. Examination of Table 3 shows that the h/h_p values increase with each evolution. For Turbo-B, $h/h_p = 2.02$ as compared to $h/h_p = 2.54$ for Turbo-BIII. The Turbo-BIII has a higher h/h_p than any of the tubes in Table 2. The Table 2 tube having performance closest to Turbo-BIII is Tube 3, which gives $h/h_p = 2.33$. The key differences between Turbo-BIII and Tube 3 are slight differences in N_s and α.

Thors et al. [9] report smooth curve experimental test results of the Table 3 tubes. The friction factor is based on the average fin height, and the average pressure drop for flow in each direction. We have used the correlations given by Eqs. (6) and (7) to predict the performance of the Table 3 Turbo B-II and Turbo B-III tubes, which are the current production versions. Note that Turbo-B, Turbo-BII, and Turbo-BIII tubes have a 49-deg helix angle, which is slightly outside the range of the Table 1 correlation database (45 deg). Error plots are shown in Fig. 8 ($f_{\mathrm{pre}}/f_{\mathrm{exp}}$) and Fig. 9 ($j_{\mathrm{pre}}/j_{\mathrm{exp}}$) for $18{,}000 < \mathrm{Re} < 90{,}000$. The j and f factors are generally predicted within ten percent. These figures also indicate the ability of the correlation to predict data outside the range of the database. The last two columns of Table 3 show $j_{\mathrm{pre}}/j_{\mathrm{exp}}$ and $f_{\mathrm{pre}}/f_{\mathrm{exp}}$ at $\mathrm{Re}=27{,}000$, which is close to the design Reynolds number for water chiller evaporator application.

Conclusions

1 This paper provides data on seven helically ribbed tubes having a wide range of internal dimensions, as defined by the rib height, number of starts, and helix angles.

2 The heat transfer and friction characteristics of the Table 1 tubes are compared and those having high performance are identified.

3 Correlations were developed for the j and f factors. Equations (10) and (11) are recommended for Prandtl numbers different from the test values (5.08–6.29).

4 Equations (6) and (7) were used to predict the performance of similar commercial tube geometries. The correlations over predicted the friction factor 0 to 15 percent and predicted the j-factor within ten percent.

5 The tested tubes appear to illustrate characteristics of both rough tubes (enhancement provided by local flow separation at the ribs) and internally finned tubes (enhancement from surface area increase).

Acknowledgment

The tubes were manufactured by Wolverine Tube Corp., Decatur, AL. The authors are grateful for the support of Wolverine in supplying the data.

Nomenclature

A = inside surface area based on nominal diameter $(\pi D_i L)$, m^2
A_c = cross-sectional area, m^2
A_o = tube outside surface area, m^2
$B(e^+)$ = friction correlating function for rough tubes $[(2/f)^{1/2} + 2.5\ln(e/D_i) + 3.75]$, dimensionless
c_p = specific heat of water, J/kg·K
C_{ST} = Seider-Tate coefficient used in Eq. (2), dimensionless
D_i = internal tube diameter, or diameter to root of fins, m
e = rib height (average value), m
$\overline{g}(e^+)$ = heat transfer correlating function, $[(f/(2\mathrm{St}) - 1)/(f/2)^{1/2} - B(e^+)]\mathrm{Pr}^{-0.57}$, dimensionless
G = mass velocity $(= m/A_c)$, kg/m^2
f = fanning friction factor, dimensionless
h = heat transfer coefficient based on $A = \pi D_i L$, W/m$^2\cdot$K
j = Colburn j factor $(= \mathrm{St}\mathrm{Pr}^{2/3})$, dimensionless
k = thermal conductivity, W/m-K
L = tube length, m
m = mass flow rate, kg/s
N_s = number of starts, dimensionless
Nu = Nusselt number $(= hD_i/k)$, dimensionless
p_n = transverse rib pitch, viewed normal to the ribs $(= \pi D_i/N_s)$, m
p_a = axial rib pitch $[(= p_n/\tan\alpha)]$, m
p_{sat} = saturation or condenser pressure, N/m^2
Pr = Prandtl number, dimensionless
R = thermal resistance, R_i (tube side), R_o (shell side), R_w (tube wall), R_{tot} (total), m^2-K/W
Re = tube-side Reynolds number $(= D_i G/\mu)$, dimensionless
St = Stanton number (h/Gc_p), dimensionless
s_f = slant height of ribs as shown on Fig. 3, m
t_b = fin thickness normal to rib at base, m
t_t = rib tip width normal to rib at tip, m
T = temperature, T_{sat} (refrigerant saturation), T_i (inlet water), T_o (outlet water), T_{ave} (average fluid bulk temperature) K
ΔT_{lm} = log-mean temperature difference, K
U = fluid velocity, m/s
UA = overall heat transfer conductance, W/K
V = material volume (tube plus enhancement), m^3

Greek Letters

α = helix angle, deg
β = included angle between sides of ribs (see Fig. 3), deg
η = efficiency index, $(h/h_p)/(f/f_p)$, dimensionless
μ = dynamic viscosity at bulk water temperature, kg/m·s
μ_w = dynamic viscosity at wall temperature, kg/m·s
ρ = fluid density, kg/m^3

Subscripts

e = enhanced surface
i = internal surface
o = outer surface
p = plain surface
pre = predicted
exp = experimental

References

[1] Webb, R. L., 1991, ''Advances in Shell Side Boiling of Refrigerants,'' Journal of the Institute of Refrigeration, **87**, pp. 75–86.
[2] Webb, R. L., 1994, *Principles of Enhanced Heat Transfer*, John Wiley and Sons, New York.
[3] Gee, D. L., and Webb, R. L., 1980, ''Forced Convection Heat Transfer in Helically Rib-Roughened Tubes,'' Int. J. Heat Mass Transf., **23**, pp. 1127–1136.
[4] Briggs, D. E., and Young, E. H., 1969, ''Modified Wilson Plot Techniques for Obtaining Heat Transfer Correlations for Shell and Tube Heat Exchangers,'' Chem. Eng. Prog. Symp. Ser., No. 92, **65**, pp. 35–45.
[5] Seider, E. N., and Tate, G. E., 1936, ''Heat Transfer and Pressure Drop of Liquids in Tubes,'' Ind. Eng. Chem., **28**, p. 1429.
[6] Incropera, F. P., and DeWitt, D. P., 1996, *Fundamentals of Heat and Mass Transfer*, 4th Ed., John Wiley and Sons, New York.
[7] Webb, R. L., Eckert, E. R. G., and Goldstein, R. J., 1971, ''Heat Transfer and Friction in Tubes With Repeated-Rib Roughness,'' Int. J. Heat Mass Transf., **14**, pp. 601–617.
[8] Ravigururajan, T. S., and Bergles, A. E., 1996, ''Development and Verification of General Correlations for Heat Transfer and Pressure Drop in Single-Phase Turbulent Flow in Enhanced Tubes,'' Exp. Therm. Fluid Sci., **13**, pp. 55–70.
[9] Thors, P., Clevinger, N. R., Campbell, B. J., and Tyler, J. T., 1997, ''Heat Transfer Tubes and Methods of Fabrication Thereof,'' U.S. Patent No. 5,697,430, assigned to Wolverine Tube.

Laminar Flow Heat Transfer and Pressure Drop Characteristics of Power-Law Fluids Inside Tubes With Varying Width Twisted Tape Inserts

A. G. Patil
Department of Chemical Engineering,
Bharti Vidyapith's College of Engineering,
Dhankawadi, Pune-411 043,
Maharashtra, India

Results of an experimental investigation of heat transfer and flow friction of a generalized power-law fluid in tape generated swirl flow inside a 25.0 mm i.d. circular tube, are presented. In order to reduce excessive pressure drops associated with full width twisted tapes, with less corresponding reduction in heat transfer coefficients, reduced width twisted tapes of widths ranging from 11.0 to 23.8 mm, which are lower than the tube inside diameter are used. Reduced width twisted tape inserts give 18 percent–56 percent lower isothermal friction factors than the full width tapes. Uniform wall temperature Nusselt numbers decrease only slightly by 5 percent–25 percent, for tape widths of 19.7 and 11.0 mm, respectively. Based on the constant pumping power criterion, the tapes of width 19.7 mm perform more or less like full width tapes. Correlations are presented for isothermal and heating friction factors and Nusselt numbers (under uniform wall temperature condition) for a fully developed laminar swirl flow, which are applicable to full width as well as reduced width twisted tapes, using a modified twist ratio as pitch to width ratio of the tape. The reduced width tapes offer 20 percent–50 percent savings in the tape material as compared to the full width tapes. [S0022-1481(00)01401-8]

Keywords: Keywords: Augmentation, Enhancement, Heat Transfer, Laminar, Non-Newtonian, Swirling

Introduction

Many fluids encountered in chemical process industries exhibit non-Newtonian behavior. Typical among such fluids are paints, soaps, detergent slurries, polymer solutions, paper pulps, and greases. Most of these fluids are pseudoplastic in nature. This is a class of time-independent power-law fluids that are described by the constitutive relationship

$$\tau = K(du/dy)^n \quad \text{where } (n<1). \tag{1}$$

These fluids are subjected to a heat exchange process in different stages of their application. Due to their viscous nature, most pseudoplastic fluids are characterized by low Reynolds number laminar flow conditions. Even with enhancement due to superimposed free convection, laminar flow heat transfer coefficients of pseudoplastic fluids in smooth circular tubes are generally low. Out of the several augmentation techniques employed in laminar flow heat exchangers, swirl flow generators like twisted tape inserts inside circular tubes are particularly attractive, as they significantly increase heat transfer rates without large increases in the associated pressure drops.

Higher heat transfer coefficients observed with pseudoplastic fluids in smooth tubes are due to variable consistency and non-Newtonian effects. Metzner et al. [1] proposed the correlation accounting for these effects

$$\mathrm{Nu} = 1.75[3n + 1/(4n)]^{1/3}(\mathrm{Gz})^{1/3}(K/K_w)^{0.14}$$
$$\text{for } \mathrm{Gz} > 20; \text{ and } n > 0.1. \tag{2}$$

For combined laminar forced convection and free convection in horizontal tube flow, Metzner and Gluck [2] recommend the equation

$$\mathrm{Nu} = 1.75[3n + 1/(4n)]^{1/3}[Gz + 12.6(\mathrm{Pr}_w \mathrm{Gr}_w (D_i/L)^{0.4}]^{1/3} \times (K'_b/K'_w)^{0.14}. \tag{3}$$

The previous investigations of Hong and Bergles [3] and Sukhatme et al. [4] for uniform heat flux condition and Marner and Bergles [5], Shivkumar and Rao [6] and Dasmahapatra and Rao [7] for uniform wall temperature condition and the numerical work of Date and Singham [8], Du Plessis and Kroger [9] have shown that tape generated swirl flow enhances Nusselt numbers by 1.5–4 times and at the same time increases friction factors by three to six times in laminar flow.

Shah and London [10] presented correlations for laminar flow isothermal friction factors for full width twisted tapes inside the smooth tube, based on the numerical work of Date and Singham [8] allowing for the thickness of the tape

$$(f\,\mathrm{Re})_i = 42.23\xi \quad \text{for } (\mathrm{Re}_i/y) \le 6.7 \tag{4a}$$

$$(f\,\mathrm{Re})_i = 38.4(\mathrm{Re}_i/y)^{0.05}\xi \quad \text{for } 6.7 \le (\mathrm{Re}_i/y) \le 100 \tag{4b}$$

$$(f\,\mathrm{Re})_i = C(\mathrm{Re}_i/y)^{0.3}\xi \quad \text{for } (\mathrm{Re}_i/y) > 100 \tag{4c}$$

where

$$\xi = [\pi/(\pi/2)]^2[(\pi + 2 - 2\delta/D_i)/(\pi - 4\delta/D_i)]^2[\pi/(\pi - 4\delta/D_i)] \tag{4d}$$

$$C = 8.8201y - 2.1193y^2 + 0.2108y^3 - 0.0069y^4. \tag{4e}$$

Contributed by the Heat Transfer Division for publication in the JOURNAL OF HEAT TRANSFER. Manuscript received by the Heat Transfer Division, Feb. 28, 1999; revision received Aug. 18, 1999. Associate Technical Editor: B. Chung.

Du Plessis and Kroger [9] developed a new way of predicting friction factors for laminar twisted tape flow using effective flow parameters and presented a single correlation applicable for the entire range of Re_i/y

$$(f_i/f_e)=[1+\{\mathrm{Re}_i/(70.y^{1.3})\}^{1.5}]^{1/3} \tag{5a}$$

where

$$f_e=3.0949[0.9692+\pi/2G']^2/\{\mathrm{Re}_i[(2y^2/\pi)(G'-1)-0.03077]^3\} \tag{5b}$$

and

$$G'=(4y^2+\pi^2)^{0.5}/2y. \tag{5c}$$

Manglik and Bergles [11] analyzed the limited uniform wall temperature heat transfer data of Marner and Bergles [5] and observed that laminar swirl flow heat transfer is affected by entrance length, fluid viscosity ratio, Prandtl number, tape twist ratio, and swirl flow Reynolds number. They proposed the equation

$$\mathrm{Nu}=4.631(\mu_b/\mu_w)^{0.14}[0.4935(\mathrm{Pr}(\mathrm{Re}_s/y)^{3.475})^{0.53}+(1+0.0954(\mathrm{Gz})^{0.8685})^{2.6316}]^{0.2}. \tag{6}$$

Dasmahapatra and Rao [7] confirmed the validity of Eq. (6) for a wide range of tape twist ratios and swirl flow Reynolds numbers.

Various geometries to augment low Reynolds number laminar flow heat transfer have been studied. Notable among these are the MC-type turbolator, wire fin insert, and wavy tube configuration. Zhu et al. [12] presented results of viscous CMC solutions flowing through smooth tubes using the MC-type turbolator (for $5<\mathrm{Re}_{\mathrm{gen}}<85$ and $5<\mathrm{Pr}_{\mathrm{gen}}<1300$). The heat transfer coefficients were four to six times and friction factors of MC-type inserts were 10 to 20 times greater than those of smooth tubes. Mukherjee [13] recommended the case of wire-fin inserts that he said to be the most cost effective in augmenting low Reynolds number flow heat transfer. Most recently Gibson [14] summarized various augmentation techniques available commercially. Of these, wavy tube configurations that cause a spiraling action in the fluid provide efficiency increases of 30–40 percent over smooth tube designs.

Several modifications in twisted tape geometries have been investigated with the aim of restricting the increase in pressure drops and achieving material savings. Shivkumar and Rao [6] reported results for laminar flow of generalized power-law fluids in smooth and spirally corrugated tubes fitted with twisted tapes ($y=3{,}5.6{,}10$). They observed that the Nusselt numbers are 1.3–3.4 times the corresponding smooth tube values. Monheit [15] made a comparative study of the thermal performance of ordinary full-width full-length twisted tapes with tapes having modified surface configurations. The modified tape was either a tape with circular holes on its surface or one with slits on its edges. For laminar flow heat transfer to lubricating oil ($\mathrm{Re}=60-3500$, $\mathrm{Pr}=150-450$) such modification offered no advantage over ordinary twisted tape. Dasmahapatra and Rao [7] studied augmentation of heat transfer to viscous non-Newtonian fluids in laminar flow using full width interrupted twisted tapes under the uniform wall temperature condition. They found that regularly spaced tapes give 15–35 percent lower friction factors and only 10–20 percent reduction of Nusselt numbers compared to full width full length twisted tapes, for the range of twist ratios ($y=2.4-5.04$) and space ratios ($S=2.2-4.0$).

Al-Fahed et al. [16,17] investigated the effect of tube-tape clearance on heat transfer under fully developed turbulent ([16]) and laminar ([17]) conditions. They have demonstrated that as the tube-tape clearance decreases, the heat transfer enhancement increases. However, they have not presented correlations for predicting the heat transfer coefficients and friction factors. They have recommended the use of loose-fit ($w=10.8$ mm) tape, in low twist ratios ($y=3.6{,}5.4$) and high pressure drop situations, since it is easier to install and remove. However, ease of installation should not be the criterion to recommend a particular geometry and the selection of the optimum geometry should be based on the hydrothermal performance of the system. Performance evaluation criteria for enhanced heat transfer surfaces are reviewed by Bergles et al. [18].

The present investigation is aimed at studying the frictional and heat transfer characteristics of laminar swirl flow of pseudoplastic type power law fluid in a circular tube using varying width twisted tapes under a uniform wall temperature condition. The objective of using varying (reduced) width twisted tapes is to reduce the pressure drops associated with full width twisted tapes without seriously impairing the heat transfer augmentation rates and to achieve material savings.

Experiments were conducted over the following ranges of independent parameters:

generalized Reynolds number	$10<\mathrm{Re}_{\mathrm{gen}}<500$
generalized Prandtl number	$600<\mathrm{Pr}_{\mathrm{gen}}<1200$
Graetz number	$100<\mathrm{Gz}<1500$
modified twist ratio	$2.69<y^*<12.27$
tape thickness to tube diameter ratio	$0.028<\delta/D_i<0.044.$

Experimental Work

The layout of tubes containing a full width and the reduced width twisted tapes is shown in Fig. 1. The tapes consist of long 304 stainless steel strips of desired width (thickness of strips=0.7–1.1 mm), which have been twisted about the longitudinal axis. Twisted tapes of four different widths (23.8, 19.7, 16.5, and 11.0 mm) were fabricated for each of the three different pitches viz. 64, 76, and 135 mm. For the case of reduced width tapes, the gap between the tube wall and the tape was maintained constant throughout the tube length by brazing metal pins to the edges of the tape as indicated in Fig. 1. The tapes of full width (23.8 mm) were inserted as is into a 25-mm-dia tube to give a sliding fit.

The test liquid used was one percent (by wt) solution of sodium carboxy methyl cellulose (SCMC) in water. The SCMC was supplied by Cellulose Products of India, Ahmedabad and was marketed as CEPOL-DV (high viscosity-pharmaceutical grade). The one percent SCMC solution was found to be pseudoplastic in nature and obeyed the generalized power-law model

$$\tau_w=K'(8\overline{v}/D_i)^{n'} \quad \text{where} \quad (n'<1) \tag{7}$$

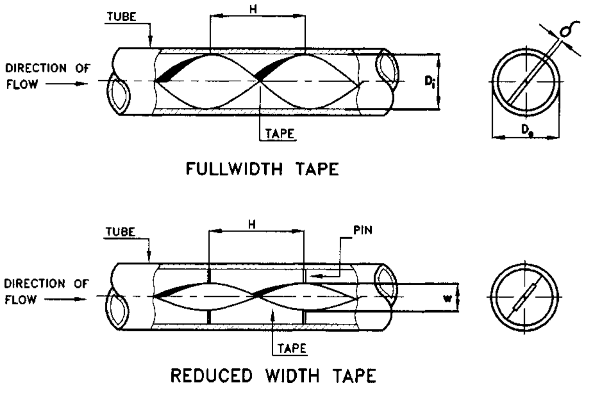

Fig. 1 Illustration of the full width and reduced width twisted tapes inside a circular tube

Table 1 Rheological properties of one percent SCMC test liquid

Liquid	Temperature (°C)	K' ($\mathrm{N\,s^{n'}/m^2}$)	n'
one percent SCMC (CEPOL-DV)	30	0.369	0.75
	40	0.359	0.75
	50	0.249	0.75

The flow constants K' and n' obtained from the rheograms using a capillary tube viscometer are listed in Table 1.

Experimental Apparatus and Procedure

The schematic diagram of the experimental setup is shown in Fig. 2. The test section consisted of a double pipe heat exchanger, 2230 mm long with the inner tube being a smooth copper tube of 25 mm i.d. and 1.5 mm tube wall thickness. The outer pipe was 55 mm i.d. galvanized iron pipe, which has openings for the passage of eight copper–constantan thermocouples, embedded in the inner tube wall at about 300 mm distance. Tube wall temperatures were recorded with a digital recorder within ±0.1°C accuracy.

The working fluid was circulated through the test section on the tube side, and hot water was circulated on the annulus side of the test section. Calibrated rotameters were used to measure the flow rates of the test liquid and hot water. Hot water was maintained at constant flow rate and essentially constant average temperature inside the annulus to achieve the uniform wall temperature condition.

The 1400-mm-long upstream and 800-mm-long downstream calming sections had the same configuration as that of the test section. These calming sections were found to be adequate for the establishment of the fully developed condition. The well-mixed inlet and exit temperatures of the tube side and annulus side fluid streams were measured by calibrated thermometers, accurate to within ±0.1°C. The pressure drops across the test section were measured by using U-tube manometers with carbon tetrachloride and monochlorobenzene as manometric liquids. The test section was sufficiently lagged with thermal insulation to make the heat loss to surroundings negligible.

Isothermal friction factors were measured at 40°C (±0.5°C) for varying flow rates in laminar flow using U-tube manometers of appropriate manometric liquid, depending upon the magnitude of generalized Reynolds number. In heat transfer and nonisothermal friction factor studies the test liquid was kept circulating through the heating test section at any desired constant flow rate, and its inlet temperature was maintained in the desired range by regulating the flow of cooling water flowing through the cooling coil placed inside the test liquid tank. Hot water was introduced into the annulus side of the test section at a constant flow rate (0.67 kg/s) and at a steady inlet temperature (60°C). The tube wall temperature variation was found to range from 0.2 to 1.4°C. At steady state, tube wall temperatures were measured and the inlet and exit temperatures of test liquid and hot water and their flow rates were noted from the respective calibrated thermometers and rotameters. Nonisothermal pressure drops were also noted from the U-tube manometer across the test section under the heated condition.

The uncertainties in the measurement of friction factor and heat transfer coefficients were found to be ±4 and ±8 percent, respectively. Further details regarding capillary tube viscometer, experimental setup, the experimental procedures, and error analysis used in the study can be found in Patil [19].

Results and Discussion

Isothermal Friction Factors Results. The isothermal pressure drop data at 40°C (±0.5°C) for laminar flow of one percent SCMC solution in smooth tubes with and without tape inserts were analyzed in terms of Fanning's friction factor given by

$$f_i = D_I \Delta P/(2L\bar{v}^2\rho). \tag{8}$$

Friction factors are shown in Fig. 3 as a function of generalized Reynolds number $\mathrm{Re}_{\mathrm{gen}}$.

The isothermal friction results for laminar flow of one percent SCMC in smooth tubes are in excellent agreement (±5 percent) with the well-known analytical equation

$$f_i = 16/\mathrm{Re}_{\mathrm{gen}} \tag{9}$$

for the range $20 < \mathrm{Re}_{\mathrm{gen}} < 400$. This served the purpose of standardization for the setup.

The isothermal friction results for swirl flow of one percent SCMC solution in smooth tube fitted with each of the full width tapes ($w = 23.8$ mm, $H = 64$, 135 mm) are compared with modified correlations of Shah and London (Eq. (4)) as shown in Fig. 3.

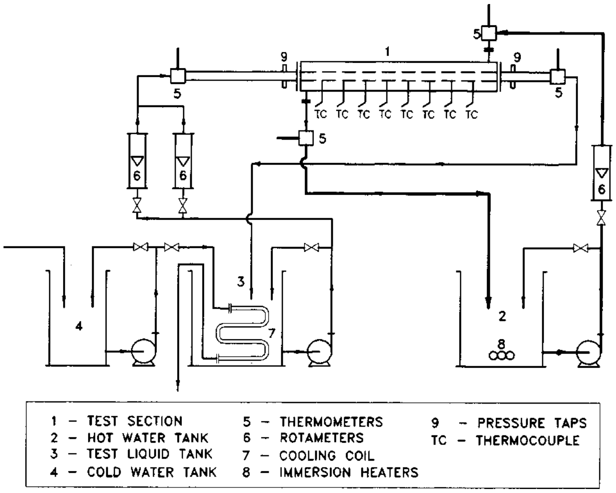

Fig. 2 Schematic diagram of experimental setup

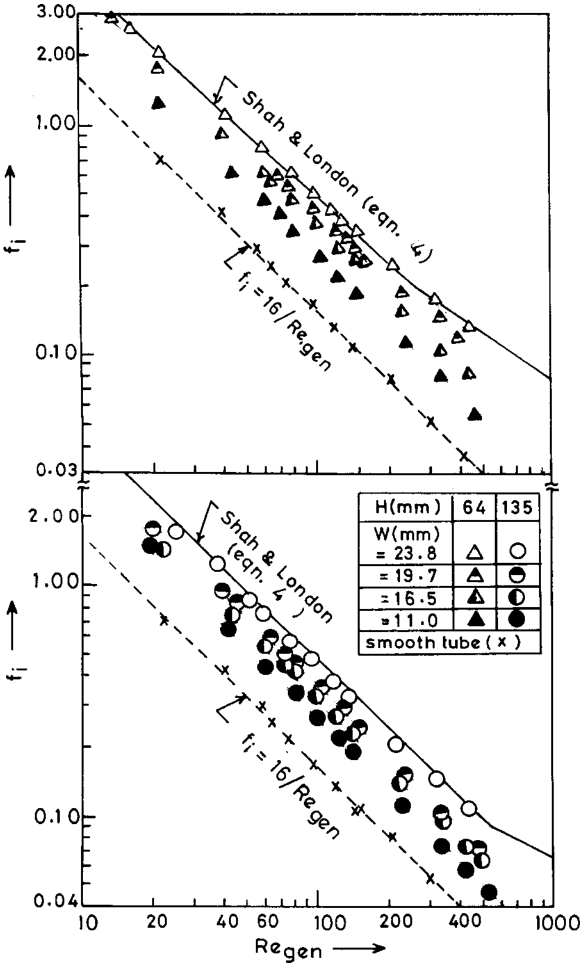

Fig. 3 Isothermal friction factors for swirl and axial flow

The experimental friction factors are consistently lower by about 35 percent over the range $20<\mathrm{Re}_{\mathrm{gen}}<400$ for both the full width tapes. This is because of the sliding fit between the tube wall and 23.8 mm tapes, whereas Eq. (4) assumes that the tape width is equal to the tube diameter ([10]).

The isothermal friction factors for reduced width tapes are also shown in Fig. 3. They are obviously affected by tape width besides $\mathrm{Re}_{\mathrm{gen}}$ and twist ratio, and are lower than that of full width tapes. The percentage reductions are about 17–25 percent, 23–40 percent, and 40–60 percent, respectively for, 19.7, 16.5, and 11.0-mm-width tapes, compared to full-width tapes.

Correlation for Isothermal Friction Factors. Isothermal friction factors for full-width twisted tapes in laminar swirl flow are accurately predicted by the modified equation of Shah and London (Eq. (4)). The friction data for reduced width tapes can be analyzed by using the modified twist ratio y^* ([19]) as tape pitch to tape width ratio, instead of the conventional twist ratio y (pitch-to-diameter ratio) used for full-width tapes. Using the modified twist ratio and swirl flow generalized Reynolds number, the present results were treated numerically to give the correlation

$$(f_i\,\mathrm{Re}_{s\mathrm{gen}})=42.23\xi^* \quad \text{for} \quad (\mathrm{Re}_{s\mathrm{gen}}/y^*)\leqslant 6.7 \tag{10a}$$

$$(f_i\,\mathrm{Re}_{s\mathrm{gen}})=38.4(\mathrm{Re}_{s\mathrm{gen}}/y^*)^{0.05}\xi^* \quad \text{for} \quad 6.7\leqslant(\mathrm{Re}_{s\mathrm{gen}}/y^*)\leqslant 100 \tag{10b}$$

$$(f_i\,\mathrm{Re}_{s\mathrm{gen}})=C^*((\mathrm{Re}_{s\mathrm{gen}}/y^*)^{0.3}\xi^* \quad \text{for} \quad (\mathrm{Re}_{s\mathrm{gen}}/y^*)>100 \tag{10c}$$

where

$$\xi^*=[\pi/(\pi/2)]^2[(\pi+2-2\delta/w)/(\pi-4\delta/w)]^2[\pi/(\pi-4\delta/w)](y/y^*) \tag{10d}$$

$$C^*=8.8201y^*-2.1193(y^*)^2+0.2108(y^*)^3-0.0069(y^*)^4. \tag{10e}$$

It can be noted that when the tape width is equal to the tube diameter, Eq. (10) reduces to Eq. (4). The experimental isothermal friction factor results for full-width and reduced-width tapes agreed within ±12 percent with those calculated by Eq. (10).

Heated (Nonisothermal) Friction Factors: Results and Correlation. The difference between isothermal and heated friction factors for the swirl flow data was found to be substantially less than the corresponding difference for a smooth tube. This is because of the difference in the cross section of flow channels. For swirl flow in tubes, the effective channel size is decreased, but the total peripheral shear stress is substantially increased. If one assumes that the viscosity correction represents the effective decrease in this shear stress due to decrease in fluid viscosity at the heated surfaces, the correction for heated friction factor would be equal for swirl and axial flow cases only if the thermal boundary layer thickness is the same at the tape surface and the tube wall. Since the heat transfer from the tape surface is negligible, it is probable that, with heat addition, the decrease in shear stress at the tape surface is less than that at the tube wall. The magnitude of the isothermal correction factor required for swirl flow would then also be less. To account for this difference, the flow consistency index ratio (K_b'/K_w') exponent of 0.43 was used to correct the empty tube heated friction factors f_h to the isothermal condition. This exponent of 0.43 was multiplied by (D_e/D_i) in order to correct the heated swirl flow data, to give the swirl flow correlation as

$$f_{\mathrm{si}}=f_{\mathrm{sh}}(K_b'/K_w')^{0.43(D_e/D_i)}. \tag{11}$$

Equation (11) accurately corrected heated swirl flow friction data for all eight tapes studied in the present investigation. It was not possible to determine the validity of this correction with the data of other investigators since information on their heated friction factors and corresponding K' ratio (K_b'/K_w') for swirl and axial flow has not been presented separately.

Heat Transfer Results. Heat transfer runs were conducted under steady-state conditions. The flow rate (0.67 kg/s) and average bulk temperature of hot water (60°C) in the annulus side were kept constant in order to keep the outside heat transfer coefficient h_0 constant and to attain a uniform wall temperature condition. For any run the variation of wall temperature throughout the test section was limited to 0.2–1.4°C. This ensured a uniform wall temperature boundary condition.

Runs with a heat balance error $(\mathrm{HBE})=100(Q_h-Q_c)/Q_h$ within ±6 percent were processed and the heat transfer coefficient was obtained from

$$h_i=Q_c/[A_i(T_w-T_c)_{\ln}]. \tag{12}$$

The mean bulk temperature $(T_c=(T_{c1}+T_{c2})/2)$ was used to calculate the property values of the test fluid.

The swirl flow generalized Prandtl number and Reynolds number were calculated as

$$\mathrm{Pr}_{\mathrm{gen}}=(C_pK'/k)(8\overline{v}/D_i)^{n'-1} \tag{13}$$

$$\mathrm{Re}_{s\mathrm{gen}}=GD_i/[K'(8\overline{v}/D_i)^{n'-1}] \tag{14}$$

where the mass flux G is evaluated on the basis of actual swirl flow area A_s, which when the tape thickness δ is taken into account, is given by

$$A_s=(A_i-\delta D_i). \tag{15}$$

The experimental heat transfer results for laminar axial and swirl flow of one percent SCMC solution are shown in Figs. 4 and 5 in terms of Nusselt number Nu_i versus Graetz number Gz and Nusselt number Nu_i versus swirl flow generalized Reynolds number $\mathrm{Re}_{s\mathrm{gen}}$ $\{(\mathrm{Re}_{s\mathrm{gen}})=R_{\mathrm{gen}}$ for axial flow$\}$ plots, respectively.

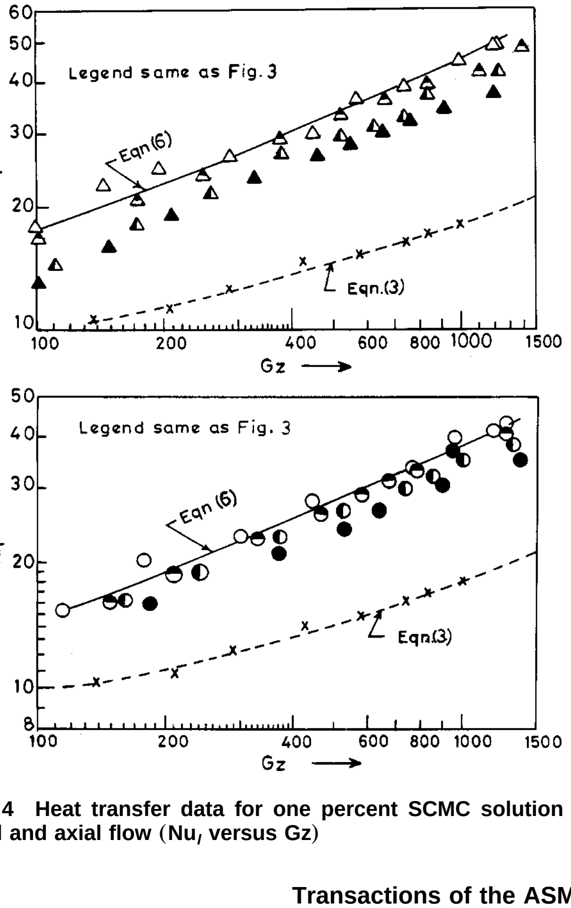

Fig. 4 Heat transfer data for one percent SCMC solution in swirl and axial flow (Nu_i versus Gz)

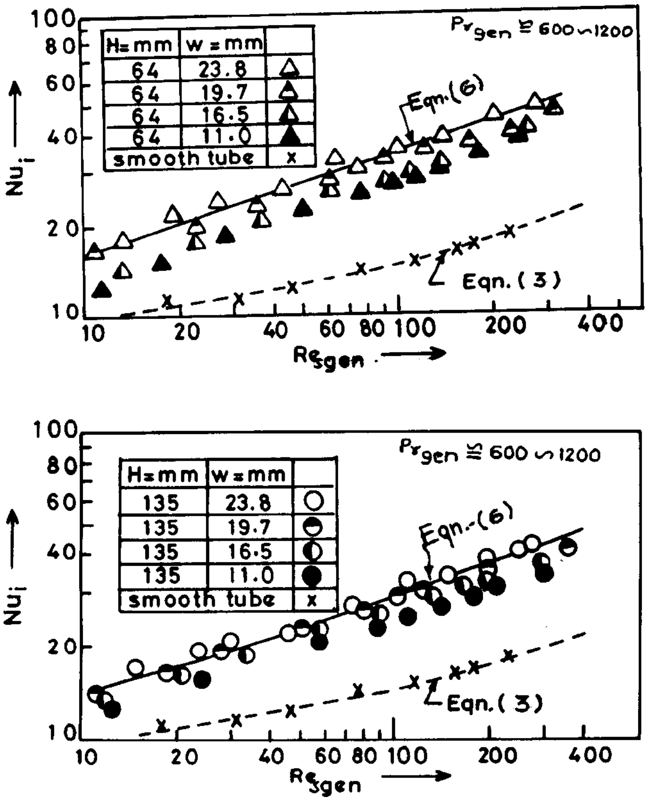

Fig. 5 Heat transfer data for one percent SCMC solution in swirl and axial flow (Nu_i versus Re_{sgen})

The smooth tube heat transfer results for laminar flow of one percent SCMC are in good agreement (±10 percent) with the correlation of Metzner and Gluck [2]. It is evident from Figs. 4 and 5 that when a twisted tape is inserted into a plain tube there is a significant improvement in Nusselt numbers because of secondary flow, with greater enhancement being realized at higher Reynolds number and tape twists. This enhancement is mainly due to the centrifugal forces resulting from the spiral motion of the fluid and partly due to the tape acting as fin. Since the tape inhibits free convection, the contribution of Grashof number Gr is unimportant in laminar swirl flow.

The experimental data for full-width twisted tapes agreed within ±10 percent with the equation of Maglik and Bergles (Eq. (6)). This served the purpose of standardization of the test setup.

It is evident from Figs. 4 and 5 that the reduction in tape width causes reduction in Nusselt numbers. The percentage reductions in Nusselt numbers for reduced width tapes compared to full width tapes are about 5–9 percent, 10–15 percent, and 20–24 percent for tape widths of 19.7, 16.5, and 11.0 mm, respectively. These are not much compared to the percentage increase in Nusselt numbers of full width tapes over smooth tube values, which are about 66–150 percent.

Heat Transfer Correlation. The heat transfer data for full width and reduced width tapes were correlated by a single equation by incorporating the modified twist ratio y^* in place of y and using (K_b'/K_w') instead of (μ_b/μ_w) in the equation of Manglik and Bergles (Eq. (6)). The resulting correlation

$$\mathrm{Nu}_i = 4.631(K_b'/K_w')^{0.14}[0.4935\{\mathrm{Pr}_{\mathrm{gen}}(\mathrm{Re}_{s\mathrm{gen}}/y^*)^{3.475}\}^{0.53} + \{1 + 0.0954(\mathrm{Gz})^{0.8685}\}^{2.6316}]^{0.2} \quad (16)$$

predicted the experimental heat transfer data within ±10 percent accuracy.

Performance Evaluation

For evaluation of hydrothermal performance of varying width tapes, the constant pumping power criterion of Bergles et al. [18] is used. The tape performance is thus expressed as the ratio of tube side heat transfer coefficients of augmented tube to smooth tube at constant pumping power given by

$$R_3 = (h_{ia} \text{ at } \mathrm{Re}_a / h_{i0} \text{ at } \mathrm{Re}_0)_{\text{for constant } D_i, L, P, T_i, \Delta T_{\ln}}, \quad (17)$$

Variations of performance ratio R_3 against smooth tube generalized Reynolds number $\mathrm{Re}_{\mathrm{gen}}$ are shown in Fig. 6. It is seen in Fig. 6 that, for tapes of widths 23.8 and 19.7 mm, R_3 curves are flat ($R_3 = 2-2.4$) for a pitch of 64 mm and show an increasing trend ($R_3 = 1.4-2.2$) for a pitch of 135 mm in the range of generalized Reynolds number from 30 to 200. Each curve seems to have a maximum at a particular generalized Reynolds number $\mathrm{Re}_{\mathrm{gen}}$, and the $\mathrm{Re}_{\mathrm{gen}}$ at which the maximum occurs decreases with the decrease in tape width. This maximum may precisely be the point (w/D_i) below which the reduction in friction factors due to the decrease in the tape width [hence in (w/D_i)] slows down, thereby giving relatively higher values of friction factors than the corresponding Nusselt numbers. The tapes of width 19.7 mm perform more or less like full-width tapes and appear to do slightly better than those for the 64-mm pitch. Even the tapes of 11.0-mm width have an R_3 value of about 1.3–1.96 times the smooth tube.

The variation of performance ratio R_3, with the fraction of tube diameter occupied by the tube w/D_i, is shown in Fig. 7. For $\mathrm{Re}_{\mathrm{gen}} = 200$ the curves are flat in the range between $w/D = 0.8$ and 1.0 for both the pitches used. However, for $\mathrm{Re}_{\mathrm{gen}} = 30$ the flatness is observed (in the same w/D range) only for the 64 mm pitch. The flatness of these curves basically represents the same performance of reduced width tapes as that of the full-width tape.

Thus the same performance can be achieved using reduced-width tapes with 20 percent material saving at higher Reynolds

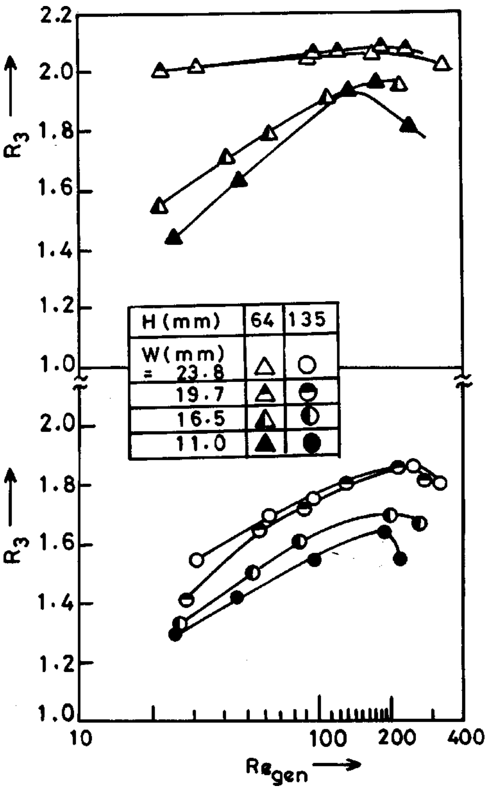

Fig. 6 Performance ratio R_3 for varying width tapes in smooth tube in one percent SCMC solution under constant pumping power

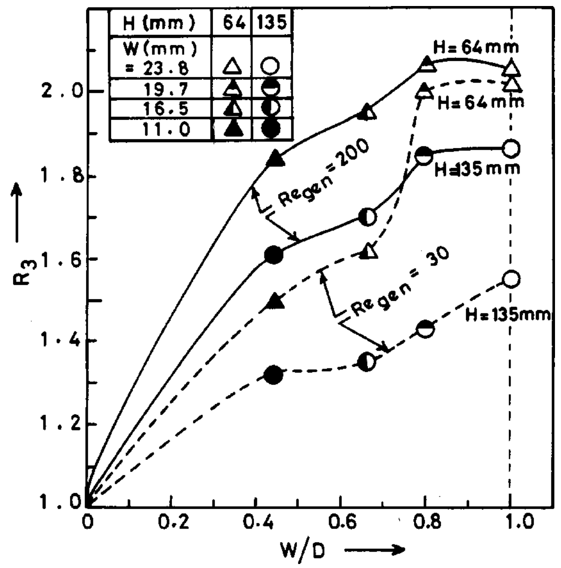

Fig. 7 Variation of performance ratio R_3 with fraction of tube diameter occupied by tape

number and/or lower twist ratios. Even for 50 percent material savings (tapes of width 11.0 mm) the performance is 1.3–1.96 times better than for a smooth tube. Thus, from the considerations of enhanced heat transfer and savings in pumping power and in tape material cost, reduced-width tape inserts are seen to be attractive for enhancing laminar swirl flow heat transfer to viscous power-law fluids of the pseudoplastic type.

Nomenclature

A = heat transfer surface area (m^2)
A_i = flow area (m^2)
A_s = cross-sectional area of tape as defined in Eq. (15)
C = defined in Eq. (4)
C^* = defined in Eq. (10)
C_p = specific heat (J/kg °C)
d,D = diameter of heat exchanger tube (m)
D_e = equivalent diameter of tube (m); $D_e=[4(\pi D_i^2/4 - \delta w)]/(\pi D_i+2w)$
f = Fanning friction factor (dimensionless)
g = acceleration due to gravity (m/s^2)
G = mass flux (kg/s m^2); $G=W/A_s$
G' = defined in Eq. (5)
H = pitch for 180 deg rotation of the tape (m)
h = heat transfer coefficient (W/m^2 °C)
l = rod length between successive tape elements (m)
k = thermal conductivity (W/m °C)
K,K' = flow consistency index ($Ns^{n'}/m^2$) defined in Eqs. (1) and (7)
L = tube length (m)
n,n' = flow behavior index (dimensionless) defined in Eqs. (1) and (7)
P = pressure (N/m^2)
ΔP = pressure drop (N/m^2)
Q = rate of heat transfer (W)
S = space ratio (dimensionless), $S=l/D_i$
T = temperature (°C)
ΔT = temperature difference (°C)
U = overall heat transfer coefficient (W/m^2 °C)
u = point velocity (m/s)
$\overline{v}$ = average velocity (m/s)
W = mass flow rate (kg/s)
w = width of twisted tape (m)
y = twist ratio (H/D_i) (dimensionless)
y^* = modified twist ratio (H/w) (dimensionless)

Greek Letters

α = angle of tape twist (deg) and tape geometry parameter defined as $[1/2y\{4y^2+\pi^2\}^{0.5}]$
β = volumetric coefficient of thermal expansion (°C^{-1})
δ = tape thickness (m)
ρ = density (kg/m^3)
μ = viscosity (kg/m s)
τ = shear stress (N/m^2) defined in Eq. (1)
ξ = defined in Eq. (4)
ξ^* = defined in Eq. (10)

Dimensionless groups

Gr = Grashof number ($\beta D_i^3 \rho^2 \Delta T g/\mu^2$)
Nu = Nusselt number (hD_i/k)
Pr = Prandtl number ($C_p\mu/k$)
$\mathrm{Pr}_{\mathrm{gen}}$ = generalized Prandtl number, $[C_p/k.K'.(8\overline{v}/D_i)^{n'-1}]$
Re = Reynolds number ($D_i\overline{v}\rho/\mu$)
$\mathrm{Re}_{\mathrm{gen}}$ = generalized Reynolds number $[(D_i^{n'}(\overline{v})^{2-n'}\rho)/(K'8^{n'-1})]$
Re_s = swirl flow generalized Reynolds number as defined in Eq. (14)
Gz = Graetz number (Wc_p/kL)

Subscripts

a = augmented case; or axial
b = bulk mean condition
c = cold fluid
e = based on equivalent diameter, D_e
gen = generalized
h = hot fluid
i = based on inside diameter
ln = logarithmic mean
m = mean value
o = based on outside diameter or smooth tube condition
s = swirl condition
$s$gen = swirl flow generalized
si = swirl flow isothermal
sh = swirl flow heated
w = wall condition
1,2 = inlet condition, exit condition

References

[1] Metzner, A. B., Vaughn, R. D., and Houghton, G. L., 1957, ''Heat Transfer to Non-Newtonian Fluids,'' AIChE. J., **3**, p. 92.
[2] Metzner, A. B., and Gluck, D. G., 1960, ''Heat Transfer to Non-Newtonian Fluids Under Laminar Flow Conditions,'' Chem. Eng. Sci., **12**, pp. 185–192.
[3] Hong, S. W., and Bergles, A. E., 1976, ''Augmentation of Laminar Flow Heat Transfer in Tubes by Means of Twisted Tape Inserts,'' ASME J. Heat Transfer, **98**, pp. 251–256.
[4] Sukhatme, S. P., Gaitonde, U. N., Shindore, C. S., and Kunlolienkar, R. S., 1987, ''Forced Convection Heat Transfer to a Viscous Liquid in Laminar Flow in a Tube with a Twisted Tape,'' *Proceedings of 9th H.M.T. Conference*, Banglore, India, pp. B1–B7.
[5] Marner, W. J., and Bergles, A. E., 1978, ''Augmentation of Tube Side Laminar Flow Heat Transfer by Means of Twisted Tape Inserts, Static Mixer Inserts and Internally Finned Tubes,'' *Proceedings of Sixth International Heat Transfer Conference*, Toronto, Hemisphere, Washington, D.C., Vol. 2, pp. 583–588.
[6] Shivkumar, C., and Raja Rao, M., 1988, ''Compound Augmentation of Laminar Flow Heat Transfer to Generalized Power Law Fluids in Spirally Corrugated Tubes by Means of Twisted Tape Inserts,'' *ASME Proceedings of National Heat Transfer Conference*, Houston, Vol.1, ASME, New York, pp. 685–692.
[7] Dasmahapatra, J. K., and Raja Rao, M., 1991, ''Laminar Flow Heat Transfer to Generalized Power Law Fluids Inside Circular Tubes Fitted with Regularly Spaced Twisted Tape Elements for Uniform Wall Temperature Condition'' *Fundamentals of Heat Transfer in Non-Newtonian Fluids*, ASME, New York, pp. 51–58.
[8] Date, A. W., and Singham, J. R., 1972, ''Numerical Prediction of Friction and Heat Transfer Characteristics of Fully Developed Laminar Flow in Tubes Containing Twisted Tapes,'' ASME Paper No. 72-HT-17.

[9] Du Plessis, J. D., and Kroger, D. G., 1987, ‘‘Friction Factor Prediction for Fully Developed Laminar Twisted Tape Flow,’’ Int. J. Heat Mass Transf., **3**, pp. 509–515.
[10] Shah, R. K., and London, A. L., 1978, ‘‘Laminar Flow Forced Convection in Ducts,’’ *Advances in Heat Transfer*, Vol. 1, Supplement-1, Academic, New York, pp. 379–381.
[11] Manglik, R. M., and Bergles, A. E., 1987, ‘‘A Correlation for Laminar Flow Enhanced Heat Transfer in Uniform Wall Temperature Circular Tubes With Twisted Tape Inserts,’’ *Advances in Enhanced Heat Transfer*, Vol. 68, ASME, New York, pp. 19–25.
[12] Zhu et al., 1992, ‘‘Augmentation of Heat Transfer for Viscous Fluids Using the Turbolator,’’ Gaoxiao Huaxue Gongcheng Xuebao **6**, pp. 56–61 (Chinese).
[13] Mukherjee, R., 1994, ‘‘Augmentation of Heat Transfer in Low Reynolds Number Flow Inside Tubes by the Use of Wire-Fin Inserts,’’ *Proceedings of the 10th International Heat Transfer Conference*, Institute of Chemical Engineering London, UK, pp. 173–176.
[14] Gibson, W. D., 1998, ‘‘Heat Exchangers: Warming up to Special Needs,’’ Chem. Eng., **105**, No. 13, pp. 45–53.
[15] Monheit, M., 1987, ‘‘Experimental Evaluation of the Convective Characteristics of Tubes with Twisted Tape Inserts,’’ *Advances in Enhanced Heat Transfer*, AMSE, New York, pp. 11–18.
[16] Al-Fahed, S., and Chakroun, W., 1996, ‘‘Effect of Tube-Tape Clearance on Heat Transfer for Fully Developed Turbulent Flow in a Horizontal Isothermal Tube,’’ Int. J. Heat Fluid Flow, **17**, No. 2, pp. 173–178.
[17] Al-Fahed, S., Chamra, L. M., and Chakroun, W., 1998, ‘‘Pressure Drop and Heat Transfer Comparison for Both Microfin Tube and Twisted-Tape Inserts in Laminar Flow,’’ Exp. Therm. Fluid Sci., **18**, No. 4, pp. 323–333.
[18] Bergles, A. E., Blumenkrantz, A. R., and Taborek, J., 1974, ‘‘Performance Evaluation Criteria for Enhanced Heat Transfer Surfaces,’’ *Proceedings of the 5th International Heat Transfer Conference*, Tokyo, Vol. 2, pp. 239–243.
[19] Patil, A. G., 1991, ‘‘Heat Transfer Augmentation in Laminar and Turbulent Flows in a Circular Tube Fitted with Varying Width Twisted Tapes,’’ M. tech. dissertation, IIT Powai, pp. 31–36.

Yuwen Zhang
Mem. ASME

A. Faghri
Fellow ASME

C. W. Buckley

T. L. Bergman
Fellow ASME

Department of Mechanical Engineering,
University of Connecticut,
Storrs, CT 06269-3139

Three-Dimensional Sintering of Two-Component Metal Powders With Stationary and Moving Laser Beams

Melting and resolidification of a mixture of two metal powders with significantly different melting points under irradiation of a stationary or a moving Gaussian laser beam were investigated numerically and experimentally. The liquid motion driven by capillary and gravity forces as well as the shrinkage of the powder bed caused by the overall density change were taken into account in the physical model. The liquid flow was formulated by using Darcy's law, and the energy equation was given using a temperature transforming model. Prediction were compared with experimental results obtained with nickel braze and AISI 1018 steel powder. The effects of laser properties and the scanning velocity on the laser sintering process were also investigated. An empirical correlation that can be used to predict the cross-sectional area of the heat affected zone is proposed. [S0022-1481(00)70201-5]

Keywords: *Heat Transfer, Laser, Manufacturing, Melting, Solidification*

1 Introduction

Selective laser sintering (SLS) is an emerging technology of solid freeform fabrication (SFF) in which three-dimensional parts can be built from CAD data ([1]). The material used in SLS includes amorphous (e.g., polycarbonate), semicrystalline (e.g., nylon), and crystalline (e.g., metal) powder. The thermal models that are available in the literature are primarily concerned with sintering of amorphous powders ([1–4]). Since amorphous powder has little crystallinity and a near zero latent heat of fusion, no phase change occurs during sintering. Some researchers simply establish the thermal model associated with sintering of an amorphous powder as a pure conduction problem ([2,3]). Kandis and Bergman [4] present an experimental investigation and a numerical prediction of the sintering of polymer powder in a square annulus with external heating and internal cooling. Kandis et al. [5] investigate sintering of a polymer powder bed under irradiation of a stationary laser beam. The effect of the powder particle motion due to shrinkage phenomena on the thermal phenomena is taken into account in Kandis and Bergman [4] and Kandis et al. [5].

SLS of metal powder involves fabrication of near full density objects from powder via melting induced by a directed laser beam (generally CO_2 or YAG) and resolidification. For sintering of metal powder, the latent heat of fusion is usually very large, and therefore melting and resolidification phenomena have a significant effect on the temperature distribution in the parts and powder, the residual stress in the part, local sintering rates, and the final quality of the parts. A significant change of density accompanies the melting process because the volume fraction of gas(es) in the powder decreases from a value as large as 0.6 to nearly zero after melting. In addition, the liquid metal infiltrates into the unsintered region due to capillary and gravity forces.

Bunnell [6] and Manzur et al. [7] propose the use of a powder mixture containing two powders with significantly different melting points, in which only the low melting point powder will be molten and resolidified during the SLS process. In this process, the low melting point powder melts and infiltrates to the unsintered region due to capillary and gravity forces. The solid particles of the high melting point powder may also move downward because the high melting point powder cannot sustain the powder bed alone. It is very clear that both liquid and solid in the powder bed have their own velocities, and these velocities may have a significant effect on the energy transport in the powder bed.

The modeling of SLS of metal powder is a very challenging task. A thorough survey of the existing literature indicates that scant attention has been paid to thermal modeling of the sintering of metal powder. Shah [8] experimentally investigated melting of a single column of solder particle (eutectic Sn–Pb) held vertically inside a glass tube. The problem is then formulated using an enthalpy model and solved using a finite difference method. Zhang and Faghri [9] analytically solve a one-dimensional melting problem in a powder bed containing a powder mixture under a boundary condition of the second kind. The results show that the shrinkage effect on the melting of the powder bed is not negligible. Zhang and Faghri [10] numerically investigate two-dimensional melting and resolidification of a two-component metal powder with a moving Gaussian heat source. The shrinkage phenomena induced by the overall density change is taken into account. However, the liquid flow driven by capillary and gravity force is neglected in Zhang and Faghri [10]. Pak and Plumb [11] present a one-dimensional thermal model of melting of two-component powder bed. The liquid motion driven by capillary and gravity forces is considered, but the velocity of nonmelting powder particle induced by shrinkage is ignored.

A three-dimensional thermal model of SLS of a metal powder bed that contains a mixture of two powders with significantly different melting points will be presented in this paper. The liquid flow driven by capillary and gravity forces and the solid particle velocity induced by shrinkage of the powder bed will be taken into account. The predicted results are compared with experimental results obtained with nickel braze and AISI 1018 steel powder. The effect of the laser beam scanning velocity on the sintering process will be discussed.

2 Physical Model

2.1 Problem Statement. The physical model of the problem is shown in Fig. 1. A powder bed, which contains two pow-

---

Contributed by the Heat Transfer Division for publication in the JOURNAL OF HEAT TRANSFER, Manuscript received by the Heat Transfer Division, Jan. 22, 1999; revision received, July 16, 1999. Associate Technical Editor: F. Cheung.

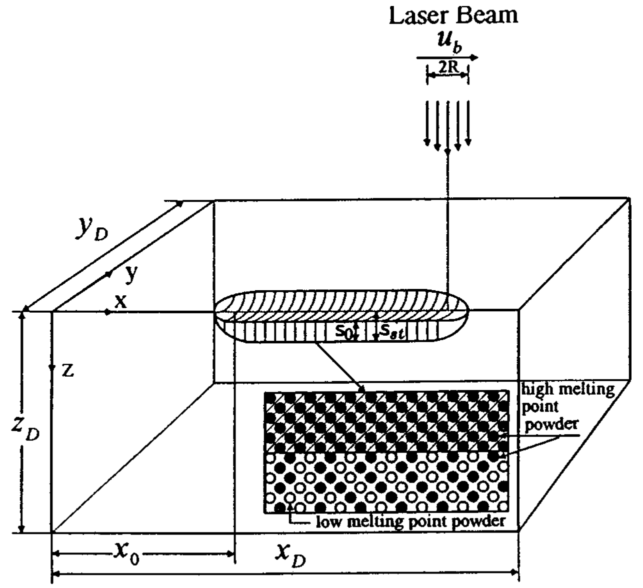

Fig. 1 Physical model of the three-dimensional sintering of two-component metal powder

ders with significantly different melting points, with a uniform initial temperature, T_i, below the melting point of the low melting point powder, T_m, is in a cavity with a size of $x_D \times 2y_D \times z_D$ (length×width×height). The coordinate system is also shown in Fig. 1. For the cases of an expanded stationary laser beam, the center of the elliptic Gaussian laser beam is located at the center of the top surface of the powder bed $(x=0, y=0)$ with the major axis of ellipse aligned with the *x*-axis. For the cases of a moving laser beam, a round Gaussian laser beam scans the surface of the cavity starting from a point $x=x_0$ toward the positive direction of the *x*-axis with a constant velocity, u_b. In practice, the temperature of the powder bed is not allowed to reach the melting point of the high melting point powder and therefore only the low melting point powder melts and resolidifies. As the laser beam interacts with the powder, the temperature of the powder increases to T_m, which induces melting. The molten metal infiltrates the unsintered region of the powder bed due to the driving forces of capillarity and gravity. The infiltration of the liquid metal affects the melting process, and from the practical point of view, it can be very helpful in producing fully densified parts ([6]). The top surface of the melted powder bed recedes since the low melting point material is molten and the high melting point material alone cannot sustain the powder bed. After the laser beam moves away, the liquid pool cools and resolidifies to form a densified heat affected zone (HAZ). These zones, formed by multiple laser scans, are subsequently interwoven to form a layer part.

For the melting of a powder bed that contains melting and nonmelting powders, both a constant volume model ([12]) and a constant porosity model ([11]) have been employed to predict the transient thermal response of the system. For the situation where the melting particles are significantly smaller than the nonmelting particles, melting particles can occupy the interstitial space between the larger particles of nonmelting material. The volume of the powder bed is unchanged after the low melting point particles change phase because the skeletal matrix formed by the nonmelting particles is able to support the powder alone. For melting and nonmelting powder particles with the sizes of same order of magnitude (which is the case for SLS of metal powder), the nonmelting powder's skeletal structure collapses after the low melting point powder is liquidified. In this case, the conservation of mass principles can be used to show that the porosity of the powder bed remains constant (while the volume of the powder bed shrinks; Pak and Plumb [11]). In addition to this constant porosity assumption, the following assumptions are made:

1 The thermal properties of both powders are independent of the temperature with exception of the surface tension of the low melting point liquid metal, which is treated as a linear function of temperature. The thermal properties of the low melting point powder are the same for both solid and liquid phases.

2 The contributions of the gas(es) to the density and heat capacity of the powder bed are negligible ([9,10]).

3 The velocity of the solid induced by the shrinkage has only a component in the *z*-direction ($\mathbf{v}_s = w_s \mathbf{k}$; Kandis et al. [5]). However, the liquid flow in all three directions is taken into account ($\mathbf{v}_l = u_l \mathbf{i} + v_l \mathbf{j} + w_l \mathbf{k}$).

4 The linear Darcy's law can be utilized to describe the liquid metal flow in the powder bed.

5 The pressure of the gas phase remains constant at one atmosphere.

2.2 Velocities and Volume Fractions. Since the system is symmetric about the (*x*, *z*) plane, only half of the cavity $(0<y<y_D)$ needs to be studied. The liquid velocities must satisfy the continuity equation

$$\frac{\partial \varphi_l}{\partial t} + \nabla \cdot (\varphi_l v_l) = \dot{\Phi}_L^0 \tag{1}$$

where $\dot{\Phi}_L^0$ is the volumetric production rate of the liquid due to melting.

Likewise, the solid low melting point powder vanishes at the same rate, i.e.,

$$\frac{\partial \varphi_s}{\partial t} + \frac{\partial (\varphi_s w_s)}{\partial z} = -\dot{\Phi}_L^0. \tag{2}$$

The high melting point powder particles have the same velocity as the particles of the low melting point powder particles. Therefore, the continuity equation for the high melting point material is

$$\frac{\partial \varphi_H}{\partial t} + \frac{\partial (\varphi_H w_s)}{\partial z} = 0. \tag{3}$$

The volume fractions of each species satisfies $\epsilon + \varphi_s + \varphi_H = 1$, where the porosity of the powder bed, ϵ, is defined as the total volume of void, including the volumes of gas and liquid, relative to the total volume of the powder bed. Adding Eqs. (2) and (3) and considering the volume fraction definition along with the constant porosity assumption, one can obtain

$$\dot{\Phi}_L^0 = -(1-\epsilon)\frac{\partial w_s}{\partial z}. \tag{4}$$

The volume production rate is zero in all the regions except at the solid-liquid interface where the phase change is taking place. The solid velocity is zero in the unsintered region. In the melted region, $\partial w_s / \partial z = 0$. Therefore, the solid velocity in the melted region is the same as the shrink velocity at the surface of the powder bed and can be expressed as $w_s = \partial s_0 / \partial t$, $s_0 < z < s$. The solid velocity can be determined by integrating Eq. (3) and the result is ([13])

$$w_s = \begin{cases} 0 & z > s \\ \dfrac{\varphi_{si}}{1-\epsilon}\dfrac{\partial s}{\partial t} & z < s. \end{cases} \tag{5}$$

The liquid flow occurs in three directions, and the velocities can be determined using Darcy's law

$$\mathbf{v}_l - w_s \mathbf{k} = -\frac{K K_{rl}}{\varphi_l \mu}(\nabla p_l - \rho_l g \mathbf{k}) \tag{6}$$

where the permeability of the porous medium, K, can be determined by use of the Carman-Kozeny equation ([14]):

$$K=\frac{d_\rho^2\epsilon^3}{180(1-\epsilon)^2}. \tag{7}$$

The relative permeability, K_{rl}, can be expressed as $K_{rl}=\psi_e^3$ ([11]), where ψ_e is the normalized saturation:

$$\psi_e=\begin{cases}\dfrac{\psi-\psi_{ir}}{1-\psi_{ir}} & \psi>\psi_{ir}\\ 0 & \psi\leqslant\psi_{ir}.\end{cases} \tag{8}$$

Considering the constant gas phase pressure assumption, Eq. (6) becomes

$$\mathbf{v}_l-w_s\mathbf{k}=\frac{KK_{rl}}{\varphi_l\mu}(\nabla p_c+\rho_l g\mathbf{k}). \tag{9}$$

The capillary pressure can be calculated using the Leverett function expressed as $p_c=a(\psi_e+b)^c\gamma^0\sqrt{\epsilon/K}$, where a, b, and c are empirical constants with values of 0.38, 0.014, and 0.27, respectively [11]. The surface tension of the low melting point liquid metal, γ^0, is expressed as a linear function of temperature, $\gamma^0=\gamma_m^0[1-\gamma^{0\prime}(T^0-T_m^0)]$.

It can be seen that the liquid velocities are functions of the saturation, ψ, which is related to the liquid fraction, φ_l, (i.e., $\varphi_l=\psi\epsilon$; [11]). On the other hand, the solution of φ_l from Eq. (1) requires the liquid velocities. Therefore, the liquid fraction and the liquid velocities must be obtained by solving Eqs. (1) and (9) simultaneously.

2.3 Energy Equation. The temperature transforming model using a fixed grid method ([15]) is employed to describe melting and resolidification in the powder bed. This model is based upon the assumption that the melting and solidification processes occur over a range of temperatures from $(T_m^0-\Delta T^0)$ to $(T_m^0+\Delta T^0)$, but it can also be used to simulate the melting and solidification processes occurring at a single temperature by using a very small value of ΔT^0. This model has the advantage of eliminating the time step and grid size limitations that are normally encountered in other fixed grid methods. In the fixed coordinate system, (x, y, z), the energy equation is

$$\begin{aligned}&\frac{\partial}{\partial t}\{[\partial_H C_H^0+(\varphi_l+\varphi_s)C_L^0)]T^0\}+\boldsymbol{\nabla}\cdot(\varphi_l\mathbf{v}_l C_L^0T^0)\\&\quad+\frac{\partial}{\partial z}[w_s(\varphi_H C_H^0+\varphi_s C_L^0)T^0]\\&=\boldsymbol{\nabla}\cdot(k\boldsymbol{\nabla}T^0)-\left\{\frac{\partial}{\partial t}[(\varphi_l+\varphi_s)S^0]\right.\\&\quad\left.+\boldsymbol{\nabla}\cdot(\varphi_l\mathbf{v}_l S^0)+\frac{\partial}{\partial z}(\varphi_s w_s S^0)\right\}.\end{aligned} \tag{10}$$

The heat capacity of the high melting point powder is

$$C_H^0=\rho_H c_{pH}. \tag{11}$$

The effective heat capacity of the low melting point metal can be expressed as

$$C_L^0(T^0)=\begin{cases}\rho_L c_{pL} & T^0<T_m^0-\Delta T^0\\ \rho_L c_{pL}+\dfrac{\rho_L h_{sl}}{2\Delta T^0} & T_m^0-\Delta T^0<T^0<T_m^0+\Delta T^0\\ \rho_L c_{pL} & T^0>T_m^0+\Delta T^0\end{cases} \tag{12}$$

and S^0 in Eq. (10) is defined as

$$S^0(T^0)=\begin{cases}0 & T^0<T_m^0-\Delta T^0\\ \frac{1}{2}\rho_L h_{sl} & T_m^0-\Delta T^0<T^0<T_m^0+\Delta T^0\\ \rho_L h_{sl} & T^0>T_m^0+\Delta T^0.\end{cases} \tag{13}$$

The thermal conductivity of the powder bed is calculated by

$$k=\begin{cases}k_{\text{eff}} & T^0<T_m^0-\Delta T^0\\ k_{\text{eff}}+\dfrac{k_l-k_{\text{eff}}}{2\Delta T^0}(T^0-T_m^0+\Delta T^0) & T_m^0-\Delta T^0<T^0<T_m^0+\Delta T^0\\ k_l & T^0>T_m^0+\Delta T^0\end{cases} \tag{14}$$

where k_{eff} is the effective thermal conductivity of the unsintered powder bed. It can be calculated using the empirical correlation proposed by Hadley [16]. When the low melting point powder is molten, the contact area between the two materials is significantly increased, and therefore it is expected that the effective thermal conductivity of the mixture of low melting point liquid metal (or resolidified low melting point metal, in the sintered region) and high melting point powder is higher than that before melting. The thermal conductivity of a liquid or resolidified part is therefore calculated using

$$k_l=(\varphi_l+\varphi_s)k_L+\varphi_H k_H. \tag{15}$$

In the arrival of Eq. (15), it is assumed the thermal resistance of the powder and the gas(es) is a parallel arrangement, and the contribution of the thermal conductivity of the gas(es) is neglected since it is much smaller than that of both powders ([9,10]).

The difference between the liquid and sintered region is that the temperature of the latter is lower than T_m, and it exists in the form of solid. It is obvious that the low melting point material in the sintered region cannot flow because it exists in the solid state. For the convenience of programming, the volume fraction of the low melting point metal is still represented by φ_l, and the summation of φ_l and φ_g holds constant, ϵ, even in the sintered region. The viscosity of the low melting point metal in the sintered region can be set as a very large value so that a low melting point metal velocity of zero can be achieved ([15]).

The boundary and initial conditions of the energy equation are

$$\begin{aligned}-k\frac{\partial T^0}{\partial z}&=\frac{\alpha_a P}{\pi R^2 A}\exp\left[-\frac{(x-x_0-u_b t)^2}{a^2}-\frac{y^2}{R^2}\right]\\&\quad-\epsilon_e\sigma[T^{04}-T_\infty^{04}]-h(T^0-T_\infty^0),\quad z=s_0(x,y)\end{aligned} \tag{16a}$$

$$\frac{\partial T^0}{\partial z}=0,\quad z=z_D \tag{16b}$$

$$\frac{\partial T^0}{\partial x}=0,\quad x=0,\ x_D \tag{16c}$$

$$\frac{\partial T^0}{\partial y}=0,\quad y=0,\ y_D \tag{16d}$$

$$\begin{gathered}T^0=T_l^0,\quad t=0,\quad 0\leqslant x\leqslant x_D,\\ 0\leqslant y\leqslant y_D,\quad 0\leqslant z\leqslant z_D.\end{gathered} \tag{17}$$

2.4 Dimensionless Governing Equations. In order to reduce the dependent variables and make the solution more general, the governing equations and the corresponding boundary conditions should be nondimensionalized. The dimensionless forms of the energy equation is obtained by nondimensionalizing Eq. (10), i.e.,

$$\frac{\partial(CT)}{\partial t}+\hat{\boldsymbol{\nabla}}\cdot(\varphi_l\mathbf{V}_lC_LT)+\frac{\partial}{\partial z}[W_s(\varphi_H+\varphi_sC_L)T]$$

$$=\hat{\boldsymbol{\nabla}}\cdot(K\hat{\boldsymbol{\nabla}}T)-\left\{\frac{\partial}{\partial\tau}[(\varphi_l+\varphi_s)S]+\hat{\boldsymbol{\nabla}}\cdot(\varphi_l\mathbf{V}_lS)\right.$$

$$\left.+\frac{\partial}{\partial Z}(\varphi_sW_sS)\right\} \tag{18}$$

where the dimensionless velocities of the liquid phase, which are calculated by the dimensionless form of Eq. (9)

$$\mathbf{V}_l-W_s\mathbf{k}=\frac{\epsilon Ma\,\psi_e^3}{\sqrt{180}(1-\epsilon)\psi}\hat{\boldsymbol{\nabla}}P_c+\frac{\epsilon^2\,\mathrm{Ma}\,\mathrm{Bo}\psi_e^3}{180(1-\epsilon)^2\psi}\mathbf{k} \tag{19}$$

satisfy the nondimensional continuity equation of the liquid, which is obtained by nondimensionalizing Eq. (1):

$$\frac{\partial\varphi_l}{\partial\tau}+\hat{\boldsymbol{\nabla}}\cdot(\varphi_l\mathbf{V}_l)=\dot{\Phi}_L\,. \tag{20}$$

The boundary condition of Eq. (18) at the top surface of the powder bed is

$$-k\frac{\partial T}{\partial Z}=N_i\exp\left[-\frac{(X-X_0-U_b\tau)^2}{A^2}-y^2\right]-N_R[(T+N_t)^4$$

$$-(T_\infty+N_t)^4]-\mathrm{Bi}(T-T_\infty),\quad Z=S_0(X,Y). \tag{21}$$

The nondimensional form of other equations can be obtained using dimensionless variables defined in the Nomenclature ([13]).

3 Numerical Solution

Equation (18) is a typical convection-diffusion equation which can be discretized by a finite volume method ([17]) and solved numerically. The simulation of the entire problem requires solutions of: (1) the velocity and the volume fraction of the solid phase of the low and high melting point powder particles; (2) the velocities and the volume fraction of melted low melting point metal, and (3) the temperature distribution and the location of solid-liquid interface, and the sintering interface. The solutions of the above three subproblems are conjugated and an iteration is needed. The outline of the solution procedure can be found in Zhang [13]. The powder bed (which includes unsintered powder, a liquid pool, and sintered region) has an irregular shape since the upper surface of the powder bed recedes due to shrinkage that occurs in the sintering process. The computational region expansion approach ([17]) is employed in this paper to deal with the irregular geometric shape.

Since Eqs. (18) and (20) are nonlinear, iterations are needed. During the iteration process, some underrelaxation is necessary. The relaxation factor used here is 0.1∼0.2. In order to simulate the melting and resolidification process occurring at a single temperature, a very small dimensionless phase-change temperature range, $\Delta T=0.01$, is used in the calculation. The grid number used in the numerical simulation was 72×37×37 (in the *x*, *y*, and *z*-directions) for stationary scanning cases and 168×37×37 for moving laser beam scanning cases. The dimensionless time step for the cases with both stationary and moving laser beam was $\Delta\tau=0.05\sim0.1$ when the laser is on and $\Delta\tau=0.5$ after the laser is shut off. A finer grid (112×52×52 for stationary laser beam and 202×82×82 for moving laser beam) and a smaller time step ($\Delta\tau=0.01$) were also used to simulate some cases, but the difference in the predicted values of the dimensionless cross-section area was less than 0.5 percent.

4 Experimental Apparatus and Procedure

It is important to note that successful fabrication of metal parts requires a careful match between the surface properties of the two materials. Specifically, the liquid phase low melting point material must wet the nonmelting solid particles in order to (1) fabricate full density parts and (2) apply the model developed here. Identification of powder pairs with these characteristics is not trivial [6] and hence specific materials are used here. Unfortunately, the thermophysical properties of the powders are not well documented and, as will become evident, some properties must be estimated in order to predict the experimental results.

Table 1 Size of the powder particles

	Average diameter	Minimum diameter	Maximum diameter	STD
nickel braze	45 μm	20 μm	93 μm	15 μm
AISI 1018 steel	68 μm	61 μm	74 μm	4.4 μm

Experiments were conducted using a mixture of 40 percent nickel braze powder and 60 percent AISI 1018 carbon steel powder by volume. The shapes of both powder particles are spherical and the size distribution of both powder particles are listed in Table 1. The experimental apparatus is shown in Fig. 2. Two types of experiments were conducted: one using a stationary line source and the other using a traversing circular beam. During the tests, the powder was contained in a block of Plexiglas with a pocket machined into it with dimensions 76.2×76.2×19 mm (length×width×height), with the surface of the powder exposed to the atmosphere. Prior to laser irradiation, the powder surface was leveled with a straight edge to obtain a smooth, flat surface. The initial porosity of the powder was determined to be 0.4 by a simple mass/volume measurement procedure.

To measure the transient temperature within the powder, Teflon coated, 0.076-mm diameter chromel-alumel (K type) thermocouples were strung across the test pocket at three different depths (2.1, 4.3, 6.5 mm±0.25 mm), with the thermocouple leads aligned parallel to the surface. A Pentium-based PC, with Keithley Metrabyte A/D and thermocouple boards, was used to acquire and log three-thermocouple readings and a voltage signal from the laser control computer. The laser signal was acquired at 20 Hz, and used to define the time the laser was turned on and off, to within ±0.05 seconds. The thermocouple readings were acquired at 7 Hz, with an estimated uncertainty of ±1.1 °C.

The irradiation was provided by a CW, 50 W (maximum), CO_2 laser (Synrad 48-5) operating at 10.6-mm wavelength with a Gaussian intensity distribution. The actual laser power was measured using an Oriel model 70266 (S/N 30362) laser power meter, positioned between the ZnSe lens and the powder surface. For the stationary line source tests, a right-angle first surface mirror and a 50.8-mm focal length, anti reflection coated ZnSe cylindrical lens was used to transform the round Gaussian beam into an ellipsoid Gaussian beam. The size of the ellipsoid laser beam can be adjusted by changing the separation distance between the lens and surface of the powder bed.

During the traversing circular beam experiments, the first surface mirror and cylindrical lens were replaced by a laser beam

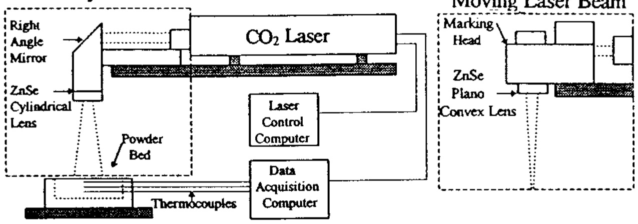

(a) Stationary laser beam system

(b) Marking head for moving laser beam system

Fig. 2 Experimental apparatus for sintering of metal powder positioning device (Synrad, SH series Marking Head, model number SH3-370CH/180), equipped with a 508 mm focal length planoconvex ZnSe lens. Two different traversing speeds (1.32 mm/s and 2.65 mm/s) were used. In both cases, the laser power was held at 31 watts and the scan length was maintained at 20 mm. The radius of the Gaussian beam measured at $1/e^2$ is 2 mm (or 1.41 mm at $1/e$).

For both stationary and traversing experiments, the solid heat affected zone formed by laser irradiation was extracted and mounted in Bakelite. The mounted specimens were sectioned in the desired location and polished for examination. Cross sections were photographed using a Nikon Metaphot reflected light microscope with a spatial resolution of 0.5 μm.

5 Results and Discussion

Radiative coupling between the laser radiation and the powder is a crucial effect to consider in the modeling since it determines the amount of laser energy delivered to the material. The value of absorptivity is usually very low for most metals at room temperature, but increases with an increase of the target material temperature ([18]). Alternatively, the absorptivity of liquid metal is not a strong function of temperature, and it is comparable to that of solid metals near their melting points ([19]). The effective absorptivity of the powder bed is expected to be much higher than that of bulk metal since the portion of the laser irradiation entering the pore space of a powder bed is trapped due to multiple reflections ([2]). The absorptivity of nickel braze bulk material is estimated to be that of Inconel [20] because the two materials' components are similar. Likewise, the absorptivity of the high melting point powder material, AISI 1018 steel, can be estimated from Brandes [21]. After a careful comparison and a trial and error procedure, the absorptivity of the powder bed is taken to be 0.5; a value which provided predictions which best agreed with the experimental results.

Thermal properties of the AISI 1018 steel are not directly available in the literature. Therefore, properties of AISI 1010 ([22]) were used. The density and the melting point of nickel braze are available from the manufacturer ([23]). Values for thermal conductivity of nickel braze can be obtained from Touloukian [20] while the specific heat of nickel braze was taken to be the weighted average of the specific heats of individual components (which are available from Brandes [21]). The latent heat of melting can be derived from the latent heats and melting points of the individual components ([21]) and the result is $h_{sl}=3.774\times10^5$ J/kg. Viscosity and surface tension for the liquid nickel braze are $\mu=5.474\times10^{-3}$ kg/sm and $\gamma=1.207-1.802\times10^{-4}(T-1271)$ N/m, which were obtained from semi-empirical equations in Iida and Guthrie [24], Bunnell [6], and Brandes [21]. Finally, the irreducible saturation, ψ_{ir}, was taken to be 0.08 ([14]). The dimensionless parameters that are used in the numerical simulation are listed in Table 2.

Numerical simulations were performed under conditions corresponding as closely as possible to those of the experiments. Numerical results were obtained in dimensionless form and were subsequently converted to dimensional form in order to compare with the corresponding experimental results. Figure 3 shows the three-dimensional shape of the powder bed surface and HAZ after irradiation of a stationary ellipsoid laser beam using a powder of 36.5 W and a processing time of 7.4 s. The minor axis of the ellipsoid laser beam (defined as the radius where the intensity of the beam is $1/e$ of the centerline intensity) is 1.4 mm. The ratio of the major axis over minor axis of the ellipsoid laser beam, A, is 3.95. It can be seen that the top depression of the HAZ is ellipsoid, which corresponds to the shape of the laser beam. Thicknesses of the sintered HAZ (in the z-direction) are greatest at the center of the beam and decrease with increasing x and y.

Table 2 The sintering parameters applied in the numerical calculation

Bi	2.94×10^{-4}	Sc	1.38
Bo	5.30×10^{-3}	T_∞	-1.0
C_L	1.07	X_D	53.88
K_g	5.38×10^{-4}	Y_D	26.94
K_L	0.20	Z_D	13.47
Ma	1042.0	ϵ	0.40
N_g	1.19×10^{-3}	φ_{si}	0.24
N_r	1.31	ψ_{ir}	0.08

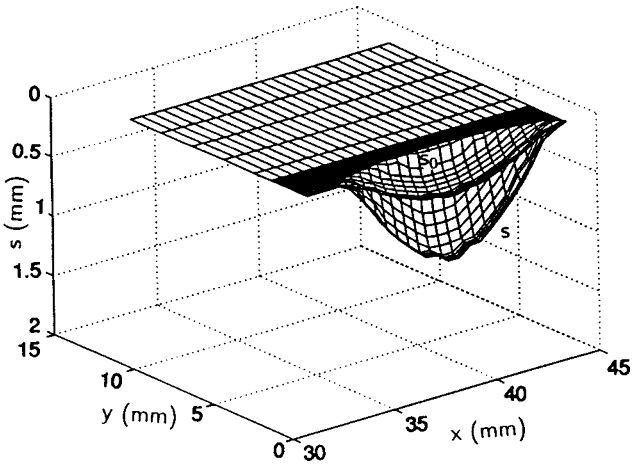

Fig. 3 Three-dimensional shape of the HAZ with a stationary ellipsoid laser beam ($A=3.95$, $N_i=0.0223$, $U_b=0$)

In order to view the shape clearly, the cross section of the HAZ at $x=38.1$ mm is plotted in Fig. 4(a). A micrograph of the cross section at $x=38.1$ mm is shown in Fig. 4(b) for comparison. The black area in the micrograph is a local void and the light area is sintered metal. The shape of HAZ, averaged locally in the x direction, corresponds to the outer boundaries of the dark region. It can be seen that the actual and predicted shapes of the HAZ are similar, but the local boundaries of the sintered and unsintered areas are somewhat different. The boundary between the sintered

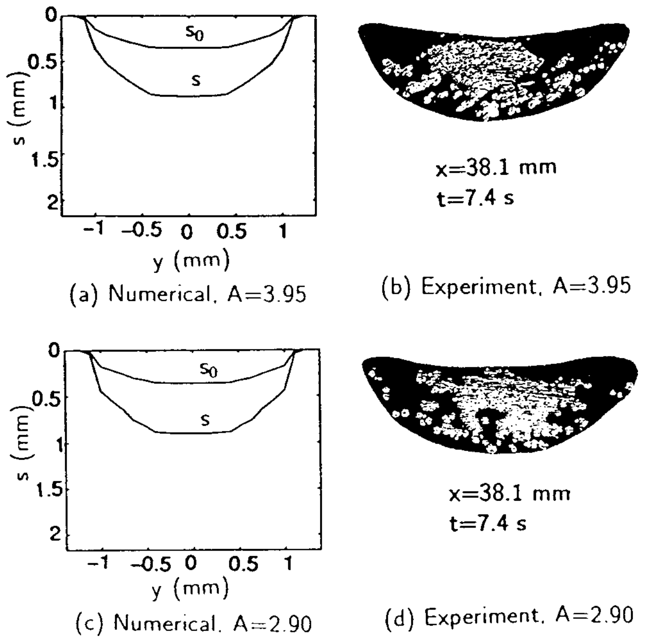

(a) Numerical, A=3.95

(b) Experiment, A=3.95

(c) Numerical, A=2.90

(d) Experiment, A=2.90

Fig. 4 Comparison of the cross-section area obtained by numerical simulation and experiment (stationary laser beam) and unsintered regions is smooth and clear for the numerical result but it is not clear for the experimental result. A large degree of local porosity is evident in the actual piece. The mophological differences between the predictions and experimental results may suggest that there is a mushy zone between the sintered and unsintered region because the low melting point liquid metal and the solid particles may not be in thermal equilibrium in such a rapid process. Another possibility is that the continuum medium assumption may not be very good because the diameter of the laser beam is only two order of magnitude greater than the particle diameter. Further efforts will be needed to reveal the cause of the nonsmooth boundary between sintered and unsintered regions.

Figures 4(*c*) and (*d*) show the numerical and experimental HAZ cross sections for different operational conditions ($P = 28.5$ W, $A = 2.9$, $t_s = 7.4$ s). Basically, the characteristics of the numerical and experimental results are similar to those at the higher laser power and longer major axis of the laser beam. Since the laser intensity at the center of the laser beam is nearly the same, the differences in the cross-sectional area are not significant for these two cases. The temperature histories at three different depths at $x = y = 0$ for the preceding two cases are shown in Figs. 5(*a*) and (*b*). It can be seen that the agreement between numerical and experimental results is excellent.

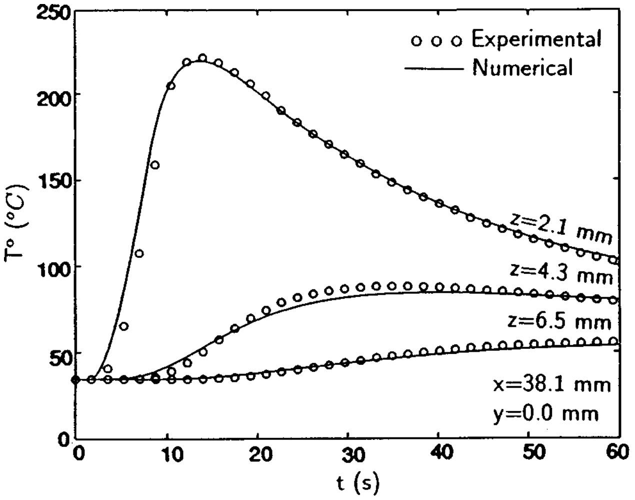

(a) A=3.95

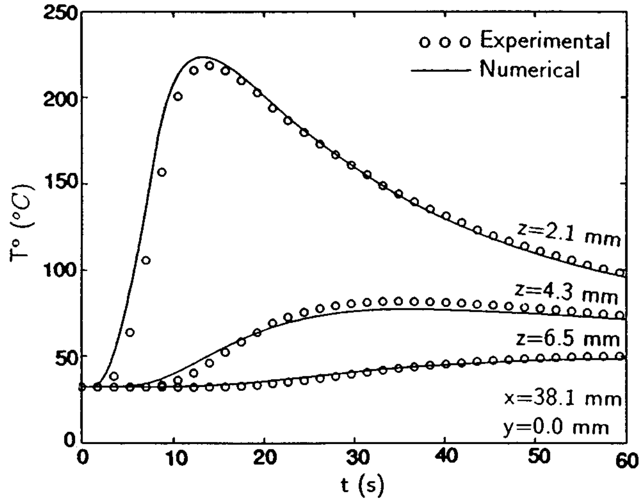

(b) A=2.90

Fig. 5 Comparison of temperature histories obtained by numerical simulation and experiment (stationary laser beam)

The SLS with a moving laser beam was investigated since it corresponds to the real process. Figure 6(*a*) shows the predicted shape of the sintered region in three different cross sections. The laser beam starts to scan the powder bed from $x = 28.1$ mm and beam irradiation is curtailed at $x = 48.1$ mm. It can be seen that the shape and size of the cross sections at the three different x are similar. This suggests that the quasi-steady state has been achieved when the laser beam travels to $x = 34.1$ mm. Figure 6(*b*) shows three cross sections corresponding to the numerical results in Fig. 6(*a*). It can be seen that the shapes of the numerical results agree fairly well with the experimental results. As can be seen from Fig. 6(*b*), some voids can be observed in the cross section of the sintered part. Again, this phenomenon was not observed in the numerical results because the porosity of the powder bed was assumed to remain constant in the process. However, the predicted and measured total volume of powder sintered in the process is very close.

In order to investigate the effect of the laser beam traversing velocity, numerical simulations and experiments were performed for a fast scanning velocity. The results are shown in Figs. 7(*a*) and (*b*). As expected, the sintered region is significantly smaller than that in Fig. 6. Like the case with slow scanning velocity plotted in Fig. 6(*a*), the predicted shape and size of the cross sections is almost the same for three different x.

Figure 8 shows the top and bottom of the HAZ for different scanning velocities at $y = 0$. For the slower scanning case, the sintered depth reaches its maximum value at $x = 31$ mm, which is about 3 mm beyond the starting point of scanning, and the sintering depth remains unchanged until $x = 47$ mm (1 mm before the stopping point of the laser scan). For the faster scanning case, the sintering starts at a slightly larger x. The variation of the sintering depth with x is similar to that of slower scanning case. Figures

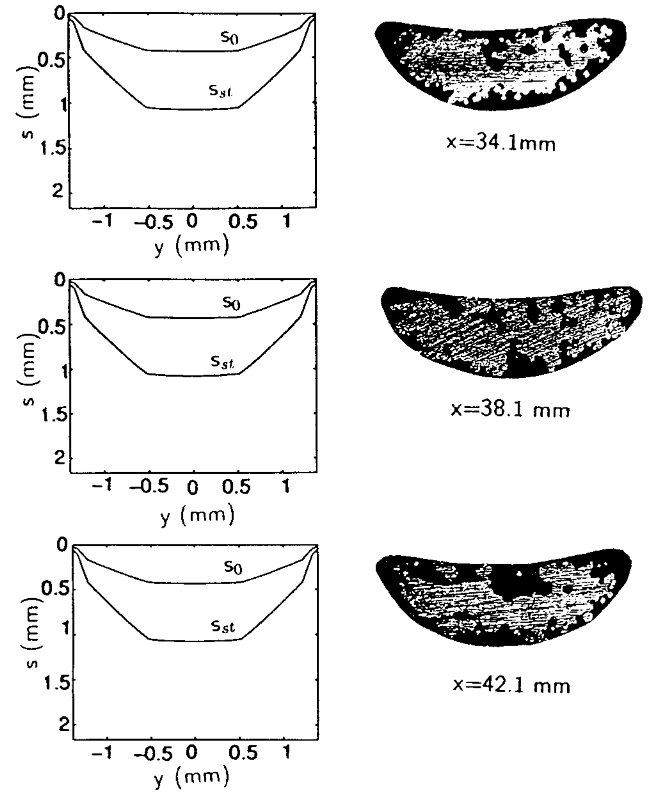

(a) Numerical (b) Experiment

Fig. 6 Comparison of the cross-section area obtained by numerical simulation and experiment (moving laser beam: $A = 1.0$, $N_i = 0.0749$, $U_b = 0.124$)

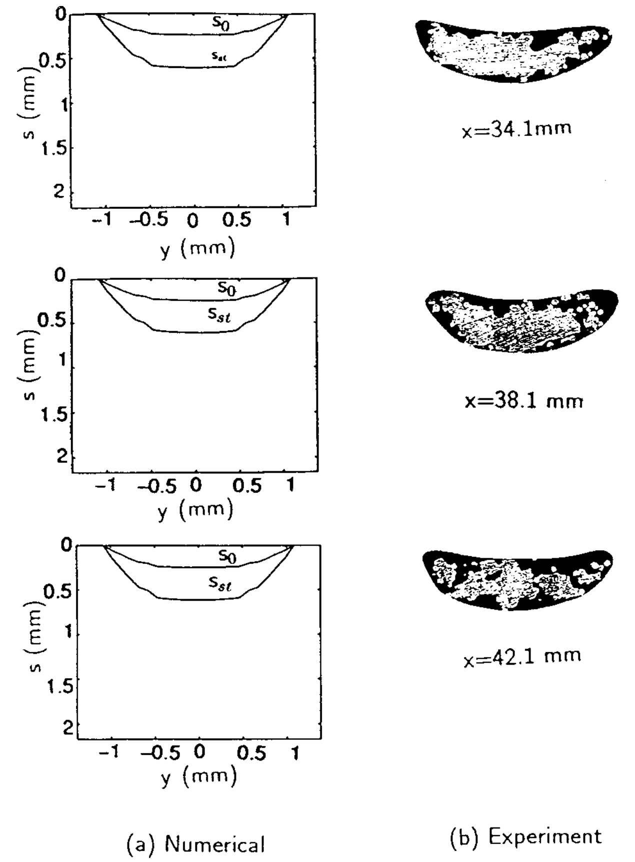

Fig. 7 Comparison of the cross-section area obtained by numerical simulation and experiment (moving laser beam: $A=1.0$, $N_i=0.0749$, $U_b=0.248$)

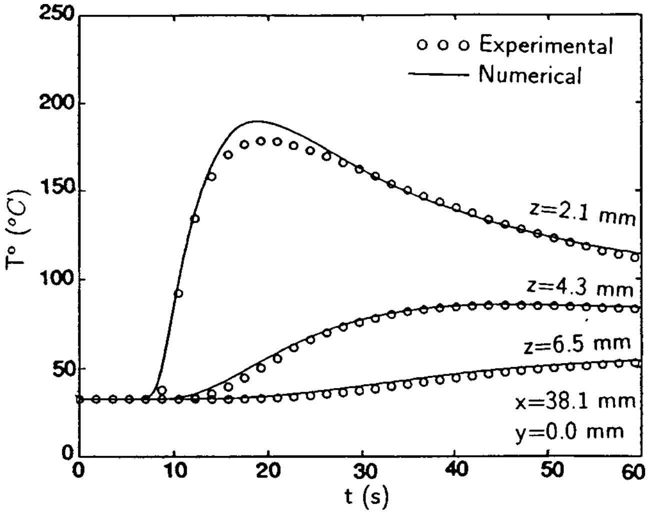

(a) $U_b=0.124$

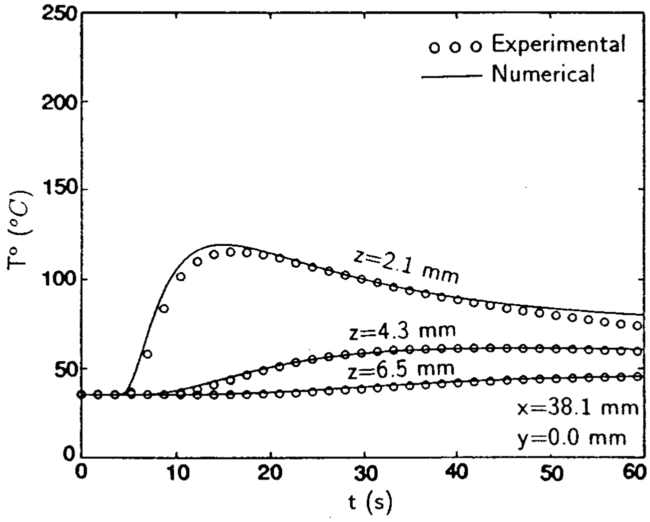

(b) $U_b=0.248$

Fig. 9 Comparison of temperature histories obtained by numerical simulation and experiment (moving laser beam: $A=1.0$, $N_i=0.0749$)

9(*a*) and (*b*) show the comparison of the temperature history obtained numerically and experimentally. The agreement between the numerical and experimental results is very good.

The variation of dimensionless HAZ cross-sectional area with the dimensionless laser intensity at two different scanning velocities is shown in Fig. 10(*a*). The predicted and measured dimensionless cross-sectional areas were obtained by

$$A_c=2\int_0^{Y_D}[\eta_{st}(X_D/2,Y)-\eta_0(X_D/2,Y)]dY$$

and by measuring the sintered area (i.e., light area in photos such as those in Figs. 6 and 7), respectively. As can be seen, both predicted and measured A_c vary linearly with N_i. The predicted cross-sectional areas are in general smaller than the measured values. Considering the uncertainty in the absorptivity and the thermal properties of both powders, as well as the uncertainty in measuring A_c, the agreement between the predicted and measured A_c is very good. Based on the experimental results in Fig. 10(*a*), an empirical correlation of A_c is proposed:

$$A_c=1.79\frac{N_i}{U_b}+0.557\,U_b-0.292. \tag{22}$$

Comparison of experimental results and Eq. (22) is shown in Fig. 10(*b*). The difference between the measured A_c and Eq. (22) is less than 15 percent. Of course, a different correlation would result if different materials are used.

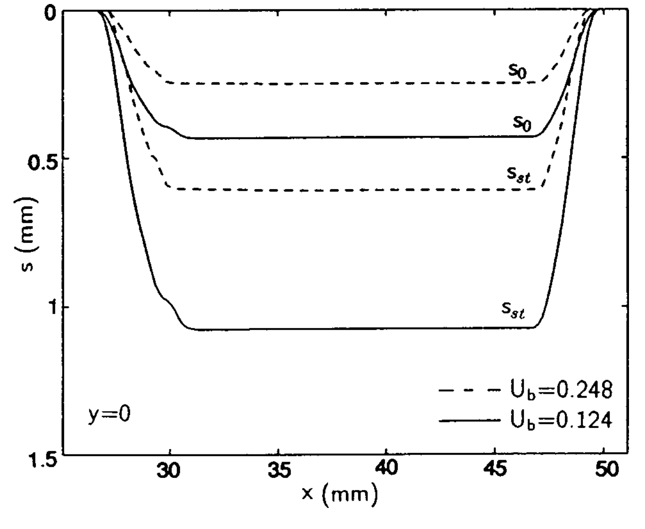

Fig. 8 Effect of the scanning velocity on the cross sections at $y=0$ (moving laser beam: $A=1.0$, $N_i=0.0749$)

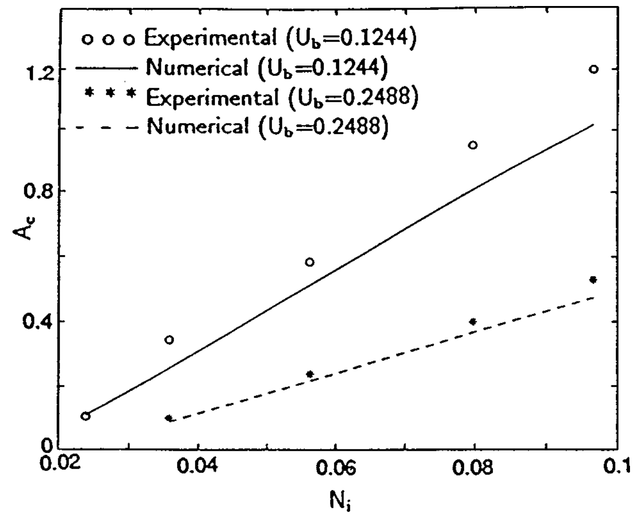

(a) Comparison of cross-section area of HAZ

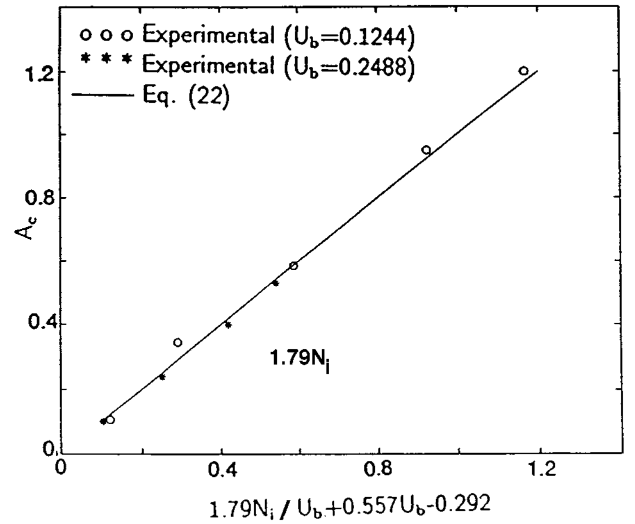

(b) Empirical correlation of cross-section area of HAZ

Fig. 10 Cross-section area of the HAZ at different laser intensities and scanning velocities

6 Conclusion

Three-dimensional sintering of two metal powders with significantly different melting points with stationary and moving laser beam has been investigated numerically and experimentally. The shrinkage of the powder bed due to the density change and the liquid flow driven by the capillary and gravity forces were taken into account. Experiments with nickel braze as the low melting point powder and AISI 1080 steel powder as the high melting point powder were performed. The numerical simulation and experiment were performed for both a stationary ellipsoid laser beam and a moving round laser beam. The temperature histories obtained by the numerical simulation and the experiment agreed very well. The boundary between sintered and unsintered powder was clear for numerical results but it was not clear for the experimental results, which may be caused by a nonequilibrium state existing between the low melting point liquid metal and the solid particles at the boundary. The effects of laser properties and scanning velocity on the SLS process were also investigated. An empirical correlation of the cross-section area of the HAZ was proposed.

Acknowledgment

CWB and TLB acknowledge the support of the National Science Foundation under Grant No. 9796186.

Nomenclature

a = major axis length of the ellipsoid laser beam (m)
A = dimensionless major axis length of the ellipsoid laser beam, a/R
A_c = dimensionless cross-section area
Bi = Biot number, hR/k_H
Bo = Bond number, $\rho_l g R d_p/\gamma_m^0$
C = dimensionless heat capacity, C^0/C_H^0
C^0 = heat capacity, ρc_p (J/m^3 K)
c_p = specific heat (J/kg °C)
d_p = diameter of the powder particle (m)
g = gravitational acceleration (m/s^2)
h = convective heat transfer coefficient (W/m^{2}K)
h_{sl} = latent heat of melting or solidification (J/kg)
i, **j**, **k** = unit vector in x, y, z-directions
k = thermal conductivity (W/m °C)
K = permeability (m^2) or dimensionless thermal conductivity, k/k_H
K_{rl} = relative permeability
Ma = Marangoni number, $\gamma_m^0 d_p/(\alpha_H\mu)$
N_i = dimensionless moving laser beam intensity, $\alpha_a P/[\pi R A k_H(T_m^0-T_i^0)]$
N_R = radiation number, $\epsilon_e\sigma(T_m^0-T_i^0)^3R/k_H$
N_t = temperature ratio for radiation, $T_m^0/(T_m^0-T_i^0)$
p = pressure (N/m^2)
P = laser power (W)
P_c = dimensionless capillary pressure, $p_c/[\gamma_m^0\sqrt{\epsilon/K}]$
R = radius of the laser beam or minor axis length of ellipsoid laser beam (m)
s = solid-liquid interface location (m)
s_0 = location of surface (m)
s_{st} = sintered depth (m)
Sc = subcooling parameter, $C_H^0(T_m^0-T_i^0)/(\rho_L h_{sl})$
T = dimensionless temperature, $(T^0-T_m^0)/(T_m^0-T_i^0)$
t = time (s)
T^0 = temperature (°C)
$\mathbf{v}$ = velocity vector, $u\mathbf{i}+v\mathbf{j}+w\mathbf{k}$ (m/s)
$\mathbf{V}$ = dimensionless velocity vector, $\mathbf{v}R/\alpha_H$
$\forall$ = volume (m^3)
x, y, z = coordinate (m)
X, Y, Z = dimensionless coordinate, $(x,y,z)/R$

Greek Letters

α = thermal diffusivity (m^2/s)
α_a = absorptivity
γ^0 = surface tension, (N/m^2)
γ = dimensionless surface tension, γ^0/γ_m^0
γ_m^0 = surface tension of low melting point metal at melting point, (N/m^2)
ΔT^0 = one-half of phase change temperature range (K)
ΔT = one-half of dimensionless phase change temperature range
ϵ = porosity for unsintered powder, $(\forall_g+\forall_l)/(\forall_g+\forall_l+\forall_s+\forall_H)$
ϵ_e = emissivity of surface
η_{st} = dimensionless sintered depth, s_{st}/R
μ = dynamic viscousity (kg/ms)
ρ = density (kg/m^3)
σ = Stefan-Boltzmann constant, 5.67×10^{-8} W/(m^2 K^4)
τ = dimensionless time, $\alpha_H/t/R^2$
φ = volume fraction, $\forall/(\forall_s+\forall_l+\forall_H+\forall_g)$
Φ_L = dimensionless volume production rate of the liquid

ψ = saturation, φ_l/ϵ
$\boldsymbol{\nabla}$ = gradient operator, $\mathbf{i}(\partial/\partial x)+\mathbf{j}(\partial/\partial y)+\mathbf{k}(\partial/\partial z)$
$\hat{\boldsymbol{\nabla}}$ = dimensionless gradient operator, $\mathbf{i}(\partial/\partial X)+\mathbf{j}(\partial/\partial X)+\mathbf{k}(\partial/\partial Z)$

Subscripts

c = capillary
g = gas(es)
H = high melting point powder
i = initial
l = liquid or sintered region
L = low melting point powder
m = melting point
s = solid particle of the low melting point powder
v = vapor

References

[1] Beaman, J. J., Barlow, J. W., Bourell, D. L., Crawford, R. H., Marcus, H. L., and McAlea, K. P., 1997, *Solid Freeform Fabrication: A New Direction in Manufacturing*, Kluwer Academic Publishers, Dordrecht.
[2] Sun, M. M., and Beaman, J. J., 1995, ''A Three Dimensional Model for Selective Laser Sintering,'' *Proceedings of Solid Freeform Fabrication Symposium 1995*, D. L. Bourell et al., eds., pp. 102–109.
[3] Williams, J., Miller, D., and Deckard, C., 1996, ''Selective Laser Sintering Part Strength as Function of Andrew Number, Scan Rate and Spot Size,'' *Proceedings of Solid Freeform Fabrication Symposium 1996*, D. L. Bourell et al., eds., pp. 549–557.
[4] Kandis, M., and Bergman, T. L., 1997, ''Observation, Prediction, and Correlation of Geometric Shape Evolution Induced by Non-Isothermal Sintering of Polymer Powder,'' ASME J. Heat Transfer, **119**, pp. 824–831.
[5] Kandis, M., Buckley, C. W., and Bergman, T. L., 1999, ''An Engineering Model for Laser-Induced Sintering of Polymer Powders,'' ASME J. Manuf. Sci. Eng., **121**, pp. 360–365.
[6] Bunnell, D. E., 1995, ''Fundamentals of Selective Laser Sintering of Metals,'' Ph.D. thesis, University of Texas at Austin, Austin, TX.
[7] Manzur, T., DeMaria, T., Chen, W., and Roychoudhuri, C., 1996, ''Potential Role of High Power Laser Diode in Manufacturing,'' presented at SPIE Photonics West Conference, San Jose, CA.
[8] Shah, A. A., 1994, ''Thermomechanical Compressive Melting of Solder Particles,'' M.S. thesis, University of Texas at Austin, Austin, TX.
[9] Zhang, Y., and Faghri, A., 1999, ''Melting of a Subcooled Mixed Powder Bed with Constant Heat Flux Heating,'' Int. J. Heat Mass Transf., **42**, pp. 775–788.
[10] Zhang, Y., and Faghri, A., 1998, ''Melting and Resolidification of a Subcooled Mixed Powder Bed With Moving Gaussian Heat Source,'' ASME J. Heat Transfer, **120**, No. 4, pp. 883–891.
[11] Pak, J., and Plumb, O. A., 1997, ''Melting in a Two-Component Packed Bed,'' ASME J. Heat Transfer, **119**, pp. 553–559.
[12] Mughal, M., and Plumb, O. A., 1993, ''Thermal Densification of Metal-Ceramic Composites,'' Scr. Metall. Mater., **29**, pp. 383–388.
[13] Zhang, Y., 1998, ''Thermal Modeling of Advanced Manufacturing Technologies: Grinding, Laser Drilling, and Solid Freeform Fabrication,'' Ph.D. dissertation, University of Connecticut, Storrs, CT.
[14] Kaviany, M., 1995, *Principles of Heat Transfer in Porous Media*, 2nd Ed., Springer-Verlag, New York.
[15] Cao, Y., and Faghri, A., 1990, ''A Numerical Analysis of Phase Change Problems Including Natural Convection,'' ASME J. Heat Transfer, **112**, pp. 812–816.
[16] Hadley, G. R., 1986, ''Thermal Conductivity of Packed Metal Powders,'' Int. J. Heat Mass Transf., **29**, pp. 909–920.
[17] Patankar, S. V., 1980, *Numerical Heat Transfer and Fluid Flow*, McGraw-Hill, New York.
[18] Von Allmen, M., 1986, *Laser-Beam Interactions with Materials*, Springer-Verlag, New York.
[19] Siegel, R., and Howell, J. R., 1992, *Thermal Radiation Heat Transfer*, 3rd Ed., Hemisphere, Washington, DC.
[20] Touloukian, Y. S., 1967, *Thermophysical Properties of High Temperature Solid Materials, Vol. 2: Nonferrous Alloys*, Thermophysical Properties Research Center, Purdue University, West Lafayette, IN.
[21] Brandes, E. A., 1983, *Smithells Metals Reference Book*, Butterworth & Co. Ltd., London.
[22] Incropera, F. P., and DeWitt, D. P., 1996, *Fundamentals of Heat and Mass Transfer*, 4th Ed., John Wiley and Sons, New York.
[23] Wall Colmonoy Corporation, 1997, Material Safety Data Sheet of Nickel Braze.
[24] Iida, T., and Guthrie, R. I. L., 1988, *The Physical Properties of Liquid Metals*, Oxford University Press, Oxford.

A Model of Dopant Transport During Bridgman Crystal Growth With Magnetically Damped Buoyant Convection

N. Ma
Assistant Professor of Mechanical Engineering,
Department of Mechanical and Aerospace
Engineering and Engineering Mechanics,
University of Missouri at Rolla,
1870 Miner Circle,
Rolla, MO 65409
e-mail: ma@umr.edu
Assoc. Mem. ASME

J. S. Walker
Professor of Mechanical Engineering,
Department of Mechanical Engineering,
and Industrial Engineering,
University of Illinois at Urbana-Champaign,
1206 West Green Street,
Urbana, IL 61801
e-mail: jswalker@uiuc.edu
Fellow ASME

This paper presents a model for the unsteady transport of a dopant during the vertical Bridgman crystal growth process with a planar crystal-melt interface and with an externally applied axial magnetic field. This dilute mass transport depends on the convective and diffusive mass transport of the dopant. The convective mass transport is driven by buoyant convection in the melt, which produces nonuniformities in the concentration in both the melt and the crystal. This convective transport is significant even for a strong magnetic field $B_o = 2\,T$. However, the electromagnetic damping of the melt motion produces a local region adjacent to the crystal-melt interface which is dominated by diffusion. Thus, this melt solidifies with a relatively radially uniform concentration, so that the radial distribution of dopants in the crystal is also relatively radially uniform. The transient model predicts the dopant distribution in the entire crystal.
[S0022-1481(00)02301-X]

Keywords: Heat Transfer, Magnetohydrodynamics, Mass Transfer

1 Introduction

Semiconductor crystals are grown from the liquid phase (melt) whose motion can be controlled by an externally applied magnetic field. The infinite number of possible magnetic field configurations provides the ability to tailor the melt motion in order to optimize the properties of the crystal. The melt is typically doped with an element to give the crystal certain electrical or optical properties. It is crucial that the distributions of these elements, called dopants, are as uniform as possible. When only a few transistors and other devices were produced on each wafer sliced from a crystal, some nonuniformity or segregation could be tolerated. With recent manufacturing advances, millions of devices are now produced on a single wafer, so that the need for a uniform dopant concentration across the wafer is more critical.

In crystal growth without a magnetic field, oscillatory melt motions produce undesirable spatial oscillations of the dopant concentration (striations) in the crystal. Since most molten semiconductors are excellent electrical conductors, an externally applied magnetic field can be used to eliminate oscillations in the melt motion, thus eliminating striations in the crystal. Chedzey and Hurle [1] and Utech and Flemings [2] published the first papers to demonstrate the benefits of applying magnetic fields during semiconductor crystal growth. Unfortunately, the elimination of mixing and a moderate electromagnetic (EM) damping of the residual steady melt motion may lead to a large variation of the dopant concentration in the crystal in the direction perpendicular to the direction of growth (lateral or radial macrosegregation) ([3]).

If the EM damping is extremely strong, then the melt motion is suppressed and has no effect on the dopant distribution in the crystal, and this diffusion-controlled mass transport may produce a dopant distribution in the crystal which is both radially and axially uniform ([3]). In order to achieve diffusion-controlled mass transport, the mass transport Péclet number, $\mathrm{Pe}_m = U_b R/D$, must be small, where U_b is the characteristic velocity for the magnetically damped melt motion and is inversely proportional to the square of the magnetic flux density B_o, while R is the inside radius of the cylindrical ampoule and D is the diffusion coefficient for the dopant in the molten semiconductor. If $\mathrm{Pe}_m \ll 1$, then the characteristic ratio of convection to diffusion of the dopant is small and the dopant transport is diffusion controlled. Diffusion-controlled growth may be achievable in a low-gravity environment where the melt motion driven by residual accelerations in an earth-orbiting vehicle can be 10,000 times smaller than the buoyant convection on earth ([4,5]). However, since typical values of D are 1 to $2\times10^{-8}\,\mathrm{m}^2/\mathrm{s}$, B_o must be extremely large for diffusion-controlled mass transport on earth. It is more practical to use magnetic fields which are strong enough to eliminate flow oscillations, but which only moderately damp the residual steady melt motion, i.e., for which Pe_m is still large and convection of dopant is important. With such fields, the objective is to tailor the melt motion in order to achieve both lateral and axial dopant uniformity in the crystal. At each stage during the growth of a crystal by any process, there are infinitely many different ways to tailor the strength and configuration of the externally applied magnetic field, the rotation rates of the crystal and crucible or ampoule or feed rod, the distribution of the heat flux into the melt, the radiative and conductive heat losses from the melt, etc., so that process optimization through trial-and-error experimental crystal growth is not practical. Models which accurately predict the dopant distribution in an entire crystal for any combination of process variables are needed to facilitate process optimization.

For a typical crystal growth process, resolution of thin mass-diffusion boundary layers having $O(\mathrm{Pe}_m^{-1})$ thicknesses is often very challenging because the mass transport Péclet number can have values as large as $\mathrm{Pe}_m = 20{,}000$ ([6]). Several grid points must be concentrated inside each layer in order to give accurate results, because these boundary layers play critical roles in the transport. As the magnetic flux density B_o of the externally applied magnetic field is increased, the value of Pe_m decreases and the mass-diffusion boundary layers become thicker, but the value of the Hartmann number $\mathrm{Ha} = B_o R(\sigma/\mu)^{1/2}$ increases, where σ and μ are the electrical conductivity and viscosity of the melt. Since there are viscous boundary layers with $O(\mathrm{Ha}^{-1})$ thicknesses, there are thin mass-diffusion or viscous boundary layers for every value of B_o. Therefore the simultaneous numerical solution of the full Navier-Stokes, internal energy, and mass trans-

---

Contributed by the Heat Transfer Division for publication in the JOURNAL OF HEAT TRANSFER. Manuscript received by the Heat Transfer Division, Nov. 11, 1998; revision received, Aug. 10, 1999. Associate Technical Editor: D. Kaminski.

port equations must always have a very fine spatial grid and a very small time step. Kaiser and Benz [7] stated that the hardware requirements and needed supercomputing time for the accurate resolution of concentration and velocity gradients are impractical. In a pair of studies, we eliminate the need for such resources by using an asymptotic approach for the unsteady dopant transport for the entire period needed to grow a crystal in a model problem ([6,8]). We demonstrated that convection leads to extremely nonuniform dopant distributions in the melt. In addition, our analyses showed that the dopant distribution in the melt is far away from that given by a steady-state model for each stage during growth of the crystal. Therefore, the dopant transport problem is intrinsically unsteady for magnetic fields which are strong enough to eliminate flow oscillations, but which are not strong enough to achieve diffusion-controlled mass transport.

In the present paper, we treat the mass transport of silicon (Si) in a germanium (Ge) melt in a vertical Bridgman ampoule with a uniform, steady, axial magnetic field. An axial magnetic field preserves the axisymmetry of the crystal, while a transverse or horizontal uniform magnetic field produces deviations from axisymmetry in the melt, composition, leading to undesirable lateral macrosegregation in the crystal. Several crystal growers are currently performing experiments on the Bridgman growth of GeSi crystals from the melt with an axial magnetic field. The present study eliminates the need for impractical computing resources by using an asymptotic approach to treat the unsteady dopant transport for the entire period needed to grow a crystal during the solidification of a GeSi crystal. This asymptotic approach provides an analytic solution for the buoyant convection in the melt, so that a numerical solution is not required for the solutions of the Navier-Stokes equations, electromagnetic and energy equations. A numerical solution is only needed for the mass transport equation, thereby facilitating a moderate requirement for computational resources. With this approach, our model provides accurate predictions for the entire period needed to grow a crystal.

The benefits of magnetic fields during semiconductor crystal growth have been reviewed by Hurle and Series [9] and Walker [10], with an emphasis on the mass transport of dopants. Our Pe_m is the same as the parameter $(\mathrm{ScGr}/\mathrm{Ha}^2)$ used by some other researchers ([11]) where Sc and Gr are the Schmidt and Grashoff numbers.

2 Melt Motion

This paper treats the unsteady, axisymmetric mass transport of silicon in a germanium melt in a vertical Bridgman ampoule with an externally applied, uniform, steady, axial magnetic field $B_o\hat{\mathbf{z}}$. Here B_o is the magnetic flux density, while $\hat{\mathbf{r}}$, $\hat{\boldsymbol{\theta}}$, and $\hat{\mathbf{z}}$ are the unit vectors for the cylindrical coordinate system. During Bridgman growth, the ampoule is moved from an isothermal hot zone where the germanium has been melted, through an adiabatic or thermal-gradient zone where the germanium solidifies, and into a cold zone where the crystal is cooled. Our dimensionless problem is sketched in Fig. 1. The coordinates and lengths are normalized by the ampoule's inner radius R, and a is the dimensionless length of the ampoule. For Bridgman growth, the values of a can be as high as 35 ([12]). The melt velocity $\mathbf{v}$ is normalized by the characteristic velocity for magnetically damped buoyant convection ([13]),

$$U_b=\frac{\rho g \beta (\Delta T)_c}{\sigma B_o^2}, \tag{1}$$

where ρ is the melt's density at the solidification temperature T_m, β is the volumetric thermal expansion coefficient, $g=9.81\,\mathrm{m/s^2}$, and $(\Delta T)_c$ is the difference between the hot-zone temperature and T_m. The crystal-melt interface moves at a constant velocity $U_g=\omega U_b$, where ω is the dimensionless interface velocity. The planar crystal-melt interface lies at $z=-b$, where the instantaneous dimensionless axial length of the melt $b(t)=a-\omega t$ decreases during growth. With time t normalized by R/U_b, the dimensionless time to grow the entire crystal is a/ω.

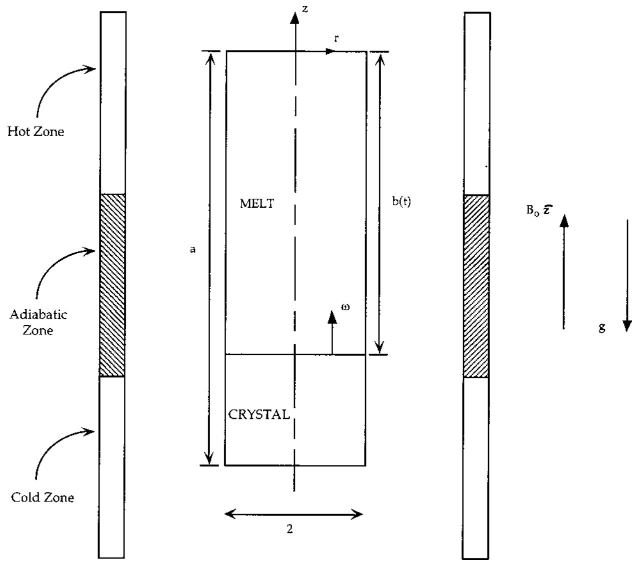

Fig. 1 **Vertical Bridgman ampoule with a uniform, steady, axial magnetic field $B_o\hat{\mathbf{z}}$ and with coordinates normalized by the ampoule's inner radius**

The electric current in the melt produces an induced magnetic field, which is superimposed upon the applied magnetic field produced by the external magnet. The characteristic ratio of the induced to applied magnetic field strengths is the magnetic Reynolds number

$$R_m=\mu_p \sigma U_b R, \tag{2}$$

where μ_p is the magnetic permeability of the melt. For all crystal-growth processes, $R_m \ll 1$ and the additional magnetic fields produced by the electric currents in the melt are negligible.

The characteristic ratio of convective heat transfer to conduction is the thermal Péclet number, $\mathrm{Pe}_t=\rho c_h U_b R/k$, where c_h and k are the melt's specific heat and thermal conductivity. For a sufficiently large value of B_o and for practical growth rates, convective heat transfer and the heat released by the cooling melt are negligible compared to the conductive heat transfer ([8]). For molten germanium with $R=7.5\,\mathrm{mm}$, $(\Delta T)_c=10\,\mathrm{K}$, and $B_o=2T$, the thermal Péclet number is $\mathrm{Pe}_t=0.02$, so that this assumption is justified. As long as the furnace is axisymmetric, the melt's temperature is independent of θ, and $T(r,\Xi)$ is the deviation of the temperature from the hot-zone temperature, normalized by $(\Delta T)_c$. The governing equation and boundary conditions are

$$\frac{1}{r}\frac{\partial}{\partial r}\left(r\frac{\partial T}{\partial r}\right)+\frac{4}{b^2}\frac{\partial^2 T}{\partial \Xi^2}=0, \quad \text{for } 0\leqslant r\leqslant 1,\ -1\leqslant \Xi \leqslant 1, \tag{3a}$$

$$T=0, \quad \text{at } \Xi=1, \tag{3b}$$

$$T=-1, \quad \text{at } \Xi=-1, \tag{3c}$$

$$\frac{\partial T}{\partial r}=\mathrm{Bi}(T_f-T), \quad \text{at } r=1, \tag{3d}$$

where $\Xi=1+2z/b$ is a rescaled axial coordinate, so that $-1\leqslant\Xi\leqslant 1$ for all time. Here, $T_f(\Xi)$ is the dimensionless furnace temperature, while the Biot number for the heat transfer from the furnace and through the ampoule wall is $\mathrm{Bi}=hR/k$, where h is the heat transfer coefficient between the outside surface of the melt and the furnace. In the hot zone, $T_f=0$ for $1<\Xi<(-b+2d)/b$, and in the thermal-gradient zone, $T_f=(\Xi+1)b/(2d)$

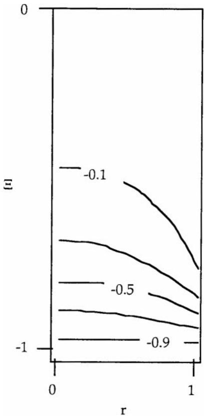

Fig. 2 **Dimensionless isotherms for Bi=10, *b*=5, and *d*=0.5**

-1 for $(-b+2d)/b<\Xi<-1$ ([14]). Here, d is the dimensionless distance between the crystal-melt interface and the vertical position in the furnace where the adiabatic and the hot-zone meet. For each instantaneous melt depth, the separation-of-variables solution for T is

$$T=\frac{1}{2}(\Xi-1)+\sum_{n=1}^{\infty}\chi_n I_o\left(\frac{n\pi r}{b}\right)\sin\left[\frac{n\pi}{2}(\Xi-1)\right], \qquad (4a)$$

$$\chi_n=\frac{\left(\dfrac{2b}{dn^2\pi^2}\right)\sin\left[\dfrac{n\pi}{b}(-b+d)\right]}{\left(\dfrac{n\pi}{b\,\mathrm{Bi}}\right)I_1\left(\dfrac{n\pi}{b}\right)+I_o\left(\dfrac{n\pi}{b}\right)}, \qquad (4b)$$

where I_0 or I_1 is the modified Bessel function of the first kind and zeroth or first order. Some typical isotherms for Bi$=10$, $b=5$, and $d=0.5$ are presented in Fig. 2. The thermal gradients are concentrated in a region of the melt near the crystal-melt interface because this region of the ampoule is adjacent to the furnace's thermal-gradient zone. The remainder of the melt which lies adjacent to the hot zone is isothermal at the hot-zone temperature. Future research will investigate the effect of the thermal environment on the distribution of dopants in the crystal.

This model is idealized because we have assumed that the crystal-melt interface is planar. The heat flux is primarily axial in the thermal-gradient zone where the crystal-melt interface occurs. Since the thermal conductivity of solid germanium is less than half that of the melt ([15]), the crystal represents a thermal barrier causing some of the heat flux to flow radially outward to the ampoule wall near the interface. This local radial heat flux causes the local isotherms and the crystal-melt interface to be concave into the crystal ([16]). The concave interface then creates two cells of circulation ([3]) instead of a single cell as shown in Fig. 2. Future research will investigate the effect of the curved crystal-melt interface on the dopant transport.

In the Navier-Stokes equation, the characteristic ratios of the electromagnetic (EM) body force term to the inertial term and to the viscous term are the interaction parameter, $N=\sigma B_o^2 R/\rho U_b$, which varies as B_o^4, and Ha^2, respectively. For molten germanium with $R=7.5$ mm, $(\Delta T)_c=10$ K and $B_o=2$ T, Ha$=664$, and $N=1.6\times10^5$. This value of N is sufficiently large that inertial effects are certainly negligible. In an asymptotic solution for Ha $\gg 1$, the melt is divided into an inviscid core, Hartmann layers with $O(\mathrm{Ha}^{-1})$ thickness adjacent to the boundaries at $\Xi=\pm1$, and a parallel layer with an $O(\mathrm{Ha}^{-1/2})$ thickness adjacent to the ampoule surface at $r=1$, as shown in Fig. 3. The Hartmann layers have a simple, local, exponential structure, which matches any radial core or parallel-layer velocities at $\Xi=\pm1$, which satisfies the no-slip conditions at the solid-liquid interfaces, and which indicates that v_z in the core or parallel layer is $O(\mathrm{Ha}^{-1})$ at $\Xi=\pm1$. Analysis of the parallel layer reveals that its thickness is actually $O[(b/\mathrm{Ha})^{1/2}]$. Since b can be as large as 35 at the beginning of the Bridgman process, the parallel layer is not actually thin as assumed in the formal asymptotic expansion for Ha$\gg1$. While a formal asymptotic analysis for Ha$\gg1$ is not appropriate, the numerical solution of the inertialess Navier-Stokes equation with all viscous terms is not necessary. The Hartmann layers represent an extremely small fraction of the melt length and have a simple exponential structure. There is no need to numerically duplicate this simple exponential structure. Therefore we use a composite core-parallel-layer solution which does not assume that the parallel-layer thickness is small. We discard the viscous terms $\mathrm{Ha}^{-2}\partial^2\mathbf{v}/\partial z^2$ in the Navier-Stokes equation, we relax the no-slip conditions at $\Xi=\pm1$ because they are satisfied by the Hartmann layers which are not part of the composite solution, and we apply the boundary conditions

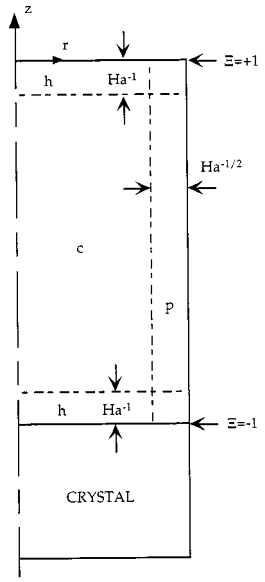

Fig. 3 **Flow subregions of the melt for Ha≫1: *c* =inviscid core, *p*=parallel layer adjacent to ampoule wall and parallel to the magnetic field, and *h*=Hartmann layers adjacent to the crystal-melt interface and the top of the ampoule**

$$v_z=0, \quad \text{at} \quad \Xi=\pm1.$$

Since these conditions neglect the $O(\mathrm{Ha}^{-1})$ perturbation velocity due to the Hartmann layers, we also discard the other viscous terms in the radial component of the Navier-Stokes equation because they are $O(\mathrm{Ha}^{-1})$ compared to the radial pressure gradient in both the core and parallel layer, and we already have an $O(\mathrm{Ha}^{-1})$ error. Therefore the dimensionless equations governing the composite solution, which assumes that the Hartmann layers have negligible thickness and which has an $O(\mathrm{Ha}^{-1})$ relative error, are

$$\frac{1}{r}\frac{\partial}{\partial r}(rv_r)+\frac{2}{b}\frac{\partial v_z}{\partial\Xi}=0, \qquad (5a)$$

$$\frac{\partial p}{\partial r}=j_\theta, \qquad (5b)$$

$$\frac{2}{b}\frac{\partial p}{\delta\Xi}=T+\mathrm{Ha}^{-2}\frac{1}{r}\frac{\partial}{\partial r}\left(r\frac{\partial v_z}{\partial r}\right), \qquad (5c)$$

$$j_\theta=-v_r, \qquad (5d)$$

where p is the deviation of the pressure from the hydrostatic pressure for the uniform density ρ, normalized by $\rho g\beta(\Delta T)_c R$, j_θ is the azimuthal component of the electric current density, normalized by $\sigma U_b B_o$, and T in (5c) is the buoyancy force with the Boussinesq approximation. Equation (5a) is conservation of mass, Eq. (5b) is the radial component of the Navier-Stokes equation with the radial EM body force due to the azimuthal electric current and the axial magnetic field, Eq. (5c) is the axial component of the Navier-Stokes equation with the buoyancy force and Eq. (5d) is the azimuthal component of Ohm's law where there is no azimuthal electric field because of axisymmetry. The boundary conditions are

$$v_z=0, \quad \text{at } \Xi=\pm 1,$$

$$v_r=v_z=0, \quad \text{at } r=1.$$

The radial velocity v_r and axial velocity v_z are given by

$$v_r=\frac{1}{r}\frac{2}{b}\frac{\partial\psi}{\partial\Xi}, \tag{6a}$$

$$v_z=-\frac{1}{r}\frac{\partial\psi}{\partial r}, \tag{6b}$$

$$\psi=-r\sum_{n=1}^{\infty}\frac{\chi_n \sin\left[\frac{n\pi}{2}(\Xi-1)\right]}{\left[1+\left(\frac{n\pi}{b\mathrm{Ha}}\right)^2\right]}\Bigg\{\lambda_n C_n \operatorname{ber}'(\lambda_n r)$$

$$+\lambda_n D_n \operatorname{bei}'(\lambda_n r)-\frac{b}{n\pi}I_1\left(\frac{n\pi r}{b}\right)\Bigg\}, \tag{6c}$$

$$C_n=\frac{1}{\Delta\lambda_n}\left[\frac{b}{n\pi}I_1\left(\frac{n\pi}{b}\right)\operatorname{ber}(\lambda_n)-\frac{1}{\lambda_n}I_0\left(\frac{n\pi}{b}\right)\operatorname{bei}'(\lambda_n)\right], \tag{6d}$$

$$D_n=\frac{1}{\Delta\lambda_n}\left[\frac{1}{\lambda_n}I_0\left(\frac{n\pi}{b}\right)\operatorname{ber}'(\lambda_n)+\frac{b}{n\pi}I_1\left(\frac{n\pi}{b}\right)\operatorname{bei}(\lambda_n)\right], \tag{6e}$$

$$\lambda_n=\left(\frac{n\pi\,\mathrm{Ha}}{b}\right)^{1/2}, \tag{6f}$$

$$\Delta=\operatorname{ber}(\lambda_n)\operatorname{ber}'(\lambda_n)+\operatorname{bei}(\lambda_n)\operatorname{bei}'(\lambda_n), \tag{6g}$$

where $I_1(x)$ is the modified Bessel function of the first kind and the first order. ber(x) and bei(x) are the Kelvin functions of the first kind and the zeroth order, defined by $\operatorname{ber}(x)+i\operatorname{bei}(x)=J_0(i^{3/2}x)$, where $i=(-1)^{1/2}$ and $J_0(x)$ is the Bessel function of the first kind and the zeroth order. Here, ber$'(x)$ and bei$'(x)$ are the first derivatives of these Kelvin functions.

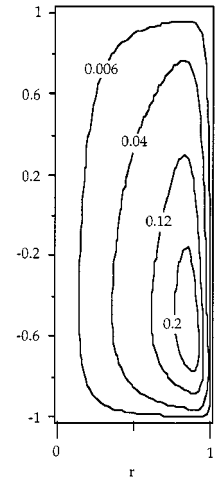

Fig. 4 Streamlines for the isotherms in Fig. 2 with $B_o=2\,T$ and $b=5$

Without a magnetic field, the local temperature gradients near the interface would drive a local buoyant convection, with very little melt motion in the isothermal region. When the electrically conducting fluid flows radially across the vertical magnetic field, it generates an induced electric field which drives an azimuthal electric current. This electric current flows across the magnetic field, creating an electromagnetic body force which opposes the radial velocity. There is no electromagnetic body force opposing flow along magnetic field lines. Therefore, the electromagnetic body force damps the flow that crosses magnetic field lines and elongates the flow along magnetic field lines ([17]), so that there is buoyant convection in the entire melt. This phenomena is demonstrated in Fig. 4 for $b=5$ and for the isotherms in Fig. 2.

3 Mass Transport

Before solidification begins, the dopant concentration is uniform, and this initial value is used to normalize the concentration C, so that $C(r,z,t)=1$ at $t=0$. Once crystal growth starts, the crystal absorbs much of the dopant during solidification, leaving a dopant-depleted region near the crystal-melt interface. The melt motion convects the melt with a low Si concentration into the rest of the melt. The dimensionless equation governing this mass transport is

$$\frac{\partial C}{\partial t}+\mathbf{v}\cdot\nabla C=\mathrm{Pe}_m^{-1}\nabla^2 C. \tag{7}$$

The velocity $\mathbf{v}=v_r\hat{\mathbf{r}}+v_z\hat{\mathbf{z}}$ is given by Eq. (6). Since dopant concentrations are generally small, the dilute approximation is appropriate. We have implicitly assumed that the dopant density has no effect on the buoyant convection.

Matching the solutions for C in the Hartmann layers, the boundary conditions at the crystal-melt interface and at the top of the ampoule are

$$\frac{2}{b}\frac{\partial C}{\partial\Xi}=\mathrm{Pe}_g(k_s-1)C, \quad \text{at } \Xi=-1, \tag{8a}$$

$$\frac{\partial C}{\partial\Xi}=0, \quad \text{at } \Xi=1, \tag{8b}$$

where $\mathrm{Pe}_g=U_gR/D=\omega\mathrm{Pe}_m$ is the Péclet number of solidification and k_s is the segregation coefficient. The boundary condition along the ampoule's vertical wall is

$$\frac{\partial C}{\partial r}=0, \quad \text{at } r=1. \tag{9}$$

We use a Chebyshev spectral collocation method for the convective and diffusive terms in Eq. (7) with Gauss-Lobatto collocations points in r and Ξ. We use a sufficient number of collocations points in order to resolve the large velocity and concentration gradients near $r=1$. All values of B_o require a significant number of collocation points in r. Either the viscous or the mass boundary layers are always thin since Ha is proportional to B_o, while Pe_m is proportional to B_o^{-2}. For the time derivative in Eq. (7), we use a second-order implicit time integration scheme to integrate from $t=0$ to t which is slightly less than a/ω. We chose a large enough number of time-steps such that the results do not change by increasing the number of time-steps.

At the beginning of crystal growth, the melt concentration, normalized with the initial uniform dopant concentration, is $C(r,z,t=0)=1$. Thus the amount of dopant initially in the melt is obtained by integrating across the ampoule's volume giving a total dopant concentration equal to πa. We verify that the sum of the total dopant in the melt and in the crystal is equal to πa at each time step.

Assuming that there is no diffusion of dopant in the solid crystal, the dopant distribution in the crystal, $C_s(r,z)$, normalized by the initial uniform dopant concentration in the melt, is given by

$$C_s(r,z)=k_s C\left(r,\Xi=-1,t=\frac{z}{\omega}\right). \qquad (10)$$

4 Results

For our germanium-silicon (GeSi) example, $k_s=4.2$ [15], and $\omega=0.01557B_o^2$, $\mathrm{Ha}=331.9B_o$ and $\mathrm{Pe}_m=72.24B_o^{-2}$. We present results for $B_o=2T$, $U_g=3\ \mu$m/s and $a=1$. For $B_o=2T$, $\omega=0.062295$, Ha$=663.8$, $\mathrm{Pe}_m=18.06$, and the time to grow a crystal is 16.05.

The constant-concentration curves in the melt at $t=0.08263$ are presented in Fig. 5(*a*). At this early stage during crystal growth, most of the melt concentration remains at its initial uniform melt concentration $C=1$. In a region near the crystal-melt interface, the dopant-depleted melt has $C<1$ because the crystal absorbs dopant during solidification. The axial magnetic field suppresses the flow adjacent to the crystal-melt interface. This $O(1)$ flow has little effect on the convection of dopant, so that the dopant transport is locally dominated by diffusion in a region near the crystal-melt interface except near $r=1$. Near $r=1$, $O(\mathrm{Ha}^{1/2})$ velocities adjacent to the ampoule's vertical wall produce a strong local upward flow which convects the dopant-depleted fluid upward. This upward flow along the ampoule wall produces the nonuniformity in the otherwise relatively horizontal constant-concentration curves in the melt.

After half of the crystal is grown, all of the melt has a concentration $C<1$ as shown in Fig. 5(*b*). The minimum melt concentration is 0.2044 and the maximum melt concentration is 0.4370. The constant-concentration curves have deviated further from the horizontal constant-concentration curves that would be given by pure diffusion, because the upward flow along the ampoule's vertical wall is convecting the dopant-depleted melt upward. The dopant-depleted melt must turn and flow adjacent to the top of the ampoule, producing constant-concentration curves that bow upward in the upper region of the melt.

As seen in Figs. 5(*a*) and 5(*b*), the concentration at the bottom of the melt adjacent to the crystal-melt interface is radially uniform except near the ampoule wall at $r=1$. Because of this uniformity, the constant-concentration curves for the crystal shown in Fig. 6 exhibit a small amount of radial macrosegregation. The maximum deviation from the concentration at $r=0$ is only 14.3 percent which occurs at horizontal cross sections for $-0.705\leqslant z\leqslant -0.720$. More than 25 percent of the crystal has less than a five percent deviation between the maximum concentration and the concentration at $r=0$ along any $z=$constant cross section, and more than 50 percent of the crystal has less than a ten percent deviation in the radial macrosegregation.

The predicted crystal composition is different from that given by the desired limiting case where dopant transport is governed by diffusion because convective mass transport plays a significant role. From a crystal-growth perspective, diffusion-dominated solidification is desirable because it leads to a radially and axially uniform dopant concentration distribution over most of the length of the crystal. Although this is highly desirable, the convective velocities are significant even for $B_o=2\ T$, so that for lower magnetic field strengths where convection would become even more significant, the dopant transport never approaches the diffusion-controlled limit.

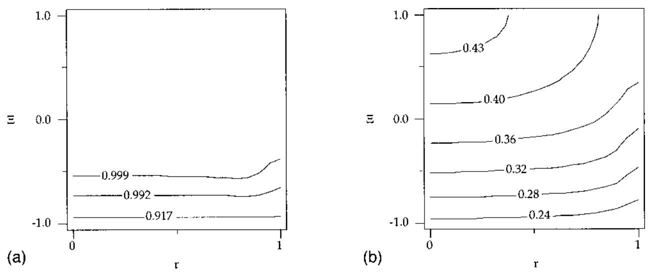

Fig. 5 Melt concentration $C(r,\Xi,t)$ for $B_o=2T$; (*a*) $t=0.08263$, (*b*) $t=8.026$

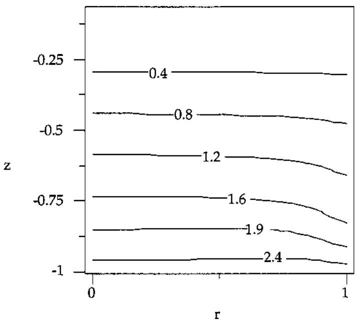

Fig. 6 Crystal concentration $C_s(r,z)$ for $B_o=2T$

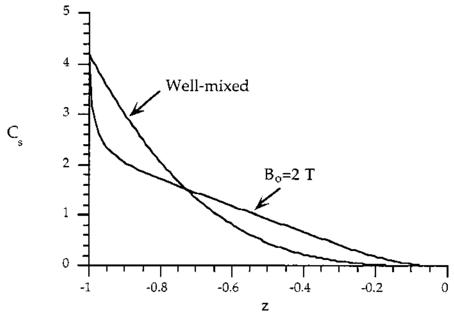

Fig. 7 Axial variation of the crystal composition for the radially averaged concentration for $B_o=2T$ and the well-mixed limit

The other limit is the well-mixed limit when the velocities provide sufficient mixing that the dopant distribution is essentially uniform throughout the melt at each time. In this case, the dopant becomes instantly uniformly distributed over the entire volume of the melt at each stage during growth. The well-mixed limit produces radially uniform dopant concentrations in the crystal, but a drastically nonuniform axial dopant distribution which is governed by

$$C_s(z)=k_s\left(-\frac{z}{a}\right)^{-(1-k_s)}. \qquad (11)$$

In Fig. 7, we show the axial variation of the crystal composition predicted by Eq. (11) and the axial variation of the radially averaged crystal composition for our GeSi example with $B_o=2\ T$. The axial variation of the dopant concentration for $B_o=2\ T$ is different from the well-mixed cases because the convection does not provide enough mixing to produce a uniform melt concentration. As shown in Fig. 5, the melt concentration is far from uniform.

The axial magnetic field has the benefit of damping the radially outward flow adjacent to the crystal-melt interface. This produces a region in the melt which is locally dominated by diffusion, so that there is only a small radial variation in the concentration. Therefore, the crystal exhibits little radial macrosegregation. A future study will investigate the effects of different magnetic field strengths, aspect ratios, and growth rates in order to determine the optimal process variables that will produce crystals with both minimal radial and axial macrosegregation.

5 Conclusions

The convective mass transport is stronger than diffusive mass transport over most of the melt, especially near the ampoule's surface at $r=1$ where $O(\mathrm{Ha}^{1/2})$ flow in the parallel layer produces significant mass transport. The flow adjacent to the crystal-melt interface is damped by the axial magnetic field, so that the diffusive mass transport is stronger than the convective mass transport in a region of the melt adjacent to the interface. The distribution of dopant in the melt adjacent to the crystal-melt interface is radially uniform except near the parallel layer at $r=1$. Therefore, this vertical Bridgman process with an axial magnetic field is a desirable situation because this flow produces a crystal composition which exhibits little radial macrosegregation.

Acknowledgments

This research was supported by the University of Missouri Research Board, by the National Aeronautics and Space Administration under Grant NAG8-1453, and by the National Science Foundation under Grant CTS 94-19484.

References

[1] Chedzey, H. A., and Hurle, D. T. J., 1966, ''Avoidance of Growth-Striae in Semiconductor and Metal Crystals Grown by Zone-Melting Techniques,'' *Nature* (London), **210**, pp. 933–934.

[2] Utech, H. P., and Flemings, M. C., 1966, ''Elimination of Solute Banding in Indium Antimonide Crystals by Growth in a Magnetic Field,'' J. Appl. Phys., **7**, pp. 2021–2024.

[3] Kim, D. H., Adornato, P. M., and Brown, R. A., 1988, ''Effect of Vertical Magnetic Field on Convection and Segregation in Vertical Bridgman Crystal Growth,'' J. Cryst. Growth, **89**, pp. 339–356.

[4] Ma, N., and Walker, J. S., 1997, ''Magnetic Damping of Melt Motions During Bridgman Crystal Growth in Microgravity,'' *SPIE International Symposium on Optical Science, Engineering and Instrumentation: Materials Research in Low Gravity*, Vol. 3123, San Diego, CA, pp. 254–261.

[5] Ma, N., and Walker, J. S., 1999, ''Segregation During Bridgman Crystal Growth in Space With an Axial Magnetic Field,'' *Proceedings of the International Colloquium: Modelling of Material Processing*, Riga, Latvia, pp. 12–16.

[6] Ma, N., and Walker, J. S., 1997, ''Validation of Strong Magnetic Field Asymptotic Models for Dopant Transport During Semiconductor Crystal Growth,'' J. Cryst. Growth, **180**, pp. 401–409.

[7] Kaiser, Th., and Benz, K. W., 1998, ''Floating-Zone Growth of Silicon in Magnetic Fields. Part III. Numerical Solution,'' J. Cryst. Growth, **183**, pp. 564–572.

[8] Ma, N., and Walker, J. S., 1997, ''Dopant Transport During Semiconductor Crystal Growth With Magnetically Damped Buoyant Convection,'' J. Cryst. Growth, **172**, pp. 124–135.

[9] Hurle, D. T. J., and Series, R. W., 1994, ''Use of a Magnetic Field in Melt Growth,'' *Handbook of Crystal Growth*, **2A**, pp. 261–285.

[10] Walker, J. S., 1999, ''Models of Melt Motion, Heat Transfer and Mass Transport During Crystal Growth With Strong Magnetic Fields,'' *The Role of Magnetic Fields in Crystal Growth: Progress in Crystal Growth and Characterization of Materials*, Vol. 38, K. W. Benz ed., Elsevier, Amsterdam, pp. 185–213.

[11] Alboussière, T., Neubrand, A. C., Garandet, J. P., and Moreau, R. 1997, ''Segregation During Horizontal Bridgman Growth Under an Axial Magnetic Field,'' J. Cryst. Growth, **181**, pp. 133–144.

[12] Watring, D. A., 1997, ''Effects of Static Axial Magnetic Fields on Directional Solidification of HgCdTe (Mercury Cadmium Telluride, Mass Transfer, Microgravity),'' Ph.D. dissertation, Massachusetts Institute of Technology, Cambridge, MA.

[13] Hjellming, L. N., and Walker, J. S., 1987, ''Melt Motion in a Czochralski Puller With an Axial Magnetic Field: Motion due to Buoyancy and Thermocapillarity,'' J. Fluid Mech., **182**, pp. 335–368.

[14] Ma, N., and Walker, J. S., 1996, ''Magnetic Damping of Buoyant Convection During Semiconductor Crystal Growth in Microgravity. Continuous Random g-Jitters,'' Phys. Fluids, **8**, pp. 944–953.

[15] Adornato, P. M., and Brown, R. A., 1987, ''Convection and Segregation in Directional Solidification of Dilute and Non-Dilute Binary Alloys: Effects of Ampoule and Furnace Design,'' J. Cryst. Growth, **80**, pp. 155–190.

[16] Ramachandran, N., and Watring, D. A., 1997, ''Convection Damping by an Axial Magnetic Field During the Growth of HgCdTe by Vertical Bridgman Method—Thermal Effects,'' 35th AIAA Aerospace Sciences Meeting and Exhibit, Paper No. 97-0450.

[17] Moreau, R., 1990, *Magnetohydrodynamics*, Kluwer, Boston.

Rayleigh Light Scattering Measurements of Transient Gas Temperature in a Rapid Chemical Vapor Deposition Reactor

J. F. Horton
Research Assistant

J. E. Peterson
Associate Professor,
e-mail: pete@cimar.me.ufl.edu

Department of Mechanical Engineering,
University of Florida,
Gainesville, FL 32611-6300

A laser-induced Rayleigh light scattering (RLS) system was used to measure transient gas temperatures in a simulated rapid chemical vapor deposition (RCVD) reactor. The test section geometry was an axisymmetric jet of carrier gas directed down, impinging on a heated wafer surface. RLS was used to measure instantaneous gas temperature at several locations above the wafer as it was heated from room temperature to 475 K. Gas flow rate and wafer temperature correspond to jet Reynolds number $Re_i=60$*, wafer maximum Grashof number* $Gr_H=4.4\times10^6$*, and maximum mixed convection parameter* $Gr_H/Re_i^2=1200$*; all conditions typical of impinging jet reactors common in the numerical literature. Uncertainty of RLS transient temperature from a propagated error analysis was* ±2*–*4 *K. Peak gas temperature fluctuations were large (in the order of 25 to 75 °C). Both flow visualization and RLS measurements showed that the flow field was momentum dominated prior to heating initiation, but became unstable by* $Gr_H/Re_i^2=5$*. It then consisted of buoyancy-induced plumes and recirculations. Up to the peak wafer temperature, the flow field continued to be highly three-dimensional, unsteady, and dominated by buoyancy. RLS measurements are shown to provide information on carrier gas instantaneous temperature and flow field stability, both critical issues in RCVD processing.* [S0022-1481(00)02401-4]

Keywords: Heat Transfer, Mixed Convection, Nonintrusive Diagnostics, Transient, Vapor Deposition

Introduction

Manufacture of integrated circuits on silicon substrate wafers is an area of substantial research and development. The integrated circuit is made by a series of chemical reaction, photolithography, and etching processes to create and modify thin film layers. These layers form resistors, wires, capacitors, and insulators required to create the desired circuitry. The silicon substrate wafer is about eight inches in diameter, and hundreds of IC chips are manufactured in parallel on this surface. Thin films of silicon are deposited by a temperature-dependent reaction called chemical vapor deposition (CVD). Traditionally, many wafers are processed simultaneously in quasi-steady state CVD reactors. However, increasing complexity of semiconductor design and higher quality results of single wafer processing has shifted the focus of microchip fabrication from conventional furnace processing to rapid thermal processing, including rapid chemical vapor deposition (RCVD) ([1]).

A typical RCVD process consists of starting a flow of silicon laden carrier gas which transports reactants to substrate wafer surface. Then radiative heating is initiated, ramping the wafer to high temperature to initiate the reaction that causes silicon to atomistically deposit on the wafer surface. The temperature is maintained for a limited period before cooling. Film quality depends on the steady and laminar supply of silicon-laden carrier gas to the wafer surface. Because the reaction is strongly temperature dependent, the carrier gas temperature is a critical parameter. While a large body of numerical work examines carrier gas in the CVD process, the accuracy of the numerical results detailing isotherms and flow lines is largely unknown and untested, and very little numerical work examines RCVD. A good summary of rapid thermal processing technology is found in Fair [2].

The present work presents transient gas temperature measurements in a simulated RCVD chamber. The reactor geometry is that of an axisymmetric jet impinging on a wafer surface, and is illustrated in Fig. 1. The problem is also of fundamental interest. Depending on flow rates and temperature, the flow field can be dominated by either momentum (creating flow patterns illustrated in Fig. 1, left side) or buoyancy (shown in Fig. 1, right side), or a combination of the two. Transient gas temperatures were sensed noninvasively by laser-induced Rayleigh Light scattering (RLS). RLS occurs because electric fields of gas molecules resonate with the electric field of the incident laser light. The result is that a small amount of light is scattered in directions different from that of the incoming light. Intensity of Rayleigh scattered light varies directly with gas molecular number density, and thus temperature

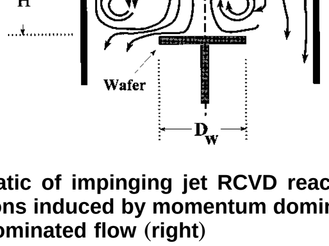

Fig. 1 Schematic of impinging jet RCVD reactor and carrier gas recirculations induced by momentum dominated flow (left) or buoyancy dominated flow (right)

Contributed by the Heat Transfer Division for publication in the JOURNAL OF HEAT TRANSFER. Manuscript received by the Heat Transfer Division, Dec. 11, 1998; revision received, Sept. 7, 1999. Associate Technical Editor: P. Menguc

of an ideal gas can be found if pressure is known. Transient temperatures were found in the RCVD test section with high spatial and temporal resolution.

Background: Rapid Chemical Vapor Deposition

Many technical publications numerically examine carrier gas temperature and flow characteristics. The goals of these works are similar: Define the geometry, operating pressure, and flow rates that will yield thin, stable boundary layers at the wafer surface, eliminate three-dimensional flow and recirculations within the reactor, and suppress the effects of buoyancy. A Boussinesq assumption is not appropriate, thus other simplifications are required to make the problem numerically tractable. The most common and questionable assumptions are of laminar steady flow and axisymmetry. Experimental verification has consisted mainly of flow visualization of a simulated CVD process, and of comparison of measured and predicted deposition rates. While commercial CVD and RCVD reactors have many internal geometries, two are studied from a fundamental point of view: horizontal duct-type reactors, and axisymmetric impinging jet reactors. In a series of publications, the effect of mixed convection on the chemical vapor deposition process was examined by Evans and Greif [3–7] and Lin, Choi, and Grief [8]. They numerically established the existence of transverse traveling waves due to the Rayleigh-Benard thermal instability, and transient effects due to buoyancy even in nominally steady-state systems. These works consider buoyancy suppression strategies including disk rotation, thermal and species diffusion, a variety of geometries, and most recently rapid thermal processing.

Flow visualization studies and numerical optimizations of rotating wafer axisymmetric reactors for organo-metallic vapor phase epitaxy (OMVPE) were conducted by Patnaik [9], Wang et al. [10,11], and Patnaik, Brown, and Wang [12] in an axisymmetric reactor. They found that quality of the deposition layer is largely determined by reactor gas dynamics, and that buoyancy-driven recirculations and other secondary flows resulting from reactor geometry have a detrimental effect on layer uniformity and interface. Three-dimensional flow effects in CVD reactors were predicted in experimental and numerical models by Moffat and Jensen [13], Jensen [14], Fotiadis et al. [15], Fotiadis, Kieda, and Jensen [16], Jensen et al. [17,18], Lie et al. [19], and Hebb and Jensen [1]. The overall thrust of this work is the complexity of the fluid mechanics and heat transfer phenomena, even in well-controlled and geometrically simplified simulations. Important phenomena had not appeared previously in numerical solutions, including effects of such practical considerations as wafer tilt, nonuniform reactor wall temperature, asymmetries in inlet conditions, and even the sequence of process steps (that is, whether carrier gas flow is initiated before or after wafer heating). It was concluded that three-dimensional transport effects are significant even when buoyancy is not important, and that the study of convective heat transfer in CVD reactors is necessary to develop more physically realistic models. Flow visualization was used to verify numerical predictions, and some temperature measurements were acquired for a horizontal CVD reactor by laser-induced Raman scattering. Due to the weak signal from Raman scattering, extremely long averaging times are required (in the order of 30 minutes), and it is not suitable for RCVD, or even for identification of transient effects in steady-state CVD processes. Most recently (in the 1995 publication), they examined the asymmetries in RCVD of wafer surface radiative properties resulting from multilayer pattern wafers.

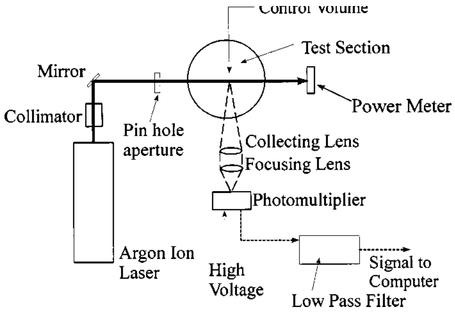

Fig. 2 Schematic of RLS optical system

Laser-Induced Rayleigh Light Scattering

The basics of Mie and Rayleigh scattering theory are detailed in many references, notably Kerker [20], and Bohren and Huffman [21]. In these works, the general solution is given of the Maxwell equations that describe independent scattering of incident electromagnetic waves by an isolated sphere. The solution is termed Mie scattering theory; a complicated series solution. Mie scattering simplifies to a single term when the scattering particles are small compared with the incident wavelength (particle diameters $<0.03\lambda$), and is termed Rayleigh scattering. The intensity of Rayleigh light scattered by a single molecule is often described in terms of a scattering cross section, σ. For an ideal gas with an index of refraction close to 1, the scattering cross section at 90 deg to the incident electromagnetic wave is written as ([22])

$$\sigma(90\ \text{deg}) = \frac{4\pi^2(n_{\text{ref}}-1)^2}{N_{\text{ref}}^2\lambda^4}. \qquad (1)$$

Using the ideal gas law to estimate the number of scatters (molecules) in the control volume, $\forall$, the intensity of Rayleigh scattered light is then written:

$$I_{\text{scat}}(90\ \text{deg}) = N_o \frac{P\forall}{\mathfrak{R}T}\sigma(90\ \text{deg})I_o. \qquad (2)$$

Thus temperature is easily found if scattered light, pressure, size of the measurement control volume, and incident power density are known. Although not well known, RLS has been successfully used for both temperature and concentration measurements, applied primarily to combustion problems ([22–24]) among others).

The RLS data acquisition system is illustrated in Fig. 2. A more complete description of the RLS system, its calibration, and its capabilities is found in Horton and Peterson [25] and Horton [26]. Laser light generated by a four watt Argon Ion laser is collimated, passed through a 1-mm diameter pinhole, and transmitted to the test section. Beam power is continuously monitored by a power meter (Newport 818T-150) as it exits the test section. The Rayleigh scattered light is collected at 90 deg by a 60-mm diameter, 248 mm focal length lens, focused with a 60-mm diameter, 125 focal length lens, passed through a slit (height 3 mm, length $=0.0155$ mm, Melles Griot), and imaged onto a photomultiplier tube (Hamamatsu HC120-01, spectral range 185–650 nm, 23 kHz bandwidth). Thus, the measurement control volume $\forall$ (and system spatial resolution), is a cylinder defined by the slit length and incident beam diameter; 0.015 mm and 1 mm in the present system. Output from the PMT is low pass filtered at 1 kHz (Frequency Devices Model 900 Tunable Filter), and transmitted to the computer through a programmable gain multiplexer and A/D board. The laser, transmission optics, and collection optics were mounted on a traverse to allow positioning the control volume at different locations in the stationary test section.

Implementation of RLS theory for temperature measurement is complicated by signal contamination from two major sources: glare from the test section and other laboratory surfaces, and Mie scattering from dust particles ([27]).

1 Intensity of light as seen by the photomultiplier tube is composed of the Rayleigh signal of interest and of glare from test section and laboratory surfaces. Glare is found by measuring PMT voltage when the test section is filled with helium ($\sigma_{\text{He}} = 0.015\sigma_{\text{AIR}}$). A PMT voltage measurement is then taken at the same location in the test section, but now at a reference condition

(most conveniently, room temperature and atmospheric pressure). Finally, heating is initiated, and instantaneous temperature is then found by subtracting the glare and rationing to known conditions:

$$T_j = T_{\text{ref}}\left(\frac{V_{\text{scat}_{\text{ref}}} - V_{gl}}{V_{\text{scat}_j} - V_{gl}}\right). \tag{3}$$

2 Contamination of the RLS signal by dust particles is relatively easy to identify as the Mie scattering signal is much stronger than RLS. To remove Mie effects, data were statistically filtered at three standard deviations. The maximum number of data points rejected was about five percent, and the lowest was zero. Additionally, the test section was observed during heating. Dust contamination was initially evenly distributed, but was driven up and away from the wafer surface by thermophoretic effects once heating was begun. Data also showed these effects. Typically, the data points with most filtered data were at low temperatures and the points at high temperature had no rejected data.

A propagated error analysis was used to assess experimental uncertainty ([28]). Principal sources of uncertainty were the error in reference temperature (±1°C), and uncertainty in the three PMT voltages of Eq. (3) was found from the standard deviation of the mean of 30 repeated measurements (95 percent confidence limits). Resulting uncertainty was 2–4°C, with about one third of the uncertainty from each of three sources: reference temperature, PMT scattered voltage, and PMT reference voltage. Uncertainty due to glare measurement was found to be negligible.

Experimental Apparatus

An axisymmetric RCVD test section was constructed as illustrated in Fig. 3. The test section consists of a cylinder of 22.9-cm diameter, 5-mm thick optical quality quartz (Heraeus Amersil). It is sealed on the bottom with a gasketed aluminum plate and on the top with gasketed PVC pipe and fittings. Highly filtered compressed air enters the test chamber through four symmetrically placed ports, passes through a porous fitted disk (Chemglass, pore size 170–220 micron) and then through flow straighteners before entering the test chamber. It leaves through four symmetric exits at the chamber bottom. The chamber is sealed and can be operated below atmospheric pressure by attaching the exhaust tubing to a vacuum pump. Gas flow path, filtering, and metering are seen in Fig. 4. Pressure in the test section was monitored by a mercury manometer during all measurements. The ''wafer'' is made of copper, with a wafer diameter to inlet diameter ratio (D_w/D_i) of 1.0 (each 15.24 cm), and heated from below with a Mica heater. Five thermocouples are mounted on the copper disk to monitor surface temperature, and are connected through the multiplexer and A/D board to the computer. Heater power is computer controlled, allowing a user selected constant temperature, or a variable temperature ramp rate to simulate the RCVD process, according to the boundary conditions wanted.

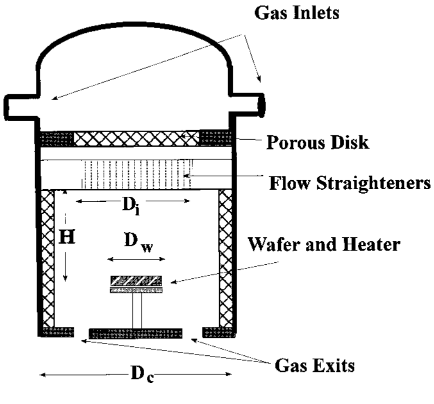

Fig. 3 Schematic of test section

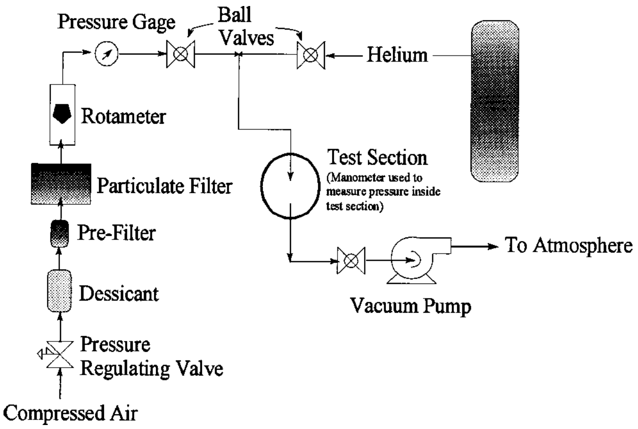

Fig. 4 Gas flow path

The test section as described above involves several project assumptions with respect to RCVD processing:

- First, a dilute limit assumption is made. With this assumption, an actual RCVD reaction need not be performed. Instead, air is used as the working fluid, and the obvious corrections in flow rates and temperatures have been made to retain Reynolds and Grashof number similarity. This simplification is valid as deposition reactions do not significantly alter the carrier gas flow or temperature distribution because reactants are present in dilute amounts (<1 percent). The energy contributions from the heats of reaction are insignificant ([17]). In fact, most numerical simulations also neglect both heats of reaction and Dufour effects in the energy conservation equation. Continuity, momentum, and energy are solved simultaneously, and then the chemical kinetics are treated as a separate problem using known velocity and temperature fields.
- The dilute limit also supports a second assumption of the present model: that growth of film on the wafer surface does not affect reactor geometry. Film thickness is typically four to six orders of magnitude below reactor length scales, and is clearly negligible.
- Third, it is assumed that carrier gas characteristics are not altered by a change in wafer heat source from radiative (as generally found in an RCVD reactor) to conduction heating by an electrical resistance unit (as in this test section). For a typical radiative source temperature of 3000 K, for example, maximum emission of radiation occurs at approximately 1000 nm. The carrier gases used in the RCVD process (nitrogen and hydrogen) are transparent in the infrared, and do not participate in the radiative heating. From a heat transfer point of view, electrical resistance heating is much simpler to achieve and does not significantly change the boundary condition (constant wafer surface temperature) as seen by the carrier gas. In a real RCVD process, there could be significant thermal emission from the reactants, an effect which requires careful assessment, and could necessitate narrow band filtering at the PMT.

Mixed Convection, Length Scales, and Flow Visualization

The four length scales defined in Figs. 1 and 3 make clear the geometric complexity of this problem, and many choices for characterization of the chamber. In the present work, the Reynolds number was based on the inlet diameter, as is appropriate for an axisymmetric jet. The Grashof number could reasonably be based on H, the height from the wafer to the chamber inlet or D_w, the wafer diameter. In the present work, H was used as at high temperatures, the momentum of the jet becomes negligible, and the

SCHEMATIC: TOP VIEW

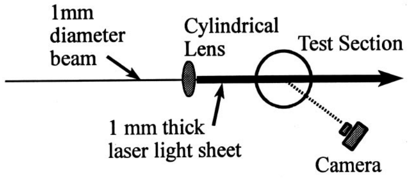

FLOW VISUALIZATON: SIDE VIEW

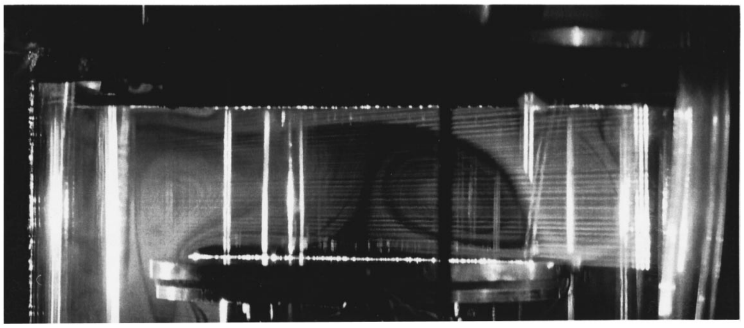

Fig. 5 (*a*) Schematic of flow visualization optical arrangement; (*b*) photograph of buoyancy-dominated flow

region above the wafer functions like an enclosure heated from below. The mixed convection flow parameter used, then, is

$$\frac{\mathrm{Gr}_H}{\mathrm{Re}_i^2}=\frac{\left(\dfrac{g\beta(T_w-T_i)H^3}{\nu_i^2}\right)}{\left(\dfrac{U_iD_i}{\nu_i^2}\right)^2}. \tag{4}$$

Flow visualizations were performed to find gas flow patterns prior to the RLS temperature measurements. A 150-mm focal length cylindrical lens was used to expand the Argon-Ion laser to a 1-mm thick sheet (Fig. 5(*a*)). The gas flow was seeded with smoke to serve as a flow tracer, and, as smoke particles are relatively large and scatter in the Mie regime, the test section was photographed from a forward angle to take advantage of the increased intensity of Mie forward scattering. The system was initially isothermal and thus momentum dominated. The sudden expansion at the chamber inlet lead to recirculation regions and momentum dominated flow pattern as illustrated in the left half of Fig. 1. When the wafer was heated, the influence of buoyancy was apparent even at low temperature. By a value of $\mathrm{Gr}_H/\mathrm{Re}_i^2$ of about 5, the boundary layer at the wafer surface became chaotic due to the buoyancy opposing jet momentum. At higher temperature, the buoyancy-dominated recirculation formed, as illustrated in Fig. 1 (right side). The photograph of Fig. 5(*b*) shows this buoyancy-dominated flow field flow. The horizontal dark streaks are caused by the extruded quartz cylinder surface. The gas was observed to be laminar, but the flow field was chaotic, and not always symmetric about the central axis. The seeding material was driven from the wafer surface by thermophoretic forces, thus the plume rising from the surface is only lightly seeded, and appears dark in the photograph. Carrier gas is completely deflected by the buoyant recirculation zones and does not impinge directly on the wafer surface. The plume is deflected to the right side, leaving a larger recirculation on the left. There are two recirculation regions to the right of the plume; the first buoyancy-driven and rotating clockwise, and the second (faintly visible at the far right edge of the cylinder) rotating counterclockwise. This flow configuration was unstable, however, as the central region of the plume moved left and right, and only occasionally assumed a stable axisymmetric appearance. As the flow visualization illuminates only one plane, the principal asymmetries were probably in the transverse plane at those times.

Transient Temperature Measurements

Transient carrier gas temperatures were measured at four radial locations at 1 cm above the wafer surface for a Reynolds number of $\mathrm{Re}_i=60$, maximum Grashof number $\mathrm{Gr}_H=4.4\times10^6$, and maximum $\mathrm{Gr}_H/\mathrm{Re}_i^2=1200$. To obtain a constant surface temperature boundary condition, the ''wafer'' was made of 1-cm thick, 15.24-cm diameter solid copper. Surface temperature uniformity was good, with temperature variations below ±2°C at 5 points continuously monitored on the wafer surface. This 1-cm wafer thickness required to obtain the consistency, however, resulted in large thermal inertia. The effect of ramp rate is a subject to be addressed in future work. At maximum power, then, the wafer was ramped from room temperature to about 200°C over an eight-minute period, as seen in Fig. 6. Ten to 15 intensity readings were taken during heating.

Figure 6 shows RLS measurements of carrier gas average temperature of 500 data points taken over the one-second sampling period. The error bars indicate uncertainty in temperature from the propagated error analysis. Mean temperature trends shown in Fig. 6 are as expected for the buoyancy-dominated flow pattern that formed for all but the first few data points when the wafer temperature was close to the inlet gas temperature. Mean temperatures at the three radii near the wafer center are highest, as these measurements are in the thermal plume rising from the hot wafer surface. In contrast, the temperature at $r/r_o=0.67$ is about 50 deg lower, indicating it is inside a recirculation cell that is not directly exposed to the hot gas rising from the wafer surface. These temperature trends are predicted in the numerical work (for example, [29,30] among others), and seen in the flow visualization photograph of Fig. 5(*b*). Figure 6 also shows that at some times, the mean temperature is significantly lower than the previous measurement at the same location (for example, the average temperature at $r/r_o=0$ is higher at 300 than at 350 seconds). The temperature change is caused by the unsteady wandering effects seen in the flow visualization, as the plume central axis varies.

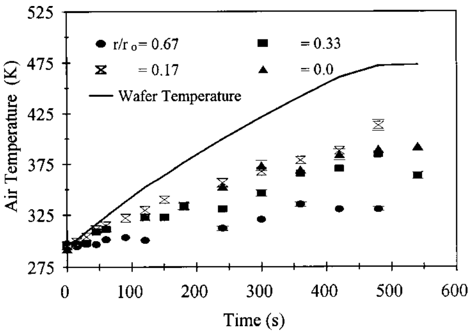

Fig. 6 Temperature as a function of time at four radial locations. Each point indicates the mean of 500 data points taken over one second. Error bars indicating uncertainty in temperature (95 percent confidence limits) are about the size of symbols.

Figures 7(*a*)–(*d*) show the instantaneous temperature for the four radial locations at four different times during the heating cycle. All four locations begin with uniform ambient temperature. The center temperature ($r/r_o=0$, as shown in Fig. 7(*a*)) shows some fluctuation and periodicity even at 120 seconds. Gas temperature climbs to about 400 K after 480 seconds, and shows irregular fluctuations of about 25 deg and frequencies in the order of 10 Hz. Figure 7(*b*) ($r/r_o=0.17$) shows similar trends to $r/r_o=0$ for times up to 300 seconds. The temperature measurement beginning at 480 seconds, however, shows high fluctuations of over 75 deg and frequency around 3 Hz. Peak temperature is significantly higher than at the other three radial locations. Both the high temperature and large fluctuations indicate that $r/r_o=0.17$ is close to the plume center, and the plume is asymmetric as shown in the photograph above.

Figure 7(*c*) shows two different flow regimes (seen most clearly at 480 seconds). The first half of the 480-second sample sees the higher frequency (~10 Hz) seen on the centerline. The second half (from 480.5–481.0 s), however, is clearly in a more stable region. Thus, this point is on the edge of the recirculation region for the first half of that sample, seeing higher temperatures of the plume core. The point is inside the recirculation for the second half, seeing cooler and more stable gas. Finally, the data point at $r/r_o=0.66$ sees little of the temperature rise and high fluctuations found in the other three graphs. Only at 480 seconds is some temperature rise seen, along with evidence of the long scale (~ 3 Hz) fluctuating nature of the flow. As both mean temperature and temperature fluctuations are low, it is concluded that this point is inside a stable recirculation region, and not in the hot unstable plume.

Summary and Conclusions

The present work presents a Rayleigh light scattering diagnostic system and its application to measurement of transient temperatures in RCVD reactor gas. The RLS system was found to be a suitable tool for diagnosis of gas temperature and flow field stability, both issues of extreme importance to the RCVD process. Uncertainty in RLS determination of transient temperature was small (±2–4°C). Transient temperature measurements were done in the RCVD test section operating at conditions typical of those found in the numerical literature. Temperature fluctuations increased significantly during the heating cycle due to buoyancy opposing momentum. The transient measurements show highly irregular wandering and chaotic flow exists, with multiple transient effects. Both the preliminary flow visualization and the RLS transient temperature measurements show the flow field, at these operating conditions, consists of an irregular buoyancy-induced plume and somewhat more stable recirculation zones, and is highly three-dimensional.

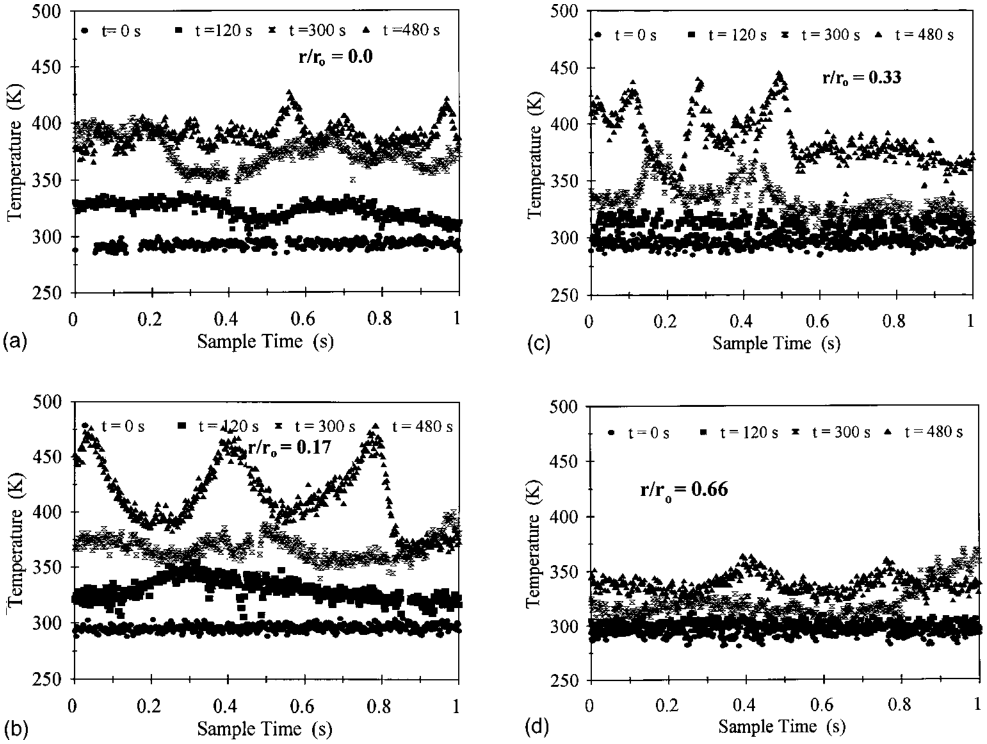

Fig. 7 Instantaneous gas temperature at four different times during the wafer heating: 0–1 s, 120–121 s, 300–301 s, and 480–481 s. (*a*) $r/r_o=0.0$; (*b*) $r/r_o=0.17$; (*c*) $r/r_o=0.33$; (*d*) $r/r_o=0.66$.

Acknowledgments

This work was supported by the National Science Foundation under Grant No. CTS-9409825. The authors would like to express their appreciation. Special thanks to Angelo Mathews for the flow visualization photograph.

Nomenclature

D_c = RCVD chamber diameter (m)
D_i = diameter of gas inlet to RCVD chamber (m)
D_w = wafer diameter (m)
Gr_H = Grashof number based on chamber inlet to wafer height, H
g = gravitational constant (m^2/s)
H = height of RCVD chamber from wafer to inlet
I_{scat} = intensity of scattered light (W)
I_o = laser power density ($\mathrm{W/m}^2$)
n_{ref} = index of refraction at reference conditions
N = gas number density ($1/\mathrm{m}^3$)
N_o = Avogadro's number (molecules/kg mol)
N_{ref} = gas number density at reference conditions ($1/\mathrm{m}^3$)
$\mathfrak{R}$ = gas constant (J/kg mol K)
r = radius (m)
r_o = chamber radius (m)
P = pressure (Pa)
Re_i = Reynolds number based chamber entrance diameter
T = instantaneous gas temperature from Eq. (2) (K)
T_w = wafer temperature (K)
T_i = inlet gas temperature (K)
T_{ref} = reference temperature (K)
U_i = inlet mean velocity (m/s)
V_{gl} = photomultiplier tube voltage due to glare
V_{scat} = photomultiplier tube voltage due Rayleigh scattered light
$V_{\mathrm{scat,ref}}$ = photomultiplier tube voltage due Rayleigh scattered light at reference conditions
$\forall$ = volume (m^3)

Greek Symbols

β = thermal expansion coefficient (K^{-1})
σ = Rayleigh scattering cross section (Eqs. (2) and (3), m^2);
λ = wavelength of light (m)
ν_i = kinematic viscosity at inlet temperature (m^2/s)

References

[1] Hebb, J. P., and Jensen, K. F., 1995, ''Length Scales and Pattern Effects in RTP Heat Transfer,'' *RTP '95*, R. B. Fair and B. Lojek, eds., RTP '95, Round Rock, TX, pp. 198–204.
[2] Fair, R. B., 1993, *Rapid Thermal Processing*, Academic Press, San Diego, CA.
[3] Evans, G., and Greif, R., 1987, ''A Numerical Model of the Flow and Heat Transfer in a Rotating Disk Chemical Vapor Deposition Reactor,'' ASME J. Heat Transfer, **109**, pp. 928–935.
[4] Evans, G., and Greif, R., 1989, ''A Study of Traveling Wave Instabilities in a Horizontal Channel Flow with Applications to Chemical Vapor Deposition,'' Int. J. Heat Mass Transf., **32**, pp. 895–911.
[5] Evans, G., and Greif, R., 1993, ''Thermally Unstable Convection with Applications to Chemical Vapor Deposition Channel Reactors,'' Int. J. Heat Mass Transf., **36**, pp. 2769–2781.
[6] Evans, G., and Greif, R., 1994, ''A Two-Dimensional Model of the Chemical Vapor Deposition of Silicon Nitride in a Low-Pressure Hot-Wall Reactor Including Multicomponent Diffusion,'' Int. J. Heat Mass Transf., **37**, pp. 1535–1543.
[7] Evans, G. and Greif, R., 1995, ''Transport in Chemical Vapor Deposition Reactors: A Two-Dimensional Model Including Multicomponent and Thermal Diffusion, and Species Interdiffusion,'' *Proceedings of the ASME-JSME Thermal Engineering Joint Conference*, Vol. 4, ASME, New York, pp. 95–101.
[8] Lin, Y. T., Choi, M., and Greif, R., 1992, ''A Three-Dimensional Analysis of Particle Deposition for the Modified Chemical Vapor Deposition (MCVD) Process,'' ASME J. Heat Transfer, **114**, pp. 735–742.
[9] Patnaik, S., 1989, ''Modeling of Transport Processes in Chemical Vapor Deposition Reactors,'' Ph.D. thesis, Massachusetts Institute of Technology, Cambridge, MA.
[10] Wang, C. A., Groves, S. H., Palmateer, S. C., Weyburne, D. W., and Brown, R. A., 1986, ''Flow Visualization Studies for Optimization of OMVPE Reactor Design,'' J. Cryst. Growth, **77**, pp. 136–143.
[11] Wang, C. A., Patniak, S., Caunt, J. W., and Brown, R. A., 1988, ''Growth Characteristics of a Vertical Rotating-Disk OMVPE Reactor,'' J. Cryst. Growth, **93**, pp. 228–234.
[12] Patnaik, S., Brown, R. A., and Wang, C. A., 1989, ''Hydrodynamic Dispersion in Rotating-Disk OMVPE Reactors: Numerical Simulation and Experimental Measurements,'' J. Cryst. Growth, **96**, pp. 153–174.
[13] Moffat, H. K., and Jensen, K. F., 1988, ''Three-Dimensional Flow Effects in Silicon CVD in Horizontal Reactors,'' J. Electrochem. Soc., **135**, pp. 459–471.
[14] Jensen, K. F., 1989, ''Transport Phenomena and Chemical Reaction Issues in OMVPE of Compound Semiconductors,'' J. Cryst. Growth, **98**, pp. 148–166.
[15] Fotiadis, D. I., Boekhold, M., Jensen, K. F., and Richter, W., 1990, ''Flow and Heat Transfer in CVD Reactors: Comparison of Raman Temperature Measurements and Finite Element Model Predictions,'' J. Cryst. Growth, **100**, pp. 577–589.
[16] Fotiadis, D. I., Kieda, S., and Jensen, K. F., 1990, ''Transport Phenomena in Vertical Reactors for Metalorganic Vapor Phase Epitaxy,'' J. Cryst. Growth, **102**, pp. 441–470.
[17] Jensen, K. F., Einset, E. O., and Fotiadis, D. I., 1991, ''Flow Phenomena in Chemical Vapor Deposition of Thin Films,'' Annu. Rev. Fluid Mech., **23**, pp. 197–232.
[18] Jensen, K. F., Fotiadis, D. I., and Mountziaris, T. J., 1991, ''Detailed Models of the MOVPE Process,'' J. Cryst. Growth, **107**, pp. 1–11.
[19] Lie, K.-N., Merchant, T. P., and Jensen, K. F., 1993, ''Simulation of Rapid Thermal Processing Equipment and Processes,'' *Materials Research Society Symposium Proceedings*, Vol. 303, MRS, Pittsburgh, pp. 197–209.
[20] Kerker, M., 1969, *The Scattering of Light*, Academic Press, New York.
[21] Bohren, C. F., and Huffman, D. R., 1983, *Absorption and Scattering of Light by Small Particles*, Wiley, New York.
[22] Pitts, W. M., and Kashiwagi, T., 1984, ''The Application of Laser-Induced Rayleigh Light Scattering to the Study of Turbulent Mixing,'' J. Fluid Mech., **141**, pp. 391–429.
[23] Richards, C. D., and Pitts, W. M., 1993, ''Global Density Effects on the Self-Preservation Behavior of Turbulent Free Jets,'' J. Fluid Mech., **254**, pp. 417–435.
[24] Dibble, R. W., Hollenbach, R. E., and Rambach, G. D., 1980, ''Temperature Measurement in Turbulent Flames via Rayleigh Scattering,'' *Laser Probes for Combustion Chemistry*, D. R. Crosley ed., American Chemical Society, pp. 435–441.
[25] Horton, J. F., and Peterson, J. E., 1999, ''Transient Temperature Measurements in an Ideal Gas by Laser-Induced Rayleigh Light Scattering,'' Rev. Sci. Instrum., **70**, No. 8, pp. 3222–3226.
[26] Horton, J. F., IV, 1998, ''Transient Gas Temperature Measurements in a Rapid Thermal Chemical Vapor Deposition Reactor Using Rayleigh Light Scattering,'' M.S. thesis, Department of Mechanical Engineering, University of Florida.
[27] Pitz, R. W., Cattolica, R., Bobben, F., and Talbot, F., 1976, ''Temperature and Density in a Hydrogen-Air Flame From Rayleigh Scattering,'' Combust. Flame, **27**, pp. 313–320.
[28] Moffat, R. J., 1985, ''Using Uncertainty Analysis in the Planning of an Experiment,'' J. Fluids Eng., **107**, pp. 173–178.
[29] Karki, K. C., Sathyamurthy, P. S., and Patankar, S. V., 1993, ''Three-Dimensional Mixed Convection in a Horizontal Chemical Vapor Deposition Reactor,'' ASME J. Heat Transfer, **115**, pp. 803–806.
[30] Karki, K. C., Sathyamurthy, P. S., and Patankar, S. V., 1993, ''Laminar Flow Over a Confined Heated Disk: Effect of Buoyancy and Rotation,'' *Advanced Computations in Materials Processing*, ASME, New York, pp. 73–81.

Journal of
Heat Transfer

Technical Notes

This section contains shorter technical papers. These shorter papers will be subjected to the same review process as that for full papers.

Determination of the Effective Thermal Conductivity Tensor of Heterogeneous Media Using a Self-Consistent Finite Element Method: Application to the Pseudo-percolation Thresholds of Mixtures Containing Nonspherical Inclusions

A. Decarlis
M. Jaeger
R. Martin
IUSTI, CNRS UMR 6595, 5 rue E. Fermi, 13453 Marseille Cedex 13, France

This paper concerns the determination of the effective thermal conductivity of heterogeneous media with randomly dispersed inclusions. Inclusions of arbitrary shape can be considered since the self-consistent problem is solved numerically with the finite element method. Results for many different cases of heterogeneous media with axially symmetrical inclusions are presented. Moreover, the influence of the inclusion's shape on the pseudo-percolation threshold is investigated. [S0022-1481(00)00801-X]

Keywords: Composites, Conduction, Finite Element, Heat Transfer, Materials

1 Introduction

The composite industry faces the need for more global modelization methods in the field of conductive processes. Consequently, simple modelization tools for calculating the ability of a heterogeneous medium to transfer heat energy are required. Basically, a heterogeneous medium means the mixture of a host material (the matrix) with a smaller amount of another material (the inclusions). In this paper, we focus on two-phase heterogeneous media in which identical inclusions (same shapes, dimensions, and compositions) are randomly dispersed in the matrix. The case of ordered distributions of inclusions has been studied in many ways since Lord Rayleigh [1] in the 19th century. This work and the bounds of Wiener [2] have been the basis for many studies. Today, this class of problem is solved by the use of numerical methods, such as the periodic homogenization method which provides accurate results. The case of random distributions involves greater analytical difficulties. Indeed, due to the number of inclusions, the use of deterministic concepts is inadequate because it is clearly impossible to determine positions, orientations, and mutual interactions of all the inclusions in the matrix. Moreover, even if this were possible, it would be useless because it would be representative of one particular case only (one realization). Many methods have been developed to circumvent this problem. We may quote methods based on the ensemble average technique ([3–5]) or the volume average technique ([6–10]). The last one is more suitable for steady state conduction problems. Among the different methods based on the volume average technique, Landauer's self-consistent scheme is a very powerful one. This scheme has been widely presented and assessed ([10]) in the literature and a wide community of researchers find attractive features in it (e.g., very good balance between complexity and accuracy). Nevertheless, this scheme provides a complete analytical solution in the case of spheroidal inclusions only. We propose an improved method which allows the generalization of the self-consistent scheme by the use of a numerical method. Numerical resolution of the self-consistent problem was first chosen by Yang et al. [11] in 1994 for the computation of simple effective elastic properties of fibrous materials. Hereby we use it to compute the effective thermal conductivity tensor of two-phase heterogeneous medium containing inclusions of any shape, and to investigate the different pseudo-percolation thresholds.

This paper begins with the presentation of the dual general equations obtained with the volume average technique for the effective thermal conductivity tensor of a two-phase heterogeneous medium. To solve these equations requires the knowledge of averaged quantities which are estimated by the use of Landauer's self-consistent scheme. After Landauer's self-consistent scheme explanation, we describe the numerical model used to solve the problem exhibited in the first part. The self-consistent finite element method and its numerical properties are presented. Then as a validation, results obtained by the self-consistent finite element method in the case of spherical inclusions are compared to known results. At last, we present the numerical results that we obtained in the case of axially symmetrical inclusions. The influence of different parameters (such as the shape of the inclusions, their orientations, or their elongation ratio) on the effective thermal conductivity tensor of mixtures involving such inclusions is investigated.

2 Expressions of the Effective Thermal Conductivity

2.1 Description of the Problem. Consider a large two phase system of total volume V_{total} composed of a matrix phase whose thermal conductivity tensor is $\mathbf{k}^{(1)}$ and volume is $V^{(1)}$, and N identical inclusions, whose thermal conductivity tensor is $\mathbf{k}^{(2)}$ and total volume is $V^{(2)}$. The inclusions are assumed to be randomly dispersed in the matrix, and the medium is assumed to be statistically homogeneous ([12]). The volume fraction of inclusion is $v^{(2)}=V^{(2)}/V_{\text{total}}$. In what follows, both phases are assumed to be homogeneous and isotropic and are denoted by r. Thus both tensor quantities $\mathbf{k}^{(r)}$ $r=1,2$ reduce to scalars: $k^{(r)}$ $r=1,2$. Let

---

Contributed by the Heat Transfer Division for publication in the JOURNAL OF HEAT TRANSFER. Manuscript received by the Heat Transfer Division, Nov. 20, 1998; revision received, Sep. 9, 1999 Associate Technical Editor: Kaviany

$T(\mathbf{X})$ be the temperature field. It is continuous inside both phases and at each matrix-inclusion interface. The intensity and heat flux vector are defined as

$$\mathbf{H}^{(r)} = -\boldsymbol{\nabla} T^{(r)}(\mathbf{X}) \quad r=1,2 \tag{1a}$$

$$\mathbf{q}^{(r)} = k^{(r)}\mathbf{H}^{(r)} \quad r=1,2. \tag{1b}$$

Under the assumption of perfect thermal contacts between matrix and inclusions, continuity of both temperature and flux normal component is assumed at the interfaces. It is well known ([10]) that under the so-called homogeneous boundary conditions:

$$T(\mathbf{X}) = -\mathbf{H}^0 \cdot \mathbf{X} \quad \text{for} \quad \mathbf{X} \in S \tag{2a}$$

or

$$\mathbf{q}_n(\mathbf{X}) = \mathbf{q}^0 \cdot n \quad \text{for} \quad \mathbf{X} \in S \tag{2b}$$

where $\mathbf{H}^0$ and $\mathbf{q}^0$ are constant vectors. The components of the effective thermal conductivities tensor in the three principal directions may be written as

$$k_i^* = k^{(1)} + (k^{(2)} - k^{(1)}) \frac{\overline{H}_i^{(2)} v^{(2)}}{H_i^0} \quad i=1,2,3 \tag{3a}$$

$$\frac{1}{k_i^*} = \frac{1}{k^{(1)}} + \left(\frac{1}{k^{(2)}} - \frac{1}{k^{(1)}}\right) \frac{\overline{q}_i^{(2)} v^{(2)}}{q_i^0} \quad i=1,2,3 \tag{3b}$$

In Eq. (3a) (respectively, (3b)) the unknown quantity is $\overline{H}_i^{(2)}$ (respectively, $\overline{q}_i^{(2)}$) which represents the average intensity (respectively, heat flux) in the ith direction throughout phase (2).

2.2 Averaging Methods. The choice of the averaging method to compute $\overline{H}_i^{(2)}$ or $\overline{q}_i^{(2)}$ to be used in Eq. (3a) or (3b) strongly depends on the problem: Basically randomness in position requires a volume average, whereas randomness in orientation requires an angular one. Thus, if inclusions are spherical or absolutely nonsymmetrical, all directions are equivalent, then a volume average is used and the effective medium is isotropic with the scalar thermal conductivity k^*. If inclusions are axially symmetrical (such as cylinder, capsules, . . .) and are all oriented in the same direction, then a volume average is used and the effective medium is anisotropic. Finally, if inclusions are axially symmetrical and are randomly oriented, then both volume and angular averages are used ([13]). The effective medium is isotropic, and the effective thermal conductivities tensor reduces to the scalar thermal conductivity.

3 The Self-Consistent Finite Element Method

3.1 The Landauer Self-Consistent Scheme. Let us work with ''flux type'' homogeneous boundary conditions (Eq. (3b)). This equation provides a formulation for the effective thermal conductivities tensor of a heterogeneous medium with statistical homogeneity. The computation of each component k_i^* is possible if the average heat flux $\overline{q}_i^{(2)}$ in the ith direction inside the inclusion medium is known. This simple form is a function of the isotropic thermal conductivity of both materials $k^{(1)}$ and $k^{(2)}$, volume fraction of the inclusion medium $v^{(2)}$, and of the average heat flux $\overline{q}_i^{(2)}$. Nevertheless, exact calculation of the latter remains impossible because of the deterministic approach problems: Positions, orientations, and mutual interactions have to be known for each realization in order to solve Laplace's equation and then evaluate the average heat flux. However, the self-consistent scheme allows the computation of an approximate value for the averaged heat flux. Landauer's physical assumption is that the actual average heat flux in the whole inclusion medium (composed by all the identical inclusions) can be estimated by the heat flux computed inside a unique representative inclusion embedded in an infinite and homogeneous effective medium of unknown properties $\mathbf{k}^*$. This effective medium is supposed to be representative (in terms of its influence on the flux $\mathbf{q}^{(2)}$ inside the representative inclusion) of the surrounding of the inclusion inside the actual medium. This means that we must take into account the coupled influences of the other inclusions in the actual medium. In Landauer's self-consistent scheme, at infinite distance from the representative particle, a homogeneous boundary condition is prescribed. Thus the field inside the representative inclusion of the self-consistent problem is defined by the boundary value problem for an infinite homogeneous medium that contains one inclusion. Consequently, the intensity field inside the inclusion turns out to be uniform in the direction of the applied flux ([10]). If the same calculation is applied to each inclusion of the actual medium, the same uniform result is obtained, thus trivially giving the desired estimated average. This problem is known as the self-consistent problem. Practically, $q_i^{(2)}$ is obviously a function of the surrounding medium property k_i^*. The use of the expression $q_i^{(2)} = f(k_i^*)$ inside Eq. (3b) leads to an expression of k_i^* in terms of itself, which is the self-consistent equation. In the case of spherical inclusions, the self-consistent equation is a second-order equation. Entire analytical resolution of this problem exists for spheroidal inclusions only. For other kind of shapes, estimation of $\overline{q}_i^{(2)}$ by $q_i^{(2)}$ inside the representative inclusion can be directly achieved by the use of a numerical method, then skipping the analytical evaluation of the ''physical'' root of the self-consistent equation.

3.1.1 Pseudo-percolation Threshold. According to Landauer's theory, in the well-known case of spherical inclusions, a specific value of the volume fraction of inclusion $v^{(2)}$ causes the behavior of the mixture to completely change. As an example, a mixture constituted with an insulating matrix and spherical conductive inclusions is an insulator for a volume fraction of inclusion up to 33 percent, and changes to a conductor for bigger volume fraction. We call this threshold value the pseudo-percolation threshold. Some authors call it ''the poor man's percolation'' ([14]). Actually some numerical evidence using the percolation theory ([15]) shows that the ''real'' threshold is about 27 percent in the case of spherical inclusions. The percolation theory involves the use of advanced mathematical concepts such as fractals or renormalization methods. This method is very powerful for the exact determination of the percolation threshold, but it is valid in the close neighborhood of the threshold only. Inversely, the self-consistent finite element method will provide an estimation of the percolation threshold for nonspherical inclusions (the pseudo-percolation threshold) and values of the effective thermal conductivities tensor for the whole set of volume fraction of inclusions.

3.2 The Finite Element Model. In our work, a finite element method is used to compute the heat flux $\mathbf{q}^{(2)}$ inside the representative inclusion of the self-consistent problem. This extension of Landauer's self-consistent scheme allows the treatment of inclusions with nonsimple shapes. By this way, the computation of effective thermal conductivity of composites containing inclusions with complex shapes such as ''cardioids'' or dodecahedrons becomes possible. Coupling the self-consistent method with the finite element method gives birth to the self-consistent finite element method. In order to compute $\mathbf{q}^{(2)}$, a finite element discretization of the representative cell (which contains the representative inclusion) is done.

4 Numerical Model

4.1 Solution Algorithm. The determination of k_i^* using Eq. (3b) is a nonlinear problem (k_i^* has to be known to compute $q_i^{(2)}$), therefore an iterative process can be used to solve it. This process is initialized with an arbitrary value. Using the first value of k_i^*, the component of the heat flux along the ith direction ($q_i^{(2)}$) is computed and provides a new value for k_i^* and so on. The iterative process is stopped when the required precision (i.e., the difference between two successive values of k_i^*) is reached.

4.1.1 Restrictions of Both Formulations. It can be shown that the use of the iterative process implies restrictions for the application of the method. The ''temperature approach'' (Eqs. (2*a*) and (3*a*)) is applicable for the whole set of volume fractions of inclusion, in the cases where $\beta \geqslant 1$ only (i.e., $k^{(2)} > k^{(1)}$). If $\beta \leqslant 1$, the method provides a nonphysical root of the problem (e.g., negative root in the case of spherical inclusions). Inversely, the flux approach (Eqs. (2*b*) and (3*b*)) is applicable for the whole set of volume fractions of inclusion in the cases where $\beta \leqslant 1$ only (i.e., $k^{(2)} < k^{(1)}$). If $\beta \geqslant 1$, the method provides a nonphysical root of the problem (e.g., the negative root in the case of spherical inclusions). We have determined that these restrictions exist for any shape of inclusion. It would be interesting to investigate whether the use of other resolution methods for the nonlinear problem would cause the same type of restrictions.

4.2 Influence of the Boundary Locations. In Landauer's self-consistent scheme the surrounding medium of the self-consistent topology is assumed to be infinite and the heat flux, under homogeneous boundary conditions, inside the whole representative inclusion is assumed to be uniform in the direction of the applied flux. In the numerical model the same constraint must be assigned. In the finite element model, the surrounding medium cannot be infinite, then the relative size of inclusion to the surrounding medium has to be such that, under homogeneous boundary conditions, the heat flux inside the inclusion medium turns out to be uniform. Numerically, all the elements comprising the representative inclusion must provide the same flux in the direction of the applied flux. A simple criterion for obtaining an acceptable grid is to minimize the variance of the flux over the ensemble of all elements constitutive of the inclusion. When the variance is minimized, the representative grid is accepted.

4.3 Sensitiveness of the Self-Consistent Finite Element Method to the Grid Density. When the relative size is chosen, the sensibility of the method to the grid refinement has to be investigated. We have focused on the relative errors between the analytical solution of the self-consistent problem with spherical inclusions ([10]), and the self-consistent finite element method for more and more refined grids. We have determined that the reduction of the error is achieved by increasing the density of the grid. We finally chose a grid built with 432 elements. The selected grid allows an error of two percent compared with the analytical solution for a mixture containing five percent of spherical inclusions, and a thermal contrast equal to 10^5. This choice optimizes the balance between computational time and precision. In the case of spherical inclusions, the self-consistent finite element method provides an accurate solution for a small number of elements. In the following parts dealing with spherical inclusions, we will always refer to the mean dense grid (432 tetrahedral elements).

4.4 Numerical Properties. The self-consistent finite element method computation process is convergent. The final value computed by the iterative process is obviously independent of the initial value. Nevertheless, the processing time depends on it: When the initial solution is chosen as one of the bounds of Wiener, the iterative process is longer than in the case of a more refined mixture law (e.g., Maxwell). We have determined the number of iterations needed to compute the effective thermal conductivity as a function of the volume fraction of inclusion for different thermal contrasts. For a fixed precision, the behavior of the number of iterations is strongly related to the thermal contrast and to the neighborhood of the pseudo-percolation threshold. For strong contrast, near the pseudo-percolation threshold, this number becomes very big (about 1000 iterations in extreme cases). In such a case, the processing time is about 5 hours and 30 minutes on a typical workstation (CPU frequency is 250 MHz and RAM is 64 MB). It can be shown that this behavior derives directly from the use of the iterative process.

5 Quality of the Computed Solution

As a first validation, the results obtained with the self-consistent finite element method have been compared to the analytical solution described by Landauer in the case of spherical inclusions. We have shown that the level of the error between computations and analytical solution is increasing with the contrast and with the proximity of the pseudo-percolation threshold.

For the general case, few comparative studies of the different methods used for the computation of effective properties do exist. Among them, a study achieved in the domain of electrical conduction of mixtures by Banhegyi [16] is of prime interest. In this study, we find the description of many EMT and the comparison of the predicted values with experimental data. Obviously, Landauer's self-consistent scheme is investigated and, according to the author, this method provides very good results in a wide variety of cases, including systems containing spherical, rods, or lamellae. The range of the average error between analytical solutions of Landauer's self-consistent scheme and experimental data is very weak (maximum value is comprised between 0.36 percent and 2.43 percent). Thus we can say that this method is an effective method to compute effective thermal conductivity of mixtures.

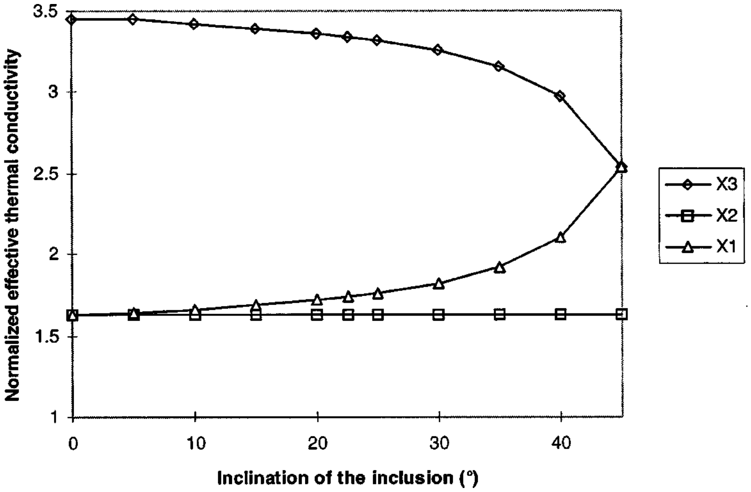

Fig. 1 Influence of the group orientation of a mixture of cylinders on the effective normalized thermal conductivity in the three principal directions ($\beta = 10^5$, $v^{(2)} = 15$ percent, $\gamma = 2$)

The remaining errors between Landauer's self-consistent scheme results and the experimental data can be assigned to different facts: inclusions may not be exactly of the prescribed shape, mixtures may be not perfect (other inclusions such as air may be present in the mixture), and self-consistent finite element method is not adequate near the pseudo-percolation threshold.

6 Numerical Results for Heterogeneous Media With Axially Symetrical Inclusions

6.1 Case of Cylindrical Inclusions Orientated in the Direction of the Heat Flux. To the best of our knowledge, no exact analytical solution exists for the case of cylindrical inclusions with finite dimensions (the case of long cylindrical fiber can be approximated with the use of ellipsoidal coordinates system ([17])). In what follows, the effective thermal conductivity is no longer isotropic. In this section, we investigate the behavior of the effective thermal conductivity along the x_3-axis (vertical axis) for mixtures containing cylinders aligned along this axis, which is also the direction of the applied flux. The cylinders that we studied present an elongation ratio equal to 2. The elongation ratio γ is defined as the ratio of its total height to its diameter. We have computed the effective thermal conductivities in the direction of the applied flux (x_3) for mixtures containing cylindrical inclusions. We have noticed a deviation of the pseudo-percolation threshold compared to the case of spherical inclusions. This deviation exists for every contrast. In the case of cylindrical inclusions aligned with the heat flux and randomly dispersed in the matrix, the pseudo-percolation threshold is about 15 percent. The deviation of the pseudo-percolation threshold in the case of cylindrical inclusions compared to the one obtained with spherical inclusions can be understood with the help of the percolation theory. This one is concerned with the determination of parameters which govern the creation of a conductive path through an insulating matrix. It is easy to understand that such a path is easier to obtain with conductive cylindrical inclusions aligned with the heat flux, than with spheres.

6.2 Case of Cylindrical Inclusions With a Group Orientation. In order to show the influence of group orientations of axially symmetrical inclusions, simulations have been completed for the whole set of angle α, which denotes an inclination in the (Ox_1, Ox_3) plane, where x_3 denotes vertical axis, x_1 denotes horizontal axis, and x_2 denotes transverse axis. In Fig. 1 we show the evolution of the effective normalized thermal conductivity (defined as the ratio of the effective conductivity to the conductivity of the matrix for a fixed direction: k_i^*/k_1) in the three principal directions for such a medium. We investigated the cases of mixtures with $\beta=10^5$, $v^{(2)}=15$ percent, and $\gamma=2$.

The effective normalized thermal conductivity increases along the x_1-axis and decreases along the x_3-axis for inclinations between 0 deg and 45 deg. These results have a physical meaning: The thermal conductivity of a mixture is maximized when both materials are arranged in slabs parallel to the heat flux ([2]). In our case, the biggest effective thermal conductivity along the x_3-axis corresponds to the case of vertical cylinders (parallel to the prescribed heat flux). The same reasoning can be made with the effective thermal conductivity along the x_1-axis: The effective thermal conductivity increases in the x_1-direction as the inclination of cylinders α increases. As expected, the effective thermal conductivity along the x_2-axis is independent of the inclination in the (Ox_1, Ox_3) plane.

6.3 Influence of the Elongation Ratio. In order to characterize axially symmetrical inclusions, we investigate the influence of the elongation ratio (sometimes named shape factor). We investigate two types of inclusions: cylinders and capsules. Capsule type inclusion is obtained when adding a half-sphere (of the same radius as the cylinder) at each base of the cylinder. We compare cylinders and capsules with the same total height and radius. Figure 2 presents the normalized effective thermal conductivity (along the x_3-axis) k_3^*/k_1 obtained by the self-consistent finite element method for cylinders and capsules aligned in the direction of the applied flux, for different elongation ratio. The computations have been achieved for mixtures with $\beta=10^5$.

The slopes of the curves exhibit an acceptable behavior: The elongation of both cylinders and capsules is increasing when the height is increasing (i.e., h/d is increasing, d is constant). In that case, the effective conductivity is increasing too. For the same elongation ratio, the "capsule" type inclusions do not imply a higher conductivity for the mixture. This can be understood using the "percolation reasoning." Consider a distribution of aligned cylinders, the possible contacts between such inclusions are lines (contacts between the lengths) and intersections of circles (contacts between extremities). For a distribution of aligned capsules (with the same value of γ), the contacts are lines—smaller than in the case of cylinders—(contacts between the lengths) and points (contacts between two spherical extremities). Thus the total possible contacts between aligned particles are smaller in the case of the capsule than in the case of the cylinder and, consequently, a conductive path is easier to appear in the case of the cylinder than in the case of the capsule.

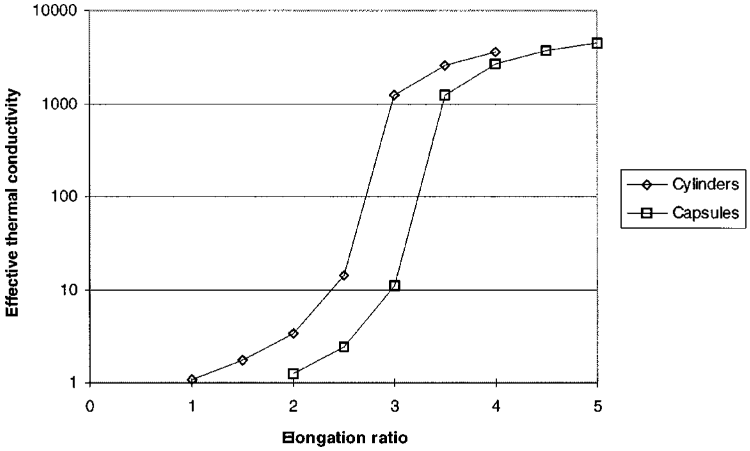

Fig. 2 Influence of the elongation ratio on the effective normalized thermal conductivity of mixtures of cylinders or capsules aligned with the applied flux ($\beta=10^5$, $v^{(2)}=15$ percent)

6.4 Pseudo-percolation Threshold for Nonspherical Inclusions.

The use of Landauer's self-consistent scheme exhibits the existence of a pseudo-percolation threshold in the case of spherical inclusions. The use of the self-consistent finite element method allows the computation of this threshold for any kind of inclusion. We define here two types of inclusions: Oblate (respectively prolate) spheroids are obtained when stretching a sphere along the direction of the flux (respectively, in both transverse directions: x_1 and x_2-axis). We have computed the different effective thermal conductivities and the pseudo-percolation threshold for different types of spheroidal inclusions (defined by the value of γ) oriented along the direction of the applied flux. We investigated the cases of mixtures with $\beta = k^{(2)}/k^{(1)} = 10^5$. A very good agreement is found with the analytical solutions ([18]): for example, the computed pseudo-percolation threshold for oblate spheroids with shape factor equal to 2 is 17 percent. In the same way, the computed pseudo-percolation threshold for prolate spheroids with shape factor equal to 0.5 is 52 percent. Both values are equal to the analytical solutions. We have also investigated the influence of the group orientation of cylindrical inclusions on the pseudo-percolation threshold. The influence of this parameter is not very important: as the angle α changes from 0 deg to 40 deg the change of the percolation threshold is smaller than three percent. The increase of the group orientation angle α of the randomly dispersed cylinders causes the effective thermal conductivity to exhibit a pseudo-percolation threshold nearer to the one for spherical inclusions. However, the influence of this parameter seems not to be preponderant with this type of inclusion.

6.5 Material With Randomly Oriented Inclusions.

In the case of axially symmetrical inclusions (cylinder, capsule, spheroid) randomly dispersed and randomly oriented, it is shown ([13]) that the randomness in orientation imposes the use of an orientation average in addition to the volume average. This can be analytically stated in the case of spherical or ellipsoidal inclusions. However, this average is generally out of reach for other shapes: From a numerical point of view, this computation may involve some problems. One simple solution is to use a distribution function for the orientation of the particle ([17]). Let $\rho(\theta,\varphi)$ be the normalized function of both angles on the spherical coordinate system. The function is defined as the number of (symmetrical) inclusions that intersect a fictitious unit sphere for a given set of angles (θ_0,φ_0). In other words this function defines the probability for one given particle to be oriented along the direction defined by (θ_0,φ_0). If $\rho=\rho_0$, where ρ_0 is a normalization factor, the angular distribution is uniform. All orientations have the same probability. In that case, the weighting is equivalent to a simple arithmetical average. Thus we may use the values obtained in Section 6.2 to compute the normalized effective thermal conductivities of a medium with randomly dispersed and randomly orientated (in the (Ox_3,Ox_1) plane) cylindrical inclusions. The different averages of the values obtained for inclinations from 0 deg to 90 deg in the plane (Ox_3,Ox_1) provide: $k_3^*/k^{(1)} = k_1^*/k^{(1)} = 2.54$ and $k_2^*/k^{(1)} = 1.63$. Although these values cannot be directly compared to an analytical solution, we can find a quantitative justification for these results. In the case of absolutely randomly dispersed and oriented spheroidal inclusions (with elongation equal to 2) the analytical normalized effective thermal conductivity is equal to 2.13. As we have noticed before, mixtures containing capsules or oblate spheroids are less conductive than mixtures containing cylinders, thus this result finds justification to a certain extent.

7 Conclusion

The self-consistent finite element method has been presented in a general way in order to allow the determination of effective conductive properties of heterogeneous media. This method is original because it mixes an old physical idea (equivalence of the solution of the self-consistent problem with the solution of the actual problem) and a modern numerical method (the finite element method). The latter brings its power to solve problems that were unsolvable up to now. The self-consistent finite element method is very simple to use since a finite element code is owned and the computational time on a standard workstation is insignificant. The use of the self-consistent finite element method in the thermal domain allows one to quickly compute the effective isotropic or anisotropic thermal conductivities tensor of heterogeneous media with inclusions of any shape. Another important feature is the ability to exhibit the pseudo-percolation threshold for any kind of two-phase mixture and to predict its behavior as a function of different parameters.

Acknowledgment

This work was carried out with the support of the DGA (Délégation Générale pour l'Armement) French Ministry of Defense.

References

[1] Lord Rayleigh, 1892, ''On the Influence of the Obstacles in Rectangular Order Upon the Properties of a Medium,'' Philos. Mag., **134**, pp. 481–502.
[2] Wiener, O., 1912, Abh. Sächs. Ges. (ahad) Wiss., **32**, p. 509.
[3] Buyevich, Y. A., 1974, ''On the Thermal Conductivity of Granular Material,'' Chem. Eng. Sci., **29**, pp. 37–48.
[4] Buyevich, Y. A., 1992, ''Heat Mass Transfer in Disperse Media-I, II,'' Int. J. Heat Mass Transf., **35**, pp. 2445–62.
[5] Furmañski, P., 1997, ''Heat Conduction in Composites: Homogenization and Macroscopic Behavior,'' Appl. Mech. Rev., **50**, p. 327.
[6] Bruggeman, D. A. G., 1935, ''Berechnung Verschiedener Physikalischer Konstanten Von Heterogenen Substanzen,'' Ann. Phys. (Paris), **24**, p. 636.
[7] Landauer, R., 1952, ''The Electrical Resistance of Binary Metallic Mixtures,'' J. Appl. Phys., **23**, p. 779.
[8] Kerner, E. H., 1956, ''The Electrical Conductivity of Composite Media,'' Proc. Phys. Soc. B, **69**, p. 802.
[9] Hashin, Z., and Shtrikman, S., 1962, ''A Variational Approach to the Theory of the Effective Magnetic Permeability of Multiphase Materials,'' J. Appl. Phys., **33l**, p. 3125.
[10] Hashin, Z., 1968, ''Assessment of the Self Consistent Scheme Approximation: Conductivity of Particulate Composites,'' J. Comp. Mat., **2**, pp. 284–300.
[11] Yang, Q. S., Tang, L., and Chen, H., 1994, ''Self-Consistent Finite Element Method: A New Method of Predicting Effective Properties of Inclusion Media,'' Finite Elem. Anal. Design, **17**, pp. 247–257.
[12] Batchelor, G. K., 1974, ''Transport Properties of Two-Phase Materials With Random Structure,'' Annu. Rev. Fluid Mech., **6**, p. 227.
[13] Miloh, T., and Benveniste, Y., 1988, ''A Generalized Self-Consistent Method for the Effective Conductivity of Composites With Ellipsoidal Inclusions and Cracked Body,'' J. Appl. Phys., **63**, pp. 789–796.
[14] Landauer, R., 1978, ''Electrical Conductivity in Inhomogeneous Media,'' *Electrical, Transport and Optical Properties of Inhomogeneous Media*, Garland & Tanner, eds., American Institute of Physics, New York, Vol. 99.
[15] Clerc, J. P., et al., 1983, ''La Percolation: Modèles, Simulations Analogiques et Numériques,'' Ann. Phys., **8**, pp. 1–108.
[16] Banhegyi, G., 1986, ''Comparison of Electrical Mixture Rules for Composites,'' Colloid Polym. Sci., **264**, pp. 1030–1050.
[17] Hatta, H., and Taya, M., 1985, ''Effective Thermal Conductivity of Misoriented Short Fiber Composite,'' J. Appl. Phys., **58**, pp. 2478–2486.
[18] Polder, D., and Van Santen, J. H., 1946, ''The Effective Permeability of Mixtures of Solids,'' Physica XII, **5**, p. 257.

An Experimental Investigation of Natural Convection in a Cubic Inclined Enclosure With Multiple Isolated Plates

Q. W. Wang[1]
e-mail: wangqw@xjtu.edu.cn

W. Q. Tao
e-mail: wqtao@xjtu.edu.cn

School of Energy and Power Engineering, Xi'an Jiaotong University, Xi'an, Shaanxi 710049, P.R. China

Z. Lin
e-mail: bsjzl@cityu.edu.hk

T. T. Chow
e-mail: bsttchow@cityu.edu.hk

Division of Building Science & Technology, City University of Hong Kong, Kowloon, Hong Kong

Natural convection in a cubic inclined enclosure with three isolated plates was investigated experimentally. The influences of the plates' spacing, the inclination angles of the enclosure, and the Rayleigh number on the heat transfer of the plate group were obtained. It was found that under a fixed Rayleigh number, there is a plate spacing at which the heat transfer rate of the three plates is approximately the same for the horizontal plate group. Under the range of Rayleigh numbers considered, the heat transfer rate of the plate group is less than that of the natural convection of the plate group in infinite space. The heat transfer rate of the plates increases with the plate inclined angle tilting from $\theta=90$ deg to $\theta=0$ deg, with the most steep increase occurring in the range of $\theta=90$ deg to 45 deg. A global correlation of the heat transfer results for all the inclination between 0 deg and 60 deg can be obtained as $Nu_{l,m}=0.5360(Ra_l \cos\theta)^{0.25}$ with a spread of ±8.9 percent. [S0022-1481(00)00501-6]

Keywords: Enclosure Flows, Experimental, Heat Transfer, Natural Convection, Steady

Introduction

Natural convection in an enclosure with isolated bodies is encountered in a number of practical applications. It has motivated a large body of experimental and analytical studies of this topic ([1–4]). However, while many studies have been performed on the heat transfer characteristics of the enclosure itself or one or two inner isolated bodies, a literature survey indicates that there has been relatively little work on the heat transfer of enclosure with multiple isolated plates and the effects of inclination of the enclosure, which can be used to simulate the arrangement of components for electronic devices.

Natural convective heat transfer between two parallel isothermal plates and their cubic isothermal enclosure has been studied by Symons et al. [4]. The two heated plates were allowed to be installed in any position or orientation inside the cubic enclosure. They found that both the presence of the enclosure and the elevation of the heated plates inside the enclosure had little effect on the overall convective heat transfer rates of the heated plates. Yang and Tao [5] found that the difference between the average Nusselt numbers of a vertical plate in a confined space and in the infinite space becomes large with increasing Rayleigh number. Sparrow and Charmchi [1] experimentally studied the natural convection in the enclosed space between two vertical cylinders with Rayleigh number ranged between 1.5×10^3 and 1.5×10^5. They found that the average Nusselt number was nearly independent of both the elevation and eccentricity of the inner cylinder.

The present work is aimed at studying the heat transfer characteristics of the multiple plates in enclosure inclined from the vertical ($\theta=0$ deg) to the horizontal ($\theta=90$ deg) positions (see Fig. 1). The boundaries of the plate group (heated surfaces) and their enclosure (cooled surfaces) were isothermal under two different temperatures. Rayleigh number based on the plate length (l) ranged from 1.86×10^4 to 2.31×10^7. The effects of the enclosure inclination, the plate spacing, and Rayleigh numbers on the plate group overall convective heat transfer and their individual characteristics were parametrically studied.

Experimental Apparatus and Procedures

The experimental arrangement, shown schematically in Fig. 1, consisted of a test enclosure, pressure box, heated plates, thermostat (water bath), and data acquisition system. The dimensions of the cube enclosure were 300 × 300 × 300 mm. The six inner walls of the enclosure, made up of aluminum, were cooled and kept isothermal (at a constant value about 30°C) to within 0.2 K by a water bath during the entire experimental period. The three heated plates were also made up of aluminum, with dimensions of 100 × 100 × 6 mm (Fig. 1). Aluminum was chosen for its high thermal conductivity. The plates were fixed in the enclosure by thin copper wires of 0.5-mm o.d. The distances between the plate group and the enclosure are adjustable along the vertical direction when $\theta=90$ deg. In the present study, the dimensionless spacing s/l varied from 0.2 to 0.9. The three plates were heated by supplying electrical currents to the resistance wires, which were sandwiched and electrically isolated in each heated plate. The power supply for each plate could be adjusted individually. All temperature data were taken by means of copper-constantan thermocouples (calibrated ±0.2 K) and logged through a computer-driven multichannel data acquisition unit. There were six thermocouples imbedded in the six inner walls of the enclosure and four thermocouples in the walls of each plate. All the thermocouples were electrically isolated. The measurement uncertainty due to the thermocouples is ±0.2 K. In order to minimize the effect of radiation heat transfer between the surfaces of enclosure and the heated plates, all inner surfaces of the enclosure and the heated plates were covered with thin aluminum foil, of which the emissivity is about 0.073. The temperatures of the heated plates were monitored on a PC, and the power input to each plate was adjusted and monitored to maintain each plate at the same desired constant temperature, that is, the temperatures of the three plates were approximately equal during the experimental procedure. The test plates and their enclosure were fixed in a larger pressure box, which was placed on a support stem and the inclination can be set with the stem. The test plates and their enclosure were inclined together with the pressure box (Fig. 1).

The power input to the aluminum heated plates was dissipated by radiation and convection. Since the thermal resistance of the plate material was very low, the plates were expected to be virtually isothermal. The three plates' resistance was connected in parallel to obtain three independent power supplies. The degree of uniformity of the surface temperature were checked by comparing the independent readings obtained in different spots of the plates.

---

[1] Corresponding author.

Contributed by the Heat Transfer Division for publication in the JOURNAL OF HEAT TRANSFER. Manuscript received by the Heat Transfer Division, Jan. 30, 1999; revision received, Sep. 17, 1999. Associate Technical Editor: M. Hunt.

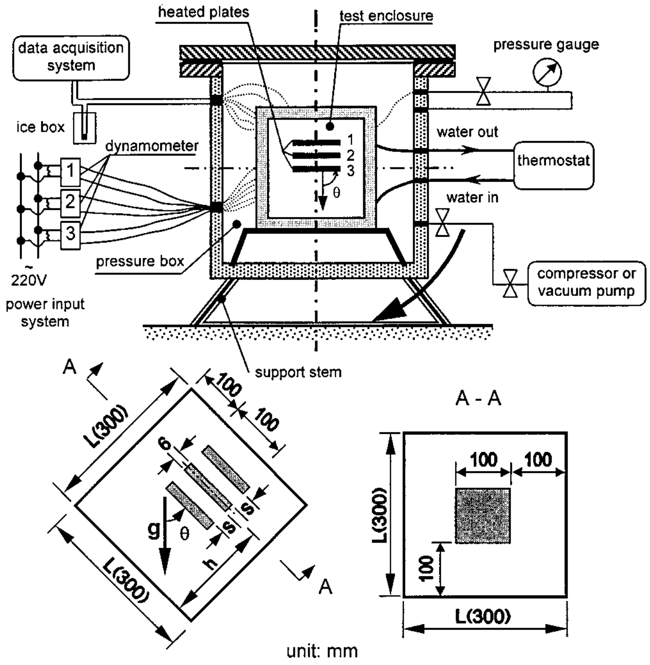

Fig. 1 Schematic diagram of the experimental apparatus and the enclosure

For all the experimental runs, the temperature readings were uniform within ±2 percent of the mean plates-to-walls temperature difference.

It was reported that the Rayleigh number is proportional to the square of pressure, i.e., p^2, when the pressure of the air is below 10 atm ([4,5]). Therefore, the range of Rayleigh number can be enlarged greatly by installing the experimental rig in a pressured box. During the experimental procedure, the enclosure and the pressure box had the same desired pressure. In the present study, the absolute pressure of the enclosure varied from 1580 Pa to 261 kPa.

After the warming-up period, power was supplied to the heating circuits, and the attainment of the steady-state condition was verified by monitoring selected plate thermocouples. In all cases, 2–2.5 h were sufficient for reaching the steady state. The wall and fluid temperatures and the heat power input were read and recorded after the temperatures of both heated plates and the enclosure inner walls were confirmed to be constant.

Data Reduction

The objective of the data reduction was to calculate the Nusselt and Rayleigh numbers, both individual and overall for the heated plates. The electric power dissipated in the heated plates was measured to determine the total heat transfer rate of the plates, which represented both radiative and convective heat losses. The net convective heat transfer rate Q_{conv} exchanged with the air in the enclosure is based on the following equations:

$$Q_{\text{conv}}=Q_{\text{tot}}-Q_{\text{rad}} \tag{1a}$$

$$Q_{\text{conv}}(i)=Q_{\text{tot}}(i)-Q_{\text{rad}}(i) \quad (i=1,2,3) \tag{1b}$$

$$Q_{\text{conv}}=\sum_{i=1}^{3} Q_{\text{conv}}(i), \quad Q_{\text{tot}}=\sum_{i=1}^{3} Q_{\text{tot}}(i), \quad Q_{\text{rad}}=\sum_{i=1}^{3} Q_{\text{rad}}(i) \tag{1c}$$

where Q_{tot} and Q_{rad} are the total heat loss and the radiative heat transfer rate, respectively, and $i=1,2,3$ represents each of the three heated plates (Fig. 1). Q_{tot} was measured experimentally, while Q_{rad} was obtained by network method ([6]). In the present study, the radiative heat transfer rate varied from 6 percent to 45 percent of the total heat transfer rate.

The individual convective heat transfer coefficients for the three heated plates and their overall-average value were defined as

$$\begin{aligned} h_1&=Q_{\text{conv}}(i)/A_i(T_{\text{hi}}-T_c) \quad (i=1,2,3) \\ h_m&=Q_{\text{conv}}\Big/\sum_{i=1}^{3} A_i(T_h-T_c) \end{aligned} \tag{2}$$

where $A_i(i=1-3)$ are the surface areas of the three heated plates, and T_h and T_c are the average temperatures of the three heated plates and six inner walls of the enclosure, respectively.

The Nusselt numbers of the plates and their overalls based on the plate length l and the spacing s between plates (Fig. 1) were calculated by

$$Nu_{s,i}=h_i s/k \quad (i=1,2,3) \quad Nu_{s,m}=h_m s/k \tag{3a}$$

$$Nu_{l,i}=h_i l/k \quad (i=1,2,3) \quad Nu_{l,m}=h_m l/k. \tag{3b}$$

The Rayleigh numbers based on plate length l or spacing s, respectively, were defined as follows using the ideal gas equation of the state for air:

$$\begin{aligned} \text{Ra}_l&=Cp^2 g\beta(T_h-T_c)c_p l^3/\mu k \\ \text{Ra}_s&=Cp^2 g\beta(T_h-T_c)c_p s^3/\mu k \end{aligned} \tag{4}$$

where $C=1/(RT_m)^2$.

The thermophysical properties in the Nusselt and Rayleigh numbers were evaluated at the reference temperature defined by

$$T_m=\left(\sum_{i=1}^{3} T_{\text{hi}}A_i+\sum_{j=1}^{6} T_{cj}A_j\right)\Big/\left(\sum_{i=1}^{3} A_i+\sum_{j=1}^{6} A_j\right) \tag{5}$$

where $A_j(j=1\sim 6)$ are surface areas of the six inner walls of the enclosure.

The uncertainties of the main quantities obtained from the experimental investigation were estimated (at the 95 percent confidence level) according to the procedure outlined by Moffat [7]. Uncertainties in Rayleigh and Nusselt numbers turned out to be 6.3 percent and 3.2 percent, respectively, at high Rayleigh numbers. At low Rayleigh numbers with relatively small temperature difference, the uncertainties could be up to 9.2 percent and 7.4 percent for Rayleigh and Nusselt numbers, respectively.

Results and Discussion

Results of Vertical Plate Group Results (θ=0 deg). Nusselt number results for the vertical plate group ($\theta=0$ deg) are plotted

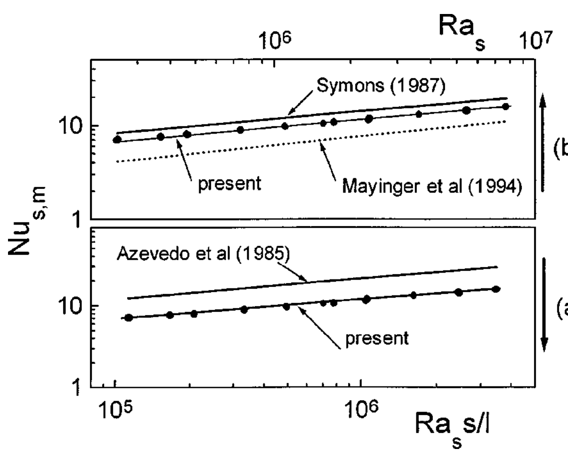

Fig. 2 Nusselt number against Rayleigh number of the vertical plate group

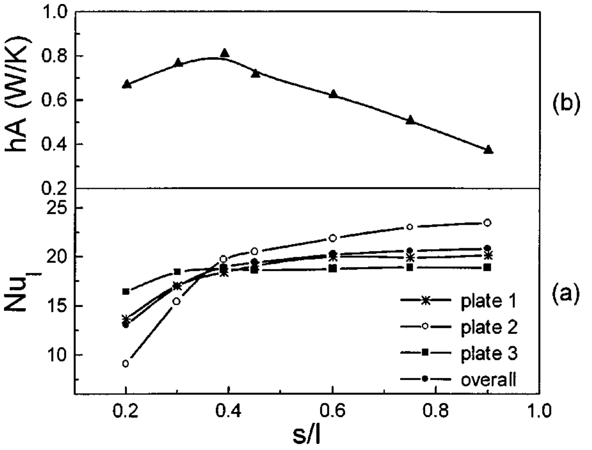

Fig. 3 Effect of s/l on the horizontal plates' heat transfer

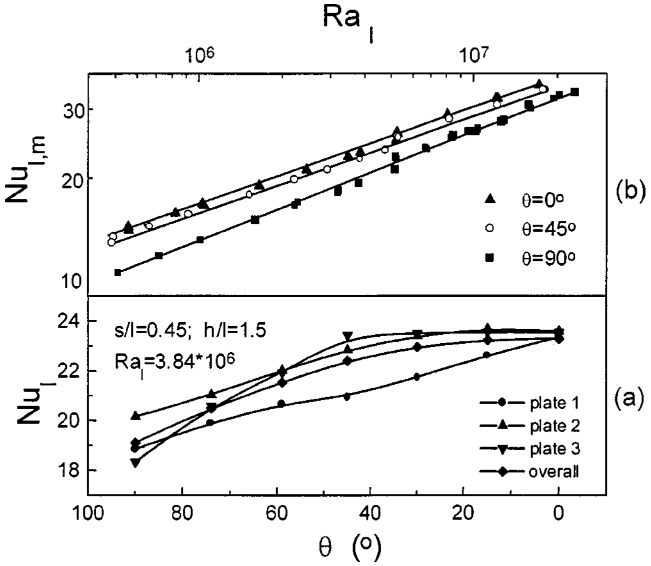

Fig. 4 Effect of inclination angle on the plates' heat transfer

Table 1 Constants m, n for Eq. (6) and the maximum deviations

θ (deg)	m	n	Maximum deviation (percent)	Range of Ra_l
0	0.5431	0.2491	2.4	$5.57\times10^5-1.73\times10^7$
	0.5360	0.25	2.59	
45	0.5461	0.2465	3.28	$4.86\times10^5-1.8\times10^7$
	0.5187	0.25	4.27	
90	0.3625	0.2654	4.44	$1.86\times10^5-2.31\times10^7$
	0.4541	0.25	7.29	

in Fig. 2 ($s/l=0.45$, $h/l=1.5$, that is, plate 2 is at the center of the enclosure, Fig. 1). In order to compare with the data in the references, the overall Nusselt number based on s, $Nu_{s,m}$, are shown as function of $\mathrm{Ra}_s s/l$ (Fig. 2(*a*)) or Ra_s (Fig. 2(*b*)). As shown in Fig. 2(*a*), the overall heat transfer of the plate group bounded in an enclosure were about 40 percent less than the plates in the infinite space ([8]). The present results for vertical plate group are also compared with those performed by Mayinger et al. [9] and Symons et al. [4], which are shown in Fig. 2(*b*). It is not surprising that there are discrepancies between the present results and the results of Mayinger and Symons, since the enclosure dimensions are different in the three cases. It was reported by Warrington et al. [3] that the enclosure dimensions have a significant effect on the temperature profile and the heat transfer results.

Results of Horizontal Plate Group Results (θ=90 deg). Attention is now turned to the horizontal plate group. By fixing the location of plate 2 at the center of the enclosure, the effects of the dimensionless spacing s/l on the Nusselt numbers based on the characteristic length l, were determined and shown in Fig. 3. From Fig. 3(*a*), it can be seen that there is a range of spacing over which the Nusselt numbers for the three plates are approximately equal. If the heat transfer at plate 2 is assumed to be the representative (i.e., it could be used to represent the heat transfer data of each plate for multiple-plates conditions), there may exist an optimal plate spacing s_{opt}, for maximizing the heat transfer rate for the plate group in the enclosure. This is because although heat transfer at each plate decreases with a decrease of s, the number of plates that may be placed in the prescribed volume (the enclosure) increases. Hence s_{opt} maximizes the heat transfer by yielding a maximum product of the heat transfer coefficient h and the plates total surface area A. The corresponding hA at different plate spacing s/l was calculated according to the test data and shown in Fig. 3(*b*). It can be seen that the total heat transfer rate reaches a maximum when s/l is at about 0.4. This finding is significant for determining a proper spacing of electronic components or ports in order to extend their service life when they have to be placed horizontally.

Effect of Inclination. Attention is now directed at the results for the effect of inclination. The Nusselt number results based on the length of the heated plate l were plotted in Fig. 4. Experiments were performed at seven different angles of inclination θ with respect to the vertical ($\theta=0$ deg, 30 deg, 45 deg, 60 deg, 75 deg, and 90 deg). From Fig. 4(*a*), where $\mathrm{Ra}_l=3.84\times10^6$ and $s/l=0.45$, $h/l=1.5$, it was found that all the individual and overall Nusselt numbers of the plate(s) increased with the decrease in θ from 90 deg to 0 deg (i.e., the plate group shifts from a horizontal to a vertical position). Furthermore, the steepest increase occurs in the range of $\theta=90$ deg–45 deg. If the plate is tilted away from the vertical position, the component of the buoyancy, which is parallel to the plate, is reduced from g to $g\cos\theta$. Since $\cos\theta$ varies from 1 to 0.707 between $\theta=0$ and 45 deg and from 0.707 to 0 between $\theta=45$ and 90 deg, the impact of the buoyancy on the fluid varies more rapidly between $\theta=45$ and 90 deg than that between $\theta=0$ and 45 deg.

At three different inclinations of 0, 45, and 90 deg, the overall Nusselt number versus Ra_l is plotted in Fig. 4(*b*). As expected, it was found that the heat transfer coefficient for $\theta=45$ deg was closer to that for $\theta=0$ deg than to that for $\theta=90$ deg.

Heat Transfer Correlation. As shown in Fig. 4(*b*), the dependence of the overall Nusselt number for the heat plate group as a function of Ra_l may be expressed as

$$\mathrm{Nu}_{l,m}=m\mathrm{Ra}_l^n. \tag{6}$$

For the three inclinations (θ=0 deg, 45 deg, and 90 deg), the constants m and n and the ranges of Ra_l are listed in Table 1 with the maximum deviations. As found from Table 1, the correlation equation exponent is close to the commonly accepted value of 0.25 for laminar natural convection. A second set of equations was then obtained using the exponent of 0.25. The corresponding results are also tabulated in Table 1.

It is known that for the inclined plate in the infinite space, the convection coefficients could be determined from the vertical plate correlation by replacing g with $g\cos\theta$ in computing the plate Rayleigh number for $0\ \mathrm{deg}\leqslant\theta\leqslant60$ deg ([6]). Based on this, the present heat transfer results for $s/l=0.45$ and $0\ \mathrm{deg}\leqslant\theta\leqslant60$ deg for all Rayleigh numbers could be correlated by the following equation with a maximum deviation of 8.9 percent:

$$\mathrm{Nu}_{l,m}=0.5360(\mathrm{Ra}_l\cos\theta)^{0.25}. \tag{7}$$

Conclusion

In general, within the range of Rayleigh numbers considered, heat transfer rate of the plates in an enclosure is less than that for plates in infinite space. The heat transfer for the vertical plate group bounded in the present enclosure was about 40 percent less than that for the same vertical plates in an infinite space. For the horizontal plate group, there is an optimal plate spacing s_{opt} at which the multiple plates have identical Nusselt number and the total heat transfer rate of the plate group reaches a maximum. The heat transfer rate of the plate group increases with a decrease of inclination from $\theta = 90$ deg (horizontal) to $\theta = 0$ deg (vertical), and with the steepest increase occurring in the range of $\theta = 90$ deg$-$45 deg. A global correlation of the heat transfer results for all the inclination between 0 deg$\leqslant \theta \leqslant$60 deg can be expressed as $\text{Nu}_{l,m} = 0.5360(\text{Ra}_l \cos\theta)^{0.25}$ with a spread of ±8.9 percent.

Acknowledgment

Support from the National Natural Science Foundation of China is gratefully acknowledged.

Nomenclature

A = surface area, m^2
c_p = specific heat, J/Kg K
C = constant in Eq. (4)
g = acceleration of gravity, 9.81 m/s^2
h = distance between the central of plate 2 and the enclosure bottom surface, m (Fig. 1) convective heat transfer coefficient, W/m^2 K
k = thermal conductivity, W/m K
l = plate length, m
L = length/height/width of enclosure, m
m,n = constants in Eq. (6)
Nu = Nusselt number
p = pressure, Pa
Q = heat transfer rate, W
R = gas constant of air, J/Kg K
Ra = Rayleigh number
s = spacing between every two heated plates (Fig. 1)
T = temperature, K
x,y,z = coordinate, m

Greek

β = coefficient of thermal expansions, 1K
ε = surface emissivity
μ = dynamic viscosity, Kg/m s
θ = angle of inclination of the plate group with the vertical
ρ = density, kg/m^3

Subscripts

1,2,3 = plate 1,2,3 (Fig. 1)
c = cold surface
conv = convective
rad = radiative
tot = total
m = overall
opt = optimal
h = heated surface
l = based on plate length l
s = based on plate spacing s

References

[1] Sparrow, E. M., and Charmchi, M., 1983, ''Natural Convection Experiments in an Enclosure Between Eccentric and Concentric Vertical Cylinders of Different Height and Diameter,'' Int. J. Heat Mass Transf., **26**, pp. 131–143.

[2] Sparrow, E. M., Stryker, P. C., and Ansari, M. A., 1984, ''Natural Convection in Enclosures with Off Center Inner Bodies,'' Int. J. Heat Mass Transf., **27**, No. 1, pp. 49–56.

[3] Warrington, R. O., and Powe, R. E., 1985, ''The Transfer of Heat by Natural Convection Between Bodies and Their Enclosures,'' Int. J. Heat Mass Transf., **28**, No. 2, pp. 319–330.

[4] Symons, J. G., Mahoney, K. J., and Bostock, T. C., 1987, ''Natural Convection in Enclosures with Through Flow Heat Sources,'' *Proceedings of the 1987 ASME-JSME Thermal Engineering Joint Conference*, Vol. 2, ASME, New York, pp. 215–220.

[5] Yang, M., and Tao, W. Q., 1995, ''Three Dimensional Natural Convection in an Enclosure with an Internal Isolated Vertical Plate,'' ASME J. Heat Transfer, **117**, pp. 619–625.

[6] Incropera, F. P., and Dewitt, D. P., 1996, *Fundamentals of Heat and Mass Transfer*, 4th Ed., John Wiley and Sons, New York.

[7] Moffat, R. J., 1988, ''Describing the Uncertainties in Experimental Results,'' Exp. Therm. Fluid Sci., **1**, pp. 3–17.

[8] Azevedo, L. F. A., and Sparrow, E. M., 1985, ''Natural Convection in Open-ended Inclined Channels,'' ASME J. Heat Transfer, **107**, pp. 893–901.

[9] Mayinger, F., and Wang, Z. G., 1994, ''Experiments on Thermal Convective Air Cooling of a PCBs Arrays in a Closed Casing with Inclination,'' *Cooling of Electronic Systems*, S. Kakac et al. eds., Kluwer, Dordrecht, The Netherlands, pp. 165–178.

Buoyancy-Driven Flow Reversal Phenomena in Radially Rotating Serpentine Ducts

J. J. Hwang
Professor

W.-J. Wang
Graduate Student

Cha'o Kuang Chen
Professor

Department of Mechanical Engineering, Chung-Hua University, Hsinchu, Taiwan 300, Republic of China
e-mail: JJHWANG@CHU.EDU.TW

Convective characteristics are analyzed numerically in a rotating multipass square duct connecting with 180-deg sharp returns. Isoflux is applied to each duct wall and periodic conditions are used between the entrance and exit of a typical two-pass module. Emphasis is placed on the phenomenon of buoyancy-driven reversed flow in the serpentine duct. Predictions reveal that the radial distance from the rotational axis to the location of flow separation in the radial-outward duct decreases with increasing the Richardson number. In addition, the local buoyancy that is required to yield the radial flow reversal increases with increasing the rotation number. This buoyancy-driven reversed flow in the radial-outward duct always results in local hot spots in the cooling channels. The critical buoyancy for the initiation of flow reversal is therefore concluded for the design purpose.
[S0022-1481(00)01101-4]

Keywords: Channel Flow, Heat Transfer, Mixed Convection, Periodic, Rotating

Introduction

Convective heat transfer mechanisms in radially rotating serpentine passages are very complicated due to the Coriolis effect as well as the rotation-induced buoyancy effect. The former always

---

Contributed by the Heat Transfer Division for publication in the JOURNAL OF HEAT TRANSFER. Manuscript received by the Heat Transfer Division, Jan. 1999; revision received, Oct. 1999. Associate Technical Editor: J. C. Han.

augments the overall heat transfer from the duct wall to the coolant ([1]), while the heat transfer benefits of the latter effect depend on the directions of coolant flow ([2,3]). Moreover, the centrifugal buoyancy can cause the radial flows to reverse themselves near the leading wall of the radial-outward flow duct ([3,4,5]). A region of zero to low velocity (stagnant) is subsequently created near the leading wall that degrades the heat transfer considerably. From the standpoint of the thermal design of rotating systems, it is very important to know the relation between the rotational buoyancy and the flow reversal phenomena. Therefore, this note extends the previous work ([3]) to numerically investigate the buoyancy effect on the reversed-flow phenomenon by varying the rotating speed and wall heat flux in the serpentine ducts. Then, the critical buoyancy that yields the flow reversal in the serpentine duct, which has not been studied previously, is concluded in the present note. Although the present prediction of laminar convection in a rotating channel is not much of an appeal to the engineering community, characterizing flow separation is still academically interesting.

Analysis

The two-pass test module is shown schematically in Fig. 1. It rotates at a constant angular speed Ω about the axis in parallel with the z-direction. The duct of square cross section is 20 De in radial length, and the distance from the axis of rotation to the test module is fixed at $x_0 = 10\,\mathrm{De}$. The radially inward flow duct and the radially outward flow duct are referred as ''RID'' and ''ROD,'' respectively. For closure of the present elliptic problem, periodical conditions are used between the inlet and the outlet of a two-pass channel and then formulate a generalization of this concept to accommodate a periodic fully developed regime in a multiple-pass serpentine duct. The periodically fully developed analysis in a rotating two-pass channel was discussed elsewhere ([3]), and all details are not elaborated on again. Basically, both pressure and temperature can be decomposed in the z-direction, i.e.,

$$p(x,y,z) = -\beta z + \hat{p}(x,y,z) \tag{1}$$

$$T(x,y,z) = \gamma z + \hat{T}(x,y,z+L_z) \tag{2}$$

where $\hat{p}$ and $\hat{T}$ are cyclic, while β and γ are constant, representing the overall pressure and temperature gradients along z-directions, respectively. Although as of now no experimental data are available that can prove the assumption of the constant pressure drop across the present test module, the pressure drops across a two-pass module of a serpentine duct away from the entrance section would be the same due to the same external forces (including body and Coriolis forces) acting on every two-pass duct. In fact, the previous experimental results revealed that after the first ([6]) and fifth ([7]) period the local heat/mass transfer characteristics have been periodical in rotating and nonrotating serpentine ducts, respectively. Here, we extend the previous experimental heat transfer characteristics to the present predictions of fluid-flow and heat transfer results.

Then, the flow is assumed to be steady and with constant properties, and the axial diffusion, viscous dissipation, and compression work are all ignored. In addition, gravitational inertia is neglected due to its small magnitude compared to the rotational induced centrifugal force. Referring to the coordinate system shown in Fig. 1, the dimensionless equations governing the mass, momentum, and energy can be written as the common form

$$\frac{\partial}{\partial x}(U\Phi) + \frac{\partial}{\partial y}(V\Phi) + \frac{\partial}{\partial z}(W\Phi) = \Gamma\left(\frac{\partial^2\Phi}{\partial X^2} + \frac{\partial^2\Phi}{\partial Y^2} + \frac{\partial^2\Phi}{\partial Z^2}\right) + S \tag{3}$$

where Φ denotes the generalized transport variable, Γ is the diffusivity, and S indicates the net source term for each variable. The

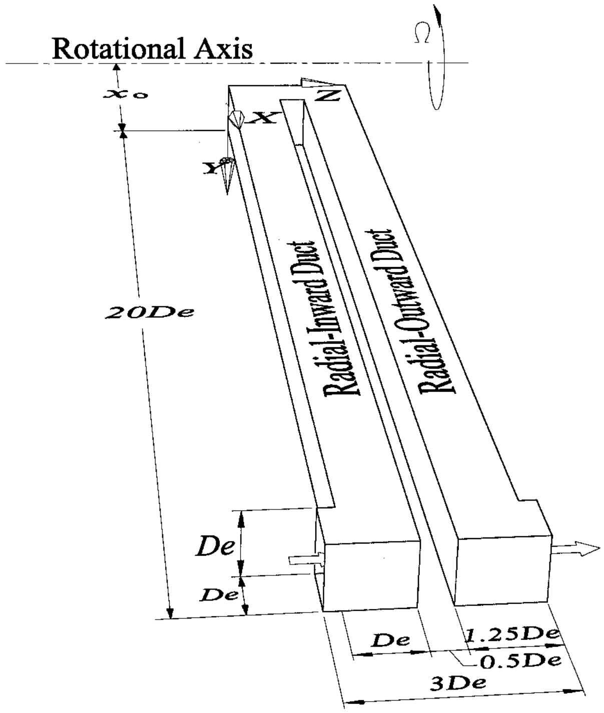

Fig. 1 Configuration, dimensions, and coordinates of the test module

Table 1 Forms of transport equations

$$\frac{\partial}{\partial x}(U\Phi) + \frac{\partial}{\partial y}(V\Phi) + \frac{\partial}{\partial z}(W\Phi) = \Gamma\left(\frac{\partial^2\Phi}{\partial X^2} + \frac{\partial^2\Phi}{\partial Y^2} + \frac{\partial^2\Phi}{\partial Z^2}\right) + S$$

Equation	Φ	Γ	S
Continuity	1	0	0
X-momentum	U	1/Re	$-(\partial P/\partial X) + 2\mathrm{Ro}V - \mathrm{Ri}(X+X_0)\vartheta$
Y-momentum	V	1/Re	$-(\partial P/\partial Y) - 2\mathrm{Ro}U - \mathrm{Ri}Y\vartheta$
Z-momentum	W	1/Re	$-(\partial P/\partial Z) + \beta'$
Energy	ϑ	1/(RePr)	$-\gamma' W$
Dimensionless Parameters	$X = x/\mathrm{De},\ Y = y/\mathrm{De},\ Z = z/\mathrm{De},\ U = u/\overline{w},\ V = v/\overline{w},\ W = w/\overline{w},\ P = \hat{p}/(\rho\cdot\overline{w}^2),$ $\vartheta = k_f(\hat{T} - T_r)/(q_w/\mathrm{De}),\ \beta' = \beta\cdot\mathrm{De}/(\rho\cdot\overline{w}^2),\ \gamma' = \gamma/(q_w/k_f),$ $\mathrm{Re} = \overline{w}\mathrm{De}/v,\ \mathrm{Ri} = \Omega^2\cdot\mathrm{De}^3\cdot\beta_T\cdot q_w/(k_f\cdot\overline{w}^2),\ \mathrm{Ro} = \Omega\mathrm{De}/\overline{w}$			

full set of transport equations as well as the dimensionless parameters within this format is listed in Table 1. No slip conditions are applied to all duct walls and each duct wall is heated uniformly. At the module inlet and outlet, the periodicity is applied for the velocity and temperature components ([3]).

The governing equations are numerically solved by the control-volume-based finite difference method ([8]). During the computational procedure, the mass flow rate (or $\overline{w}$) is not known a priori. Solution for a given flow rate is attained by iteratively updating the value of the global pressure gradient parameter β until convergence is reached. The quantity of β may be regarded as an assignable parameter, the given value of which will generate a corresponding mass flow rate. Usually, the initial value of β for a required mass flow rate is estimated arbitrarily, as is done in the present work, and then is updated by ''trial-and-error'' until the convergent solution is attained. This procedure is time consuming. If the value of β selected is based on the available experimental data, generally, the convergence of the solution will be very fast ([9]). All computations are performed on $72\times 20\times 50$ (X by Y by Z) straight-line grids in the present work. Additional runs for the coarser meshes, $60\times 15\times 40$, and the finer meshes, $72\times 20\times 50$, are taken for a check of grid independence, which shows a maximum change of 1.6 percent in Nusselt number distribution between the solutions of $72\times 20\times 50$ and $90\times 30\times 70$ grids. According to Kim et al. [10], solutions are converged at each test condition after the following two criteria are satisfied. That is the maximum local value of the relative change over two consecutive iterations of the dependent variable is smaller than 5.0×10^{-6}, and the nondimensional sum of the local residual magnitude is below 1.0×10^{-3}. Numerical computation of the periodically fully developed flow is rendered difficult by the fact that no boundary information is available in the main flow direction along which the discritezation coefficients are largest. Partly due to this reason, the code takes as high as 5000–9000 iterations for convergence. On Convex-C3840, this translated to about 10–40 hours of CPU time.

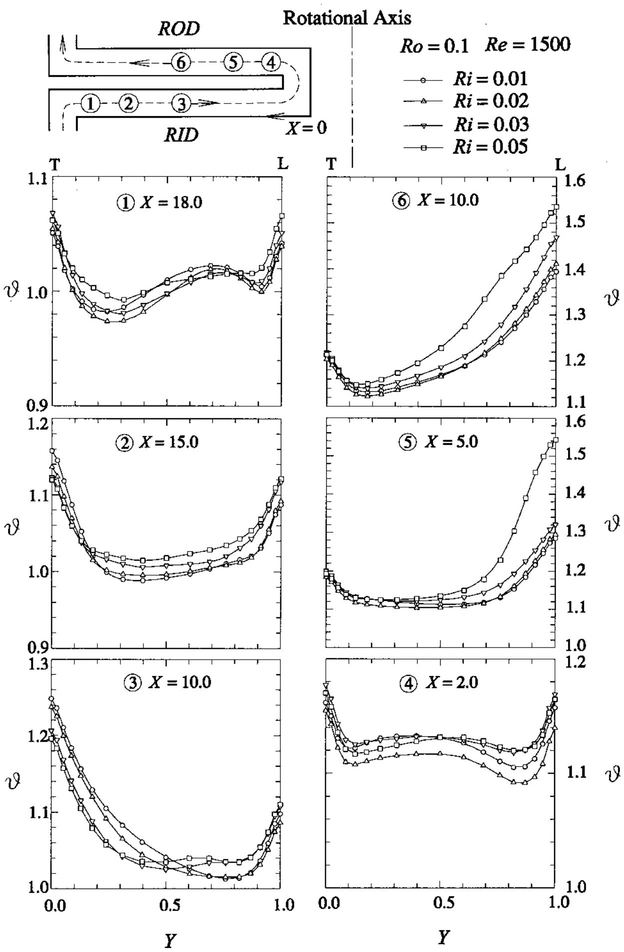

Fig. 2 Effect of Ri on temperature profiles at several axial stations of RID and ROD

Results and Discussions

Thermal-Fluid Fields. The validation of the present numerical code by comparing to experimental data has been proved in Hwang and Lai [3,9] under rotating and nonrotating conditions, and therefore is not repeated in the present note due to space limitation. Figure 2 shows the effect of Ri on the temperature profiles cutting across the duct centerlines ($Z=0.5$ and 2.0) between the high and low-pressure surfaces at several axial stations. The letters L and T denote the leading wall and the trailing wall, respectively. In the RID, owing to the Coriolis effect, the temperature increment near the trailing wall along the axial distance is faster than that near the leading wall. In addition, the higher the centrifugal buoyancy is, the lower the trailing-wall temperature becomes. This is because the assisting buoyancy accelerates the fluid near the trailing wall, and subsequently reduces the trailing-wall temperatures ([3,9]). Similarly in the ROD due to the Coriolis effect, the temperature rise near the trailing wall is less rapid than that near the leading wall. As the flow proceeds from $X=2.0$ to 5.0, the temperature near the leading wall abruptly increases for Ri$=0.05$ (square symbols). This is because the radial flow starts reversely between $X=2.0$ and 5.0. A similar phenomenon is observed for Ri$=0.03$ after $X\geq 5.0$, but not for Ri ≤ 0.02. This means that the radial distance from the rotational axis to the initiation of flow reversal decreases with increasing buoyancy when the Ro and Re are fixed constantly.

Figure 3 compares the local Nusselt numbers on four duct walls and the fluid isotherms at $X=10$ between the RID and the ROD. The dashed line in each graph represents the value of fully developed stationary flows. In the RID, the departure of local Nusselt number between the high and the low-pressure surfaces is less than that in the ROD. In the ROD, the buoyancy augments/degrades the trailing-wall/leading-wall heat transfer, which enlarges the discrepancy of heat-transfer coefficient between them. In the RID, the assisting buoyancy flattens the temperature profiles (Fig. 2), resulting in a reduction of the heat-transfer difference between the trailing and leading surfaces. Note that the heat transfer on the leading wall of the ROD is largely deteriorated, even lower than the stationary fully developed values.

Critical Local Buoyancy. From the above discussion, the radial flow separates from the leading surface in the ROD under high opposed buoyancy conditions. The initiation of flow reversal largely deteriorates the local heat-transfer performance in rotating channels. From the viewpoint of thermal design in the rotating cooling passages, it is very essential to avoid the flow separation near the leading wall under actual operating conditions. Therefore, critical buoyancy parameters that yield the radial flow reversal are determined as follows. The flow separates from the near-wall region, so the convective and the Coriolis force terms in the x-momentum equation listed in Table 1 are neglected because the near-wall velocities are very small. In addition, the viscous effects are ignored in the x and z-directions. The resulting x-momentum equation is

$$\frac{\partial p}{\partial x}+\rho\Omega^2(x+x_0)\beta_T T=\mu\,\frac{\partial^2 u}{\partial y^2}. \qquad (4)$$

The fact of flow separation under adverse buoyancy conditions can be inferred from a consideration of the velocity distribution

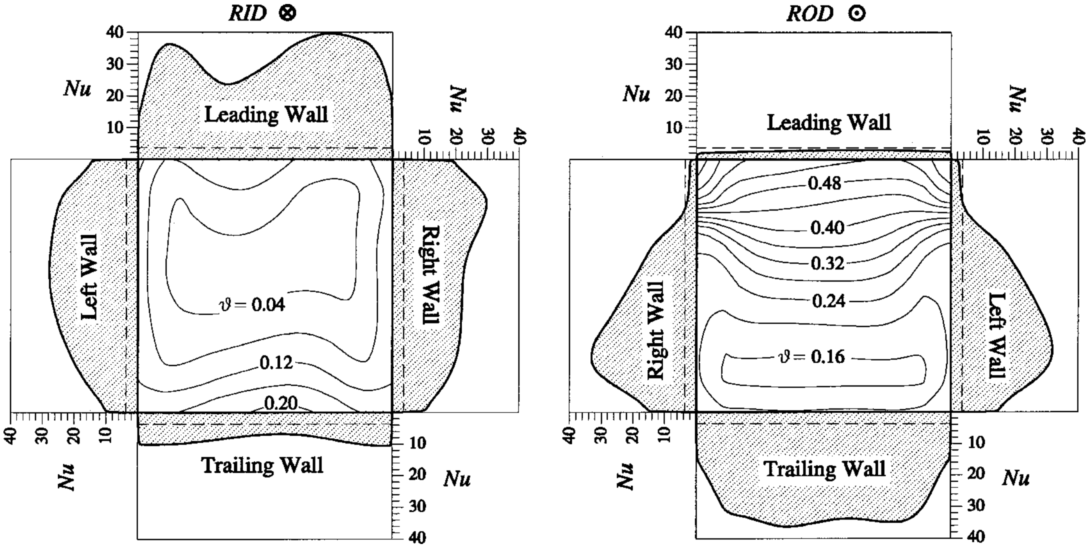

Fig. 3 Comparison of local Nusselt number distributions and isotherms at $X=10$ between the RID and ROD

$u(y)$. In the immediate neighborhood of the leading wall the curvature of the velocity profile depends on the sum of the pressure gradient and the centrifugal buoyancy. Therefore, the curvature of the velocity profile at the wall changes its sign with the left-hand side of the above equation. In the region of decelerated flow, we find $\partial^2 u/\partial y^2>0$. However, since in any case $\partial^2 u/\partial y^2<0$ at a large distance from the wall, there must exist a point for which $\partial^2 u/\partial y^2=0$ (point of inflection). This gives an indication that, at the point of flow separation, the antibuoyancy force always balances the favorable pressure gradient, i.e., $-\partial p/\partial x \sim \rho\Omega^2(x+x_0)\beta_T T$, Then

$$\frac{\rho\Omega^2(x+x_0)\beta_T T}{(\partial p/\partial x)}=\frac{\mathrm{Gr}}{\mathrm{Re}^2}(X+X_0)=\mathrm{Ri}(X+X_0). \tag{5}$$

Physically, the local nondimensional buoyancy force $\mathrm{Ri}(X+X_0)$ should be of order of unity for flow separation to occur. From Eq. (5), the factors that influence the magnitude of rotating buoyancy include the rotation speed Ω, radial distance from the rotating axis x_0+x, and wall heat flux q_w (or coolant density ratio). In the present numerical test, the wall heat flux varies (increases) until the flow reversal is predicted for each rotation number. The data points shown in Fig. 4(*a*) are the actual numerical predictions. The open symbols stand for the results that the flow reversal is not observed, while the solid symbols mean that the flow reversal has been predicted. Figure 4(*b*) further shows the local critical Richardson number, $\mathrm{Ri}(X_0+X_s)$ as a function of the rotation number. In this expression, the value of X_s is the axial distance from $X=0$ to the separation point of the radial flow. The dashed curve represents the lower limit of the buoyancy that the flow-reversal phenomena is observed. To avoid local hot spots in the serpentine duct, the operating conditions selected in a rotating flow system should be below this curve. As clearly shown in this figure the local buoyancy that is required to yield the radial flow reversal increases with increasing rotation number.

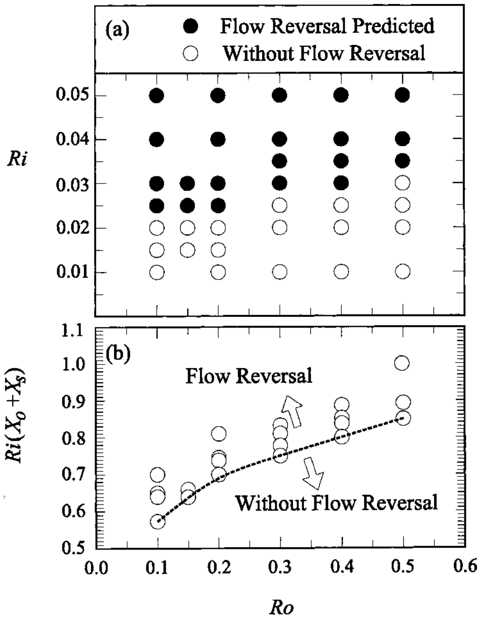

Fig. 4 (*a*) Predictions of flow-reversal phenomenon in the ROD; (*b*) critical local buoyancy for the initiation of the flow reversal in the ROD

Conclusions

The influences of centrifugal buoyancy on heat transfer characteristics in the RID and ROD have been examined numerically, and compared thereafter in the present study. The major contribution is to conclude the critical buoyancy for the initiation of flow reversal in the ROD. In general, the critical buoyancy increases with increasing rotation number. The buoyancy-driven reversed flow in the radial outward duct always results in local hot spots in the cooling channels. In addition, the radial distance from the rotational axis to the location of flow separation in the ROD decreases with increasing Richardson number when rotation number remains constant. Increasing the rotation number will delay the initiation of flow reversal in the ROD when the Richardson number is fixed.

Acknowledgment

Support for this work was provided by the National Science Council of the Republic of China under Contract No. NSC 85-2212-E-216-003.

Nomenclature

De = duct hydraulic diameter
Gr = rotational Grashof number, $\Omega^2 \cdot \beta_T \cdot q_w \cdot \text{De}^5/(\nu^2 k_f)$
k_f = air thermal conductivity
Nu = local Nusselt number, $q_w \cdot \text{De}/[k_f \cdot (T_w - T_b)]$
P,p = dimensionless and dimensional pressures
Pr = Prandtl number
q_w = wall heat flux
Re = Reynolds number, $\overline{w}\text{De}/\nu$
Ri = Richardson number, Gr/Re^2
Ro = rotation number, $\Omega \text{De}/\overline{w}$
T = temperature
U,V,W,u,v,w = dimensionless and dimensional velocities in x, y and z, respectively
$\overline{w}$ = averaged through flow velocity in the duct
X,Y,Z,x,y,z = dimensionless and dimensional rectangular coordinates
X_0, x_0 = Dimensionless and dimensional distances from $X=0$ to the test module
β', β = Dimensionless and dimensional pressure drop parameters
β_T = thermal expansion coefficient
γ', γ = dimensionless and dimensional air enthalpy rise parameters
ϑ = dimensionless temperature, $T/(q_w \cdot \text{De}/k_f)$
ν = kinematics viscosity
ρ = air density
Ω = angular rotation speed

References

[1] Han, J. C., and Zhang, Y. M., 1992, ''Effect of Uneven Wall Temperature on Local Heat Transfer in a Rotating Square Channel With Smooth Walls of Radial Outward Flow,'' Trans. ASME, Ser. C: J. Heat Transfer, **114**, pp. 850–858.

[2] Wagner, J. H., Johnson, B. V., and Kopper, F. C., 1991, ''Heat Transfer in Rotating Serpentine Passages With Smooth Walls,'' Trans. ASME J. Turbomachinery, **113**, pp. 321–330.

[3] Hwang, J. J., and Lai, D. Y., 1998, ''Three Dimensional Mixed Convection in a Rotating Multiple-Pass Square Channel,'' Int. J. Heat Mass Transf., **41**, pp. 979–991.

[4] Prakash, C. V., and Zerkle, R., 1992, ''Prediction of Turbulent Flow and Heat Transfer in a Radially Rotating Square Duct,'' Trans. ASME J. Turbomachinery, **114**, pp. 835–846.

[5] Dutta, S., Andrews, M. J., and Han, J. C., 1996, ''On Flow Separation With Adverse Rotational Buoyancy,'' Trans. ASME, Ser. C: J. Heat Transfer, **118**, pp. 977–979.

[6] Yang, W. J., Zhang, N., and Chiou, J., 1992, ''Local Heat Transfer in a Rotating Serpentine Flow Passage,'' Trans. ASME, Ser. C: J. Heat Transfer, **114**, pp. 354–361.

[7] Choi, J. M., Anand, N. K., Lau, S. C., and Kukreja, R. T., 1996, ''Heat (Mass) Transfer in a Serpentine Channel with Right-Angled Turns,'' Trans. ASME, Ser. C: J. Heat Transfer, **118**, pp. 211–213.

[8] Patankar, S. V., 1980, *Numerical Heat Transfer and Fluid Flow*, Hemisphere, Washington, D.C.

[9] Hwang, J. J., and Lai, D. Y., 1998, ''Three Dimensional Laminar Flow in a Rotating Multiple-Pass Square Channel With 180-deg Turns,'' Trans. ASME, J. Fluids Eng., **120**, pp. 488–495.

[10] Kim, N., Anand, N. K., and Rhode, D. L., 1998, ''A Study on Convergence Criteria for a Simple-Based Finite-Volume Algorithm,'' Numer. Heat Transfer, B, **34**, pp. 401–417.

Analysis of the Two-Flux Model for Predicting Water Spray Transmittance in Fire Protection Application

S. Dembele[1]
e-mail: s.dembele@kingston.ac.uk

J. X. Wen

Combustion and Fire Modelling Group, School of Mechanical, Aeronautical and Production Engineering, Kingston University, Roehampton Vale, Friars Avenue, London SW15 3DW, England

J. F. Sacadura
Centre de Thermique de Lyon (CETHIL), 20, ave. Albert Einstein, 69621 Villeurbanne Cedex, France

An investigation is carried out to assess the two-flux model for evaluating the attenuation ability of a water spray curtain in fire protection. Transmittances calculated with this model are compared with the ''exact'' discrete ordinates solutions for a range of water curtains under practical conditions. The results show the unsuitability of the two-flux method under a collimated incidence boundary condition, even if some improvements could be expected with very small droplets. Whereas the diffuse incidence type provides relatively better results, it is more reliable for transmittance calculations. [S0022-1481(00)00101-8]

Keywords: Droplet, Heat Transfer, Radiation, Sprays

Introduction

For practical engineering applications, many approximate solutions of the radiative transfer equation have been suggested, as alternatives to the mathematically complex and rigorous solutions. Among these, the two-flux model first suggested by Schuster [1] and extended by Hamaker [2] and Churchill and Chu [3] has received a wider attention. The method is based on the assumption of semi-isotropic distribution of radiative intensity. Daniel et al. [4] have applied the two-flux model for radiative calculations in shallow ponds and concluded its unsuitability in comparison to the six-flux and the discrete ordinates methods. The major drawback of the model, for this particular application, was due to its inability to account for the step change of refractive index at the air-water interface, which gave rise to a rather pronounced anisotropic distribution of intensity. Brewster and Tien [5] assessed the predictive capability of the two-flux model without relying on any empirical constants. Acute anisotropic scattering, it was noted, is the prime cause of inaccuracy in the two-flux model, and the combination of large optical thicknesses with strong forward scattering is the worst case. However, because any engineering application is a particular case of utilization, the two-flux method has not been discredited in general. In fire protection by water sprays, the two-flux method has been widely used ([6–8]) without deeper criticism and assessment of its suitability for such applications.

---

[1] Corresponding author.

Contributed by the Heat Transfer Division for publication in the JOURNAL OF HEAT TRANSFER. Manuscript received by the Heat Transfer Division, Feb. 14, 1999; revision received, Aug. 2, 1999. Associate Technical Editor: J. Gore.

This situation is mainly due to the lack of more experimental data available on water sprays. An attempt is made in this work to assess this model for radiative transfer in water sprays under practical conditions encountered in fire protection. The predicted transmittances of the two-flux model are compared to the more accurate discrete ordinates solutions. Main tendencies and guidelines are provided for fire protection modelers.

Theoretical Model

The analysis is carried out for a one-dimensional geometry (plane parallel slab) for both diffuse and collimated incident radiation. The water spray curtain used to shield fire radiation (Fig. 1) is formed by droplets, which are the only phase considered here, although water vapor contribution may be important in some cases ([9]). The radiative transfer equation for azimuthally symmetric radiation is ([10,11])

$$\mu \frac{\partial I_\nu(\tau,\mu)}{\partial \tau} = -I_\nu(\tau,\mu) + (1-\omega_\nu) I_{b\nu}[T_{\text{spray}}] + \frac{\omega_\nu}{2}\int_{-1}^{1} P_\nu(\mu,\mu') I_\nu(\tau,\mu')\, d\mu', \qquad (1)$$

where I is the intensity, ν the frequency of radiation, P the phase function of the water droplets, and $\omega=\sigma/\beta$ their albedo (ratio of the scattering to extinction coefficients). μ is the directional cosine with respect to a direction perpendicular to the water curtain, and τ the optical depth. The subscript b refers to blackbody properties at a given temperature T. In the traditional two-flux model considered here, the intensity distribution is assumed to be semi-isotropic, and divided into forward $I_\nu^+(\tau)$ $(0<\mu<1)$ and backward $I_\nu^-(\tau)$ $(-1<\mu<0)$ components ([10]).

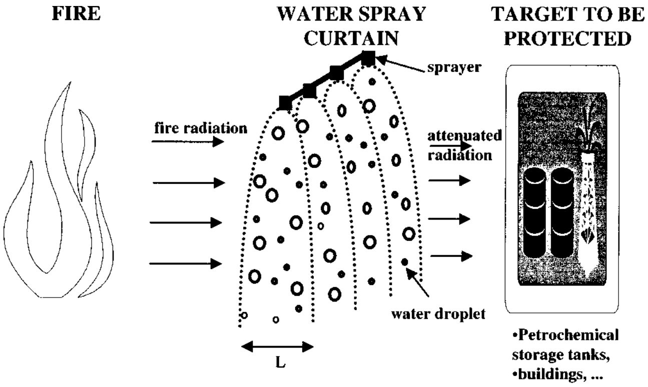

Fig. 1 Attenuation of fire thermal radiation with water spray curtain

For diffuse externally incident radiation, introducing these assumptions into the integral term in Eq. (1) and integrating over $-1\leqslant\mu\leqslant 1$ provides the following first ordinary differential equations ([11]):

$$\begin{cases} +\dfrac{1}{2}\dfrac{dI_\nu^+(\tau)}{d\tau} = -(1-\omega_\nu+\omega_\nu B)I_\nu^+(\tau) + \omega_\nu B I_\nu^-(\tau) + (1-\omega_\nu)I_{b\nu}[T_{\text{spray}}] \\ -\dfrac{1}{2}\dfrac{dI_\nu^-(\tau)}{d\tau} = -(1-\omega_\nu+\omega_\nu B)I_\nu^-(\tau) + \omega_\nu B I_\nu^+(\tau) + (1-\omega_\nu)I_{b\nu}[T_{\text{spray}}], \end{cases} \qquad (2)$$

where

$$B=\frac{1}{2}\int_{\mu=0}^{1}\int_{\mu'=-1}^{0} P_\nu(\mu',\mu)\, d\mu'\, d\mu.$$

Equation (2) is solved analytically with the following boundary conditions for the water spray curtain of length L (Fig. 1), standing between the fire and the vessel to be protected (incident flux from fire at $\tau=0$):

$$\begin{cases} I_\nu^+(\tau=0)=I_{b\nu}[T_{\text{fire}}] & \mu>0 \\ I_\nu^-(\tau_L=\beta_\nu L)=0 & \mu<0. \end{cases} \qquad (3)$$

For large liquefied natural gas pool fires, it has been proved from experimental measurements ([12]) that the flame emission spectrum is similar to that of a blackbody radiating at the temperature T_{fire} ($\cong 1300$ K). The single particle efficiencies for the water drops (absorption, scattering, extinction) and phase function are calculated using Mie theory [13]. The spectral refraction indexes of water were taken from Hale and Querry [14]. It has been shown that for most actual industrial sprayers, the independent scattering assumption is valid ([15]) and therefore the volume properties of the water spray are obtained by summing the single-particle ones ([11]). The phase function is obtained by a numerical integration from the Mie single particle calculations, involving the azimuthal angles ([11]).

The transmittance of the water curtain, i.e., the fraction of the incident radiation transmitted through the curtain, is the main quantity of interest in fire protection engineering. The attenuation ability of the curtain, and the heat flux reaching the target (e.g., hydrocarbon fuel tank) can be evaluated from calculated transmittances. For diffuse incidence, the following expression is found when the emission term (relatively negligible) is omitted in Eq. (2):

$$\mathrm{Tr}_{\nu-\text{diff}} = L_\nu^+(\tau_L)/L_\nu^+(0) = \frac{2g e^{-g\tau_L}}{\alpha+g-(\alpha-g)e^{-2g\tau_L}}, \qquad (4)$$

where $\alpha=2(1-\omega+\omega B)$, $g=\sqrt{\alpha^2-(2\omega B)^2}$.

For a collimated incident radiation along a direction μ, the transmittance is given by ([16]):

$$\mathrm{Tr}_{\nu-\text{coll}} = \frac{2g^* e^{-g^*\tau_L/\mu}}{1-\omega F+g^*-(1-\omega F-g^*)e^{-2g^*\tau_L/\mu}}, \qquad (5)$$

where

$$F=\frac{1}{2}\int_{\mu'=0}^{1} P_\nu(\mu',\mu)\, d\mu', \quad B^*=\frac{1}{2}\int_{\mu'=-1}^{0} P_\nu(\mu',\mu)\, d\mu'$$

and $g^*=\sqrt{(1-\omega F)^2-(\omega B^*)^2}$.

Results and Discussion

Solutions are presented in terms of the water spray curtain transmittance, and compared for the ‘‘exact’’ discrete ordinates and two-flux predictions. A complete discussion of the discrete ordinates solution for planar geometry can be found elsewhere ([10,11]). The in-scattering integral in Eq. (1) is approximated by a Gaussian quadrature formula that discretizes the intensity field into a finite number of streams (ordinates). The study covers a

Table 1 Comparative transmittance between two-flux method and ''exact'' discrete ordinates solutions

		Collimated incidence			Diffuse incidence		
		Tr_{coll} ''exact'' (percent)	Tr_{coll} two-flux (percent)	Relative difference (percent)	Tr_{diff} ''exact'' (percent)	Tr_{diff} two-flux (percent)	Relative difference (percent)
Case 1 $L=0.6$ m $d=350$ μm	Subcase 1-1 $f_v=0.24\times10^{-3}$, $\tau=1.24$	29	62.7	—	25	16.2	35.2
	Subcase 1-2 $f_v=1\times10^{-3}$, $\tau=5.25$	0.53	18	—	2.6	1.0	61.5
	Subcase 1-3 $f_v=2\times10^{-3}$, $\tau=10.5$	0.0044	6.8	—	0.6	0.22	63.3
Case 2 $L=0.25$ m $d=90$ μm	Subcase 2-1 $f_v=0.05\times10^{-3}$, $\tau=0.44$	64.5	86.7	34.4	61.2	54.6	10.8
	Subcase 2-2 $f_v=0.55\times10^{-3}$, $\tau=4.8$	0.8	29.3	—	7.2	3.6	50
	Subcase 2-3 $f_v=1.7\times10^{-3}$, $\tau=15$	0.0024	10.4	—	0.8	0.32	60
Case 3 $L=1.0$ m $d=10$ μm	Subcase 3-1 $f_v=0.001\times10^{-3}$, $\tau=0.4$	68.7	93.2	35.6	74.3	68.5	8
	Subcase 3-2 $f_v=0.015\times10^{-3}$, $\tau=5.7$	0.82	45	—	11.3	6	47
	Subcase 3-3 $f_v=0.03\times10^{-3}$, $\tau=11.4$	0.035	27.4	—	4.2	2	51

wide range of curtain length (geometrical and optical), water droplets size, and volume fraction (f_v) encountered in practical situations. The influence of these parameters on the predicted attenuation by the two methods is analyzed. Table 1 presents the cases and subcases considered. Case 1 and Subcase 1-1 correspond to a sprayer full cone (ref. 402.962, Lechler S.A.) operating at 8 bars pressure (52.4 L/min flow rate). The water curtains operating under this condition have shown their attenuation ability and wind stability in large-scale experiments without total evaporation ([17,15]). The diameter *d* is the mean Sauter diameter of the distribution. For Subcases 1-2 and 1-3, the volume fraction was varied to quantify the influence of the optical thickness. Case 2 and Subcase 2-1 are typical of a sprayer TG03 (Spraying Systems Co.) operating under 5 bar pressure (0.3 L/min) used in laboratory investigations ([9]). The volume fraction was varied in Subcases 2-2 and 2-3. Case 3 and Subcases 3-1, 3-2, 3-3 describe a theoretical water spray, chosen to analyze the influence of very small droplets. The wavelength range considered for spectral integration is from 0.8 to 20 μm and the discrete ordinates solutions are based on 20 Gaussian quadrature points. A blackbody incident spectrum (1300 K) is considered. All the results are summarized in Table 1 for both diffuse and collimated incidences. The relative differences $|\mathrm{Tr}(\text{``exact''})-\mathrm{Tr}(\text{2-flux})|/\mathrm{Tr}(\text{``exact''})$ larger than 100 percent are not mentioned, indicating a large failure of the two-flux solutions. For the collimated incidence, it is seen that the two-flux model overestimates the total transmittance with comparison to the ''exact'' solutions. For the Subcase 1-1, corresponding to large drop size (350 μm) and strong anisotropic scattering, the discrepancies are very large (relative difference >100 percent). The same tendency is observed for smaller drop size and large optical thickness. The relative error is, however, smaller only for Subcases 2-1 (34.4 percent) and 3-1 (35.6 percent), which correspond to a smaller drop size and optically thin water curtain ($\tau=0.4$). For the diffuse incidence, the results between the two methods, as shown in Table 1, are in rather good agreement. The relative differences are 35.2 percent, 10.8 percent, and 8 percent, respectively, for the Subcases 1-1, 2-1, and 3-1. Transmittances predicted by the two-flux method are very close to the ''exact'' solution for Subcases 2-1 and 3-1, which correspond to a smaller drop size and optically thin curtain. For a given case (1, 2, or 3), an increase in the optical depth leads, in general, to larger discrepancies. The large errors related to the collimated incidence can be explained by the assumption of semi-isotropic intensity distribution in the traditional two-flux method which, strictly speaking, is more valid for diffuse incidence. The combination of large drops (anisotropic scattering), an optically thick curtain, and collimated incidence is the worst scenario for the two-flux method to be used for water sprays transmittance calculation. The two-flux method is generally suitable for diffuse incidence. The combination of diffuse incidence, small drops (rather semi-isotropic phase function), and an optically thin curtain is an ideal scenario, where this method can give reliable predictions (e.g., Subcase 3-1). However, according to our experience based on large hydrocarbon fire tests ([15,17]), water curtains of droplet diameters smaller than 100 μm are more susceptible to wind effects and present a risk of total evaporation. The most realistic situation in an industrial environment is to use droplets larger than 300 μm (e.g., Case 1) which do not present these disadvantages although their attenuation ability is lower.

Conclusions

A comparative study of the two-flux method and ''exact'' discrete ordinates solutions for predicting water spray curtain transmittance has been presented. Although some similar comparative studies have been carried out in the past for various media, the current work has the particular feature of being based on practical water sprays parameters. The results clearly show that the use of the two-flux model with collimated incidence (used by some fire protection modelers) should be avoided in calculating a curtain transmittance. The predictions for collimated incidence are improved slightly for very small droplets (diameter <100 μm) and an optically thin water curtain. The two-flux model may be reasonably used for diffuse incidence where its predictions could be in close agreement with the ''exact'' solution of the discrete ordinates method. The best results are obtained for small drop size and an optically thin medium. However, based on our experience, for the water curtain to be wind stable and resistant to total evaporation, droplets diameter should be larger than 300 μm. Use of the two-flux model, only with diffuse incidence for such drop sizes, can provide acceptable accuracy depending on the optical thickness (35 percent relative difference with exact solution for $\tau=1.2$ here). Thus for fire protection modelers using water spray curtains, diffuse incidence boundary should be used to achieve more reliable results. This is contrary to the collimated boundary conditions. Moreover, the curtain parameters investigated in this work can be used by other workers as a guideline for this particular absorbing and scattering medium.

References

[1] Schuster, A., 1905, ''Radiation Through a Foggy Atmosphere,'' Astrophys. J., **217**, pp. 1–22.

[2] Hamaker, H. C., 1947, ''Radiation and Heat Conduction in Light Scattering Material,'' Philips Res. Rep., **2**, pp. 55–67, 103–125, 420.

[3] Churchill, S. W., and Chu, C. M., 1955, ''Numerical Solution of Problems in Multiple Scattering of Electromagnetic Radiation,'' J. Phys. Chem., **59**, pp. 855–863.

[4] Daniel, K. J., Laurendeau, N. M., and Incropera, F. P., 1979, ''Prediction of Radiation Absorption and Scattering in Turbid Water Bodies,'' ASME J. Heat Transfer, **101**, pp. 63–67.

[5] Brewster, M. Q., and Tien, C. L., 1982, ''Examination of the Two-Flux Model for Radiative Transfer in Particular Systems,'' Int. J. Heat Mass Transf., **25**, pp. 1905–1907.

[6] Thomas, P. H., 1952, ''Absorption and Scattering of Radiation by Water Sprays of Large Drops,'' Br. J. Appl. Phys., **3**, pp. 385–393.

[7] Stephenson, S., and Coward, M. J., 1986, ''Attenuation of Radiant Heat on LNG/LPG Carriers With Freestanding Water Curtains,'' *Gastech 86 LNG/LPG Conference*, Hamburg, pp. 157–168.

[8] Coppalle, A., Nedelka, D., and Bauer, B., 1993, ''Fire Protection: Water Curtains,'' Fire Safe. J., **20**, pp. 241–255.

[9] Dembele, S., Delmas, A., and Sacadura, J. F., 1997, ''A Method for Modeling the Mitigation of Hazardous Fire Thermal Radiation by Water Spray Curtains,'' ASME J. Heat Transfer, **119**, pp. 746–753.

[10] Chandrasekhar, S., 1960, *Radiative Transfer*, Dover, New York.

[11] Brewster, M. Q., 1992, *Thermal Radiative Transfer and Properties*, John Wiley and Sons, New York.

[12] Nedelka, D., Moorhouse, J., and Tucker, R. F., 1989, ''The Montoir 35 m Diameter LNG Pool Fire Experiments,'' *Liquefied Natural Gas-9 Congress, Nice*, France.

[13] Bohren, C. F., and Huffman, D. R., 1983, *Absorption and Scattering of Light by Small Particles*, John Wiley and Sons, New York.

[14] Hale, G. M., and Querry, M. R., 1973, ''Optical Constants of Water in the 200-nm to 200 μm Wavelength Region,'' Appl. Opt., **12**, pp. 555–563.

[15] Dembele, S., 1998, ''Mitigation of Hydrocarbon Fires Radiation by Water Spray Curtains: Modelling and Experimental Validations,'' Ph.D. dissertation, INSA Lyon, No. 98 ISAL 0043, France.

[16] Hottel, H. C., and Sarofim, A. F., 1967, *Radiative Transfer*, McGraw-Hill, New York.

[17] Dembele, S., Delmas, A., and Sacadura, J. F., 1998, ''Water Sprays for Protection From Fire Thermal Radiation Hazards,'' *9th International Symposium Loss Prevention Safety Prom. Proc. Ind.*, Barcelona, Vol. 2, pp. 668–677.

Average Boiling and Condensation Heat Transfer Coefficients of the Zeotropic Refrigerant Mixture R22/R142b in a Coaxial Tube-in-Tube Heat Exchanger

J. P. Meyer[1]
J. M. Bukasa
S. A. Kebonte
Department of Mechanical and Manufacturing Engineering, Rand Afrikaans University, Laboratory for Energy, PO Box 524, Auckland Park, 2006, Johannesburg, South Africa

Average boiling and condensation heat transfer coefficients were determined experimentally for a coaxial tube-in-tube heat exchanger used in hot water heat pumps. During manufacturing, the heat exchanger geometry used for the experiments changed from round tubes to elliptical tubes as no spacers were used to keep the inner tube from touching the outer tube. The refrigerant used was two different mixtures of R22 with R142b in mass ratios of 80 percent/20 percent and 60 percent/40 percent. The results were compared to theoretical results for straight tubes. It was concluded that the theoretical modes do not predict the heat transfer coefficients very well in coaxial tube-in-tube heat exchangers where the annulus touches the inside of the outer tube. [S0022-1481(00)01001-X]

Keywords: Experimental Heat Transfer, Boiling, Condensation, Refrigerants, R22, R142b, Coaxial, Tube-in-Tube, Heat Exchanger

Introduction

The air conditioning and refrigeration industry is in the midst of an unprecedented transition, catalyzed by environmental concerns regarding the impact of refrigerant emissions. Refrigerants containing chlorine, though less frequently used than compound bromide, are being phased out. Production of chlorofluorocarbons (CFCs) ended in 1995 in developed countries. It was agreed at the last followup conference held in Vienna in 1995, that the worldwide phaseout of hydrochlorofluorocarbons (HCFCs) in industrialized countries has to be fulfilled by 2030 and in developing countries by 2040 ([1]). In nonindustrialized countries where air-conditioning, heat pump, and refrigeration equipment are being developed, which are not usually manufactured in industrialized countries, HCFCs are still being used for new equipment under development such as hot-water heat pumps.

Hot-water heat pumps are especially used in countries with a mild climate in winter that have no natural gas and where electrical heating is usually used for the heating of water. Heating of water with heat pumps is extremely energy efficient. Savings of approximately 67 percent can be realized, compared to heating with direct electrical resistance heaters ([2,3]). Hot-water heat pumps are vapor compression cycles, which use water-cooled condensers for heating hot water. The most widely used refrigerant for hot-water heat pumps is R22 ($CHClF_2$) with which a maximum hot-water temperature of 60–65°C is possible with approximately the same condensing temperatures. This is possible by making use of the refrigerant's superheat, which is approximately 120°C at the compressor outlet. The maximum condensation temperature is limited by the maximum condensing pressure to control the amount of wear in the compressor bearings, the load on the bearings, and to keep the lubrication oil from decomposing at higher compressor discharge temperatures.

Although hot-water temperatures of 60–65°C are adequate for domestic use, they are low when compared to temperatures that can be delivered by fossil fuel and direct electric resistance systems. This limits the potential applications of hot-water heat pumps. Smit and Meyer [4] as well as Johannsen [5] showed analytically that a zeotropic mixture of R22 and R142b ($CClF_2CH_3$) can be used to obtain higher temperatures. Theoretically, a hot-water outlet temperature of 120°C is possible if only R142b is used. The disadvantage of using only R142b is that its heating capacity is 15 percent lower and its heating coefficient of performance (COP) is seven percent lower when compared to R22. Furthermore, it is flammable, but the flammability is decreased by adding R22. A mixture of 60 percent R22 with 40 percent R142b or 80 percent R22 with 20 percent R142b by mass is recommended. With these mixtures the heating capacities are about the same as just R22, but its COP is increased, while hot-water temperatures of 80°C (80 percent R22) to 90°C (60 percent R22) can be achieved. Mixtures of R22 with R142b form zeotropic mixtures with glides of 7 and 5°C for 60 percent and 80 percent R22, respectively.

Literature searches by Smit [6], Kebonte [7], and Bukasa [8] showed that heat transfer coefficients for the recommended con-

---

[1] Author to whom correspondence should be addressed.

Contributed by the Heat Transfer Division for publication in the JOURNAL OF HEAT TRANSFER. Manuscript received by the Heat Transfer Division, 1999; revision received, Oct. 1999.

centrations of R22 with R142b are not readily available for coaxial tube-in-tube heat exchangers. In this investigation these average heat transfer coefficients (that is at 60 percent R22 mixed with 40 percent R142b and 80 percent R22 mixed with 20 percent R142b, by mass) during condensation and evaporation are determined experimentally. The heat exchanger configuration is used in hot-water heat pumps as usual.

Experimental Apparatus and Procedures

The experimental apparatus and procedure were the same as used by Schlager et al. [9] except for the following differences. (1) For condensing experiments, the inside and outside diameters of the inner tube of the test section were 8.11 and 9.53 mm, respectively. The inside diameter of the outer tube was 14.26 mm. For the evaporation experiments, the inside and outside diameters of the inner tube of the test section were 14.26 and 15.88 mm, respectively. The inside diameter of the outer tube was 20.23 mm. Both tubes were soft drawn copper tubes and experiments were conducted in a counter flow direction with the refrigerant flowing through the inner tube and water in the annulus. The test section was coiled as shown in Fig. 1 and no spacers were used to keep the inner tube from touching the outer tube. During the bending process into a coil the tube geometry changes from round to elliptical. This bending practice is usually used in the manufacturing of hot-water heat pumps. For condensation measurements, the heat exchange length was 7.93 m and for evaporation, it was 4.89 m. (2) The water and refrigerant mass flows were measured with Coriolis mass flowmeters with an accuracy of ±0.02 percent. (3) Temperatures were measured with Pt100s, calibrated to measure temperature differences to within ±0.02°C.

The uncertainty of the heat transfer coefficients is ±10 percent using a propagation-of-error analysis, whose technique is based on the method of Kline and McKlintock [10]. Experiments were also conducted with straight tube-in-tube heat exchangers with only R22 and the heat transfer coefficients were compared to those of Schlager et al. [9]. The comparison was within ±20 percent.

The condensation and evaporation tests through the coiled tube were conducted at three different mass concentrations of R22 (i.e., 100 percent, 80 percent, and 60 percent). The tests conditions are summarized in Table 1.

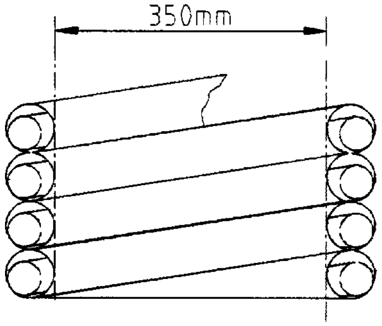

Fig. 1 Schematic representation of coiled test section (not to scale)

Table 1 Summary of test conditions

	Condensation	Evaporation
G (kg/m^2 s)	180–450	160–280
q (kW/m^2)	10–24	25–93
P (MPa)	1.7–1.9	0.6–0.9
$T_{\mathrm{dew}}(°C)$	46–70	0–10
X_{in} (percent)	90–95	20–30
X_{out} (percent)	0	90–95

Results

The results of the average heat transfer coefficients during condensation are given in Fig. 2. The heat transfer coefficients decrease when the mass percentage of R22 is decreased and the R142b is increased. The results were also compared to theoretical predictions for a straight tube using the models of Akers et al. [11], Cavallini and Zecchin [12], Travis et al. [13], and Azer et al. [14]. Only the results of Akers [11] are shown in Fig. 2. It was found that in general the Akers method gave the best agreement to measurements although it overpredicts the average heat transfer coefficients for the mixtures by 40 percent and by 10 percent for R22. The other methods overpredict the coefficients even more. It can be deduced that prediction methods do not determine the average heat transfer coefficients during condensation very well in coaxial tube-in-tube heat exchangers where the annulus touches the outer tube.

The boiling heat transfer coefficients are given in Fig. 3. Again, the measured heat transfer coefficients decrease when R142b is added to R22. The decrease is not as drastic as during condensation. The results were also compared to the correlations of Jung et al. [15], Murata and Hashizume [16], and Thome [17] for straight tubes. Only the results of Jung et al. [15] are shown in Fig. 3 as it was found that in general this method gave the best agreement, although it underpredicts the measured heat transfer coefficients by 100 percent–130 percent. The other methods underpredict the coefficients for the mixtures even more. It can be

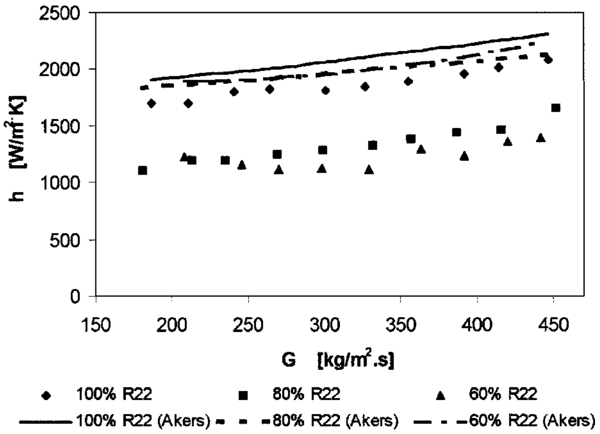

Fig. 2 Average heat transfer coefficients during condensation as function of mass flux

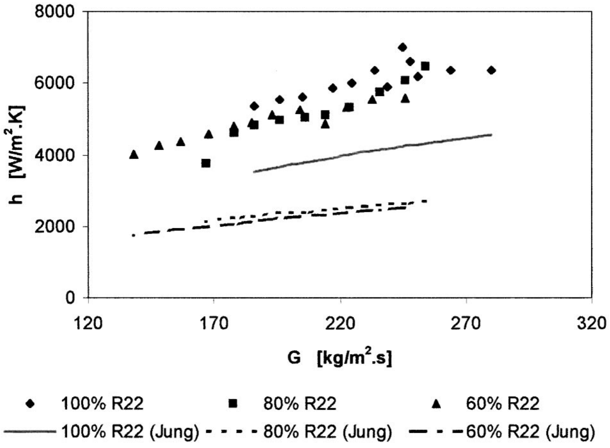

Fig. 3 Average heat transfer coefficients during evaporation as function of mass flux

deduced that theoretical methods do not predict the average heat transfer coefficients correctly in coaxial tube-in-tube heat exchangers where the annulus touches the outer tube.

Conclusions

Theoretical models exist that predict the average heat transfer coefficients during condensation and evaporation in straight tubes quite accurately. It was found that these models do not predict the coefficients very well in coaxial tube-in-tube heat exchangers where the annulus touches the inside of the outer tube. During condensation, the measured heat transfer coefficients were lower than predicted theoretically, while they were higher for evaporation. It was also found that the heat transfer coefficients decreased for R22/R142b mixtures as the mass ratio of R142b increased. For condensation, the decrease in heat transfer coefficients was more than for evaporation.

Nomenclature

G = mass flux, kg/m^2 s
h = average heat transfer coefficient, W/m^2 K
P = pressure, Pa
q = heat flux, W/m^2
T_{dew} = dew point temperature, °C
X_{in} = inlet vapor quality
X_{out} = outlet vapor quality

References

[1] Kruse, H. H., and Tiedemann, T., 1997, ''Experience With HC Refrigerants and Projections for Future Applications, Current and Projected Use of Refrigerants in Europe,'' Refrigerants for the 21st Century, ASHRAE/NIST Refrigerants Conference, Gaithersburg, MD, pp. 44–56.
[2] Meyer, J. P., and Greyvenstein, G. P. 1991, ''Hot Water for Homes in South Africa,'' Energy Int. J. **16**, pp. 1039–1044.
[3] Meyer, J. P. and Greyvenstein, G. P. 1992, ''Hot Water for Large Residential Units, Hospitals and Laundries with Heat Pumps in South Africa: A Techno-economic Analysis,'' Energy Convers. Manage. **33**, No. 2. pp. 135–143.
[4] Smit, F. J. and Meyer, J. P., 1998, ''Investigation of the Potential Effect of Zeotropic Refrigerant Mixture on Performance of a Hot-Water Heat Pump,'' ASHRAE Trans., **104**, pp. 387–394.
[5] Johannsen, A. F. B., 1992, ''Potential of Non-azeotropic Refrigerant Mixtures for Water-Heating Heat Pumps in South Africa,'' Department of Mineral and Energy Affairs, Pretoria, South Africa, Report No. ED 8807.
[6] Smit, F. J., 1996, ''The Influence of a Non-azeotropic Refrigerant Mixture on the Performance of a Hot-Water Heat Pump,'' M. Eng. dissertation, Rand Afrikaans University, Johannesburg, South Africa.
[7] Kebonte, S. A., 1999, ''Condensation Heat Transfer and Pressure Drop Coefficients of R22/R142b in a Water Cooled Helically Coiled Tube-in-Tube Heat Exchanger,'' M. Eng. dissertation, Rand Afrikaans University, Johannesburg, South Africa.
[8] Bukasa, J. M., 1999, ''Average Boiling Heat Transfer and Pressure Drop Coefficients of R22/R142b in a Helically Coiled Water Heated Tube-in-Tube Heat exchanger,'' M. Eng. dissertation, Rand Afrikaans, University, Johannesburg, South Africa.
[9] Schlager, L. M., Pate, M. B., and Bergles, A. E., 1990, ''Evaporation and Condensation Heat Transfer and Pressure Drop in Horizontal, 12.7-mm Microfin Tubes with Refrigerant 22,'' ASME J. Heat Transfer **112**, pp. 1041–1047.
[10] Kline, S. J., and McClintock, F. A. 1953, ''Describing Uncertainties in Single Sample Experiments,'' Mech. Eng., **75**, pp. 3–8.
[11] Akers, W. W., Beans, H. A., and Crosser, O. K. 1959, ''Condensation Heat Transfer Within Horizontal Tubes,'' Chem. Eng. Prog. Symp. Ser., **55**, No. 29 pp. 171–176.
[12] Cavallini, A., and Zecchin, R. A., 1974 ''A Dimensionless Correlation for Heat Transfer in Forced Convention Condensation,'' 6th International Heat Transfer Congress, Tokyo, Japan, Vol. 3, pp. 309–313.
[13] Travis, D. P., Rohsenov, W. M., and Baron, A. B., 1973, ''Forced Convection Condensation Inside Tubes: A Heat Transfer Equation for Condenser Design,'' ASHRAE Trans., **79**, pp. 157–165.
[14] Azer, N. Z., Abis, L. V., and Soliman, H. M. 1972, ''Local Heat Transfer Coefficient During Forced Convection Condensation Inside Horizontal Tube,'' ASHRAE Trans., **77**, Part 1, pp. 182–201.
[15] Jung, D. S., McLinden, M., Radermacher, R., and Didion, D., 1989, ''Horizontal Flow Boiling Heat Transfer Experiments With a Mixture of R22/R114,'' Int. J. Heat Mass Transf., **32**, pp. 131–145.
[16] Murata, K., and Hashizume, K. 1993, ''Forced Convective Boiling of Non-Azeotropic Refrigerant Mixtures Inside Tubes,'' J. Heat Transfer, **115**, pp. 680–688.
[17] Thome, J. R. 1996, ''Boiling of New Refrigerants: A State of the Art Review,'' Int. J. Refrig., **19**, pp. 435–457.

Effect of Tube Inclination on Pool Boiling Heat Transfer

M.-G. Kang
Department of Mechanical Engineering Education,
Andong National University, 388 Songchun-dong,
Andong-city, Kyungbuk 760-749, Korea

An experimental parametric study of a tubular heat exchanger has been carried out under pool boiling conditions to determine effects of the tube inclination angle on pool boiling heat transfer. Through the study, it can be concluded that (1) tube inclination gives much change on pool boiling heat transfer and the effect of the inclination angle is more strongly observed in the smooth tube and (2) if a tube is properly inclined, enhanced heat transfer is expected due to the decrease in bubble slug formation on the tube surface and easy liquid access to the surface.

[S0022-1481(00)01201-9]

Keywords: Boiling, Enhancement, Experimental, Geometry, Heat Transfer

Introduction

The mechanisms of pool boiling heat transfer have been studied for a long time since it is closely related to the designs of more efficient heat exchangers and heat removal systems. Recently, they have been widely investigated in nuclear power plants for application to the design of new passive heat removal systems employed in the advanced light water reactors (ALWRs) designs ([1,2]). To determine the required heat transfer surface area as well as to evaluate the system performance during postulated accidents, a detailed analysis on pool boiling heat transfer applicable for the systems is needed. Through the review of published results it can be concluded that one of the efficient ways to increase the heat transfer rate is the orientation of a heated surface.

Jakob [3] suggested empirical correlations containing orientation effects. According to the results, the horizontal type ($\theta = 0$ deg) is more efficient than the vertical type ($\theta = 90$ deg) in the low heat flux region (i.e., $q'' < 11.8\,\mathrm{kW/m^2}$) while the opposite is true in the high heat flux region. Stralen and Sluyter [4] performed a test to find out boiling curves for platinum wires with various orientations (i.e., $\theta = 0$ deg, 45 deg, and 90 deg) at atmospheric pressure. They said that the horizontal type was more effective than the vertical type both in the natural convection and boiling regions. Nishikawa et al. [5] studied the orientation effect using a flat plate in the water. According to the results, boiling heat transfer in the vertical type is more efficient than the horizontal type in the low heat flux region (less than 100 kW/m^2) and orientation effects become negligible as heat flux on the surface increases more than 100 kW/m^2. Chyu and Mghamis [6] studied the effects of orientation using twisted cylinders in line contact. According to the results, twisted tubes in line contact can change the tendency of heat transfer followed by tube orientation. Most recently, Chun and Kang [7] studied the effect of tube orientation (i.e., $\theta = 0$ deg and 90 deg) on pool boiling heat transfer in combination with tube surface roughness. According to them the slope of heat flux q'' versus tube wall superheat ΔT curve of the vertical tube becomes smaller than that of the horizontal tube as surface rough-

---

Contributed by the Heat Transfer Division for publication in the JOURNAL OF HEAT TRANSFER. Manuscript received by the Heat Transfer Division, Jan. 1999; revision received, Oct. 1999. Associate Technical Editor: T. Chu.

ness decreases. That is, when surface roughness is $\varepsilon = 26.2\,\mathrm{nm}$, the slopes of two q'' versus ΔT curves for horizontal and vertical tubes shift and cross each other around $q'' = 50.0\,\mathrm{kW/m^2}$. Summarizing the works, it can be said that the effect of an inclination angle on pool boiling heat transfer closely depends on the heating surface geometry (i.e., wire, plate, or tube) and surface roughness.

Although many workers have in the past two generations investigated the effect of the inclination angle on pool boiling heat transfer along with the effects of pressure and fluid properties, some areas still must be identified. One of them is a detailed study on the tube type geometry which is frequently encountered in the designs of passive heat exchangers ([2]). Therefore, the present study is aimed at the determination of effects of the tube inclination angle on pool boiling heat transfer to investigate potential areas for improvement of the thermal design of the passive heat exchangers.

Experiments

A schematic view of the present experimental apparatus is shown in Fig. 1. The water storage tank is made of stainless steel and has a rectangular cross section (790 × 860 mm) and a height of 1000 mm. This tank has a glass view port (595 × 790 mm) which permits viewing of the tubes and photographing. The heat exchanger tubes are simulated by resistance heaters made of stainless steel tubes, whose heating length and diameter are 530.5 and

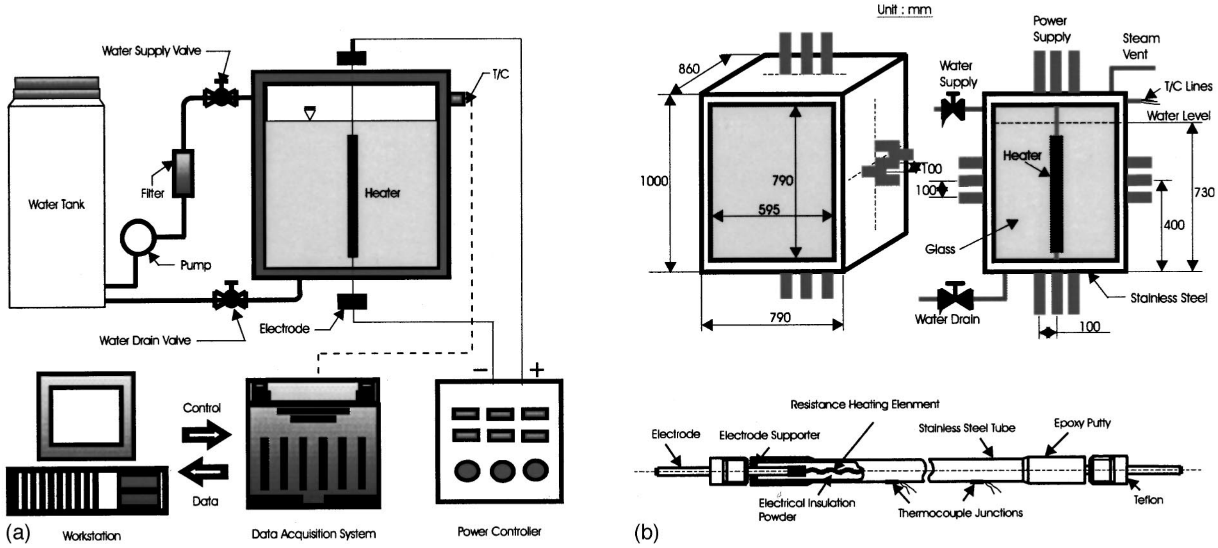

Fig. 1 Schematic diagram of the experimental appratus: (*a*) overall arrangement, (*b*) water storage tank and heated tube

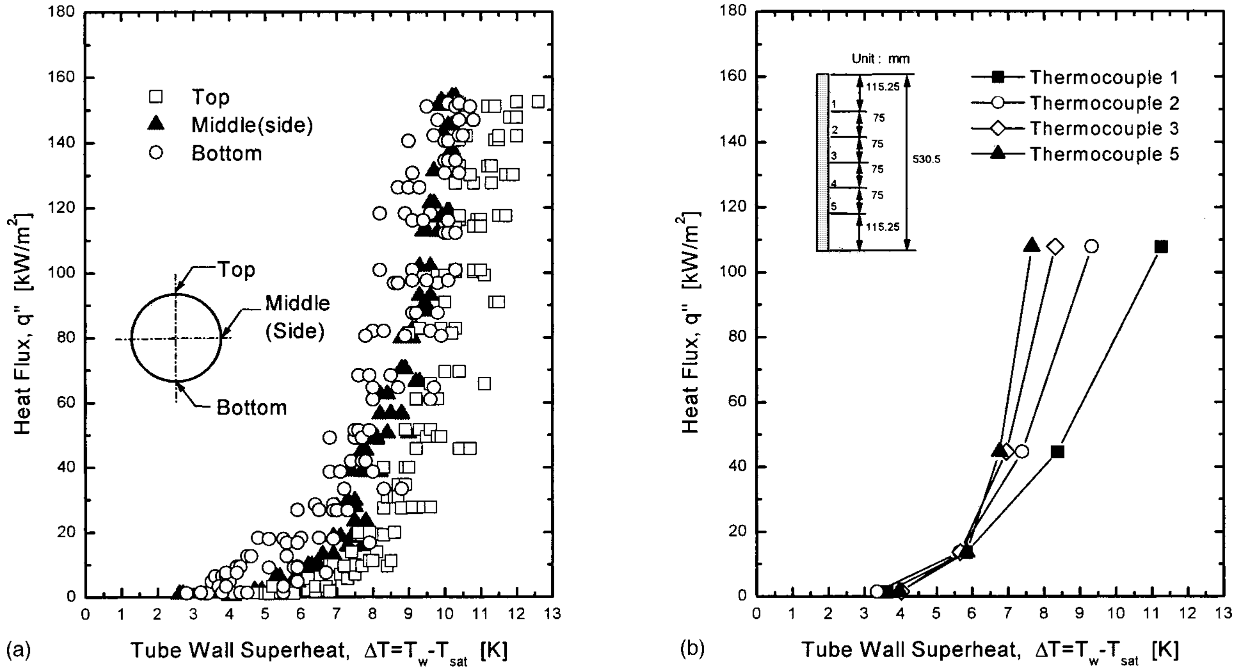

Fig. 2 Changes in heat flux and tube wall superheat due to thermocouple location: (*a*) horizontal tube (θ=0 deg); (*b*) vertical tube (θ=90 deg)

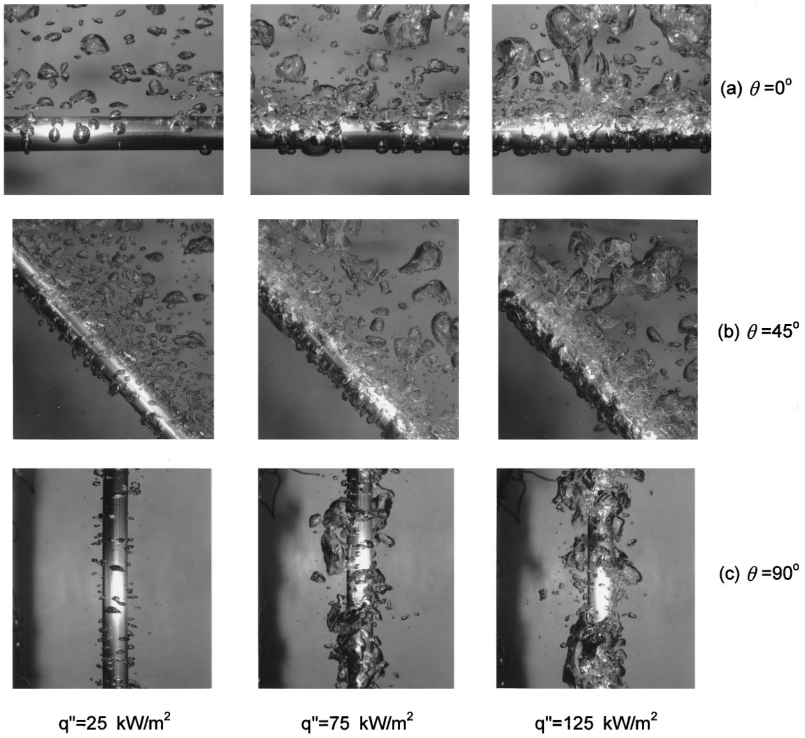

Fig. 3 Bubble generation and coalescence on the heated tube surface ($D=19.05$ mm, $\varepsilon=60.9$ nm) for various heat fluxes: (*a*) $\theta=0$ deg, (*b*) $\theta=45$ deg, and (*c*) $\theta=90$ deg

19.05 mm, respectively. The surfaces of the tubes were instrumented with five thermocouples outside the surface of the tube. The thermocouple tip (about 10 mm) has been bent at a 90 deg angle and brazed the bent tip on the tube wall. The first and the fifth thermocouples are placed at 115.25 mm from both ends of the heating element and the space between other thermocouples is 75 mm.

To determine effects of the tube inclination angle on pool boiling heat transfer one tube diameter ($D=19.05$ mm), two different surface roughness (15.1 and 60.9 nm in root mean square (rms) measured by the phase measuring interferometer), and three different orientations of the heat exchanger tube (i.e., $\theta=0$ deg, 45 deg, and 90 deg) are used to obtain the heat flux q'' versus wall

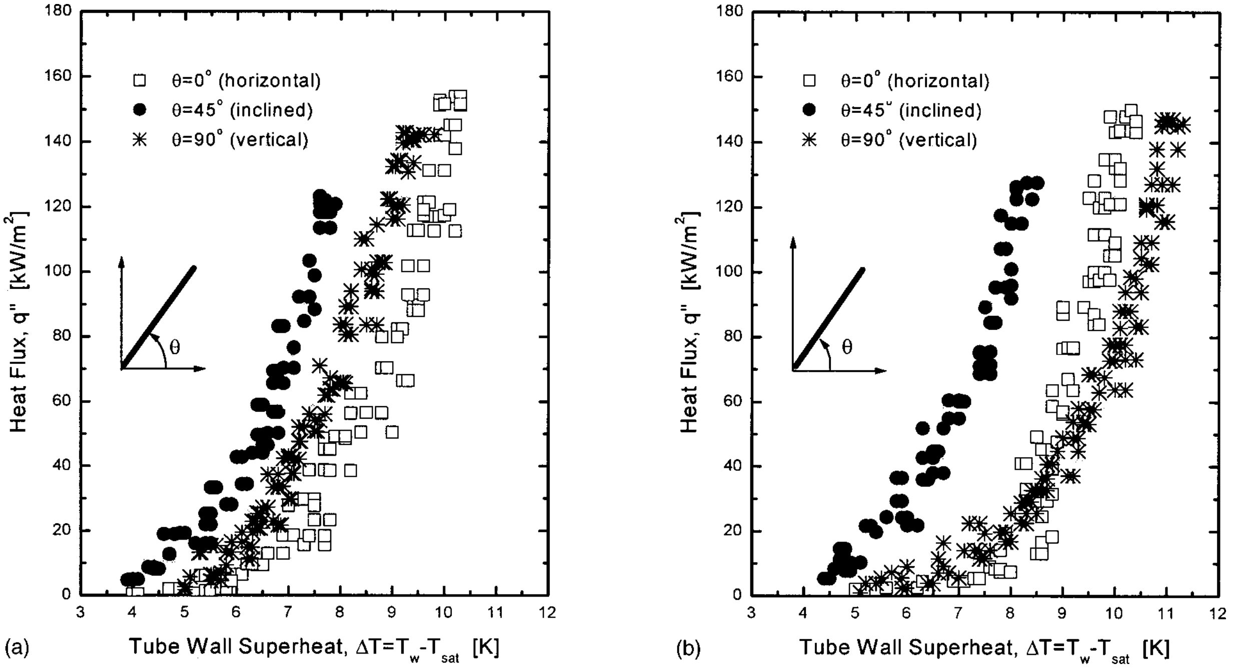

Fig. 4 Effects of tube ($D=19.05$ mm) inclination on pool boiling heat transfer: (*a*) rough surface ($\varepsilon=60.9$ nm) and (*b*) smooth surface ($\varepsilon=15.1$ nm)

superheat ($\Delta T = T_w - T_{sat}$) data. The uncertainty (errors from measurement, instruments, and environmental conditions) in the heat flux, the measured temperature, and surface roughness is estimated to be ±1.0 percent, ±1.0 percent, and ±5.0 nm, respectively.

The water storage tank is filled with water until the initial water level is reached at 730 mm and the water is then boiled for 30 minutes at saturation temperature to remove the dissolved air. The temperatures of the water and heater surfaces are measured while the heater power is set at constant value. However, once the water temperature has reached saturation value (i.e., 100°C since all the tests are run under atmospheric pressure condition), the temperatures of the water and tube surfaces are measured when they are at steady state while controlling the heat flux on the tube surface with input power. In this manner a series of experiments has been performed for various combinations of test parameters.

The heat flux from the electrically heated tube surface is calculated from the measured values of the power input as follows:

$$q'' = \frac{q}{A} = \frac{EI}{\pi DL} = h_b(T_w - T_{sat}) = h_b \Delta T \tag{1}$$

where E and I are the supplied voltage (V) and current (A), and D and L are the outside diameter and the length of the heated tube, respectively. The tube surface temperature T_w used in Eq. (1), on the other hand, is the arithmetic average value of the temperatures measured by five thermocouples brazed on the tube surface. A more detailed description for the experimental apparatus and the test procedure can be found in Chun and Kang's paper [7].

Results and Discussion

The temperature distribution on the horizontal and the vertical tube surfaces during pool boiling tests in the saturated water at atmospheric pressure (i.e., 0.1 MPa) is shown in Fig. 2 and some photos are shown in Fig. 3. For the horizontal tube ($\theta = 0$ deg) shown in Fig. 2(*a*), surface temperatures are measured at the top, middle, and bottom of the tube circumference. These data are a combination of three different tests rotating the tube each test. As shown in the figure, the temperature corresponding to the same heat flux increases from the bottom to the top positions. The main cause of that temperature difference is presumed to be the inherent boiling characteristics of the horizontal tubes. For horizontal tubes, bubbles generated at the bottom side of the tube circumference driven by buoyancy force move toward the top of the tube wall through the tube circumference as shown in Fig. 3(*a*). These bubbles coalesce with other bubbles during traveling, continue growing into large bubbles, and finally depart from the tube surface near the top region of the circumference. Therefore, there exist large bunches composed of bubble and liquid to decrease active nucleation sites on the tube wall. Bubble slug formation also prevents the easy access of liquid to the heating surface, such that the heat transfer rate becomes reduced as the location of the thermocouple approaches the top region. Results of the temperature distribution through the height of the vertical tube are introduced in Fig. 2(*b*). In the figure, temperature changes for four heat fluxes of 1.42, 13.64, 44.68, and 107.9 kW/m^2 are introduced as a function of thermocouple location. As shown in the figure, a large difference in the temperatures of the bottom and the top regions of the vertical tube is observed as heat flux increases. At low heat flux ($q'' = 1.42$ kW/m^2) it is observed that the temperature of thermocouple 1 installed at the upper side of the tube is lower than the temperature of thermocouple 5 installed at the lower side of the tube. The temperature of thermocouple 1, on the other hand, is higher than the temperature of thermocouple 5 by more than 3.5 K at high heat flux ($q'' = 107.9$ kW/m^2). This phenomenon is due to boiling characteristics of the vertical tubes. For vertical tubes, bubbles generated at the bottom can be developed into large bubbles while traveling through the tube height by coalescing with relevant bubbles and finally departing at the top position as shown in Fig. 3(*c*). At low heat flux these bubble slugs agitate relevant liquid and increase heat transfer rate at the top region. At high heat flux, on the other hand, these bubble slugs prevent easy liquid access to the heating surface and result in somewhat rapid convective flow, which could act to suppress boiling near the top regions. That is, as heat flux increases the temperature near the top region also increases significantly compared with the bottom region due to the decrease of the active site density and the creation of the rapid convective flow. Therefore, one of the heat transfer enhancing methods in vertical and horizontal tubes is related to minimizing bubble coalescence at the top region.

If a tube is properly inclined ($\theta = 45$ deg for the present) bubbles move upward and depart before getting to the top regions of the tube circumference and the tube upper side as shown in Fig. 3(*b*). Such that enhanced heat transfer is expected due to the increase in active sites and easy liquid access to the surface followed by: (1) the decrease in bubble slug formation near the top regions, (2) higher liquid agitation and smaller bubble traveling time on the tube surface than the horizontal tube, and (3) the decrease in convective flow near the tube upper side. Figure 4 shows that the effect of tube inclination angle on pool boiling heat transfer is very large. For example, q'' increases 311 percent (from 18 to 74 kW/m^2) when θ is increased from 0 deg (horizontal) to 45 deg and increases 124 percent (from 33 to 74 kW/m^2) when θ is decreased from 90 deg (vertical) to 45 deg at the given wall superheat ($\Delta T = 7$ K) and the tube surface roughness ($\varepsilon = 60.9$ nm). Since much bubble coalescence is expected on the smooth tube surface for the horizontal and the vertical tubes due to the smaller liquid agitation than the rough tube surface, the effect of the tube inclination angle is more strongly observed on the smooth tube. As shown in Fig. 4(*b*) q'' increases more than 360 percent (from 28 to 130 kW/m^2) when θ is decreased from 90 deg (vertical) to 45 deg whereas q'' increases 189 percent (from 45 to 130 kW/m^2) when θ is increased from 0 deg (horizontal) to 45 deg at the given wall superheat ($\Delta T = 8.5$ K) and the tube surface roughness ($\varepsilon = 15.1$ nm).

Conclusions

An experimental parametric study of a tubular heat exchanger (for the case, $L = 530.5$ mm) has been carried out under pool boiling conditions to determine effects of the tube inclination angle on pool boiling heat transfer. Through the study for the three inclination angles ($\theta = 0$ deg, 45 deg, and 90 deg) and two surface roughness ($\epsilon = 15.1$ and 60.9 nm) the following conclusions can be obtained:

1 Tube inclination gives much change on pool boiling heat transfer and the effect of the inclination angle is more strongly observed in the smooth tube.

2 If a tube is properly inclined ($\theta = 45$ deg for the present) enhanced heat transfer is expected due to the decrease in bubble slug formation on the tube surface and easy liquid access to the surface.

Nomenclature

A = heat transfer area, m^2
D = tube outer diameter, m or mm
E = supplied voltage, V
h_b = boiling heat transfer coefficient, kW/m^2 K
I = supplied current, A
L = tube length, m
q'' = heat flux, kW/m^2
q = total heat transfer, kW
T_{sat} = saturated water temperature, K or °C
T_w = tube wall temperature, K or °C
ΔT = degree of superheat of the heating surface ($T_w - T_{sat}$), K
ε = average tube surface roughness in rms value, nm

References

[1] Corletti, M. M., and Hochreiter, L. E., 1991, ''Advanced Light Water Reactor Passive Residual Heat Removal Heat Exchanger Test,'' Proceedings of the 1st JSME/ASME Joint International Conference on Nuclear Engineering, Tokyo, Japan, pp. 381–387.

[2] Kang, M. G., 1998, ''Experimental Investigation of Tube Length Effect on Nucleate Pool Boiling Heat Transfer,'' Ann. Nucl. Energy, **25**, No. 4-5, pp. 295–304.

[3] Jakob, M., and Hawkins, G. A., 1957, *Elements of Heat Transfer*, 3rd. ed., John Wiley and Sons, New York, pp. 206–210.

[4] van Stralen, S. J. D., and Sluyter, W. M., 1969, ''Investigations on the Critical Heat Flux of Pure Liquids and Mixtures Under Various Conditions,'' Int. J. Heat Mass Transf., **12**, pp. 1353–1384.

[5] Nishikawa, K., et al., 1984, ''Effect of Surface Configuration on Nucleate Boiling Heat Transfer,'' Int. J. Heat Mass Transf., **27**, No. 9, pp. 1559–1571.

[6] Chyu, M. C., and Mghamiz, A. M., 1991, ''Nucleate Boiling on Two Cylinders in Line Contact,'' Int. J. Heat Mass Transf., **34**, No. 7, pp. 1783–1790.

[7] Chun, M. H., and Kang, M. G., 1998, ''Effects of Heat Exchanger Tube Parameters on Nucleate Pool Boiling Heat Transfer,'' ASME J. Heat Transfer, **120**, pp. 468–476.

Effects of Vapor Superheat and Condensate Subcooling on Laminar Film Condensation

J. Mitrovic

Institut für Energie- und Verfahrenstechnik, Thermische
Verfahrenstechnik und Antagentechnik, Universität
Paderborn, 33095 Paderborn, Germany
e-mail: mitrovic@vt.uni-paderborn.de

Nusselt's model is employed to illustrate the effects of vapor superheat and condensate subcooling on laminar film condensation occurring under simultaneous actions of gravity and interfacial shear. The vapor superheat affects the condensation kinetics in cooperation with heat transfer in both phases. Under comparable conditions, the condensate film is thinner and the heat transfer coefficient larger for superheated than for saturated vapor. The heat flux on the cooling surface arising from the sensible heat of condensate increases as the critical point of the condensing substance is approached and, at this point, the Nusselt condensation model gives the single-phase boundary layer solutions. [S0022-1481(00)00701-5]

Keywords: Condensation, Film, Heat Transfer, Laminar, Phase Change, Plate

1 Introduction

Since the experiments by Joule [1] and the theory by Nusselt [2], condensation of vapors has been the subject of numerous studies. Kruzhilin [3] supplemented Nusselt's idea by accounting for the condensate inertia. Examining the role of condensate subcooling, both Rohsenow [4] and Labuntsov [5] provided detailed energy balances. Labuntsov, in addition, extended Kruzhilin's model by obtaining the interfacial shear from the momentum change of the vapor crossing the vapor-liquid interface. In all these studies, the wall temperature was considered as constant. Parr [6] first assumed the heat flux to be constant. His theory, however, being not as elegant as that of Nusselt, prompted Jakob [7] to stress that—in light of Nusselt's analysis—the work by Parr was superfluous.

Meanwhile, Nusselt's theory of condensation has been extended in various directions (see, e.g., Rose [8,9] and Marto [10]). Several authors, e.g., Cess [11], Chen [12], Koh [13], and Shekriladze and Gomelauri [14], assuming a saturated vapor, dealt with the effect of interfacial shear on condensation kinetics. Following Webb [15], relatively little is published on methodology of convective condensation of superheated vapors. However, already Nusselt [2] has briefly treated the issue, whereas Stender [16] provided a detailed analysis. Also Kutateladze [17] and Isachenko [18] gave some hints on how to account for the superheat effect. Neglecting vapor convection, Mills [19] reduced condensation of a superheated to that of saturated vapor, as was also done by Sparrow and Eckert [20], Minkowycz and Sparrow [21,22], Ferreira [23], and Fujii [24]. Sparrow and Eckert neglected vapor convection, while Minkowycz and Sparrow [21] considered a quiescent vapor. Heat transfer correlations with condensation of a superheated vapor both in forced flow (without gravity) and pure gravity flow at no condensate subcooling have been developed by Fujii [24].

Insofar as the author of the present paper is aware, condensation of a superheated vapor with simultaneous effects of gravity, interfacial shear, condensate subcooling, and vapor convection has not been studied previously. Here, we incorporate these effects into the Nusselt model. The condensing vapor is taken to be a pure substance of constant physical properties, the cooling surface is a flat vertical plate, and the flow of condensate is governed both by gravity and an interfacial shear.

2 Basic Relationships

The physical picture adopted is illustrated in Fig. 1. The interfacial temperature ϑ_I is below the vapor bulk temperature ϑ_G, resulting in a heat flux q_{IG} on the vapor side of the interface.

At constant physical properties, an energy balance (with $h(0°\mathrm{C})=0$), written for an element of condensate film, sandwiched between the cooling surface and the vapor–liquid interface, gives

$$q_W=q_{IG}+(c_{pL}\vartheta_I+\Delta h)\frac{d\dot{M}}{\mathfrak{J}dz}-\frac{d\dot{H}}{\mathfrak{J}dz}. \tag{1}$$

The heat fluxes q_W and q_{IG} are related to the area $\mathfrak{J}dz$ of the wall surface, $\mathfrak{J}$ being its extension orthogonal to the $y_l z$-plane; Δh is the latent heat of condensation, whereas c_{pL}, $\dot{M}$, and $\dot{H}$ denote the specific heat, the mass, and the enthalpy flows of condensate, respectively.

Defining a local heat transfer coefficient α_W on the wall as

$$q_W=\alpha_W(\vartheta_I-\vartheta_W)=\frac{\lambda_L}{\delta}(\vartheta_I-\vartheta_W) \tag{2}$$

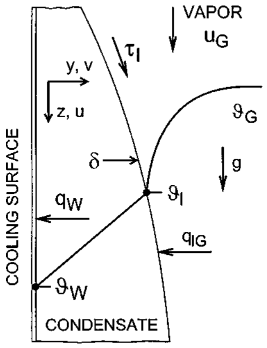

Fig. 1 Illustration of condensation of a superheated vapor on a vertical surface

---

Contributed by the Heat Transfer Division for publication in the JOURNAL OF HEAT TRANSFER. Manuscript received by the Heat Transfer Division, Oct. 9, 1998; revision received, Aug. 9, 1999. Associate Technical Editor: C. Beckermann.

where λ_L is the thermal conductivity of condensate, obtaining the mass and enthalpy flows in the condensate film according to Nusselt's model and combining Eqs. (1) and (2) gives

$$\frac{\lambda_L(\vartheta_I-\vartheta_W)}{\delta}=q_{IG}+\frac{d}{\mathfrak{J}dz}\left(\left(\frac{1}{3}\left(1+\frac{3}{8}\mathrm{Ku}\right)+\frac{1}{2}\left(1+\frac{1}{3}\mathrm{Ku}\right)\frac{\tau_I}{g\delta\Delta\rho}\right)\frac{g\delta^3\mathfrak{J}\Delta\rho\Delta h}{\nu_L}\right) \tag{3}$$

where τ_I is the interfacial shear stress and Ku is the phase-change (Kutateladze) number,

$$\mathrm{Ku}=\frac{c_{pL}(\vartheta_I-\vartheta_W)}{\Delta h}. \tag{4}$$

Equation (3) allows variation of ϑ_W, q_{IG}, $\mathfrak{J}$, and τ_I, and hence a construction of several model cases (see Mitrovic [25]). In what follows, ϑ_W and $\mathfrak{J}$ are always constant while, for illustration reasons, the other two quantities are first considered as independent of z.

3 Film Thickness and Heat Transfer Coefficient

3.1 Constant Heat Flux and Shear Stress at the Interface. For constant τ_I and q_{IG}, Eq. (3) can be rearranged into

$$\frac{\lambda_L(\vartheta_1-\vartheta_W)}{\Delta h}dz=\left(1+\frac{3}{8}\mathrm{Ku}\right)\frac{g\Delta\rho}{\nu_L}\frac{\delta^3 d\delta}{1-a\delta}+\left(1+\frac{1}{3}\mathrm{Ku}\right)\frac{\tau_I}{\nu_L}\frac{\delta^2 d\delta}{1-a\delta}, \tag{5}$$

and solved to give

$$\frac{\lambda_L(\vartheta_I-\vartheta_W)z}{\Delta h}=-\left(1+\frac{3}{8}\mathrm{Ku}\right)\frac{g\Delta\rho}{\nu_L a^4}\left(\ln(1-a\delta)+a\delta+\frac{1}{2}(a\delta)^2+\frac{1}{3}(a\delta)^3\right)-\left(1+\frac{1}{3}\mathrm{Ku}\right)\frac{\tau_I}{\nu_L a^3}\left(\ln(1-a\delta)+a\delta+\frac{1}{2}(a\delta)^2\right) \tag{6}$$

if $\delta=0$ at $z=0$; the quantity a, introduced by Nusselt [2], represents the reciprocal of a length

$$a=\frac{q_{IG}}{\lambda_L(\vartheta_I-\vartheta_W)}. \tag{7}$$

The product $a\delta$ in Eq. (6) can be obtained from Eqs. (2) and (7) as

$$a\delta=\frac{q_{IG}}{q_W}, \tag{8}$$

requiring $a\delta<1$ for condensation to occur; for $a\delta=1$, no phase change is possible at a net rate, and this case is excluded from the present treatment.

For graphical illustration, Eq. (6) is written nondimensionally as

$$\frac{az}{B_1}=-\left(\ln(1-a\delta)+a\delta+\frac{1}{2}(a\delta)^2+\frac{1}{3}(a\delta)^3\right)-\frac{B_2}{B_1}\left(\ln(1-a\delta)+a\delta+\frac{1}{2}(a\delta)^2\right) \tag{9}$$

where

$$B_1=\left(1+\frac{3}{8}\mathrm{Ku}\right)\frac{g\Delta\rho}{\nu_L a^3}\frac{\Delta h}{\lambda_L\Delta\vartheta}, \tag{10}$$

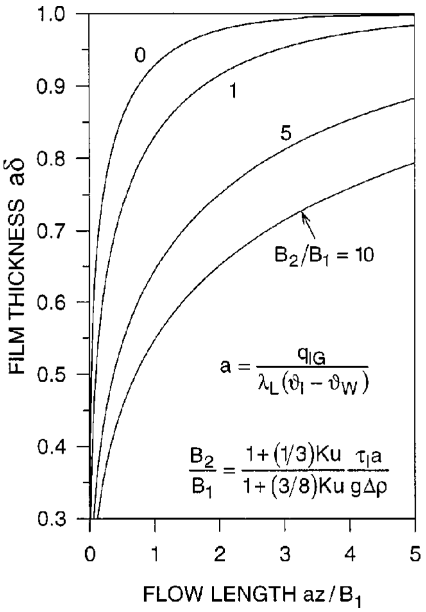

Fig. 2 Variation of dimensionless film thickness $a\delta$ along cooling surface at some values of $B_2/B_1\sim\tau_I a/(g\Delta\rho)\sim\tau_I q_{IG}$. The curve $B_2/B_1=0$ correspond to the gravity region; when the roles of B_1 and B_2 are interchanged, this curve represents (approximately) also the shear stress region.

$$B_2=\left(1+\frac{1}{3}\mathrm{Ku}\right)\frac{\tau_I}{\nu_L a^2}\frac{\Delta h}{\lambda_L\Delta\vartheta}. \tag{11}$$

Two limiting condensation regimes are obvious from Eq. (9). For $B_1=0$, the condensate flow is governed by interfacial shear, while for $B_2=0$ by gravity. These regimes should be examined separately in the following. Prior to this, however, we may introduce a nondimensional heat transfer coefficient

$$\frac{\alpha_W}{\lambda_L a}=\frac{1}{a\delta}=\frac{q_W}{q_{IG}}, \tag{12}$$

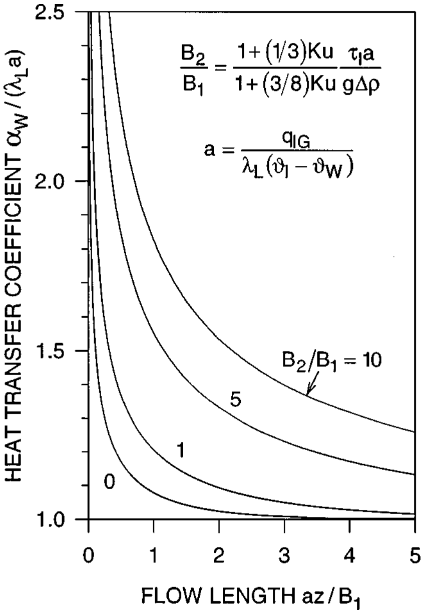

Fig. 3 Heat transfer modulus $\alpha_W/(\lambda_L a)$ corresponding to the film thickness in Fig. 2

with α_W according to Eq. (2), and illustrate the distributions of both $a\delta$ and $\alpha_W/(\lambda_L a)$ along the cooling surface.

Figure 2 pictures Eq. (9) and Fig. 3 Eq. (12) for a few values of $B_2/B_1 \sim \tau_I a/(g\Delta\rho) \sim \tau_I q_{IG}$. As may be inferred from these figures, an increase of the ratio B_2/B_1 reduces the film thickness, thus improving heat transfer. The curve $B_2/B_1 = 0$ represents the pure gravity regime. The other limiting case, $B_1/B_2 = 0$, the shear condensation, is not shown in the figures, but is easily obtained, at least qualitatively, by interchanging the roles of B_1 and B_2.

3.1.1 Gravity Region of Condensate Flow. At approximately equal velocities of vapor bulk and film surface, the effect of vapor shear on the condensate flow is negligible and, for $\tau_I \to 0$, Eq. (6) reduces to

$$\frac{\lambda_L(\vartheta_I-\vartheta_W)z}{\Delta h} = -\left(1+\frac{3}{8}\mathrm{Ku}\right)\frac{g\Delta\rho}{\nu_L a^4}\left(\ln(1-a\delta) + a\delta + \frac{1}{2}(a\delta)^2 + \frac{1}{3}(a\delta)^3\right). \tag{13}$$

For Ku = 0, this equation becomes identical to the one derived by Nusselt [2] except for a typographical error in his expression.

Expanding the logarithm into a series, Eq. (13) takes the shape

$$\frac{\lambda_L(\vartheta_I-\vartheta_W)z}{\Delta h} = \left(1+\frac{3}{8}\mathrm{Ku}\right)\frac{g\Delta\rho}{\nu_L}\left(\frac{1}{4}\delta^4 + a^{-4}\sum_{m=5}^{\infty}\frac{(a\delta)^m}{m}\right). \tag{14}$$

Setting $a=0$, we obtain the Nusselt equation for a saturated vapor ($\delta=\delta_0$)

$$\frac{\lambda_L(\vartheta_I-\vartheta_W)z}{\Delta h} = \left(1+\frac{3}{8}\mathrm{Ku}\right)\frac{g\Delta\rho}{\nu_L}\frac{\delta_0^4}{4}, \tag{15}$$

which, when combined with Eq. (14), delivers

$$\delta_0^4 - \delta^4 = 4a^{-4}\sum_{m=5}^{\infty}\frac{(a\delta)^m}{m}. \tag{16}$$

Since $a>0$, $\delta<\delta_0$. Thus, under otherwise identical conditions, the condensate film is thinner for superheated than for saturated vapor. This is qualitatively in agreement with the results Fujii [24] obtained from a different way of treatment.

The effect of condensate subcooling, that is of Ku, on condensation heat transfer has been analyzed by many authors, see, e.g., Sadasivan and Lienhard [26] and Fujii [24], but the case of a very large Ku has not been pursued in earlier studies. For large Ku to be established requires a correspondingly large temperature difference through the condensate film (maximum: condensation minus freezing temperature), or condensation near the thermodynamic critical point of the substance. In the latter case, the specific heat capacity increases and the latent heat decreases as the critical point is approached. At this point, $\Delta h \to 0$, and we get $\mathrm{Ku}\to\infty$, thereby leaving the two-phase and entering the single-phase region.

At the critical point the vapor superheat loses its physical significance concerning the common (first-order) phase change, and we may set $a=0$. Thus, for $\mathrm{Ku}\to\infty$, Eq. (14) reduces to

$$\delta = \left(\frac{32}{3}\frac{\lambda_L\nu_L z}{c_{pL}g\Delta\rho}\right)^{1/4} \tag{17}$$

with the density difference $\Delta\rho$ depending on the bulk-to-wall temperature difference, whereas the quantity δ may now be identified as a thickness of a boundary layer, giving a local heat transfer coefficient as

$$\alpha_W = \left(\frac{3}{32}\frac{c_{pL}g\Delta\rho\lambda_L^3}{\nu_L z}\right)^{1/4}. \tag{18}$$

Equation (18) coincides qualitatively with the boundary layer expression for single phase, laminar, free convection past a vertical plate where the constant deduced from the boundary layer considerations is about 0.508, at large Prandtl number. This is approximately by nine percent less than in Eq. (18). Hence, the Nusselt theory ''smoothly'' connects the condensation heat transfer with the single-phase convection via the critical point.

3.1.2 Shear Stress Driven Condensate Film. When vapor shear dominates the condensate flow and the gravity effect is neglected, Eq. (6) yields

$$\frac{\lambda_L(\vartheta_I-\vartheta_W)z}{\Delta h} = -\left(1+\frac{1}{3}\mathrm{Ku}\right)\frac{\tau_I}{\nu_L a^3}\left(\ln(1-a\delta) + a\delta + \frac{1}{2}(a\delta)^2\right), \tag{19}$$

which for $a=0$ (saturated vapor, $\delta=\delta_0$) becomes

$$\frac{\lambda_L(\vartheta_I-\vartheta_W)z}{\Delta h} = \frac{1}{3}\left(1+\frac{1}{3}\mathrm{Ku}\right)\frac{\tau_I\delta_0^3}{\nu_L}. \tag{20}$$

Applying the same procedure as for the gravity region, Eqs. (19) and (20) give

$$\delta_0^3 - \delta^3 = 3a^{-3}\sum_{m=4}^{\infty}\frac{(a\delta)^m}{m}, \tag{21}$$

showing, like Eq. (16), a smaller film thickness δ at a larger q_{IG}. This is generally in agreement with the numerical studies of Fujii [24] and Minkowycz and Sparrow [22].

Corresponding to Eq. (20), we have

$$\alpha_W = \left(\frac{1}{3}\frac{\tau_I\Delta h\lambda_L^2}{\nu_L(\vartheta_I-\vartheta_W)z}\left(1+\frac{1}{3}\mathrm{Ku}\right)\right)^{1/3}. \tag{22}$$

Finally, if, despite the assumptions of a constant interfacial shear, τ_I is taken from the single-phase laminar boundary layer solution for an impermeable wall,

$$\tau_I = 0.332\rho_G u_G^2\,\mathrm{Re}_{Gz}^{-1/2}, \tag{23}$$

(see, e.g., Schlichting [27]), Eq. (22) results in

$$\alpha_W = \left(\frac{0.332}{3}\right)^{1/3}\frac{\lambda_L}{z}\mathrm{Re}_{Gz}^{1/2}\mathrm{Pr}_L^{1/3}\mathrm{Ku}^{-1/3}\left(1+\frac{1}{3}\mathrm{Ku}\right)^{1/3}\left(\frac{\rho_G}{\rho_L}\frac{\nu_G^2}{\nu_L^2}\right)^{1/3}. \tag{24}$$

Here, $\mathrm{Re}_{Gz}=u_G z/\nu_G$ is the local vapor Reynolds number, u_G is the relative vapor velocity, and Pr_L is the Prandtl number of condensate. At the critical temperature ($\mathrm{Ku}\to\infty$), Eq. (24) simplifies to the boundary layer plate solution for single-phase laminar forced convection.

Introducing the parameter $G=(\mathrm{Ku}/\mathrm{Pr}_L)(\rho_L^2\nu_L/\rho_G^2\nu_G)^{1/2}$, Eq. (24) can be written as

$$\mathrm{Nu}_z\,\mathrm{Re}_{Lz}^{-1/2} = 0.480G^{-1/3}\left(1+\frac{1}{3}\mathrm{Pr}_L\left(\frac{\nu_G}{\nu_L}\frac{\rho_G^2}{\rho_L^2}\right)^{1/2}G\right)^{1/3} \tag{25}$$

where $\mathrm{Nu}_z=\alpha_W z/\lambda_L = z/\delta$ and $\mathrm{Re}_{Lz}=u_G z/\nu_L$. Expressions of this form are well known from the literature (see, e.g., Rose [8] and Marto [10]). The effect of Pr_L and $(\rho_L^2\nu_L)/(\rho_G^2\nu_G)$ on the product $\mathrm{Nu}_z\,\mathrm{Re}_{Lz}^{-1/2}$ disappears asymptotically as G goes to zero, which is in agreement with the numerical treatments of the boundary layer equations (see, e.g., Koh [13]).

For $\mathrm{Re}_{Gz}=u_G z/\nu_G > 5\times10^5$, the vapor boundary layer is turbulent, thus with

$$\tau_I = 0.0296\rho_G u_G^2\,\mathrm{Re}_{Gz}^{-1/5} \tag{26}$$

and $G=(\mathrm{Ku}/\mathrm{Pr}_L)(\rho_L^5\nu_L/\rho_G^5\nu_G)^{1/5}$, Eq. (22) gives

$$\mathrm{Nu}_z\,\mathrm{Re}_{Lz}^{-3/5} = 0.214\;G^{-1/3}\left(1+\frac{1}{3}\mathrm{Pr}_L\left(\frac{\nu_G}{\nu_L}\frac{\rho_G^5}{\rho_L^5}\right)^{1/5}G\right)^{1/3}. \tag{27}$$

In a similar way, equations for condensation in tubes could also be obtained. For a superheated vapor, however, no simple expressions are deducible from the basic Eq. (19). Note that Eqs. (25) and (27) require a very low condensation rate ($G \to 0$) and a hydrodynamically smooth condensate surface.

3.2 Effect of Condensation Rate on Interfacial Shear Stress and Heat Flux. As is well known, condensation of a vapor is a typical example of fluid flow with suction, the suction rate being governed thermally. Vapor suction thins the boundary layer, thereby increasing both the interfacial shear and vapor convection. The simplest and, at the same time, most frequently used expression for the shear stress τ_I with fluid suction can be written (see, e.g., Bird et al. [28]) as

$$\frac{\tau_I}{\tau_{I0}} = \frac{\varepsilon}{1-\exp(-\varepsilon)} \tag{28}$$

where τ_{I0} is the shear stress at no suction (Eqs. (23) and (26)) and $\varepsilon = \rho_G v_{IG} u_G / \tau_{I0} > 0$ is the suction parameter. The latter quantity depends via the condensation rate, $\rho_G v_{IG} = (1/\mathfrak{J}) d\dot{M}/dz$, on heat transfer.

The heat flux q_{IG} may be calculated by a method well established in condensation of vapor mixtures (see, e.g., Webb [29], Mitrovic and Gneiting [30]). Thus,

$$q_{IG} = \alpha_{IG}(\vartheta_G - \vartheta_I) \tag{29}$$

where

$$\frac{\alpha_{IG}}{\alpha_{IG0}} = \frac{\rho_G v_{IG} c_{pG} / \alpha_{IG0}}{1-\exp(-\rho_G v_{IG} c_{pG} / \alpha_{IG0})} \tag{30}$$

with α_{IG0} and α_{IG} as the vapor-side heat transfer coefficients without and with vapor suction, respectively.

Expressions (28) and (30) for τ_I and q_{IG} do not allow an analytical integration of Eq. (3). Solutions for a saturated vapor ($\tau_{I0} = 0$) in the shear stress region at $\tau_{I0} = 0$ giving $\tau_I = \rho_G v_{IG} u_G$ are summarized, e.g., by Rose [8]. In the following, we shall briefly discuss a solution for a superheated vapor at a negligible vapor convection and specify the conditions of its applicability.

Neglecting vapor convection ($\alpha_{IG0} = 0$), Eq. (29) becomes

$$q_{IG} = \rho_G v_{IG} c_{pG}(\vartheta_G - \vartheta_I), \tag{31}$$

expressing the heat flux which arises from the condensation rate when cooled as vapor from the bulk down to the interfacial temperature. Supplementing this equation by latent heat, we get the heat flux on the cooling surface to be

$$q_W = \rho_G v_{IG}(\Delta h + c_{pG}(\vartheta_G - \vartheta_I)) = \frac{\Delta h + c_{pG}(\vartheta_G - \vartheta_I)}{\mathfrak{J}} \frac{d\dot{M}}{dz}, \tag{32}$$

if the subcooling of condensate is disregarded. Equations (31) and (32) were first derived by Stender [16]. For a flowing vapor, he added to Eq. (32) a convection term.

Combining Eqs. (3) and (31) and taking ϑ_G and τ_I as constant, one obtains

$$\frac{\lambda_L(\vartheta_I - \vartheta_W)z}{\Delta h_*} = \left(1 + \frac{3}{8}\mathrm{Ku}_*\right)\frac{g\Delta\rho}{\nu_L}\frac{\delta^4}{4} + \left(1 + \frac{1}{3}\mathrm{Ku}_*\right)\frac{\tau_I}{\nu_L}\frac{\delta^3}{3} \tag{33}$$

where $\Delta h_* = \Delta h + c_{pG}(\vartheta_G - \vartheta_I)$ and $\mathrm{Ku}_* = c_{pL}(\vartheta_I - \vartheta_W)/\Delta h_*$. This equation, when correspondingly adapted, describes the numerical results of Sparrow and Eckert [20] for $\mathrm{Ku}_* < 0.4$ and $1 < \mathrm{Pr}_L < 100$ with a deviation less than approximately five percent.

Because of its simplicity, it seems useful to specify the applicability range of Eq. (33) under common condensation conditions. Confining ourselves to the gravity region ($\tau_I = 0$) assuming

$$\alpha_{IG0} \leqslant \rho_G v_{IG} c_{pG}, \tag{34}$$

further, requiring Eq. (31) to be also valid at $\alpha_{IG0} \neq 0$ and combining Eqs. (32) and (34), gives

$$\rho_G v_{IG} = \left(\frac{1}{4}\frac{g\Delta\rho\lambda_L^3}{\nu_L z\Omega}\right)^{1/4}\left(\frac{\vartheta_I - \vartheta_w}{\Delta h}\right)^{3/4}, \tag{35}$$

$$\Omega = 1 + \frac{3}{8}\frac{c_{pL}(\vartheta_I - \vartheta_W)}{\Delta h + c_{pG}(\vartheta_G - \vartheta_I)}, \tag{36}$$

$$\alpha_{IG0} \leqslant \left(\frac{1}{4}\frac{g\Delta\rho c_{pG}\lambda_L^3}{\nu_L z\Omega}\right)^{1/4}\left(\frac{c_{pG}(\vartheta_I - \vartheta_W)}{\Delta h}\right)^{3/4}. \tag{37}$$

For a numerical illustration, we may take water at $\vartheta_I = 100°\mathrm{C}$. Then, setting $z = 1$ m, $\vartheta_G - \vartheta_I = 40$ K, and $\vartheta_I - \vartheta_W = 5$ K, Eq. (37) delivers $\alpha_{IG0} \leqslant 23\ \mathrm{W/(m^2\,K)}$.

When the criterion Eq. (37) is not satisfied, Eq. (6), or the corresponding limit expressions Eqs. (13) and (19), although obtained at constant both q_{IG} and τ_I, may be combined with Eqs. (28)–(30) and used for local calculations. However, higher accuracy is achieved when Eqs. (28)–(30) are introduced in Eq. (3) and evaluation is performed stepwise along the cooling surface.

4 Conclusions

The effects of vapor superheat, condensate subcooling, gravity, interfacial shear, and vapor convection on laminar film condensation have been examined on the basis of Nusselt's model. The expressions obtained show the vapor convection to reduce the condensate film thickness in comparison to saturated vapor. The consequence of this effect is a lowering of the transport resistance of condensate which increases the condensation rate.

Expressions for both interfacial shear and heat flux deduced from the film theory contain a condensation rate which changes along the flow path. This leads to a strong nonlinearity of the balance equations requiring their numerical treatment. A criterion derived in this paper specifies the applicability range of the equation valid for a superheated vapor at negligible convection in the gravity flow region.

It is further demonstrated that the Nusselt condensation theory ''smoothly'' connects the condensation heat transfer with single-phase convection via the thermodynamic critical point of the condensing substance.

Acknowledgment

The author wishes to express his thanks to the reviewers for their remarks and recommendations.

Nomenclature

a = reciprocal of length arising from vapor superheat, Eq. (7)
B = nondimensional quantity (B_1 Eq. (10), B_2 Eq. (11))
c_p = specific heat capacity
g = acceleration due to gravity
G = nondimensional parameter
$\dot{H}$ = enthalpy flow of condensate
Δh = latent heat of condensation
Ku = phase-change (Kutateladze) number, Eq. (4)
$\dot{M}$ = condensate flow rate
Nu = Nusselt number
Pr = Prandtl number
q = heat flux
Re = Reynolds number
u = velocity in z-direction
v = velocity in y-direction
y = coordinate orthogonal to cooling surface
z = coordinate along cooling surface
α = heat transfer coefficient
δ = thickness of condensate film
ϑ = temperature
$\Delta\vartheta$ = temperature difference through condensate film
ε = suction parameter
λ = thermal conductivity

ν = kinematic viscosity
ρ = density, $\Delta\rho$ liquid-to-vapor density difference
τ = shear stress
$\mathfrak{J}$ = extension of cooling surface orthogonal to condensate flow

Subscripts

I = at vapor-liquid interface
G = vapor
L = liquid
0 = without suction, also saturated vapor
W = at cooling surface
z = local value

References

[1] Joule, J. P., 1861, ''On the Surface Condensation of Steam,'' Philos. Trans. R. Soc. London, **151**, pp. 133–160.
[2] Nusselt, W., 1916, ''Die Oberflächenkondensation des Wasserdampfes,'' Z VDI, **60**, pp. 541–546, 569–575.
[3] Kruzhilin, G. N., 1937, ''Improvement of the Nusselt Theory of Heat Transfer with Condensation,'' J. Tech. Phys., **7**, pp. 2011–2017.
[4] Rohsenow, W. M., 1956, ''Heat Transfer and Temperature Distribution in Laminar-Film Condensation,'' Trans. ASME, **78**, pp. 1645–1648.
[5] Labuntsov, D. A., 1956, ''On the Influence of Convection and Inertia of Condensate on Heat Transfer with Laminar Film Condensation,'' Therm. Eng., **12**, pp. 47–50.
[6] Parr, P. H., 1921, ''The Water Film on Evaporating and Condensing Tubes,'' Engineer, **131**, pp. 559–561.
[7] Jakob, M., 1921, ''Die Wasserhaut an Verdampfer-und Kondensatorrohren,'' Z. VDI, **65**, pp. 1244–1246.
[8] Rose, J. W., 1988, ''Fundamentals of Condensation Heat Transfer: Laminar Film Condensation,'' JSME J. Ser. II, **31**, pp. 357–375.
[9] Rose, J. W., 1998, ''Condensation Heat Transfer Fundamentals,'' Trans. Inst. Chem. Eng., **76**, Pt. A, pp. 143–152.
[10] Marto, J. P., 1998, ''Condensation,'' in *Handbook of Heat Transfer*, 3rd ed., W. M. Rohsenow et al., ed., McGraw-Hill, New York.
[11] Cess, R. D., 1960, ''Laminar-Film Condensation on a Flat Plate in the Absence of a Body Force,'' Z. Angew. Math. Phys., **11**, pp. 426–433.
[12] Chen, M. M., 1961, ''An Analytical Study of Laminar Film Condensation: Part 1-Flat Plate,'' ASME J. Heat Transfer, **83**, pp. 48–54.
[13] Koh, J. C. Y., 1962, ''Film Condensation in a Forced-Convection Boundary-Layer Flow,'' Int. J. Heat Mass Transf., **5**, pp. 941–954.
[14] Shekriladze, I. G., and Gomelauri, V. I., 1966, ''Theoretical Study of Laminar Film Condensation of Flowing Vapour,'' Int. J. Heat Mass Transf., **9**, pp. 581–591.
[15] Webb, R. L., 1998, ''Convective Condensation of Superheated Vapor,'' ASME J. Heat Transfer, **120**, pp. 418–421.
[16] Stender, W., 1925, ''Der Wärmeübergang bei kondensierendem Heissdampf,'' Z. VDI, **69**, pp. 905–909.
[17] Kutateladze, S. S., 1937, ''On the Use of the Similarity Theory in the Process of Condensation of Saturated Vapor,'' J. Tech. Phys., **7**, pp. 282–293.
[18] Isachenko, V. L., 1977, *Heat Transfer with Condensation*, Energiya, Moscow.
[19] Mills, A. F., 1999, *Heat Transfer*, 2nd edition, Prentice Hall, Englewood Cliffs, NJ.
[20] Sparrow, E. M., and Eckert, E. R. G., 1961, ''Effects of Superheated Vapor and Non-Condensable Gases on Laminar Film Condensation,'' A.I.Ch.E. J., **7**, pp. 474–477.
[21] Minkowycz, W. J., and Sparrow, E. M., 1966, ''Condensation Heat Transfer in the Presence of Noncondensables, Interfacial Resistance, Superheating, Variable Properties, and Diffusion,'' Int. J. Heat Mass Transf., **9**, pp. 1125–1144.
[22] Minkowycz, W. J., and Sparrow, E. M., 1969, ''Effect of Superheating on Condensation Heat Transfer in a Forced Convection Boundary Layer,'' Int. J. Heat Mass Transf., **12**, pp. 147–154.
[23] Ferreira, S. M. M., 1973, ''Forced Convection Condensation of Vapor Flowing Around a Circular Cylinder: Effect of the Presence of Inert Gas, Gravitation Field and Superheating,'' Chem. Eng. J., **6**, pp. 81–90.
[24] Fujii, T., 1991, *Theory of Laminar Film Condensation*, Springer, Berlin.
[25] Mitrovic, J., 1998, ''The Nusselt Condensation and Nonisothermality,'' Int. J. Heat Mass Transf., **41**, pp. 4055–4061.
[26] Sadasivan, P., and Lienhard, J. H., 1987, ''Sensible Heat Correction in Laminar Film Boiling and Condensation,'' ASME J. Heat Transfer, **109**, pp. 545–547.
[27] Schlichting, H., 1979, *Boundary-Layer Theory*, McGraw-Hill, New York.
[28] Bird, R. B., Stewart, W. E., and Lightfoot, E. N., 1960, *Transport Phenomena*, Wiley, New York.
[29] Webb, D. R., 1990, ''Multicomponent Condensation,'' Proceedings of the 9th International Heat Transfer Conference, Vol. 1, pp. 287–304.
[30] Mitrovic, J., and Gneiting, R., 1996, ''Kondensation von Dampfgemischen,'' *Forschung im Ingenieurwesen*, Vol. 62, Springer-Verlag, New York, pp. 1–10, 33–42, and 81–89.

Predicting the Influence of Compressibility and Thermal and Flow Distribution Asymmetry on the Frequency-Response Characteristics of Multitube Two-Phase Condensing Flow Systems

C. J. Kobus
Visiting Assistant Professor, Mem. ASME, Oakland University, Rochester, MI 48309
e-mail: cjkobus@oakland.edu

G. L. Wedekind
John F. Dodge Professor of Engineering, Mem. ASME, Oakland University, Rochester, MI 48309
e-mail: wedekind@oakland.edu

B. L. Bhatt
Professor and Associate Dean of Engineering and Computer Science, Mem. ASME, Oakland University, Rochester, MI 48309
e-mail: bhatt@oakland.edu

An equivalent single-tube model concept was extended to predict the frequency-response characteristics of multitube two-phase condensing flow systems, complete with the ability to predict the influence of compressibility and thermal and flow distribution asymmetry. The predictive capability of the equivalent single-tube model was verified experimentally with extensive data that encompassed a three-order-of-magnitude range of frequencies, and a wide range of operating parameters. [S0022-1481(00)00601-0]

Keywords: Condensation, Heat Transfer, Heat Exchangers, Two-Phase, Unsteady

Introduction

The research presented in this paper is associated with the influence of compressibility on the frequency-response characteristics of multitube condensing flow systems. To the best knowledge of the authors, the archival literature does not contain any theoretical models for predicting the frequency-response characteristics of such systems. There is also very little experimental data. Filling these knowledge gaps is the focus of this research.

Kobus et al. [1] extended the predictive capability of the equivalent single-tube model to predict the frequency-response characteristics of multitube condensing flow systems when compressibility effects are negligible. The influence of compressibility on transient flow surges in multitube condensing flow systems was investigated by Wedekind et al. [2]. The effects of compressibility on a *single-tube* condensing flow system had also been studied earlier ([3]). Given the complexity of the physical mechanisms involved, and the fact that most of them are coupled in some way, a significant step is involved between successfully

---

Contributed by the Heat Transfer Division for publication in the JOURNAL OF HEAT TRANSFER. Manuscript received by the Heat Transfer Division, Aug. 25, 1998; revision received, Aug. 23 1999. Associate Technical Editor: M. Kaviany.

modeling the frequency-response characteristics in a single-tube condenser, and having the same level of success when the condenser is multitube. The major purpose of this research, then, is to investigate the requirements for extending the equivalent single-tube model so that it can successfully predict the influence of compressibility on the frequency-response characteristics for a multitube system, and to verify the model by comparing its predictions with experimental data.

Formulation of Governing Differential Equations

The formulation of the governing differential equations, including the effects of compressibility, was presented in previous research ([2]), but solved for the case of *transient flow surges*. Therefore, details of the development of these governing equations will not be repeated here. The solution of the equations, however, will be presented for the special case of a sinusoidal inlet vapor flowrate $m_{t,i}(t)$.

Equivalent Single-Tube Model . The equivalent single-tube model is based on the system mean void fraction model, which is a one-dimensional, two-fluid, distributed parameter *integral model* developed in previous research ([2]). It represents a way of modeling the transient characteristics of the effective point of complete condensation $\eta(t)$. The system mean void fraction model incorporates the concept of a system mean void fraction $\overline{\alpha}$. The differential equation governing the effective point of complete condensation for a representative jth tube, $\eta_j(t)$, obtained from the conservation of mass and energy principles ([2]), is expressed as follows:

$$\tau_{c,j}\frac{d\eta_j(t)}{dt}+\eta_j(t)=x_i\frac{(h'-h)}{\overline{f}_{q,j}P_j}\gamma_j m_{t,i}(t) \tag{1}$$

where

$$\tau_{c,j}=\frac{\rho'(h'-h)\overline{\alpha}A_{t,j}}{\overline{f}_{q,j}P_j}. \tag{2}$$

In the above equations, $\overline{f}_{q,j}$ represents the spatially averaged heat flux for a representative jth tube, x_i the inlet flow quality, $A_{t,j}$ and P_j the tube cross-sectional area and periphery, respectively, and ρ' and $(h'-h)$ the saturated vapor density and heat of vaporization.

The system mean void fraction $\overline{\alpha}$ is defined in terms of the local area void fraction $\alpha(z,t)$, and represents the integral form of the mean value theorem. The particular void fraction model used is that of Zivi [4], chosen for its simplicity, yet is sufficiently accurate for these types of condensing flow problems. However, any void fraction-flow quality relationship that is valid over the full range of flow qualities would yield similar results. It was established in previous early research that the system mean void fraction is essentially time invariant. This has the effect of uncoupling the conservation of mass and energy principles in the two-phase region from the transient form of the momentum principle; thus, only the steady-state form of the momentum principle is required. The system mean void fraction $\overline{\alpha}$ can therefore be expressed as

$$\begin{aligned}\overline{\alpha}&\equiv\frac{1}{\eta(t)}\int_{z=0}^{\eta(t)}\alpha(z,t)dz\\&=\frac{1}{(1-a)}+\frac{a}{x_i(1-a)^2}\,\mathrm{Ln}\left|\frac{a}{a+(1-a)x_i}\right|;\quad a=(\rho/\rho')^{2/3}.\end{aligned} \tag{3}$$

The equivalent single-tube model is an approximation technique that has been shown to be successful in predicting various transient characteristics associated with multitube condensing flow systems ([2,1]). This approximation technique has the effect of reducing the equations governing the multitube system, which contain complex summations ([2]), to an approximation where the summations are eliminated. The resulting approximation has the appearance of being an equivalent single-tube condensing flow system, but where the associated parameters are weighted with determinable multitube parameters. The equivalent single-tube model contains an equivalent single-tube condensing flow system time constant $\tau_{c,s}$ which is a weighted average of the condensing flow system time constants of each of the individual tubes $\tau_{c,j}$, thus

$$\tau_{c,s}=\sum_{j=1}^{n}\gamma_j\tau_{c,j}=\tau_{c,1}\sum_{j=1}^{n}\gamma_j\beta_j;\quad \beta_j=\overline{f}_{q,1}/\overline{f}_{q,j} \tag{4}$$

where the flow distribution parameter γ_j is defined as the fraction of the total mass flowrate entering tube j. In general, $0\leqslant\gamma_j\leqslant 1$. A flow distribution parameter $\gamma_j=1/n$ signifies flow distribution symmetry in an n-tube system. The parameter β_j is the heat flux ratio between a reference tube (usually designated as tube 1) and the jth tube in the system. In general, $\beta_j\geqslant 0$. $\beta_j=1$ signifies thermal symmetry of the multitube system. In this phase of the model development, both the thermal and flow distribution parameters are treated as parameters in the classical sense ([2]).

Outlet Liquid Flowrate. The differential equation governing the transient outlet liquid flowrate $m_{t,o}(t)$ is the same as that presented in the aforementioned research; thus,

$$\begin{aligned}\tau_{f,s}\frac{dm_{t,o}(t)}{dt}+m_{t,o}(t)&=\{[(\rho/\rho')-1]x_i+1\}m_{t,i}(t)\\&\quad-[(\rho/\rho')-1]\sum_{j=1}^{n}\frac{\overline{f}_{q,j}P_j\eta_j(t)}{(h'-h)}\end{aligned} \tag{5}$$

where

$$\tau_{f,s}=\left(\frac{\rho}{\rho'}\right)\left\{\left(\frac{\rho'}{\rho}\right)\{[(\rho/\rho')-1]x_i+1\}V_{u,t}+V_{2\phi}+V_{p,\mathrm{eff}}\right\}\gamma^*k_0^*. \tag{6}$$

The compressible flow system time constant $\tau_{f,s}$ incorporates fluid properties, system vapor volumes, and flow resistances ([2]). For the case where the effects of compressibility are negligible, $\tau_{f,s}=0$, Eq. (5) reduces to an algebraic equation identical to that obtained in the work of Kobus et al. [1]. Also, for the case of a single-tube condenser, $n=1$, Eq. (5) reduces to the governing differential equation that appears in the work of Bhatt and Wedekind [3].

A solution of Eq. (5) is obtained by first solving the set of equations represented by Eq. (1), then substituting these solutions into the summation in Eq. (5), and then solving. As mentioned earlier, this was carried out in previous work where the inlet flowrate to the condensing flow system $m_{t,i}(t)$ produces transient flow surges ([2]). In this current work, however, the inlet flowrate is a sinusoidal function of the form

$$m_{t,i}(t)=\overline{m}+a^*\cos(\omega t) \tag{7}$$

where a^* and ω are the amplitude and angular frequency of the inlet flowrate oscillations, respectively, and $\overline{m}$ is the mean flowrate about which the oscillations occur. Carrying out the solution, the frequency-response characteristics of the transient outlet liquid flowrate, $m_{t,o}(t)$, for an n-tube condensing flow system, can be expressed by the following generalized, yet comparably simple expressions:

$$G_m=\left\{\frac{1+\{[(\rho/\rho')-1]x_i+1\}^2(\omega\tau_{c,s})^2}{[1+(\omega\tau_{f,s})^2][1+(\omega\tau_{c,s})^2]}\right\}^{1/2} \tag{8}$$

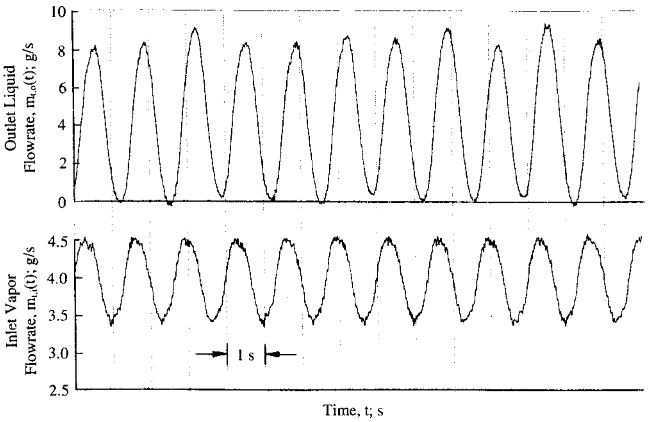

Fig. 1 Strip chart record of measured outlet liquid and inlet vapor flowrates for an oscillatory inlet vapor flowrate

Table 1 Physical properties and parameters

Data set	α [ ]	$\tau_{c,1}$ [s]	$V_{2\phi,1}$ [cm^3]	$V_{2\phi,2}$ [cm^3]	k_0^* [N s /cm^{2}kg]	$\tau_{c,s}$ [s]	$\tau_{f,s}$ [s]
1fr-618b	0.831	0.79	245	—	67.7	0.79	0.95
1fr-620	0.831	0.79	245	—	364.4	0.79	5.10
1fr-620b	0.830	0.81	244	—	19.3	0.81	0.26
2fr-623	0.830	0.79	120	120	16.3	0.79	0.26
2fr-707	0.830	0.81	123	123	57.7	0.81	0.93
2fr-707b	0.830	0.81	123	123	312.4	0.81	5.02
2fr-714b	0.826	0.84	98	343	265.5	2.09	5.00

$$\Phi_m=\tan^{-1} \times \left\{ \frac{\left\{\left[\left(\frac{\rho}{\rho'}\right)-1\right]x_i+1\right\}(\omega\tau_{c,s})-\frac{[(\omega\tau_{c,s})+(\omega\tau_{f,s})]}{[1-(\omega\tau_{c,s})(\omega\tau_{f,s})]}}{1+\left\{\left[\left(\frac{\rho}{\rho'}\right)-1\right]x_i+1\right\}(\omega\tau_{c,s})\frac{[(\omega\tau_{c,s})+(\omega\tau_{f,s})]}{[1-(\omega\tau_{c,s})(\omega\tau_{f,s})]}} \right\}. \tag{9}$$

For the case where the effects of compressibility are negligible, $\tau_{f,s}=0$, Eqs. (8) and (9) reduce to Eqs. (1) and (2) in the research of Kobus et al. [1]. Note that the above solution is greatly simplified by the equivalent single-tube model, where the summation in Eq. (5) is eventually assimilated by the definition of the condensing flow system time constant $\tau_{c,s}$, Eq. (4).

Experimental Verification

As was pointed out in earlier research ([2]), a two-tube condensing flow system with significant thermal asymmetry may very well represent a worst-case situation for the equivalent single-tube model. For this reason, and to keep the experimental apparatus tractable, experimental verification was carried out using a parallel two-tube configuration.

Experimental Apparatus and Measurement Uncertainties. The experimental apparatus used in the present research is similar to that used by Kobus et al. [1]. Therefore, the details will not be repeated here. Uncertainties in the experimental measurements were also discussed in detail in the aforementioned research, and will not be repeated. The experimental data pertaining to the gain characteristics had an average maximum uncertainty of ±10 per-

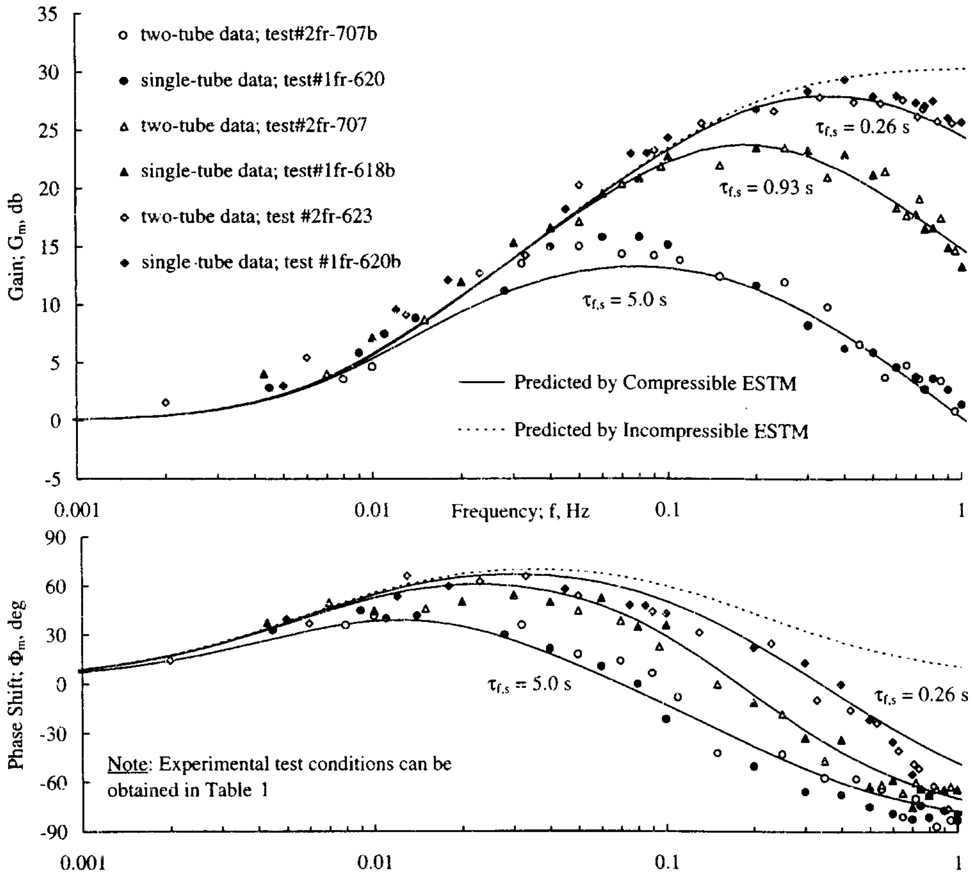

Note: Experimental test conditions can be obtained in Table 1

Fig. 2 Influence of compressibility on frequency-response characteristics of outlet liquid flowrate relative to inlet vapor flowrate for a two-tube condensing flow system; comparison of experimental data with equivalent single-tube model (equivalent single-tube model)

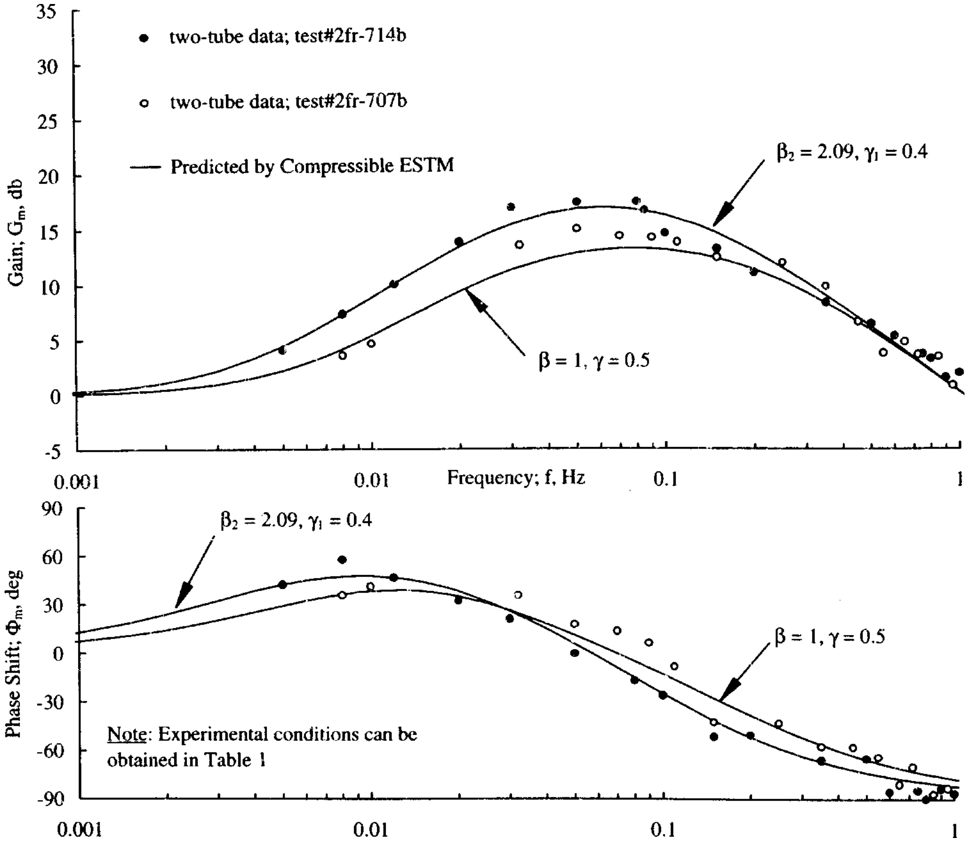

Fig. 3 Influence of thermal and flow distribution asymmetry on frequency-response characteristics of outlet liquid flowrate relative to inlet vapor flowrate for a two-tube condensing flow system; comparison of experimental data with predictions of equivalent single-tube model (equivalent single-tube model)

cent, whereas the uncertainty associated with the phase shift characteristics was slightly higher at ±15 percent. A sample strip-chart trace of the inlet and outlet flowrate variations, $m_{t,i}(t)$ and $m_{t,o}(t)$, respectively, for the two-tube system is shown in Fig. 1. It demonstrates the clarity and repeatability of the experimental measurements.

In calculating the compressible flow system time constant $\tau_{f,s}$ the total upstream vapor volume in the two-tube system was 464 cm^3, while that in the single-tube system was 486 cm^3. The test sections were copper tubes with an inside diameter of 0.80 cm. All of the forthcoming experimental data were run at constant conditions of $\overline{m} = 4.31$ g/s, $x_i = 1.0$, $\overline{f_{q,1}} = 11.1\ \text{kW/m}^2$, and at a condensing pressure of approximately 690 kPa, which in turn yields a liquid-to-vapor density ratio $(\rho/\rho') = 33.7$. Table 1 lists other relevant parameters associated with the calculations necessary to predict the frequency-response characteristics in the current research.

Experimental Verification of Equivalent Single-Tube Model. The theoretical predictions of the equivalent single-tube model, Eqs. (6) and (7), for the frequency-response characteristics of a two-tube condensing flow system, are compared with experimental data for several different condensing flow conditions.

Influence of Compressibility. Similar to what was done by Kobus et al. [1], frequency-response tests were carried out initially with a two-tube condenser. But this time the effects of compressibility were made to be more significant. The results, along with the theoretical predictions of the present compressible equivalent single-tube model, are depicted in Fig. 2. Note the very dramatic attenuating effect that compressibility can have on the frequency-response characteristics; the experimental data corresponding to the most significant compressibility, $\tau_{f,s} = 5.0$ s, having roughly a quarter the maximum amplitude in the gain (one-half the gain in decibels, db) to that of the experimental data corresponding to the lowest magnitude of compressibility, $\tau_{f,s} = 0.26$ s. The agreement between the experimental data and the compressible equivalent single-tube model predictions are seen to be exceptionally good over the entire three-order-of-magnitude range of frequencies.

As a further means of model verification, the compressible equivalent single-tube model was used to design a test for a single-tube condenser, which theoretically would yield the exact same frequency-response characteristics as that of the two-tube condenser, even though the refrigerant flowrate in each of the two tubes was different from what it was for the single-tube condenser. The results of the designed experiments are superimposed in Fig. 2. The equivalent single-tube model predicts that the frequency-response characteristics of symmetric or asymmetric multitube systems are identical to that of a single-tube system as long as the equivalent condensing system time constant $\tau_{c,s}$ and the compressible flow system time constant $\tau_{f,s}$ for the multitube system are the same as τ_c and τ_f for a single-tube system. As can be seen from the figure, the measured frequency-response characteristics were virtually identical for both the single- and the two-tube condensers, as the equivalent single-tube model predicted.

Influence of Thermal and Flow Distribution Asymmetry Thermally and hydrodynamically asymmetric experimental data are depicted in Fig. 3 for a two-tube condenser for the case where there is considerable compressibility. One set of data depicts the condition where thermal and flow distribution symmetry was present ($\beta = 1.0$, $\gamma = 0.5$); the other set of experimental data possessed significant thermal and flow distribution asymmetry between the two tubes ($\beta_2 = 2.09$, $\gamma_1 = 0.4$). Note the significant influence of thermal and flow distribution asymmetry. Superimposed in the figure is the frequency response predicted by the compressible equivalent single-tube model. It is important to note that there is no empiricism or ''curve fitting'' involved in the equivalent single-tube model predictions. All of the parameters in Eqs. (8) and (9) are known or determined analytically ([2]). Again, the agreement between the experimental data and the equivalent single-tube model is seen to be quite good for both the symmetric and asymmetric conditions, even at the higher frequencies. The incompressible equivalent single-tube model was incapable of predicting the attenuating effects of compressibility ([1]). More experimental data are available at other levels of compressibility by referring to the work of Kobus [5]. As can be seen, the agreement between the experimental data and the compressible equivalent single-tube model is again exceptionally good over the entire range of frequencies presented, which represents three orders of magnitude.

Conclusions

It seems appropriate to emphasize the significance of the degree of agreement between all of the single- and the two-tube experimental data presented, and the predictive capability of the compressible equivalent single-tube model. The experimental data represent both single- and two-tube condensers, with different flowrates, heat fluxes, having a wide range of compressibility effects, as well as significant thermal and flow distribution asymmetries. The equivalent single-tube model is seen to predict the effects of all of these different system characteristics very well, over a three order of magnitude range of frequencies.

The experimental data not only confirm the predictive capability of the equivalent single-tube model, they demonstrate its accuracy and its wide range of application. This confirming experimental data also establishes the applicable frequency range of the dynamic viability of the system mean void fraction model, which is an integral part of the equivalent single-tube model. The true value of the equivalent single-tube model can only be appreciated when consideration is given to the complexity of the numerous physical mechanisms involved, and the remarkable accuracy of such a relatively simple model; a model which can be solved, and graphically demonstrated, on typical ''spread-sheet'' software.

Acknowledgments

The authors would like to acknowledge the National Science Foundation, Thermal Transport and Thermal Processing Program, Division of Chemical and Transport Systems, for its part in the support of this research under Grant No. CTS-9420853. The support of the NASA/Michigan Space Grant Consortium is also acknowledged.

References

[1] Kobus, C. J., Wedekind, G. L., and Bhatt, B. L., 1998, ''Application of an Equivalent Single-Tube Model for Predicting Frequency-Response Characteristics of Multitube Two-Phase Condensing Flow Systems With Thermal and Flow Distribution Asymmetry,'' ASME J. Heat Transfer, **120**, No. 2, pp. 528–530.

[2] Wedekind, G. L., Kobus, C. J., and Bhatt, B. L., 1997, ''Modeling the Characteristics of Thermally Governed Transient Flow Surges in Multitube Two-Phase Condensing Flow Systems With Compressibility and Thermal and Flow Distribution Asymmetry,'' ASME J. Heat Transfer, **119**, No. 3, pp. 534–543.

[3] Bhatt, B. L., and Wedekind, G. L., 1980, ''Transient and Frequency Response Characteristics of Two-Phase Condensing Flows: With and Without Compressibility.'' ASME J. Heat Transfer, **102**, pp. 495–500.

[4] Zivi, S. M., 1964, ''Estimation of Steady-State Steam Void Fraction by Means of the Principle of Minimum Entropy Production,'' ASME J. Heat Transfer, **86**, p. 247.

[5] Kobus, C. J., 1998, ''Application of the System Mean Void Fraction Model in Formulating an Equivalent Single-Tube Model for Predicting Various Transient and Unstable Flow Phenomena Associated with Horizontal Multitube Two-Phase Condensing Flow Systems With and Without the Effects of Compressibility, Inertia, and Thermal and Flow Distribution Asymmetry,'' Ph.D. thesis,Oakland University, Rochester, MI.

An Experimental Study of Electrohydrodynamic Induction Pumping of a Stratified Liquid/Vapor Medium

M. Wawzyniak[1]
J. Seyed-Yagoobi
G. L. Morrison
Department of Mechanical Engineering, Texas A&M University, College Station, TX 77843-3123

Electrohydrodynamic induction pumping of a stratified liquid/vapor medium is quantitatively assessed utilizing Laser Doppler Anemometry. Data are presented suggesting that pumping is due to both interfacial and bulk effects. Values of turbulence intensity associated with this type of flow are briefly discussed for the various cases studied. [S0022-1481(00)00401-1]

Keywords: Electric Fields, Heat Transfer, Pumps, Stratified, Two-Phase

Introduction

Electrohydrodynamic induction pumping is based on charges induced in the fluid and delayed at a gradient or discontinuity of the electric conductivity. A traveling electric wave then attracts or repels these induced charges, leading to fluid motion. Electrohydrodynamic pumps are generally lightweight, produce no vibrations, require little to no maintenance, are easily controllable by adjusting the applied voltage, and have low power consumption. They are also useful for the enhancement of heat transfer, as an increase in mass transport often translates to an augmentation of the heat transfer.

Melcher [1] provided the first theoretical model of electrohydrodynamic induction pumping due to charges at a liquid/air interface. He then presented an improved version of his theoretical model which also described the pumping of a liquid/liquid interface ([2]). This theory was recently examined in more detail by Wawzyniak and Seyed-Yagoobi [3,4]. The above theoretical models are built around a number of simplifying assumptions leading to a linear velocity profile (Couette flow), the most significant of which are that: (1) flow is laminar, isothermal, and one-dimensional, (2) charges are induced and consequently an electric force is present only at the interface, and (3) the pressure is constant in the direction of motion. It will later be shown that these assumptions are not met and that improvements have to be made to the existing theoretical model of Wawzyniak and Seyed-Yagoobi [3,4] to accurately describe and predict the phenomena encountered in two-phase flow electrohydrodynamic induction pump.

For this experimental study, induction pumping of a stratified liquid/vapor medium is carried out. Specifically, velocity and turbulence intensity measurements inside a liquid film of HCFC-123 are conducted by means of a one-dimensional LDA system as functions of location, frequency, and voltage.

---

[1] Current address: Behr GmbH& Co., Abt.E-T, Postfach 30 09 20, 70449 Stuttgart, Germany.

Contributed by the Heat Transfer Division for publication in the JOURNAL OF HEAT TRANSFER. Manuscript received by the Heat Transfer Division, Dec. 1, 1998; revision received, Aug. 1, 1999. Associate Technical Editor: P. Ayyaswamy

Experimental Setup and Procedure

The details of the experimental setup and procedure are given in Wawzyniak [5]. The AC power supply utilized in this study is capable of generating sine, square, and triangle waves at voltages of 0–12 kV (zero to peak) and frequencies of 0–13 Hz. The pumping channel with a rectangular cross-section width of 50 mm and a height of 36 mm is milled directly into a single piece of PVC (see Fig. 1). Two straight sections measuring 390 mm in length are connected by half-round sections with a centerline radius of 150 mm. The pump is equipped with three view ports along one of the straight pumping sections. These view ports are located at 37.5, 195.0, and 352.5 mm from the start of the straight section, respectively. Each view port measures 45 mm in width by 25 mm in height and extends from the bottom of the pumping channel up. The pumping channel is covered with a plate made from high-density polyethylene, which is equipped with ports for a pressure transducer, a vacuum gauge, and two thermocouple probes. The pumping channel and support lines are initially evacuated to a vacuum better than 250 μm of mercury. The apparatus is then charged with refrigerant HCFC-123.

Two integrated electrode boards are mounted into the bottoms of the two straight sections of the induction pump. Each board, a schematic of which is shown in Fig. 1, measures 50 mm in width, 390 mm in length, and 1.5 mm in thickness. The board laminate is made from the epoxy resin FR-4, a material commonly used for printed circuit boards, while the electric lines are tin covered copper. The top of each board features 39 electrodes and the bottom holds the three bus lines. The electrodes are 1 mm wide and extend across the entire width of the board, and subsequent electrodes are spaced 10 mm apart (center to center). To completely eliminate the possibility of direct charge injection ([5]), a coating of epoxy 0.8 mm in thickness was applied to the top surface of both electrode plates. This material was compatible with the working fluid. The three bus lines running along the length of the board are also 1 mm in width, but they are located 17 mm from each other (center to center) with the second bus line placed in the middle of the board. The first, second, and third bus lines are connected to electrodes 1, 4, 7, . . . 2, 5, 8, . . . , and 3, 6, 9, . . . , respectively, by means of through-plated holes. The bus lines in turn are linked to the high-voltage power supply.

The one-dimensional LDA system measures the main velocity component and turbulence intensity in the *x*-direction (see Fig. 1 for the definition of *x*, *y*, and *z*-directions). Light from an argon-ion laser is passed through a prism, with the green color component ($\lambda = 514\,\text{mm}$), being used for the measurement. The optical train consists of a polarization unit, a Bragg cell, a 3.75 × beam expander, and a lens with a focal length of 450 mm. Light reflected from particles in the flow is collected in an on-axis

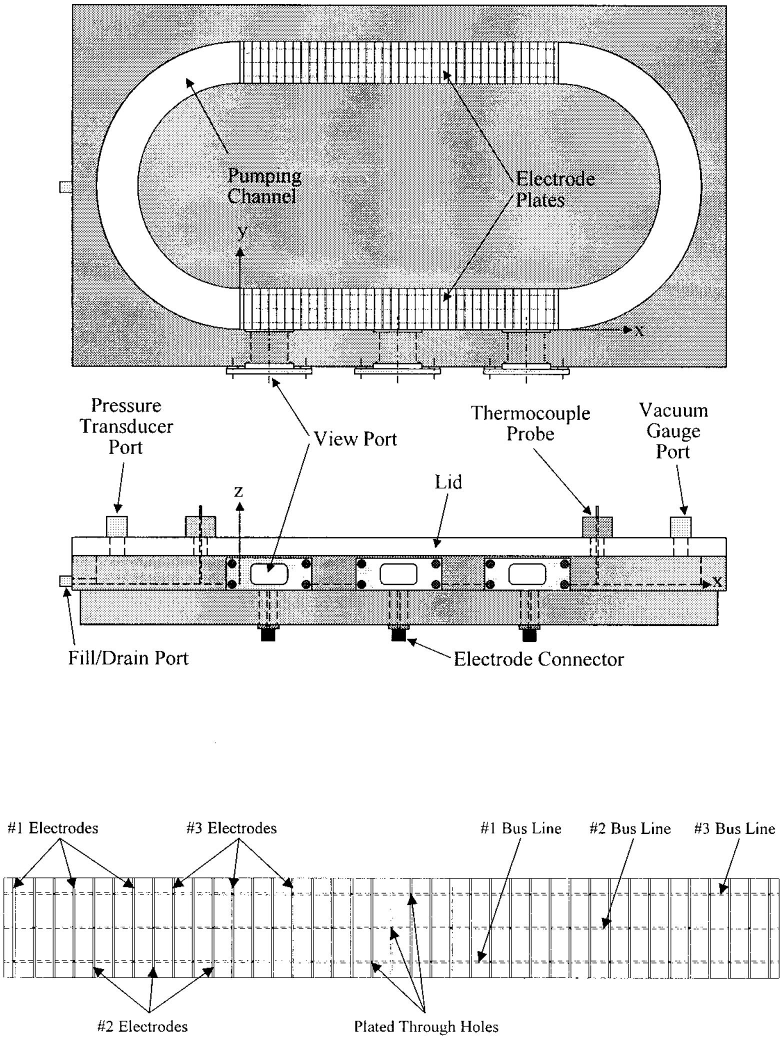

electrode plate (electrodes on top side, bus lines on underside)

Fig. 1 Schematic of electrohydrodynamic induction pump and electrode plate

back scatter mode through a photomultiplier tube. This optical arrangement in conjunction with the refractive indices of the glass and the working fluid HCFC-123 yield a measurement volume $0.066 \times 0.066 \times 0.629$ mm in size. The entire optical system is situated on a traverse table allowing it to be moved in space with a resolution of 0.0025 mm and a repeatability of 0.010 mm. The LDA traverse table is leveled to within 0.05 mm/m. The photomultiplier tube is connected to the data acquisition computer through a low and a high pass filter and a signal processor. The data are reduced statistically, i.e., all measurements are weighed equally.

Impurities in the fluid proved adequate to generate Doppler bursts and therefore data points. However, data rates realized without the addition of any particles were extremely low and generally below 10 Hz. Mean velocities were obtained by averaging up to 4096 data points at each location, however, at positions close to the channel bottom and interface as well as at low flow velocities, this number was frequently not attained. The error associated with each individual data point was due to uncertainties in the burst timing mechanism, the Bragg shift frequency, and the beam angle. The method of Kline and McClintock [6] was used to calculate an error in the mean velocity of no greater than two percent. All of the following results were obtained at room temperature $(18^\circ\mathrm{C} \leq T \leq 23^\circ\mathrm{C})$. All measurements were performed in the streamwise center of a view port and for a liquid film height of 7.5 mm measured from the top of the electrodes' coating. Due to the measurement difficulties near the interface, only data up to a film height of 7.0 mm are presented.

Results

Figure 2 shows profiles for velocity and turbulence intensity in the y-direction (across the pumping channel) at the downstream view port for a voltage of 6 kV (zero to peak) and for frequencies of 6.0, 10.0, and 13.5 Hz, respectively. The turbulence intensity data will be discussed later. Measurements were conducted at a height of $z=3.0$ mm, which was chosen due to the relatively high attainable data rate at this elevation. The collection of data becomes more difficult with increasing y value due to the attenuation of both incoming beams and reflected beams resulting from the fluid. This effect was most pronounced at higher settings of the laser power and, therefore, all experiments were carried out at laser power levels between 300 and 500 mW.

According to Fig. 2, the velocity profiles are quite similar for the three electric wave frequencies, showing a thin boundary layer of approximately 3.0 mm thickness extending from the side walls, followed by a nearly flat region to about 10.0 mm from the side wall. Values for the velocities in this region are 0.110, 0.120, and 0.140 m/s for frequencies of 6.0, 10.0, and 13.5 Hz, respectively. The velocities then increase to their peaks, which are reached at the center of the channel. These maxima are 0.150 m/s for a frequency of 6.0 Hz and about 0.160 m/s for frequencies of both 10.0 and 13.5 Hz. Theoretical results derived from Wawzyniak and Seyed-Yagoobi [3] suggest that the velocity will peak at frequency one order of magnitude higher than the maximum frequency that the power supply employed in this study is capable of generating. The theory also indicates that the velocity–frequency dependency curve is relatively flat even over the frequency range studied here. This may explain why some of the experimental data show poor separation for the frequencies presented here. The back portions of the velocity profiles approximately mirror those of the front portion, but exact symmetry is neither attained nor is it a realistic expectation and the velocities decay to zero roughly 2.0 mm in front of the far side wall. This is presumably due to the difficulties related to data collection at the far side of the channel as described above.

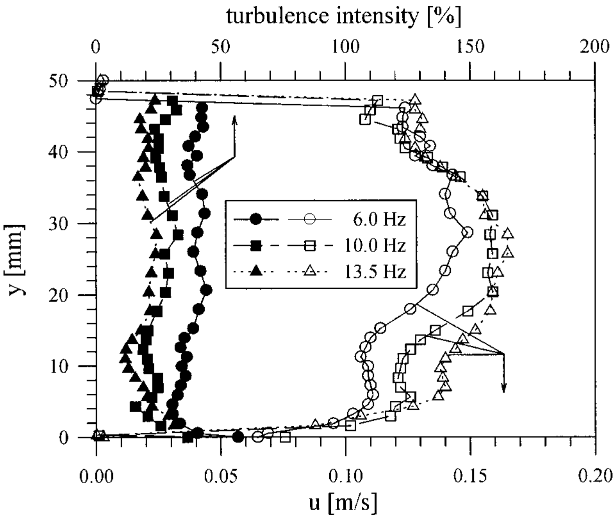

Fig. 2 Cross-streamwise velocity and turbulence intensity profiles in downstream view port ($z=3$ mm, applied voltage $=6$ kV)

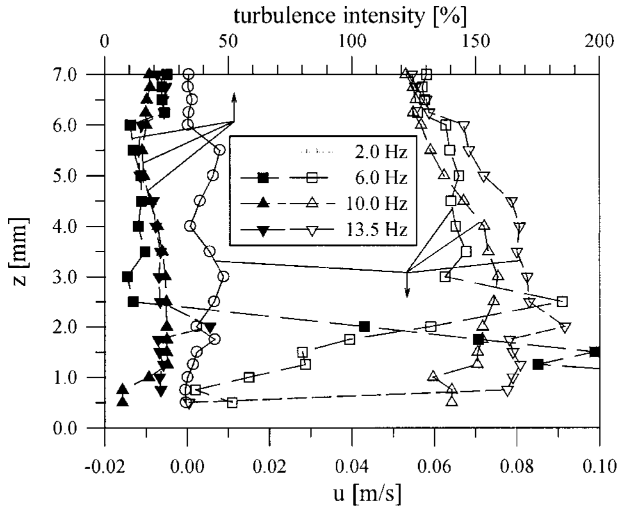

Fig. 3 Effect of frequency on vertical velocity and turbulence intensity profiles ($y=10$ mm, applied voltage$=6$ kV)

Data as a function of vertical position (z) in the center window were obtained at a horizontal location of $y=10.0$ mm. This horizontal position was chosen because it is far enough away from the window to avoid any significant reduction of the velocities, yet close enough to the front of the view port to yield data that are satisfactory in both quality and quantity. The results of the velocity measurements in the z-direction are displayed in Fig. 3. Turbulence intensity data are also presented in the same figure, but again will be discussed later. At a frequency of 2.0 Hz speeds of merely up to 0.01 m/s are produced. Peak velocities for frequencies of 6.0, 10.0 and 13.5 Hz are near 0.070, 0.075, and 0.085 m/s, respectively. These maxima occur at distances of 2.0–3.5 mm from the bottom of the channel. The velocity profiles shift to higher values with increasing frequency. However, it is of note that the profiles converge to a value of about 0.050 m/s close to the interface for all but the lowest frequency.

The most surprising feature of the results plotted in Fig. 3 is not the magnitude of the velocities, but the shape of the velocity profiles. With charge injection eliminated by the coating, only induced charges are available to be acted upon by the electric field and procure pumping. Intuition predicts that these charges may only be induced at the interface due to the prevailing difference in conductivity between the vapor and the liquid. The velocity profile corroborating this expectation would have to be linear under laminar conditions (Couette flow), and even under turbulent con-

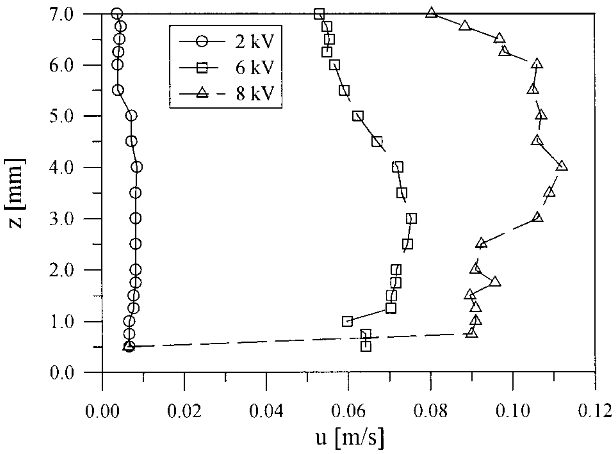

Fig. 4 Effect of voltage on vertical velocity profiles (y=10 mm, f=10 Hz)

ditions, the point of maximum velocity is constrained to the interface. Yet, Fig. 3 shows velocity maxima much closer to the electrodes than the interface. Thus, it must be concluded that charges are induced also in the bulk of the liquid. This, however, requires a conductivity gradient within the liquid. It was observed that fluid temperature and vapor pressure in the apparatus rise slightly over the course of several hours while the electrodes are energized. Margo and Seyed-Yagoobi [7] demonstrated that electrohydrodynamic induction pumping can be accomplished in dielectric liquids exhibiting a temperature gradient of less than 1°C since the electric conductivity of dielectric liquids is a strong function of temperature. It is conceivable that in experiment at hand Joule heating from the electrodes and cooling of the pump walls from the ambient caused temperature gradients within the liquid layer, allowing for the induction of charges throughout the bulk of the liquid. Assuming that these temperature gradients are relatively uniform throughout the pumping channel, more charges will be induced close to the electrodes due to the higher electric field strength. Also, these charges will experience a stronger electric force than those closer to the interface, again because of the greater electric field strength. The combination of these effects lead to the appearance of the velocity profiles as shown in Fig. 3. Neither Joule heating nor the temperature gradient were quantified in this study and demand further research.

Figure 4 displays the significance of the applied voltage at a fixed frequency of 10.0 Hz. The profile for 2 kV is quite flat with speeds not exceeding 0.010 m/s. At 6 kV the flow velocity reaches its largest magnitude of 0.075 m/s at a height of 3.0 mm, whereas at 8 kV it peaks at 0.110 m/s at 4.0 mm from the channel bottom. An increase in the applied voltage results in a stronger electric field, which in turn leads to higher fluid velocities. The upper voltage limit is imposed by the breakdown strength of the liquid. This limit could not be approached with the power supply used for this study. The value of 8 kV (zero to peak) was the highest at which the power supply could be properly operated for extended time periods and it can be assumed that higher pumping velocities could be realized with a different power supply.

The turbulence intensity is somewhat of a misdemeanor when describing electrohydrodynamic induction flows. Fluid may advance in cellular motion, or, particularly at low frequencies, move back and forth, all in a quite organized fashion. However, the corresponding values of the turbulence intensity can be high. Plots presented in Fig. 2 show the cross-stream dependence of the turbulence intensity at three frequencies. Average values are approximately 40 percent, 25 percent, and 20 percent, respectively, for frequencies of 6, 10, and 13.5 Hz. Comparing these levels to the velocity profiles, it can be concluded that the turbulence intensity of the flow decreases with increasing velocity. This effect can be accounted for by the cellular motion of the flow, which is more pronounced at the lower frequencies. The turbulence intensity values generally increase towards the side walls, but these data need to be used with caution due to their limited availability in these regions. Data points with unreasonably high values of turbulence intensity in the vicinity of the side walls have been omitted from the plots. Vertical turbulence intensity plots are shown in Fig. 3 for three frequencies. Values for an applied frequency of 2 Hz have been omitted from the figure as they exceed 200 percent across the entire liquid film. For the remaining frequencies, turbulence intensity values are relatively close and reach values between 10 percent and 25 percent. The only exception is for a frequency of 6 Hz, where the turbulence intensity increases dramatically below 2.5 mm from the channel bottom. It is in this area that the corresponding flow velocity quickly decays to zero. At an average flow velocity of 0.05 m/s the corresponding Reynolds number is 3700.

In summary, in this work, detailed velocity profiles inside a liquid film pumped by electrohydrodynamic forces have been generated with the help of an LDA system. The results illustrated the complexity of the phenomena involved in this family of flows. The velocity profiles permitted assessment of mechanisms responsible for producing fluid motion. Turbulence intensity generally decreased with increasing velocity and frequency of the applied electric field under the operating conditions explored in this study.

References

[1] Melcher, J. R., 1966, ''Traveling-Wave Induced Electro-convection,'' Phys. Fluids, **9**, No. 8, pp. 1548–1555.
[2] Melcher J. R., 1981, *Continuum Electromechanics*, MIT Press, Cambridge, MA, pp. 5.49–5.54.
[3] Wawzyniak, M., and Seyed-Yagoobi, J., 1999, ''An Analytical Study of Electrohydrodynamic Pumping of a Stratified Liquid/Vapor Medium,'' IEEE Trans. Ind. Appl., **35**, pp. 231–239.
[4] Wawzyniak, M., and Seyed-Yagoobi, J., 1999, ''Stability of Electrodrodynamic Induction Pumping of a Stratified Liquid/Vapor Medium in the Presence of an External Load,'' IEEE Trans. Ind. Appl., **35**, No. 5, pp. 1211–1217.
[5] Wawzyniak, M., 1999, ''Fundamental Study of Electrohydrodynamic Induction Pumping of a Stratified Liquid/Vapor Medium,'' Ph.D. dissertation, Texas A&M University, College Station, TX.
[6] Kline, S. J., and McClintock, F. A., 1953, ''Describing Uncertainties in Single Sample Experiments,'' Mech. Eng., **75**, pp. 3–8.
[7] Margo, B. D., and Seyed-Yagoobi, J., 1994, ''Heat Transfer Enhancement Under Various Orientations Resulting From Attraction Mode Induction Electrohydrodynamic Pumping,'' ASME J. Heat Transfer, **116**, pp. 598–603.

An Analytical Model for Decaying Swirl Flow and Heat Transfer Inside a Tube

Hui-Ying Wu
Institute of Engineering Thermophysics, Department of Power and Energy Engineering, Shanghai Jiaotong University, Shanghai 200030, China
e-mail: whysri@online sh.ch

Hui-Er Cheng
Institute of Engineering Thermophysics, Department of Power and Energy Engineering, Shanghai Jiaotong University, Shanghai 200030, China

Ren-Jun Shuai
Department of Mechanical and Electrical Engineering, Nanjing Institute of Architectural and Civil Engineering, Nanjing 210009, China

Qiang-Tai Zhou
Department of Power Engineering, Southeast University, Nanjing 210096, China

Decaying swirl flow can enhance the heat transfer inside a tube. For the decaying swirl flow of which maximum tangential velocity is located in the immediate vicinity of the wall, an analytical model based on the fluid theorem about the moment of momentum is proposed for the local maximum tangential velocity, local friction factor, and local Nusselt number in this paper. The analytical solutions compare favorably with the experimental data. Influences of the Reynolds number, wall roughness and initial tangential-to-axial velocity ratio on the decaying characteristics of the friction factor and Nusselt number have been analyzed. The analytical results show that the swirl flow decays more rapidly at the initial segment; for same conditions, the friction factor decays more severely than the Nusselt number; relative to the values of the nonswirl flow, the friction factor increases more intensely than the Nusselt number. [S0022-1481(00)70401-4]

Keywords: *Analytical, Enhancement, Flow, Heat Transfer, Swirling*

Introduction

The concept that the swirl flow can enhance the heat transfer inside a tube was proposed by Kreith and Margolis [1]. Since then, a lot of experimental investigations were made on the friction and heat transfer characteristics of the swirl flow ([2–6]). It's regarded that the swirl tangential velocity increases the composite velocity ([2]), thins the boundary layer ([7]), enhances the tangential and radial turbulent fluctuation ([8]), and therefore causes the increase in friction and heat transfer inside a tube.

Generally, the swirl flow can be classified as two kinds: the continuous swirl flow and the decaying swirl flow. The twisted tapes inserted along the whole tube generate the continuous swirl flow, and various inlet swirlers generate the decaying swirl flow inside a tube.

Problems of friction and heat transfer for the decaying swirl flow inside a tube are of practical importance in designing the equipment, like combustion chambers and heat transfer promoters in different kinds of heat exchangers. For the decaying swirl flow, the friction factor and heat transfer coefficient decrease with the axial distance, while for the continuous swirl flow, the friction factor and heat transfer coefficient keep constant. Though there are lots of experimental and a few theoretical studies reported in the literature ([6–10]), there is still no satisfactory analytical method to predict the local friction and heat transfer characteristics for the decaying swirl flow.

The aim of this paper is to establish an approach to compute the local maximum tangential velocity, the local friction factor, and the local Nusselt number of the decaying swirl flow if the maximum tangential velocity is very near the wall and the initial flow conditions are known.

Friction and Heat Transfer Decaying Model

We know that for the decaying swirl flow, the friction factor and Nusselt number are greatly influenced by the tangential velocity, so it's necessary to obtain the decaying equation of the tangential velocity. If u, w, x, r, d represent the axial velocity, tangential velocity, axial distance, radial distance, and tube inside diameter, respectively, then the tangential moment of momentum flowing in the element δx shown in Fig. 1 per second, M_i, is

$$M_i=\int_0^{d/2}(\rho u\cdot 2\pi r\cdot dr)\cdot wr. \tag{1}$$

The tangential moment of momentum flowing out per second, M_o, is

$$M_o=\int_0^{d/2}(\rho u\cdot 2\pi r\cdot dr)\cdot\left(w+\frac{\partial w}{\partial x}\cdot\delta x\right)\cdot r, \tag{2}$$

and the tangential moment of force which acts on the element δx, M, is

$$M=\left(\mu\frac{\partial w}{\partial r}\bigg|_w\cdot\pi d\cdot\delta x\right)\cdot\frac{d}{2}. \tag{3}$$

According to the fluid theorem about the moment of momentum, we have

$$M=M_o-M_i. \tag{4}$$

Substituting Eq. (1) to Eq. (3) into Eq. (4) and rearranging, we obtain

$$\mu\frac{\partial w}{\partial r}\bigg|_w=\frac{4\rho}{d^2}\int_0^{d/2}u\frac{\partial w}{\partial x}r^2dr. \tag{5}$$

The experimental study by Yajnik and Subbaiah [7] regarded that for the decaying swirl flow without adverse current near the central axis, the variance of axial velocity in the radial direction, can be ignored. So we assume

$$u=u_{av} \tag{6}$$

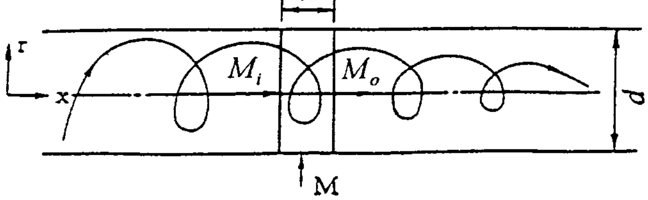

Fig. 1 Decaying swirl flow inside a tube

Contributed by the Heat Transfer Division for publication in the JOURNAL OF HEAT TRANSFER. Manuscript received by the Heat Transfer Division, Dec. 1, 1997; revision received, June 16, 1999. Associate Technical Editor: R. Douglass.

and for the decaying swirl flow generated by the inlet twisted tape, inlet vane swirler, and similar other devices, Yajnik and Subbaiah [7] and Shen [11] found that the tangential velocity approximately follows the distribution

$$\frac{w}{w_m}=\frac{2r}{d} \tag{7}$$

where w_m is the maximum tangential velocity, which is located in the immediate vicinity of the wall.

Substituting Eq. (6) and Eq. (7) into Eq. (5), and integrating, we obtain

$$\mu\frac{\partial w}{\partial r}\bigg|_w=\frac{\rho d u_{av}}{8}\frac{\partial w_m}{\partial x}. \tag{8}$$

Assuming that the swirl flow resistance at element δx is equivalent to the resistance of an axial flow with velocity $\sqrt{u_{av}^2+w_m^2}$ over length $(\sqrt{u_{av}^2+w_m^2}/u_{av})\delta x$, based on the principle of straightening out the streamlines and the equivalent velocity, we have the following force equilibrium equation:

$$\tau_s \pi d\cdot\delta x=\lambda\cdot\frac{\sqrt{(u_{av}^2+w_m^2)/u_{av}^2}\cdot\delta x}{d}\cdot\frac{\rho(u_{av}^2+w_m^2)}{2}\cdot\frac{\pi d^2}{4} \tag{9}$$

where τ_s is the actual wall frictional stress,

$$\tau_s=\sqrt{\tau_u^2+\tau_w^2}=\sqrt{\left(\mu\frac{\partial u}{\partial r}\bigg|_w\right)^2+\left(\mu\frac{\partial w}{\partial r}\bigg|_w\right)^2}. \tag{10}$$

Substituting Eq. (10) into Eq. (9) and rearranging, we obtain

$$\mu\frac{\partial w}{\partial r}\bigg|_w=-\frac{\lambda\rho u_{av}^2}{8}\cdot\sqrt{\left(\frac{u_{av}^2+w_m^2}{u_{av}^2}\right)^3-1}. \tag{11}$$

Substituting Eq. (11) into Eq. (8) and rearranging, we have

$$\frac{\partial(w_m/u_{av})}{\partial(x/d)}=-\lambda\sqrt{[(w_m/u_{av})^2+1]^3-1}. \tag{12}$$

Let $\begin{cases} z=w_m/u_{av}\\ \bar{x}=x/d\end{cases}$, and Eq. (12) can be transformed to

$$\int_{z0}^{z}\frac{1}{\sqrt{(z^2+1)^3-1}}dz=\int_0^{\bar{x}}-\lambda d\bar{x}. \tag{13}$$

Noting that λ in the above equations is the friction factor of the axial flow for which the inlet segment influence can't be ignored if the tube length-to-diameter ratio L/d is less than 60, we use the expression ([12])

$$\lambda=\lambda_s(1+1.5e^{-0.25\bar{x}}) \tag{14}$$

where λ_s is the friction factor of the fully developed turbulent axial flow inside a tube. For the smooth tube, it can be calculated by Blasius equation ([13])

$$\lambda_s=0.3164/\mathrm{Re}^{0.25} \tag{15}$$

and for the rough tube, it can be calculated by Lange equation ([13])

$$\lambda_s=0.0096+\sqrt{\xi/d}+\sqrt{2.88/\mathrm{Re}}, \tag{16}$$

where ξ is the tube wall roughness.

Substituting Eq. (14) into Eq. (13) and integrating, we determine the local maximum tangential velocity for the decaying swirl flow

$$\ln\left(\frac{6+2z^2+2\sqrt{3}\sqrt{z^4+3z^2+3}}{2\sqrt{3}+2\sqrt{3}z^2-2\sqrt{z^4+3z^2+3}}\right)=2\sqrt{3}\lambda_s(\bar{x}-6e^{-0.25\bar{x}}+6)+C_0 \tag{17}$$

where C_0 is dependent on the initial velocity ratio z_0 ($z_0=w_{m0}/u_{av}$)

$$C_0=\ln\left(\frac{6+2z_0^2+2\sqrt{3}\sqrt{z_0^4+3z_0^2+3}}{2\sqrt{3}+2\sqrt{3}z_0^2-2\sqrt{z_0^4+3z_0^2+3}}\right). \tag{18}$$

Let λ_x represent the local friction factor of the decaying swirl flow inside a tube, then according to Eq. (9), we have

$$\lambda_x\cdot\frac{\delta x}{d}\cdot\frac{\rho u_{av}^2}{2}\cdot\frac{\pi d^2}{4}=\lambda\cdot\frac{\sqrt{(u_{av}^2+w_m^2)/u_{av}^2}\cdot\delta x}{d}\cdot\frac{\rho(u_{av}^2+w_m^2)}{2}\cdot\frac{\pi d^2}{4}. \tag{19}$$

Substituting Eq. (14) into Eq. (19) and rearranging, we get the equation for the local friction factor of the decaying swirl flow

$$\lambda_x/\lambda_s=(1+1.5e^{-0.25\bar{x}})(1+z^2)\sqrt{1+z^2}. \tag{20}$$

Considering that the heat transfer is influenced and determined by the thermal resistances of the wall-adjoining layer, which consists of a viscous sublayer and a turbulent core, Migay and Golubev [12] introduced a thermodynamical analogy relation:

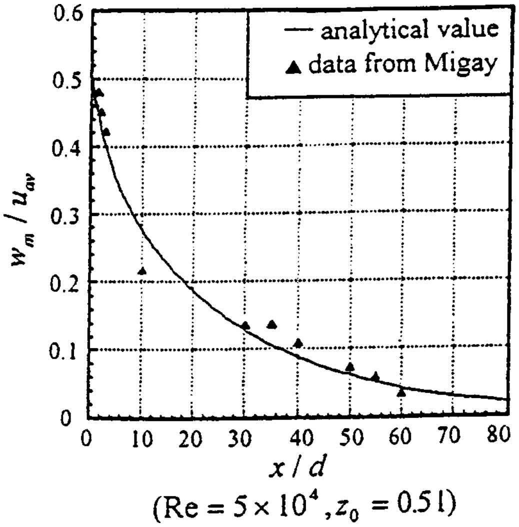

Fig. 2 Decay of w_m/u_{av} with x/d

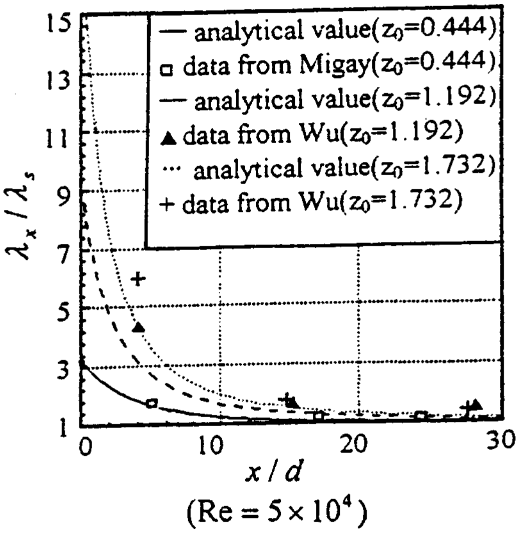

Fig. 3 The decay of λ_x/λ_s with x/d

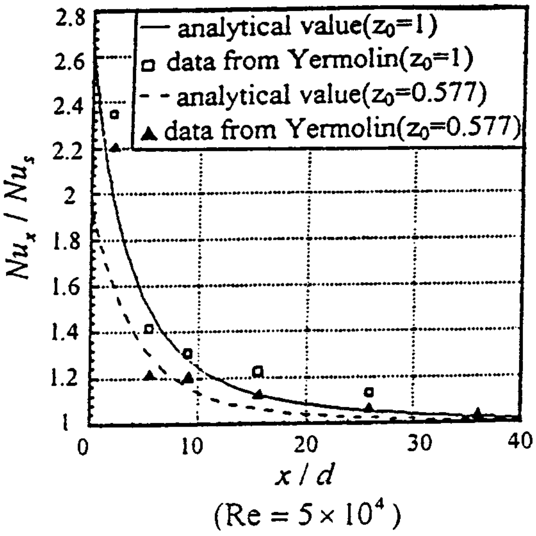

Fig. 4 The decay of $\mathrm{Nu}_x/\mathrm{Nu}_s$ with x/d

$$\mathrm{Nu}=[1+1.75/(\mathrm{Pr}+8)]\mathrm{Re}\,\mathrm{Pr}/\sqrt{8/\lambda}\{\sqrt{8/\lambda}(1.325\sqrt{\lambda}+1)\times[1-(30/\mathrm{Re}\sqrt{\lambda/32})]+5\,\mathrm{Pr}[(1.285/\mathrm{Pr}^{0.21})-(0.265/\mathrm{Pr}^{1.2})]+5\ln(5\,\mathrm{Pr}+1)\}. \tag{21}$$

The expression in braces changes very little, and Migay and Golubev [12] further wrote, to within five percent, that

$$\mathrm{Nu}_x/\mathrm{Nu}_s=\sqrt{\lambda_x/\lambda_s} \tag{22}$$

where Nu_x is the local Nusselt number of the decaying swirl flow, and Nu_s is the Nusselt number of the fully developed turbulent axial flow in a tube.

Substituting Eq. (20) into Eq. (22), we obtain the equation of the local Nusselt number for the decaying swirl flow:

$$\mathrm{Nu}_x/\mathrm{Nu}_s=(1+1.5e^{-0.25\bar{x}})^{1/2}(1+z^2)^{3/4}. \tag{23}$$

Validation

Migay [12], Yermolin [14], and Wu [13] made the experimental investigations on the flow and heat transfer characteristics of the decaying swirl flow inside a smooth tube. Their experimental data are plotted in Figs. 2–4. The figures also provide the analytical curves according to Eq. (17), Eq. (20), and Eq. (23). It is shown that the analytical values of the local maximum tangential velocity, the local friction factor, and the local Nusselt number are in reasonable agreement with the experimental data, with the errors no more than −18.6 percent∼+26.8 percent, −12.1 percent ∼+27.0 percent, and −26.4 percent∼+8.3 percent, respectively.

Discussion

In this part we will discuss the decaying characteristics in terms of the decaying rate and decaying extent. The decaying rate is defined as the slope of the decaying curve. The decaying extent δ is defined as the ratio of the decaying quantity to the initial quantity. For the local maximum tangential velocity, local friction factor, and local Nusselt number, δ is calculated by

$$\delta_z=\frac{z_0-z_x}{z_0} \tag{24}$$

$$\delta_\lambda=\frac{\lambda_0-\lambda_s}{\lambda_0} \tag{25}$$

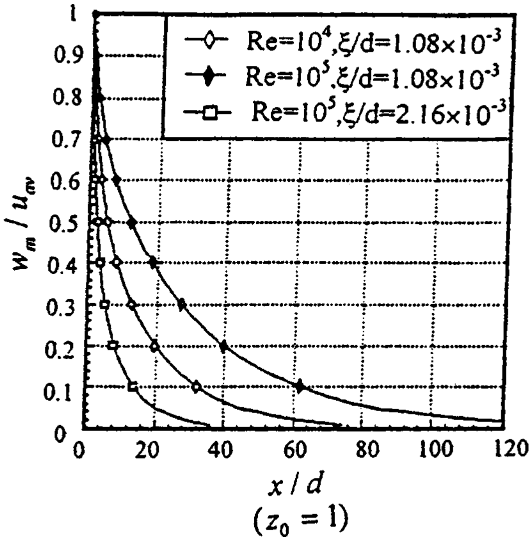

Fig. 5 Influence of Re and ξ on decay of w_m/u_{av}

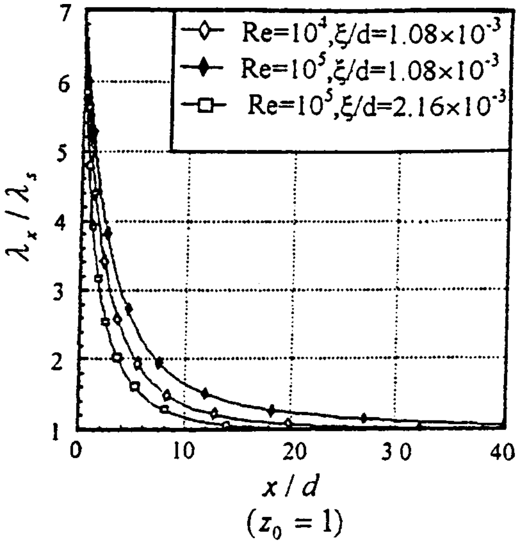

Fig. 6 Influence of Re and ξ on decay of λ_x/λ_s

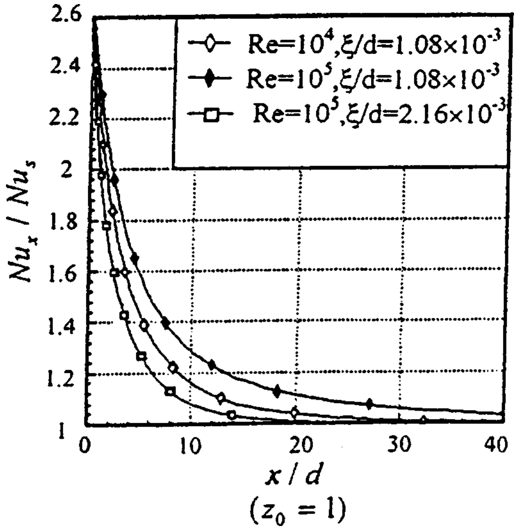

Fig. 7 Influence of Re and ξ on decay of $\mathrm{Nu}_x/\mathrm{Nu}_s$

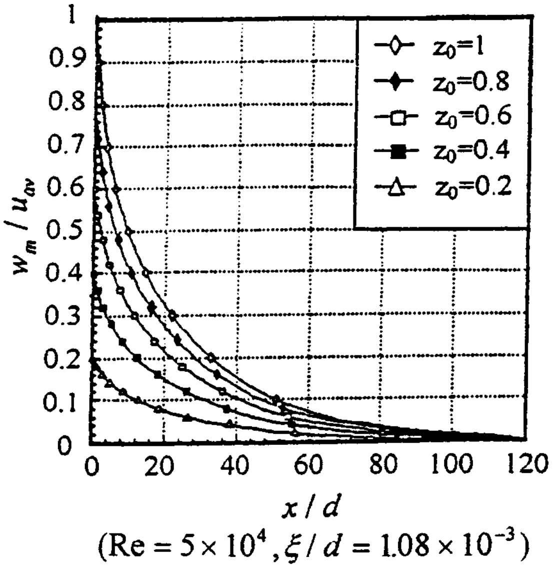

Fig. 8 Influence of z_0 on decay of w_m/u_{av}

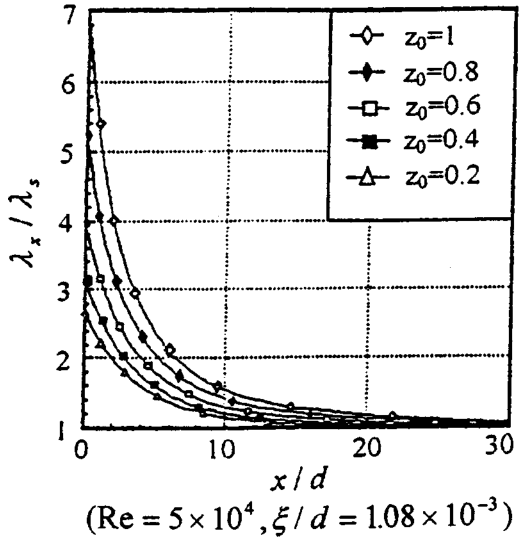

Fig. 9 Influence of z_0 on decay of λ_x/λ_s

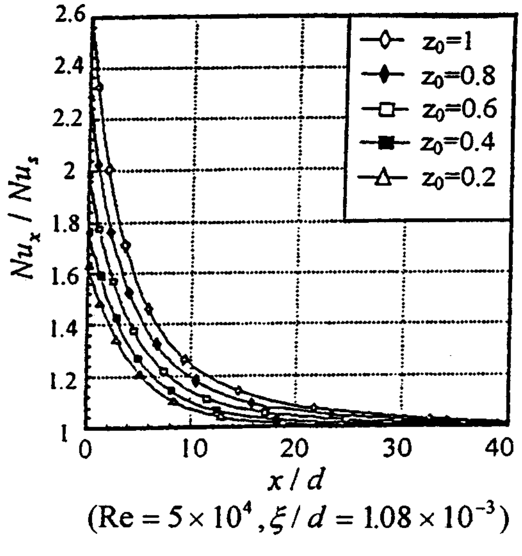

Fig. 10 Influence of z_0 on decay of $\mathrm{Nu}_x/\mathrm{Nu}_s$

$$\delta_{\mathrm{Nu}}=\frac{\mathrm{Nu}_0-\mathrm{Nu}_x}{\mathrm{Nu}_0}. \tag{26}$$

For the same conditions, the larger the decaying slope, the more rapid the decay is; the larger the value of δ, the more severe the decay is.

Substituting Eq. (15) or Eq. (16) into Eq. (17), Eq. (20), and Eq. (23), we can obtain the analytical decaying curves for different conditions. Figures 5–10 show the influence of x/d, Re, z_0, and ξ on the decaying characteristics of the local maximum tangential velocity, local friction factor, and local Nusselt number. It can be seen that

1 for any decaying curve, the slope of the initial segment is larger, that is to say, the swirl is damped out more rapidly at the initial segment. As $x/d\rightarrow\infty$, w_m/u_{av}, λ_x/λ_s and $\mathrm{Nu}_x/\mathrm{Nu}_s$ tend asymptotically to 0, 1, and 1, respectively.

2 the Reynolds number, initial tangential-to-axial velocity ratio, and wall roughness have a fair influence on the decaying characteristics. For the same conditions, a decrease in Re, or an increase in z_0 or ξ will result in an increase in the decaying rate and decaying extent. The reason for this is that with the decrease in Re or the increase in z_0 or ξ, the fluid inertia force is weakened, and the fluid viscous force is strengthened, which cause a more rapid and severe decay of the tangential velocity, and further cause a more rapid and severe decay of the friction factor and Nusselt number.

3 given the same x/d, Re, z_0 and ξ, there exists $\delta_\lambda>\delta_{\mathrm{Nu}}>\delta_z$. This shows that with the axial distance, the friction factor decays more severely than the Nusselt number, and the latter decays more severely than the maximum tangential velocity.

4 for the same conditions, $\lambda_x/\lambda_s>\mathrm{Nu}_x/\mathrm{Nu}_s>1$. This shows that the decaying swirl flow can enhance the heat transfer inside a tube, and this enhancement is at the cost of the increase in friction. Relative to the values of the nonswirl axial flow, the friction factor for the decaying swirl flow increases more intensely than the Nusselt number.

Conclusions

An analytical model for the decaying swirl flow inside a tube has been developed in an attempt to describe the decaying characteristics of the flow and heat transfer. When compared to the experimental data, the model predicts the proper decaying trends for the local maximum tangential velocity, local friction factor, and local Nusselt number for different conditions.

The model shows that (1) the swirl flow decays more rapidly at the initial segment, and with the increase in axial distance x, it tends asymptotically to the nonswirl flow; (2) for the same conditions, the friction factor decays more severely than the Nusselt number, and the Nusselt number decays more severely than the maximum tangential velocity; (3) for the same conditions, a decrease in Re, or an increase in the initial tangential-to-axial velocity ratio or wall roughness will result in an increase in the decaying rate and decaying extent; (4) relative to the values of the nonswirl axial flow, the friction factor increases more intensely than the Nusselt number.

Nomenclature

d = tube inside diameter, m
k = thermal conductivity, W/(mK)
L = tube length, m
M = force moment acting on element δx, Nm
M_i = tangential moment of momentum flowing in element δx per second, Nm
M_o = tangential moment of momentum flowing out element δx per second, Nm
Nu = Nusselt number, $= \alpha d/k$
Nu_s = Nusselt number for fully developed turbulent axial flow

Nu_x = local Nusselt number for decaying swirl flow
r = radial distance, m
u = axial velocity, m/s
u_{av} = mean axial velocity, m/s
w = tangential velocity, m/s
w_m = maximum tangential velocity, m/s
x = axial distance, m
$\overline{x}$ = nondimensional axial distance, $=x/d$
z = tangential-to-axial velocity ratio, $=w_m/u_{av}$
z_0 = initial tangential-to-axial velocity ratio
δx = element length, m
δ_z = decaying extent of tangential velocity, $=(z_0-z_x)/z_0$
δ_λ = decaying extent of friction factor, $=(\lambda_0-\lambda_x)/\lambda_0$
δ_{Nu} = decaying extent of Nusselt number, $=(\mathrm{Nu}_0-\mathrm{Nu}_x)/\mathrm{Nu}_0$
λ = friction factor
λ_s = friction factor for fully developed turbulent axial flow
λ_x = local friction factor for decaying swirl flow
α = heat transfer coefficient, $\mathrm{W/(m^2K)}$
μ = dynamic viscosity, $\mathrm{N/(m^2s)}$
ρ = density, $\mathrm{kg/m^3}$
τ_s = actual wall frictional stress, $\mathrm{N/m^2}$
τ_u = axial wall frictional stress, $\mathrm{N/m^2}$
τ_w = tangential wall frictional stress, $\mathrm{N/m^2}$
ξ = tube wall roughness, m

Subscripts

av = mean value
m = maximum value
s = value for fully developed turbulent axial flow
u = axial value
v = tangential value
x = local value for decaying swirl flow
0 = initial value

References

[1] Kreith, F., and Margolis, D., 1959, ''Heat Transfer and Friction in Turbulent Vortex Flow,'' Appl. Sci. Res., **8**, pp. 457–473.
[2] Smithberg, E., and Landis, F., 1964, ''Friction and Forced Convection Heat Transfer Characteristics in Tubes With Twisted Tape Swirl Generator,'' ASME J. Heat Transfer, **86**, pp. 39–49.
[3] Hay, N., and West, P. D., 1975, ''Heat Transfer in Free Swirling Flow in a Pipe,'' ASME J. Heat Transfer, **97**, pp. 411–416.
[4] Guo, Z., and Dhir, V. K., 1989, ''Single- and Two-Phase Heat Transfer in Tangential Injection-Induced Swirl Flow,'' Int. J. Heat Fluid Flow, **10**, pp. 203–210.
[5] Manglik, R. M., Bergles, A. E., and Manglik, R. M., 1993, ''Heat Transfer and Pressure Drop Correlations for Twisted-Tape Inserts in Isothermal Tubes: Part II—Transition and Turbulent Flows,'' ASME J. Heat Transfer, **115**, pp. 890–896.
[6] Chang, F., and Dhir, V. K., 1995, ''Mechanisms of Heat Transfer Enhancement and Slow Decay of Swirl in Tubes Using Tangential Injection,'' Int. J. Heat Fluid Flow, **16**, pp. 78–87.
[7] Yajnik, K. S., and Subbaiah, M. V., 1973, ''Experiments on Swirling Turbulent Flows Part 1. Similarity in Swirling Flows,'' J. Fluid Mech., **60**, pp. 665–687.
[8] Kitoh, O., 1991, ''Experimental Study of Turbulent Swirling Flow in a Straight Pipe,'' J. Fluid Mech., **225**, pp. 445–479.
[9] Narezhny, E. G., and Sudarev, A. V., 1972, ''Local Heat Transfer in Air Flowing in Tubes with a Turbulence Promoter at the Inlet,'' Heat Transfer-Sov. Res., **4**, pp. 62–66.
[10] Algifer, A. H., Bhardwaj, R. K., and Rao, Y. V. N., 1988, ''Heat Transfer in Turbulent Decaying Swirl Flow in a Circular Pipe,'' Int. J. Heat Mass Transf., **31**, pp. 1563–1568.
[11] Shen, Y. P., 1988, ''Study on the Heat Transfer Enhancement by Axial Vane Swirlers,'' M.S. thesis, Southeast University, China.
[12] Migay, V. K., and Golubev, L. K., 1970, ''Friction and Heat Transfer in Turbulent Swirl Flow with a Variable Swirl Generator in a Pipe,'' Heat Transfer-Sov. Res., **2**, pp. 68–73.
[13] Wu, H. Y., 1997, ''Study on the Decaying Swirl Flow and its Compound Enhanced Heat Transfer in Tubes,'' Doctoral dissertation, Southeast University, China.
[14] Yermolin, V. K., 1979, ''The Effect of Local Flow Swirl on Heat Transfer in the Initial Section of a Cylindrical Pipe,'' Heat Transfer-Sov. Res., **11**, pp. 71–76.

Heat (Mass) Transfer in a Diagonally Oriented Rotating Two-Pass Channel With Rib-Roughened Walls

C. W. Park
C. Yoon
S. C. Lau
Department of Mechanical Engineering, Texas A&M University, College Station, TX 77843-3123

Naphthalene sublimation experiments have been conducted to examine the effects of channel orientation, rotational Coriolis force, ad a sharp turn, on the local heat (mass) transfer distributions in a two-pass square channel with rib-roughened walls, rotating about a perpendicular axis. The test channel was oriented so that the direction of rotation was perpendicular or at a 45 deg angle to the leading and trailing walls. In the two straight passes of the test channel, there were parallel 90 or 60 deg ribs on the leading and trailing walls. The test channel modeled serpentine cooling passages in modern gas turbine blades. The results showed that the heat (mass) transfer was very low on the leading wall of the first pass when the channel was oriented with the rotating direction normal to the leading and trailing walls. There were regions of very low heat (mass) transfer on both the leading and trailing walls in the turn, especially on the trailing wall in the turn when the channel with transverse ribs was oriented diagonally. For the given diagonal channel orientation, rotational Coriolis forces caused the leading and trailing wall heat (mass) transfer to be high near the outer edges of the walls in the channel with transverse ribs; rotation-induced secondary flows dominated near wall rib-induced secondary flows in the channel with angled ribs, since the heat (mass) transfer was generally higher near the outer edges of the walls than near the inner edges in the first and second straight passes. [S0022-1481(00)00201-2]

Keywords: Forced Convection, Heat Transfer, Mass Transfer, Rotating, Turbines

Introduction

Naphthalene sublimation experiments have been conducted to examine the effects of channel orientation, rotational Coriolis force, and a sharp turn, on the local heat (mass) transfer distributions in a two-pass square channel with rib-roughened walls, rotating about a perpendicular axis. The test channel was oriented so that the direction of rotation was perpendicular or at a 45 deg angle to the leading and trailing walls. In the two straight passes of the test channel, there were parallel 90 deg or 60 deg ribs on the leading and trailing walls. The height of the ribs was equal to one-tenth of the channel hydraulic diameter, and the spacing between two ribs was equal to ten times the rib height. The test channel modeled serpentine cooling passages in modern gas turbine blades.

The analogy between heat and mass transfer was applied to relate mass transfer distributions to heat transfer distributions. Since the test channel walls and the flow of naphthalene vapor-air mixture were both at room temperature, and the naphthalene vapor partial pressure and concentration at the test channel walls are very small, there was no significant density variation in the test channel. Thus, buoyancy effect in the test channel was negligible.

Contributed by the Heat Transfer Division for publication in the JOURNAL OF HEAT TRANSFER. Manuscript received by the Heat Transfer Division, Nov. 14, 1997; revision received, Aug. 12, 1999. Associate Technical Editor: T. Ayyaswamy.

The experimental results of this investigation will enhance understanding of turbulent heat transfer for flows through rotating rib-roughened channels, and will help the turbine designer validate computer codes that are used to predict hot spots and high thermal stress regions in gas turbine blades under actual operating conditions.

Detailed descriptions of the test apparatus, the test procedure, and the data reduction method, along with a list of relevant publications, have been given in Park et al. [1] and Park and Lau [2], and will not be repeated here. The experimental results reported here are for an average airflow velocity of 5.3 m/s and a rotational speed of 770 rpm, corresponding to a Reynolds number Re of 5500 and a rotation number Ro of 0.24, respectively. The local and regional average mass transfer coefficients are presented as normalized local and regional average Sherwood numbers, Sh/Sh_0 and $\overline{Sh}/Sh_0$, respectively, where $Sh_0=0.023\,Re^{0.8}Sc^{0.4}$ (for fully developed turbulent flow through a stationary smooth tube; Sc is the Schmidt number). According to the analogy between heat and mass transfer, $Nu/Nu_0=Sh/Sh_0$ and $\overline{Nu}/Nu_0=\overline{Sh}/Sh_0$, where $Nu_0=0.023\,Re^{0.8}\,Pr^{0.4}$ (Pr is the Prandtl number).

Presentation and Discussion of Results

In Figs. 1 and 2, the distributions of the local Sherwood number ratios, Sh/Sh_0, on the leading and trailing walls with transverse and angled ribs, respectively, are compared. The figures clearly show the effect of channel orientation on the local mass transfer distribution. In the two figures, sketches are also included to illustrate the rotation-induced and the near wall rib-induced secondary flows in the two straight passes.

Channels With Transverse Ribs (Fig. 1). In the two straight passes of the diagonally oriented channel, the mass transfer is higher near the outer edges of both the leading and trailing walls than near the inner edges. The higher mass transfer near the outer edges is caused by the rotational secondary flows that shift the core flow toward the outer edges of the walls. In the first pass of the normally oriented channel, there is very little spanwise variation of the trailing wall mass transfer. On the opposite wall, the mass transfer is very low, with the peak Sh/Sh_0 values of between 2.00 ad 2.25 over small regions near the middle of the wall between two ribs. The leading wall mass transfer is much lower in the first pass of the normally oriented channel than in the first pass of the diagonally oriented channel, where the Sh/Sh_0 values are at least 2.25 almost everywhere between two ribs, with values of over 4.50 along the outer edge.

The mass transfer on both the leading and trailing walls in the turn of the diagonally oriented channel is lower than the corresponding mass transfer in the turn of the normally oriented channel. The mass transfer on the trailing wall in the turn of the diagonally oriented channel is especially low, with Sh/Sh_0 values of less than 2.5 over a large portion of the trailing wall in the turn and upstream of the first rib in the second straight pass. In the downstream half of the turn, including the region upstream of the first rib in the second straight pass, in the diagonally oriented channel, the leading wall mass transfer is also very low, with typical Sh/Sh_0 values of less than 2.75.

On the leading wall in the turn of the normally oriented channel, the mass transfer is low near the tip of the inner wall and is high along the outer edge of the wall. The local mass transfer on the leading wall is the highest near the tip wall, where the Sh/Sh_0 values are about 5.0.

The local mass transfer distributions on the leading and trailing

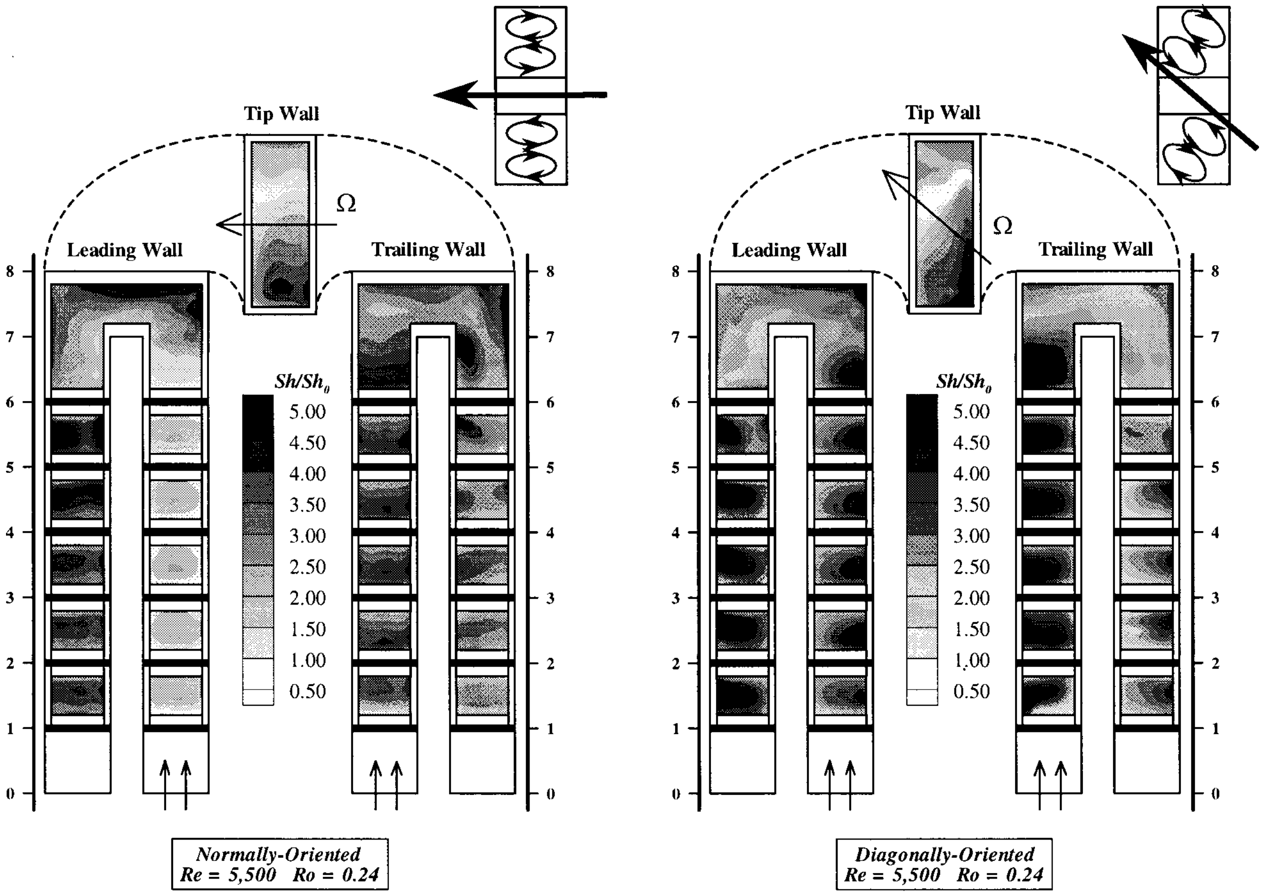

Fig. 1 Effect of channel orientation on local mass transfer distribution in channel with transverse ribs

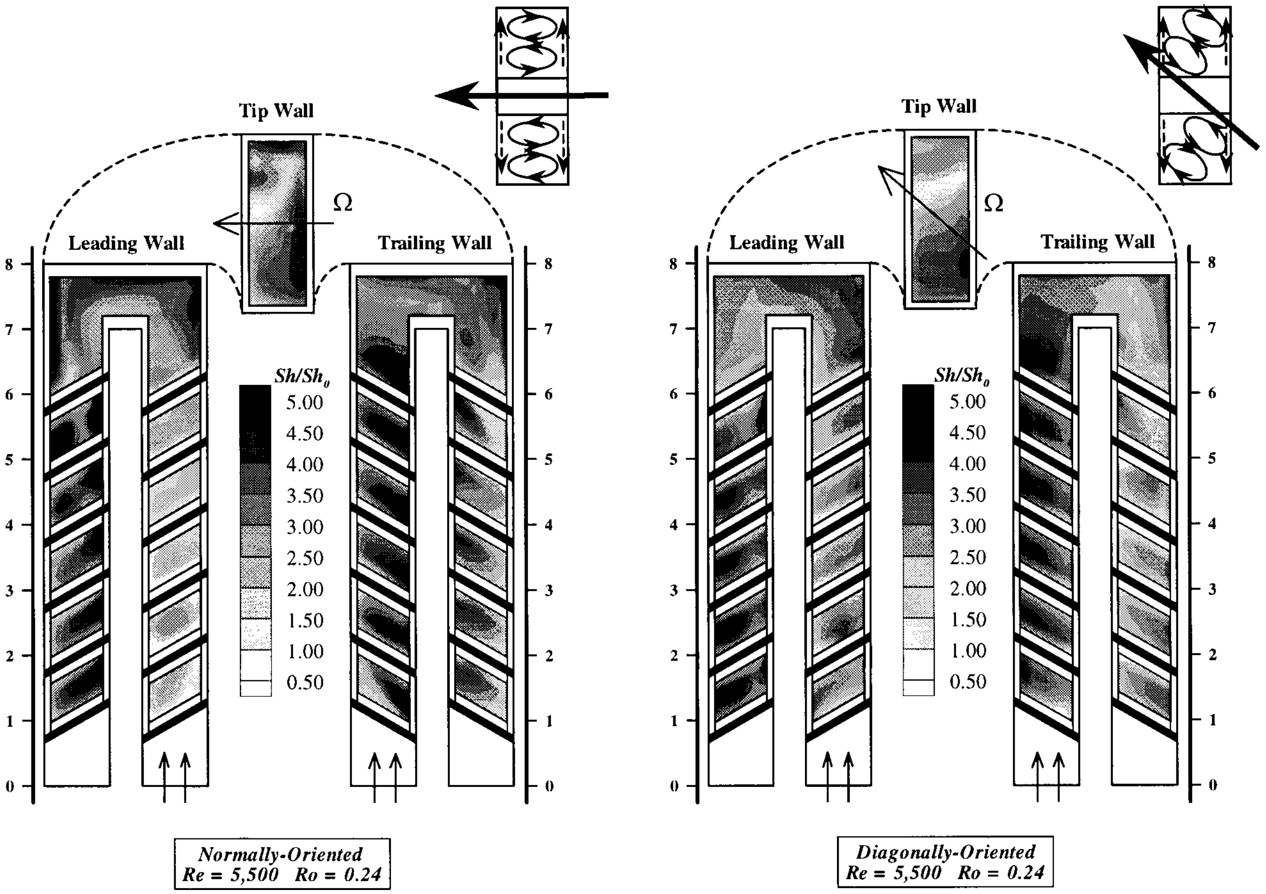

Fig. 2 Effect of channel orientation on local mass transfer distribution in channel with angled ribs

Table 1 Regional average mass transfer in normally oriented and diagonally oriented channels

Channel Orientation			Leading and Trailing walls Oriented Normal to Rotation Direction (Normally Oriented Channel)			Leading and Trailing walls Oriented At 45° to Rotation Direction (Diagonally Oriented Channel)		
Rib Configuration			No Ribs	Transverse Ribs	Angled Ribs	No Ribs	Transverse Ribs	Angled Ribs
Leading Wall	First Pass		0.59	1.53	1.76	1.15	3.02	2.25
	Turn	Upstream Region	3.57	3.78	3.75	3.53	3.38	3.46
		Middle Region	3.24	3.43	3.16	3.18	2.70	2.88
		Downstream Region	3.63	3.36	3.79	3.52	2.58	2.70
	Second Pass		2.19	3.43	3.39	2.27	3.36	3.03
Trailing Wall	First Pass		1.59	3.22	3.40	1.43	3.78	3.28
	Turn	Upstream Region	2.38	2.90	2.82	2.32	2.38	2.97
		Middle Region	2.59	3.02	2.96	2.79	1.98	2.56
		Downstream Region	3.54	3.55	3.67	3.30	2.35	2.65
	Second Pass		1.68	2.66	2.59	1.71	2.50	2.17
Tip Wall	Upstream Half		2.79	3.09	3.16	2.48	3.22	3.27
	Downstream Half		2.34	1.98	2.73	2.34	1.93	1.94

walls in the turns of the two channels with transverse ribs are different from those in the turns of corresponding stationary and rotating channels with all smooth walls ([1]).

The mass transfer is higher in the upstream half of the tip wall than in the downstream half in each of the two channels with transverse ribs. The tip wall mass transfer distribution is more asymmetric in the diagonally oriented channel than in the normally oriented channel. The highest Sh/Sh_0 value of about 5.0 on the tip wall of the diagonally oriented channel is along the trailing wall near the upstream corner of the wall. The peak Sh/Sh_0 value on the tip wall of the normally oriented channel is only between 4.0 and 4.25. A region of very low mass transfer is evident along the leading edge of the tip wall in each channel, directly across from the tip of the inner wall, where the Sh/Sh_0 value is about or below 1.0.

In the second straight pass of each channel, Coriolis forces in the radial inward flow cause the mass transfer to be higher on the leading wall than on the trailing wall. There are less spanwise variations of the Sh/Sh_0 distributions on the walls in the normally oriented channel than in the diagonally oriented channel.

In the diagonally oriented channel, the trailing wall mass transfer in the second straight pass is the lowest among the four ribbed-walls in the two straight passes.

Channels With Angled Ribs (Fig. 2). The local mass transfer distributions in the two channels with angled ribs have some of the features of those in the two channels with transverse ribs. In each channel with angled ribs, the mass transfer is again higher on the trailing wall in the first straight pass (with radial outward flow) and on the leading wall in the second straight pass (with radial inward flow) than on the respective opposite walls.

In the first straight pass of the diagonally oriented channel, the mass transfer is higher near the outer edges of both the leading and trailing walls and lower near the inner edges. Since the near wall rib-induced secondary flows should cause lower mass transfer near the outer edges of the walls, it is evident that the rotation-induced secondary flows dominate the rib-induced secondary flows.

In the first straight pass of the normally oriented channel, however, the trailing wall mass transfer is higher near the inner edge and lower near the outer edge. Also, the mass transfer is much lower on the leading wall than on the trailing wall (also lower than on the walls in the second pass). Each of the local distributions between two successive ribs on the leading wall between $X/D = 3.0$ and 6.0 has two peaks, the values of which increase along the main stream direction.

There are regions of very low mass transfer in the turns of both the normally oriented and diagonally oriented channels. In the downstream half of the turn in the diagonally oriented channel, including the region immediately upstream of the first rib on each wall in the second straight pass, the mass transfer is low on both the leading and trailing walls. The $\mathrm{Sh}/\mathrm{Sh}_0$ values are as low as 1.50 on the trailing wall and as low as 1.75 on the leading wall. The mass transfer decreases around the turn on both the leading and trailing walls.

The mass transfer distribution on the leading wall of the normally oriented channel has the largest variation among the distributions on the walls at the turns. The $\mathrm{Sh}/\mathrm{Sh}_0$ values there are over 5.0 along the outer edges and below 2.0 near the tip of the inner wall.

The mass transfer is again higher in the upstream half of the tip wall than in the downstream half in each of the two channels. The tip wall mass transfer is higher near the trailing wall and lower near the leading wall. The mass transfer distribution is more asymmetric in the normally oriented channel than in the diagonally oriented channel.

Between the first two ribs on the leading wall in the second straight pass of the diagonally oriented channel, the mass transfer is high along both the inner and outer edges of the wall. Further downstream in the second straight pass, the leading wall mass transfer is higher near the outer edge than near the inner edge. Immediately downstream of the turn on the trailing wall, the mass transfer is higher along the inner edge. The peak of the mass transfer distribution between two ribs shifts toward the outer edge of the trailing wall along the second pass. The mass transfer distribution between two ribs on the trailing wall near the exit of the second straight pass is very similar to that on the leading wall immediately upstream of the turn in the first straight pass.

On each of the two walls of the second pass in the normally oriented channel, the mass transfer between two ribs decreases along the direction of the rib axes (higher along the inner edge and lower along the outer edge), except in the region immediately downstream of the turn on the leading wall. Between the first and the third ribs in the second straight pass, the leading wall mass transfer distribution has two peaks with very large $\mathrm{Sh}/\mathrm{Sh}_0$ values. The sharp turn, however, does not increase the mass transfer along the outer edge of the trailing wall in the second straight pass.

Regional Average Mass Transfer. The weighted averages of the local Sherwood number ratios, $\overline{\mathrm{Sh}}/\mathrm{Sh}_0$, on the various regions of the leading, trailing, and tip walls (not including the rib surfaces) in the normally oriented and diagonally oriented channels are presented in Table 1. Included also in the table for comparison are the corresponding $\overline{\mathrm{Sh}}/\mathrm{Sh}_0$ values in the case of rotating channels with smooth walls.

The $\overline{\mathrm{Sh}}/\mathrm{Sh}_0$ values of 1.53 and 1.76, respectively, are the lowest on the leading walls in the first passes of the normally oriented channels with transverse and angled ribs. The $\overline{\mathrm{Sh}}/\mathrm{Sh}_0$ values are also quite low on both the leading and trailing walls in the turns of the diagonally oriented channels with transverse and angled ribs, especially on the trailing wall in the turn of the channel with transverse ribs (where $\overline{\mathrm{Sh}}/\mathrm{Sh}_0$ values range between 2.0 and 2.4). The $\overline{\mathrm{Sh}}/\mathrm{Sh}_0$ value on the tip wall of each channel is always lower in the downstream half of the wall than in the upstream half. Finally, for the given diagonal channel orientation and the given angled rib configuration, the leading and trailing wall $\overline{\mathrm{Sh}}/\mathrm{Sh}_0$ values are lower in both the first and second passes of the channel with angled ribs than those on the corresponding walls roughened with transverse ribs.

Conclusions

The results of the investigation show that the direction of rotation, a sharp turn, and the rib configuration significantly affect the local heat (mass) transfer distributions in a rotating two-pass square channel with rib-roughened leading and trailing walls. The heat (mass) transfer is very low on the leading wall of the first pass when the channel is oriented with the rotating direction normal to the leading and trailing walls. There are regions of very low heat (mass) transfer on both the leading and trailing walls in the turn, especially on the trailing wall in the turn when the channel with transverse ribs is oriented diagonally. For the given diagonal channel orientation, rotational Coriolis forces cause the leading and trailing wall heat (mass) transfer to be high near the outer edges of the walls in the channel with transverse ribs; rotation-induced secondary flows dominate near wall rib-induced secondary flows in the channel with angled ribs, since the heat (mass) transfer is generally higher near the outer edges of the walls than near the inner edges in the first and second straight passes.

Acknowledgments

This research was sponsored by the NASA Lewis Research Center, Cleveland, Ohio (Grant No. NAG3-1980).

References

[1] Park, C. W., Lau, S. C., and Kukreja, R. T., 1998, ‘‘Heat/Mass Transfer in a Rotating Two-Pass Square Channel With Transverse Ribs,’’ AIAA J. Thermophys. Heat Transfer, **12**, pp. 80–86.

[2] Park, C. W., and Lau, S. C., 1998, ‘‘Effect of Channel Orientation on Local Heat (Mass) Transfer Distributions in a Rotating Two-Pass Square Channel With Smooth Walls,’’ ASME J. Heat Transfer, **120**, pp. 624–632.